CMBE11

2nd International Conference on Computational & Mathematical Biomedical Engineering

30st March – 1st April, 2011, Swansea University, UK

Edited by:

Perumal Nithiarasu
Civil and Computational Engineering Centre
School of Engineering, Swansea University
Swansea, UK

Rainald Löhner
Center for Computational Fluid Dynamics
College of Sciences, George Mason University
Fairfax, Virginia, US

Raoul van Loon
Civil and Computational Engineering Centre
School of Engineering, Swansea University
Swansea, UK

Igor Sazonov
Civil and Computational Engineering Centre
School of Engineering, Swansea University
Swansea, UK

Xianghua Xie
Department of Computer Science, Swansea University
Swansea, UK

2nd International Conference on Computational & Mathematical Biomedical Engineering, 2011, Swansea, UK

First edition, March 2011

Printed for CMBE by: All American Printing inc, Alexandria, VA, US

ISBN: 978-0-9562914-1-7

PREFACE

It is our pleasure to welcome all participants of the *2nd International Conference on Computational and Mathematical Biomedical Engineering* (**CMBE11**) to George Mason University. This is the second in the series, after a successful first meeting that was held at Swansea University, UK in 2009. The increased number of abstracts received for CMBE11 clearly shows a great deal of interest in this area. In order to maintain a very high quality, the number of standard presentations in CMBE11 is limited to a maximum of 120. We are hoping to maintain a similar number of presentations in the future conferences by introducing a more rigorous review process. It is encouraging to learn that this conference represents an interdisciplinary forum of scientists with expertise ranging from imaging to CFD, from algorithmic developments to clinical applications and from respiratory flows to protein mechanics. We hope that the interaction between scientists during the conference leads to new topics of research and new collaborations.

CMBE11 consists of three plenary lectures nine keynotes, ten organized mini-symposia and eight standard sessions. We anticipate that some of the presentations will be published in the '*International Journal for Numerical Methods in Biomedical Engineering*'.

We thank CMBE11 sponsors, supporters, mini-symposium organizers, executive, scientific and local committee members for their support.

Perumal Nithiarasu
Swansea University
United Kingdom

Rainald Löhner
George Mason University
United States of America

SPONSORS

SUPPORTING ORGANISATIONS

Swansea University
Prifysgol Abertawe

COMMITTEES

Co-chairs

P. Nithiarasu, Swansea University, UK
R. Löhner, George Mason University, USA

Executive committee

F. Baaijens, Eindhoven University of Technology, The Netherlands
R. Feijoo, Coordenação de Ciência da Computação, Brazil
T.J.R. Hughes, The University of Texas at Austin, USA
G.A. Holzapfel, Royal Institute of Technology, Sweden and Graz University of Technology, Austria
J. Humphrey, Texas A&M University , USA
W.K. Liu, Northwestern University, USA
J. Middleton, Cardiff University, UK
J.T. Oden, The University of Texas at Austin, USA

International Advisory Committee

D. Drikakis, Cranfield University, UK
L. Formaggia, Politecnico di Milano, Italy
K. Garikipati, University of Michigan, USA
J-F. Gerbeau, Stanford University, USA and INRIA, France
M. Heil, University of Manchester, UK
A. Lee, Institute of High Performance Computing (IHPC), Singapore
G.R. Liu, National University of Singapore, Singapore
X. Luo, Glasgow University, UK
A.G. Malan, CSIR, South Africa
M. Oshima, University of Tokyo, Japan
J. Peiro, Imperial College, UK
D. Reddy, University of Cape Town, South Africa
J.N. Reddy Texas A&M University, USA
A.M. Robertson University of Pittsburgh, USA
K.N. Seetharamu, IEEE EMBS section and PES College, India.
S.J. Sherwin, Imperial College, UK
N. Smith, University of Oxford, UK
D. Steinman, University of Toronto, Canada
J. Suri, Idaho State University, USA
T. Tezduyar, Rice University, USA
M. Vázquez, Barcelona Supercomputing Center, Spain
Y. Ventikos, University of Oxford, UK
F. Van de Vosse, Eindhoven University of Technology, The Netherlands
W. Wall, Technical University of Munich, Germany
G.W. Wei, Michigan State University, USA
X.Y. Xu, Imperial College, UK

Local organizing committee

Swansea University, UK
R. Bevan
J.W. Jones
P.H. Saksono
I. Sazonov
R. Van Loon
X. Xie

George Mason University, USA
J.R. Cebral
F. Mut
D. Sforza

CONTENTS

Keynote & Plenary Lectures

A BIOENGINEER'S VIEW OF RECENT DEVELOPMENT IN VPH/PHYSIOME PROJECT
P. Hunter

INTERIOR TOMOGRAPHY
G. Wang 3

REAL-TIME FINITE ELEMENT AND MESHLESS METHODS FOR MODELLING NEUROSURGERY
K. Miller 4

THINKING OUTSIDE THE BENCH
D. Steinman 6

NANO-DEVICES IN BIOTECHNOLIOGY AND DRUG DELIVERY
W-K. Liu, A. Adnan, A. Kopacz 7

COMPUTATIONAL MODELLING OF THE HEART IN THE CLINIC
A. Cookson, A. de Vecchi, P. Lamata, J. Lee, S. Krittian, M. McCormick, C. Michler, S. Niederer, D. Nordsletten, N. Smith 11

USE OF COMPUTATIONAL FLUID DYNAMICS FOR THE DESIGN AND DEVELOPMENT OF ANIMAL MODELS FOR STUDIES OF THE PATHOPHYSIOLOGY OF CEREBRAL ANEURYSMS
A. M. Robertson, Z. Zeng, M.J. Durka, D.F. Kallmes, R. Kadirvel, Y. Ding, D. Dai, D. Lewis, M.R. Hill, S.C.Watkins 15

MULTISCALE MODELS FOR NANO-BIO SYSTEMS
G-W Wei, Z. Chen 19

MULTISCALE PROCESSES IN ANALYSIS OF NANOTUBE REINFORCED TISSUE ENGINEERING BIOREACTORS
J.N. Reddy, G.U. Unnikrishnan, V.U. Unnikrishnan 23

A DIMENSIONALLY HETEROGENEOUS MODEL FOR THE ENTIRE CARDIOVASCULAR SYSTEM BASED INTEGRATED WITH A MODEL OF THE AUTONOMIC NERVOUS SYSTEM
P.J. Blanco, R.A. Feijóo 24

APPLICATION OF REDUCED ORDER MODELING FOR MECHANICAL AND ELECTRICAL ASPECTS OF THE CARDIOVASCULAR SYSTEM
Jean-Frédéric Gerbeau 28

G SPACE THEORY AND WEAKENED WEAKFORM (W2) METHODS FOR EFFICIENT AND CERTIFIED SOLUTIONS FOR BIO-SYSTEMS
G.R. Liu 29

MS-1: Cerebral Arteries

Organised by Juan R. Cebral, Christopher M. Putman and Jay Humphrey

A NUMERICAL STUDY ON THE FEASIBILITY OF ANEURYSM PROPERTY IDENTIFICATION AT THE PRESENCE OF UNKNOWN STRESS-FREE GEOMETRY
J. Lu, X. Zhao 35

VORTEX CORELINE DETECTION FOR THE ANALYSIS OF BLOOD FLOW PATTERNS IN CEREBRAL ANEURYSMS
G.Byrne, F. Mut, J.R. Cebral 39

PATIENT-SPECIFIC MODELLING OF CEREBRAL ANEURYSM EVOLUTION
P.N. Watton, A. Selimovic, H. Chen, H. Thompson, Y. Ventikos 43

FLUID-STRUCTURE INTERACTION SIMULATION OF CEREBRAL ANEURYSM WITH THE EFFECTS OF PERIPHERAL NETWORK
M. Oshima, M. Toma, A. Krdy, S. Takagi 47

AN EQUIVALENT WALL THICKNESS ESTIMATION FOR CEREBRAL ANEURYSMS
E. L. Johnson, Y. Zhang, K. Shimada 51

INTRACRANIAL ANEURYSMS: STUDY OF X-RAYS TIME-INTENSITY-CURVES (TIC) PULSATILITY
R. Ouared, O. Brina, O. Bonnefous, A Groth, T Brunjs, D. Babic, P. Bijlenga, K Schaller, K. Lovblad, V. Pereira 55

CONTRIBUTIONS OF IMAGE-BASED CFD TO THE EVALUATION OF INTRACRANIAL ANEURYSMS RUPTURE RISK
J.R. Cebral, F. Mut, D. Sforza, C.M. Putman 59

COMPUTATIONAL AND STATISTICAL ANALYSIS OF ICA MORPHOLOGY AND HEMODYNAMICS
T. Passerini, M. Piccinelli, A. Veneziani, L.M. Sangalli, P. Secchi, S. Vantini 63

EFFECT OF FLOW DIVERTERS ON IA FLOW DYNAMICS: ASSESSMENT IN 23 ANEURYSMS
I. Larrabide, M. Aguilar, H. Morales, S. Cito, D. Rüfenacht, Z. Kulcsar, S.Wetzel, A.F. Frangi 67

TECHNIQUES FOR AUTOMATIC ANEURYSM NECK PLANE DETECTION AND GEOMETRIC CHARACTERIZATION OF 3D ANEURYSMAL SAC
M. Piccinelli, Y. Hoi, A. Veneziani, D.A. Steinman, L. Antiga 71

SENSITIVITY TO MATHEMATICAL MODEL CHOICE AND LEVEL OF GEOMETRY DESCRIPTION IN IDEALISED CONDUITS AND A PATIENT SPECIFIC CEREBRAL ANEURYSM.
A.M. Gambaruto, A.B. Moura, A. Sequeira 75

HIGH RESOLUTION HEMODYNAMICS OF SMALL INTRACRANIAL ANEURYSMS USING PHASE CONTRAST MRI
S.R. Kecskemeti, K.M. Johnson, Y. Wu, P. Turski, O. Wieben 79

COMPARING GEOMETRY AND HEMODYNAMICS OF MCA ANEURYSMS
A.J. Geers, I. Larrabide, H.G. Morales, M.C. Villa-Uriol, A.F. Frangi 83

CHARACTERIZATION OF THE MORPHOMETRY AND HEMODYNAMICS OF CEREBRAL ARTERIAL TREES IN HEALTHY HUMANS: A PRELIMINARY STUDY
F. Mut, S. Wright, G. Ascoli, J.R. Cebral 87

MS-2: Heart Valve Modelling

Organised by Raoul van Loon and Daniel Einstein

APPLICATION OF GRADIENT WEIGHTED MOVING FINITE ELEMENTS TO LAGRANGIAN BIOMEDICAL FLUID-STRUCTURE INTERACTION PROBLEMS**A. P. Kuprat, F. del Pin, K.S. Kunzelman, D.R. Einstein** 91

SIMULATING AORTIC HEART VALVE DYNAMICS BY THE IMMERSED BOUNDARY METHOD
B.E. Griffith 95

A SIMPLE VERSATILE MODEL OF VALVE DYNAMICS FOR USE IN LUMPED PARAMETER AND ONE-DIMENSIONAL CARDIOVASCULAR MODELS
J.P. Mynard, M.R. Davidson, D.J. Penny, J.J. Smolich 99

A REALISTIC COMPUTATIONAL MODEL TO SIMULATE AORTIC VALVE REPAIR
M.R. Labrosse, M. Boodhwani, C.J. Beller 103

THE INFLUENCE OF THE UPSTREAM BOUNDARY CONDITION IN THE NUMERICAL SIMULATION OF THE OPENING OF AN AORTIC BMHV
S. Annerel, J. Degroote, T. Claessens, P. Van Ransbeeck, P. Segers, P. Verdonck, J. Vierendeels 107

IN-VIVO DYNAMIC STRESS HISTORY OF THE MITRAL VALVE ANTERIOR LEAFLET
R. Amini, C.E. Eckert, C.A. Carruthers, K. Koomalsingh, M. Minakawa, J.H. Gorman, R.C. Gorman, M.S. Sacks 111

IMAGING-BASED CARDIAC VALVE LAGRANGIAN-FSI IN LS-DYNA
F. Del Pin, D.R. Einstein, A.P. Kuprat, X. Jiao, J.P. Carson, K.S. Kunzelman 115

OPTIMAL UNLOADED LEAFLET SHAPE FOR THE OVINE PULMONARY VALVE SINGLE LEAFLET REPLACEMENT SURGERY
R. Fan, C.M. Hobson, A. Bayoumi, J.E. Mayer, W.R. Wagner, M.S. Sacks 119

MS-3: Biomechanical Imaging

Organised by Paul E. Barbone, Assad A. Oberai and Isaac Harari

BREAST LINEAR AND NONLINEAR REAL-TIME ULTRASOUND ELASTOGRAPHY
A. Samani S. Shavakh, M. Amooshahi, S.R. Mousavi 123

AN ERROR IN CONSTITUTIVE EQUATIONS APPROACH FOR ELASTICITY IMAGING
W. Aquino, M. Bonnet 127

CORRELATION OF BIOMECHANICS TO TISSUE REACTION IN AORTIC ANEURSYMS ASSESSED BY FEM AND FDG-PET-CT
M.W. Gee, W.A.Wall, A. Maier, C. Reeps, M. Essler 129

4D IMAGE-BASED CFD OF A COMPLIANT VESSEL
E. Haber, L. Mirabella, T. Passerini, M. Piccinelli, A. Veneziani 132

4D IMAGE-BASED APPROACH FOR CFD IN COMPLIANT BLOOD VESSELS
L. Mirabella, M. Piccinelli, T. Passerini, M. Restrepo, E. Haber, A.P. Yoganathan, A.Veneziani 136

MICROCRACK LOCAL STRESS FIELD IN HUMAN HAVERSIAN CORTICAL BONE
E. Budyn, J. Jonvaux, T. Hoc 140

MOTION TRACKING STRATEGIES FOR BIOMECHANICAL IMAGING
T.J. Hall, J. Jiang 144

MODELING SHEAR WAVES IN SOFT TISSUE RESULTING FROM ACOUSTIC RADIATION FORCE EXCITATION**K.H.F. Lee, A.M. Maniatty**

148

MS-4: Fluid Structure Interaction in Haemodynamics

Organised by Luca Formaggia, Fabio Nobile, Christian Vergara

FSI ANALYSIS OF A DISEASED HUMAN TRACHEA BEFORE AND AFTER PROSTHESIS IMPLANTATION
M. Malvè, A. Pérez del Palomar, S. Chandra, J.L. López-Villalobos, E. Finol, A. Ginel, M. Doblaŕe

152

VALIDATION AND COMPARISON AMONG DIFFERENT FLUID-STRUCTURE INTERACTION SCHEMES
F. Nobile, M. Pozzoli, C. Vergara 156

FSI ANALYSIS OF A HUMAN CAROTID BIFURCATION UNDER IMPEDANCE-BASED BOUNDARY CONDITIONS
M. Malvè, S. Chandra, A. García, M.A. Martínez, E. Finol, M. Doblaré 160

ADVANCED COMPUTATIONAL APPROACHES FOR FLUID-STRUCTURE INTERACTION IN HEMODYNAMICS
W.A.Wall, M.W. Gee, T. Klöppel, U. Küttler, A. Popp 164

MORPHOGENESIS: A MULTIPHYSICS MODEL FOR CELL MECHANICS
D. Aubry, R. Allena 167

MS-5: High Performance Computational Biomechanics

Organised by Mariano Vázquez, Guillaume Houzeaux and Raúl Cebral

MODELLING BLOOD FLOW THROUGH SUBJECT-SPECIFIC CAROTID BIFURCATIONS WITH PARTICULAR ATTENTION TO WALL SHEAR STRESS
R.L.T. Bevan, P. Nithiarasu, R. van Loon, I. Sazonov, H. Luckraz 172

NUMERICAL SIMULATION OF BLOOD FLOWS AROUND AORTIC VALVE LEAFLETS BY VIRTUAL FLUX METHOD
T. Fukui, K. Morinishi 176

SIMULATION OF THE BLOOD FLOW IN THE LEFT VENTRICLE USING A FINITE ELEMENT METHOD WITH MOVING GEOMETRIES BASED ON ULTRASOUND MEASUREMENTS
J.H. Spühler, J. Hoffman, J. Jansson, U. Gustafsson, M.Broomé, M.G. Larson, P. Vesterlund 180

RUNNING HAEMODYNAMIC SIMULATIONS ON GPUS
R. Löhner, A. Corrigan, F. Camelli, F. Mut, J.R. Cebral 184

FLUID-STRUCTURE INTERACTION FINITE ELEMENT ANALYSIS ON THE RELATIONSHIP BETWEEN LEFT VENTRICULAR PUMP FUNCTION AND FIBER STRUCTURE WITHIN THE WALL
H. Watanabe, S. Sugiura, T. Hisada 188

PARALLEL COMPUTATIONAL ELECTROPHYSIOLOGY IN NVIDIA GPUS
F. Rubio, M. Hanzich, R. Arís, M. Vázquez, G. Houzeaux 192

STRATEGIES FOR HIGH PERFORMANCE COMPUTATION OF HEMODYNAMICS IN CEREBRAL ANEURYSMS**R. Löhner, F. Mut, F. Camelli, J.R. Cebral** 195

MS-6: Meshing Challenges in Subject-Specific Biomedical Modelling

Organised by Igor Sazonov and Perumal Nithiarasu

QUALITY MESHING ALGORITHMS FOR ACCURATE AND EFFICIENT CARDIOVASCULAR SIMULATIONS
E. Marchandise, E. Sauvage, J.-F. Remacle 198

MESHING CHALLENGES FOR PATIENT-SPECIFIC CARDIOVASCULAR SYSTEMS
Y. Zhang 199

HEXAHEDRAL MESH GENERATION FOR IMAGE-BASED COMPUTATIONAL FLUID DYNAMIC INVESTIGATION OF VASCULAR DISTRICTS
G. De Santis, M. De Beule, P. Segers, P.Verdonck, B. Verhegghe 200

HIGH-ORDER MESHING AND FLOW SIMULATION OF THE RABBIT ARTERIAL SYSTEM
A. Plata, J. Peiró, S.J. Sherwin, V. Peiffer 204

SEMI-AUTOMATIC MESH GENERATION AND COSMETICS FOR SUBJECT-SPECIFIC BIOMEDICAL GEOMETRIES
I. Sazonov, P. Nithiarasu 209

GENERATING SMOOTH SURFACE MESHES FROM LABELLED MEDICAL DATA SETS
V. d'Otreppe, R. Boman, J.P. Ponthot 213

ROBUST MEDIAL CURVE COMPUTATION FOR BIOMEDICAL GEOMETRIES
V. Dyedov, D. Einstein, X. Jiao 217

MESH GENERATION TECHNOLOGY FOR DOMAINS WITH SMALL STRUCTURAL ELEMENTS
A.A. Danilov, Y.V. Vassilevski 221

EVALUATION OF MESH MORPHING AND MAPPING TECHNIQUES IN PATIENT SPECIFIC MODELING OF THE HUMAN PELVIS
Z. Salo and C. Whyne 225

VARIATIONAL GENERATION OF HYBRID PRISM-TETRAHEDRAL MESHES FOR BIOMEDICAL APPLICATIONS
D.R. Einstein, V. Dyedov, A.P. Kuprat, N. Ray, X. Jiao 229

MS-7: Shape and Deformable Modelling in Biomedical Image Analysis

Organised by Xianghua Xie and Majid Mirmehdi

LOCAL PHASE BASED AUTOMATIC IVUS MEDIA-ADVENTITIA BORDER DETECTION
E. Essa, X. Xie, I. Sazonov, P. Nithiarasu 233

LEARNING PATIENT-SPECIFIC MOTION BASED ON DECOMPOSING A MULTILINEAR SHAPE MODEL
Y. Hu and D. Barratt 237

VARIATIONAL LEVEL SET SEGMENTATION USING SHAPE PRIOR
S.Y. Yeo, X. Xie, I. Sazonov, P. Nithiarasu 241

USING 4D PHASE-CONTRASTS MRI TO DETERMINATE BLOOD FLOW PATTERNS IN THE AORTIC DISEASES
E. Soudah, J.S. Ronda, M. Rodriguez, H. Hervilla, F. Carreras, E. Oñate 245

MS-8: Inverse Vascular Mathematics

Organised by Alessandro Veneziani and Christian Vergara

A VARIATIONAL APPROACH FOR ESTIMATING THE COMPLIANCE OF CARDIOVASCULAR TISSUES
M. Perego, A. Veneziani, C. Vergara 250

INVERSE STRESS ANALYSIS IN AAA CONSIDERING THROMBUS
S. Hu, J. Lu 254

NON-INVASIVE AND INVERSE PROPERTY ESTIMATION OF ARTERIAL WALLS
A.S. Kapoor, P. Nithiarasu, R. van Loon 258

INTEGRATION OF ULTRASOUND COLOR DOPPLER IMAGING
K. Funamoto, T. Kato, T. Hayase 262

REDUCED ORDER MODELLING FOR INVERSE PROBLEMS IN HAEMODYNAMICS
A. Manzoni, A. Quarteroni, G. Rozza 266

INVERSE IDENTIFICATION OF THE IN VIVO ARTERIAL WALL THICKNESS AND ANISOTROPY
S. Zeinali-Davarani, L.G. Raguin, D.A. Vorp, S. Baek 267

A DATA ASSIMILATION PROCEDURE FOR INCLUDING NOISY MEASUREMENTS OF BLOOD VELOCITY INTO HEMODYNAMICS SIMULATIONS
M. D'Elia, M. Perego, A. Veneziani 271

DESIGN OF STATE ESTIMATORS IN FLUID-STRUCTURE INTERACTION FOR DATA ASSIMILATION IN LARGE ARTERIES
C. Bertoglio, D. Chapelle, M. Fernández, J-F. Gerbeau, P. Moireau 275

SOLVING PULMONARY HEMODYNAMIC INVERSE PROBLEMS BY TUNING MODELS WITH MULTIPLE LEVELS OF DETAIL
R.L. Spilker, J.A. Feinstein, C.A. Taylor 276

BIOMECHANICAL IMAGING: INFERRING TISSUE MICROSTRUCTURE AND PATHOLOGY
A.A. Oberai, P.E. Barbone, R. Leiderman, S. Goenezen, J-F. Dord 280

MS-9: Processing and Analysis in Biomedical Imaging

Organised by João Manuel R. S. Tavares, R. M. Natal Jorge and Yongjie Zhang

REGISTRATION OF PLANTAR PRESSURE IMAGES
F.P.M. Oliveira, J.M.R.S. Tavares 282

FINITE ELEMENT COMPARISON OF DENTAL IMPLANTS WITH STANDARD AND PLATFORM SWITCHING PROSTHETIC COMPONENTS
M.A. Neto, P. Nicolau, S. Rocha, R.P. Leal 286

CHALLENGES IN IMAGE-BASED GEOMETRIC MODELING AND MESH GENERATION
Y. Zhang 288

AN INTEGRATED METHOD FOR INTENSITY INHOMOGENEITY CORRECTION AND LOCAL IMAGE ENHANCEMENT OF MRI BASED ON CURVELET TRANSFORM
K. Tsai, J. Wu, D. Ye, J. Ma 290

IMAGE REGISTRATION FOR TISSUE BIOMECHANICS IMAGING
M.S. Richards, P.E Barbone, A.A. Oberai 294

GEOMETRIC ANALYSIS AND DECOMPOSITION OF 3-D CLOSED SURFACES FOR APPLICATIONS IN DIAGNOSTIC MEDICAL IMAGING
J. Wu, J.C. Brigham 297

MINIATURIZED LASER SPECKLE CONTRAST IMAGING MICROSCOPE
J. Senarathna, K. Murari, N. Li, R. Etienne-Cummings, N.V. Thakor 301

SEGMENTATION OF MAGNETIC RESONANCE IMAGES FROM FEMALE PELVIC CAVITY
Z. Ma, R.N.M. Jorge, T. Mascarenhas, J.M.R.S. Tavares 305

INTEGRATING COMPUTATIONAL BIOMECHANICS AND ULTRASOUND SIMULATIONS TO IMPROVE ULTRASONIC VISUALIZATION AND QUANTIFICATION OF ARTERIAL MECHANICS
A. Swillens, L. Lovstakken, J. Degroote, J. Vierendeels, P. Segers 309

IMAGE-BASED 3D SHAPE RECONSTRUCTION OF ABDOMINAL AORTIC ANEURYSM
K. Shimada 313

MS-10: Methods of Numerical Cardiac Electro-Mechanics

Organised by Lucia Mirabella, Mauro Perego and Alessandro Veneziani

LARGE SCALE ELECTROMECHANICAL CARDIAC SIMULATIONS
P. Lafortune, R. Arís, M. Vázquez, G. Houzeaux, A. Jérusalem 317

MODEL ADAPTIVE METHODS FOR THE BIDOMAIN EQUATIONS IN ELECTROCARDIOLOGY
L.G. Giorda, L. Mirabella, M. Perego, A. Veneziani 320

EFFICIENT PRECONDITIONERS FOR THE BIDOMAIN SYSTEM IN ELECTROCARDIOLOGY
L. Gerardo-Giorda, L. Mirabella, M. Perego 324

ON SOME NUMERICAL ASPECTS OF AN ACTIVE STRAIN FORMULATION IN CARDIAC MECHANICS
A. Quarteroni, S. Rossi, R. Ruiz-Baier 328

SS-1: Waves and Acoustics

TIME-DOMAIN ULTRASONIC WAVE PROPAGATION IN ANISOTROPIC POROELASTIC BONE PLATE
V-H Nguyen, S. Naili 335

ACOUSTICAL ANALYSIS OF SWALLOWING MECHANISM
S.S. Shirazi, Z. Moussavi 339

SS-2: Respiratory

COMPUTATIONAL ANALYSIS OF DROPLET EVAPORATION AND DEPOSITION IN A REALISTIC RESPIRATORY TRACT SUBJECT TO PUFF-LIKE INHALATION WAVEFORMS
Y. Feng, C. Kleinstreuer 343

COMPUTATIONAL MODEL OF TISSUES IN THE HUMAN UPPER AIRWAY
J-P.V. Pelteret, B.D. Reddy 347

SS-3: Biosolid

A THREE-DIMENSIONAL DESCRIPTION OF ARTERIAL GROWTH AND REMODELING
I. Karšaj, J. Sorić, J.D. Humphrey 351

A NON-LINEAR HOMOGENEOUS MODEL FOR BONE-LIKE MATERIALS UNDER COMPRESSIVE LOAD.
M. Mengoni, R. Voide, D. Toye, A. Léonard, G.H. van Lenthe, J.P. Ponthot 355

SS-4: Cardiovascular

TISSUE LENGTH DEPENDENCE AND LEFT VENTRICULAR BLOOD FLOW IN THE HUMAN HEART
D. Nordsletten, M McCormick, D. Kay, N. Smith 359

A MATHEMATICAL MODEL OF BIDIRECTIONAL GLENN HEMODYNAMICS WITH AN INCREMENT IN PULMONARY VASCULAR RESISTANCE
C.Vallecilla, N. Sandoval, J. C. Briceño 363

PATIENT-SPECIFIC FINITE ELEMENT ANALYSIS OF CAROTID ARTERY STENTING: IMPACT OF CONSTITUTIVE VESSEL MODELING ON VESSEL WALL STRESS DISTRIBUTION
F. Auricchio, M. Conti, A. Ferrara, S. Morganti, A. Reali 367

THE MECHANICAL RESONSE OF THE HUMAN CORONARY ARTERY: SIMULATION BY HIGH ORDER FINITE ELEMENT ANALYSIS
E. Priel, Z. Yosibash 371

REGIONAL DIFFERENCES IN MECHANICAL BEHAVIOR OF THE THORACIC AORTA DURING PRESSURE-INDUCED INFLATION
J. Kim, S. Baek 375

COMPUTATIONAL STUDY OF BLOOD FLOW WITHIN A MULTI-BRANCHED MODEL OF THE RABBIT THORACIC AORTA
A. M. Plata, P. E. Vincent, A. A. E. Hunt, S. J. Sherwin, P. D.Weinberg 379

SWIRLGRAFT VERSUS CONVENTIONAL STRAIGHT GRAFT AS VASCULAR ACCESS: A FULL CFD-ANALYSIS
K. Van Canneyt, G. De Santis, S. Eloot, P. Segers, P. Verdonck 383

NUMERICAL MODEL FOR THE CFD-SIMULATION OF THE FLOW FIELD IN THE ANASTOMOSIS REGION OF CORONARY BYPASSES
M. De Witte, A. Swillens, L. Løvstakken, H. Nordgaard, D. Van Loo, B. Trachet, J. Vierendeels, P Segers 387

RESULTS OF THE FDA INTERLABORATORY COMPUTATIONAL
S.F.C. Stewart, P. Hariharan, E.G. Paterson, G.W. Burgreen, V. Reddy , S.W. Day, M. Giarra, K.B. Manning, S. Deutsch, M.R. Myers, M.R. Berman, R.A. Malinauskas 391

VESSEL WALL MODELING FOR 1D HAEMODYNAMICS
S.S. Simakov, Y.V. Vassilevski, V.Yu. Salamatova, Y.A. Ivanovy, T.K. Dobroserdova 395

SS-5: Surgical Simulation

A COMPUTATIONAL FRAMEWORK FOR UNCERTAINTY QUANTIFICATION AND ROBUST OPTIMIZATION OF CARDIOVASCULAR BYPASS GRAFT SURGERIES.
Sankaran, A.L. Marsden 399

APPLICATION OF GENETIC ALGORITHM AND FINITE ELEMENT METHOD IN DESIGN OF THE SCAFFOLDS FOR TISSUE ENGINEERING
M.K. Heljak, W. Swieszkowski K.J. Kurzydlowski 403

MODELLING VENTRICULAR FUNCTION UNDER LVAD SUPPORT
M. McCormick, D. Nordsletten, D. Kay, N. Smith 407

SS-6: Analysis Models

A SALIENCY-BASED VISUAL ATTENTION MODEL FOR DYNAMICAL SCENE ANALYSIS.
J.F. Ramirez-Villegas, D.F. Ramirez-Moreno 411

POINT-CLOUD METHOD FOR IMAGE-BASED BIOMECHANICAL ANALYSIS
J. Qian, M. Chiang, J. Lu 415

SS-7: Blood

HEMODYNAMICS IN THE LOWER-LIMB BYPASSES USING WAVE SEPARATION AND WAVE INTENSITY ANALYSIS
M. Willemet, V. Lacroix, E. Marchandise, A. Khir 418

COMPUTATIONAL RHEOLOGY OF SICKLE CELL
O.L. Castillo, A.L. Gonzalez 422

A FLUIDO-CHEMICAL MODEL OF THROMBUS FORMATION
J. Biasetti, T.C. Gasser 426

EFFECT OF ROLL ANGLE ON THE BUBBLE TRANSPORT IN A SYMMETRIC BIFURCATING MICROCHANNEL
J. Poornima, S. Vengadesan 429

FONTAN SURGICAL DESIGN FOR IMPROVED HEPATIC FLOW DISTRIBUTION USING CFD AND DERIVATIVE-FREE OPTIMIZATION
W. Yang, I.E. Vignon-Clementel, G. Troianowski, S.Shadden, V.M. Reddy, J.A. Feinstein, A.L. Marsden 433

MATHEMATICAL MODELING OF SWIRLING INTRACARDIAC FLOW USING EXACT SOLUTION OF UNSTEADY-STATE HYDRODYNAMIC EQUATIONS FOR THE CLASS OF SELF-ORGANIZING TORNADO-LIKE FLOWS OF VISCOUS MEDIUM
L.A. Bokeriya, G.I. Kiknadze, A.V. Bogevolnov, A.Yu. Gorodkov 437

Poster Abstracts

MODELING HEAT AND MASS TRANSFER IN RADIANT WARMER
M.J. Rojczyk, I.A. Szczygieł 443

ESTIMATION FO PULSE WAVE VELOCITY DERIVED FROM 2D AND 4D FLOW-SENSITIVE MAGNETIC RESONANCE IMAGING
A.L. Wentland, A. Frydrychowicz, K.M. Johnson, C.J. Francois, T.M. Grist, and O. Wieben 447

DIGITAL SIGNAL CONTROLLER DM 330011 BASED REAL TIME SYSTEM FOR DETECTION OF ECG SIGNAL
D. Bansal, M. Khan, A.K. Salhan 451

CONTROLLABLE SEPARATION OF SSDNA MOLECULES BY A POLARIZED CNT MEMBRANE SUBJECTED TO A PULSED ELECTRIC FIELD
Y.H. Xie, A.K. Soh 455

MODELING AND CONTROL OF AN INDUCIBLE GENE EXPRESSION SYSTEM
N. Barbosa, A. Olarte, C.A. Clavijo, H. Diaz 459

A NEW FRACTAL MODEL OF CHROMOSOME AND DNA PROCESSES
K.Bouallegue 463

FINITE ELEMENT ANALYSIS ON THE FLUID FILTRATION IN A CAPILLARY-TISSUE SYSTEM
Y. He, R. Himeno 467

A CONSTITUTIVE MODEL FOR VASCULAR TISSUE THAT INTEGRATES FIBRIL, FIBER AND CONTINUUM LEVELS
T.C. Gasser, G. Martufi, M. Auer 471

MYOCARDIAL TISSUE DEFORMATION DUE TO PACEMAKER LEAD CONTACT - THE IMPACT OF MATERIAL ANISOTROPY.
C. Forsell, T.C. Gasser 475

NUMERICAL IMPLEMENTATION OF A CONTINUUM LEVEL THROMBOSIS MODEL: SIMULATION OF THROMBUS GROWTH AND FLUID-THROMBUS INTERACTION
S.B. Samra, E.G. Paterson 478

IMPORTANCE OF THORACIC AORTIC CURVATURE IN THE PATHOGENESIS OF THORACIC AORTIC DISSECTION
D.P. Nathan, T.J. Eperjesi, A. Pouch, A.S. Jassar, C. Xu, J.H. Gorman III, R.C. Gorman, B.M. Jackson 482

BLOOD FLOW DYNAMICS IN PATIENT SPECIFIC ARTERIAL NETWORK IN HEAD AND NECK
S. Rhode, M.C. Pauly, E. Martens, D.F. Campbell 486

SIMULATION AND ANALYSIS OF FLOW IN DIFFERENTS GEOMETRICAL ARRAYS OF A VASCULAR GRAFT
J.F. García, A. Gonzalez, C. Vallecilla, J.C. Briceño 490

ASYMMETRIC ARTERY STENOSIS - NUMERIC MODEL
M. Brand, M. Teodorescu, I. Avrahami, J. Rosen 494

FINITE ELEMENT ANALYSIS OF STENTLESS VALVE IMPLANT IN PATIENT-SPECIFIC AORTIC ROOT GEOMETRY
F. Auricchio, M. Conti, S. Morganti, P. Totaro, M. Viganò 498

INTRACRANIAL ANEURYSMS: TOWARDS DISCRIMINATION OF HEMODYNAMICALLY STABLE AND UNSTABLE 3D VIRTUAL PATIENT SPECIFIC GEOMETRIES
R. Ouared, O. Brina, A. Narata, A. Marcos, P. Bijlenga, K. Schaller, K.Lovblad, V. Pereira 501

INFLUENCE OF SIPHON BENDS ON THE FLOW PATTERNS OF THE INTERNAL CAROTID ARTERY
M. Piccinelli, T. Passerini 505

ANEURYSM ENLARGEMENT USING A FIBER-BASED GROWTH MODEL
Fred Nugen, L. Dedé, T.J.R. Hughes 509

TOWARDS THE VALIDATION OF A VIRTUAL COILING TECHNIQUE USING A REAL VERSUS A SIMULATED BOLUS INJECTION
H.G. Morales, I. Larrabide, M. Villa-Uriol, A.J. Geers, A.F. Frangi 512

Keynote Lectures

Interior Tomography

Ge Wang
SBES Division / ICTAS Center for Biomedical Imaging, VT-WFU School of Biomedical Engineering & Sciences, Virginia Polytechnic Institute and State University, USA
wangg@vt.edu

SUMMARY

While classic CT theory is for exact reconstruction of a whole cross-section or an entire object, real-world applications often focus on smaller regions of interest (ROIs). The long-standing "interior problem" is to reconstruct an internal ROI only from truncated projections associated with x-rays through the ROI. In 2007, mathematical analysis and numerical results were published demonstrating that the interior problem can be solved in an exact and stable fashion if a subregion in the ROI is known. Such knowledge of a subregion is often available in practice; for example, the x-ray linear attenuation coefficients of air, water, blood, or other calibrated structures. Even without exact subregion knowledge, it was recently shown that interior tomography could still be exactly performed via compressive sensing. In this presentation, I will discuss the principles and implications of interior tomography to minimize radiation dose, handle large objects, improve temporal resolution, and be extended into other imaging modalities such as MRI, SPECT, and electron tomography.

2nd International Conference on Mathematical and Computational Biomedical Engineering – CMBE2011
March 30 – April 1, 2011, Washington D.C., USA
P. Nithiarasu and R. Löhner (eds)

REAL-TIME FINITE ELEMENT AND MESHLESS METHODS FOR MODELLING NEUROSURGERY

Karol Miller
Intelligent Systems for Medicine Laboratory
The University of Western Australia
35 Stirling Highway, Crawley WA 6009, AUSTRALIA
Email: kmiller@mech.uwa.edu.au
http://www.mech.uwa.edu.au/ISML/
and
Leverhulme Visiting Professor
C2EC, Swansea University

SUMMARY

Mathematical modeling and computer simulation have proved tremendously successful in engineering. Computational mechanics has enabled technological developments in virtually every area of our lives. One of the greatest challenges for mechanists is to extend the success of computational mechanics to fields outside traditional engineering, in particular to biology, biomedical sciences, and medicine (Oden et al., 2003). By extending the surgeon's ability to plan and carry out surgical interventions more accurately and with less trauma, Computer-Integrated Surgery (CIS) systems could help to improve clinical outcomes and the efficiency of health care delivery. CIS systems could have a similar impact on surgery to that long since realized in Computer-Integrated Manufacturing (CIM).

However, before this vision can be realized the following two challenges must be met:

Challenge 1. Real-time (or near-real-time) computations.
Rationale: In surgical simulation interactive (haptic) rates (i.e. at least 500 Hz) are necessary for force and tactile feedback delivery. In intra-operative image registration one needs to provide a surgeon with updated images in less than 40 seconds. To achieve these, highly non-linear models with ca. 50 - 100 thousand degrees of freedom must be solved in close-to-real-time on commodity computing hardware.

Challenge 2. Efficient generation of computational grids from medical images of human organs.
Rationale: In clinical workflow 3D images (e.g. magnetic resonance images) are acquired. In order for biomechanical computations to be practical, a computational grid must be obtained from these images (semi-)automatically and rapidly.

At Intelligent Systems for Medicine Laboratory we have addressed Challenge 1 by developing Total Lagrangian Explicit Dynamics finite element and meshless algorithms and implementing them on Graphics Processing Units [2, 3, 4, 5].

We are also addressing Challenge 2 by developing a concept of "an image as a computational model". We discretize the entire image volume with the cloud of points for the solution interpolation, insert an underlying regular cubic grid for volumetric integration and assign mechanical properties to integration cells based on probabilistic tissue classification algorithms. This approach leads to almost instantaneous computational model generation.

We have successfully applied the techniques mentioned above to modeling brain deformations during surgery and intra-operative neuroimage registration, Figure 1.

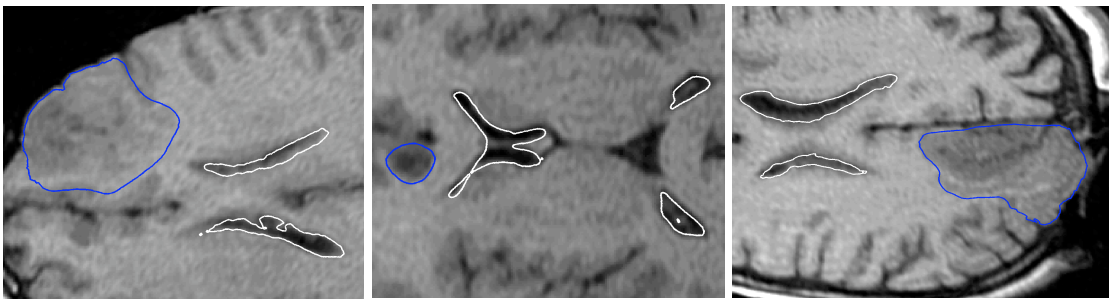

Figure 1. An example demonstrating the accuracy of the modeling and simulation techniques: the predicted contours of a brain tumor (blue) and ventricles (white) are overlaid on the MR images taken during surgery. Intraoperative images courtesy of CRL, Harvard.

Key Words: *computational biomechanics, brain, finite element method, meshless methods, graphics processing unit.*

REFERENCES

[1] J.T Oden, T. Belytschko, I. Babuska and T.J.R. Hughes, Research directions in computational mechanics. *Comput. Methods Appl. Mech. Eng. 2003;* **192**, 913-922.

[2] K. Miller, G. Joldes, D. Lance and A. Wittek, Total Lagrangian explicit dynamics finite element algorithm for computing soft tissue deformation, *Commun. Numer. Meth. Engng.* 2007; **23**:121–134

[3] A. Horton, A. Wittek, G. R. Joldes and K. Miller, A meshless Total Lagrangian explicit dynamics algorithm for surgical simulation, *Int. J. Numer. Meth. Biomed. Engng.* 2010; **26**:977–998

[4] G.R. Joldes, A. Wittek and K. Miller, Real-time nonlinear finite element computations on GPU — Application to neurosurgical simulation, *Comput. Methods Appl. Mech. Eng.* (2010), doi:10.1016/j.cma.2010.06.037

[5] Wittek, A., G. Joldes, M. Couton, S.K. Warfield and K. Miller, Patient-specific non-linear finite element modelling for predicting soft organ deformation in real-time; Application to non-rigid neuroimage registration, *Progress in Biophysics and Molecular Biology* (2010), doi:10.1016/j.pbiomolbio.2010.09.001

THINKING OUTSIDE THE BENCH

David A. Steinman
Biomedical Simulation Laboratory, Mechanical & Industrial Engineering, University of Toronto, 5 King's College Road, Toronto, ON, Canada, steinman@mie.utoronto.ca

ABSTRACT

Nearly half a century has passed since the first modern hemodynamic hypotheses of vascular disease were framed [1]. More than a quarter of a century has passed since engineering experiments confirmed direct links between hemodynamic forces and vascular pathology [2]. And well over a decade has passed since image-based computational fluid dynamics (CFD) was introduced as a means of bringing hemodynamic knowledge from bench to bedside [3]. Yet, despite the fact that hemodynamic disturbances are almost universally acknowledged to play a central role in vascular (patho)physiology, clinical decision-making still rarely incorporates this knowledge in a systematic way. Reasons for this were neatly summarized by Lieber *et al.* [4]:

> *Clinical acceptance of new methodologies and tools depends on criteria that are usually not observed in developing engineering concepts: they need to be relatively uncomplicated, fast (no lengthy offline analysis), quantitative ('threshold mentality'), and economically affordable. Widespread acceptance also hinges on successful clinical trials proving efficacy and safety for the patient and physician (evidence-based medicine).*

In this presentation I will discuss our experiences and efforts in confronting these clinical realities. For example, "virtual imaging" – recognizing and exploiting clinical visual vocabularies – has proven to be a useful adjunct to our usual engineering visualization conventions. Our software tools, crafted by engineers for engineers, can be intimidating or inscrutable when presented to a clinical audience, which only serves to widen rather than bridge the gap between the bench and the clinic. Most important, we have come to appreciate that our engineering models may be relied upon in a qualitative, but not necessarily quantitative sense. As a result, we can (and should) be willing to sacrifice accuracy for efficacy in the same way that clinicians must balance the desire for sensitivity and specificity with practicalities of obtaining it.

REFERENCES

[1] C.G. Caro, Discovery of the role of wall shear in atherosclerosis, *Arterioscler Thromb Vasc Biol,* 29, 158-161, 2009.

[2] S. Glagov, C. Zarins, D.P. Giddens, and D.N. Ku, Hemodynamics and atherosclerosis: Insights and perspectives gained from studies of human arteries, *Arch Pathol Lab Med*, 112, 1018-1031, 1998.

[3] C.A. Taylor, and D.A. Steinman. Image-based modeling of blood flow and vessel wall dynamics: Applications, methods and future directions, *Ann Biomed Eng*, 38, 1188-1203, 2010.

[4] B.B. Lieber, M. Siebes, and T. Yamaguchi, Correlation of hemodynamic events with clinical and pathological observations. *Ann Biomed Eng*, 33, 1695–1703, 2005.

2nd International Conference on Mathematical and Computational Biomedical Engineering – CMBE2011
March 30 – April 1, 2011, Washington D.C., USA
P. Nithiarasu and R. Löhner (eds)

NANO-DEVICES IN BIOTECHNOLIOGY AND DRUG DELIVERY

WING KAM LIU*, ASHFAQ ADNAN[+] and ADRIAN KOPACZ[!]
*Walter P. Murphy Professor of Mechanical Engineering, Northwestern University, and World Class University Professor at SKKU, w-liu@northwestern.edu
[+]Mechanical and Aerospace Engineering, The University of Texas at Arlington, aadnan@uta.edu
[!] Mechanical Engineering, Northwestern University, a-kopacz@northwestern.edu

SUMMARY

The fundamental challenge in the study of nanodevices in biotechnology and drug delivery stems from the fact that the basic mechanisms of the devices involve mechanics and materials at multiple length scale. Most of the nanodevices that are typically in the centimeter scale or above are developed using nanoparticles with a size scale in the nanometer scale. In this talk, we will discuss our studies on multiscale analysis of two types of nanodevices - one being used as DNA detector and the other as cancer therapeutic delivery. In nanoparticle based DNA detection devices, nanoparticle concentration is crucial for disease diagnosis and drug discovery. The major challenge for such concentration is in the low abundance of nanoparticles. For example, to concentrate DNA from sample mixture, current methods involve microfiltration and centrifugation. DNA is then extracted and amplified by Polymerase Chain Reaction (PCR) for detection. However, these methods are inefficient, cumbersome and time consuming. To overcome this challenge, we are designing a concentration tool composed of the nanotips that are similar to nanoparticles in size. On the other hand, a broad range of materials have been explored as candidates for the imagery/diagnosis and therapeutic release towards cancer. The development of a platform approach towards rationally designed nanocarbon-enabled imagery and drug delivery that is broadly applicable would then generate an important advance towards material-driven enhancements in therapy. In this talk, we first described various nanocarbon-materials for therapeutic and diagnostic applications. We will then demonstrate that nanodiamonds (NDs) represent as one of the most promising candidate materials as they have much higher potential for mass production, yet still possess properties common to nanotubes and bucky balls such as the ultrahigh surface-to-volume ratio. Then, we outline an experimentally validated and nansocale science based simulation technique for the development of ND-enabled drug delivery system capable of performing both therapeutics and diagnostics functions. We will exclusively focus our quantitative analysis of pH-dependent interactions between doxorubicin hydrochloride (DOX) cancer therapeutic and faceted nanodiamond (ND) nanoparticle carriers using a constant-pH molecular dynamics simulation approach.

Key Words: *constant pH MD simulation, doxorubicin, nanodiamond, multiscale analysis, uncertainty quantification techniques, nanodevices, medicine.*

1. INTRODUCTION

1.1 Nanodevices for DNA detection

A critical challenge in the field of medicine is to develop a low cost sensor competent of detecting specific bacterial pathogens via a precise deoxyribonucleic acid (DNA) sequence. In order to identify such biological agents in a patient's blood or other bodily fluids at the onset of infection, detection of specific pathogen genomic DNA is considered a reliable approach. Current techniques involving multiplex DNA/RNA detection arrays or immunoassays [1] require cumbersome sample preparation, aggressive nucleic acid amplification protocols and must be

operated by trained personnel. The goal of this work is to develop a unique simulation tool that will help guide the design of the device, characterize its fundamental mechanisms at the nanometer scale and optimize distinct parameters for its high sensitivity throughput.

1.2 Nanodevices for Drug delivery

It has been demonstrated from recent studies that nanodiamonds (NDs) based nano-devices have tremendous potential as drug carriers due to their exceptional biocompatibility and unique surface properties (5-10). Understanding the fundamental mechanism of ND-based drug delivery is a major challenge because of multiple length scale involved in the delivery process, and the goal of our current research is to develop a multiscale modeling technique to understand the fundamental mechanism of a ND-based cancer therapeutic drug delivery system. The major components of the proposed device include nanodiamonds (ND), parylene buffer layer and doxorubicin (DOX) drugs, where DOX loaded self-assembled nanodiamonds are packed inside parylene capsule. In this work, we have employed a constant-pH molecular dynamics simulation approach to provide a quantitative analysis of pH-dependent interactions between doxorubicin hydrochloride (DOX) cancer therapeutic and faceted nanodiamond (ND) nanoparticle carriers.

2. MAIN BODY

2.1 DNA detection

An electric field is used to concentrate target DNA molecules in the vicinity of a nanotip where probe molecules are immobilized. However, submicron particle manipulation requires very high field strengths resulting in AC electroosmosis and possible deterioration of biomolecules [2]. Our primary aim is to increase the local density of target DNA molecules and the molecular flux at the nanotip in a large volume of 10μL-1mL. This is accomplished by controlling the frequency and amplitude of an AC electric field, the conductivity of the suspending medium, sample size, nanotip and counter electrode geometry. A simulation based modelling is used to predict electrohydrodynamics and the dominant electrokinetic forces at the nanometer scale while varying the aforementioned conditions. In this study, the immersed finite element method is extended by coupling it with various multiphysics features [3,4].

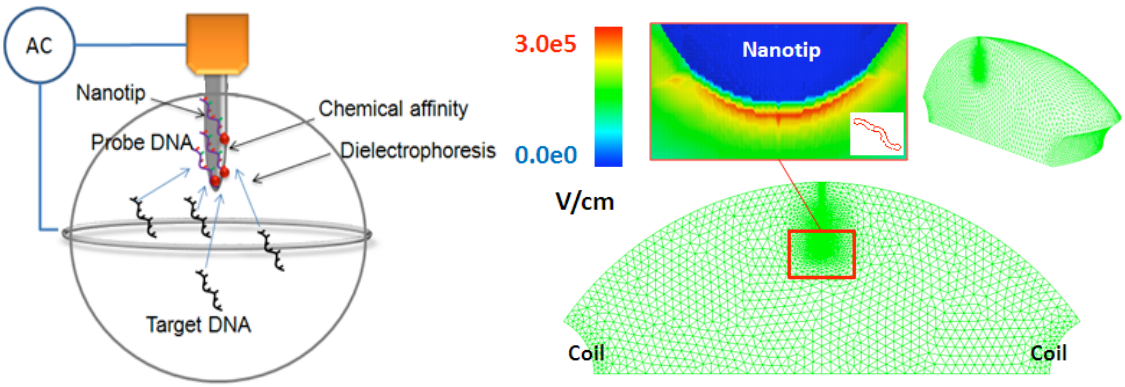

(a) (b)

Figure 1. (a) Enrichment system using a nanotip where circulatory flow is generated on a nanotip surface by electroosmosis and attraction is conducted by dielectrophoresis. Binding is determined by probe molecules that are immobilized on a nanotip surface. (b) Vrms of 3.54 at 5MHz is prescribed across the nanotip and the coil. Max electric field is located just below the nanotip.

As depicted in Figure 1(b), maximum electric field is present just below the apex of the nanotip. Our calculations suggest that the maximum DEP force that is exerted on a DNA molecule within the vicinity of the nanotip is on the order of 1nN. However, couple microns away from the nanotip, the magnitude of the DEP force exerted on a DNA molecule drops exponentially to under 1pN. Hence, the DEP force is dominant close to the nanotip while forces such as those due to the average motion of the suspended medium caused by thermal fluctuations, i.e. Brownian forces, become important couple microns away from the nanotip.

2.1 ND-DOX Interaction

Here we have adopted a constant pH Molecular Dynamics Simulation (CpHMD) (11) technique to explore the pH dependent interactions between DOX and ND. As shown in Fig. 2, this model consists of 8 truncated octahedral ND with a diameter of 3.5nm plus several DOX molecules, counterions and water molecules. The properties of the surface carbon atoms are modified to reflect functionalization whose properties are only poorly known. MD simulations at various pH levels have been performed for pH in the range from 6 to 11 with an interval of 0.5. In Fig. 3, MD simulation results for the number of drug adsorption per ND are plotted versus pH and have been compared with experimental results (6). We consider a DOX molecule to be bound to the ND surface when the amino group of the DOX maintains a Van der Waals separation distance (<~3.5 nm) from the ND. It can be observed that presence of 30% and 20% functional groups on ND surface has yielded similar results. For the 10% functional group case, the trend in results with respect to pH variation remain the same but the total number of DOX binding on ND surface is seen to be reduced substantially.

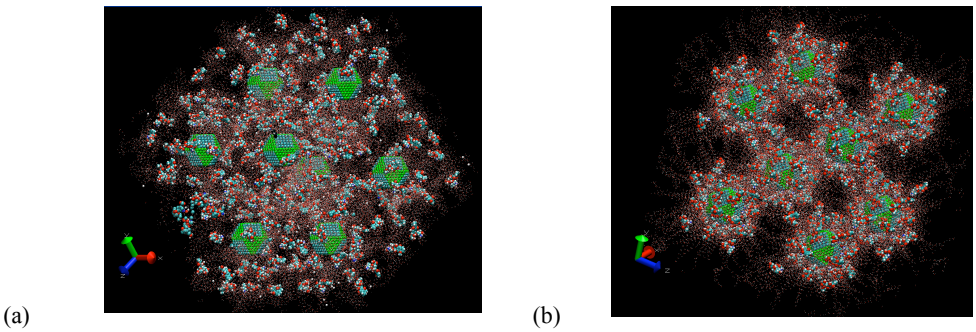

Figure 2: Representative final MD snapshots for the DOX-ND interaction simulation at different pH level: (a) large model with 8 NDs and 208 DOX in the solvent.

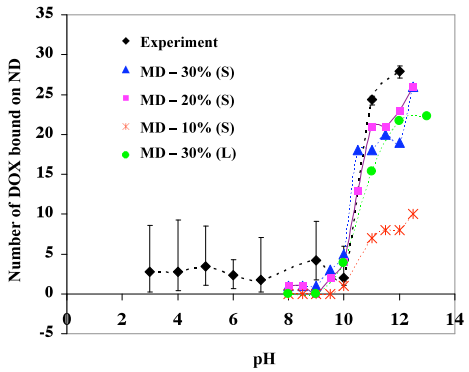

Figure 3: pH dependent DOX-ND binding capacity. "S" and "L" represents smaller MD model and larger MD model, respectively.

3. CONCLUSIONS

In order to achieve optimum device sensitivity for large sample volumes, it is imperative to understand the underlying forces present at the nanoscale. Forces of interest include DEP force, forces due to Brownian motion and forces due to DNA particle-particle interaction. The immersed molecular electrokinetic finite element method is currently being implemented that will help guide the design of the device, characterize its fundamental mechanisms at the nanometer scale and optimize distinct parameters for its high sensitivity throughput.

The effect of pH on the ND-DOX interactions has been investigated. Some discrepancies between experiment and simulation have been observed and can be attributed to several factors including improper surface charge distribution and pKa of ND, DOX concentration, ND surface groups etc. Nevertheless, our study clearly suggests that pH is a critical factor to DOX interaction with ND. This work paves the way for the continued and optimized development of a pH controlled drug delivery method using NDs carriers (5,6).

4. ACKNOWLEDGEMENT

The support of this research by NSF CMMI 0856492, NSF CMMI 0856333 and the World Class University program (R33-10079) under the Ministry of Education, Science and Technology, Republic of Korea, are gratefully acknowledged.

REFERENCES

1. E. Sada, D. Aguilar, M. Torres, and T. Herrera, Journal of Clinical Microbiology 30, 2415-2418 (1992).
2. Müller T, Gerardino A, Schnelle T, Shirley SG, Bordoni F, DeGasperis G, Leoni R, Fuhr G. Trapping of micrometre and sub-micrometre particles by high-frequency electric fields and hydrodynamic forces. J. Phys. D: Appl. Phys. Vol 29 340-349 1996.
3. L Zhang, A Gerstenberger, X Wang, and W K Liu. Immersed finite element method. Computer Methods in Applied Mechanics and Engineering, 193(21-22):2051-2067, 2004.
4. Y. Liu, W.K. Liu, T. Belytschko, N. Patankar, A. C. To, A. Kopacz, J.H. Chung. Immersed electrokinetic finite element method. International Journal for Numerical Methods in Engineering 71:379-405, 2007.
5. Huang, H.; Pierstorff, E.; Osawa, E.; Ho, D. Active Nanodiamond Hydrogels for Chemotherapeutic Delivery. *Nano Letters,* **2007**, 7, 3305-3314.
6. Ashfaq Adnan, Robert Lam, Hanning Chen, Jessica Lee, Daniel J. Schaffer, Amanda S. Barnard, George C. Schatz, Dean Ho, Wing Kam Liu, "Atomistic Simulation and Measurement of pH dependent Cancer Therapeutic Interactions with Nanodiamond Carrier", *Molecular Pharmaceutics*, In Review (conditionally accepted), 2010
7. Wing Kam Liu, **Ashfaq Adnan, "**Multiscale Bio-chemo mechanics for Nanodiamond-based Therapeutic Delivery", 9th World Congress on computational Mechanics and 4th Asian Pacific Congress on Computational Mechanics (WCCM/APCOM2010) 19-23 July 2010, Sydney, Australia.
8. **Ashfaq Adnan,** Wing Kam Liu, "Electrostatic self-assembly of Functionalized Nanodiamonds and their Binding Capacity with Doxorubicin drugs", 1st Global Congress on NanoEngineering for Medicine and Biology (NEMB**)**, Houston, Texas, Feb 07 – 10, 2010.
9. Wing Kam Liu**, Ashfaq Adnan, "**Multiscale Modeling of Nanodiamond enabled drug delivery system", 1st Global Congress on NanoEngineering for Medicine and Biology (NEMB**)**, Houston, Texas, Feb 07 – 10, 2010 *(invited)*.
10. **Ashfaq Adnan,** Wing Kam Liu, "Mechanics of pH Mediated Adsorption/Desorption of Doxorubicin Drug From Functionalized Nanodiamond", 2009 ASME International Mechanical Engineering Congress & Exposition, Lake Buena Vista, Florida - November 13-19, 2009
11. Baptista, A. M.; Teixeira, V. H., Soares, C. M. Constant-pH molecular dynamics using stochastic titration. *J. Chem. Phys***. 2002**, 117, 4184-4196.

2nd International Conference on Mathematical and Computational Biomedical Engineering – CMBE2011
March 30 – April 1, 2011, Washington D.C., USA
P. Nithiarasu and R. Löhner (eds)

COMPUTATIONAL MODELLING OF THE HEART IN THE CLINIC

Andrew Cookson, Adelaide de Vecchi, Pablo Lamata, Jack Lee, Sebastian Krittian, Mathew McCormick, Christian Michler, Steven Niederer, David Nordsletten, Nic Smith
Department of Biomedical Engineering, King's College London
Computing Laboratory, University of Oxford

SUMMARY

The loss of cardiac pump function accounts for a significant increase in both mortality and morbidity in western society. There is currently a 1 in 4 lifetime risk of cardiac disease and an acceleration of the costs associated with acute and long-term hospital treatments. The significance of this disease has motivated the application of state of the art clinical imaging techniques to aid diagnosis and clinical planning. Measurements of cardiac function currently provide high-resolution data sets for characterizing cardiac patients. However, the clinical practice of using population-based metrics derived from separate image sets often indicates contradictory treatment plans due to inter-individual variability in pathophysiology. To address this issue the goal of our work, demonstrated in this study through three specific clinical applications, is to integrate multiple types of functional data into a consistent framework using multi-scale computational modelling.

Key Words: *Multi-Physics, Multi-scale, Cardiac Modelling.*

1. INTRODUCTION

Cardiovascular disease (CVD) is a highly significant contributor to loss of quality and quantity of life [1]. It is most commonly a consequence of diseases such as coronary artery disease (CAD), congestive heart failure (HF), and cardiac arrhythmias. Thus the early detection and prediction of the progression of CVD are key requirements towards improved treatment and hence a reduction in mortality and morbidity.

The diversity and quantity of currently available imaging data, including measurements of cardiac wall motion, chamber flow patterns, coronary perfusion and electrical mapping, presents a significant opportunity to improve clinical care of CVD. However, despite imaging advances, determining optimal treatment strategies for CVD patients remains problematic. To exploit the full value of imaging technologies, and the combined information content they produce, requires the ability to integrate multiple types of anatomical and functional data into a consistent framework.

2. MAIN BODY

An exciting and highly promising strategy for contributing to this integration is through the personalisation of bio-physically based mathematical models. The development of such models presents the ability to capture the complex and multi-factorial cause and effect relationships which link underlying pathophysiological mechanisms. This in turn provides the capacity to derive parameters that are not directly observable but play a key mechanistic role in the disease

process (for example tissue stress and measures of pump efficiency) to assist treatment decisions. Across international efforts to develop these types of models the heart is arguably one of the most advanced current examples of an integrated organ model. As such it represents an excellent organ system with which to demonstrate the translation of models to clinical application. Specifically, detailed anatomical finite element based models of the heart now accurately represent both cardiac anatomy and detailed microstructure. These mathematical descriptions serve as spatial frameworks for embedding functional cellular models of electrical activation, and the resultant tension generation which produces cardiac contraction. These cell and organ components have been combined through the application of continuum equations to simulate whole organ cardiac electro-mechanics, perfusion and ventricular fluid dynamics in a number of clinical contexts:

Cardiac Electro-mechanics: Cardiac resynchronisation therapy (CRT) has emerged as one of the few effective and safe treatments for HF. Identifying patients that will benefit from CRT remains controversial and this situation is exacerbated by the cost and invasiveness of the procedure. To address this issue a biophysically-based patient-specific coupled electromechanics heart model has been developed, which links the cellular and sub-cellular mechanisms that regulate cardiac function to the whole organ function observed clinically before and after CRT [2]. The model integrates diagnostic data from ECG, left ventricle (LV) pressure catheter, cine MRI, late enhancement MRI and electrical activation maps (see figure 1) collected from a specific individual into a consistent quantitative framework. Anatomy, electrical and mechanical function have been validated against MRI derived deformation patterns at baseline, and against EnSite maps and pressure catheter data collected under paced conditions. A sensitivity analysis of the model has identified the length-dependence of tension as a significant contributor to the efficacy of CRT. Further simulation analysis using simulations packages CARP[1] and Cmiss[2] has demonstrated that in the whole heart, length-dependent tension development in the sarcomere is key not only for the beat-to-beat regulation of stroke volume (Frank-Starling mechanism) but also the homogenisation of tension development and strain. The model has identified that in individuals with effective Frank-Starling mechanism the length dependence of tension facilitates the homogenisation of stress and strain. This can result in synchronous contraction despite asynchronous electrical activation. Thus, in individuals with effective Frank-Starling mechanism of tension, we are able to conclude that the synchronising electrical activation through CRT may have minimal benefit.

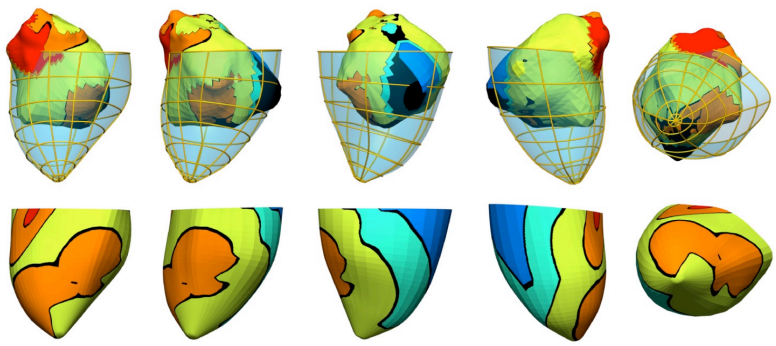

Figure 1: Ensite LV endocardial geometry and activation map for sinus rhythm (solid surface) with MRI geometry (transparent mesh surface) overlaid (top). LV endocardial activations times from 3D whole heart simulation with fitted conductivities (bottom).

[1] http://carp.meduni-graz.at/
[2] http://www.cmiss.org/

Modelling Coronary Perfusion:
Like HF, CAD is also a major cause of mortality, but again, despite its significance, the determination of optimal clinical diagnosis and treatment strategies for CAD patients remains problematic. Exacerbated by the high risk of the disease, and the difficulty in excluding it, the clinical problem is tangibly demonstrated by the large number of patients who currently unnecessarily undergo invasive angiography and achieve negative results.
The numerical simulation of coronary perfusion thus has the potential to play a vital role in advancing the understanding of important aspects of coronary heart disease and improving treatment. However, the simulation of this phenomenon has to overcome several major challenges. To date, it has been very difficult to obtain accurate anatomical information of the human coronary vascular network ranging from the millimeter to the micrometer scale. But even if one had exact anatomical information available in so much detail, simulating blood flow on such a vast vascular tree would be prohibitive in terms of computational complexity. Moreover, the interaction between blood flow and tissue mechanics requires the accurate coupling of those different types of physics [3].

To address these challenges, we have modelled blood flow through the microscopic vasculature as a porous media flow. The solid constituent, on the other hand, is modelled using the theory of finite elasticity, in order to address the large strain deformation the cardiac muscle experiences. This results in a volume-coupled model where Darcy flow and finite elasticity co-exist on the same homogenised domain while the coupling is expressed through conditions characterising the respective material laws and constitutive relations. Figure 2 demonstrates that the Darcy flow model can be solved on a realistic left ventricle geometry undergoing physically meaningful deformations.

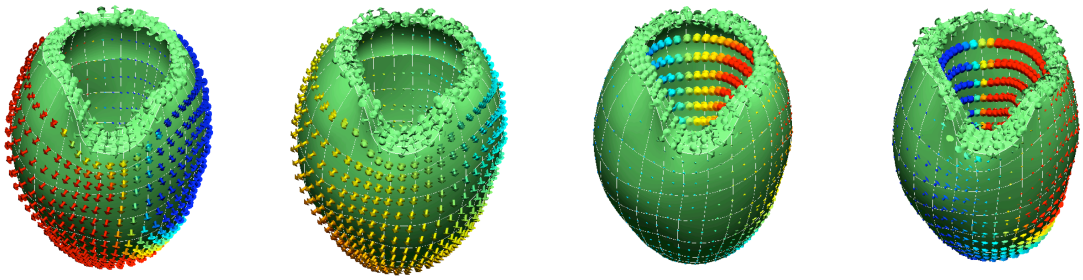

Figure 2: Numerical solution of the Darcy problem with deformation-dependent material properties under prescribed geometry movement and homogeneous Neumann boundary conditions. Snapshots at times t = 0.18T, t = 0.45T, t = 0.73T and t = 0.91T with T the period of the heart cycle. Velocity vectors are coloured by the magnitude of the x-velocity. Velocity vectors are absolute velocities and, therefore, not relative to the motion of the heart.

Ongoing work is focused on the application of these models to quantitatively link the measured contrast agent transport to myocardial contraction, epicardial and microcirculatory coronary perfusion.

Fluid Structure Interaction: Hypo-plastic left heart is a condition that affects 4–5 children out of 10,000 births and poses a serious threat to life, requiring immediate surgical treatment in the majority of the cases. Hypo-plastic left heart patients rely solely on the right ventricle as a motor for the systemic and the pulmonary circulation, the left one being atrophied or underdeveloped. To assist the surgeon in planning the intervention, we are using biophysical simulations [4] to assess diastolic dysfunction through the analysis of pressure gradients and myocardial relaxation

(Figure 3). In the rapid filling phase (early diastole), the annular velocity during the ventricle elongation, *e'*, is recorded as well as the velocity of the inflow at the inlet valve, *E*. Previous studies in the literature have demonstrated that the ratio *E/e'* is an important clinical parameter to predict the filling pressures and to highlight diastolic abnormalities. The flow propagation and vortex formation mechanism is analyzed in the hypo-plastic left heart cases and compared to the previous results obtained with patients affected by congenitally corrected transposition of the great arteries (CCTGA). Our goal in this work is to use the information provided by the model to underpin a clinical trial at the end of the project to test the value of computational metrics for selecting patients who will respond to surgical treatment.

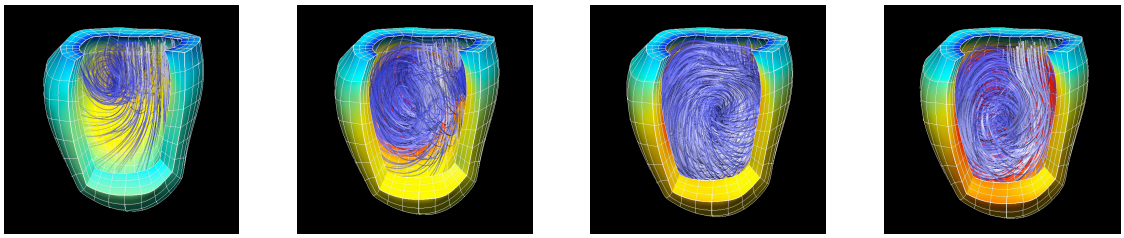

a) **b)** **c)** **d)**

Figure 3: The vortex formation in the systemic right ventricle of a patient with hypo-plastic left heart. The ring vortex is formed during the peak *E* wave in proximity of the aortic valve, as shown in (a). During the deceleration period it expands and travels axially away from the formation region (b). At diastasis (c) the maximum volume expansion is attained on a circumferential plane located just below the valve orifices and the two vortices merge into one complex swirling structure. No additional vortex pair is observed during the atrial contraction (d), unlike in the normal left ventricle filling, where a weak ring vortex appears near to the mitral inlet.

3. CONCLUSIONS

The results of this work demonstrate the capacity of mathematical models to integrate multiple clinical data sets into a consistent framework to facilitate patient treatment. Through this work our goal is to support a paradigm shift away from predefined clinical indices determining treatment options and a move towards true personalisation of care based on an individual's specific physiology.

REFERENCES

[1] Liu, J. L. Maniadakis, N. et al. , The economic burden of coronary heart disease in the UK. Heart 88(6): 597-603,2002

[2] Niederer S.A., Plank G., Chinchapatnam P., Ginks M., Lamata P., Rhode K.S., Rinaldi C.A., Razavi R., Smith N.P. Length-Dependent Tension in the Failing Heart and the Efficacy of Cardiac Resynchronisation Therapy, Cardiovascular Reserach (accepted), 2010.

[3] Lee J., Niederer S.A., Nordsletten D.A., Smith N.P. Coupling Contraction, Excitation, Ventricular and Coronary Blood Flow across scale and physics in the Heart, Phil. Trans. 2009,367, 2311-2331, 2009

[4] Nordsletten D. A., Niederer S. A., Nash M. P., Hunter P. J., Smith N. P. Coupling Multi-Physics Models to Cardiac Mechanics, Prog. Bio. Phys. Mol. Bio. (in press), 2010

2nd International Conference on Mathematical and Computational Biomedical Engineering - CMBE2011
March 30 - April 1, 2011, Washington D.C, USA
P. Nithiarasu and R. Löhner (Eds.)

Use of Computational Fluid Dynamics for the Design and Development of Animal Models for Studies of the Pathophysiology of Cerebral Aneurysms

A. M. Robertson,[⋆], Z. Zeng[⋆⋆], M. J. Durka[⋆⋆], D. F. Kallmes[⋆⋆⋆], R. Kadirvel[⋆⋆⋆], Y. Ding[⋆⋆⋆], D. Dai[⋆⋆⋆], D. Lewis[⋆⋆⋆], M. R. Hill[⋆⋆], S. C. Watkins [⋆⋆⋆⋆]

[⋆]University of Pittsburgh, Pittsburgh, PA, 15261, rbertson@pitt.edu

[⋆⋆]University of Pittsburgh, Pittsburgh, PA, 15261

[⋆⋆⋆]Mayo Clinic College of Medicine, Rochester, MN, 55905

[⋆⋆⋆⋆]Center for Biological Imaging, Pittsburgh, PA, 15261

SUMMARY

Intracranial aneurysms (IAs) are saccular abnormalities of cerebral arterial walls that can rupture, leading to subarachnoid hemorrhage with an associated high rate of morbidity and mortality. It is therefore desirable to identify and treat high risk lesions prior to rupture. It is generally agreed that hemodynamics play a critical role in the development, progression and rupture of IAs. However, the determination of which mechanical stimuli are important and their role in the various stages of aneurysm evolution remains elusive. This poor understanding of the disease process limits treatment planning and the development of pharmaceutical therapies. This is in sharp contrast to diseases such as such as atherosclerosis in which detailed knowledge of the pathobiology has led to development of preventative treatment strategies using statins.

Animal models provide a mechanism for fundamental studies of disease pathophysiology and have been heavily used in studies of atherosclerosis. Ideally, these animal models would mimic the anatomy, physiology, biology, and response to therapy of human aneurysms during all stages of the disease. However, cerebral aneurysms have not been shown to occur naturally in animals. Therefore, the relevance of the animal model to human IAs must be carefully established. In this talk, we consider an elastase induced aneurysm model in rabbits (EIAR) and discuss how computational fluid dynamics (CFD) has been used to (i) evaluate its hemodynamic relevance to cerebral aneurysms in humans, (ii) reconfigure this animal model to extend the range of its applicability, (iii) enable an assessment of coupling between hemodynamics and wall remodeling.

Key Words: *cerebral aneurysm, animal model, hemodynamics, remodeling.*

1 The Elastase Induced Aneurysm Model in Rabbits (EIAR)

A number of animal models have been created for studying aneurysm pathogenesis including those in mice, rats, rabbits, canines, swine and primates. In this work, we consider an elastase induced, saccular aneurysm model in rabbits that offers some merits such as similarity in size between parent vessels in the EIAR and those of human IAs, lower cost compared with larger animal models, ease of imaging and handling as well as a comparable clotting response compared with human IAs [6]. Briefly, the right common carotid artery (RCCA) in New Zealand white rabbits is exposed and ligated distally and a balloon catheter is advanced to the origin of the RCCA at the right subclavian artery and used to achieve flow arrest in the RCCA, [1].

Porcine elastase is incubated above the inflated balloon for 20 minutes, after which the balloon is deflated and catheter system removed. The RCCA is then ligated at its mid-portion. Dilated, arterial segments thus formed from the stump of the RCCA, are termed “aneurysms”, Fig. 1A

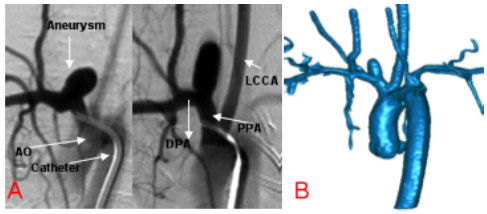

Figure 1: A: 2D angiography of elastase-induced rabbit aneurysms, left: low AR model; right: high AR case; B: 3D reconstructed geometric models of the aneurysm and segments of the peripheral vasculature.

1.1 Computational Model

Geometric models of the luman surface of the aneurysm and sections of local vasculature were generated from 3D reconstruction of animal specific data obtained from three-dimensional rotational angiography, Fig.1B. Blood flow in the reconstructed models was simulated based on the unsteady, 3D Navier-Stokes equations, using the finite element method with ADINA software (64 bit) (ADINA Inc.). Blood was modeled as an incompressible linearly viscous fluid with density and viscosity specified as $\rho = 1050 \text{kg/m}^3$ and $\mu =$ 3.5 mPa·s, respectively. The vessel wall was idealized as rigid and the no-slip boundary condition was applied. Animal specific in vivo doppler measurements in the DPA and LCCA were obtained using transthoracic duplex doppler ultrasound imaging and provided estimates of the time averaged flow rate at the these locations [12, 10]. A structured hexahedral mesh was used with element numbers ranged from 40,000 to 60,000 depending on the geometric complexity [10]. CFD analyses were performed for each model for two cardiac cycles using 100 time steps per cycle using using a 3-GHz dual Xeon processor work station with 8-GB of memory.

A central question in any hemodynamic study is the extent of vasculature to include in the study so as to avoid needless computational effort without degrading the accuracy of CFD results. In the EIAR, the aortic arch as well as up-stream and down-stream bifurcations are in close proximity to the aneurysm cavity, Fig. 1B. In a previous study, the sensitivity of CFD results to the extent of the vascular domain was shown to vary between the low and high aspect ratio (AR) cases. Based on these results, in future studies the computational domain for high AR EIAR included the LCCA, proximal parent artery, DPA and aneurysm while low AR models included this computational domain and the downstream bifurcation /quadrification structure, [10].

1.2 Relevance of the EIAR to Humans

The EIAR must have geometries representative of human IA, if they are to be useful for studying human IA development and treatment. Further, a large range of geometries are needed if the EIAR are to be used to test current hypothesis about the role of geometry in aneurysm development. Kallmes et al. developed protocols for creating statistically different neck sizes and sac volumes in the EIAR by adjusting the balloon and ligation positions, respectively, [4, 3]. Using the new protocols, a wide range of geometries were created in 51 EIAR. The 3D reconstructed geometries were retrospectively analyzed and compared with published values for human aneurysms [10]. The neck width, aneurysm height, maximum sac diameter, aneurysm surface area, aneurysm volume (V) and parent artery diameter (P) were all within the range of reported values for human IAs. The aspect ratio (AR = H/N), D/H, and BF = D/N [5] were also within reported human limits.

CFD was recently used to assess flow in the pool of 51 EIAR and compared with published results for human IA [10]. The flow structure could be categorized as Type A flows with a single, stationary circulation inside the aneurysm sac (n = 33, 65%) and Type B flows with a transient

secondary circulation in the dome as well as a primary (larger) stationary circulation below this (n = 18, 35%). Cebral et al. classified the flow in 62 cerebral aneurysms in humans into four types based on the nature of the inflow jet and the number and stability of vortices in the sac [2]. Flow types A and B in the EIAR are of types I and III, respectively, corresponding to flow found in 61% of the IA analyzed in [2]. The Reynolds and Womersley numbers also fall within the human range [10]. The spatial distributions of wall shear stress (WSS) and oscillatory shear index (OSI) in and around the rabbit aneurysm sac were shown to be typical for large groups of human IA [10].

1.3 Aspect Ratio Studies

Clinical studies suggest AR is a useful indicator for assessing IA rupture risk (e.g. [8]). The importance of AR is hypothesized to arise from the dependence of hemodynamic wall stress on the geometry of the sac [9]. Using CFD studies, Zeng et al. demonstrated the range and distribution of AR in the EIAR are suitable for evaluating this conjecture, [10]. Further, flow in the low and high AR models was shown to be significantly different [10, 11]. Low, transitional and high AR categories could be defined such that a single circulation was observed in low AR sac and a transient, slower secondary circulation with an associated separation point was seen in high AR sacs. This high AR flow environment has been associated with deleterious changes to the wall and may trigger wall degradation and general mechanical weakening of the aneurysm sac.

1.4 Aneurysm Wall Degradation and Remodeling

The previous work lays the foundation for future applications of the EIAR to studies of the coupling between local intra-aneurysmal hemodynamics and wall structure. In a related work in this direction, differential gene expression was compared in high and low AR aneurysms in 11 EIAR [7]. High AR was associated with differential expression of inflammatory/immunomodulatory genes, structural genes, and genes related to proteolytic enzymes, and extracellular matrix-related genes. Endothelial cells are present along the intima of the EIAR sacs, but they are more disordered and less uniformly distributed than in control arteries. In ongoing work, wall structure and histology are being compared in EIAR and human IA walls.

1.5 Extension of the current RCCA EIAR

Though the hemodynamic parameters in the current EIAR all fall within values reported in human IA, only two out of four flow types identified in [2] are created in the current model. Recently, a range of new EIAR have been produced and assessed using CFD including a model with a “flow modulating” arterial venous malformation downstream from the aneurysm cavity that generates antegrade peri-aneursymal flows. In addition, a bifurcation EIAR was developed by utilizing the LCCA rather than the RCCA. Using CFD analysis, the intra-aneurysmal flow in the LCCA EIAR with downstream AVF was found to display a third flow type reported in [2]. The flow displayed a second stationary circulation pattern and an oscillating impingement region. This flow type is associated with increased risk of rupture compared with the previous two flow types [2].

2 CONCLUSIONS

An elastase induced aneurysm model in rabbits displays similar geometries and hemodynamic environments to those seen in humans. CFD analysis has shown that three of the four flow types identified in human IAs can be created in the EIAR using a previously created RCCA model as

well as a new high flow LCCA model. A wide range of ARs can be created in the rabbit model. CFD studies demonstrate distinct flow types in low and high AR models. Flow in the high AR aneurysms appears to be more deleterious to the wall, displaying larger regions of pathologically low WSS, elevated OSI than in the low AR sacs. Future studies will be directed at rigorously assessing wall remodeling and degradation in the EIAR to evaluate its relevance to humans.

References

[1] TA Altes, HJ Cloft, JG Short, A DeGast, HM Do, GF Helm, and DF Kallmes. 1999 ARRS Executive council award. Creation of saccular aneurysms in the rabbit: A model suitable for testing endovascular devices. *American Journal of Roentgenology*, 174(2):349–354, 2000.

[2] JR Cebral, MA Castro, JE Burgess, R Pergolizzi, MJ Sheridan, and CM Putman. Characterization of cerebral aneurysm for assessing risk of rupture using patient-specific computational hemodynamics models. *AJNR Am J Neuroradiol*, 26:2550–2559, 2005.

[3] YH Ding, D Dai, MA Danielson, R Kadirvel, DA Lewis, HJ Cloft, and DF Kallmes. Control of aneurysm volume by adjusting the position of ligation during creation of elastase-induced aneurysms: a prospective study. *Am J Neuroradiol*, 28:857–859, 2007.

[4] YH Ding, D Dai, DA Lewis, MA Danielson, R Kadirvel, JN Mandrekar, HJ Cloft, and DF Kallmes. Can neck size in elastase-induced aneurysms be controlled? A prospective study. *Am J Neuroradiol*, 26(9):2364–2367, 2005.

[5] K Ebina, T Shimizu, M Sohma, and T Iwabuchi. Clinico-statistical study on morphological risk factors of middle cerebral artery. *Acta Neurochir (Wien)*, 106(3-4):153–159, 1990.

[6] CB Heilman, E Kwan, and JK Wu. Aneurysm recurrance following endovascular balloon occlusion with either silicon or latex balloons. *J Neurosurg*, 77:260264, 1992.

[7] R Kadirvel, YH Ding, D Dai, DA Lewis, and DF Kallmes. Differential expression of genes in elastase-induced saccular aneurysms with high and low aspect ratios. *Neurosurgery*, 66:578–584, 2010.

[8] RR Lall, CS Eddleman, BR Bendok, and HH Batjer. Unruptured intracranial aneurysms and the assessment of rupture risk based on anatomical and morphological factors: sifting through the sands of data. *Neurosurg Focus*, 26(5):E2, 2009.

[9] H Ujiie, H Tachibana, O Hiramatsu, AL Hazel, T Matsumoto, Y Ogasawara, H Nakajima, T Hori, K Takakura, and F Kajiya. Effects of size and shape (aspect ratio) on the hemodynamics of saccular aneurysms: a possible index for surgical treatment of intracranial aneurysms. *Neurosurgery*, 45(1):119–129; discussion 129–130, 1999.

[10] Z Zeng, M Durka, DF Kallmes, R Kadirvel, Y Ding, D Lewis, and AM Robertson. Hemodynamics and anatomy of elastase-induced rabbit aneurysm models–Similarity with human cerebral aneurysms? *AJNR Am J Neuroradiol*, 2011 (in press).

[11] Z Zeng, M Durka, DF Kallmes, and AM Robertson. Effects of aspect ratio on the hemodynamics in elastase induced rabbit aneurysms. In *Fifth European Conference on Computational Fluid Dynamics (ECCOMAS CFD 2010)*, June 14th - 17th 2010.

[12] Z Zeng, DF Kallmes, M Durka, Y Ding, D Lewis, R Kadirvel, and AM Robertson. Sensitivity of CFD based hemodynamic results in rabbit aneurysm models to idealizations in surrounding vasculature. *J Biomech Eng-T ASME*, 132(9):091009 (10 pages), 2010.

2nd International Conference on Mathematical and Computational Biomedical Engineering – CMBE2011
March 30 – April 1, 2011, Washington D.C., USA
P. Nithiarasu and R. Löhner (eds)

MULTISCALE MODELS FOR NANO-BIO SYSTEMS

Guo-Wei Wei* and Zhan Chen*
*Department of Mathematics, Michigan State University, East Lansing, MI48824, USA
e-mail: wei@math.msu.edu

SUMMARY

We propose a differential geometry based multiscale paradigm for the description and analysis of aqueous chemical, biological systems, such as protein complex, molecular motors, ion channels, and PEM fuel cells. Our multiscale paradigm provides a macroscopic continuum description of the fluid or solvent, a microscopic discrete description of the macromolecule, a differential geometric formulation of the micro-macro interface, and a mixed micro-macro description of the electrostatic interaction. In the proposed framework, we have derived four types of governing equations for different parts of complex systems: fluid dynamics, molecular dynamics, electrostatic interactions, and surface dynamics. These four types of governing equations are generalized Navier–Stokes equations, Newton's equations, generalized Poisson or Poisson–Boltzmann equations, and hypersurface evolution equations. For systems far from equilibrium, coupled geometric evolution equations, generalized Navier–Stokes equations, Newton's equations, and Poisson–Nernst–Planck (PNP) equations are formulated. For excessively large chemical and biological systems, we replace the expensive molecular dynamics with a macroscopic elastic description and develop alternative differential geometry based fluid-electro-elastic models.

Key Words: *Differential geometry based multiscale modeling, Ion channels, Proteins, Solvation analysis, Molecular dynamics.*

1. INTRODUCTION

Recently, multiscale modeling and multiscale simulation have emerged as powerful approaches in physical, biological, mathematical, and engineering sciences. The popularity of these approaches is driven by the human curiosity and desire to understand the behavior of complex systems, such as complex fluids, turbulent flows, micro-fluidics, solids, interface problems, structure and fluid interactions, wave propagation in random media, stochastic processes, and statistically self-similar problems, to name only a few. In general, multiscale models and methods allow efficient descriptions of key elements in a physical phenomenon such that the subsequent simulations are feasible with the current computational capability, and the simulation results offer insights to the understanding of the phenomenon. The most intriguing and fascinating phenomenon on Earth is life. Amazingly, life encompasses over more than twenty orders of magnitude in time scales from electron transfer, proton dislocation, on the scale of femtoseconds to organism lifetimes on the scale of years; and over ten orders of magnitude in spatial scales from electrons to organisms. Since life has so many scales in space and time, biology is subdivided into molecular biology, cellular biology, development biology, evolutionary biology, organismic biology, population biology, etc., not to mention emerging fields such as systems biology, ecology, and bioinformatics. Biology at each scale and level collects enormous amount information which can

easily outrace the theory needed to understand it. Quantitative understanding and theoretical prediction have emerged as a key discipline in the contemporary biology. Therefore, the complexity of life and the need for its understanding present an extraordinary opportunity for multiscale modeling and simulation.

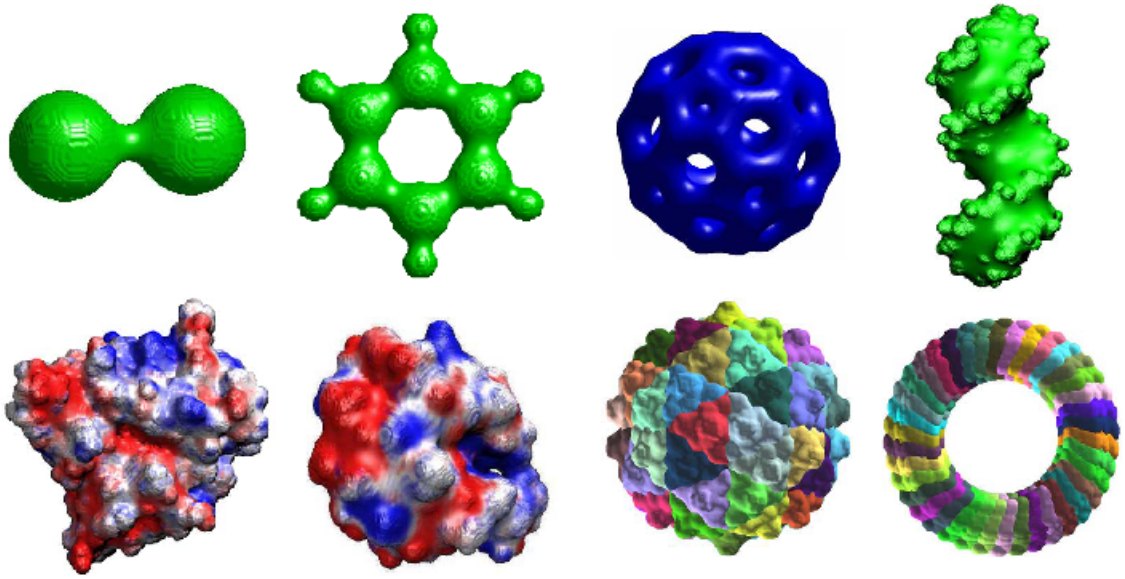

Figure 1: Minimal molecular surfaces (MMSs) constructed by geometric flows and their application to biomolecular analysis. First row: from left to right, MMSs of diatom, benzene, C60 and DNA; Bottom row: from left to right, surface electrostatic potential of protein 1b4l, surface electrostatic potential of protein 451c, MMS of nodamura virus (1nov), and MMS of toxin pneumolysin virus (2bk1).

2. DIFFERENTIAL GEOMETRY BASED MULTISCALE MODELS

Large chemical and biological systems such as fuel cells, ion channels, molecular motors, and viruses are of great importance to the scientific community and public health. Typically, these complex systems in conjunction with their aquatic environment pose a fabulous challenge to theoretical description, simulation, and prediction. In this work, we propose a differential geometry based multiscale paradigm to model complex macromolecular systems, and to put macroscopic and microscopic descriptions on an equal footing. In our approach, the differential geometry theory of surfaces and geometric measure theory are employed as a natural means to couple the macroscopic continuum mechanical description of the aquatic environment with the microscopic discrete atomistic description of the macromolecule. Multiscale free energy functionals, or multiscale action functionals are constructed as a unified framework to derive the governing equations for the dynamics of different scales and different descriptions. Two types of aqueous macromolecular complexes, ones that are near equilibrium and others that are far from

equilibrium, are considered in our formulations. We show that generalized Navier–Stokes equations for the fluid dynamics, generalized Poisson equations or generalized Poisson-Boltzmann equations for electrostatic interactions, and Newton's equation for the molecular dynamics can be derived by the least action principle. These equations are coupled through the continuum-discrete interface whose dynamics is governed by potential driven geometric flows. Comparison is given to classical descriptions of the fluid and electrostatic interactions without geometric flow basedmicro-macro interfaces. The detailed balance of forces is emphasized in the present work. We further extend the proposed multiscale paradigm to micro-macro analysis of electrohydrodynamics, electrophoresis, fuel cells, and ion channels.We derive generalized Poisson–Nernst–Planck equations that are coupled to generalized Navier–Stokes equations for fluid dynamics, Newton's equation for molecular dynamics, and potential and surface driving geometric flows for the micro-macro interface. For excessively large aqueous macromolecular complexes in chemistry and biology, we further develop differential geometry based multiscale fluid-electro-elastic models to replace the expensive molecular dynamics description with an alternative elasticity formulation.

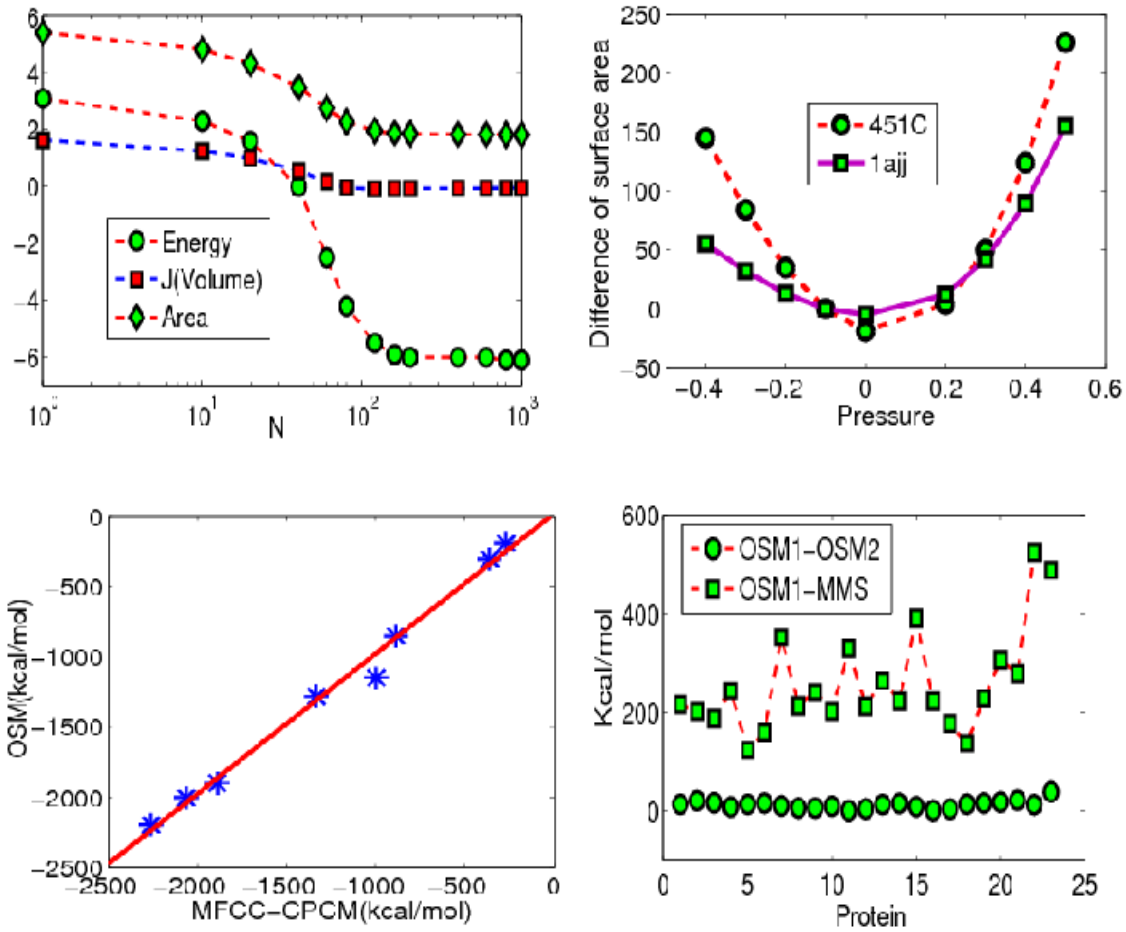

Figure 2, Results of differential geometry based solvation models. Upper left: Convergence history of the total energy, volume and area for protein 1ajj; Upper right: Impact of pressure to the surface areas indicating the MMS having the smallest surface area for protein 1ajj and 451C; Lower left: The correlation of electrostatic salvation free energies of 8 proteins between the MFCC-CPCM model and our optimized surface model (OSM); Lower right: Differences in solvation free energies for 23 proteins between computed with our optimized surface model (OSM) and our minimal molecular surface (MMS) model.

3. CONCLUSIONS

This work creates a fundamental paradigm, i.e., a differential geometry based multiscale variational framework, to address the aforementioned challenges in implicit solvent models and Poisson–Nernst–Planck (PNP) theories. Though these challenges originate from a large number of atoms and a variety of interactions in macromolecular systems including the aquatic environment, the lack of multiscale models to provide an appropriate description of the solvent has led to the current inadequacy in understanding. Utilizing the differential geometry theory of surfaces, we formulate a multiscale paradigm that puts the macroscopic description of the solvent and the microscopic description of solute on an equal footing. We describe the biomolecule in the atomistic detail and describe the transport properties of the solvent with mechanical variables. The interface of the macroscopic and microscopic subsystems is naturally described by the differential geometry theory of surfaces. We set up new free energy functionals for equilibrium analysis and action functionals for non-equilibrium studies of the solvation process.

REFERENCES

[1] Guo Wei Wei, Differential Geometry Based Multiscale Models, *Bulletin of Mathematical Biology*, 72, 1562–1622, 2010.

[2] Zhan Chen, Nathan Baker and G. W. Wei, Differential geometry based salvation model I: Eulerian formulation, *Journal of Computational Physics*, 229, 8231–8258, 2010.

2nd International Conference on Mathematical and Computational Biomedical Engineering - CMBE2011
March 30 - April 1, 2011, Washington D.C, USA
P. Nithiarasu and R. Löhner (Eds.)

Multiscale Processes in Analysis of Nanotube Reinforced Tissue Engineering Bioreactors

J. N. Reddy*, G. U. Unnikrishnan, and V. U. Unnikrishnan
Advanced Computational Mechanics Laboratory, Department of Mechanical Engineering,
Texas A&M University, College Station, TX-77843-3123 U.S.A
*e-mail: jnreddy@tamu.edu

ABSTRACT

Bioreactors simulate the physiological environment required for the development of tissue substitutes and play an important role in tissue engineering. The bioreactors maintain optimal environments for tissue growth by controlling the temperature, pH, and nourishment as in an *in-vivo* environment. The major operational difficulty of a bioreactor is maintaining adequate supply of nourishment to the growing tissue and removal of the waste materials from the scaffold. Therefore, transfer of nutrients through diffusion from the boundary of the scaffolds limits the size of the cultured tissue, making it clinically unusable. Hollow fiber membrane bioreactors (HFMB), which consist of a network of semi-permeable hollow fibers embedded in a porous scaffold, are capable of overcoming the limitations due to inadequate nutrient transport. In an HFMB the nutrient diffuses through the semi-permeable fiber membrane into the porous scaffold and similarly the waste materials get transferred into the membrane to be removed at the end of bioreactor. Estimates of nutrient distributions in HFMB are available primarily for the scaffold region only and does not consider the fluid-scaffold interactions. In this work, we present a new model for analyzing the movement of nutrients in a scaffold from the fluid using fluid-biphasic finite element models.

In the first part of this talk, we discuss the finite element framework based on biphasic theory to study the open fluid domain flow over a porous channel. The model considers open channel-porous domain as a single continuous domain, with the momentum and mass transfer occurring at the interface. The nutrient transfer is then studied by incorporating convection-diffusion equations into the finite element framework. The developed finite element model would be a great tool in the study of both fluid flows through the porous-open channels as well as optimizing the nutrient distribution in the HFMB.

In the second part of this talk, a multiscale modeling strategy to estimate the properties of carbon nanotube polymeric scaffold is discussed. Carbon nanotube polymeric scaffolds for tissue engineering applications have gained attention recently due to the enhanced mechanical properties of carbon nanotubes. The extremely high mechanical strength of carbon nanotubes is found to result in a nanofiber capable of withstanding tremendous mechanical stresses. The properties of these nano-biomaterials can be obtained from various experimental investigations, but a thorough understanding of the properties and its interactions with the surrounding materials can only be obtained by advanced computational models. The analysis is carried out at the atomistic scale using MD simulations, and the properties are scaled-up using homogenization schemes. A nonlinear hyperelastic material based homogenization is also developed utilizing the experimentally obtained deformation profile of nanotube systems. The effective property of the nanofiber scaffold is then incorporated in the finite element model to analyze the influence of the property on the behavior of HFMB.

Acknowledgement: The authors gratefully acknowledge the support of this research through Oscar S. Wyatt Endowed Chair funds at Texas A&M University.

2nd International Conference on Mathematical and Computational Biomedical Engineering - CMBE2011
March 30 - April 1, 2011, Washington D.C, USA
P. Nithiarasu and R. Löhner (Eds.)

A dimensionally heterogeneous model for the entire cardiovascular system based integrated with a model of the autonomic nervous system

P. J. Blanco[⋆,⋆⋆] **and R. A. Feijóo**[⋆,⋆⋆]
[⋆]LNCC - National Laboratory for Scientific Computing
[⋆⋆]INCT-MACC - National Institute for Science and Technology in Medicine Assisted by Scientific Computing,
Av. Getúlio Vargas 333, Quitandinha, 25651-075, Petrópolis, RJ, Brazil,
E-mail: pjblanco@lncc.br; feij@lncc.br

SUMMARY

In the present work a computational model of the entire closed cardiovascular system (CVS) interacting with the autonomic nervous system (ANS) is developed. In this model the arterial tree is described by a one dimensional model in order to simulate the propagation phenomena that takes place at the larger arterial vessels. The inflow and outflow locations of this 1D model are coupled with proper lumped parameter descriptions (0D model) of the remainder part of the circulatory system. We incorporate the peripheral circulation in arterioles and capillaries by using a 0D 3-component Windkessel models. In turn, the whole peripheral circulation converges to the venous system through the upper and lower parts of the body, for which we set two corresponding major venous circulation circuits. Then, the right and left heart circulations, as well as the pulmonary circulation, are accounted by means of 0D models. Particularly for the four cardiac valves we employ a valve model allowing for the regurgitation phenomenon during the valve closing. Finally, the 0D model of the left ventricle is coupled with the inflow boundary in the 1D model, closing the system. In addition, we consider the existence of 3D models accounting for the detailed aspects of blood flow in specific vessels of interest. The resulting CVS model (3D-1D-0D coupled model) forms a closed loop network capable of taking into account the interaction between the global circulation (1D-0D models) and the local hemodynamics (3D models). Furthermore, a model for the ANS ensuring the inclusion of the main reflex branches participating in the nervous reflex regulation is also developed. The interaction between the proposed CVS and ANS Models results in a framework capable to simulate the roles of different underlying mechanisms in the hemodynamics regulation. Situations of interest are presented showing the capabilities of the model.

Key Words: *closed-loop system, dimensionally-heterogeneous models, multi-scale analysis, autonomic nervous system, baroreflex regulation.*

1 INTRODUCTION

Our aim in this work is to develop a computational model of the entire closed-loop of the CVS integrated with a model for the ANS in such a way that changes in the physiological state of the CVS will activate short-term control mechanisms which play a leading role in maintaining hemodynamics state levels through regulation of total blood volume, heart rate, vascular tone, among others.

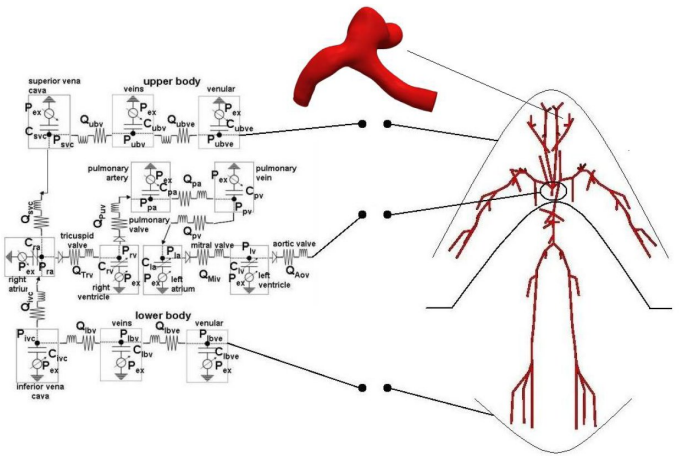

Figure 1: Scheme of the 1D-0D closed-loop model with a 3D patient-specific aneurism embedded in it.

2 THE MODEL FOR THE CARDIOVASCULAR SYSTEM

A computational model of the entire cardiovascular system is established accounting for specific vessels, systemic arteries, systemic veins, pulmonary and heart circulation and real valve functioning. In this context we perform the integration of different levels of circulation. This approach is usually recognized as multiscale modeling of the cardiovascular system. Following [1, 5] the arterial tree is described by a one dimensional model with 128 arterial segments in order to simulate the propagation phenomena that takes place at the larger arterial vessels. The inflow and outflow locations of this 1D model are coupled with proper lumped parameter descriptions (0D model) of the remainder part of the circulatory system. At each outflow point we incorporate the peripheral circulation in arterioles and capillaries by using a 0D three-component Windkessel model (see [12]). The whole peripheral circulation converges to the venous system through the upper and lower parts of the body (superior and inferior vena cava), with corresponding 0D models for such parts (in the spirit of [9]). Then, the right and left heart circulation, as well as the pulmonary circulation, are also accounted for by means of 0D models. Particularly we point out the modeling of the four heart valves, which is carried out by using a non-linear model which allows for the regurgitation phase during the valve closing according to [6]. Finally, the 0D model of the left ventricle is coupled with the inflow boundary in the 1D model, closing the cardiovascular loop. The entire 0D model which performs the coupling between the outflow and inflow in the arterial tree consists of 14 compartments. Furthermore and following [2, 13], we can consider the existence of 3D models accounting for the detailed aspects of blood flow in specific vessels of interest (see Figure 1).

The resultant integrated model (0D-1D-3D coupled model) forms a closed loop network that accounts for the interaction between the global circulation (0D-1D Models) and the local hemodynamics (3D models). Summing up, this is carried out by putting together the following mathematical representations: (i)1D Models for the larger systemic arteries; (ii) 0D Models (R - C windkessel models) for the arterioles and capillaries; (iii) 0D Models (R - L - C models) for venules and veins to model the upper and lower body parts; (iv) 0D Models (R - L - C models) for inferior and superior vena cava, pulmonary veins and pulmonary arteries; (v) 0D models (elastance models) for each of the four heart chambers; (vi) 0D Models (non-linear non-ideal diode models) to approximate the behavior of the tricuspid, pulmonary, mitral and aortic valves; and (vii) 3D Models for the specific vessels of interest. The whole model with all the elements is presented in Figure 1.

3 A MODEL FOR THE AUTONOMIC NERVOUS SYSTEM

Despite the fact that the mechanisms by which the ANS works still remain incompletely understood, for modeling purposes it is usually divided it into four functional compartments. Our model is based on several models proposed in the literature in particular: (i) the model proposed by Ursino [14], (ii) Olufsen et al. [10] and (iii) Liang et al. [8] and includes the receptors at the afferent end, the CNS, the effectors responsive to control signals, and the sympathetic and parasympathetic nerves.

4 NUMERICAL SIMULATIONS

In the context introduced in the previous paragraphs, this work presents a computational model of the entire CVS integrated with a model of the ANS borrowing the most important features of the different models available in the literature. Thus, this integrative model has more descriptive capabilities than the models currently available in the literature.

The parameters used in the 1D-0D model have been assigned or estimated based on the data reported in [3, 4, 7, 8-11, 15]. The values of the parameters used in model for the peripheral circulation, the heart model and model of the cardiac valves are based on the data reported in [3, 4, 9]. The parameters used in the 1D model of the arterial tree and those corresponding to the Windkessel elements that account for the arterioles and capillaries has been built according to the guidelines given in [1,12]. The parameters for the ANS have been also estimated based on data reported in [8, 10, 14].

The numerical approximation of the model for the arterial tree network, eventually with an embedded 3D model, is carried out as in [2, 13]. The discretization of the 0D models is done following a second order Crank-Nicolson method combined with fixed point iterations for dealing with the non-differentiable non-linearity of the valve models.

In particular, in Figure 2 and Figure 3 show the behavior of the 1D-0D entire model described in this work and the pressure and flow rate at the proximal coupling interface of the patient-specific aneurism embedded in it.

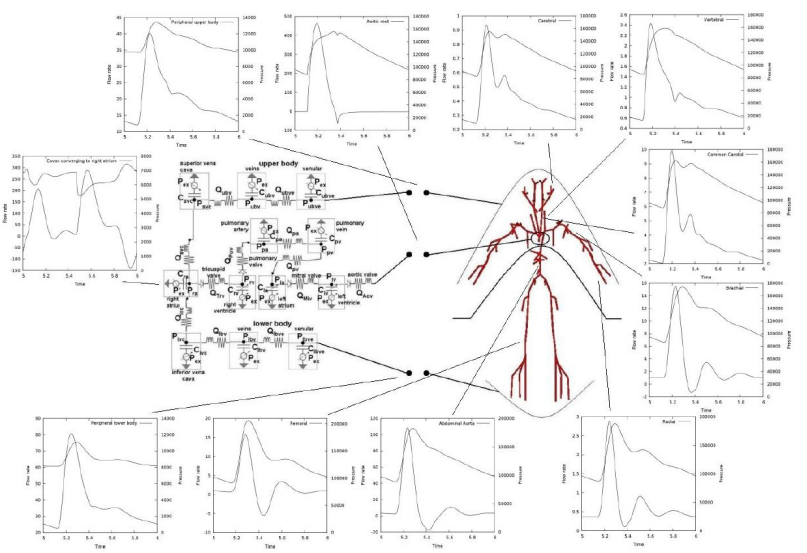

Figure 2: Results throughout the entire 1D-0D cardiovascular model.

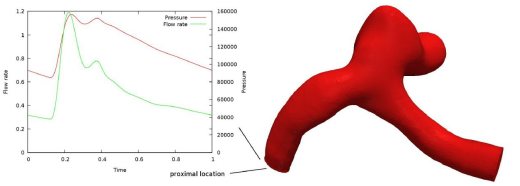

Figure 3: Pressure and flow rate at the proximal coupling interface.

REFERENCES

[1] A.P. Avolio. Multi-branched model of the human arterial system. Med. Biol. Engrg. Comp., 18:709-718, 1980.

[2] P. J. Blanco , R. A. Feijóo, and S. Urquiza. A unified variational approach for coupling 3D-1D models and its blood flow applications. Comp. Meth. Appl. Mech. Engrg., 196:4391-4410, 2007.

[3] T. Heldt, E.B. Shim, R.D. Kamm, and R.G. Mark. Computational modeling of cardiovascular response to orthostatic stress. J. Appl. Physiol., 92:1239-1254, 2002.

[4] F.C. Hoppensteadt and C.S. Peskin. Modeling and Simulation in Medicine and the Life Sciences. Texts in Applied Mathematics, Springer, 2002.

[5] T.J.R. Hughes. A Study of the One-Dimensional Theory of Arterial Pulse Propagation. PhD thesis, University of California, Berkeley, 1974.

[6] T. Korakianitis and Y. Shi. Numerical simulation of cardiovascular dynamics with healthy and diseased heart valves. J. Biomech., 39:1964-1982, 2006.

[7] F. Liang and H. Liu. A closed-loop lumped parameter computational model for human cardiovascular system. JSME International Journal, 48:Series C, 2005.

[8] F. Liang and H. Liu. Simulation of hemodynamic responses to the valsalva maneuver: An integrative computational model of the cardiovascular system and the autonomic nervous system. J. Physiol. Sci., 56:45-65, 2006.

[9] F. Liang and S. Takagi. Multi-scale modeling of the human cardiovascular system with applications to aortic valvular and arterial stenoses. Med. Biol. Eng. Comput., 47:743-755, 2009.

[10] M.S. Olufsen, J.T. Ottesen, H.T. Tran, L.M. Ellwein, L.A. Lipsitz, and V. Novak. Blood pressure and blood flow variation during postural change from sitting to standing: model development and validation. J. Appl. Physiol., 99:1523-1537, 2005.

[11] G. Pontrelli. A multiscale approach for modelling wave propagation in an arterial segment. Comp. Meth. Biomech. Biom. Engrg., 7:79-89, 2004.

[12] N. Stergiopulos, D.F. Young, and T.R. Rogge. Computer simulation of arterial ow with applications to arterial and aortic stenoses. J. Biomech., 25:1477-1488, 1992.

[13] S. Urquiza , P. J. Blanco , M. J. Vénere , and R. A. Feijóo. Multidimensional modeling for the carotid blood flow. Comp. Meth. Appl. Mech. Engrg., 195:4002-4017, 2006.

[14] M. Ursino. Interaction between carotid baroregulation and the pulsating heart: a mathematical model. Am J Physiol., 275:H1733-47, 1998.

[15] K. van Heusden, J. Gisolf, W.J. Stok, S. Dijkstra, and J. M. Karemaker. Mathematical modeling of gravitational effects on the circulation: importance of the time course of venous pooling and blood volume changes in the lungs. Am. J. Physiol. Heart Circ. Physiol., 291:H2152-H2165, 2006.

2nd International Conference on Mathematical and Computational Biomedical Engineering - CMBE2011
March 30 - April 1, 2011, Washington D.C, USA
P. Nithiarasu and R. Löhner (Eds.)

Application of Reduced Order Modeling for Mechanical and Electrical aspects of the Cardiovascular System.

Jean-Frédéric Gerbeau
INRIA Paris-Rocquencourt, 78153 Le Chesnay Cedex, France, jean-frederic.gerbeau@inria.fr

Key Words: *blood flow, electrophysiology, reduced order modeling.*

SUMMARY

We are interested in the application of reduced order modeling by proper orthogonal decomposition (POD) in two different aspects of the modeling of the cardiovascular system.

The first application deals with blood flows. We will present a method which combines atlas-based techniques and model reduction approaches in order to perform faster patient-specific simulations, based on prior simulations on an average anatomy [1].

We will also consider an application in cardiac electrophysiology. We will show how reduced order modeling can be combined with evolutionary algorithms in order to estimate, from an electrocardiograms, the parameters of a model of the electrical activity of the heart.

Reference

[1] McLeod, Caiazzo, Fernandez, Mansi, Vignon-Clementel, Sermesant, Pennec, Boudjemline, Gerbeau, *Atlas-Based Reduced Models of Blood Flows for Fast Patient-Specific Simulations*, Lecture Notes in Computer Science, Vol. 6364, p 95-103, 2010, Springer.

2nd International Conference on Mathematical and Computational Biomedical Engineering – CMBE2011
March 30 – April 1, 2011, Washington D.C., USA
P. Nithiarasu and R. Löhner (eds)

G space theory and weakened weakform (W2) methods for efficient and certified solutions for bio-systems

G. R. Liu
School of Aerospace Systems
University of Cincinnati, USA
liugr@uc.edu

SUMMARY

This talk introduces the G space theory and some of the weakened weak (W2) formulations for solving mechanics problems in bio-systems, considering large deformation in soft bio-tissues submerged in fluids. Important properties and inequalities for G spaces are proven, leading to the so-called weakened weak (W2) formulations that guarantee stable and convergent solutions. Bound properties of the W2 formulations will also be discussed. Examples of red-blood-cells traveling in micro-veins will be simulated using a typical W2 method: edge-based smoothed finite element method or ES-FEM that works well with triangular/tetrahedral mesh and less sensitive to mesh quality and much more efficient computationally compared to the standard FEM.

Key Words: *G space theory, W2 formulation, solution bounds, Blood flow, S-FEM.*

1. INTRODUCTION

Bio-systems are extremely sophisticated in nature. Computer modelling for such systems is a must for studying and examining the behaviour of the systems, diagnostics, healthy monitoring, and "engineering" illness treatments and prevention. The necessary requirements for an effective computational method have now become stability, convergence, automation, solution certification, adaptation, highly efficient and even real-time computation. This talk introduces a G space theory [1]-[4] and some of the weakened weak (W2) formulations [3][4] for solving mechanics problems in bio-systems with extremely large deformation in soft bio-tissues submerged in fluids.

2. The Theory

The G space theory is a relatively new theory in functional analysis of mechanics problems. The theory allows the use of a class of discontinuous functions in creating computational methods. It is a basic theory for a unified formulation of a wide class of compatible and incompatible methods based on FEM [5] and meshfree settings [6][7]. Important properties and inequalities for G spaces are proven, leading to the so-called weakened weak (W2) formulation that guarantees stable and convergent solutions. We then present some possible W2 models that meet all these challenges: 1) linearly conformability ensuring the stability and convergence; 2) softening effects leading to certified solutions [13][14] and real-time computational models; 3) insensitivity to the

quality of mesh allowing effective uses of triangular/tetrahedral meshes best suited for automatic adaptive analyses.

3. Applications

A large number of benchmarking examples and practical examples will be presented to examine the theory and various numerical models, including material behaviour at various extreme situations, dynamic behaviour and interactions of red blood cells, inverse identification of material properties and cracks in engineering structural systems, and integrity assessment of dental implant systems via inverse analysis with real-time computation. Examples of red-blood-cells traveling in micro-veins will be simulated using a typical W2 method, smoothed finite element method [9]-[12]. Figure 1 show a simulated result of a snapshot of an army of 5 Red blood cells travelling in a simulated micro-vein. The details for fluid-structure interaction problems using the S-FEM are given in [15].

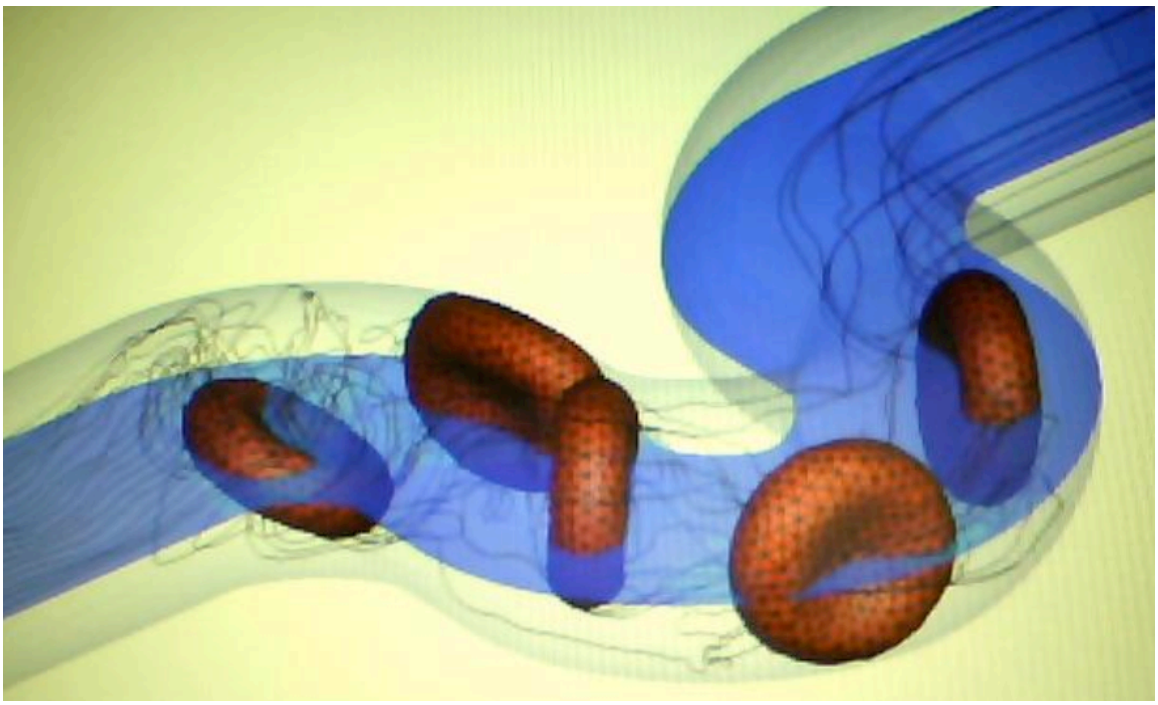

Figure 1. A snapshot of an army of 5 Red blood cells travelling in a simulated micro-vein.

4. CONCLUSIONS

The W2 methods offer a class of effective methods for solving mechanics problems in bio-systems, considering large deformation in soft bio-tissues submerged in fluids. These methods are found working well with triangular/tetrahedral mesh and less sensitive to mesh quality and much more efficient computationally compared to the standard FEM.

5. ACKNOWLEDGEMENTS

This work was partially completed at the National University of Singapore (NUS) supported by A*Star, Singapore. It is also partially supported by the Open Research Fund Program of the State

Key Laboratory of Advanced Technology of Design and Manufacturing for Vehicle Body, Hunan University, P.R.China under the grant number 40915001.

REFERENCES

[1] Liu, G. R., On a G space theory. *International Journal of Computational Methods*, 6(2): 257-289, 2009.

[2] Liu, G. R., Zhang, G. Y., A normed G space and weakened weak (W^2) formulation of cell-based smoothed point interpolation method. *International Journal of Computational Methods*, 6(1): 147-179, 2009.

[3] Liu, G. R., A G space theory and a weakened weak (W^2) form for a unified formulation of compatible and incompatible methods: Part I theory. *International Journal for Numerical Methods in Engineering*, 81: 1093-1126, 2010.

[4] Liu, G. R., A G space theory and a weakened weak (W^2) form for a unified formulation of compatible and incompatible methods: Part II applications to solid mechanics problems. *International Journal for Numerical Methods in Engineering*, 81: 1127-1156, 2010.

[5] G.R. Liu, and Quek, S.S., *Finite Element Method: a practical course*, BH, Burlington, MA, 2003.

[6] Liu GR, *Meshfree Methods – Moving beyond the finite element method*, 2nd Ed., CRC Press, 2009.

[7] Liu, G. R., Liu, M. B., *Smoothed Particle Hydrodynamics—A Meshfree Practical Method*. World Scientific: Singapore, 2003.

[8] J.S. Chen, C.T. Wu, S. Yoon, Y. You, A stabilized conforming nodal integration for Galerkin mesh-free methods. *Int. J. Numer. Mech. Engrg.*, 50: 435-466, 2001.

[9] Liu GR and Nguyen Thoi Trung, *Smoothed Finite Element Methods*, CRC Press, 2010.

[10] Liu, G. R., Dai, K. Y. and Nguyen, T. T. (2007). A smoothed finite element method for mechanics problems. *Computational Mechanics*; 39: 859-877.

[11] G.R. Liu, T. Nguyen-Thoi, H. Nguyen-Xuan, K.Y. Lam. A node-based smoothed finite element method (NS-FEM) for upper bound solution to solid mechanics problems. *Computers and Structures*, 87: 14-26, 2009.

[12] G.R. Liu, X. Xu, G.Y. Zhang, Y. T. Gu, An extended Galerkin weak form and a point interpolation method with continuous strain field and superconvergence using triangular mesh. *Computational Mechanics*, 43: 651-673, 2009.

[13] Liu, G. R. and Zhang, G. Y., Upper bound solution to elasticity problems: A unique property of the linearly conforming point interpolation method (LC-PIM). *International Journal for Numerical Methods in Engineering*, 74: 1128-1161, 2008.

[14] Zhang, G. Y., Liu, G. R., Nguyen, T. T., Song, C. X., Han, X., Zhong, Z. H., Li, G. Y., The upper bound property for solid mechanics of the linearly conforming radial point interpolation method (LC-RPIM). *International Journal of Computational Methods*, 4(3): 521-541, 2007.

[15] Z.Q. Zhang and G.R. Liu, Immersed deformable solids method for Fluid-Structure Interaction using Characteristic-based Algorithm and Smoothed Finite Element Method, *International Journal of Computational Method*s. 2010 (submitted).

Mini-Symposia

2nd International Conference on Mathematical and Computational Biomedical Engineering - CMBE2011
March 30 - April 1, 2011, Washington D.C, USA
P. Nithiarasu and R. Löhner (Eds.)

A numerical study on the feasibility of aneurysm property identification at the presence of unknown stress-free geometry

Jia Lu, Xuefeng Zhao
Department of Mechanical and Industrial Engineering, Center for Computer Aided Design,
The University of Iowa, Iowa City, IA 52242-1527, jia-lu@uiowa.edu

SUMMARY

Characterizing aneurysm properties in vivo presents a tremendous challenge. Aside from the limitation of image resolution, a pressing issue is that the pulsation data do not expose the stress-free geometry. This is compounded by the nonlinearity, anisotropy, and heterogeneity of the constitutive behavior. Recently, the authors proposed a pointwise approach for characterizing thin tissues and tested the applicability numerically in cerebral aneurysm, under the assumption that the stress geometry is known. This article further evaluates the feasibility for the case of unknown stress-free geometry. An image-based aneurysm sac is considered. The wall tissue is described as nonlinear anisotropic hyperelastic material with spatially varying parameters. Forward finite element simulation is conducted to generate a series of deformed configurations between the diastolic and the systolic pressures. Taking these mesh data as input, the material properties are identified together with the zero-stress geometry using the pointwise method. The recovered parameters are in good agreement with their reference values. The predictability of the identified model is evaluated through a forward analysis at an elevated pressure; the nodal displacement deviation is found to be within 0.6% over the entire mesh.

Key Words: *Cerebral aneurysms, tissue property, pointwise method, in vivo identification.*

1 INTRODUCTION

The elastic property of the aneurysm wall is fundamental for understanding the mechanical behavior the lesion, and is a biomarker for vascular tissue fragility. A possible approach for characterizing vascular tissues, although not feasible presently due to the limitation of image resolution. is to assess the wall properties non-invasively from in vivo pulsation data and blood pressure measurement. Hopefully, the advent of imaging technology and/or image registration method will eventually provide sufficiently accurate image data for this inverse problem. Aside from the image limitations, there are several obstacles on the mechanics side that can also hamper this approach. The first one relates to the fact that the visible wall motion, which corresponds to pulsation between the diastolic and the systolic pressures, does not expose the stress-free geometry of the lesion. To characterize the tissue properties requires one to take into account of the unknown stress-free geometry. Another difficulty lies in material heterogeneity. The elastic properties of the wall tissue normally varies spatially due to the difference in growth and remodeling history and pathological condition. In the traditional optimization-based approaches, the parameters over the entire sac must be optimized simultaneously. This can easily leads to prohibitively expensive computations and lack of algorithmic robustness.

Recently, the authors developed a pointwise identification method to address heterogeneous properties [1]. In [2], a numerical study was conducted to examine this method in the context of aneurysm identification. An imaged-based sac was considered. The wall tissue was described by the nonlinear structural model by Kroon et al. [4]. We used simulated wall motion to inversely characterize the property maps. The novelty of the pointwise method lies in that the stress computation and parameter identification are un-coupled. The stress data were acquired independently of the material parameters in question. The optimization problem is formulated individually at each materials point and solved independently. The number of parameters for optimization is fixed.

This pointwise approach provides a suitable framework for dealing with unknown reference geometries, at least in theory. As is well-understood in classical mechanics, the stress-free configuration of an elastic body is a local concept, because the stress at a material point depends only on the local motion in the vicinity of that point. As such, it is possible to represent the stress-free configuration pointwisely with appropriate geometric parameters [3]. For a thin membrane, the local stress free configuration can be represented by surface metric tensor containing three parameters. The geometric parameters have distinctly different pattern of influence in comparing to the elasticity parameters, and therefore it is possible to identify them together with the elasticity parameters. In the pointwise approach, this amounts to adding three parameters in the optimization problem, which should be readily handled. In this study, we report a numerical test on a nonlinear anisotropic heterogeneous aneurysm model.

2 METHOD AND RESULTS

Kinematics

The aneurysm wall is described as an elastic membrane, and the convected surface coordinate setting in [1, Part I] is followed. With respect to the surface coordinate system, the Cauchy-Green deformation tensor is written as

$$\mathbf{C} = g_{\alpha\beta}\mathbf{G}^{\alpha} \otimes \mathbf{G}^{\beta}. \tag{1}$$

The meanings of various quantities are described in [1]. This tensor is regarded as a metric tensor that describes the deformed geometry, as the fundamental form $ds^2 = d\mathbf{X} \cdot \mathbf{C}d\mathbf{X}$ characterizes the deformed length of a reference line element $d\mathbf{X}$. The reference configuration is an accessible configuration between the diastolic and the systolic configurations, therefore pre-strained, and the Euclidean geometry does not describe the undistorted (natural) geometry. We assume that at every material point there is a metric tensor $\mathfrak{G}$ describing the natural geometry, in the sense that the fundamental form $dS^2 = d\mathbf{X} \cdot \mathfrak{G}d\mathbf{X}$ characterizes the undistorted length of the line element $d\mathbf{X}$. In the surface coordinate system, $\mathfrak{G}$ admits the form

$$\mathfrak{G} = \mathfrak{G}_{\alpha\beta}\mathbf{G}^{\alpha} \otimes \mathbf{G}^{\beta}. \tag{2}$$

The change of local geometry from the natural to the deformed state is completely described by the tensors $\mathbf{C}$ and $\mathfrak{G}$. The square stretch of a line element alone the direction $\mathbf{N}$ is given by

$$\lambda^2 = \frac{N^{\alpha} g_{\alpha\beta} N^{\beta}}{N^{\delta}\mathfrak{G}_{\delta\gamma}N^{\gamma}}. \tag{3}$$

The strain invariants I_1 and I_2, which measure respectively the average square-stretches of all line elements emanating at a point and the square of the area ratio. are found to be

$$I_1 = g_{\alpha\beta}\mathfrak{G}^{\alpha\beta}, \qquad I_2 = \frac{\det[g_{\alpha\beta}]}{\det[\mathfrak{G}_{\alpha\beta}]}. \tag{4}$$

Therefore, any constitutive equations represented as functions of I_2, I_2, and line stretches can be readily expressed as functions of $\mathbf{C}, \mathfrak{G}$ and a family of fiber directions, $\mathbf{N}_I$.

Constitutive model

We utilize the aneurysmal tissue model proposed by Kroon and Holzapfel [4] to describe the wall elasticity. The strain energy function of this model is

$$w = \sum_{I=1}^{8} \frac{k_I}{8a} \left(exp[a(\lambda_I^2 - 1)^2] - 1 \right). \tag{5}$$

The stress components $t^{\alpha\beta}$ are given by

$$Jt^{\alpha\beta} = \sum_{I=1}^{8} \frac{k_I}{2} exp\left[a(\lambda_I^2 - 1)^2\right](\lambda_I^2 - 1) \left(N_I^\delta G_{\delta\gamma} N_I^\gamma \right)^{-1} N_I^\alpha N_I^\beta. \tag{6}$$

The model assumes that there are eight families of collagen fibers for which λ_I are the corresponding stretches, computed according to $\lambda_I^2 = \frac{N_I^\alpha g_{\alpha\beta} N_I^\beta}{N_I^\delta G_{\delta\gamma} N_I^\gamma}$ where $\mathbf{N}_I$ is the direction vector of the Ith fiber. k_I, $I = 1, 2, ..., 8$, define the fiber stiffness of these fibers, a is a dimensionless material constant. It is further assumed that the fiber stiffness k_I are functions of two elastic parameters E_1 and E_2 which designate the tissue stiffness in the material's principal symmetry directions. Once E_1 and E_2 are given, the fiber stiffness parameters are determined.

Numerical experiments

The sac in Figure 1 was considered. Forward finite element analysis was conducted to generate 17 configurations uniformly placed between $80\ mmHg$ (diastolic) and $160\ mmHg$ (systolic) pressures, using an assumed property distribution. The elasticity parameters were carefully selected to ensure that strains relative to the diastolic configuration are 1-2.5%, which is consistent with the reported physiological range. The parameters E_1 and E_2 and the principal fiber direction were prescribed to vary continuously across the sac. Two patterns of variation were considered, one has a linearly decreasing stiffness from the neck to the dome, and the other contains a weaker region in the dome. Inverse stress analysis [5] was applied individually to each of the pressurized configuration to compute the wall stresses. The diastolic state was taken as the reference, relative to which the deformation tensor $\mathbf{C}$ were computed. The reference configuration was endowed with an unknown metric tensor, represented by three parameters $\mathfrak{G}_{11}$, $\mathfrak{G}_{22}$, and $\mathfrak{G}_{12}$ at every Gauss point. The stress function (6), containing the material parameters E_1, E_2, a, the angle Θ of the principal fiber direction, and the metric parameters $\mathfrak{G}_{11}$, $\mathfrak{G}_{22}$, $\mathfrak{G}_{12}$, were fitted pointwisely to the inversely computed stress data at every Gauss point. A sequential quadratic programming software (SNOPT) was utilized to solve the optimization problem.

Table 1 presents the means and standard deviations of the pointwise percentage difference between the identified and the prescribed parameter values. The means are less than 4% for the major parameters. The metric component $\mathfrak{G}_{12}$ are close to zero and therefore there relative error are larger ($> 100\%$ for most points). However, the error norm of $\mathfrak{G}$ (the last column in Table 1) remains small, indicating that the seemingly large $\mathfrak{G}_{12}$ error is in fact immaterial. A forward verification was also conducted to predict the deformed configuration at $170\ mmHg$ using the identified material model. A comparison to the the predictions of the prescribed model shows that the nodal displacement differences are within 0.6%.

3 CONCLUSIONS

We tested the feasibility of identifying heterogeneous aneurysms properties without knowing the stress-free configuration. The stress-free configuration was represented locally by three parame-

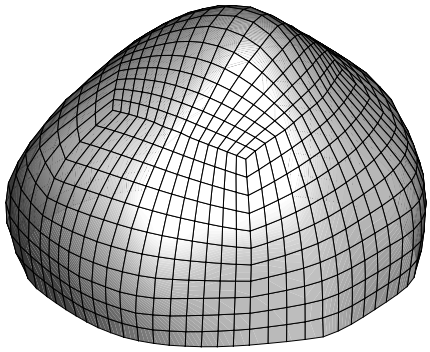

Figure 1: The aneurysm sac considered in this study.

Table 1: Mean, standard deviation, minimum and maximum of the identification error.

	Err(E_1)	Err(E_2)	Err(a)	Err($\mathfrak{G}_{11}$)	Err($\mathfrak{G}_{22}$)	Err($\|\mathfrak{G}\|$)
Mean (%)	1.64	2.21	3.86	0.10	0.09	0.056
SD (%)	1.45	1.66	4.73	0.095	0.074	0.05
Min (%)	1.43E-3	1.95E-3	2.65E-3	6.16E-5	9.57E-5	1.37E-4
Max (%)	11.04	15.09	24.51	0.86	0.74	0.395

ters, which were inversely identified together with the unknown material parameters. The numerical experiment demonstrated the effectiveness of this method.

REFERENCES

[1] J. Lu, X. Zhao, and X. Chen, Pointwise identification of elastic properties in nonlinear hyperelastic membranes. Part I: Theoretical and computational developments; *Journal of Applied Mechanics*, 76, 061013/1-061013/10, 2009. Part II: Experimental validation, *ibid*, 76, 061014/1-061014/8, 2009.

[2] X. Zhao, M. L. Raghavan, and J. Lu, Identifying heterogeneous anisotropic properties in cerebral aneurysms: a pointwise approach. *Biomechanics and Modeling in Mechanobiology*, in press, DOI 10.1007/s10237-010-0225-7.

[3] J. Lu, A covariant constitutive theory for pre-strained anisotropic hyperelastic solids. *Mathematics and mechanics of Solids*, in review, http://css.engineering.uiowa.edu/˜jialu.

[4] M. Kroon, G. A. Holzapfel, A new constitutive model for multilayered collagenous tissues. *Journal Biomechanics*, 41, 2766-2771, 2008.

[5] J. Lu, X. Zhou, and M. L. Raghavan, Inverse method of stress analysis for cerebral aneurysms. *Biomechanics and Modeling in Mechanobiology*, 7:477-486 2009.

2nd International Conference on Mathematical and Computational Biomedical Engineering – CMBE2011
March 30 – April 1, 2011, Washington D.C., USA
P. Nithiarasu and R. Löhner (eds)

VORTEX CORELINE DETECTION FOR THE ANALYSIS OF BLOOD FLOW PATTERNS IN CEREBRAL ANEURYSMS

Greg Byrne*, Fernando Mut*, and Juan R. Cebral*
*Center for Computational Fluid Dynamics, George Mason University,
4400 University Drive, Fairfax, VA 22030, USA, jcebral@gmu.edu

SUMMARY

We construct one-dimensional sets known as vortex corelines for computational fluid dynamic (CFD) simulations of blood flow in patient specific cerebral aneurysm models. These sets identify centers of swirling blood flow that may play an important role in the biological mechanisms causing aneurysm growth, rupture, and thrombosis. We highlight three specific applications in which vortex corelines are used to assess flow complexity and stability in cerebral aneurysms, validate numerical models against PIV-based experimental data, and analyze the effects of flow diverting devices used to treat intracranial aneurysms.

Key Words: *cerebral aneurysm, hemodynamics, vortex coreline detection.*

1. INTRODUCTION

Blood flows in cerebral aneurysms are characterized by three-dimensional rotating flow structures. It has been speculated that swirling flows play an important role in the mechanisms governing the natural history of intracranial aneurysm and their thrombosis. These flow structures are identified through the use of vortex corelines; one-dimensional sets that pass through centers of swirling flow. In this work we study the effects of swirling flow by using vortex corelines in three strategic areas of research; assessing the risk of aneurysm rupture, treatment with flow diverters, and validation against experimental data.

Our risk assessment study uses vortex corelines as a way to characterize blood flow patterns and look for signatures of swirling flow that could be linked to aneurysmal growth, bleb formation, or rupture. In our treatment study, we use vortex corelines to identify vortical structures in the aneurysm before and after the deployment of flow diverting stents. Analyzing changes in the flow structure is important for understanding the long term effects of flow diverting devices since thrombus formation and organization are thought to be related to flow stasis and recirculation within the aneurysm sac [1]. Our validation study uses vortex corelines to compare the large-scale flow structures generated by computational fluid dynamic (CFD) simulations to those generated by experimental in vitro particle image velocimetry (PIV) data.

2. METHODS

Vortex corelines are defined in this work by the locus of points that satisfy the two following equivalent properties [2, 3]: (1) the velocity and acceleration vectors are parallel, and (2) the instantaneous streamline curvature is zero. Mathematically, these conditions can be expressed in the form of an eigenvalue equation:

$$U \cdot u = \lambda u \tag{1}$$

that is satisfied by points in the computational domain where the velocity vector u is an eigenvector of the velocity gradient tensor U. Corelines are computed algorithmically in the

computational domain using the eigenvector method of Sujudi and Haimes [4]. For each tetrahedral element, the following steps are applied:

- Compute and diagonalize the Jacobian matrix for the host element.
- Verify that the eigenvalue spectrum consists of one real eigenvalue and a pair of complex conjugate eigenvalues. If this condition is not satisfied, skip to the next element.
- Form a reduced velocity vector *w* at each node in the element by subtracting the components of the velocity that point along the eigenvector associated with the real eigenvalue ξ_R. The reduced velocity can then be expressed as: $w = u - (u \cdot \xi_R)\,\xi_R$.
- For each face on the element, use linear interpolation to determine if there is a point on that face where the reduced velocity is zero. If two faces are found to have a zero point, the element is marked to contain a coreline segment.

This procedure is used to construct vortex core lines in a variety of patient-specific cerebral aneurysm geometries derived from 3D medical images and physiologic flow conditions.

RESULTS

Characterization of Cerebral Aneurysm Blood Flow Patterns

The first application illustrates the use of vortex corelines for characterizing blood flow patterns in cerebral aneurysms. Previous studies have suggested that the flow pattern complexity and stability may be associated with aneurysmal rupture [5]. Flow patterns were classified as simple if they contained one main vortex structure and complex if they had more than one vortex. If the vortex structures remained stationary and were not created or destroyed during the cardiac cycle the flow pattern was classified as stable, otherwise as unstable. This analysis was done by inspection of flow visualizations created using streamlines. The use of vortex corelines can greatly aid this flow analysis and categorization. Two examples are presented in Figure 1.

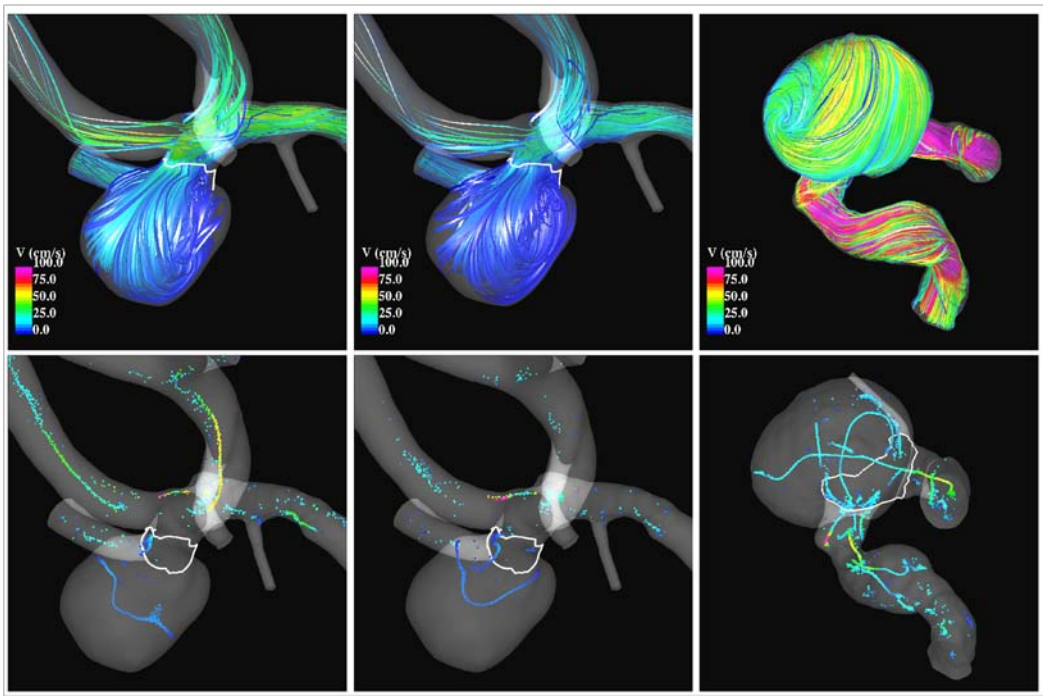

Figure 1: Examples of aneurysms with different flow structures. Top row: streamline visualizations. Bottom row: vortex corelines visualizations. Left column: aneurysm with simple/unstable flow pattern at peak systole. Center column: aneurysm with simple/unstable flow pattern at end diastole. Right column: complex/unstable flow pattern at peak systole.

The first example corresponds to an aneurysm at the middle cerebral artery bifurcation previously classified as having a simple/unstable flow pattern. Visualizations of vortex corelines indicate that there is only one major vortex and that the centreline of this vortex bends during the cardiac cycle. This is consistent with the previous characterization that classified this flow structure as simple/unstable. The second example corresponds to a large aneurysm in the internal carotid artery with a flow pattern previously classified as complex/unstable. Visualization of vortex corelines reveals several vortical structures within the aneurysm. Specifically, we observed that a swirling flow jet enters the aneurysm at the proximal end of the neck, recirculates inside the aneurysm in a complex manner and exits the aneurysm at the distal end of the neck. We also observed a strong secondary flow in the distal portion of the aneurysm orifice and parent artery. Additionally, a small vortex coreline is detected near a small bleb demonstrating a counter current recirculation that takes place inside the bleb.

Comparison of CFD and PIV Cerebral Aneurysm Models

The second application illustrates the use of vortex corelines for comparing flow structures obtained using computational fluid dynamics (CFD) and in vitro particle image velocimetry (PIV) models of a cerebral aneurysm constructed from CTA image data [6]. After building a 3D vector field from orthogonal 2D sets of PIV measurements and interpolating to a common grid, the CFD and PIV fields were visualized using streamlines (Figure 2 left and center) and vortex corelines (Figure 2 right). These visualizations show that, despite differences observed mainly near the aneurysm wall, the CFD and PIV data provide a consistent description of the intra-aneurysmal flow structures. In this particular aneurysm the flow enters at the distal part of the neck, recirculates around a single main vortex structure and swirls into the two daughter vessels.

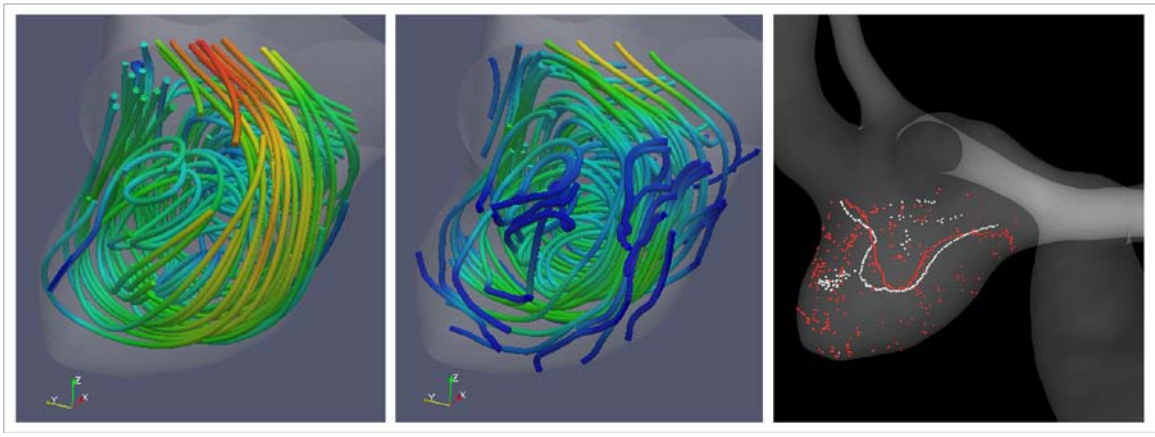

Figure 2: Comparison of flow structures obtained with CFD and PIV models of a growing cerebral aneurysm. Left to right: CFD streamlines, PIV streamlines, CFD (white) and PIV (red) vortex corelines.

Analysis of Effects of Flow Diverting Devices

The final application illustrates the use of vortex corelines for analyzing blood flows before and after treatment of intracranial aneurysm with flow diverting devices. Figure 3 presents results for a giant cerebral aneurysm treated solely with flow diverting stents. These visualizations show that before stenting a swirling stream of blood flows into the aneurysm through the proximal part of the aneurysm orifice, then recirculates around a large vortex, and exits the aneurysm at the distal end of the orifice in a swirling manner. After stenting, the intra-aneurysmal flow velocity is reduced. It can also be seen that the swirling of the inflow and outflow streams have been eliminated. In other words, the flow patterns in the inflow and outflow regions (and the distal parent artery) have been made parallel. Additionally, the visualizations demonstrate a small shift of the main vortex structure within the aneurysm. These observations may be important for

further understanding the thrombosis processes (and thrombus organization) induced by the implantation of this type of devices.

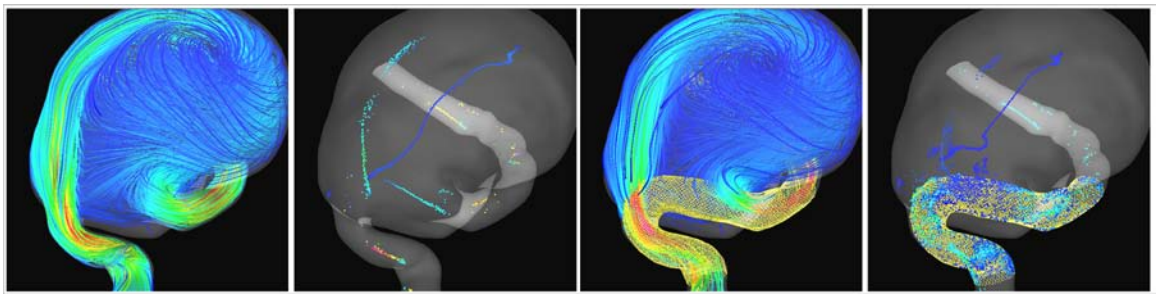

Figure 3: Comparison of flow structures in a giant cerebral aneurysm before and after treatment with a flow diverting stent. Left to right: streamlines before treatment, vortex corelines before treatment, streamlines after treatment, vortex corelines after treatment.

3. CONCLUSIONS

We have successfully computed one-dimensional sets called vortex corelines that identify swirling blood flow in experimental and computational models based on patient-specific vascular geometries and physiologic flows conditions. Vortex corelines provide a powerful tool that simplifies the analysis of complex hemodynamics in cerebral aneurysms. We have illustrated this point in three diverse applications; (1) characterization of blood flow patterns in order to study aneurysm evolution and rupture, (2) comparison of blood flow structures in pre- and post-stented aneurysm models for understanding the processes of thrombosis and aneurysmal occlusion, and (3) comparison of large-scale flow structures between computational and experimental models of intracranial aneurysm hemodynamics.

REFERENCES

1. Lieber, B.B., A.P. Stancampiano, and A.K. Wakhloo, *Alteration of hemodynamics in aneurysm models by stenting: influence of stent porosity.* Annals of Biomedical Engineering, 1997. **25**(3): p. 460-469.
2. Roth, M. and R. Peikert, *A higher-order method for finding vortex core lines*, in *Proc. IEEE Visualization Conference '98*. 1998. p. 143-150.
3. Peikert, R. and M. Roth, *The parallel vectors operator-A vector field visualization primitive*, in *Proc. IEEE Visualization Conference '99*. 1999. p. 263-270.
4. Sujudi, D. and R. Haimes, *Identification of swirling flow in 3D vector fields.* Tech. Report, Dept. of Aeronautics and Astronautics, MIT, Cambridge, MA, 1995.
5. Cebral, J.R., et al., *Association of hemodynamic characteristics and cerebral aneurysm rupture.* AJNR American Journal of Neuroradiology, 2011. **in press**.
6. Raschi, M., et al., *Computational and experimental hemodynamic analysis of an intracranial aneurysm*, in *IX Argentinian Congress on Computational Mechanics (MECOM) and XXXI Iberian-Latin-American Congress on Computational Methods in Engineering (CILAMCE)*. 2010: Buenos Aires, Argentina.

2nd International Conference on Mathematical and Computational Biomedical Engineering - CMBE2011
March 30 - April 1, 2011, Washington D.C, USA
P. Nithiarasu and R. Löhner (Eds.)

Patient-Specific Modelling of Cerebral Aneurysm Evolution

Paul N. Watton*, Alisa Selimovic*, Haoyu Chen*, Harry Thompson* and Yiannis Ventikos*
*Institute of Biomedical Engineering, Department of Engineering Science,
University of Oxford, Oxford, UK.
Paul.Watton@eng.ox.ac.uk

SUMMARY

We present a novel fluid-solid-growth computational framework for the evolution of sidewall saccular cerebral aneurysms on physiological sections of cerebral vasculature. Sidewall saccular aneurysms are identified from clinical imaging data. The vasculature is segmented and centrelines generated. The section of vasculature that contains the aneurysm is removed and replaced with a cylindrical section, hereon referred to as *aneurysmal section*; this simulates an idealised section of healthy artery prior to formation of the aneurysm. The *aneurysmal section* utilises a realistic constitutive model of the arterial wall [1] that accounts for the structural arrangement of collagen fibres in the medial and adventitial layers, the natural reference configurations in which the collagen fibres are recruited to load bearing and the mass of the elastinous and collagenous constituents. It is reconnected to the upstream and downstream sections of the vasculature using an automated algorithmic method [2]: boundary curves propogate along a centreline to smoothly morph the surface sections together. Integrating the aneurysmal section within a realistic vasculature geometry enables growth and remodelling to be explicitly linked to physiologically realistic haemodynamic stimuli. In addition, a quasi-static analysis is employed to obtain the geometry of the aneurysmal section at systolic and diastolic pressures, enabling growth and remodelling (G&R) to be explicitly linked to the magnitude of the cyclic stretches of cells. Initially, the degradation of elastin is prescribed to create a small outpouching of the computational domain and perturb the haemodynamic environment [3]. Subsequent elastin degradation is linked to low WSS in a localised region of the computational domain [4], whilst the collagen fabric adapts to restore its strain to the homeostatic value. To our knowledge, this is the first patient-specific model of cerebral aneurysm evolution that incorporates a realistic constitutive model of the arterial wall and explicitly links G&R to pulsatile mechanical stimuli. It will provide the basis for further investigating and elucidating the aetiology of the disease.

Key Words: *cerebral aneurysm, mechanobiology, growth and remodelling, wall shear stress, cyclic stretch*

1 INTRODUCTION

Intracranial aneurysms appear as sac-like outpouchings of the cerebral vasculature wall; inflated by the pressure of the blood that fills them. They are relatively common and affect up to 5% of the adult population. Fortunately, most remain asymptomatic. However, there is a small but inherent risk of rupture: 0.1% to 1% of detected aneurysms rupture every year. If subarachnoid haemorrhage does occur there is a 30% to 50% chance of fatality. Consequently, if an aneurysm is detected, clinical intervention may be deemed appropriate. Therapy is currently aimed at pre-rupture

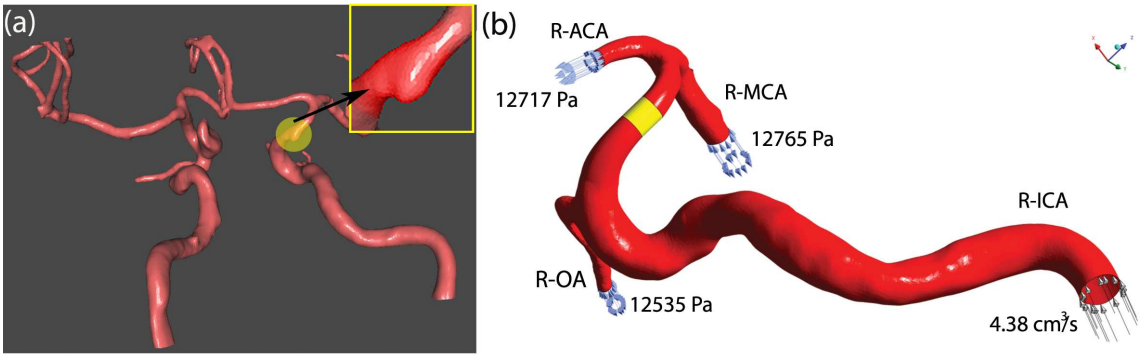

Figure 1: (a) Clinical MRI data is automatically segmented using @neufuse software. A small sidewall saccular aneurysm developing on the right internal carotid artery is identified. (b) Boundary conditions for the haemodynamic computational domain. The original aneurysm has been removed and replaced with a short cylindrical section which is then reconnected to the vasculature. It is on this section that aneurysm evolution is simulated.

detection and preventative treatment. However, interventional procedures are not without risk to the patient. Relatively recent developments in imaging technology have led to new healthcare policies in terms of application of medical imaging modalities. This trend has led to a dramatic increase in the number of coincidentally detected asymptomatic cerebral aneurysms. Moreover, there has been an increase in the number of cases where intervention is deemed necessary, in spite of the lack of robustly founded rupture risk indicators. The improvement and optimisation of interventional techniques is an important concern for patient welfare and is necessary for rationalisation of healthcare priorities. Hence there is a need to develop methodologies to assist in identifying those ICAs most at risk of rupture. Biomechanics has an essential role to play in this respect. It offers the potential for computational tools to assist clinical diagnostic procedures.

2 Fluid-Structure-Growth Computational Framework

We propose a novel Fluid-Structure-Growth computational framework for modelling ICA evolution. Sidewall saccular aneurysms are identified from clinical imaging data (see (Fig. 1(a))). The data is automatically segmented and centrelines are created through the vasculature. The section of vasculature that contains the aneurysm is removed and replaced with a cylindrical section (see (Fig. 1(b))), hereon referred to as aneurysmal section, to represent an idealised section of healthy artery on which the aneurysm develops. The aneurysmal section utilises a realistic constitutive model of the arterial wall that accounts for the structural arrangement of collagen fibres in the medial and adventitial layers, the natural reference configurations in which the collagen fibres are recruited to load bearing and the mass of the elastin and collagenous constituents [1]. The *aneurysmal section* is then reconnected to the upstream and downstream sections of the vasculature using an automated algorithmic method [2]: boundary curves propogate along a centreline to smoothly morph the surface sections together.

Figure 2 illustrates the computational methodology. The computational modelling cycle begins with a structural analysis of the aneurysmal section to solve the equilibrium deformation field for given pressure and boundary conditions. The structural analysis quantifies the stress and stretch, and the cyclic deformation, of the ECM components and the cells (each of which may have different natural reference configurations). The (systolic) geometry of the aneurysmal section is exported to be prepared for haemodynamic analysis. To achieve physiologically realistic flow in

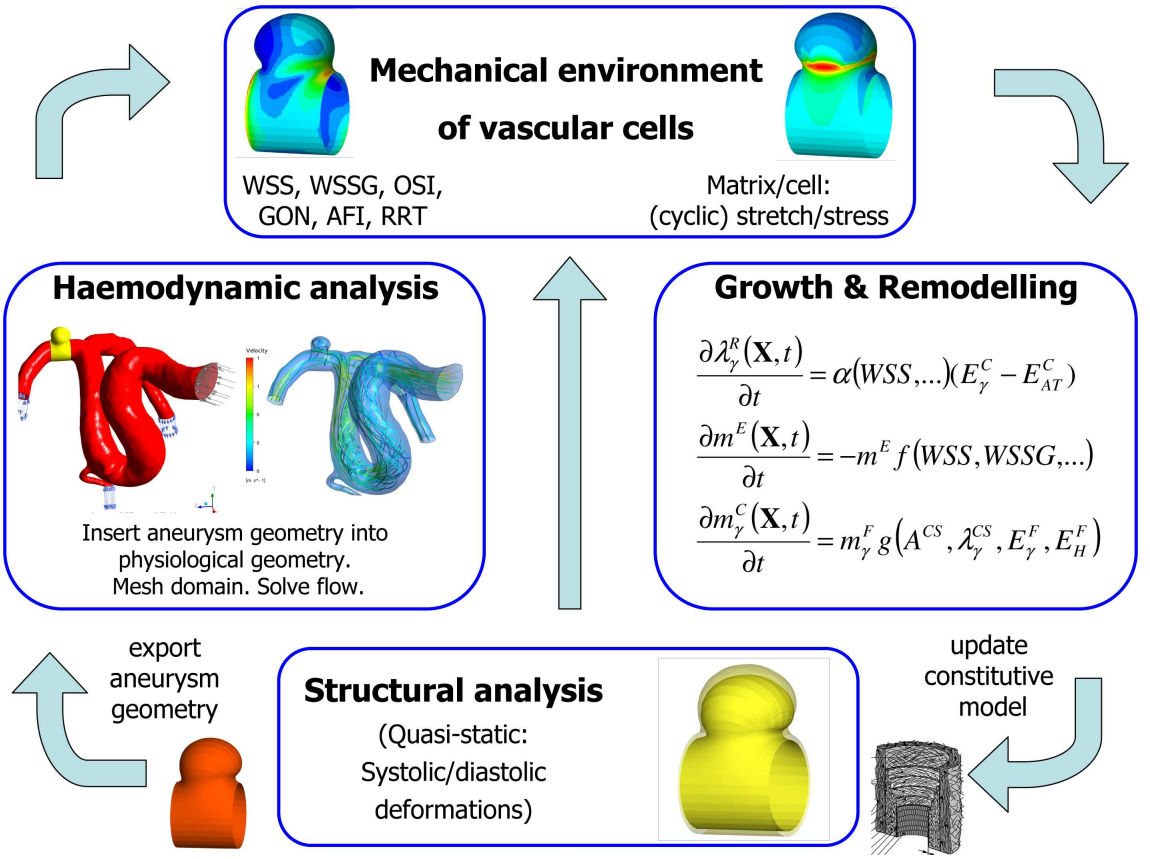

Figure 2: Fluid-Solid-Growth computational framework for modelling aneurysm evolution.

the region where the aneurysm develops, the aneurysm geometry is integrated into a physiological geometrical domain, which is then automatically meshed with ANSYS ICEM (ANSYS Inc, Canonsburg, PA) ; physiological flow rate and pressure boundary conditions are applied. The flow is solved with ANSYS CFX assuming rigid boundaries for the haemodynamic domain. The haemodynamic quantities of interest, for example, WSS, WSSG are then exported and interpolated onto the nodes of the structural mesh: each node of the structural mesh contains information regarding the mechanical stimuli obtained from the haemodynamic and structural analyses. G&R algorithms simulate cells responding to the mechancial stimuli and adapting the tissue: the constitutive model of the aneurysmal tissue is updated. The structural analysis is executed to calculate the new equilbrium deformation fields. The updated geometry is exported for haemodynamic analysis. The cycle continues and as the tissue adapts an ICA evolves.

Initially, the degradation of elastin is prescribed to create a small outpouching of the computational domain to perturb the haemodynamic environment [3]. Subsequent elastin degradation is then linked to low WSS in this localised region of the computational domain [4], whilst the collagen fabric adapts (throughout the arterial domain) to restore its strain to the homeostatic value. The evolving geometry alters the spatial distribution of haemodynamic stimuli that act on the endothelial layer of the artery. Figure 3 illustrates the WSS, WSSG and pressure distributions on the arterial domain following the development of a sidewall saccular aneurysm. Elevated regions of WSS/WSSG are observed distal to the aneurysm and close to the bifurcation. The variation in pressure is negligible over the aneurysm region.

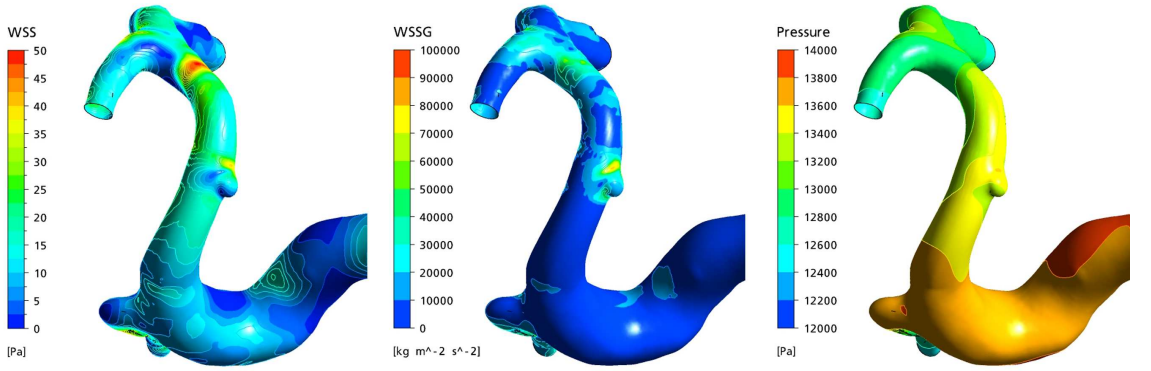

Figure 3: WSS, WSS spatial gradients and pressure distributions following the evolvement of a model of an ICA on patient-specific vasculature. Patient-specific inlets and outlet geometries yield physiologically realistic haemodynamics within the aneurysmal region. Consequently, the haemodynamic stimuli that are incorporated into the G&R algorithms have realistic magnitudes and spatial distributions.

3 CONCLUSIONS

We propose a novel FSG computational framework for the evolution of sidewall saccular aneurysms on physiological sections of vasculature. This approach enables growth and remodelling to be explicitly linked to physiologically realistic mechanical stimuli. Computational models provide an ideal basis to explore hypotheses for how ICAs form and evolve and have the potential to yield insight into the aetiology of the disease. The long term objective is that such models may ultimately have diagnostic application, for example, patient -specific stress analysis and prediction of future growth/rupture. In the shorter term however, they present us with excellent in silico testbeds for theory and hypothesis evaluation.

REFERENCES

[1] P. Watton and Y. Ventikos, Modelling Evolution of Saccular Cerebral Aneurysms, *Journal of Strain Analysis*, 44, 375-389, 2009.

[2] H. Chen, An Automated Method to Reconstruct Healthy Vasculature from Medical Imaging Depicting Cerebral Aneurysm, *MSc Thesis in Biomedical Engineering*, Department of Engineering Science, University of Oxford, 2009.

[3] P.N. Watton, N.B Raberger, G.A. Holzapfel and Y. Ventikos, Coupling the Haemodynamic Environment to the Evolution of Cerebral Aneurysms: Computational Framework and Numerical Examples, *ASME Journal of Biomechanical Engineering*, 131(10):101003, 2009.

[4] P.N. Watton, A. Selimovic, N.B. Raberger, P. Huang, G.A. Holzapfel and Y. Ventikos, Modelling Evolution and the Evolving Mechanical Environment of Saccular Cerebral Aneurysms, *Biomechanics and Modelling in Mechanobiology*, DOI: 10.1007/s10237-010-0221-y, 2010.

2nd International Conference on Mathematical and Computational Biomedical Engineering – CMBE2011
March 30 – April 1, 2011, Washington D.C., USA
P. Nithiarasu and R. Löhner (eds)

Fluid-Structure Interaction Simulation of Cerebral Aneurysm with the Effects of Peripheral Network

Marie Oshima*, Milan Toma*, Absei Krdy and Shu Takagi**
*Institute of Industrial Science, The University of Tokyo, 4-6-1 Meguru-ku, Tokyo, Japan, marie@iis.u-tokyo.ac.jp
**Graduate School of Engineering, The University of Tokyo, 7-3-1 Hongo, Bynkyo-ku, Tokyo, Japan, takagi@mech.t.u-tokyo.ac.jp

SUMMARY

The cerebral aneurysms are caused by the degeneration of blood vessel wall, which is initiated by hemodynamic forces, particularly wall shear stresses. Therefore it is important to simulate the blood flow and the blood vessel wall as well as the interaction between them. In order to achieve a realistic in-vivo simulation, modeling of appropriate boundary conditions is a crucial issue. The aim of the present research is to develop a numerical simulation system, which considers the interaction between the blood flow and the blood vessel wall of the cerebral aneurysm using finite element method, as well as the effect of the peripheral vessels network of the cerebral arteries. The peripheral vessels network was modeled using coupling multi-scale model of 1D and STI (Structure Impedance Model), and then applied as outflow boundary condition to the 3D simulation of patient specific model.

Key Words: F*luid-structure interaction, Middle cerebral aneurism, Multi-scale model*

1. INTRODUCTION

The formation and growth of cerebral aneurysm depends on hemodynamic factors such as WSS (Wall Shear Stress) or blood pressure induced by blood flow[1]. The WSS is known as one of the mechanical forces induced by blood flow causing damages on endothelial cells, which leads to degeneration of blood vessels. Therefore it is important to obtain information on the location and the magnitude of local high and low shear stresses to be able to predict consequences.

The hemodynamic simulation combined with medical images can estimate WSS as well as flow features quantitatively, in a patient-specific manner, if an appropriate initial- and boundary conditions are estimated. Especially the fluid-structure interaction simulation is very sensitive regarding those conditions. The peripheral vessels network of cerebral artery, including the small arteries and the arterioles, plays an important role in determining the outflow pressure of the middle cerebral artery. Since this network cannot be resolved by medical images, it is necessary to develop a numerical model that predicts the effect of the peripheral network on the 3D outflow boundary.

Based on models introduced by Olufsen et al[2], the peripheral network is modeled as the binary symmetric tree attached to the outlet of the 3D model as shown in Fig.1. The small arteries are modeled using 1D model, whereas the arterioles or one smaller than 100μm down to 5 μm are modeled using STI model.

This paper aims to develop a multi-scale model (1D - STI) for the cerebral peripheral network, and is applied as an outflow boundary condition for a 3D model of the middle cerebral artery.

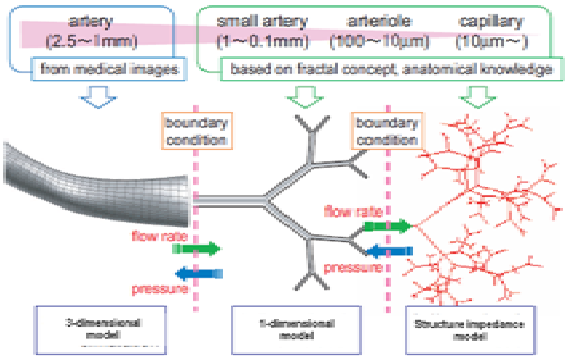

Fig.1 Schematic illustration of the multi-scale outflow boundary model.

2. NUMERICAL MEHTOD

2.1 1D model:

The small peripheral arteries, with diameters ranging approximately down to 0.1 mm, are modeled using 1D model[3]. Predicting blood flow and pressure, for the small arteries, requires three equations. Two equations ensure conservation of volume and momentum:

$$\frac{\partial}{\partial x}\begin{pmatrix} q \\ A \end{pmatrix} + \frac{\partial}{\partial t}\begin{pmatrix} \frac{4}{3}\frac{q^2}{A} + \frac{f}{\rho}\sqrt{A_0 A} \\ A \end{pmatrix} = \begin{pmatrix} 0 \\ -8\pi\nu\frac{q}{A} \end{pmatrix} \tag{1}$$

The equation of the relationship between the pressure and the area is given by

$$p(x,t) - p_0 = \frac{4}{3}\frac{Eh}{r_0}\left(1 - \sqrt{\frac{A_0}{A}}\right) \tag{2}$$

where **q** is the flow-rate, **A** is the cross sectional area, **p** is the pressure, **ρ** is the density, **ν** is dynamic viscosity, **E** is Young's modulus, **h** is the wall thickness and $\mathbf{r_0}$ is the initial radius.

The compliance of the blood vessel is modeled using he following formula[4]

$$\frac{Eh}{r_0} = k_1 \exp(k_2 r_0) + k_3 \tag{3}$$

where $k_1 = 2.0\text{x}10^6$ kg/(sec^2 m), $k_2 = -2.253\text{x}10^3$ m^{-1}, and $k_3 = 8.65\text{x}10^4$ kg/(sec^2 m) are constants.

The 1D model tree was assumed to be bifurcating symmetrically until it reaches the threshold of approximately 0.1mm in diameter. Since the diameter becomes smaller than 0.1 mm, the vessels tend to become rigid, the STI model is used to make the entire simulation efficient.

2.2 STI model

The arterioles, with diameters ranging from approximately 0.1 mm to 5μm, are modeled using the structure tree impedance model. An expression for the impedance in the frequency domain at the root of the STI model was derived using a semi-analytical approach based on a linearized version of the governing equations. Using the analogy from electrical circuit, the pressure-drop relationship of the STI model can be related to the flow rate in the frequency domain as follows

$$P(x,\omega) = Z(x,\omega)Q(x,\omega) \tag{4}$$

where $Z(x,\omega)$ is the impedance at the root of the STI model transferring this relation to the time domain yields the outflow boundary of the 1D model.

The STI model, also, was assumed to be bifurcating symmetrically until it reaches the threshold diameter (approximately 5μm).

The non-Newtonian effect of the blood was taken in account in this model. Hematocrits of the blood decreases as the diameter of blood vessel become smaller than 300μm[5]. Pries suggested, the apparent viscosity of the blood can be directly written as a function of the hematocrit and the diameter of the vessel[6].

2.3 3D FSI simulation

The present FSI simulation is based on finite element ALE (Arbitrary Lagrangian-Eulerian) method using strong coupling method. The governing equations for the fluid part consist of the following continuity and Navier-Stokes equations:

$$\nabla \cdot u = 0 \tag{5}$$

$$\rho^f \left(\frac{\partial u}{\partial t} + \bar{u} \cdot \nabla u \right) + \nabla \cdot \sigma^f + \rho^f f = 0 \tag{6}$$

where u is the velocity, $\bar{u}$ is the relative velocity. ρ^f is the density of the fluid. And σ^f is expressed as follows:

$$\sigma^f = -PI + 2\mu\varepsilon(u) \tag{7}$$

$$\varepsilon(u) = \frac{1}{2}\left(\nabla u + (\nabla u)^T\right) \tag{8}$$

here P is pressure, andμ is the viscous coefficient.

The structure analysis deals with the following equilibrium equation;

$$\rho^s \frac{\partial^2 v}{\partial t^2} = \nabla \cdot \sigma^s \tag{9}$$

where v is displacement and ρ^s is the density of the structure.

High order Mooney-Rivlin model is used to fit an experimentally-derived stress-strain curve for the arterial wall. The blood is considered to be incompressible and Newtonian with kinematic viscosity 4.06×10^{-3} Pa.sec and density 1000 kg/sec^3.

From the medical data of a 49 year-old patient, a 3D geometry of the middle cerebral artery with the aneurism is extracted by our in-house program as shown in Fig.2.

Fig.3. 3D model of middle cerebral aneurysm

Ultrasound Doppler-measured velocity profile is used as the inflow boundary condition at the inlet of the 3D model. The outflow pressure boundary is modeled using the multi-scale model, which predicts the pressure at the outlets of the middle cerebral artery, taking in account the effect of the peripheral vessels network.

3. CONCLUSIONS

In order to investigate the effects of Newtonian versus non-Newtonian blood flow in the STI model, the simulation has been conducted for 2 cases with different types of viscosity models: 1) Newtonian and 2) non=Newtonian.

Case 1 of Newtonian assumption shows the pressure-drop at the inlet of the STI model to be over-estimated (70mmHg) compared to Case 2 of non-Newtonian assumption (50mmHg). The difference in viscosity model in the STI model leads to an increase in pressure range over the 1D model since the pressure in the STI is used to obtain one for the 1-D calculation. The pressure-difference at the inlet of 1D model remained constant (45mmHg), in both Newtonian and non-Newtonian cases as shown in Fig.3.

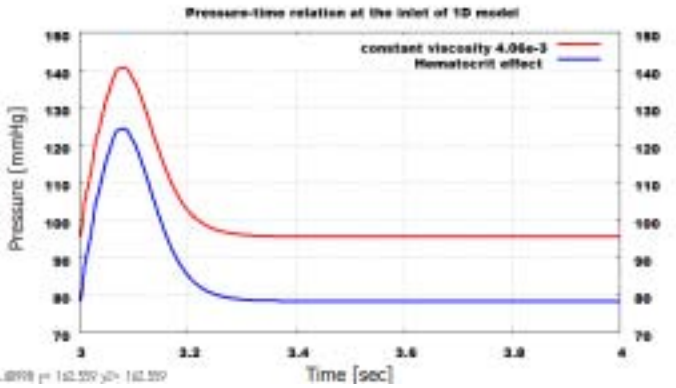

Fig.3 Comparison between the pressure at the inlet of 1D model between Newtonian and non-Newtonian cases

The results are compared with and without multi-scale boundary conditions in order to investigate the effects of the boundary conditions on the hemodynamics as well as arterial wall structural properties.

REFERENCES

[1] H. J. Steiger. Pathophysiology of development and rupture of cerebral aneurysms. Acta Neurochirurgica Supplement, 8,1–57, 1990.

[2] M. S. Olufsen, C. S. Peskin, W. Y. Kim, E. M. Perdersen, A. Nadim, and J. Larsen. Numerical simulation and experimental validation of blood flow in arteries with structured-tree outflow conditions. Annals of Biomedical Engineering, 28,1281–1299, 2000.

[3] Oshima, M., Torii, R., Tokuda, S., Yamada, S., Koizumi, A., ‘’Patient-Specific Modeling and Multi-Scale Blood Simulation for Computational Hemodynamic Study on the Human Cerebrovascular System’’, to be submitted to Current Pharmaceutical Biotechnology

[4] Segers, P., F. Dubois, D. DeWachter, and P. Verdonck. Role and relevancy of a cardiovascular simulator. Cardiovasc. Eng. 3,48–56, 1998.

[5] Freitas Jr., R. A. Nanomedicine, Volume I: Basic Capabilities. Landes Bioscience, 1999.

[6] Pries, A. R., Secomb, T. W., GeBner, T., Sperandio, M.B., Gross, J. F., and Gaehtgens, P. Resistance to blood flow in microvessels in vivo. Circulation Research, 75, 904–915, 1994.

2nd International Conference on Mathematical and Computational Biomedical Engineering – CMBE2011
March 30 – April 1, 2011, Washington D.C., USA
P. Nithiarasu and R. Löhner (eds)

An Equivalent Wall Thickness Estimation for Cerebral Aneurysms

Erick L. Johnson*, Yongjie Zhang and Kenji Shimada****
*Sandia National Laboratories, Albuquerque, NM, erick.l.johnson@gmail.com
**Carnegie Mellon University, Pittsburgh, PA

SUMMARY

Computational simulations are making significant strides within the biomedical community; however, the accuracy of the results can only be as good as the geometry used. While current imaging techniques are able to capture the shape of a cerebral aneurysm, they are still unable to adequately resolve the wall thickness and result in patient-specific models that do not use patient-specific thicknesses. An equivalent wall thickness estimation approach is proposed that approximates the weakening wall as a change in the wall thickness and is related to the elastic deformation of the aneurysm model. Fluid-structure interaction simulations are used to validate the proposed method for patient-specific models.

Key Words: Cerebral a*neurysm, principal wall stress, wall thickness, deformation.*

1. INTRODUCTION

Computational fluid dynamic (CFD) simulations have been a significant tool for engineers looking at and have provided insight into the human cardiovascular system. In beginning to tailor these simulations toward patient-specific problems an accurate representation of the fluid domain is required, which medical imaging and geometry creation is able to provide. Unfortunately, the geometry used in a CFD simulation is not sufficient for fluid-structure interaction (FSI) analyses, as there is no need for a wall thickness in the former. Additionally, the imaging techniques are not capable of capturing the thin walls of cerebral arteries and aneurysms. This leaves a vacuum of data that researches have to fill with best-guesses and approximations.

Until recently it was common to use a uniform wall thickness when performing a structural simulation of any aneurysm. More recently smoothing techniques [34] and using a discrete size for the healthy and aneurysm regions [4] have provided improved approximations for the geometry; however, the former would yield the same thickness distribution for a healthy and aneurysm model of the same domain, and the latter still does not account for the elastic stretching of the vessel wall. A separate body of work is using the growth and remodelling of collagen to demonstrate the formation of an aneurysm from a healthy vessel, but has not been extended to patient-specific models [18].

An alternative approach is proposed that approximates the weakening of a cerebral aneurysm wall through surface parameterization and non-linear spring relaxation. This equivalent wall thickness represents both the changing thickness and structural properties as an aneurysm develops. The resultant wall thickness is smooth and is thinnest near the apex of a patient-specific aneurysm.

The wall thickness is compared against literature and FSI simulations are performed to provide further validation.

2. AN EQUIVALENT WALL THICKNESS AND RESULTS

The pathogenesis of cerebral aneurysms is still not fully understood. Yet, it has been shown the vessel wall loses its linear-elastic region after high-strain loading [12] and can be modelled with an exponential equation [16]. To reinforce the weakened wall the rate of collagen growth is increased, though this appears to occur more slowly than the initial growth of the aneurysm. The disparity in time scales may account for why relatively small aneurysms rupture and some large ones have not. That is, as the aneurysm growth slows, the collagen is able to strengthen the weakest regions of the wall allowing larger aneurysms to remain unruptured longer. This leads to a primary assumption of this work, mainly: The mass of the vessel wall remains a constant during the *initial* growth. It needs to be repeated, however, that the goal is not to capture the exact wall thickness, but the relative strength of the wall; so even if this assumption can be improved upon, the wall never returns to its healthy strength and is still able to be represented by a thinning wall.

Capturing the thinning wall is achieved by deforming a model of the healthy vessel into the aneurysm, taking into account the elastic stretching of the vessel tissue. Surface parameterization is able to quickly move the surface mesh of the healthy model onto the aneurysm surface. Relaxation of a non-linear spring system using an isotropic variation of the Fung equation gives an approximation of the true stretching the vessel has undergone. This second assumption, that the vessel wall is an isotropic material, is based on the inability to measure the true material directions for patient-specific aneurysms *in situ* and a realization the severity of deformation with a fixed amount of material will smooth anisotropic effects. The change in wall thickness is then inversely proportional to the area change of the individual mesh elements. A one-dimensional cartoon illustrates this in Figure 1.

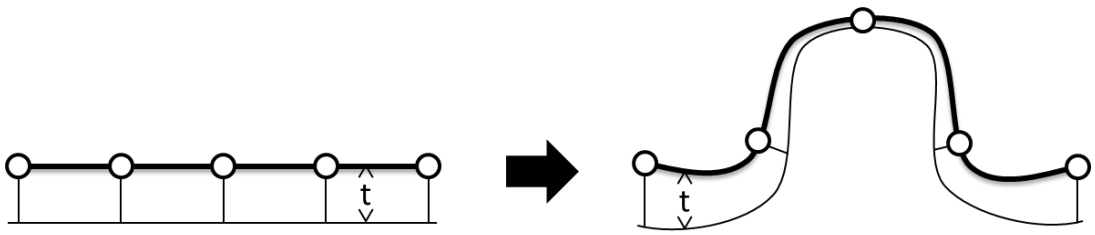

Figure 1: The change in wall thickness is inversely proportional to the change in element area.

The equivalent wall thickness smoothly transitions from the healthy regions of the cerebral artery into the thinnest regions near the peak of the aneurysm dome and is seen in Figure 2(b). The minimum thickness is 43 μm and is 16% of the initial thickness. This is in contrast to a current method that solves the Laplace equation over the aneurysm with the boundary thicknesses fixed at 20% of the local radius, where the minimum thickness occurs at one of the outlets; see Figure 2(a). The minimum thickness for a sampling of patient-specific cerebral aneurysms falls within the range presented in literature.

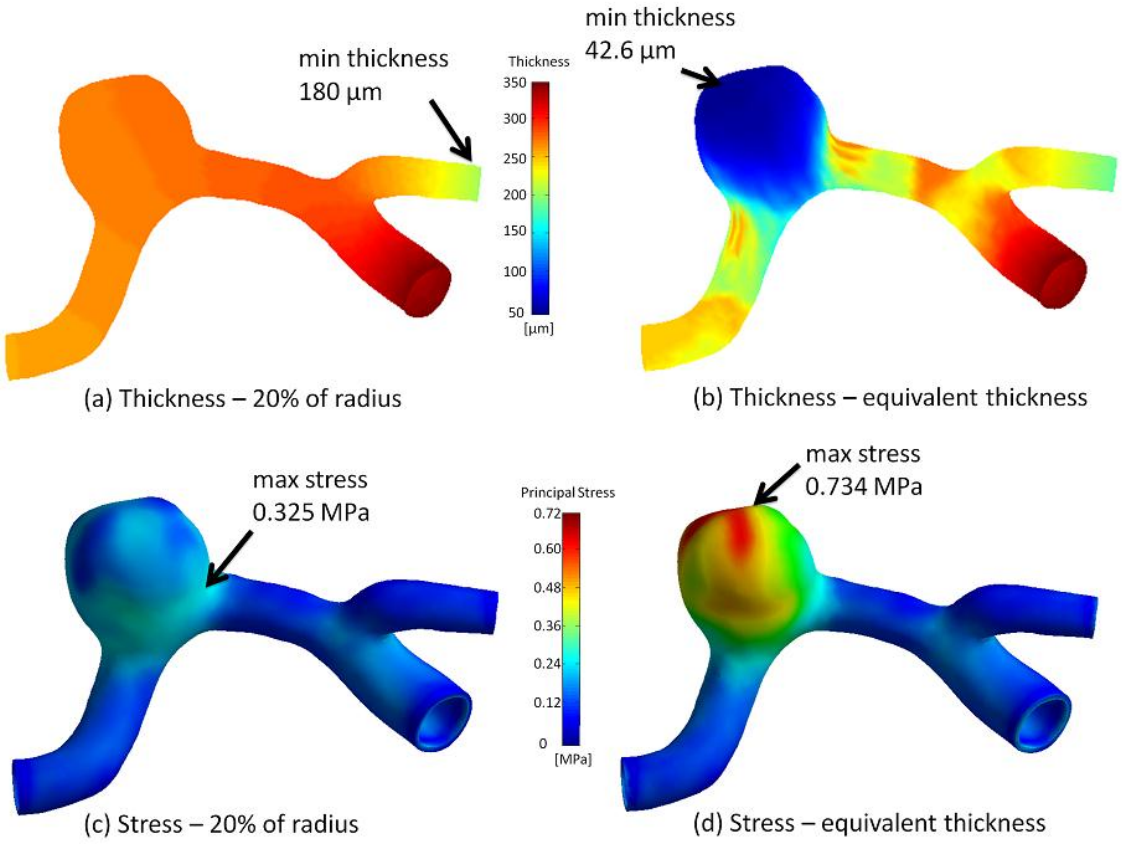

Figure 2: The wall-thickness (a,b) and absolute principal stresses (c,d) for a patient-specific aneurysm at peak systole. (a,c): the wall thickness of 20% of the radius and (b,d): the equivalent wall thickness. Arrows point to the location of minimum wall thickness and maximum stress.

FSI simulations were performed to determine the value and location of maximum principal stress. The inlet and outlets were given a pulsatile velocity and pressure waveform, respectively, and the wall was modelled as an isotropic, Mooney-Rivlin material. The absolute principal stress for the 20% of the radius and equivalent walls are shown in Figures 2(c) and 2(d), respectively. As can be seen with the equivalent wall thickness model the maximum principal stress occurs at the dome of the aneurysm, as would be expected. Additionally, the maximum stress is within the range blood vessel tissue may be expected to rupture (0.73 to 1.9 MPa) [41].

3. CONCLUSIONS

The proposed method provides a new method to estimate a patient-specific cerebral aneurysm wall thickness. This equivalent wall model is representative of the weakened structure of an aneurysm and is capable of bridging the gap between the surface model generation and structural simulation. Good agreement exists between the computed minimum thickness and maximum principal stress against those values found in literature. The results also show a stress distribution that more closely matches expected results, with the maximum occurring near the apex of the aneurysm dome.

REFERENCES

[1] Y. Bazilevs, M. C. Hsu, Y. Zhang, W. Wang, T. Kvamsdal, S. Hentschel, and J. G. Isaksen, Computational vascular fluid-structure interaction: methodology and application to cerebral aneurysms, *Biomechanics and Modeling in Mechanobiology*, 2010, DOI:10.1007/s10237-010-0189-7.

[2] R. Torii, M. Oshima, T. Kobayashi, K. Takagi, and T. E. Tezduyar, Influence of wall thickness on fluid-structure interaction computations of cerebral aneurysms, *International Journal for Numerical Methods in Biomedical Engineering*, 26, 336-347, 2010.

[3] M. Kroon and G. A. Holzapfel, A model for saccular cerebral aneurysm growth by collagen fibre remodelling, *Journal for Theoretical Biology*, 247, 775-787, 2007.

[4] S. Scott, G. G. Ferguson, and M. R. Roach, Comparison of the elastic properties of human intracranial arteries and aneurysms, *Canadian Journal of Physiology and Pharmacology*, 50, 328-332, 1972.

[5] Y. C. Fung, K. Fronek, and P. Patitucci, Pseudoelasticity of arteries and the choice of its mathematical expression, *American Journal of Physiology – Heart and Circulatory Physiology*, 237, H620-H631, 1979.

[6] D. J MacDonald, H. M. Finlay, and P. B. Canham, Directional wall strength in saccular brain aneurysms from polarized light microscopy, *Annals of Biomedical Engineering*, 28, 533-542, 2000.

Intracranial Aneurysms: Study of X-rays Time-Intensity-Curves (TIC) Pulsatility

R. Ouared*, O. Brina*, O. Bonnefous*, A Groth**, T Brunjs**, D. Babic**, P. Bijlenga*, K Schaller*, K. Lovblad* and V. Pereira***
*Hospital of Geneva, Rue Gabrielle-Perret-Gentil 4, 1211 Geneva 14, Switzerland
**Philips Medical Systems, Veenpluis 4-6, 5684 PC, Netherlands
***Laboratoires d'Electronique Philips, Limaille-Brevanne 94450, France

rafik.ouared@unige.ch, olivier.brina@hcuge.ch, vitor.mendespereira@hcuge.ch

SUMMARY

In a recent study led in our group at hospital of Geneva we made a non-exhaustive study of X-rays time-intensity-curves on 35 patients harbouring aneurysms, with a high temporal resolution CsI flat panel detector. 2D regions-of-interest have been delimited in both aneurysms and supporting vessels and related TICs have been compared. A pulsatility feature has emerged and used by PMS for angio cine purpose. On our side, we rather focused on the characterization of such pulsatility and how it could be related to clinical assessment. We observed several interesting features, essentially: 1/ pulsatility of TICs can be very well correlated with ECG, 2/ it depends on contrast agent injection rates, 3/ it somehow varies with geometrical parameters of intracranial aneurysms and their related locations. Even though data processing is still going on, we have established that TICs can well reflect the complexity of flow patterns in aneurysms, hence providing a potential tool to validate blood flow simulation. Preliminary results are presented in this symposium.

Key Words: *Time-Intensity-Curves , TIC, pulsatility , aneurysm, Flow Dynamics, Geometry.*

1. INTRODUCTION

Some years ago, TICs have been studied to assess efficacy of stents in endovascular treatments of intracranial aneurysms. This study was based on the assumption that the best stents could induce more blood flow dispersion than advection in aneurysm hence reducing the washout and accumulating the bulk of platelets and clotting factors for thrombogenesis. Though this question is not settled down so far, it is interesting to notice that all those study were based on curves with no pulsatility. That was due to constant contrast agent injection rates masking physiological conditions. In this model, both the advective and dispersive parts were characterized by two parameters each: density and decay time [1].

In a more recent study [2], it has been suggested a new parameterization based on restrictive observations that TICs have a gamma-variate distribution form which allow cumulative distribution functions based parameterization. Several characteristic times have been defined and used to measure blood flow velocity.

At Hug, pulsatility of TICs has been obtained with high speed X-rays detector at hospital of Geneva. The oscillating TIC pattern has been first used by Philips Medical Systems to measure velocity field in parent artery with a validation from transcranial Doppler measurements. Those figures and the fine level of details for temporal resolution have been used to validate submitted work on virtual angiography and based on in-vitro experiments.

We have conducted a consecutive series study on 35 patients harbouring aneurysms. TransCranial Doppler measurements were used to find the best injection rate to obtain an optimal curve and to validate flow measurements. 2DSA acquisitions were coupled to ECG trigger. ROIs in both aneurysms and parent vessels have been systematically delimited and related TICs compared and analyzed.

2. MAIN BODY

Following an ethical committee approved protocol to evaluate epidemiology and flow in intracranial aneurysms, we included a consecutive series of 35 patients, suffering from ruptured and un-ruptured cerebral saccular aneurysms. They were submitted to diagnostic angiogram and eventually underwent endovascular treatment if indicated. Patients with intraventricular drainage, hydrocephalus or intracranial hematoma were excluded as well as patients without a good accessibility for the trans-cranial Doppler.

The angiographic data was collected with a monoplane angiographic C-arm allura FD20 (Philips, health Care, Best, the Netherlands) equipped with a high speed imaging prototype detector. This detector was able to acquire runs at 150 images per second, with a very high spatial resolution providing very high quality angiographic sequences. During diagnostic angiogram, after femoral artery seldinger approach, a 3D rotational sequence was performed in order to determine the best projection angle to avoid superimposed artery branches of the distal vascular tree and to discriminate the aneurysm from the parent vessel. The ECG signal, synchronized to the acquisition, was recorded for each run and used as reference for pulsatility and frequency analysis X-ray acquisition duration was fixed to 6 seconds in order to limit patient exposition and X-ray tube overweight. The injection duration was limited to 3 seconds enough to cover the intra aneurismal wash-out. The contrast agent, *iopamiro 300* (Bracco Industria Chimica, Milan) was injected with a 5F / 0.035 inches diagnostic catheter which was positioned at the same locations in either the internal carotid artery or the vertebral artery portions.

We divided the study in two steps: On the first part of the study, the aim was to determinate an optimal injection rate. We included 21 patients carrying 23 aneurysms, we acquired in the same projection 3 runs with different injection rates: 1.5, 2.0 and 3.0 ml/s. The purpose was to understand how the CA injection can influence the pulsatile flow pattern. A transcranial Doppler measurement on internal carotid artery (ICA) and on vertebral artery (VA) was done by the same trained neurologist. The data was extracted and parent vessel diameter was measured on the 3D reconstruction Xtravision. the velocity profiles from the Doppler curves were used to extract the mean blood flow rate with Matlab code developed for this purpose (The MathWorks, Inc, Natick, MA)
On the second part of the study, we included 35 patients all of them having ECG trigger, TCCD and at least one CA injection rate. The analysis was focused on the relationship between the TICs of the aneurysm and of the parent artery and aneurismal geometrical and clinical features.
The image datasets were loaded on the open source ImageJ software (developed at National Institutes of Health, USA) and regions of interest (ROI) were interactively delimited around the

aneurysm. In the whole process, manned intervention was performed by the same technician. A ROI was also delimited in the inlet parent vessel in a straight part as close as possible to the aneurysm inlet. The average gray value over all pixels within the ROI is calculated for each image and plotted with regard to time, hence providing the TICs.
Aspect ratios, volumes, locations and neck sizes of aneurysms were measured and calculated on 3D Xtravision work station (Philips, Best, Netherlands). All the data have been captured and integrated in a Matlab data structure. Matlab tools have been developed to measure TIC and ECG frequencies along with mean pulsatility, and to analyze all the correlations.

Figure 1 shows one frame of the angiogram and the aneurysm ROI depicted in yellow.

Figure 1: one frame of the angiogram. The ROI is depicted in yellow around the aneurysm.

At every frame, the average gray level intensity in given region of interest (ROI) is calculated and TIC plotted. Figure 2 demonstrate that peaks of pulses are detected correctly (detection efficiency is 99%). The TIC-cycle time is averaged over inter-peak distances. The detection efficiency does not depend on level of pulsatility. We observed also that pulsatility decreases with the injection rate ratio index (defined as the ratio between injection rate and mean flow rate).

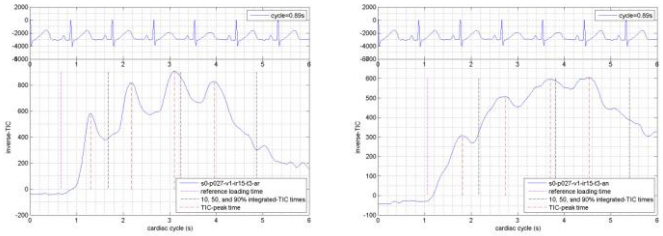

Figure 2: To get a positive scale, inverted-TIC in artery ROI is plotted on left, and right in aneurysm ROI, for the same injection rate at 1.5ml/s and in same view. ECG figure is superposed to the TIC at the top of both images.

The linear regression with ECG cycle time is shown in Figure 3.

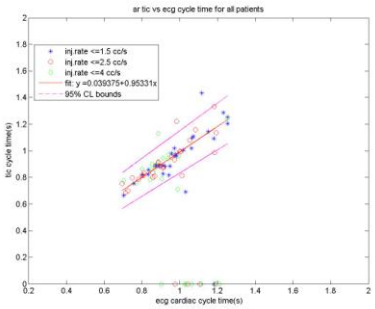

Figure 3: linear regression between TIC-cycle time and ECG cycle time. The slope is close to 1. The 95%CI limits are also shown.

In Figure 4, one can notice that the normalized pulsatility is reduced in the seven ruptured aneurysm (rupture state=1) compared with the non ruptured cases (rupture state=0).

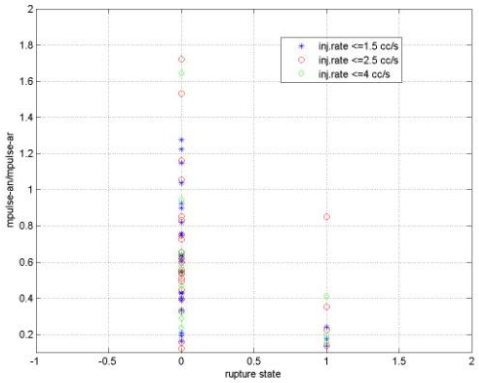

Figure 4: attenuation of pulsatility in aneurysm wrt artery. Rupture state 1 in the horizontal axis indicates a state of rupture. The mean pulsatility in ruptured cases is significantly smaller by a factor 6 compared with their non-ruptured counterparts (p=0.05).

3. CONCLUSIONS

The pulsatility of Time-Intensity-Curves can be used to assess intra-aneurismal flow and daily clinical assessment. They can determine cardiac frequency and provide a mathematical signal object that can be analyzed with linear methods. This pulsatility can be controlled with a precise injection protocol if mean flow rate in parent artery is measured. We observed that the aneurismal geometry and locations could influence the TIC patterns, with potential applications in evaluating unruptured aneurysms status or impact of devices used as treatment. TICs could also be used to reveal complexity of flows, which may help in validating simulations and measuring stent performance without carrying heavy experiments like PIV.

REFERENCES

[1] C. Sadasivan, B.B. Lieber, M.J. Gounis, D.K. Lopes, and L.N. Hopkins, Angiographic quantification of contrast medium washout from cerebral aneurysms after stent placement *AJNR Am. J. Neuroradiol.*, 23, 1214-1221, 2002.

[2] H. Tenjin, F. Asakura, Y. Nakahara, K. Matsumoto, T. Matsuo, F. Urano, and S. Ueda, Evaluation of Intraaneurysmal Blood Velocity by Time-Density Curve Analysis and Digital Subtraction Angiography, *Am J Neuroradiol 19*, 1303–1307, 1998.

[3] I. Waechter, J. Bredno, R. Hermans, J. Weese, D.C. Baratt, D.J. Hawkes, Model-based blood flow quantification from rotational angiography, *Medical Image Analysis*, 12, 586-602, 2008

2nd International Conference on Mathematical and Computational Biomedical Engineering – CMBE2011
March 30 – April 1, 2011, Washington D.C., USA
P. Nithiarasu and R. Löhner (eds)

CONTRIBUTIONS OF IMAGE-BASED CFD TO THE EVALUATION OF INTRACRANIAL ANEURYSMS RUPTURE RISK

Juan R. Cebral*, Fernando Mut*, Daniel Sforza*, and Christopher M. Putman**
*Center for Computational Fluid Dynamics, George Mason University,
4400 University Drive, Fairfax, VA 22030, USA, jcebral@gmu.edu
**Interventional Neuroradiology, Inova Fairfax Hospital,
3300 Gallows Rd, Falls Church, VA 22042, christopher.putman@inova.com

SUMMARY

Evaluating the risk of rupture of cerebral aneurysms requires the establishment of statistical associations between hemodynamic and geometric variables to aneurysmal rupture as well as a better understanding of the underlying mechanisms governing the natural history of intracranial aneurysms. This article summarizes recent results towards these two ends using image-based computational fluid dynamics models.

Key Words: *cerebral aneurysm, hemodynamics, growth and rupture.*

1. INTRODUCTION

Advances in neuroimaging technology have resulted in the detection of increased numbers of unruptured cerebral aneurysms. While the risks of surgical and endovascular interventions are well known and improving, little is known about the natural rupture risks of intracranial aneurysms. However, planning elective interventions requires judging the relative weight of the natural and procedural risks. Currently, risk assessment is based on aneurysm size, location and some morphologic factors such as aspect ratio as well as the patient's clinical status. But hemodynamics is thought to be an important factor in the processes of aneurysm development, growth and rupture. Thus, improving rupture risk analysis requires on one hand the establishment of statistical correlations between geometric and hemodynamic variables and aneurysmal rupture, and on the other hand a better understanding of the mechanisms governing the natural history of cerebral aneurysms that explain the observed correlations. The purpose of our work is then twofold: to identify hemodynamic variables associated with rupture, and to improve our understanding of the role of hemodynamics in the underlying mechanisms responsible for aneurysm formation, progression and rupture.

2. METHODS

Patient-specific computational fluid dynamics (CFD) models are constructed from 3D medical images using previously developed methods [1]. Blood flows are represented by the unsteady incompressible Navier-Stokes equations, which are numerically solved using finite element methods on unstructured tetrahedral grids. Pulsatile physiologic flow conditions are derived from measurements on normal subjects. The resulting flow fields are visualized and the flow patterns are classified according to the following characteristics: a) complexity (simple/complex), b) stability (stable/unstable), c) inflow concentration (diffuse/concentrated), and d) impingement size (large/small). Additionally, the vascular models are subdivided into different geographic regions: a) aneurysm orifice, b) aneurysm neck, c) aneurysm body, d) aneurysm dome, e) near

parent artery, and f) far parent artery (see Figure 1 – bottom right). A number of hemodynamic variables or measures are then calculated using this geographic subdivision, including [2]: a) maximum aneurysmal wall shear stress (MWSS), b) inflow concentration index (ICI), c) shear concentration index (SCI), d) low shear area (LSA), e) low shear index (LSI), f) kinetic energy ratio (KER), g) viscous dissipation ratio (VDR). The mean values of these variables computed over groups of ruptured and unruptured aneurysms were then statistically compared. In order to study the relationship between the local hemodynamic environment and the progression of cerebral aneurysms, patient-specific CFD models are constructed from longitudinal CTA images of stable and growing aneurysms. The vascular models corresponding to consecutive imaging studies are aligned trying to maximize the coincidence of the parent arteries. Deformation fields are then obtained by computing the shortest distance between consecutive surface models, and regions of aneurysmal enlargement or deformation are identified. Hemodynamic variables are then averaged over the growing and non-growing regions and compared. Additionally, possible contacts with extra-vascular structures such as bone are identified in the CTA images. If such contacts are observed, the extra-vascular structures are segmented and the regions of contacts are identified by computing the distances between the vascular and extra-vascular surface models.

3. RESULTS

A total of 210 patient-specific cerebral aneurysms were analyzed. Each aneurysm was visually inspected and by two investigators and classified into each of the hemodynamic categories described before. Then, the numbers of ruptured and unruptured aneurysms in each category were counted and statistically analyzed using 2x2 contingency tables. The results are presented in Figure 1 (top-left) [3]. This figure shows that ruptured aneurysms are statistically more likely to have complex flow patterns, unstable flow structures, concentrated inflows and small impingement regions. The analysis also revealed a low inter-observer variability (not shown).

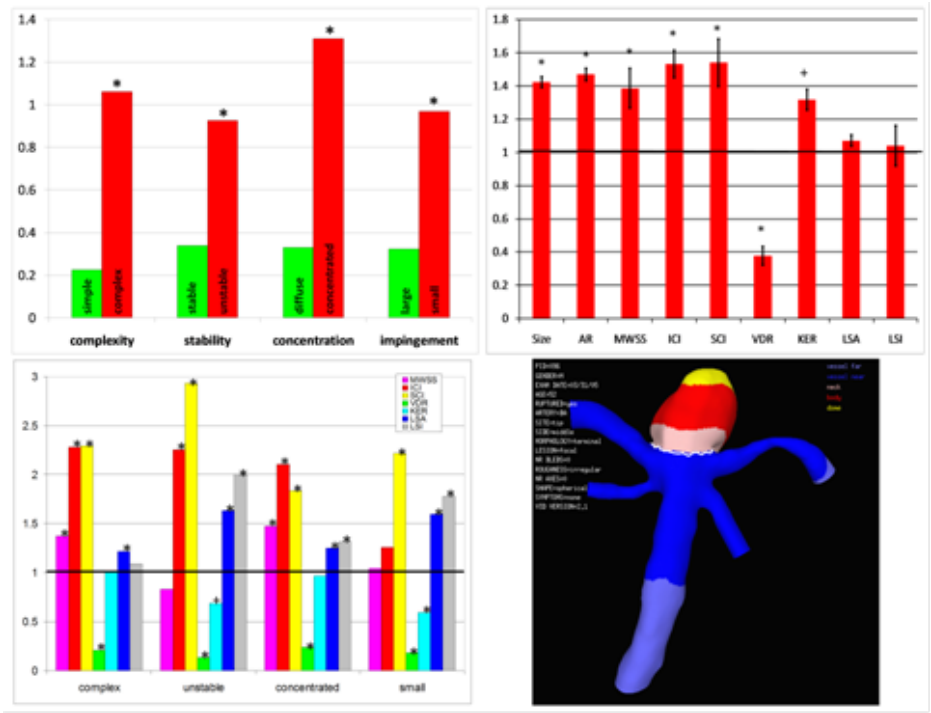

Figure 1: Top left: relative number of ruptured to unruptured aneurysms into each hemodynamic category. Top right: ratio of hemodynamic variables averaged over the ruptured and unruptured groups. Bottom left: ratio of hemodynamic variables averaged over each hemodynamic category. Bottom right: example of geographic subdivision of aneurysm model.

Subsequently, a number of quantitative hemodynamic measures were calculated for each aneurysm. The mean values of these variables averaged over the rupture and the unruptured aneurysm groups were computed and statistically compared using Student's t-test. The results are presented in Figure 1 (top-right) [4]. The results indicate that ruptured aneurysms are statistically associated to higher maximum WSS, larger inflow concentration indices, larger shear concentration indices, larger kinetic energy ratios (only 90% confidence), and smaller viscous dissipation ratios, as well as larger sizes and aspect ratios. In contrast, the low shear area and low shear indices were not significantly different between ruptured and unruptured aneurysm groups. The error bars in this plot represents the variability with respect to the choice of physiologic flow conditions, showing that the statistical associations are maintained under different flow conditions. Finally, the relationships between the different qualitative hemodynamic characteristics and quantitative measures are presented in Figure 1 (bottom-left) [2].

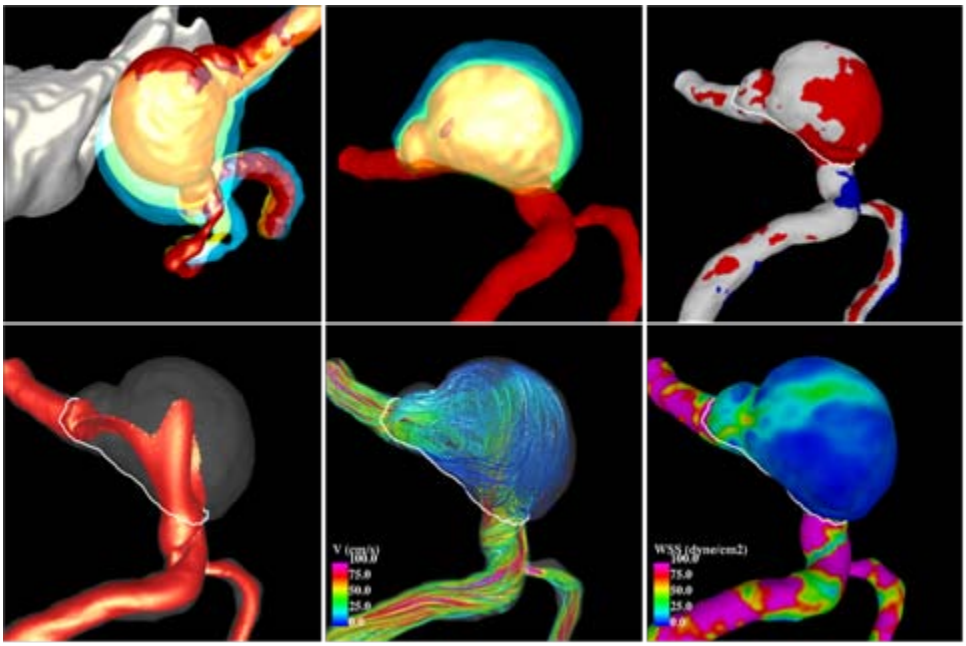

Figure 2: Example of a growing aneurysm in contact with peri-aneurysmal environment structures (bone). Top, left to right: vascular models during aneurysm evolution aligned to the bone, models aligned to the parent artery, regions of aneurysmal displacement. Bottom, left to right: inflow jets, flow pattern, wall shear stress at peak systole.

The importance of including contacts with extra-vascular structures in studies of the relationship between hemodynamics and aneurysm growth is illustrated with a case study of a growing basilar artery aneurysm. As this aneurysm grows, it pushes against the bone inducing a change in the parent artery geometry (Figure 2, top-left) that in turn affects the intra-aneurysmal hemodynamics. Alignment of the evolving vascular geometries with respect to the parent artery (Figure 2, top-center) may then result in underestimations of the aneurysm progression in the region of contact (Figure 2, top-right). In this particular aneurysm, the region of contact with bone is aligned with the inflow jet and subject to moderate to high wall shear stress (Figure 2, bottom row). Additionally, a "notch" near the distal end of the aneurysm, which is also subject to moderate to high WSS, is seen to enlarge in subsequent follow up geometries. The region of lowest WSS is also seen to expand outwards, but this could be the result of pushing against the bone on the distal side of the aneurysm body.

4. CONCLUSIONS

A computational hemodynamics modelling framework for the analysis of cerebral aneurysms has been developed. This framework has been used to explore possible relationship between hemodynamic characteristics and aneurysm rupture that could potentially be used for rupture risk stratification. Interesting statistical associations between qualitative hemodynamic characteristics as well as quantitative measures and aneurysm rupture were found in set of 210 cerebral aneurysms. These associations were largely independent from the choice of physiologic flow conditions and showed low inter-operator variability. Finally, the analysis framework was extended to the study of aneurysm progression based on longitudinal image data. Preliminary results indicate that vascular models representing different stages of the aneurysm evolution must be carefully aligned in order to determine regions of aneurysm growth, and that contacts with peri-aneurysmal environment structures such as bone can substantially affect the results and alter the aneurysmal hemodynamics and therefore must be considered. Combining studies of the association of hemodynamic characteristics and rupture with investigations of the underlying mechanisms responsible for aneurysm progression and rupture is important for building reliable rupture risk stratification systems and ultimately improving patient care.

REFERENCES

1. Cebral, J.R., et al., *Efficient pipeline for image-based patient-specific analysis of cerebral aneurysm hemodynamics: Technique and sensitivity*. IEEE Transactions in Medical Imaging, 2005. **24**(1): p. 457-467.
2. Mut, F., et al., *Computational hemodynamics framework for the analysis of cerebral aneurysms.* Int J Num Meth Biomed Eng, 2011. **in press**.
3. Cebral, J.R., et al., *Association of hemodynamic characteristics and cerebral aneurysm rupture.* AJNR American Journal of Neuroradiology, 2011. **in press**.
4. Cebral, J.R., et al., *Quantitative characterization of the hemodynamic environment in ruptured and unruptured brain aneurysms.* AJNR American Journal of Neuroradiology, 2011. **in press**.

2nd International Conference on Mathematical and Computational Biomedical Engineering - CMBE2011
March 30 - April 1, 2011, Washington D.C, USA
P. Nithiarasu and R. Löhner (Eds.)

Computational and Statistical Analysis of ICA Morphology and Hemodynamics

Tiziano Passerini[⋆], **Marina Piccinelli**[⋆], **Alessandro Veneziani**[⋆], **Laura M. Sangalli**[⋆⋆], **Piercesare Secchi**[⋆⋆] **and Simone Vantini**[⋆⋆]

[⋆]Department of Mathematics and Computer Science, Emory University, 400 Dowman Dr., W401 Atlanta, GA 30322, tiziano@mathcs.emory.edu, ale@mathcs.emory.edu

[⋆⋆]MOX, Department of Mathematics, Politecnico di Milano, via Bonardi 9, 20133 Milano, laura.sangalli@polimi.it, piercesare.secchi@polimi.it, simone.vantini@polimi.it

SUMMARY

Stemming from previous works presented by the coauthors, this research aims at defining a set of parameters describing both the morphologic features and hemodynamics of the internal carotid artery (ICA), that significantly and jointly correlate with the location of aneurysms and possibly with their tendency to rupture.

Key Words: *blood flow, wall shear stress, aneurysm, functional data analysis.*

1 INTRODUCTION

As many concurrent causes appear to underlie the occurrence and development of cerebral aneurysms, an integrated approach is required to understand the interplay between the different factors. It is suggested that the association of several conditions rather than the evidence of a single factor would lead to a more effective risk stratification. On the other hand, there is still no clear agreement on which features to choose as the most significant risk indicators. The number of possible risk factors is large, so that statistical analyses on large data sets are in order to compare intra-patient with inter-patient variability pointing out subjects (or even groups of subjects) that strongly deviate from the average physiological condition. To this aim, retrospective studies, despite having the intrinsic limitation of not being able to evaluate the history of the pathology progression, can shed a light on the significant associations of risk factors to the onset of the disease.

It has been shown that morphological characterization of the cerebral vasculature allows to define parameters which are measurable in a robust and reproducible way [1], and that correlate with the aneurysm location and rupture [2,3,4]. In the context of CFD modeling, it has become more and more evident that it is necessary to take into account both local and non local features of blood flow in the cerebral circulation. The significance of risk factors identified by considering the local flow features may be strongly altered by concurring non-local circumstances, which should not be neglected [5]. This motivates the approach followed in the present work, in which the internal carotid artery (ICA) is studied both as a possible site for aneurysms development and as a feeding vessel for the downstream arteries. In the cerebral circulation, the morphological features of the feeding arteries could determine a hemodynamics environment which is more or less protective from the disease. Results of a recent work from some of the coauthors seem to support this conjecture, by considering the number and shape of bends in the siphon of the ICA

[6]. The syphon seems to act like a damper for stresses induced by the fluid dynamics in the brain vasculature.

The Aneurisk research project (2005-2008) was developed by a joint venture of different subjects: academic and non academic research centers (MOX - Department of Mathematics, and LaBS - Department of Structural Engineering, Politecnico di Milano; "M. Negri" Institute for Farmacological Research, Bergamo), medical centers (Dipartimento di Neurochirurgia, Università degli Studi di Milano; Ospedale Niguarda Ca' Granda di Milano; Ospedale Maggiore Policlinico di Milano), industrial partners (Siemens Medical Solutions Italy; Fondazione Politecnico di Milano). In this work we plan to adopt the methods and models from Aneurisk to perform statistical analysis correlating morphology and blood dynamics features of the ICA, for outlining possible conditions triggering the development of the pathology in the cerebral circulation. The outcome is two-fold. On the one hand, we present a framework for geometric and hemodynamic studies of cardiovascular problems, discussing in particular how we can achieve robustness and reproducibility of our analysis. On the other hand, our results support the assumption that a combined evaluation of blood flow features and vascular morphology can increase the descriptive capability of statistical techniques applied to large data sets of patients, and possibly their predictive potential.

2 METHODOLOGY AND RESULTS

Geometrical processing. VMTK (www.vmtk.org) is the adopted tool for the geometric characterization of aneurysms and their parent vasculature. Blood vessels can be effectively represented by centerlines, synthetic descriptors of the geometry and the topology of vascular networks. For the purposes of this work, a centerline is defined as the weighted shortest path traced between the inlet and the outlet of a vessel, the weight depending on the distance from the surface [1]. The construction of centerlines is particularly useful in the study of bifurcating vessels, since it allows the identification and characterization of the bifurcation points. Moreover, after splitting the centerlines into tracts corresponding to the bifurcation branches, the same partition can be induced in the surface representing the vessel, associating each surface point to its nearest centerline point. A curvilinear reference system can be defined on each centerline branch, centered in the bifurcation point.

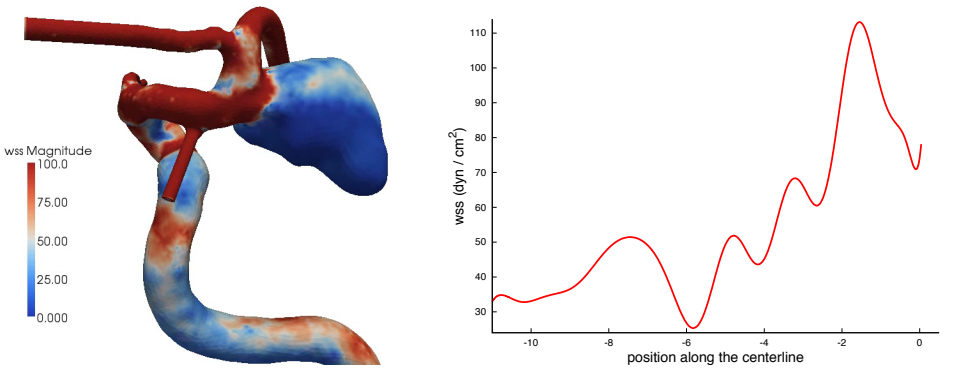

Figure 1: Definition of the WSS as a function of the curvilinear abscissa. To each value of the curvilinear abscissa an average WSS is associated. The origin of the reference system is placed at the terminal bifurcation of the ICA.

Fluid dynamics has been simulated in patient-specific 3D models using a software based on LifeV (www.lifev.org). The computational domain was assumed to be fixed, corresponding to the hypothesis of rigid vascular walls which has been shown to be acceptable for intracranial vasculature

[7]. We further assumed that blood can be modeled as a continuous incompressible Newtonian fluid, so that the blood flow problem can be described by the incompressible Navier-Stokes equations. For each vascular geometry, three cardiac cyles were simulated, in order to reduce the effects of the initial conditions and obtain the periodic solution in the last simulated heartbeat. Proper boundary conditions were prescribed, producing the same flow regime in all the computational domains. The wall shear stress (WSS) was computed on the lateral surface of each geometry, representing the vascular wall. After processing the geometry with VMTK, each surface point was associated to a value of the centerline curvilinear abscissa. Conversely, to each value of the curvilinear abscissa along the centerline we associated a measure of the average WSS exerted by the blood flow on the corresponding tract of the arterial wall.

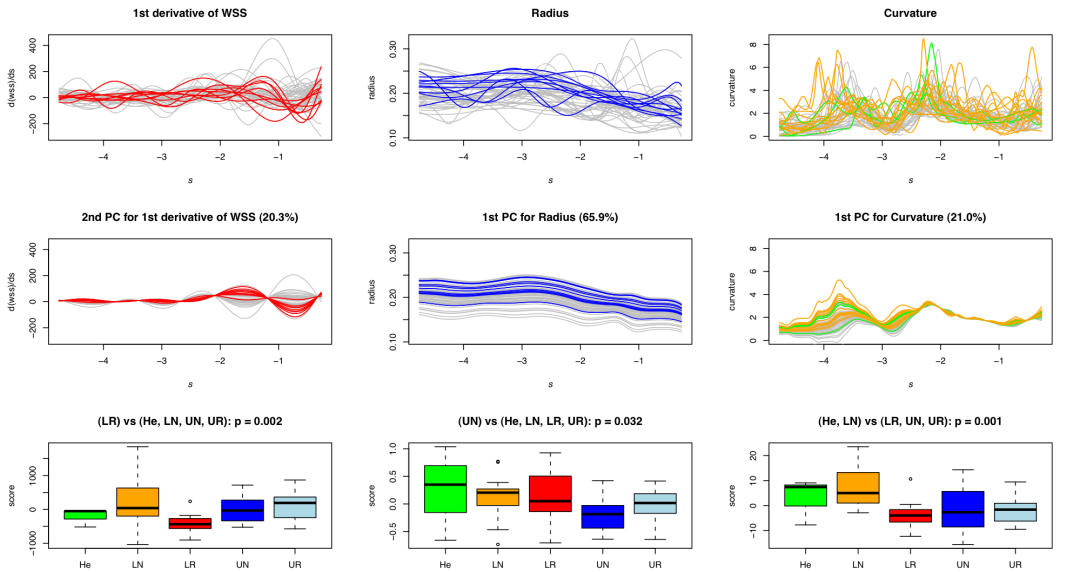

Figure 2: First row: functional data set (first derivatives of WSS, radius of ICA, and curvature of ICA centerlines, respectively). Second row: some main modes of variability detected by functional principal component analysis. Third row: boxplots of the variability manifested by the patients along the corresponding modes of variability, divided by pathological groups.

Statistical analysis. Following the approach adopted in Aneurisk [3], the geometric features of the centerline (radius, curvature) and its hemodynamic attributes (average WSS on tracts of the arterial wall), together with their derivatives with respect to the curvilinear abscissa, were modeled as the realization of random functions of the curvilinear abscissa. A suitable estimation step was devised for eliminating artefacts and bias of the data due to the different size of the vascular districts in different patients or to differences in image acquisition [8]. A joint clustering and alignment of functional data was obtained by means of a two-mean alignment of the centerlines [6]. The main modes of variability present in the functional data set were extracted by means of a Functional Principal Component (PC) Analysis, and finally a classification of the patients was established, based on the Quadratic Discriminant Analysis (QDA) [3]. This statistical analysis was intended to identify the morphological/fluid dynamical features significantly correlated with the location of the disease in the cerebral circulation and with the event of rupture.

A data set of 45 3D computed rotational angiography (CRA) images was considered, and the described steps were performed for each case. A multivariate analysis of variance of the reduced functional data set suggests the joint presence of just one siphon along the ICA and of a small average radius of the ICA to be significantly associated to the presence of a ruptured aneurysm in

the cerebral circulation; moreover the location of the ruptured aneurysm seems to be associated to a peak of the WSS in the same location. On the other hand, either a wider radius of the ICA or the presence of two siphons along to ICA seems to be sufficient for not having rupture events (even when an aneurysm is present). These preliminary results suggest that the presence of more marked bends in the ICA could have a protective effect on the vasculature downstream the terminal bifurcation. This is likely due to larger dissipation of the blood flow energy induced by the geometry. This protective effect is enhanced by a larger radius of the ICA and the absence of abrupt localized changes of the WSS along the centerline.

3 CONCLUSIONS

In the framework here described, geometrical reconstruction and characterization of the vascular structures can be obtained in a semi-automatic and reproducible manner. We describe the fluid dynamics parameters as functions of the curvilinear abscissa along the centerline, to achieve synthesis through dimensional reduction and to feed data to a statistical analysis technique proven to be effective for the characterization of large data sets. Future work includes the application of the proposed approach to the complete set of 159 patient-specific geometrical models available in the Aneurisk database, in view of the identification of existing correlations and recurrent geometrical/fluid dynamical patterns and possibly the definition of a potential rupture risk index.

REFERENCES

[1] M. Piccinelli, A. Veneziani, D. A. Steinman, A. Remuzzi and L. Antiga, A framework for geometric analysis of vascular structures: application to cerebral aneurysms, *IEEE Transactions on Medical Imaging*, 28(8), 1141-55, 2009.

[2] M. Tremmel, S. Dhar, E. I. Levy, J. Mocco and H. Meng, Influence of intracranial aneurysm-to-parent vessel size ratio on hemodynamics and implication for rupture: results from a virtual experimental study, *Neurosurgery*, 64 (4), 622-30, 2009.

[3] L. M. Sangalli, P. Secchi, S. Vantini, A. Veneziani, A Case Study in Exploratory Functional Data Analysis: Geometrical Features of the Internal Carotid Artery, *Journal of the American Statistical Association*, 104 (485), 37-48, 2009.

[4] M. Piccinelli, S. Bacigaluppi, E. Boccardi, B. Ene-Iordache, A. Remuzzi, A. Veneziani and L. Antiga, Geometry of the ICA and recurrent patterns in location, orientation and rupture status of lateral aneurysms: an image-based computational study, *Neurosurgery*, in press, 2010.

[5] M. A. Castro, C. M. Putman and J. R. Cebral, Patient-specific computational fluid dynamics modeling of anterior communicating artery aneurysms: a study of the sensitivity of intra-aneurysmal flow patterns to flow conditions in the carotid arteries, *AJNR American journal of neuroradiology*, 27, 2061-2068, 2006.

[6] L. M. Sangalli, P. Secchi, S. Vantini, and V. Vitelli, K-mean alignment for curve clustering, *Computational Statistics & Data Analysis*, 54 (5), 1219-1233, 2010.

[7] D. M. Sforza, R. Loehner, C. Putman, J. R. Cebral, Hemodynamic analysis of intracranial aneurysms with moving parent arteries: Basilar tip aneurysms, *International Journal for Numerical Methods in Biomedical Engineering*, 26 (10), 1219-1227, 2010.

[8] L. M. Sangalli, P. Secchi, S. Vantini, A. Veneziani, Efficient estimation of three-dimensional curves and their derivatives by free-knot regression splines, applied to the analysis of inner carotid artery centrelines, *Journal of the Royal Statistical Society, Series C (Applied Statistics)*, 58(3), 285-306, 2009.

2nd International Conference on Mathematical and Computational Biomedical Engineering - CMBE2011
March 30 - April 1, 2011, Washington D.C, USA
P. Nithiarasu and R. Löhner (Eds.)

Effect of flow diverters on IA flow dynamics: assessment in 23 aneurysms

I. Larrabide[†⋆], M. Aguilar[†⋆], H. Morales[⋆†], S. Cito[⋆†], D. Rüfenacht[§], Z. Kulcsar[§], S. Wetzel[§] and A. F. Frangi[⋆†‡]

[⋆] Center for Computational Imaging & Simulation Technologies in Biomedicine (CISTIB), Universitat Pompeu Fabra, Barcelona, Spain

[†] Networking Center on Biomedical Research (CIBER-BBN), Barcelona, Spain

[§] Department of Neuroradiology, Swiss Neuro Institute, Hirslanden Klinic, Zürich, Switzerland

[‡] Institució Catalana de Recerca i Estudis Avançats (ICREA), Barcelona, Spain

ignacio.larrabide@upf.edu

SUMMARY

The treatment of intracranial aneurysms with flow diverters is becoming more frequent between neuro-interventionists. Despite this, the effect of these new devices on the local hemodynamics is not fully understood and contradictory clinical outcomes have been reported in the literature. Twenty-three intracranial aneurysms of different size and shape have been virtually treated and hemodynamic alterations after treatment have been analyzed using CFD. In general, the effect of the placement of the device was to considerably alter the flow inside the aneurysm and diminish its activity.

Key Words: *cerebral aneurysm, flow diverters, CFD*

1 INTRODUCTION

In the recent years, a variety of new alternatives for endovascular treatment of intracranial aneurysms have appeared, which have substantially improved the therapeutic outcome. Still, the effect of some of these treatments on local hemodynamics is not fully understood. In particular, the use flow diverting devices has not been thoroughly described so far, and the published reports of this experience are scarce [8]. Flow diverters are stent-like devices specially designed to reconstruct the parent artery and divert blood flow along the normal anatomical course of the vessel and away from the aneurysm neck and dome. Some recent studies have been showing different clinical outcomes for this therapy [3]. Also, different studies have been developed to study their effect in a controlled environment. In-vitro studies by Canton et al. [4] uses Particle Image Velocimetry (PIV) to quantify the velocity related variables before and after treatment. The work of Augsburguer et al. [2] focused on the effect of such devices on shear driven and inertia driven aneurysm geometries.

The effect of these devices on realistic geometries has not been largely addressed so far. The use of Computational Fluid Dynamics (CFD) can provide a better and more detailed insight of the effect of these devices on patients. The objective of the present study was to assess the "device-induced" alterations on the intra-aneurysmal flow dynamics using CFD in realistic geometries. In the current study we present the results obtained for a series of 23 intracranial aneurysms virtually treated with a flow diversion device.

2 MATERIALS AND METHODS

The anatomical models studied in this paper have been obtained from diagnostic 3D rotational angiographic (3DRA) images, which have been acquired using either an Integris^{TM} Allura System (Philips Healthcare, Best, The Netherlands) or an AXIOM Artis (Siemens Medical Solutions, Erlangen, Germany). Voxel sizes in the reconstructed 3D images ranged from 0.208 mm^3 to 0.378 mm^3. All the aneurysms correspond to three locations along the internal carotid artery (ICA), which are normally treated using flow diverter devices, namely anterior choroidal artery (AChA), ophthalmic artery (Opht) and posterior communicating artery (PComm). From a set of forty aneurysms, three independent clinicians were asked to select the appropriate treatment for each aneurysms. The aneurysms were selected for the study if at least two clinicians selected them for treatment with flow diverter, thus our population was reduced to 23 aneurysms. The remaining aneurysms were considered as not appropriate for this treatment because they were more suitable for stent assisted coiling, or because they presented small neck or branches near the aneurysm. The studied aneurysms were located along the ICA as follows: 3 (13%) for the AChA, 11 (47%) for the Opht and 9 (38%) for the PComm. The aneurysm sizes ranged between 1.3 to 22 mm of depth. The size of the aneurysms (small, medium and large/giant) has been determined based on the measurements used in a study by Ishibashi et al. [6]. For the group under study we have 10 (43%) small, 9 (39%) medium, and 4 (17%) large/giant aneurysms. The gender of the patients was females 70% and males 30% and their average age was 50 (SD$\pm$8) at the moment the aneurysm was discovered. Regarding the shape of the aneurysms 65% were saccular and 35% were fusiform.

The patient images were segmented using Geodesic Active Regions (GAR) [5]. From the vasculature segmentation, a 3D model consisting of a triangulated surface mesh was generated. In some cases these models contained artifacts and vessels that were not of interest for the study. Triangle removal, hole filling and volume preserving Laplacian smoothing of the vessel was necessary to reduce any imperfections on the vessel wall. The stent deployment was performed using the Fast Virtual Stenting method proposed by Larrabide et al. [7]. The diameter of the stent strut was set to 0.06 mm, following Silk device (Balt Extrusion, Montmorency, France) specifications. From the skeleton of the vascular region of interest, a point under the aneurysm neck was selected to specify the location of the stent longitudinal center. All volumetric meshes were generated using the commercial software ANSYS ICEM CFD (Ansys Inc., Canonsburg, PA, USA) and were composed of unstructured tetrahedral and 8-node prism elements. A mesh independency test showed that an element size of 1.6×10^{-5}m around the stent struts was appropriate. Following the study of Appanaboyina et al. [1], the part of the stent laying over the vessel was removed and only the portion of the stent covering the aneurysm ostium were considered for the CFD analysis. The resulting meshes were approximately 7.6×10^5 elements for the untreated cases and 7.36×10^6 elements for the treated cases. Boundary conditions were imposed according to a 1D mathematical model of the systemic tree. At the inlet, which was the internal carotid artery for all the selected patients, a mass flow rate was imposed, whereas pressure was imposed at the outlets.

3 RESULTS

Different variables were studies before and after the implantation of the device for the CFD results. These were the wall shear stress (WSS) in the aneurysm dome, the 90 percentile highest WSS in the aneurysm dome (WSS90), inflow in the aneurysm per second (Q_{an}) and flow velocity at the aneurysm ($\overline{\mathbf{v}}_{an}$).

In Figure 1 are presented three selected cases corresponding to a large, a medium and a small aneurysm. The first two columns present the WSS before and after treatment, which is alleviated

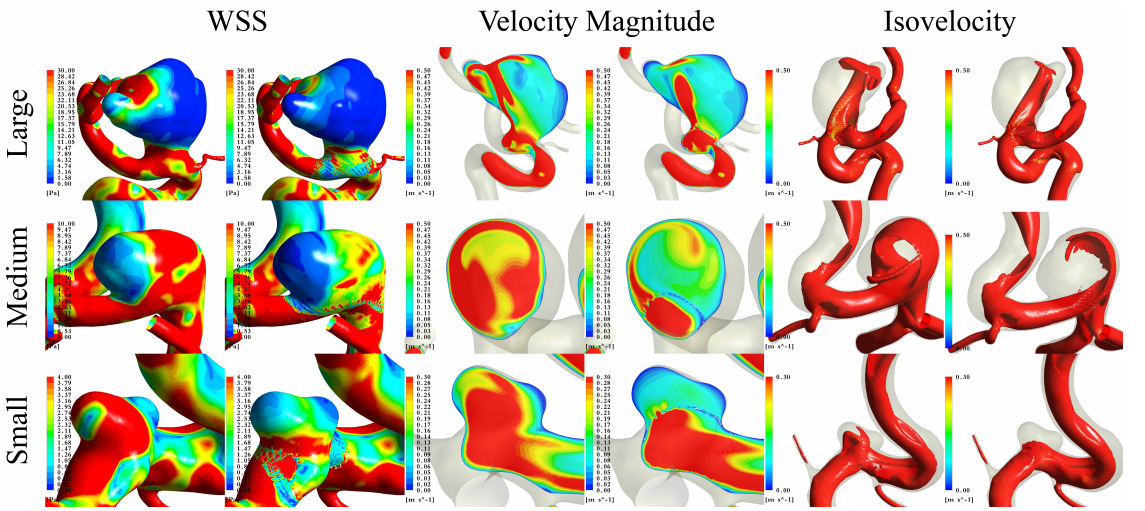

Figure 1: Results for the CFD simulations. Images for the WSS (column 1 and 2), velocity contours at a middle plane in the aneurysm (columns 3 and 4) and isosurface (columns 5 and 6), both before and after the treatment are presented. Results correspond to peak systole.

by the presence of the device. The velocity magnitude contours at the aneurysm middle plane are presented in the third and fourth columns before and after the treatment, respectvely. The effect of the device is clearly visible. It can be observed that high velocities are redirected away from the aneurysm dome into the parent vessel. This can laso be observed from the iso-velocities (fifth and sixth columns for untreated and treated, respectively). The results shown correspond to the peak systole.

Table 1 summarizes the results obtained from the study. The twenty-three aneurysms have been classified according to two different characteristics. First, all the aneurysms been classified for their size (i.e, small, medium and large/giant). From this we observe a larger impact of the device on small aneurysms regarding the reduction of WSS90 and WSS. Regarding the velocity, similar reductions are observed. In the worst case, the WSS is alleviated by a minimum of 50%. For the Q_{an} and $\overline{\mathbf{v}}_{an}$, the differences observed between groups are negligible. Secondly, they have been grouped according to their shape (i.e., fusiform and saccular). In this case, the WSS90, WSS and $\overline{\mathbf{v}}_{an}$ we observe a larger impact on saccular aneurysms than on fusiform ones. Regarding Q_{an}, the effect on both groups is similar.

		WSS	WSS90	Q_{an}	$\overline{\mathbf{v}}_{an}$
Giant/Large	Max	79%	80%	79%	80%
	min	52%	55%	28%	42%
	Avg	64%	64%	56%	62%
Medium	Max	79%	80%	67%	77%
	min	58%	61%	42%	42%
	Avg	65%	66%	49%	59%
Small	Max	95%	97%	74%	95%
	min	52%	52%	33%	38%
	Avg	73%	73%	51%	63%

Table 1.1: Results organized by aneurysm size.

		WSS	WSS90	Q_{an}	$\overline{\mathbf{v}}_{an}$
Fusiform	Max	79%	80%	79%	80%
	min	52%	55%	28%	42%
	Avg	65%	65%	52%	59%
Saccular	Max	95%	97%	74%	95%
	min	52%	52%	33%	38%
	Avg	73%	73%	52%	64%

Table 1.2: Results organized by aneurysm shape.

Table 1: Percentages of reduction with respect to the untreated configuration. Max = maximum, min = minimum, Avg = average.

4 CONCLUSIONS

In this study, an analysis of the effect of flow diverter devices used in intracranial aneurysms using CFD was done. A population of twenty-three aneurysms was considered and intra-aneurysmal hemodynamics were studied before and after the implantation of the device. The group was separated by two means. First the aneurysms were separated by their size and second they were separated by their shape. As a conclusion, we can mention that the effect of flow diverters significantly reduced all hemodynamic variables studied. The largest effect was observed for saccular aneurysms.

5 ACKNOWLEDGEMENTS

This research has been partially funded by the Industrial and Technological Development Center (CDTI) under the CENIT-CDTEAM and CENIT-cvREMOD programs and by the European Commissions project @neurIST (IST-2005-027703).

References

[1] S. Appanaboyina, F. Mut, R. Löhner, C. Putman, and J. Cebral. Simulation of intracranial aneurysm stenting: Techniques and challenges. *Comput. Meth. Appl. Mech. Eng.*, 198(45-46):3567 – 3582, 2009. Models and Methods in Computational Vascular and Cardiovascular Mechanics.

[2] L. Augsburger, M. Farhat, P. Reymond, E. Fonck, Z. Kulcsar, N. Stergiopulos, and D. Rfenacht. Effect of flow diverter porosity on intraaneurysmal blood flow. *Clinical Neuroradiology*, 19(3):204–214, August 2009.

[3] J.R. Cebral, F. Mut, M. Raschi, E. Scrivano, R. Ceratto, P. Lylyk, and C.M. Putman. Aneurysm rupture following treatment with flow-diverting stents: Computational hemodynamics analysis of treatment. *Am. J. Neuroradiol.*, XX(YY):DOI:10.3174/ajnr.A2398, 2010.

[4] C. Gádor, D. I. Levy, and L. C. Lasheras. Hemodynamic changes due to stent placement in bifurcating intracranial aneurysms. *J. Neurosurg.*, 103(1):146–155, 2005.

[5] M. Hernandez and A. F. Frangi. Non-parametric geodesic active regions: Method and evaluation for cerebral aneurysms segmentation in 3DRA and CTA. *Med. Image Anal.*, 11(3):224–241, 2007.

[6] T. Ishibashi, Y. Murayama, M. Urashima, T. Saguchi, M. Ebara, H. Arakawa, K. Irie, H. Takao, and T. Abe. Unruptured intracranial aneurysms: Incidence of rupture and risk factors. *Stroke*, 40(1):313–316, 2009.

[7] I. Larrabide, M. Kim, L. Augsburger, M. C. Villa-Uriol, D.Rüfenacht, and A. F. Frangi. Fast virtual deployment of self-expandable stents: method and in-vitro evaluation for intracranial aneurysmal stenting. *Med. Image Anal.*, DOI: http://dx.doi.org/10.1016/j.media.2010.04.009, 2010.

[8] I. Szikora, Z. Berentei, Z. Kulcsar, M. Marosfoi, Z. S. Vajda, W. Lee, A. Berez, and P. K. Nelson. Treatment of intracranial aneurysms by functional reconstruction of the parent artery: The budapest experience with the pipeline embolization device. *Am. J. Neuroradiol.*, page ajnr.A2023, February 2010.

2nd International Conference on Mathematical and Computational Biomedical Engineering – CMBE2011
March 30 – April 1, 2011, Washington D.C., USA
P. Nithiarasu and R. Löhner (eds)

Techniques for automatic aneurysm neck plane detection and geometric characterization of 3D aneurysmal sac

M.Piccinelli[1], Y. Hoi[2], A. Veneziani[1], D.A. Steinman[2] and L. Antiga[3]
[1]Math&CS Department, Emory University, Atlanta, US, marina@mathcs.emory.edu, ale@mathcs.emory.edu
[2] Department of Mechanical and Industrial Engineering, University of Toronto, Toronto, Canada, ymhoi@mie.utoronto.ca, steinman@mie.utoronto.ca
[3] Orobix srl, Bergamo, Italy, luca.antiga@orobix.com

SUMMARY

The three dimensional (3D) morphology of aneurysms is presumably one of the key factors reflecting the biomechanical mechanisms that contribute to rupture. A computational technique is presented for detection of aneurysm neck and delineation of sac from 3D surface models of cerebral aneurysms and their parent vasculature. The extraction of 3D geometric features may improve our ability in designing more reliable geometry-based rupture risk indexes.

Key Words: *Cerebral aneurysms, 3D geometry, rupture risk.*

1. INTRODUCTION

In recent years, the increasing rate of detection of unruptured intracranial anuerysm (IA) and the catastrophic consequences of subarachnoid haemorrhage have drawn attention to the crucial issue of whether these lesions should be treated or just followed up. In fact, the ideal situation would be to clinically address only those aneurysms that are more likely at risk of rupture.

A huge amount of work has been done in order to devise proper rupture risk indexes that could be applied in clinical settings. Hemodynamics has indeed been regarded as one of the crucial factors in IA development, growth and rupture and has been extensively explored, but the mechanisms involved are still to be clearly established and elucidated. Since geometry has a major impact on blood dynamics, one alternative approach is to examine vascular geometric features as they may become valid surrogates of specific flow conditions and shed light on hemodynamics associations with the disease.

As a consequence, aneurysmal sac morphology and more recently parent vasculature geometry have been independently investigated and have been found to correlate with aneurysm outcome. In addition, from a more pragmatic perspective, morphological measurements are the main guidance in handling IA in clinical practice. The most common geometric features span from one-dimensional (1D) measures like height or neck diameter to volumes and surfaces, to various ratios in order to obtain more comprehensive shape indexes[1,2] (i.e. aspect ratio as one of the most accepted).

Nevertheless, crucial issues still have to be addressed in geometry-based approaches. IA are characterized by a complex three dimensional (3D) structure which presumably play a role in aneurysm rupture, but that can be difficult to capture with one dimensional measures. Also, most of these measurements still rely on tedious and time consuming procedures where the “right” angiographic 2D projection should be detected and the measurement performed.

While this is partially due to the intrinsic difficulty of dealing with the large variability of cerebral anatomies and geometries, the lack of standardized definitions (for example of

aneurysm neck) and robust methodologies to cope with the complexity of 3D configurations might also hamper the development of more sophisticated approaches.

In the following we present a fully automated technique for localization of the neck section and extraction of 3D shape of the aneurysmal sac from surface models of cerebral aneurysms and their parent vasculature. The computation of some preliminary geometric primitives for the characterization of 3D sac morphology is also presented.

2. MAIN BODY

Our approach for localization of the aneurysm neck and geometric characterization of the 3D sac relies on the concepts of Voronoi diagram (VD), centerline and tube function as described in [3,4] and on their implementation within the Vascular Modeling Toolkit (VMTK)[5].

The methodologies were applied to a group of ninety-seven 3D surface models of saccular IA and their parent vasculature taken from the ANEURISK cohort[4]; the reconstructions were antecedently obtained by way of a segmentation step from 3D rotational angiography (3D-RA) images[4]. The selected group included 38 sidewall and 59 terminal aneurysm models; 42 were ruptured, 55 unruptured.

Given the 3D segmented surface, the starting point is the reconstruction of a plausible parent vessel by digitally removing the aneurysm sac[6], an operation performed by means of an automatic technique previously published by the authors (Figure 1A).

Since the two models, prior to and following aneurysm removal, differ only in the aneurysm sac protruding out of the diseased parent vessel, the aneurysmal surface can be retrieved by means of the tube function[3,4] of the centerline of the reconstructed artery, as the portion of the complete model lying far from the tube surface. Being the tube surface by construction strictly included in the lumen of the vascular segment, the sac surface hence obtained is an irregular saddle shape containing also tracts of the local parent vasculature (Figure 1B).

A distance metric is then defined on the sac as the shortest distance of every point to the tube surface; this allows us to move consistently away from the parent vessel within the aneurysm by means of an interpolated spline constructed over the barycenters of a set of iso-contours drawn on this distance field (Figure 1C).

Having the barycenter spline as a hinge through the aneurysmal shape, the sac surface is sliced at each spline point first perpendicularly to the spline and subsequently, with an array of planes that wobble around the barycenter by regularly changing their orientation with respect to the first perpendicular plane. For each slice, two main geometric parameters are considered: its area and, given the irregular shape of the sac surface at the interface with the parent vessel, where the neck actually localizes, whether this is an open or closed section. According to our approach the aneurysm neck is selected as the first closed section for which the area has a local minimum. Once the aneurysm neck has been identified, the “true” aneurysm sac without portions of parent vessels is considered by clipping the sac surface at the neck section plane (Figure 1D).

To characterize the 3D morphology of the aneurysm sac, we resort to its VD and subsets of it. The VD is a non manifold surface whose points are the centers of the maximal spheres inscribed in the shape; by computing the envelope of these spheres we obtain the 3D original object (Figure 1E). A subset of this VD, called the Voronoi core (VC) is also taken into consideration as the set of centers of spheres with radii greater than 75% of the maximum Voronoi radius; its envelope represents a smaller portion of the segmented aneurysm sac. The rationale behind the use of the VC and its envelope is to identify the most stable part of the 3D sac shape where ambiguous surface irregularities such as blebs and/or daughter sacs are excluded (Figure 1F). Volumes and surface areas of both envelopes are readily computable.

According to methodologies previously presented[3,4], the sac centerline is automatically extracted over the VC. Being computed on the VC, it represents the aneurysm sac along its most stable 3D direction of development, that is the core centerline will not travel into blebs or daughter sacs. For the estimation of the actual sac length, the maximum inscribed sphere radius at the last centerline point is added to the length of the centerline (Figure 1G).

In order to complete the characterization of the 3D nature of the sac, the VC envelope is also approximated with an inscribed ellipsoid that provides radii along the three main directions of the 3D sac shape (Figure 1H), similarly to [7].

By way of demonstration, these techniques were successfully applied to all 97 models; Figure 2-Rows A,C shows a small subgroup of them. In order to demonstrate the robustness of the techniques and to prove their applicability to clinical environments, where 3D segmentation tools may not be available, we applied our techniques to the same models obtained by means of isosurface thresholding of the 3D-RA images; in Figure 2-Rows B,D neck localization on those thresholded models is shown for a qualitative comparison. Differences in position of neck plane barycenters (Δp) and normals orientation ($\Delta\theta$) in segmented vs thresholded models were evaluated to test the robustness of the whole procedure: mean $\Delta p=0.72\pm0.65$ mm; mean $\Delta\theta=7.8\pm5.4$ degrees.

The goal behind the extraction of 3D measurements is to identify analogues of 2D quantities commonly used or to shape new indexes that can better account for sac morphology: the core centerline represents an example of a 3D definition of aneurysm length, ratios of the inscribed ellipsoid radii may provide a way to categorize the sac shape, VC envelope can robustly extract a stable portion of the sac volume in order to identify blebs or in general to define quantities related to surface irregularities. Whether this 3D geometry-based approach can be useful to better predict aneurysms rupture as well as their clinical significance are subject of ongoing work.

3. CONCLUSIONS

We presented a methodology for automatic identification of aneurysm neck plane and delineation of aneurysmal sac from 3D surface models of saccular aneurysms and their parent vasculature. Some basic geometric primitives for the characterization of 3D shapes and the computation of 3D measures were illustrated in order to provide 3D analogues of commonly used 2D measurements.

While representing a technical improvement, as future work these methodologies and definitions will be tested for their clinical significance, their actual ability to add information and improve the design of a reliable rupture risk index, and their applicability in a clinical setting.

REFERENCES

[1] M.L. Raghavan, B. Ma, R.E. Harbaugh, Quantified aneurysm shape and rupture risk, *J Neurosurg,*102(2), 355-62, 2004.

[2] S. Dhar, M. Tremmel, J. Mocco, M. Kim, J. Yamamoto, A.H. Siddiqui, L.N. Hopkins, H. Meng, Morphology parameters for intracranial aneurysm rupture risk assessment, *Neurosurgery,* 63(2), 185-96, 2008.

[3] L. Antiga, D.A. Steinman, Robust and objective decomposition and mapping of bifurcating vessels, *IEEE Transactions on Medical Imaging*, 23(6), 704-13, 2004.

[4] M. Piccinelli, A. Veneziani, D.A. Steinman, A. Remuzzi, L. Antiga, A framework for geometric analysis of vascular structures: application to cerebral aneurysms, *IEEE Transactions on Medical Imaging,* 28(8), 1141-55, 2009.

[5] L. Antiga, D.A. Steinman, Vascular Modeling Toolkit, Nov. 9, 2010. Available at http://www.vmtk.org.

[6] M.D. Ford, Y. Hoi, M. Piccinelli, L. Antiga, D.A. Steinman, An objective approach to digital removal of saccular aneurysms: technique and applications, *British Journal of Radiology*, 82 Spec No 1, S55-61.

[7] M.Raghavan, J. Torner, J. Zhang, I. Meissner, D. Piepgras, J. Houston, R. Brown, Assessment of intracranial aneurysm morphology in a large patient population, *The 6th World Congress on Biomechanics, Singapore*, 2010.

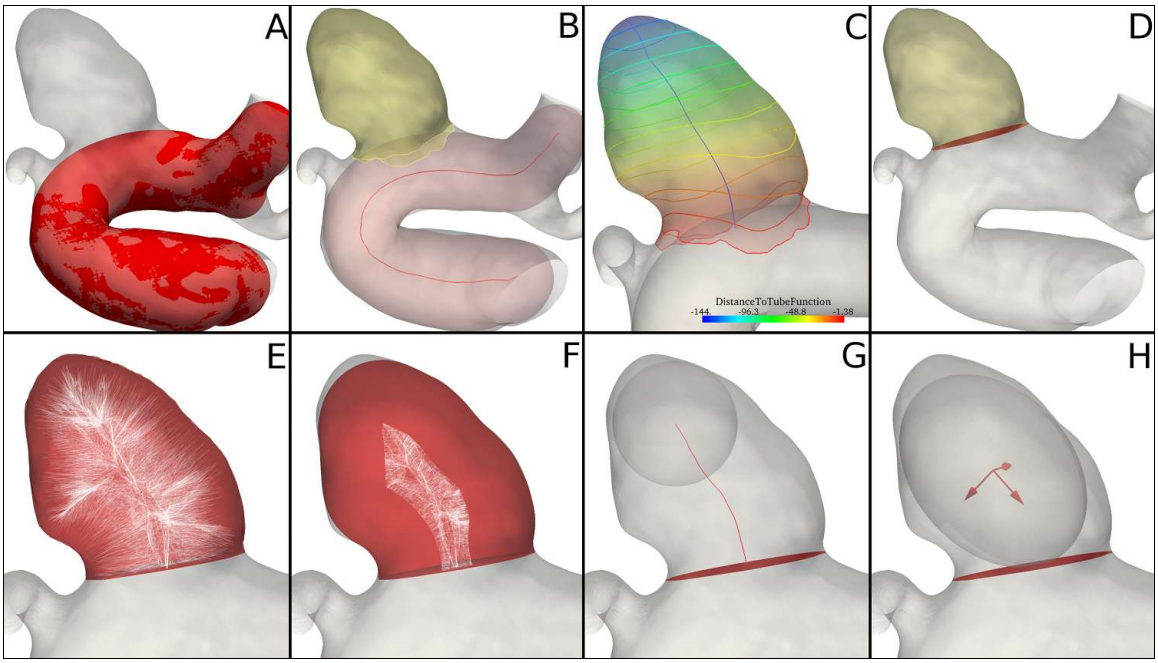

Figure 1. Top row. Steps for localization of neck section and delineation the aneurysm sac: A. one of the 3D surface models analysed and the reconstructed parent artery (red) with the aneurysm sac removed; B. delineation of the sac surface (yellow) from the parent artery tube function (light red); C. computation on the aneurysm sac of the distance to the tube surface of the parent artery; in blue the barycenter centerline; D. aneurysm neck plane section and sac surface clipped at the neck level. Bottom row. Some of the geometric primitives to characterize the aneurysm sac 3D shape: E. Voronoi diagram of the aneurysm sac (white) and its envelope (red); F. Voronoi core (white) and its envelope (red); G. core centerline; the last maximum inscribed sphere is explicitly represented; G. inscribed ellipsoid into the VC envelope; the directions of its three radii are also depicted.

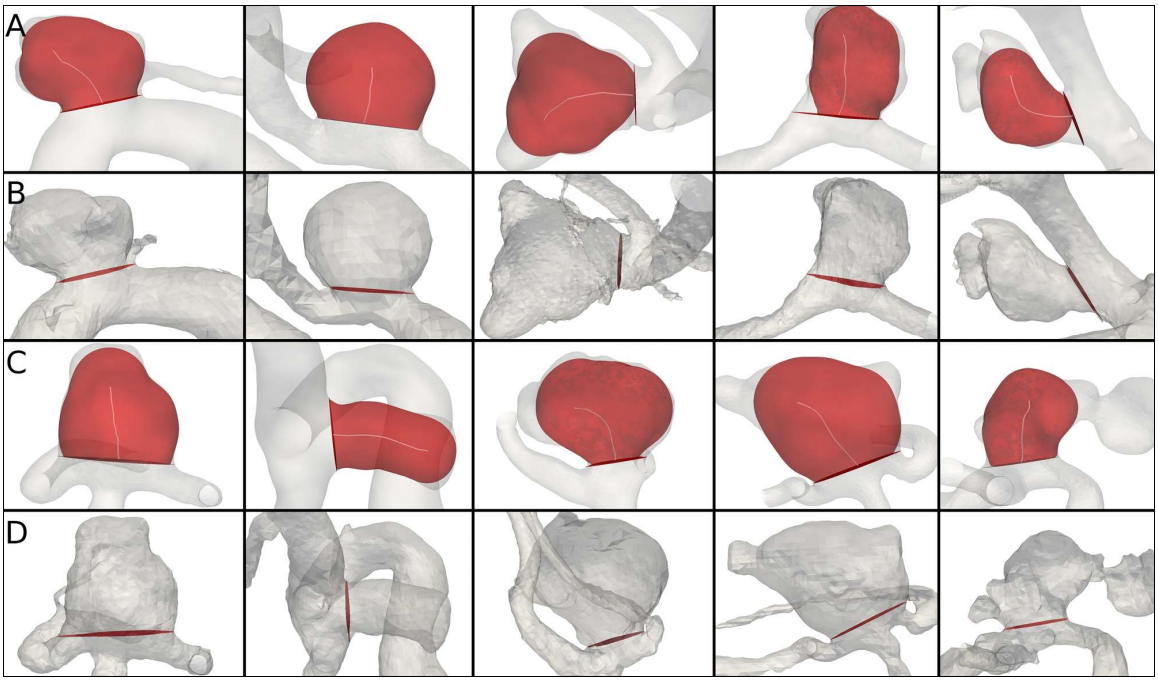

Figure 2. Application of the described techniques to a small subset of the analyzed group for segmented (A,C) vs thresholded (B,D) models. For the segmented models, the original surface, the aneurysm neck, the VC envelope (red) and the core centerline are depicted. For the thesholded only the neck is displayed.

2nd International Conference on Mathematical and Computational Biomedical Engineering - CMBE2011
March 30 - April 1, 2011, Washington D.C, USA
P. Nithiarasu and R. Löhner (Eds.)

Sensitivity to mathematical model choice and level of geometry description in idealised conduits and a patient specific cerebral aneurysm.

A.M. Gambaruto*, A.B. Moura* and A. Sequeira*
*Department of Mathematics and CEMAT - Center for Mathematics and its Applications,
Instituto Superior Ténico, Av. Rovisco Pais, 1, 1049-001, Lisboa, Portugal
agambar@math.ist.utl.pt, alexandra.moura@math.ist.utl.pt, adelia.sequeira@math.ist.utl.pt

SUMMARY

Mathematical models as well as the detail of the bounding geometry can be described by increasing levels of detail. Commonly the increasing level of detail can be thought to have a lesser influence on the resulting flow field at the cost of more expensive computations. For these reasons usually, as well as the more complex nature of the problem to be resolved they are commonly disregarded. In this work, taking as example idealised geometries and an anatomically realistic cerebral vasculature with aneurysm, these effects are compared and quantified.

Key Words: *blood flow, side branches, fluid-structure interaction, boundary conditions, 3D-1D coupling.*

1 INTRODUCTION

It is useful to study the sensitivity of changes in parameters to the resulting computed solution. In this work a patient specific geometry of a cerebral aneurysm and idealised test cases are considered, as shown in figure1. This is in part to be able to quantify expected error bounds in the solutions obtained with respect to choice of mathematical models that represent the physical problem. Variations in the mathematical modelling appear as hierarchy complexity, here studied as the choice of rheological models for blood (Newtonian versus shear-thinning), the compliance of the vessel walls (rigid versus deformable), and the flow boundary conditions (time varying 0D or 1D). Of concern is also the geometric representation, that apart from uncertainty in model definition due to medical imaging limitations of signal noise and resolution, in regards to the upstream and downstream regions that should be included in the computational domain. In this respect, the inclusion or omission of side branches is studied in this work, while a single segmentation is used and no sensitivity is performed to the thresholding and model reconstruction.

The effects of each of these modelling challenges are taken individually and compared to eachother.

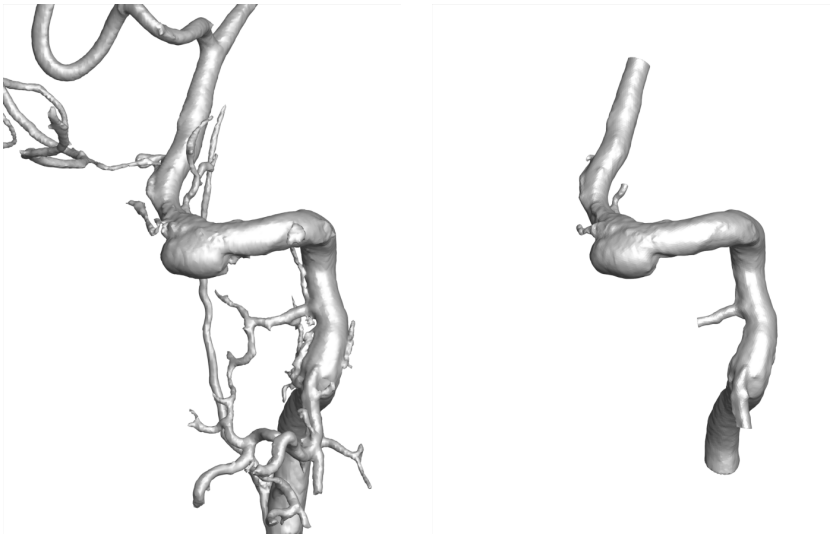

Figure 1: Details of surface definition of cerebral fasculature after segmentation (left) and identification of region of interest to include side initial portions of the side branches (right).

2 THE MODELS

In this work, blood is modelled as an incompressible fluid, governed by the conservation of mass and linear momentum equations:

$$\nabla \cdot \boldsymbol{u} = 0, \quad \text{in } \Omega^t, \tag{1}$$

$$\rho \left(\frac{\partial \boldsymbol{u}}{\partial t} + \boldsymbol{u} \cdot \nabla \boldsymbol{u} \right) = -\nabla p + \nabla \cdot \boldsymbol{\tau}, \quad \text{in } \Omega^t, \tag{2}$$

where ρ is the constant fluid density, $\boldsymbol{u}$ and p are the fluid velocity and pressure, and $\boldsymbol{\tau}$ is the deviatoric or extra stress tensor. The rheological properties of blood are modeled through the specification of a constitutive relation for $\boldsymbol{\tau}$. In this study, we will compare results using Newtonian and non-Newtonian models. The Newtonian behaviour is described through the constitutive law $\boldsymbol{\tau} = \mu(\nabla \boldsymbol{u} + \nabla \boldsymbol{u}^T)$, where μ is the fluid constant viscosity. In the non-Newtonian case the fluid viscosity varies and the only effect that will be taken into account here is the shear-thinning viscosity, which can be described by means of a generalised Newtonian model:

$$\boldsymbol{\tau} = \mu(\dot{\gamma})(\nabla \boldsymbol{u} + \nabla \boldsymbol{u}^T), \tag{3}$$

where the viscosity μ is now a function of the shear rate $\dot{\gamma}$, which is a scalar measure of the strain rate tensor, given by

$$\dot{\gamma} = \sqrt{\frac{1}{2}(\nabla \boldsymbol{u} + \nabla \boldsymbol{u}^T) : (\nabla \boldsymbol{u} + \nabla \boldsymbol{u}^T)}. \tag{4}$$

Here, the Carreau viscosity function (see [2,3]) is considered:

$$\mu(\dot{\gamma}) = \mu_\infty + (\mu_0 - \mu_\infty)(1 + (\lambda \dot{\gamma})^2)^{(n-1)/2},$$

where μ_0 and μ_∞ are the asymptotic viscosities at zero and infinite shear rate, respectively. Parameters λ, n, μ_∞ and μ_0 are obtained by fitting experimental data as described in [2,3].

Equations (1) - (2) will be coupled with a structure model, and the domain where they are defined will change in time. The reference domain is denoted as Ω^0, while the current domain is Ω^t, with

$t \in I = [0, T]$. As initial condition we take $\mathbf{u} = \mathbf{u}_0$ in Ω^0. The boundary condition on the physical wall, denoted Γ_w^t, will be given by the coupling with the structural model.

For the vessel wall model we consider the equation of the 3D quasi-incompressible elastic structure:

$$\rho_w \frac{\partial^2 \boldsymbol{\eta}}{\partial t^2} - \mathrm{div}_0 (\mathbf{P}) = \mathbf{0}, \quad \text{in } \Sigma^0, \forall t \in I, \tag{5}$$

where Σ^0 is the solid reference domain, $\boldsymbol{\eta}$ is the unknown displacement vector, ρ_w is the wall density, div_0 is the divergence operator with respect to the Lagrangian coordinates, and $\mathbf{P}$ is the first Piola-Kirchhoff tensor. We consider a St Venant-Kirchhoff material, for which the response function for the second Piola-Kirchhoff tensor is linear as a function of the Green - St Venant strain tensor $\mathbf{e} = \frac{1}{2}\left(\nabla_0^T \boldsymbol{\eta} + \nabla_0 \boldsymbol{\eta}\right)$: $\mathbf{S} = \lambda \,\mathrm{tr}(\mathbf{e})\mathbf{I} + 2\mu\mathbf{e}$, with $\lambda = \frac{E\xi}{(1+\xi)(1-2\xi)}$ and $\mu = \frac{E}{2(1+\xi)}$ the Lamé constants, where E is the Young modulus and ξ the Poisson ratio. In this study we consider a nearly incompressible material by setting a Poisson ratio close to 0.5 and a constant mass density ρ_w.

The initial condition for (5) is set to be $\boldsymbol{\eta} = \boldsymbol{\eta}_0$, and $\dot{\boldsymbol{\eta}} = \dot{\boldsymbol{\eta}}_0$ in Σ^0. In view of the coupling with the fluid, the structure initial conditions must verify the compatibility constraint $\dot{\boldsymbol{\eta}}_0 = \mathbf{u}_0$, on Γ_w^t. At the exterior boundary we assume that the stress is zero.

At the interface with the fluid Γ_w^0, the boundary condition is given by the fluid-structure interaction (FSI) coupling, which is performed through the following matching conditions.

$$\begin{aligned} \mathbf{u} &= \dot{\boldsymbol{\eta}}, \quad \forall t \in I, \text{ on } \Gamma_w^t, \\ -\left(\det \nabla_{\mathbf{0}} \boldsymbol{\eta}\right) \boldsymbol{\sigma}(\mathbf{u}, P) \left(\nabla_{\mathbf{0}}{}^{-T} \boldsymbol{\eta}\right) \cdot \mathbf{n}_0 &= \mathbf{P}(\boldsymbol{\eta}) \cdot \mathbf{n}_0, \quad \forall t \in I, \text{ on } \Gamma_w^0, \end{aligned}$$

where $\nabla_{\mathbf{0}}$ indicates the gradient with respect to the Lagrangian coordinates, and $\mathbf{n}_0$ is the outward unit vector to Γ_w^0. The first is the no-slip conditions and the second establishes the continuity of the normal stresses.

On the atrificial sections, the boundary conditions must account for the remaining parts of the system, and for the case of FSI models should be absorbing.

The 1D model is derived from the 3D FSI model by making simplifying assumptions and through an average procedure, and it describes very well the wave propation nature of blood flow in arteries. The unknowns are the cross-section area $A(z)$, which is related to the mean pressure $\overline{p}(z)$ through an algebraic relation (see [2]), and the flow rate $Q(z)$. It is described through a hyperbolic system of equations, having two distinct eigenvalues $\lambda_{1,2} = \overline{u} \pm \sqrt{\frac{\beta}{2\rho A_0}} A^{\frac{1}{4}}$, with $\overline{u} = \dfrac{Q}{A}$ the mean velocity and $\beta = \frac{\sqrt{\pi} h_0 E}{1-\xi^2}$, with A_0 the cross-section reference area at rest, E the Young modulus, h_0 the wall thickness, and ξ the Poisson ratio. Under physiological conditions in hemodynamics, the eigenvalues $\lambda_{1,2}$ have opposite signs, *i.e.* the flow is sub-critical. Their corresponding eigenfunctions or characteristic variables are

$$W_{1,2}(Q, A) = \overline{u} \pm 4\sqrt{\frac{\beta}{2\rho A_0}} \left(A^{\frac{1}{4}} - A_0^{\frac{1}{4}}\right), \tag{6}$$

where W_1 is the incoming characteristic at the left extremity (inflow) of the vessel, and W_2 is the incoming characteristic at the right extremity (outflow) of the vessel. Imposing $W_2(Q, \bar{p}) = 0$ at the right extremity corresopnds to an absorbing boundary condition at the end of the 1D model.

In order to prescribe adequate boundary conditions, the 3D outflow section is coupled to a 1D model, that can represent a singular cylinder or a network of arteries. The coupling is performed

imposing the continuity of the normal stresses and the fluxes:

$$p\mathbf{n} - 2\mu(\dot{\gamma})\mathbf{D}(\mathbf{u}) \cdot \mathbf{n} = \left(\overline{p}_{1D} + \frac{\rho}{2}|\overline{u}_{1D}|^2\right)\mathbf{n}, \quad (7)$$

$$Q_{3D} = \int_{\Gamma_a^t} \mathbf{u} \cdot \mathbf{n} d\gamma = Q_{1D}. \quad (8)$$

The 3D-1D coupling is performed imposing (7) into the 3D model, and (8) into the 1D one, *i.e.* the total pressure computed on the 1D model is provided to the 3D model through a constant Neumann boundary condition, while the flow rate computed on the 3D artificial section is prescribed at the 1D inflow boundary. A staggered numerical algorithm is used, consisting of an iterative procedure between the 3D FSI and 1D subproblems. This iterative scheme can be considered explicit or implicit.

Different absorbing boundary conditions can be obtained by imposing the absorbing boundary condition of the 1D outflow point, $W_2(Q, \bar{p}) = 0$, directly on the 3D FSI outflow section. In this case there is no need for solving a 1D problem.

It has been shown in [2] that, for physiological values of the Young modulus for the arterial tissue, condition $W_2(Q, \bar{p}) = 0$ between mean pressure $\bar{p}$ and flow rate Q is almost linear, and an absorbing linear boundary condition relating mean pressure and flow rate can be derived:

$$Q \approx \frac{\sqrt{2}A_0^{5/4}}{\sqrt{\rho\beta}}\bar{p}. \quad (9)$$

Expression (9) provides a way of setting the proper resistence at the artificial section of interest, in order to be absorbing. Indeed, a boundary condition of this type, where the mean pressure to be prescribed is linearly computed from the flow rate on that section, can be seen as a coupling bewteen the 3D FSI problem and a simple RL lumped parameters model.

3 CONCLUSIONS

In this work idealised models of vessels are initially studied to observe the influence of different models on the computed flow field. These include rheological models, boundary conditions of the flow and the wall structural models. Importantly the effect of inclusion of side-branches as geometric detail is considered, and the appropriate boundary conditions that these require. The extension to a anatomically accurate geometry of cerebral arterial system with an aneurysm is then studied.

REFERENCES

[1] A. Kazakidi, S.J. Sherwin and P.D. Wienberg, Effect of Reynolds number and flow division on patterns of heamodynamic wall shear stress near branch points in the descending thoracic aorta, *J .R. Soc. Interface*, 6 (2009) 539–548.

[2] J. Janela, A. Moura and A. Sequeira, Absorbing bondary conditions for a 3D non-Newtonian fluid-structure interaction model for blood flow in arteries, *Int. J. Eng. Sci.*, (2010) doi: 10.1016/j.ijengsci.2010.08.004.

[3] A.M. Gambaruto, J. Janela, A.B. Moura, A. Sequeira. Sensitivity of hemodynamics in a patient specific cerebral aneurysm to vascular geometry and blood rheology. *Mathematical Biosciences and Engineering*. Accepted (2010)

[4] J.R. Cebral, M.A. Castro, S. Appanaboyina, C.M. Putman, D. Millan and A. Frangi. Efficient pipeline for image-based patient-specific analysis of cerebral aneurysm hemodynamics: technique and sensitivity. *IEEE Transactions on medical imaging*, **24**(4) (2005) 457–467.

2nd International Conference on Mathematical and Computational Biomedical Engineering - CMBE2011
March 30 - April 1, 2011, Washington D.C, USA
P. Nithiarasu and R. Löhner (Eds.)

High Resolution Hemodynamics of Small Intracranial Aneurysms using Phase Contrast MRI

Steven R. Kecskemeti*, Kevin M. Johnson, Yijing Wu, Patrick Turski and Oliver Wieben
* Correspondence to: Steven Kecskemeti, University of Wisconsin-Madison, Department of MR/CT Research, Room 1005, Wisconsin Institutes for Medical Research (WIMR), 1111 Highland Ave., Madison, WI 53705-2275. E-mail: kecskemeti@wisc.edu

SUMMARY

A new, cardiac gated, volumetric three directional phase contrast (PC) magnetic resonance imaging (MRI) technique has been used to image and gather hemodynamic information on 12 small intracranial aneurysms, including 7 that are 4mm or smaller. The new approach uses radial undersampling to obtain high spatial and temporal resolutions that would be clinically unfeasible using standard Cartesian based acquisitions. The high spatial resolution has shown flow patterns not detectable with the lower resolutions of conventional PC MRI, but seen in computational fluid dynamic (CFD) models. The new technique may therefore be useful in providing patient specific input parameters in future CFD simulations.

Key Words: *blood flow, wall shear stress, aneurysm.*

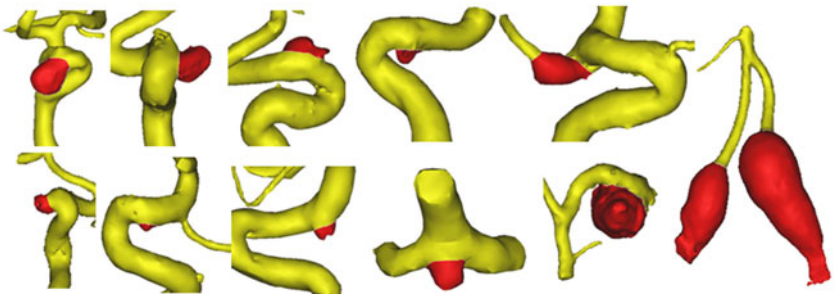

Figure 1: Surface renderings of the 12 aneurysms (red). Each case is individually scaled and rotated for beat visualization.

1 INTRODUCTION

Phase contrast (PC) magnetic resonance imaging (MRI) can provide both an anatomical angiogram depicting vasculature anatomy as well as hemodynamical information such as velocity, flow, pressure, and wall sheer stress. This could be valuable in patient specific computational fluid dynamic (CFD) models. However, several complications exist that must be overcome before PC MRI can become a valuable resource for CFD inputs. Primarily, spatial and temporal resolutions are typically reduced in order to overcome the long scantime inherent to the PC method itself. Since only the average velocity per imaging voxel can be calculated, the decreased spatial resolution therefore degrades the accuracy of velocity inputs, especially in areas of complex, turbulent, or helical flow

such as aneurysms. The method presented in this work addresses these limitations through the use of a hybrid radial-Cartesian k-space readout [1].

The inplane radial readout serves several purposes. Of most importance, spatial resolution in radial MRI is determined by the readout length in k-space, as opposed to the number of collected lines (phase encodes) in Cartesian MRI. Scantime is reduced by sampling fewer radial lines than required by the Nyquist sampling theorem, trading scantime for increased levels of artifact. However, the sparsness provided by the inherent subtraction of stationary tissues removes much of the artifact, allowing large degrees of undersampling compared to other techniques. Maintaining a Cartesian readout through-plane allows for target volumetric acquisitions with higher SNR than multi-slice [2] or three-dimensional radial k-space trajectories [3]. The SNR advantage is in turn used to acquire even higher spatial resolution.

2 MAIN BODY

Eleven patients with 12 known intracranial aneurysms were imaged on a clinical 3T scanner (MR 750, GE Healthcare, Waukesha, WI) using an 8 channel head coil after obtaining IRB approval and written informed consent from all subjects.. Following a contrast enhanced MRA, patients were scanned with PC SOS and 5-pt velocity encoding [4] using: FOV 220x220x30-40mm, acquired resolution 0.43x0.43x0.7-1.0mm, TE/TR = 3.7/8.0ms, tip angle = 20 deg, BW = 83.3 kHz, scantime = 9 minutes. PC derived angiograms were analyzed for aneurysm conspicuity and were used to construct surface renderings. Dynamic velocity fields were reconstructed with retrospective ECG gating and radial view sharing [5] with 40ms temporal resolution and used for hemodynamic visualization with a dedicated software package (EnSight, CEI Inc., Apex, NC).

All 12 aneurysms were successfully identified in the 11 PC SOS exams (see surface rendered images in Fig.(1)). A representative PC MRA used for anatomical diagnosis, surface renderings, and masks for hemodynamic analysis in EnSight is shown in Fig.(2). The high spatial resolution

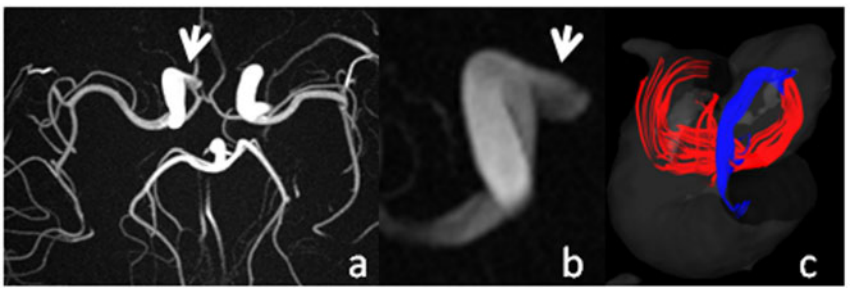

Figure 2: Example images of a 3.8 mm aneurysm (arrow) in the right carotid artery demonstrating the fine vessel conspicuity, high spatial resolution, and superior background suppression of PC SOS (a/b) Full/limited axial MIPs from PC SOS angiogram. Streamlines (c) depicting inflow/outflow colored with blue/red to illustrate the 3D circulation pattern within the aneurysm.

and strong background suppression typical of PC SOS aid in visualization and segmentation of this aneurysm, measured to be 3.8mm at its neck. The high spatial resolution aids in proper visualization of streamlines here showing a helical circulation pattern within the aneurysm, despite its small size.

A small carotid terminus aneurysm, measured as 2.3mm at its neck is used to demonstrate the benefits and necessity for high spatial resolution obtained. Velocity vectors, shown in Fig.(3) show the blood entering the aneurysm from the internal carotid artery with high speed and then

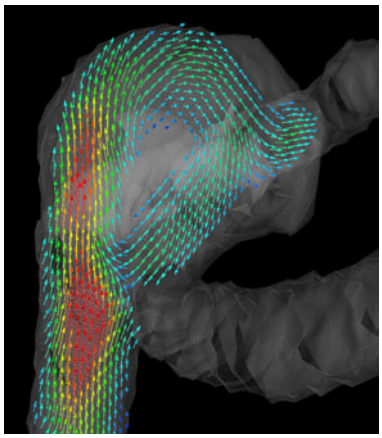

Figure 3: A 2.3mm aneurysm in the carotid terminus shows higher velocity blood traveling up from the left internal carotid artery, circulating around the aneurysm, and finally entering the left anterior cerebral and left communicating artery.

slowing as it circulates and eventually exits to the anterior cerebral and communicating arteries. Flow maps calculated at a plane placed at the aneurysm neck Fig.(4), demonstrate this behavior in the original images. However, when the same velocity maps were visualized after MR image reconstruction from the identical k-space data but at lower spatial resolutions of 1.0x1.0x1.0mm and 1.5x1.5x1.5mm, typical of Cartesian 4D PC MR acquisitions, this behavior was not observed (Fig. 3d,e). Velocity maps appear smoothed and do not demonstrate regions with strong in or outflow as typically seen in terminus aneurysms [6].

3 CONCLUSIONS

We conclude that 4D cardiac gated PC SOS is a well suited approach to study flow and pathological conditions in and around intracranial aneurysms. We have found that the improved spatial resolution enables characterization of regions with complex flow in small vascular structures. By better visualizing the regions of high inflow, as in Fig.(4), the improved spatial resolution could prove useful in the diagnosis, monitoring of disease progression, and monitoring surgical treatment of aneurysms. For example, the inability to visualize the regions of high-inflow in the low resolution reconstructions of Fig. 3e could incorrectly suggest successful treatment in post-op exams. In addition, the high spatial resolution data are well suited to derive hemodynamic parameters such as pressure gradients and wall shear stress which can serve as patient specific input parameters for CFD models.

References

[1] S. Kecskemeti, K. Johnson, O. Wieben, and C. Mistretta. Phase contrast stack of stars imaging. In *Sixteenth Annual Meeting of the Society of Magnetic Resonance in Medicine*, 2008.

[2] A V Barger, D C Peters, W F Block, K K Vigen, F R Korosec, T M Grist, and C A Mistretta. Phase-contrast with interleaved undersampled projections. *Magn Reson Med*, 43(4):503–509, Apr 2000.

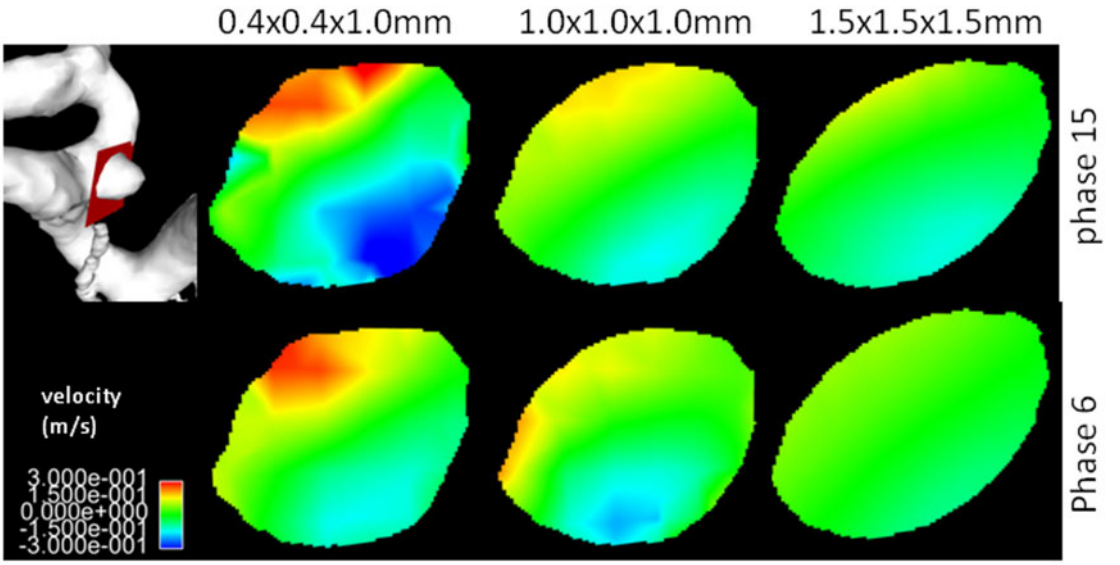

Figure 4: UPPER LEFT: Anatomical view of placement of plane used for velocity maps showing flow into and out of the aneurysm. The high spatial resolution of 0.4x0.4x1.0mm shows a nice delineation between high flow entering the aneurysm and that leaving it. The same dataset, reduced to resolution of 1.0x1.0x1.0mm and 1.5x1.5x1.5mm does depict as well the high speed entering and low speed exiting the aneurysm. Shown are cardiac phases 6 and 15 out of 16 total.

[3] K M Johnson, D P Lum, P A Turski, W F Block, C A Mistretta, and O Wieben. Improved 3d phase contrast mri with off-resonance corrected dual echo vipr. *Magn Reson Med*, 60(6):1329–1336, Dec 2008.

[4] K M Johnson and M Markl. Improved snr in phase contrast velocimetry with five-point balanced flow encoding. *Magn Reson Med*, 63(2):349–355, Feb 2010.

[5] A V Barger, W F Block, Y Toropov, T M Grist, and C A Mistretta. Time-resolved contrast-enhanced imaging with isotropic resolution and broad coverage using an undersampled 3d projection trajectory. 48(2):297–305, Aug 2002.

[6] Aishwarya R. Mantha, Goetz Benndorf, Andres Hernandez, and Ralph W. Metcalfe. Stability of pulsatile blood flow at the ostium of cerebral aneurysms. *Journal of Biomechanics*, 42(8):1081 – 1087, 2009.

2nd International Conference on Mathematical and Computational Biomedical Engineering - CMBE2011
March 30 - April 1, 2011, Washington D.C, USA
P. Nithiarasu and R. Löhner (Eds.)

COMPARING GEOMETRY AND HEMODYNAMICS OF MCA ANEURYSMS

A.J. Geers[⋆†], I. Larrabide[†⋆], H.G. Morales[⋆†], M.C. Villa-Uriol[⋆†], A.F. Frangi[⋆†‡]
[⋆]Center for Computational Imaging & Simulation Technologies in Biomedicine (CISTIB),
Universitat Pompeu Fabra, Barcelona, Spain
[†]Networking Center on Biomedical Research (CIBER-BBN), Barcelona, Spain
[‡]Institució Catalana de Recerca i Estudis Avançats (ICREA), Barcelona, Spain
{arjan.geers,alejandro.frangi}@upf.edu

SUMMARY

Twenty-six MCA bifurcation aneurysms from the @neurIST database were examined. Geometric variables were compared with both qualitative and quantitative hemodynamic variables as a first step in search for geometric markers that could serve as surrogate markers for aneurysmal blood flow.

Key Words: *cerebral aneurysm, geometry, hemodynamics.*

1 INTRODUCTION

Intracranial aneurysms are pathologic dilatations of cerebral arteries, most commonly found in the circle of Willis. The growth and rupture of aneurysms have been related to the intra-aneurysmal hemodynamics and computational blood flow simulations using image-based geometries could potentially assist rupture risk assessment. Patient-specific blood flow simulations are known to be sensitive to the vascular geometry and the boundary conditions imposed at the in- and outlets of the vasculature [3]. However, the main flow characteristics are robust and show promising correlations with rupture risk [4]. Furthermore, there is an ongoing trend to reduce the complexity of hemodynamic datasets, even to the extend of exploring geometric variables that might serve as surrogate markers of pathological blood flow [7,11]. Such a simplified approach to hemodynamics might be relatively easy to adopt into clinical practice.

Geometric variables describing the shape of the aneurysm dome and the relationship between parent vessel and aneurysm have been proposed and have been related to rupture risk [5,9]. Many of these variables were designed with a hemodynamic motivation, but not many studies have compared the shape descriptors with hemodynamic simulations in image-based geometries. The aim of this study is to look at qualitative and quantitative hemodynamic variables and find correlations with geometric ones. Besides using established geometric variables, such as the aspect ratio (aneurysm depth / neck width), we also propose new variables as a first step to finding robust markers for the flow field in aneurysm and surrounding vasculature.

2 MATERIALS AND METHODS

Twenty-six MCA bifurcation aneurysms (11 ruptured, 14 unruptured, 1 unknown) were drawn from the database of the European project @neurIST [6]. Three-dimensional rotational angiography (3DRA) images and clinical data came

from 3 hospitals and was processed by 4 operators from 1 research group. Using @neuFuse, the computational tool-chain developed within @neurIST, the 3DRA images were segmented with a geodesic active regions approach. The triangulated surface mesh was post-processed to correct the topology, smooth the surface, and improve the mesh quality.

Based on the surface mesh, a volume mesh was generated in ANSYS ICEM CFD v11.0 with the following specifications: tetrahedral and prismatic elements; node spacing of 0.4 mm; total height of 3 prism layers of 0.12 mm; on average, 3 million elements. ANSYS CFX v11.0 was employed to solve the Navier-Stokes equations for the computational domain. We used the following specifications: rigid wall; incompressible Newtonian fluid (density = 1066 kg m^{-3}; viscosity = 0.0035 Pa s); no-slip boundary conditions; 160 timesteps per cardiac cycle of 0.8 s; 3 cardiac cycles calculated with the results of the last cycle stored for post-processing; boundary conditions computed using the 1D circulation model developed by Reymond et al. [10]; flow rate waveform at inlet; pressure waveform at outlets; fully developed velocity profile from Womersley equation imposed on circular inlet.

Aneurysm dome shape descriptors were automatically calculated by @neuFuse after the operator manually outlined the aneurysm neck. The Vascular Modeling Toolkit was used to measure bifurcation angles and cross-sectional areas of parent and daughter vessels at 2 maximally inscribed spheres distance from the bifurcation (Fig. 1,G-H) [1,8].

Four dichotomous qualitative hemodynamic variables proposed by Cebral et al. [4] were measured using visualizations as shown in Fig. 1: flow complexity, flow stability, inflow concentration, and flow impingement. As part of the @neurIST tool chain, many quantitative hemodynamic variables were derived from the simulation; most of them related to the wall shear stress (WSS), pressure, or flow rate distribution. All reported values are measured at peak systole.

3 RESULTS

Fig. 3 shows boxplots of geometric and hemodynamic variables grouped by the categories of the qualitative hemodynamic variables. The reported p-value was calculated with the Mann-Whitney U test. We found complex flow aneurysms to have a significantly higher non-sphericity index than simple flow aneurysms. Aneurysms with concentrated inflow jets had, as expected, significantly smaller parts of the neck through which the blood went into aneurysm. Concentrated inflow jets were found more often in large volume aneurysms and aneurysms with high aspect ratios. The qualitatively measured impingement size corresponded well with the size of the aneurysm wall part that experienced elevated pressure (i.e. pressure higher than 50% of the maximum pressure on the aneurysm). Large impingement regions were found in aneurysms with small non-sphericity indices, small volumes, and small aspect ratios. No significant geometric differences were found between aneurysms with stable or unstable flow fields.

Fig. 2 shows scatter plots of geometric and hemodynamics variables. The part of the flow in the parent vessel that entered the aneurysm correlated well with the size of the neck area (Pearson's $r = 0.71$; $p < .0001$). We reasoned that the volume-averaged velocity magnitude in the aneurysm should be related to the aneurysm volume and the influx into the aneurysm. Since the volume-averaged velocity magnitude in turn correlated strongly with the area-averaged WSS on the aneurysm dome ($r = 0.98$; $p < .0001$), the following was proposed:

$$\text{WSS} \propto Q_{an}^{k} \cdot V_{an}^{l} \tag{1}$$

where Q_{an}^{k} and V_{an}^{l} are the influx into the aneurysm and the volume of the aneurysm, respectively. By taking the logarithm on both sides, the equation becomes linear. Parameters k and l were found through the least squares method to be: $k = 0.63$ and $l = -0.67$, and the right-hand side of Eq. (1) showed good correlation with the WSS ($r = 0.81$; $p < .0001$).

Similarly, we attempted to find a relationship between the bifurcation angles and areas, and the flow split from parent vessel to daughter vessels. The following was proposed:

$$\frac{Q_{d_1}}{Q_{d_2}} \propto \frac{A_{d_1}^{m} \cdot \alpha_{d_1}^{n}}{A_{d_2}^{m} \cdot \alpha_{d_2}^{n}} \tag{2}$$

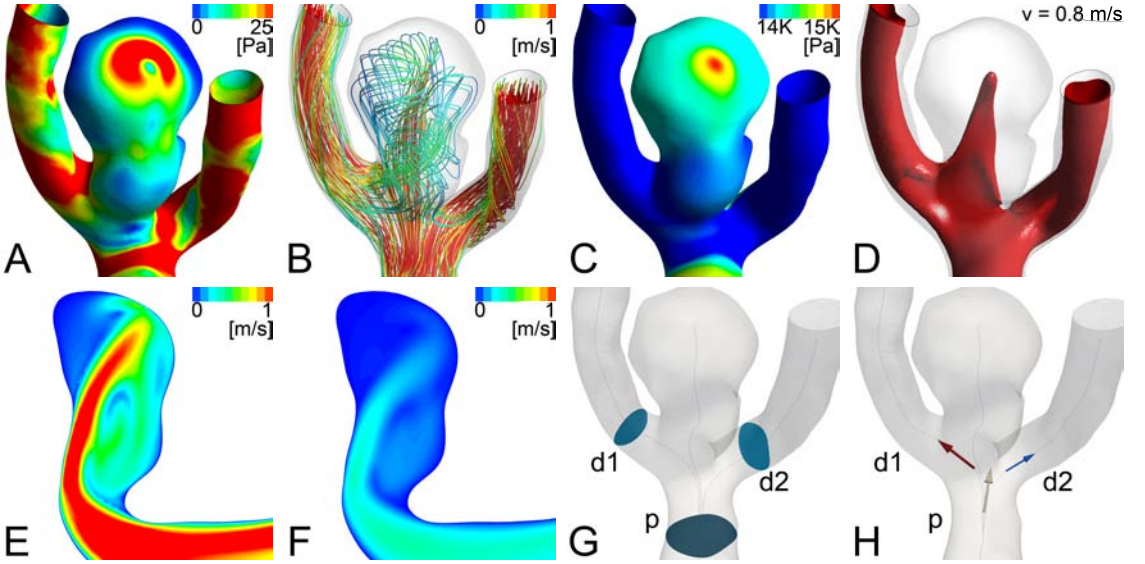

Figure 1: Visualization of geometry and hemodynamics. WSS distribution (A); instantaneous streamlines color-coded by the velocity magnitude (B); pressure distribution (C); velocity isosurface at 0.8 $ms{-}1$ (D); cutplane along parent vessel midline color-coded by velocity magnitude (E); same as image E but at end diastole to visualize slight change in direction of flow jet (F); cross-sectional areas at two maximally inscribed spheres distance from the bifurcation (G); bifurcation vectors for the parent vessel (p) and the two daughter vessels (d1 and d2) (H).

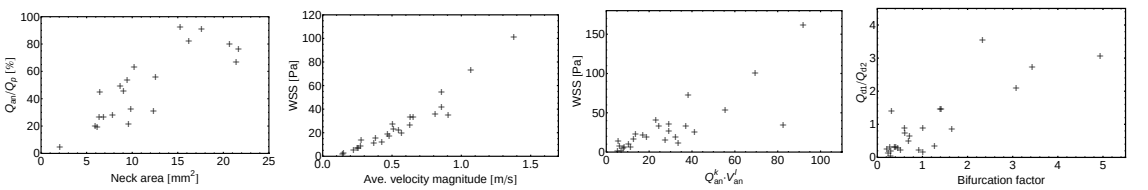

Figure 2: Scatter plots of several geometric and hemodynamic correlations.

where Q_{d_λ}, A_{d_λ}, and α_{d_λ} are the flow rate, the cross-sectional area, and the angle with the parent vessel of daughter vessel d_λ, respectively. The parameters were found to be: $m = 0.99$ and $n = -1.20$. Correlation of the right-hand side of Eq. (2) with the flow split at the aneurysm bifurcation was better ($r = 0.86$; $p < .0001$) than for each of the fractions $A^m_{d_1}/A^m_{d_2}$ ($r = 0.69$; $p < .0001$) and $\alpha^n_{d_1}/\alpha^n_{d_2}$ ($r = -0.64$; $p < .0001$) independently.

No significant differences were found for any variables between ruptured and unruptured aneurysms, which can be explained by the small population size.

4 CONCLUSIONS

Relationships between simple geometric descriptors and qualitative and quantitative hemodynamic variables were found. The strong link between geometry and blood flow should be exploited by defining new geometric features that could serve as surrogate markers of certain flow conditions. Future work should include multivariate regression analyses to identify geometric variables that show significant correlations with hemodynamic variables when controlling for correlations be-

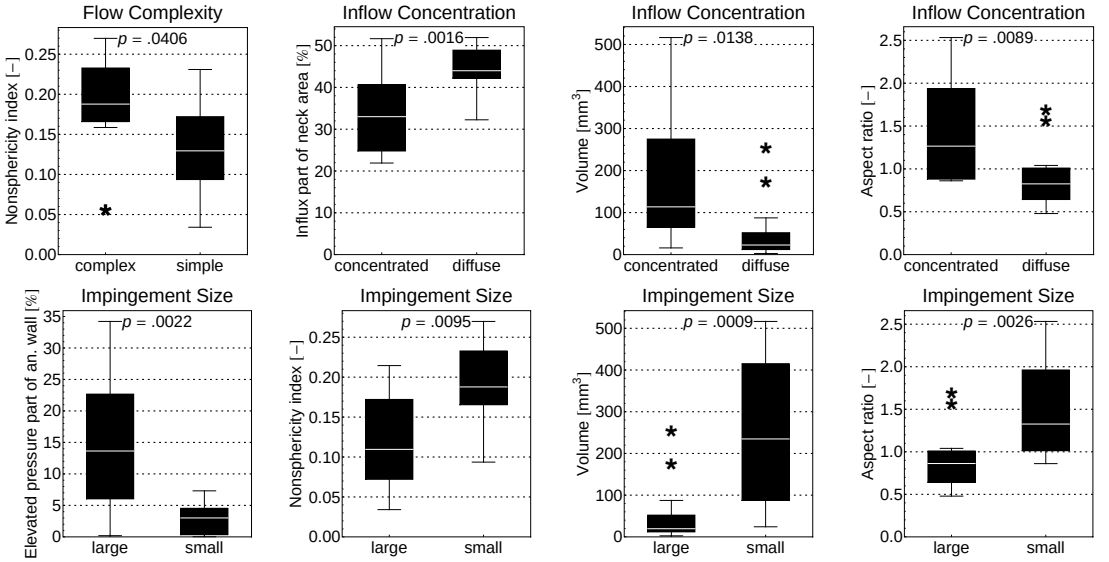

Figure 3: Boxplots of geometric and hemodynamic quantitative variables for categories of the dichotomous qualitative variables. Outliers at 1.5 IQR from the 25th and 75th percentile are indicated with asterisks.

tween the variables themselves. Since the parent vessel geometry is of great importance to the aneurysmal flow [2], taking the shape of that vessel into account could potentially further refine geometric variables.

REFERENCES

[1] L. Antiga, D.A. Steinman, *Vascular Modeling Toolkit*, `http://www.vmtk.org`, last access: Nov 15, 2010

[2] M.A. Castro, C.M. Putman, J.R. Cebral, Computational fluid dynamics modeling of intracranial aneurysms: Effects of parent artery segmentation on intra-aneurysmal hemodynamics, *American Journal of Neuroradiology*, 27(8), 1703-1709, 2006.

[3] J.R. Cebral, M.A. Castro, S. Appanaboyina, C.M. Putman, R.D. Millan, A.F. Frangi, Efficient pipeline for image-based patient-specific analysis of cerebral aneurysm hemodynamics: technique and sensitivity, *IEEE Transactions on Medical Imaging*, 24(4), 468-476, 2005.

[4] J.R. Cebral, F. Mut, J. Weir, C.M. Putman, Association of hemodynamic characteristics and cerebral aneurysm rupture, *IEEE American Journal of Neuroradiology*, *In Press*, 2011.

[5] S. Dhar, M. Tremmel, J. Mocco, M. Kim, J. Yamamoto, A.H. Siddiqui, L.N. Hopkins, H. Meng, Morphology parameters for intracranial aneurysm rupture risk assessment, *Neurosurgery*, 63(2), 185-196, 2008.

[6] A.F. Frangi, D.R. Hose, D.A Rüfenacht, The neurIST project: Towards understanding cerebral aneurysms, *SPIE Newsroom*, 2007.

[7] S.W. Lee, L. Antiga, J.D. Spence, D.A. Steinman, Geometry of the carotid bifurcation predicts its exposure to disturbed flow, *Stroke*, 39(8), 2341-2347, 2008.

[8] M. Piccinelli, A. Veneziani, D.A. Steinman, A. Remuzzi, L. Antiga, A framework for geometric analysis of vascular structures: Application to cerebral aneurysms, *IEEE Transactions on Medical Imaging*, 28(8), 1141-1155, 2009.

[9] M.L. Raghavan, B. Ma, R.E. Harbaugh, Quantified aneurysm shape and rupture risk, *Journal of Neurosurgery*, 102(2), 355-362, 2005.

[10] P. Reymond, F. Merenda, F. Perren, D. Rüfenacht, N. Stergiopulos, Validation of a one-dimensional model of the systemic arterial tree, *AJP - Heart and Circulatory Physiology*, 297(1), H208-H222, 2009.

[11] C.A. Taylor, D.A. Steinman, Image-based modeling of blood flow and vessel wall dynamics: Applications, methods and future directions, *Annals of Biomedical Engineering*, 38(3), 1188-1203, 2010.

2nd International Conference on Mathematical and Computational Biomedical Engineering – CMBE2011
March 30 – April 1, 2011, Washington D.C., USA
P. Nithiarasu and R. Löhner (eds)

CHARACTERIZATION OF THE MORPHOMETRY AND HEMODYNAMICS OF CEREBRAL ARTERIAL TREES IN HEALTHY HUMANS: A PRELIMINARY STUDY

Fernando Mut*, Susan Wright **, Giorgio Ascoli and Juan R. Cebral***
*Center for Computational Fluid Dynamics, George Mason University,
**Krasnow Institute, George Mason University,
4400 University Drive, Fairfax, VA 22030, USA, fmut@gmu.edu

SUMMARY

This paper describes a preliminary study of the morphometric and hemodynamic characteristics of the brain vascular trees using 61 reconstructed models from healthy humans. In the first part, a few morphometric variables are defined, namely, the length and diameter ratios as a function of the branch generation, and computed using the 61 reconstructed models. In the second part of the paper, the feasibility of computational hemodynamics calculations in these 3D complex models is demonstrated. For this, 3 out of the 61 models were selected and corresponding three-dimensional meshes were generated, and the unsteady solutions of the incompressible Navier-Stokes equations were computed.

Key Words: *cerebral arterial trees, hemodynamics, morphometrics.*

1. INTRODUCTION

Understanding the vascular structure and hemodynamics of the brain is important for gaining insight into a variety of pathological conditions and the development and progression of cerebrovascular diseases. The construction of a hemodynamics atlas or a population averaged model of the brain is useful to characterize the hemodynamics conditions of normal subjects and to provide a baseline for studying pathological cases. This work represents the first steps towards these aims. Specifically, this study focused on the morphometric characterization of brain arterial trees of healthy human subjects with the objective of providing information required for the construction of generic arterial tree models. Secondly, CFD simulations were performed to demonstrate the feasibility of computing 3D arterial blood flows in complex arterial networks, which will be used for computing typical values of local hemodynamics variables along the different arterial branches.

2. METHODS

Brain Vascular Reconstruction and Morphometric Characterization.

Human arterial arborizations from 61 healthy adults were digitally traced using image stacks acquired from 3T time-of-flight MRA that spanned the entire cerebral volume at 0.6mm isotropic resolution [1]. The segmentation process was performed using previously developed tools used to create 3D neuronal reconstructions [2]. The six mayor subtrees stemming from the circle of Willis were identified for each of the data sets and represented as a series of interconnected tapering cylinders characterized by their ending XYZ coordinates, diameter, and link to the

previous node. In order to characterize the morphometry of the arterial trees, a number of geometrical properties have to be calculated. For instance, the branch length and diameter ratios at each of the bifurcation nodes, are obtained from:

$$R_L^i = \frac{(L_{i+1}^{(1)} + L_{i+1}^{(2)})/2}{L_i} \qquad R_D^i = \frac{(D_{i+1}^{(1)} + D_{i+1}^{(2)})/2}{D_i}$$

where R_L^i and R_D^i are the branch length and branch diameter ratios respectively, computed at the *i*th bifurcation (or equivalent, at the *i*th branch generation). The length (diameter) of a branch (L/D) is the sum (average) of the lengths (diameters) of the individual cylinders that define the branch. Since, at the bifurcations, a single branch (parent) splits into two branches (daughters), the corresponding geometrical variables of the daughter branches are averaged in order to get a single value.

Computational Hemodynamics Modelling.

The computational arterial network model consists in the circle of Willis and its six stemming trees. The process of generating a three-dimensional mesh suitable for finite element computations starts by generating triangulated tubular surfaces along each of the branches of the arterial model. This is carried out by fitting a cubic spline using the coordinates and diameters from the reconstructed vessels and generating corresponding tubular surfaces following the splined curve. Triangulated spheres are also placed at both ends of the tubular surfaces in order to generate a closed discrete surface model. This collection of intersecting (but disconnected) discrete surfaces is merged into one single watertight surface that represents the vascular wall. This step is carried out by first embedding the collection of discrete surfaces into a three-dimensional background mesh. This mesh is adaptively refined several times around the discrete surfaces in order to capture in detail the surface topography. Then, the (signed) distance function to each of the surfaces is computed and an iso-surface of zero-value is extracted. Using information from the reconstructed arterial vessels, the tips of all the terminal branches (inflows/outflows) are identified and cut perpendicularly to the vessel axis. The surface mesh is then fed into a three-dimensional advancing front mesh generator [3] which produces the three-dimensional volumetric grid.

The unsteady solution of the incompressible Navier-Stokes equations is computed using an implicit incompressible flow solver [4]. Boundary conditions are specified by prescribing pulsatile flows at the outlets, constant pressure at the inlets and no-slip boundary conditions at the wall. This selection of the boundary condition is consistent with the fact that at the inflow of the circle of Willis, the pressure is assumed to be roughly constant, while the pulsatile outflow conditions allows for a fine tuning of internal flow division in order to get a realistic result.

3. RESULTS

Preliminary Morphometric Characterization of the Arterial Trees Reconstructions.

The 61 reconstructed arterial trees where characterized by computing the length and diameter ratios as a function of the branch generation for the six mayor subtrees stemming from the circle of Willis, namely, left and right MCA, ACA and PCA. Figure 1 shows the evolution of the length and diameter ratios for each one of the six mayor subtrees. The length ratios up to generation 13 are all above one, indicating that at the beginning, the daughter/son branches are larger than the parent branches. However, it appears that the total average value (average of the 6 subtrees values) decreases as the branch generation order increases, which may indicate that the length ratio will eventually fall bellow one (daughter branches smaller than parent branches) after a

certain number of generations. On the other hand, the diameter ratios seem to have a constant (fractal) behavior, with a total average value close to 0.9. The increase in the variability of the diameter ratios for generations above 10 is most likely due to the fact that not all the reconstructed subtrees have that many generations and consequently the average value is computed with just a few values.

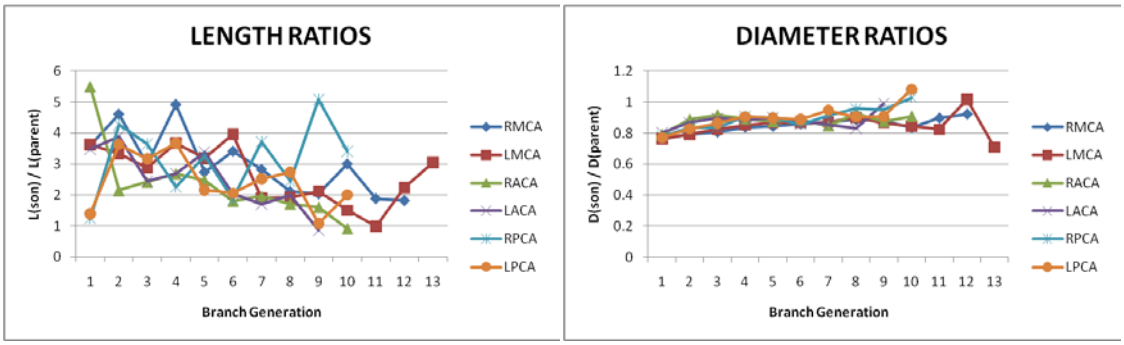

Figure 1: Average values of the length and diameter ratios as a function of the branch generation from the 61 reconstructed cerebral trees models.

Feasibility of Computational Hemodynamic Modelling.

Three cerebral vascular models were selected to demonstrate the feasibility of 3D pulsatile CFD calculations. Meshes of about 20 million tetrahedral elements were obtained for each of the models. Pulsatile boundary conditions at the outflows were selected so that the wall shear stress (WSS) at all the terminal branches is about 15 dyne/cm^2. A constant pressure (p=0) was set at the three inflow boundaries. Two complete cardiac cycles were computed for each of the three cases. The total compute time was about 42 hours for each run on a desktop workstation (32GB of ram). Figure 2 shows the WSS distributions obtained for each of the cases.

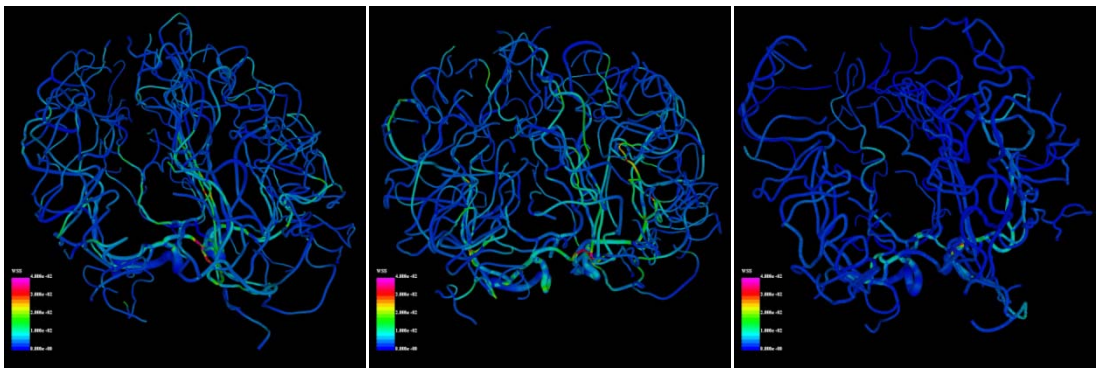

Figure 2: Peak wall shear stress distribution corresponding to computational hemodynamics simulation of three reconstructed brain vascular models.

The highest values of the WSS were observed between generations one and two of the six principal subtrees. However, these values were found to be unphysiologic high. This is due to an improper balance of the blood flow within the arterial trees, which produces very high velocities in small arteries in order to comply with the total outflow condition. This suggests that a better criteria for selection of boundary conditions is required. For instance, inspired be the principle of minimum work, this new criteria should seek to produce more balanced flow divisions and a WSS distribution that is as uniform as possible across the model.

4. CONCLUSIONS

Human arterial networks were reconstructed from 61 healthy adults using 3T time-of-flight MRA images that spanned the entire brain. The six mayor subtrees emanating from the circle of Willis were extracted from the models and analyzed using a few morphometric variables, namely, the length and diameter ratios as a function of the branch order. The results showed that these morphometric characterizations could be successfully used to build a baseline population averaged brain vascular model.

The feasibility of computational hemodynamics calculations was demonstrated using three subject specific geometries and pulsatile flows. The results showed that this type of calculations can be successfully performed in a reasonable time frame (less than 2 days for each model). Boundary conditions for these types of simulations need to be studied in order to obtain more realistic results. In particular, a new criteria to impose the flow divisions within the arterial trees, and subsequently, the total distribution of the WSS need to be investigated. This type of calculations will provide detailed information about the local hemodynamics variables along the arterial branches of the cerebrovasculature, which can ultimately be used for constructing a baseline statistical model of the brain hemodynamics.

REFERENCES

1. Wright, S.N., et al. *Digital reconstruction and morphometric analysis of human brain vasculature from magnetic resonance angiography*. in *Society of Neuroscience Annual Meeting*. 2007. San Diego, CA.
2. Brown, K.M., et al., *A cross-platform freeware tool for digital reconstruction of neuronal arborizations from image stacks.* Neuroinformatics, 2005. **3**: p. 343-360.
3. Löhner, R. and E. Oñate, *A general advancing front technique for filling space with arbitrary objects.* International Journal for Numerical Methods in Engineering, 2004. **61**: p. 1977-1991.
4. Cebral, J.R., et al., *Efficient pipeline for image-based patient-specific analysis of cerebral aneurysm hemodynamics: Technique and sensitivity.* IEEE Transactions in Medical Imaging, 2005. **24**(1): p. 457-467.

2nd International Conference on Mathematical and Computational Biomedical Engineering - CMBE2011
March 30 - April 1, 2011, Washington D.C, USA
P. Nithiarasu and R. Löhner (Eds.)

APPLICATION OF GRADIENT WEIGHTED MOVING FINITE ELEMENTS TO LAGRANGIAN BIOMEDICAL FLUID-STRUCTURE INTERACTION PROBLEMS

Andrew P. Kuprat[⋆], Facundo del Pin[⋆⋆], Karyn S. Kunzelman[⋆⋆⋆], and Daniel R. Einstein[⋆]
[⋆]Pacific Northwest National Laboratory, 902 Battelle Blvd., P.O. Box 999; MSIN P7-58, Richland, WA 99352, andrew.kuprat@pnl.gov, daniel.einstein@pnl.gov
[⋆⋆]Livermore Software Technology Corp., 7374 Las Positas Road, Livermore, CA 94551, fdelpin@lstc.com
[⋆⋆⋆]University of Maine, 219 Boardman Hall, Orono, Maine 04469-5711 kunzelka@msn.com

SUMMARY

Interfacial shear stresses play a biologically important role in the environs of the cardiac valve. Thus, it is highly desirable to treat the interface in a Lagrangian framework, where fluid shear stresses can be correctly resolved. Adoption of a Lagrangian framework, however, poses significant challenges in terms of grid management, especially during contact and re-opening of the valve. Herein, we present a novel numerical paradigm for ALE motion that reduces the need for expensive edge flip operations even in the presence of motions such as contact where other approaches break down. Specifically, we apply the method of gradient-weighted moving finite elements (GWMFE) to optimize mesh motion throughout the simulation. Element collapse is prevented by adopting regularization force that is related to integrator truncation error. As a result, contact and re-opening are dealt with in a very natural way. No offsets nor fictitious forces need be defined. We first present the broad outlines of the approach and then demonstrate its application to two canonical problems which illustrate the robustness of the technique even in the absence of local edge-flipping operations.

This work was in part supported by National Institutes of Health (NIH) Research R01HL092926-01A2 (Karyn S. Kunzelman, PI)

Key Words: *cardiac valves, fluid-structure interaction, blood flow, wall shear stress.*

1 INTRODUCTION

Computational mesh dynamics (CMD) in ALE-based fluid-structure interaction (FSI) simulations strongly influences simulation performance, robustness and accuracy. To be effective, CMD algorithms should preserve element quality and anisotropy over the simulation while minimizing the need for remeshing. At the same time, they should be problem-independent. FSI simulations of cardiac valves are among the most challenging problems for CMD because a mesh singularity occurs when the valve opens and closes changing the topology of the problem. Typically, interface capturing techniques are used to address this problem, such that the valve mesh travels though the fluid mesh, both having separate topologies. However, this approach sacrifices accuracy at the interface and furthermore mechanisms must be introduced to deal with contact between the valve surfaces. Below we present a novel paradigm for CMD that robustly enables Lagrangian tracking of the valve interface, while handling contact in a natural way.

2 THEORY

Briefly, the momentum equation for the fluid is given as:

$$\rho \frac{Du_i}{Dt} = \frac{\partial \sigma_{ij}}{\partial x_j} + \rho f_i, \tag{1}$$

where D is the material derivative, u is the velocity, σ_{ij} is the stress tensor, ρ is the density and f_i is a vector of external body forces. In an ALE formulation, the material derivative is expressed as:

$$\frac{Du_i}{Dt} = \frac{\partial u_i}{\partial t} + \frac{\partial u_i}{\partial x_j}(u_j - v_j), \tag{2}$$

where v_j is the mesh velocity. The focus of the approach to CMD based on GWMFE is the robust specification of v_j in the presence of large deformation and contact-related mesh singularities.

Applied to motion of surfaces, GWMFE evolves a piecewise linear triangular mesh to minimize the error in normal surface velocity over the set of all possible nodal motions. In [1] the method was used to compute mean curvature motion of surfaces with additional equations added to evolve an attached tetrahedral mesh.

The surface velocities in [1] were driven by mean curvature motion, while here they are driven by solution of Equation 1. However, the situation is similar: a) normal surface velocities represent motions derived from physical considerations b) tangential surface velocities can be arbitrary in nearly planar regions since they do not affect normal surface motion, and c) interior node velocities are completely arbitrary. Since the velocities in b) and c) are arbitrary, we are free to devise velocities that improve mesh quality and CFD solution quality. A key observation is that the arbitrariness of the tangential surface velocities hinges on the notion of what is 'nearly planar'. In fact, if the triangular surface neighborhood of a vertex V can be sandwiched between two parallel planes separated by no more than η – the truncation error of the integrator – then computationally the neighborhood of V is indistinguishable from a perfect planar neighborhood. Thus, in [1] as well as this work, regularization forces are introduced whose strength is a function of the truncation error.

Assuming the FSI solver suggests velocities $\mathbf{v}_0$ on the solid-fluid interface, GWMFE solves for final velocities $\mathbf{v}$ on the surface and in the fluid domain (Algorithm 1). The normal velocity components of supplied surface velocity will be essentially preserved, so that

$$\mathbf{v}_i \cdot \hat{\mathbf{n}} \approx \mathbf{v}_{0,i} \cdot \hat{\mathbf{n}}, \tag{3}$$

where i is an interface node and $\hat{\mathbf{n}}$ is surface normal. To obtain the velocities $\mathbf{v}_i = \dot{\mathbf{x}}_i$, the following ODE system is solved with an implicit solver using timesteps $dt_{\mathbf{GWMFE}}$ independent of timesteps $dt_{\mathbf{FSI}}$ used in the FSI solver:

$$\begin{aligned} &\left[\int (\hat{\mathbf{n}}\hat{\mathbf{n}}^T \alpha_i \alpha_j + \mathbf{I}_3 \epsilon_{\text{visc}} (\nabla_{\mathbf{s}} \alpha_i \cdot \nabla_{\mathbf{s}} \alpha_j))\, dS \;+\; \int \mathbf{I}_3 \tilde{\epsilon}_{\text{visc}} (\nabla \tilde{\alpha}_i \cdot \nabla \tilde{\alpha}_j)\, dV \right] \dot{\mathbf{x}}_j \\ &\quad = \int \mathbf{v}_0 \cdot \hat{\mathbf{n}}\hat{\mathbf{n}} \alpha_i \, dS \;-\; \epsilon_{\text{qual}} \nabla_{\mathbf{x}_i} Q^{\text{tri}} - \; \tilde{\epsilon}_{\text{qual}} \nabla_{\mathbf{x}_i} Q^{\text{tet}} \,, \quad 1 \le i \le N. \end{aligned} \tag{4}$$

When regularization terms involving $\epsilon_{\text{visc}}, \tilde{\epsilon}_{\text{visc}}, \epsilon_{\text{qual}}, \tilde{\epsilon}_{\text{qual}}$ are neglected, what remains is the unregularized GWMFE method

$$\left[\int \hat{\mathbf{n}}\hat{\mathbf{n}}^T \alpha_i \alpha_j \, dS \right] \dot{\mathbf{x}}_j = \int \mathbf{v}_0 \cdot \hat{\mathbf{n}}\hat{\mathbf{n}} \alpha_i \, dS. \tag{5}$$

Here α_i is the piecewise linear hat function for the ith surface node which is 1 at $\mathbf{x}_i$ and is zero at all other surface nodes j. $\mathbf{v}_0$ is the surface velocity, which is assumed to vary piecewise linearly, and is supplied by the FSI solver. It is easy to show that solution of (5) gives (3) with equality, but a unique solution will not exist when the surface exhibits planar degeneracy at any point, so regularization is needed.

The second term on the left-hand side of (4) is surface grid viscosity:

$$\left[\int \mathbf{I}_3 \epsilon_{\text{visc}} (\nabla_{\mathbf{s}} \alpha_i \cdot \nabla_{\mathbf{s}} \alpha_j) \, dS\right] \dot{\mathbf{x}}_j. \tag{6}$$

Here $\mathbf{I}_3$ is the 3x3 identity matrix and $\nabla_{\mathbf{s}} \alpha_i$ is gradient with respect to surface parametrization of the surface piecewise linear basis function α_i. This term creates a viscous medium for node motions within the surface and removes the ambiguity of GWMFE node motion when the surface has planar degeneracy.

The last term on the left-hand side is volume grid viscosity:

$$\left[\int \mathbf{I}_3 \tilde{\epsilon}_{\text{visc}} (\nabla \tilde{\alpha}_i \cdot \nabla \tilde{\alpha}_j) \, dV\right] \dot{\mathbf{x}}_j. \tag{7}$$

Here $\tilde{\alpha}_i$ is the piecewise linear tetrahedral basis function which is 1 on node i and zero at other nodes. This term can be seen as the inner product of $\tilde{\alpha}_i$ with $-\tilde{\epsilon}_{\text{visc}} \nabla^2 \left(\sum_j \tilde{\alpha}_j \dot{\mathbf{x}}_j\right)$, the negative Laplacian of the grid velocity in the fluid interior, multiplied by the tiny parameter $\tilde{\epsilon}_{\text{visc}}$. The presence of this term ties all grid node motions together and essentially makes nodes travel in a viscous medium. It also reveals the connection of GWMFE to standard ALE formulations.

The middle and last terms on the right hand side of (4) are grid quality regularization terms that tend to prevent collapse of triangles within the surface and to prevent collapse of tetrahedra within the volume. Here Q^{tri} is a 'triangle quality energy' which is essentially the sum of the squares of the aspect ratios of all the surface triangles and Q^{tet} is a 'tetrahedral quality energy' which is essentially the sum of the squares of the aspect ratios of all the interior tetrahedra. The factors ϵ_{qual}, $\tilde{\epsilon}_{\text{qual}}$ are chosen in system (4) so that collapse is averted when inscribed radius is on the order of η, the truncation error used by the integrator when solving the system. Arguably, this is the most "natural" choice possible.

Data: initial time t, simulation end time t_{end}, grid node positions $\mathbf{x}$, mesh topology, and field variables $\mathbf{u}$
while $t < t_{\text{end}}$ **do**
  [determine appropriate FSI timestep based on values of $\mathbf{x}$ and $\mathbf{u}$]
  dt_{FSI} =GETFSITIMESTEP($\mathbf{x}$,$\mathbf{u}$)
  $t_{\text{targ}} \leftarrow t + dt_{\text{FSI}}$
  [FSI code determines proposed surface velocities $\mathbf{v}_0$ for time interval $[t, t_{\text{targ}}]$]
  $\mathbf{v}_0$ = GETFSISURFACEVELOCITIES(t,t_{targ},$\mathbf{x}$,$\mathbf{u}$)
  [Compute final surface and interior fluid velocities $\mathbf{v}$ using GWMFE with timestepping dt_{GWMFE} independent of dt_{FSI}]
  $\mathbf{v}$ = GETGWMFEVELOCITIES(t,t_{targ},$\mathbf{x}$,$\mathbf{v}_0$)
  [update field variables $\mathbf{u}$, grid node positions $\mathbf{x}$, and time t]
  call UPDATEFSIFIELDVARIABLES(t,t_{targ},$\mathbf{x}$,$\mathbf{v}$,$\mathbf{u}$)
  $\mathbf{x} \leftarrow \mathbf{x} + \mathbf{v} \cdot dt_{\text{FSI}}$
  $t \leftarrow t_{\text{targ}}$
end

Algorithm 1: Coupling of FSI code with GWMFE computational mesh dynamics

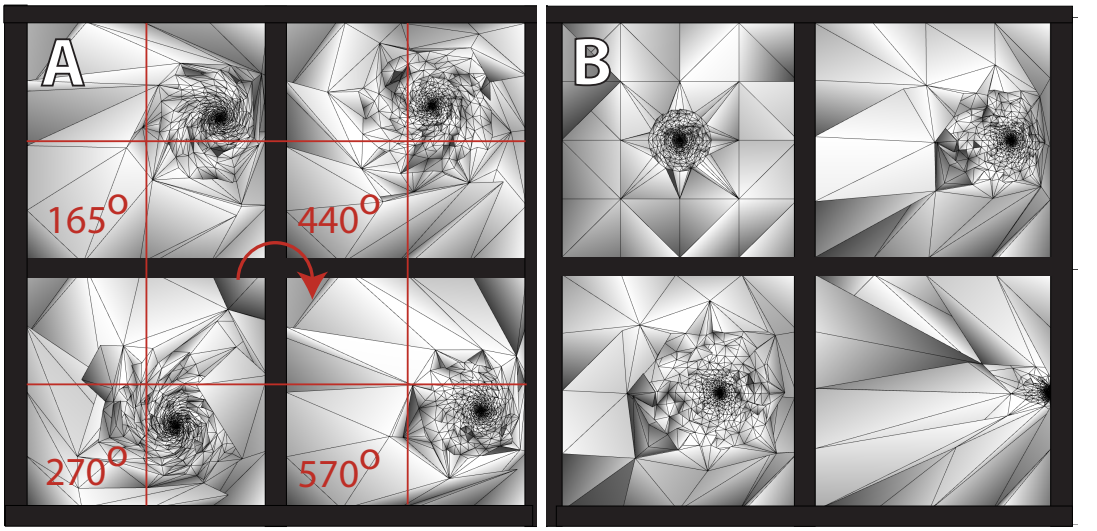

Figure 1: A: indefinite rotation of ball without mesh inversion with no topology change. B: Collision of ball with wall, keeping all elements positively oriented. Asymptotic solution of mesh movement system is no motion with elements trapped between ball and wall having inscribed radii on the order of the integrator truncation error.

3 CANONICAL EXAMPLE

In Figure 1 on the left, we show the effect of regularized GWMFE motion on the grid surrounding a ball that is rotating in a 3D domain with constant angular velocity. Without any grid reconnection, the mesh maintains positive tet volumes, while the surface triangles on the the ball all maintain correct orientation. This happy situation is maintained for an indefinite number of rotations.

On the right we translate a ball with constant velocity to the right side of the domain. At a certain time the problem becomes ill-defined, since the ball should penetrate the wall, yet the wall is rigid. The GWMFE system elegantly solves the problem in a *natural* fashion by continuing the motion of the ball until the tetrahedra that are trapped between the ball and the wall get inscribed radii on the order of η the truncation error. At this point, the regularization terms in the system take over and lock up the trapped tetrahedra.

4 CONCLUSIONS

We have developed a robust mesh movement system that couples FSI surface movement to fluid mesh movement. The terms appearing in the system allow for unparalleled robust mesh movement which is necessary for challenging realistic cardiac FSI simulations.

REFERENCES

[1] A.P. Kuprat, Modeling Microstructure Evolution Using Gradient-Weighted Moving Finite Elements, *Siam J. Sci. Comput*, 22, 535-560, 2000.

2nd International Conference on Mathematical and Computational Biomedical Engineering - CMBE2011
March 30 - April 1, 2011, Washington D.C, USA
P. Nithiarasu and R. Löhner (Eds.)

Simulating aortic heart valve dynamics by the immersed boundary method

Boyce E. Griffith
Leon H. Charney Division of Cardiology, Department of Medicine, New York University School of Medicine, 550 First Avenue, New York, NY 10016 USA, boyce.griffith@nyumc.org

SUMMARY

The immersed boundary (IB) method is a mathematical and computational approach to fluid-structure interaction problems in which an elastic structure is immersed in a viscous incompressible fluid. The IB approach to such problems is to describe the elasticity of the structure in Lagrangian form, and to describe the momentum, viscosity, and incompressibility of the coupled fluid-structure system in Eulerian form. Lagrangian and Eulerian variables are coupled by integral transforms with Dirac delta function kernels. Many IB models describe the elasticity of the immersed structure in terms of families of elastic fibers; however, the use of fiber-based elasticity models is not an essential aspect of the IB formulation. We shall describe one possible extension of the IB method to use more general elasticity models that permit finite element discretizations, and we shall present results obtained by applying both the conventional IB method and also our extended IB method to the simulation of the three-dimensional fluid dynamics of the aortic heart valve.

Key Words: *heart valves, blood flow, fluid-structure interaction.*

1 INTRODUCTION

Approximately 250,000 procedures are performed annually to repair or replace damaged or destroyed heart valves, and approximately 50,000 aortic valve replacements are performed annually to treat severe aortic stenosis. Many of the difficulties of replacement cardiac valves are related to the fluid dynamics of the replacement valve. Mathematical and computational models of cardiac fluid-structure interaction can offer insight into the mechanisms of valve function and dysfunction and therefore have the potential to improve the treatments available to the many patients suffering from valvular heart diseases.

The immersed boundary (IB) method [1] is a mathematical and computational approach to fluid-structure interaction problems that was introduced to model the fluid dynamics of heart valves [2,3], and has subsequently been applied to a broad range of problems in biological fluid mechanics. The IB formulation treats problems in which an elastic structure is immersed in a viscous incompressible fluid. The IB approach to such problems is to describe the elasticity of the immersed structure in Lagrangian form, to describe the momentum, viscosity, and incompressibility of the coupled fluid-structure system in Eulerian form, and to couple the Lagrangian and Eulerian variables by integral equations with Dirac delta function kernels. Discretized versions of the IB method generally approximate the Lagrangian variables on a moving curvilinear mesh and the Eulerian variables on a Cartesian grid. The Lagrangian-Eulerian interaction equations are approximated by replacing the singular delta function with a regularized version of the delta function.

Many IB models of fluid-structure interaction describe the elasticity of the immersed structure in terms of families of fibers. Although fiber-based elasticity models are well-suited to describe the anisotropic materials commonly encountered in biological applications, it is difficult combine the fiber-based modeling approach with experimentally characterized constitutive laws. The use of fiber models is not essential to the IB methodology, however, and several recent extensions of the IB method allow for more general elasticity models that permit finite element discretizations [4–6]. We shall describe a new approach to employing finite element mechanics models with the IB method [7] and present initial results obtained by using this method to simulate the mechanics of the aortic heart valve. We shall also present recent simulations of the aortic valve that use an improved version of a more conventional IB method [8,9]. These simulations are among the first three-dimensional IB models of cardiac fluid dynamics to consider multiple cardiac cycles with realistic driving and loading conditions.

2 MATHEMATICAL FORMULATION

Let $\mathbf{x} = (x_1, x_2, x_3) \in \Omega$ denote Cartesian physical coordinates, with $\Omega \subset \mathbb{R}^3$ denoting the physical region that is occupied by the coupled fluid-structure system; let $\mathbf{s} = (s_1, s_2, s_3) \in U$ denote Lagrangian material coordinates that are attached to the immersed elastic structure, with $U \subset \mathbb{R}^3$ denoting the Lagrangian coordinate domain; and let $\mathbf{X}(\mathbf{s}, t) \in \Omega$ denote the physical position of material point $\mathbf{s}$ at time t. The IB formulation of the equations of motion for the fluid-structure system is:

$$\rho\left(\frac{\partial \mathbf{u}}{\partial t}(\mathbf{x},t) + \mathbf{u}(\mathbf{x},t)\cdot\nabla\mathbf{u}(\mathbf{x},t)\right) = -\nabla p(\mathbf{x},t) + \mu\nabla^2\mathbf{u}(\mathbf{x},t) + \mathbf{f}(\mathbf{x},t), \tag{1}$$

$$\nabla\cdot\mathbf{u}(\mathbf{x},t) = 0, \tag{2}$$

$$\mathbf{f}(\mathbf{x},t) = \int_U \mathbf{F}(\mathbf{s},t)\,\delta(\mathbf{x}-\mathbf{X}(\mathbf{s},t))\,\mathrm{d}\mathbf{s}, \tag{3}$$

$$\frac{\partial \mathbf{X}}{\partial t}(\mathbf{s},t) = \int_\Omega \mathbf{u}(\mathbf{x},t)\,\delta(\mathbf{x}-\mathbf{X}(\mathbf{s},t))\,\mathrm{d}\mathbf{x}, \tag{4}$$

$$\mathbf{F}(\mathbf{s},t) = \boldsymbol{\mathcal{F}}[\mathbf{X}(\cdot,t)], \tag{5}$$

in which $\mathbf{u}(\mathbf{x},t)$ is the Eulerian velocity field, $p(\mathbf{x},t)$ is the Eulerian pressure, $\mathbf{f}(\mathbf{x},t)$ is the Eulerian elastic force density (i.e., the elastic force density with respect to the physical coordinate system, so that $\mathbf{f}(\mathbf{x},t)\,\mathrm{d}\mathbf{x}$ has units of force), $\mathbf{F}(\mathbf{s},t)$ is the Lagrangian elastic force density (i.e., the elastic force density with respect to the material coordinate system, so that $\mathbf{F}(\mathbf{s},t)\,\mathrm{d}\mathbf{s}$ has units of force), $\boldsymbol{\mathcal{F}} : \mathbf{X} \mapsto \mathbf{F}$ is a functional that specifies the Lagrangian elastic force in terms of the deformation of the structure, and $\delta(\mathbf{x}) = \delta(x_1)\,\delta(x_2)\,\delta(x_3)$ is the three-dimensional delta function.

For a fiber-based elasticity models, it is convenient to assume a fiber-aligned Lagrangian coordinate system, so that (s_1, s_2) labels a particular fiber and the mapping $s_3 \mapsto \mathbf{X}(s_1^0, s_2^0, s_3)$ is a parametric representation of the fiber labeled by $(s_1, s_2) = (s_1^0, s_2^0)$. With this coordinate system, it is possible to determine the Lagrangian elastic force density via [9]

$$\mathbf{F}(\mathbf{s},t) = \frac{\partial}{\partial s_3}\left(T\boldsymbol{\tau}\right) + \frac{\partial^2}{\partial s_3^2}\left(c_{\mathrm{b}}(\mathbf{s})\left(\frac{\partial^2\bar{\mathbf{X}}}{\partial s_3^2} - \frac{\partial^2\mathbf{X}}{\partial s_3^2}\right)\right), \tag{6}$$

in which T is the fiber tension, $\boldsymbol{\tau} = \partial\mathbf{X}/\partial s_3 / \left|\partial\mathbf{X}/\partial s_3\right|$ is the fiber-aligned unit tangent vector, $c_{\mathrm{b}}(\mathbf{s})$ is the fiber bending rigidity, and $\bar{\mathbf{X}} = \bar{\mathbf{X}}(\mathbf{s})$ is a reference configuration.

It is also possible to specify the elasticity of the immersed structure in terms of a Lagrangian elastic stress tensor. In the IB formulation, it is most convenient to use the first Piola-Kirchhoff elastic

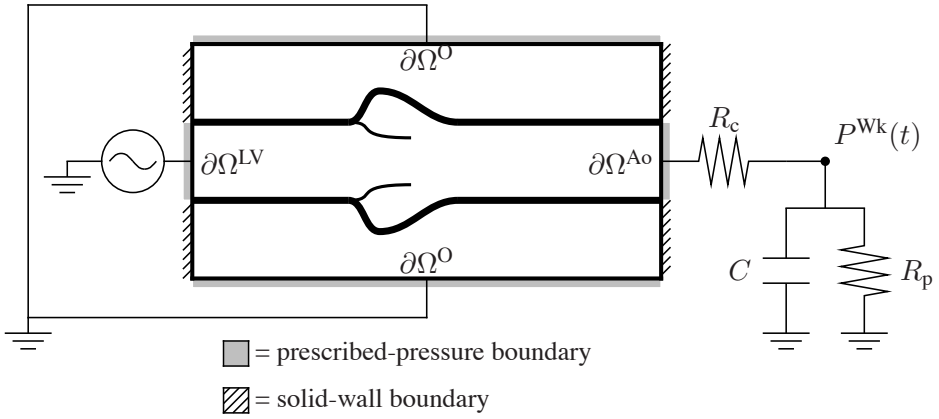

Figure 1: Schematic diagram of the model showing the coupling between the detailed fluid-structure interaction model and the reduced circulation models that provide physiological driving and loading conditions. The model vessel is coupled via the upstream boundary $\partial\Omega^{\mathrm{LV}}$ to a prescribed left-ventricular pressure source that drives flow through the valve. At the downstream boundary $\partial\Omega^{\mathrm{Ao}}$, the model vessel is coupled to a circulation model that provides a realistic pressure load. The open boundary $\partial\Omega^{\mathrm{O}}$ provides a constant-pressure fluid reservoir that balances any changes in the volume of the vessel.

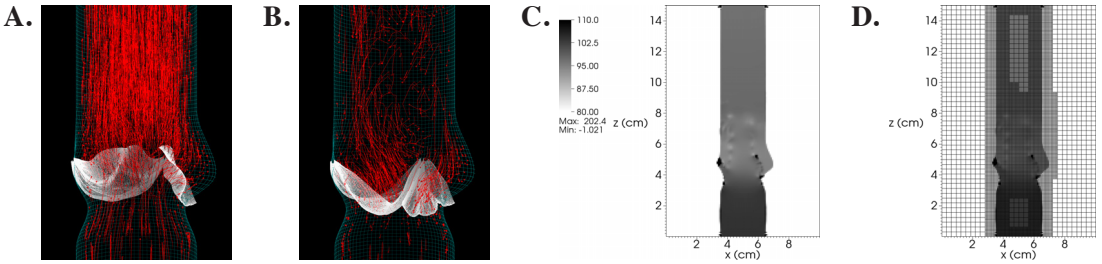

Figure 2: Results from a three-dimensional adaptive IB simulation of the aortic valve. **A–B:** Flow through the model valve as indicated by passively advected markers particles. **C:** Pressure in the model valve plotted along a plane that bisects one of the valve leaflets at the time of peak flow. At this point in the simulation, the pressure difference across the valve is 7.9 mmHg. The maximum systolic pressure difference is 12.9 mmHg, which is in good agreement with experimental observations [10]. **D:** Same as **C**, but also showing the two-level adaptive grid.

stress tensor $\mathbb{P}^{\mathrm{e}}(\mathbf{s},t)$, and to use a weak formulation to determine the corresponding Lagrangian elastic force density, so that $\mathbf{F}(\mathbf{s},t)$ is defined in terms of $\mathbb{P}^{\mathrm{e}}(\mathbf{s},t)$ via [7]

$$\int_U \mathbf{F}(\mathbf{s},t)\cdot\mathbf{v}(\mathbf{X}(\mathbf{s},t))\,d\mathbf{s} = -\int_U \mathbb{P}^{\mathrm{e}}(\mathbf{s},t) : \nabla_{\mathbf{s}}\mathbf{v}(\mathbf{X}(\mathbf{s},t))\,d\mathbf{s}, \tag{7}$$

in which $\mathbf{v}(\mathbf{x})$ is an arbitrary test function that is not assumed to vanish on ∂U.

3 RESULTS

Using an adaptive version of the IB method, we have performed simulations of the fluid dynamics of the aortic valve. A schematic diagram of our aortic valve model is shown in fig. 1. Representative results obtained using a fiber-based elasticity model are shown in fig. 2. Preliminary results obtained by using a finite element model of the aortic wall are shown in fig. 3.

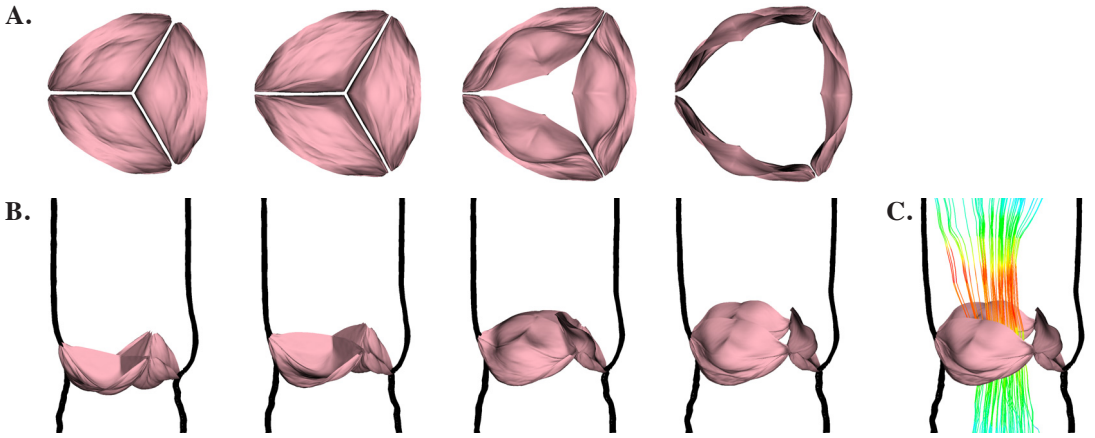

Figure 3: Preliminary results from a three-dimensional adaptive IB simulation of aortic valve dynamics using a finite element model of the vessel wall. **A.** The opening dynamics of the valve, shown at equally spaced time intervals, as viewed from the ascending aorta. **B.** Same as **A**, but also showing a cross-sectional view of the vessel wall. **C.** Same as the rightmost panel of **B**, but also showing instantaneous flow streamlines.

References

[1] C. S. Peskin. The immersed boundary method. *Acta Numer*, 11:479–517, 2002.

[2] C. S. Peskin. *Flow patterns around heart valves: A digital computer method for solving the equations of motion*. PhD thesis, Albert Einstein College of Medicine, 1972.

[3] C. S. Peskin. Numerical analysis of blood flow in the heart. *J Comput Phys*, 25(3):220–252, 1977.

[4] L. Zhang, A. Gerstenberger, X. Wang, and W. K. Liu. Immersed finite element method. *Comput Meth Appl Mech Eng*, 193(21–22):2051–2067, 2004.

[5] W. K. Liu, Y. Liu, D. Farrell, L. Zhang, X. S. Wang, Y. Fukui, N. Patankar, Y. Zhang, C. Bajaj, J. Lee, J. Hong, X. Chen, and H. Hsu. Immersed finite element method and its applications to biological systems. *Comput Meth Appl Mech Eng*, 195(13–16):1722–1749, 2006.

[6] D. Boffi, L. Gastaldi, L. Heltai, and C. S. Peskin. On the hyper-elastic formulation of the immersed boundary method. *Comput Meth Appl Mech Engrg*, 197(25–28):2210–2231, 2008.

[7] B. E. Griffith and X. Luo. Immersed boundary method with finite element elasticity. Submitted, preprint available from `http://www.cims.nyu.edu/~griffith`.

[8] B. E. Griffith, R. D. Hornung, D. M. McQueen, and C. S. Peskin. An adaptive, formally second order accurate version of the immersed boundary method. *J Comput Phys*, 223(1):10–49, 2007.

[9] B. E. Griffith, X. Luo, D. M. McQueen, and C. S. Peskin. Simulating the fluid dynamics of natural and prosthetic heart valves using the immersed boundary method. *Int J Appl Mech*, 1(1):137–177, 2009.

[10] T. E. Driscol and R. W. Eckstein. Systolic pressure gradients across the aortic valve and in the ascending aorta. *Am J Physiol*, 209(3):557–563, 1965.

2nd International Conference on Mathematical and Computational Biomedical Engineering - CMBE2011
March 30 - April 1, 2011, Washington D.C, USA
P. Nithiarasu and R. Löhner (Eds.)

A simple versatile model of valve dynamics for use in lumped parameter and one-dimensional cardiovascular models.

Jonathan P. Mynard*, Malcolm R. Davidson, Daniel J. Penny* and Joseph J. Smolich***
*Heart Research Group, Murdoch Childrens Research Institute, Flemington Rd. Parkville, VIC, Australia, jonathan.mynard@mcri.edu.au
**Department of Chemical and Biomolecular Engineering, University of Melbourne, Australia

SUMMARY

Lumped parameter (0D) and one-dimensional (1D) models of the cardiovascular system generally employ ideal cardiac and/or venous valves that open and close instantaneously. However, under normal or pathological conditions, valves can exhibit complex motions that are mainly determined by the instantaneous difference between upstream and downstream pressures. We present a simple valve model that predicts valve motion on the basis of this pressure difference, and can be used to investigate not only valve pathology, but a wide range of cardiac and vascular factors that are likely to influence valve motion.

Key Words: *aortic valve, pulmonary valve, mitral valve, tricuspid valve, venous valve, stenosis, regurgitation, pulmonary hypertension.*

1 INTRODUCTION

Cardiac and venous valves play a crucial role in the function of the cardiovascular system and in recent modelling studies have been treated in one of two ways. First, in what might be termed 'valve-centric' modelling, 3D fluid-structure interactions are modelled in order to study, for example, detailed fluid and cusp dynamics associated with mechanical or stenosed valves [1,2]. On the other hand, in 'circulation-centric' modelling, valves form just one component of a more global cardiovascular model and are generally represented as perfect diodes that open and close instantaneously or with a prescribed time-course, triggered on the basis of pressure difference or flow thresholds [3,4]. The first approach provides information about valve dynamics, but only with respect to local phenomena. In the second approach, a wide range of cardiovascular interactions are accounted for, but their influence on valve dynamics remains unclear. The purpose of this study was therefore to formulate a simple model of valve dynamics that can be easily incorporated into 0D/1D models and applied to any cardiac or vascular valve, thus allowing study of system-level cardio-valvar-vascular interactions.

2 MAIN BODY

Although valve motion is known to be influenced by a number of complex factors, such as vortex dynamics and the function of the valvar apparatus, the most important factor appears to be the dynamic pressure difference across the valve. In order to formulate a simple model, we therefore assume that the rate of valve opening and closure is determined by only two variables, 1) the

pressure difference (Δp), and 2) the current position (or 'state') of the valve. The net pressure drop across an open valve can be approximated by the Bernoulli equation [4] as

$$\Delta p = Bq\,|q| + L\frac{dq}{dt} \tag{1}$$

where q is flow. The Bernoulli resistance (B) governs pressure differences related to convective acceleration and dynamic pressure losses caused by the diverging flow field downstream to the vena contracta, and is given by $B = \rho/(2A_{\text{eff}}^2)$, where A_{eff} is an effective cross-sectional area and ρ is blood density (1.06 g/cm^3). Blood inertance (L) accounts for the component of Δp related to blood acceleration and is given by $L = \rho l_{\text{eff}}/A_{\text{eff}}$, where l_{eff} is an effective length. Note that A_{eff} incorporates pressure recovery downstream to the vena contracta and is therefore generally larger than the commonly-employed 'effective orifice area'. To model dynamic A_{eff}, we define an index of valve state ($0 \le \zeta \le 1$; $\zeta = 0$, closed valve; $\zeta = 1$, open valve) such that

$$A_{\text{eff}}(t) = \left[A_{\text{eff,max}}(t) - A_{\text{eff,min}}(t)\right]\zeta(t) + A_{\text{eff,min}}(t) \tag{2}$$

To allow representation of valve regurgitation, stenosis and varying annulus area (A_{ann}), maximum ($A_{\text{eff,max}}$) and minimum ($A_{\text{eff,min}}$) valve areas can be further expressed as

$$A_{\text{eff,min}}(t) = M_{\text{rg}}A_{\text{ann}}(t) \quad , \quad A_{\text{eff,max}}(t) = M_{\text{st}}A_{\text{ann}}(t) \tag{3}$$

In this study, we assume A_{ann} is constant. The parameters M_{rg} and M_{st} take values between 0 and 1. For a healthy valve, $M_{\text{rg}} = 0$ and $M_{\text{st}} = 1$. A valve with $M_{\text{rg}} > 0$ corresponds to a leaky (or regurgitant) valve, since $A_{\text{eff,min}} > 0$ and total closure cannot occur. In the limit, $M_{\text{rg}} = 1$ corresponds with an absent valve. By contrast, $M_{\text{st}} < 1$ corresponds to a stenosed valve (reduced $A_{\text{eff,max}}$) or in the extreme, when $M_{\text{st}} = 0$, an atretic valve.

Smooth valve motion requires that the rate of opening/closure approach zero as the valve approaches a fully open/closed position. Assuming that valve opening commences when Δp exceeds a threshold pressure (p_{open}), the rate of opening is thus considered to proceed according to

$$\frac{d\zeta}{dt} = (1-\zeta)\,K_{\text{vo}}\,(\Delta p - p_{\text{open}}) \tag{4}$$

where K_{vo} is a rate coefficient (units: mmHg^{-1}s^{-1}) for valve opening. Thus, valve opening occurs at a faster rate when the instantaneous pressure difference is greater and, for a given pressure difference, at a slower rate as the valve approaches a fully open position. Similarly, valve closure commences when $\Delta p < p_{\text{close}}$ and is governed by the rate coefficient K_{vc},

$$\frac{d\zeta}{dt} = \zeta K_{\text{vc}}\,(\Delta p + p_{\text{close}}) \tag{5}$$

To demonstrate the versatility of the proposed valve model, the four cardiac valves as well as one venous valve are incorporated into a simple closed-loop 0D/1D model of the circulation (Figure 1A). The mitral and tricuspid valves form part of a 0D atrium-valve-ventricle compartment (Figure 1B) in which heart chambers are represented by the standard time-varying elastance model. The left/right ventricles (LV/RV) are coupled to short 1D outflow tract segments and the aortic/pulmonary valves. Large arteries and veins are represented as 1D vessels [3], while systemic and pulmonary peripheral vascular beds are represented by the 0D compartment shown in Figure 1C. All valve threshold pressures are assumed to be zero, except for p_{close} of the venous valve (3 mmHg), based on [5]. See legend of Figure 2 for other valve parameter values.

For a generic valve, Figure 1D demonstrates the dependence of valve state on instantaneous Δp. Note that as the amplitude of Δp increases, the valve opens or closes at a faster rate. Figure 2 shows

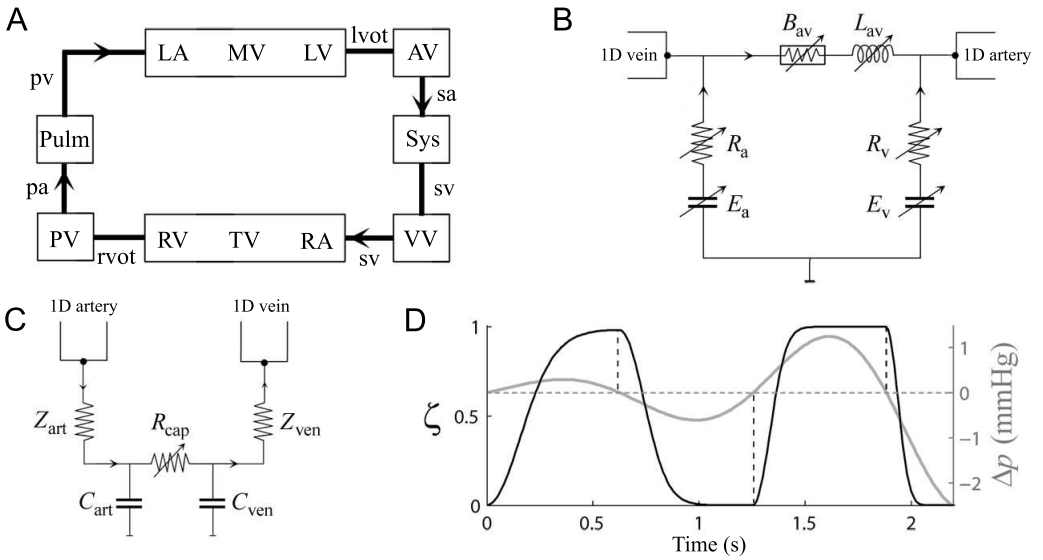

Figure 1: (A) Schematic of the 0D/1D circulation model, where 0D compartments (boxes) are connected by 1D segments (thick lines). (B) An atrium('a')-valve('av')-ventricular('v') compartment represents left/right sides of the heart. Each chamber is represented as a time-varying elastance (E) and pressure-dependent source resistance (R). See text for description of valve parameters. (C) Peripheral vascular bed model, instantiated as 'Sys' and 'Pulm' in (A), consisting of arterial and venous characteristic impedances (Z_{art}, Z_{ven}) and compliances (C_{art}, C_{ven}), and a pressure-dependent capillary resistance (C_{cap}). (D) The dependence of valve state (ζ, black line) on a time-varying pressure difference (Δp, grey line) of increasing amplitude. Abbreviations: AV=Aortic Valve; LA=Left Atrium; LV=Left Ventricle; lvot=left ventricular outflow tract; MV=Mitral Valve; pa=pulmonary artery; Pulm=Pulmonary vascular bed; pv=pulmonary vein; PV=Pulmonary valve; RA=Right Atrium; RV=Right Ventricle; rvot=right ventricular outflow tract; sa=systemic artery; sv=systemic vein; Sys=Systemic vascular bed; TV=Tricuspid Valve; VV=Venous Valve

the simulated valve dynamics for all valves in the 0D/1D model under normal haemodynamic conditions (black lines) and under various pathological conditions (grey lines), as described below.

Under normal conditions, the *aortic valve* (Figure 2A) exhibits four phases that have been observed *in vivo* [6,7] and are predicted by the model, 1) rapid valve opening when LV pressure initially rises above aortic pressure, followed by 2) a short period in which the valve remains fully open, 3) a slow closure phase during the second-half of systole and 4) rapid closure when the ventricle begins relaxing. With aortic stenosis, the valve opens and closes more slowly (e.g. due to calcification of valve cusps) and reaches a smaller A_{eff} when maximally open [7].

The *pulmonary valve* (Figure 2B) has a similar motion to the aortic valve under normal conditions, although there is no clear distinction between slow and rapid valve closure phases [8]. A prominent mid-systolic notching is commonly seen in patients with pulmonary hypertension [8] and is predicted by the model.

The normal *mitral valve* (Figure 2C) undergoes 1) rapid opening in early diastole when LV pressure falls below left atrial (LA) pressure, 2) partial closure during diastasis when LV-LA Δp reverses and then oscillates around zero, 3) full re-opening when LA contraction causes Δp to rise and 4) rapid closure due to LA relaxation and LV contraction [9]. The stenosed mitral valve is restricted when open (lower A_{eff}) but remains open throughout diastole [9].

The *tricuspid valve* (Figure 2D) has a similar motion to the mitral valve under normal conditions [10]. With tricuspid regurgitation, the valve never achieves full closure, leading to substantial retrograde flow during ventricular systole and a loss of the partial closure phase during diastole.

Venous valves (Figure 2E) are normally open throughout the cardiac cycle, despite a small amount of reverse flow [5]. However, tricuspid regurgitation leads to elevated right atrial pressure and probably causes substantial venous valve motion to prevent reflux [11].

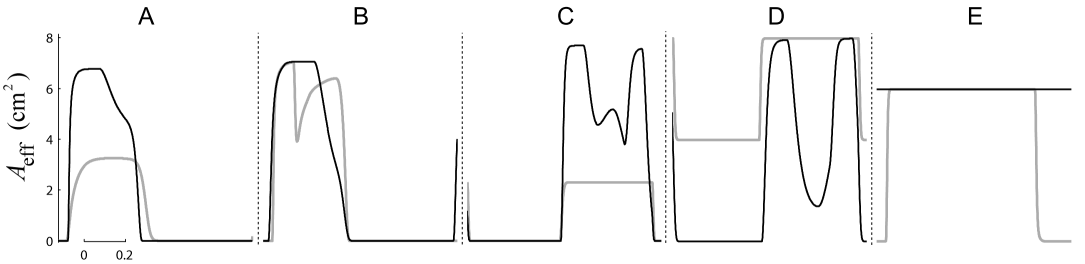

Figure 2: Instantaneous effective valve area (A_{eff}) for the valves in the closed-loop circulation model (Figure 1A) under normal physiological conditions (black line) and for a pathological state (grey line) as follows, (A) Aortic valve, aortic stenosis ($M_{\mathrm{st}} = 0.5$, $K_{\mathrm{vo}} = K_{\mathrm{vc}} = 0.001$); (B) pulmonary valve, pulmonary hypertension (Pulmonary $R_{\mathrm{art}} \uparrow$, $C_{\mathrm{art}} \downarrow$, $E_{\mathrm{RV}} \uparrow$); (C) mitral valve, mitral stenosis ($M_{\mathrm{st}} = 0.3$); (D) tricuspid valve, tricuspid regurgitation ($M_{\mathrm{rg}} = 0.5$, $E_{\mathrm{RA}} \uparrow$, $E_{\mathrm{RV}} \uparrow$); (E) venous valve, tricuspid regurgitation (as in D). For normal valves, estimated $K_{\mathrm{vo}}/K_{\mathrm{vc}}$ values are (A) 0.012/0.012, (B) 0.02/0.02, (C) 0.03/0.04, (D) 0.03/0.04 and (E) 0.03/0.03.

3 CONCLUSIONS

The simple model of valve dynamics proposed in this study is suitable for 0D/1D cardiovascular models and is able to predict typical features of valve motion in normal and pathological conditions. Further work is required to elucidate the limitations and potential uses of this model.

REFERENCES

[1] F. Sotiropoulos and I. Borazjani. A review of state-of-the-art numerical methods for simulating flow through mechanical heart valves. *Med Biol Eng Comput*, 47, 245-256, 2009.

[2] R. van Loon, Towards computational modelling of aortic stenosis. *Int J Num Meth Biomed Eng*, 26, 405-420, 2010.

[3] J.P. Mynard and P. Nithiarasu, A 1D arterial blood flow model incorporating ventricular pressure, aortic valve and regional coronary flow using the locally conservative Galerkin (LCG) method, *Commun Num Meth Eng*, 24, 367-417, 2008.

[4] Y. Sun, B.J. Sjoberg, P. Ask, D. Loyd and B. Wranne, Mathematical model that characterizes transmitral and pulmonary venous flow velocity patterns. *Am J Physiol Heart Circ Physiol*, 268(1): H476-489, 1995.

[5] P.S. van Bemmelen, K. Beach, G. Bedford and D.E.Jr. Strandness, The mechanism of venous valve closure: Its relationship to the velocity of reverse flow, *Archiv Surg* 125, 617-619, 1990.

[6] M.J. Thubrikar, J.L. Heckman and S.P. Nolan, High speed cine-radiographic study of aortic valve leaflet motion, *J Heart Valve Dis*, 2, 653-661, 1993.

[7] M. Handke, G. Heinrichs, F. Beyersdorf, M. Olschewski, C. Bode and A. Geibel, In vivo analysis of aortic valve dynamics by transesophageal 3-dimensional echocardiography with high temporal resolution, *J Thorac Cardiovasc Surg*, 125, 1412-1419, 2003

[8] A.E. Weyman, J. C. Dillon, H. Feigenbaum and S. Chang, Echocardiographic patterns of pulmonic valve motion with pulmonary hypertension, *Circulation*, 50, 905-910, 1974.

[9] A. Zaky, W.K. Nasser, and H. Feigenbaum. A study of mitral valve action recorded by reflected ultrasound and its application in the diagnosis of mitral stenosis. *Circulation*, 37: 789-799, 1968.

[10] B. Anderson, *Echocardiography: the normal examination and echocardiographic measurements.*, Manly, Queensland, Australia, MGA Graphics, 2000 (p. 52).

[11] J. Fisher, F. Vaghaiwalla, J. Tsitlik, H. Levin, J. Brinker, M. Weisfeldt and F. Yin, Determinants and clinical significance of jugular venous valve competence, *Circulation*, 65, 188-196, 1982.

2nd International Conference on Mathematical and Computational Biomedical Engineering – CMBE2011
March 30 – April 1, 2011, Washington D.C., USA
P. Nithiarasu and R. Löhner (eds)

A REALISTIC COMPUTATIONAL MODEL TO SIMULATE AORTIC VALVE REPAIR

Michel R. Labrosse[*], Munir Boodhwani[**], Carsten J. Beller[***]
[*]Department of Mechanical Engineering, University of Ottawa,
161 Louis Pasteur, Ottawa, K1N 6N5 Ontario, Canada;
[**]Department of Cardiac Surgery, University of Ottawa Heart Institute,
42 Ruskin Street, Ottawa, K1Y 4W7 Ontario, Canada;
[***]Department of Cardiac Surgery, University of Heidelberg,
INF 326 2.OG, 68120 Heidelberg, Germany

SUMMARY

Key Words: *Aortic valve, regurgitation, leaflet prolapse, repair, leaflet correction*

1. INTRODUCTION

Recent finite element (FE) models provide increasingly accurate descriptions of the deformations, stresses and dynamics experienced by the aortic valve [1,2]. To gain clinical applicability and facilitate planning for aortic valve repair, these models must make it possible to address asymmetric valves of various sizes, correct dimensions of specific valve components and represent the valve transformations from unpressurized to physiologically loaded. The goal of this study was to create such a model and evaluate its capability to simulate: 1) correct function in normal valves, 2) aortic regurgitation due to annular dilatation and/or leaflet prolapse in diseased valves, and 3) surgical techniques for the correction of leaflet dimensions.

2. METHODS AND RESULTS

Methods: Fifteen three-dimensional points and eight additional parameters were defined to represent a typical trileaflet aortic valve without symmetries. From these data, lines and curves were drawn using MatLab (The MathWorks) to represent the leaflet contours in partially closed position, the aortic sinuses, the left ventricular outflow tract (LVOT) and the ascending aorta. These curves formed the edges of linear and bicubic Coons surfaces [3], each of which was discretized using structured meshing. The process was repeated to produce several layers. A structured hexahedral FE mesh of the whole valve (Fig. 1) was finally generated by connecting the nodes from adjacent surfaces. All subsequent analyses of the valve were done with commercial FE software LS-Dyna (LSTC). The leaflets and the aortic

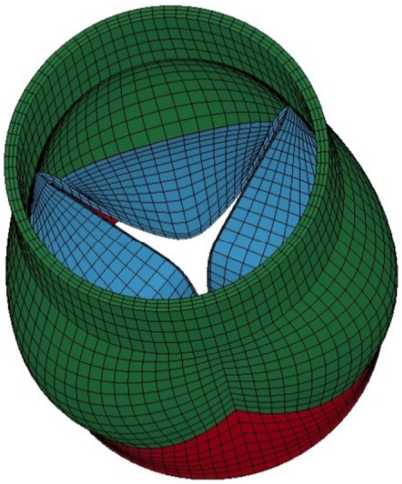

Figure 1: Scalable finite element model of an aortic valve. Green: ascending aorta and aortic sinuses; blue: leaflets; red: base of the valve, including the LVOT.

tissues were modeled as hyperelastic, transversely isotropic materials using Guccione et al.'s model [4]. The dimensions for a symmetric model (Table 1) were obtained from published measurements of a rubber silicone mold cast in an unpressurized human aortic valve: series 7 in [5]. The material constants c_1, c_2, c_3 in Table 1 were determined such as to reproduce the deformations of the valve under static pressurization from 0 to 120 mmHg as described in [5].

Table 1: Symmetric model parameters. Dimensions in mm. C: commissure; L: leaflet; A: aorta.

Base radius	C. radius	Valve height	Sinus height	L. height	L. length
11.75	9.10	17.8	18.33	16	30
C. height	L. thickness	A. thickness	Sinus radius	Sinus max. radius height	
7.1	0.50	1.52	13.30	10	
A. c_1 (kPa)	A. c_2 (-)	A. c_3 (-)	L. c_1 (kPa)	L. c_2 (-)	L. c_3 (-)
14.30	4.55	6.10	1.00	200	50

The valve model was then studied over one cardiac cycle by application of known pressure pulses. Since the analysis started from the unpressurized geometry, the pressure was ramped from 0 up to 80 mmHg before the cardiac cycle started in early systole. In addition, a longitudinal stretch ratio of 1.20 was applied to the whole valve to mimic physiological conditions [6]. The geometric orifice area (GOA) as a function of time was measured from the valve model to evaluate its opening and closing characteristics. Since real valves are rarely symmetric, the individual leaflets dimensions shown in Table 2, and consistent with published measurements [7], were implemented in an asymmetric model.

Table 2: Asymmetric model parameters. Dimensions in mm. FE: leaflet free edge length, LH: leaflet height.

Right FE	Right LH	Left FE	Left LH	Non-coron. FE	Non-coron. LH
31	15	29	16	30	16

In further modifications of the symmetric and asymmetric models, the LVOT and commissural radii were increased, and the longitudinal stretch ratio decreased until the closed valve exhibited a central hole. This created regurgitant (leaky) valves whose surgical repair was to be simulated.

During a repair procedure of the remodeling type, the aortic sinuses and the ascending aorta are replaced by a Dacron tube graft recreating pseudo sinuses [8]. In the model, the graft material was idealized as isotropic, linearly elastic, with an elastic modulus of 6 MPa, and a Poisson's ratio of 0.49 [9]. The graft size is chosen to bring back functional dimensions to the ascending aorta, the sinotubular junction and the aortic sinuses. Additional annuloplasty may be used to decrease the dilated LVOT. Depending on the valve geometry and degree of asymmetry, leaflet prolapse, where one leaflet free edge sits below the others while the valve is closing, may compromise the correct sealing of the valve. This requires a customized correction of the leaflet dimensions.

Herein, three existing leaflet correction techniques [10] were simulated: leaflet resuspension (sutures are run all along the leaflet free edge), leaflet central plication (sutures are placed at the leaflet center, and run perpendicular to the free edge over 5-10 mm) and leaflet commissural plication (sutures are placed at both commissures of the leaflet). Accordingly, depending on the case, special finite elements representing 7-0 polypropylene sutures were placed along the leaflet free edge length, at the leaflet center or the leaflet commissures. Each of these elements connected two selected nodes of the leaflet tissue and was instructed to shrink by a controlled amount, thereby mimicking a suture performed by the surgeon.

Results: The approach described above successfully produced a scalable FE mesh of a trileaflet valve (Fig. 1). Analysis of the static pressurization results showed that the dimensional discrepancies between the symmetric model and the data in [5] were less than 12% over the 0-120 mmHg static pressure range.

During a cardiac cycle, both the symmetric and asymmetric valve models showed a maximum GOA of 4.75 cm^2, a rapid valve opening velocity of 70 cm^2/s, a slow closing velocity of 6 cm^2/s and a rapid closing velocity of 33 cm^2/s. These values compare well with in vivo data obtained from transesophageal echography (TEE) in normal aortic valves [11]. While the symmetric valve model had a perfectly symmetric closure, the right leaflet showed a slight prolapse in the asymmetric valve model. Maximum Von Mises stresses of 840 and 1,012 kPa were observed in the leaflets, at the commissures, during diastole, in the symmetric and asymmetric models, respectively.

An increase by 2 mm in the LVOT diameter and by 6 mm in the commissural diameter, combined with a decrease in the longitudinal stretch ratio to 1.00, produced regurgitant valves with a central hole of 1 and 2 mm^2 in the symmetric (Fig. 2a) and asymmetric models (Fig. 2b), respectively. The right leaflet of the asymmetric valve showed a pronounced prolapse (Fig. 2b).

Replacement of the dilated aorta by a 24-mm graft with pseudo sinuses restored correct sealing in the symmetric valve model. The asymmetric valve model still exhibited a pronounced prolapse of the right leaflet, which warranted individual leaflet correction.

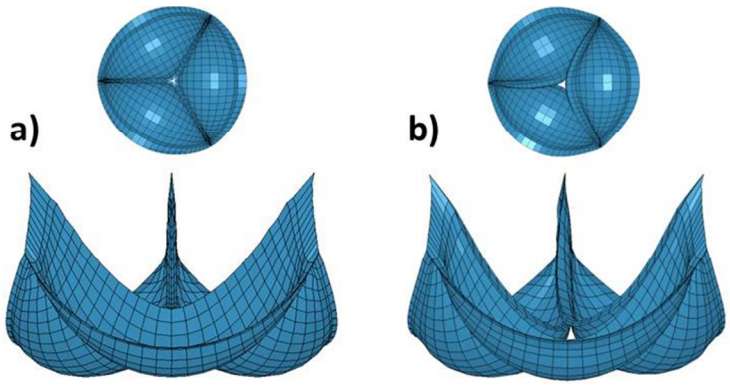

Figure 2: Top and side views of a) the regurgitant symmetric valve model, b) the regurgitant asymmetric valve model with prolapse of the right leaflet.

A 1-mm reduction in the free edge length of the right leaflet was implemented using resuspension, central plication and commissural plication. The simulation results are summarized in Table 3. In all the cases, the maximum stress in the leaflets was observed at the commissures, the maximum opening of the valve was large to the point that the leaflets hit the graft wall, and the rapid opening and slow closing velocities were about twice as large as in normal valves, while the rapid closing velocities were in the higher normals [11]. Although all three techniques produced competent valves, the leaflets never perfectly closed at the same level, inducing small amounts of prolapse for different leaflets depending on the technique. Commissural plication yielded the largest central coaptation height, and central plication the smallest.

Table 3: Descriptors of the valve function after repair combining placement of a 24-mm graft with a 1-mm reduction in the right leaflet free edge length by three different techniques. VM: Von Mises; GOA: valve geometric orifice area; RVO: rapid valve opening; SC: slow closing; RC: rapid closing. L: left; N: non-coronary; R: right.

Leaflet Correction Technique	Max. VM Stress (kPa)	Max. GOA (cm^2)	Coaptation Height (mm)	RVO Velocity (cm^2/s)	SC Velocity (cm^2/s)	RC Velocity (cm^2/s)	Comments
Resuspension	712	5.39	2.7	89	19	70	Slight prolapse of L&N leaflets
Central Plication	752	5.37	1.6	91	19	70	Slight prolapse of R leaflet
Commissural Plication	757	5.28	2.9	91	18	70	Slight prolapse of R&N leaflets

Discussion: To the authors' knowledge, this is the first time that leaflet prolapse has been shown in a computational model. It appears as the direct consequence of valve asymmetry. The results from the simulation of different leaflet correction techniques illustrate that repairing an asymmetric aortic valve can be quite challenging, a fact well known to cardiac surgeons [10]. In the particular case considered, commissural plication produced the best overall sealing characteristics along with acceptable dynamic performance, despite marginally higher leaflet stresses. More analyses are granted now that a well validated computational model of the whole aortic valve has been established. For instance, attempts can be made to minimize the interference between the leaflets and the graft in repaired valves, and explore different amounts of leaflet correction.

3. CONCLUSIONS

The proposed FE modeling approach gives access to unprecedented details in the function of normal, diseased and repaired aortic valves. This could facilitate aortic valve repair planning.

REFERENCES

[1] T.M. Koch, B.D. Reddy, P. Zilla and T. Franz, Aortic valve leaflet mechanical properties facilitate diastolic valve function, *Computer Methods in Biomechanics and Biomedical Engineering*, 13(2), 225-234, 2010.

[2] M.R. Labrosse, K. Lobo and C.J. Beller, Structural analysis of the natural aortic valve in dynamics: from unpressurized to physiologically loaded, *Journal of Biomechanics*, 43, 1916-1922, 2010.

[3] D. Salomon, *Curves and Surfaces for Computer Graphics*, Springer, 2006.

[4] J. Guccione, A. McCulloch and L. Waldman, Passive material properties of intact ventricular myocardium determined from a cylindrical model, *Journal of Biomechanical Engineering*, 113, 42-55, 1991.

[5] W.M. Swanson and R.E. Clark, Dimensions and geometric relationships of the human aortic valve as a function of pressure, *Circulation Research*, 22, 871-882, 1974.

[6] H.C. Han and Y.C. Fung, Longitudinal strain of canine and porcine aortas, *Journal of Biomechanics*, 28(5), 637-641, 1995.

[7] M.A. Sliver and W.C. Roberts, Detailed anatomy of the normal functioning aortic valve in hearts of normal and increased weight, *American Journal of Cardiology*, 55, 454-461, 1985.

[8] R. De Paulis, G.M De Matteis, P. Nardi, R. Scaffa, M.M. Buratta and L. Chiariello, Opening and closing characteristics of the aortic valve after valve-sparing procedures using a new aortic valve conduit, *Annals of Thoracic Surgery*, 72, 487-494, 2001.

[9] J.M. Lee and G.J. Wilson, Anisotropic tensile viscoelastic properties of vascular graft materials tested at low strain rates, *Biomaterials*, 7, 423-431, 1986.

[10] M. Boodhwani, L. de Kerchove, D. Glineur, P. Noirhomme and G. El Khoury, Repair of aortic valve cusp prolapse, *Multimedia Manual of Cardiothoracic Surgery*, doi:10.1510/mmcts.2008.003806.

[11] M. Handke, G. Heindrichs, F. Beyerdorf, M. Olshewski, C. Bode and A. Geibel, In vivo analysis of aortic valve dynamics by transesophageal 3-dimensional echocardiography with high temporal resolution, *Journal of Thoracic and Cardiovascular Surgery*, 125, 1412-1419, 2003.

2nd International Conference on Mathematical and Computational Biomedical Engineering – CMBE2011
March 30 – April 1, 2011, Washington D.C., USA
P. Nithiarasu and R. Löhner (eds)

THE INFLUENCE OF THE UPSTREAM BOUNDARY CONDITION IN THE NUMERICAL SIMULATION OF THE OPENING OF AN AORTIC BMHV

Sebastiaan Annerel*, Joris Degroote*, Tom Claessens, Peter Van Ransbeeck**, Patrick Segers***, Pascal Verdonck*** and Jan Vierendeels***
*Ghent University, Department of Flow, Heat and Combustion Mechanics,
Sint-Pietersnieuwstraat 41, B-9000 Ghent, Belgium
e-mail: {Sebastiaan.Annerel,Joris.Degroote,Jan.Vierendeels}@UGent.be
**University College Ghent, BioMech, Department of Mechanics,
Schoonmeersstraat 52, B-9000 Ghent, Belgium
e-mail: {Tom.Claessens,Peter.VanRansbeeck}@HoGent.be
***Ghent University, IBiTech-bioMMeda,
De Pintelaan 185, B-9000 Ghent, Belgium
e-mail: {Patrick.Segers,Pascal.Verdonck}@UGent.be

SUMMARY

In this paper, the influence of the upstream boundary condition for the numerical simulation of an aortic Bileaflet Mechanical Heart Valve (BMHV) is studied. Two types of upstream boundary conditions are discussed and evaluated. First, an inflow velocity profile is imposed at the inlet of the valve. Secondly, a geometrical boundary condition is used, which implies that the flow rate is governed by the geometrical contraction of the left-ventricle (LV). Both boundary conditions are used to simulate a 3D case with the same BMHV. The change in time of the LV volume is calculated such that the flow rate through the valve is identical in both cases. The dynamics of the BMHV are modelled using fluid-structure interaction (FSI) and only the opening phase of the valve is simulated. The simulations show that although the results for the two cases are similar, differences occur in the leaflet movement. In particular, when using the velocity profile, the leaflets impact the blocking mechanism at their open position with a 25% larger angular velocity. Therefore, when one wants to simulate the dynamics of such an impact, the upstream boundary condition needs to be chosen carefully.

Key Words: *Boundary condition, Left-ventricle, Bileaflet Mechanical Heart Valve, FSI*

1. INTRODUCTION

When numerically simulating Bileaflet Mechanical Heart Valves (BMHVs), several types of upstream boundary conditions can be used [1,2]. However, since the dynamic movement of the valve leaflets is driven by the resulting flow field, the imposed boundary condition needs to be chosen carefully.
Commonly, an inflow velocity profile is imposed at the inlet [1]. Another approach is to implement a geometrical boundary condition. For a BMHV in the aortic position, this can be done by a contracting left-ventricle (LV), as is discussed in [2].
In this paper, the use of these two upstream boundary conditions is discussed and evaluated through 3D numerical simulations.

2. METHODS

In this section, the used 3D cases are discussed. First, the numerical simulation of the dynamics of a BMHV is described. Subsequently, the details of the used boundary conditions are discussed.

2.1 Fluid-Structure Interaction simulation of the BMHV

The numerical simulation of a BMHV is a complex Fluid-Structure Interaction (FSI) problem because the movement of the leaflets strongly interacts with the surrounding fluid motion and, therefore, the dynamic equilibrium at the fluid-structure interface needs to be taken into account.
The dynamics of the BMHV with rigid leaflets is calculated by a recently developed FSI algorithm [1]. This strong coupling algorithm uses separated solvers for the flow and the structural domain. It predicts the moments (and thus the angular accelerations) for the next coupling iteration through a linearization of Newton's Second Law with a finite difference approximation of the Jacobian. The components of this Jacobian are the derivatives of the moments (exerted by the flow on the leaflets) with respect to changes in leaflet angular accelerations. The Jacobian is numerically derived from the flow solver by variations of the leaflet positions. A more detailed description of the FSI algorithm can be found in [1].
The BMHV used in the simulations, is a simplified model of the 25mm ATS Open Pivot Standard Heart Valve in aortic position with the orifice inner diameter measuring 20.8mm [1].

2.2 Boundary Conditions

Downstream of the valve, the geometry consists of a rigid straight tube with diameter 22mm. A pressure is imposed at the outlet boundary, since in a rigid geometry the pressure level does not affect the flow field (only the pressure gradient appears in the equations).

Upstream of the valve, the flow rate is specified. This is done by the use of two different boundary conditions, which results in two cases, as is visualised in Figure 1.

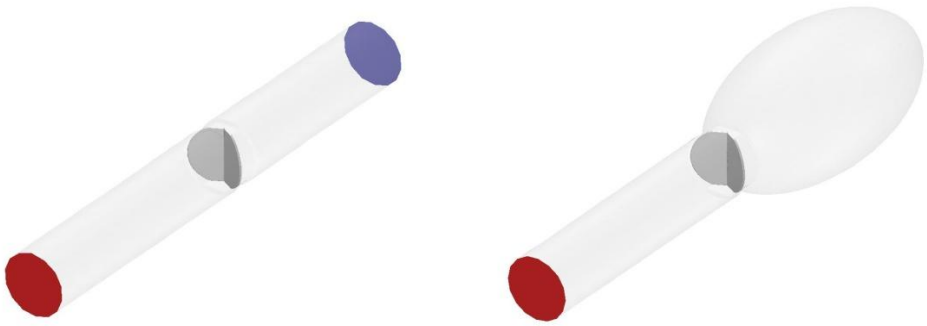

(*a*) (*b*)

Figure 1: View on the geometry of the simulated cases, with the boundary conditions. Downstream: pressure outlet (in red). Upstream: (*a*) inflow velocity profile (in blue), (*b*) contracting LV.

In the first case, a rigid straight tube (with diameter 22mm) is placed upstream with a velocity profile imposed at the inlet. The used velocity profile is an aortic flow pulse with a time cycle of 1s and is displayed in Figure 3.a. It is the same uniform velocity profile that is used in [1].
The second case consists upstream of a contracting LV, as is done in [2]. The shape of such a LV is usually modelled as a prolate spheroid [3]. The short-to-long-axis ratio of the spheroid is kept constant at 0.5, which is considered the normal reference for a human LV [4]. The change in time of the LV volume is calculated such that the flow rate through the valve is identical in both cases.

An end-diastolic volume of 111ml is chosen. Contraction results in an end-systolic LV volume of approximately 41ml. Both volumes are well within the reference range for healthy men [3].
Both geometries are meshed with approximately 800 000 tetrahedral cells. Blood is modelled as a laminar incompressible Newtonian fluid with density and viscosity equal to respectively 1050 kg/m^3 and 4E-3 Pa·s. A no-slip boundary condition is applied at the walls.

3. RESULTS

The opening phase of the valve leaflets is simulated from t = 0s (begin of systole) to t = 0.125s (peak of systole). The velocity flow field is visualised in Figure 2 on a longitudinal cut plane at t = 0.2s. It shows that the flow through the valve is similar in both geometries.

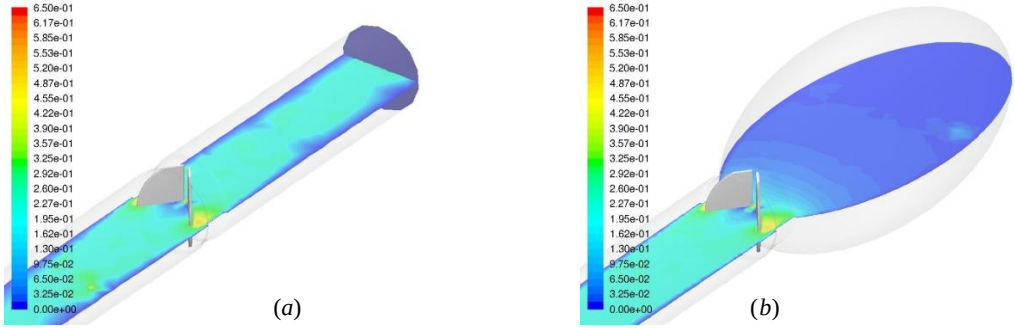

Figure 2: Velocity flow field (in m/s) at t=0.2s. (*a*) inflow velocity profile, (*b*) contracting LV.

The movement of the leaflets is depicted in Figure 3. Since the resulting leaflet motion is symmetric, only one of the two leaflets of each case is shown for clarity. The angular positions (Figure 3.a) are calculated relative to the fully opened position. Therefore, 0% refers to the closed position and 100% refers to a fully opened leaflet.

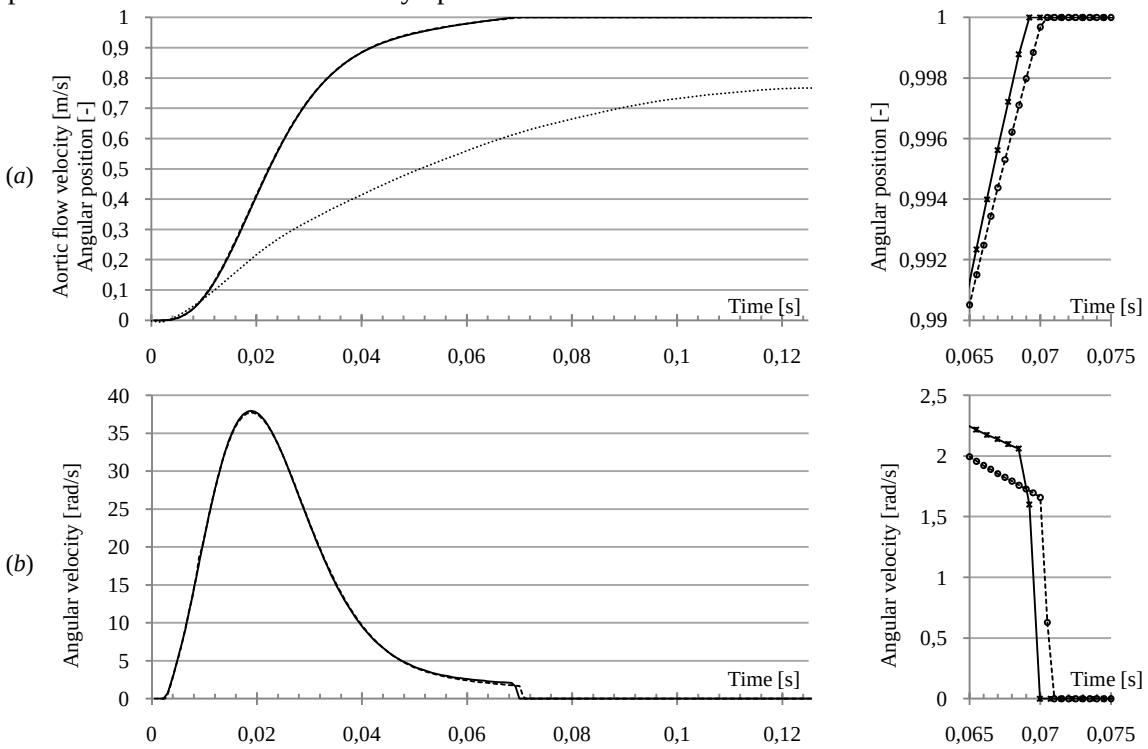

Figure 3: Plot of the aortic flow velocity (*a*) and the leaflet movement: angular position (*a*), angular velocity (*b*). Aortic flow velocity (···), Leaflet with ventricle (---), Leaflet with velocity profile (—). The impact at the open position is zoomed at the right.

It can be seen that although the results for the two cases are similar, differences occur in the leaflet movement. In particular, the leaflet reaches the fully open position a little sooner when using the velocity profile. Furthermore, when using the velocity profile, the leaflet impacts the blocking mechanism with a 25% larger angular velocity which will result in larger stresses in the leaflets. Also, the moments on the leaflets in the open position (after the impact) remain the largest when using the velocity profile (Figure 4).

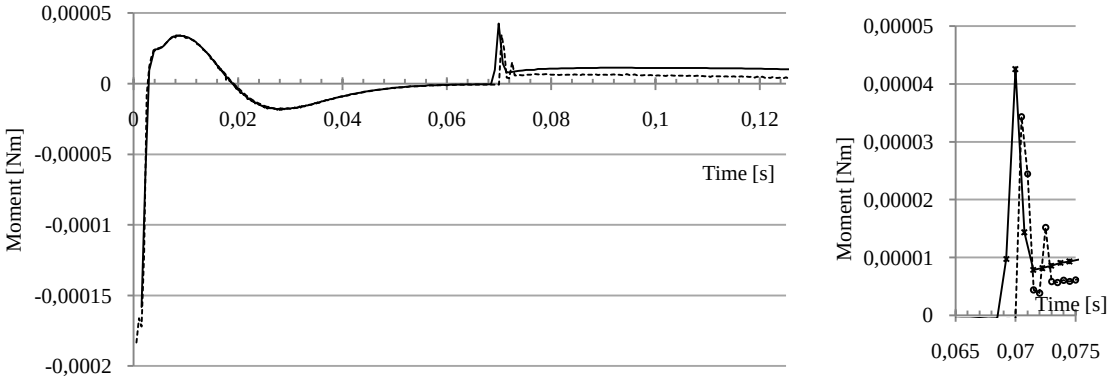

Figure 4: Plot of the moments: Leaflet with ventricle (---), Leaflet with velocity profile (—). The impact at the open position is zoomed at the right.

4. CONCLUSIONS

In this paper, two types of upstream boundary conditions are used to simulate the dynamics of a BMHV. A first case consists of a rigid straight tube with a velocity profile imposed at its inlet. In the second case, the upstream rigid tube is replaced by a contracting LV. The contraction of the LV at every time level induces a flow rate that is identical to the flow rate due to the velocity profile. It is shown that a change in the specified upstream boundary condition can result in different leaflet motion. In particular, when using the velocity profile, the leaflets impact the blocking mechanism at their open position with a 25% larger angular velocity. Therefore, when one wants to simulate the dynamics of such an impact, the upstream boundary condition needs to be chosen carefully.

REFERENCES

[1] S. Annerel, J. Degroote, T. Claessens and J. Vierendeels, Evaluation of a new Implicit Coupling Algorithm for the Partitioned Fluid-Structure Interaction Simulation of Bileaflet Mechanical Heart Valves, *IOP Conference Series: Materials Science and Engineering*, 10, 012124, 2010.

[2] C.J. Carmody, G. Burriesci, I.C. Howard and E.A. Patterson, An approach to the simulation of fluid-structure interaction in the aortic valve, *Journal of Biomechanics*, 39, 158-169, 2006.

[3] R. Lang, M. Bierig, R. Devereux, F. Flachskampf, E. Foster, P. Pellikka, M. Picard, M. Roman, J. Seward, J. Shanewise, S. Solomon, K. Spencer, M. Sutton and W. Stewart, Recommendations for chamber quantification, *European Journal of Echocardiography*, 7, 79-108, 2006.

[4] H.F. Choi, J. D'hooge, F.E. Rademakers and P. Claus, Influence of the left-ventricular shape on passive filling properties and end-diastolic fiber stress and strain, *Journal of Biomechanics*, 43, 1745-1753, 2010.

2nd International Conference on Mathematical and Computational Biomedical Engineering – CMBE2011
March 30 – April 1, 2011, Washington D.C., USA
P. Nithiarasu and R. Löhner (eds)

IN-VIVO DYNAMIC STRESS HISTORY OF THE MITRAL VALVE ANTERIOR LEAFLET

Rouzbeh Amini*, Chad E. Eckert*, Christopher A. Carruthers*, Kevin Koomalsingh, Mashito Minakawa**, Joseph H. Gorman**, Robert C. Gorman**, and Michael S. Sacks***

*Department of Bioengineering and McGowan Institute for Regenerative Medicine, 450 Technology Drive, Suite 300 Pittsburgh, PA 15219, msacks@pitt.edu

**Department of Surgery, School of Medicine, University of Pennsylvania, Philadelphia, PA 19036

SUMMARY

Mitral valve repair surgeries are performed for a wide variety of cardiac pathologies. The *in-vivo* dynamic stress history is an essential step in the study of the repair durability. In this work, we employed a nonlinear structural constitutive model to estimate the stress in an ovine mitral valve anterior leaflet during the full cardiac cycle using *in-vivo* deformation measurements. To obtain the leaflet mechanical properties, a series of biaxial tests were performed on the anterior leaflets and the stress-strain data was fitted to the nonlinear constitutive model. The maximum second Piola-Kirchhoff stress was 355 kPa and 302 kPa in the circumferential and radial directions, respectively. The proposed method could be used to predict the dynamic changes in the leaflet stress when the valve structure and/or loading are changed via surgical procedures.

Key Words: *repair surgery, nonlinear curve fit, dynamic stress.*

1. INTRODUCTION

Application of mitral valve (MV) repair surgeries is ubiquitous. Nowadays, all patients with degenerative valvular diseases and the majority of patients with other types of valvular diseases benefit from MV repair surgeries [1]. Currently, the main three principles of repair surgeries defined by Carpentier [2] are: (i) preserving or restoring full leaflet motion, (ii) creating large surface of coaptation, and (iii) remodeling and stabilizing the annulus. Following Carpentier's principles has reduced MV-repair-related intra-operative and short-term post-operative mortality. Recent long-term studies using more rigorous definitions of failure, however, have identified less optimistic results for repair durability. In most cases, failures were a result of disruption at the leaflet, chordal, or annular suture lines. These failure modes suggest excessive tissue stress as an etiologic factor.

The purpose of this study was to develop a method to compute the stress in the center of the MV anterior leaflet from the dynamic *in-vivo* strain measured experimentally. Numerous *in-vivo* and *in-vitro* studies (e.g.[3, 4]) have been conducted to quantify MV dynamic strain. In the current work, we used *in-vivo* strain data obtained from our well-established ovine model [4] and a nonlinear structural constitutive model [5] to calculate the leaflet *in-vivo* stress.

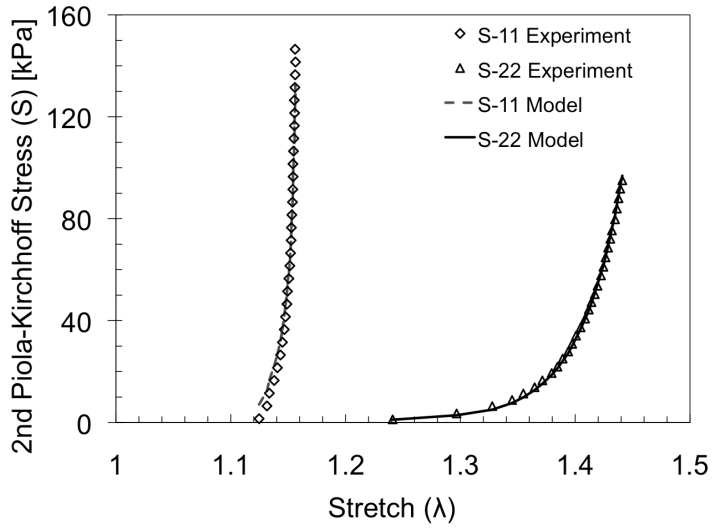

Figure 1. Second Piola-Kirchhoff stress versus stretch for a typical equi-stress biaxial mechanical test along with the model predicted values. S11 and S22 are the normal stress components of the second Piola-Kirchhoff stress tensor along the circumferential and radial directions, respectively. The data points are thinned 10 folds only for the purpose of illustration.

2. METHODOLOGY

Our structural constitutive model was described previously [5]. Briefly, the tissue level second Piola-Kirchhoff stress tensor $\mathbf{S}$ was defined by

$$\mathbf{S} = \int_{-\pi/2}^{\pi/2} R(\theta)\, S^{ens} \mathbf{N} \otimes \mathbf{N}\, d\theta \tag{1}$$

with θ being the fiber orientation and $\mathbf{N}$ being the unit vector along the undeformed fiber, both defined in the material (undeformed) coordinate system. The effective fiber ensemble stress S^{ens} and the fiber angular distribution $R(\theta)$ were defined by

$$S^{ens} = d_1 \exp\left(d_2 \varepsilon^{ens} - 1\right) \tag{2}$$

$$R(\theta) = \frac{1}{\sigma\sqrt{2\pi}} \exp\left[\frac{-(\theta-\mu)^2}{2\sigma^2}\right] \tag{3}$$

where d_1 and d_2 were fiber ensemble material parameter and $R(\theta)$ was defined by a Gaussian distribution with μ and σ being its mean and standard deviation, respectively. The ensemble Green strain ε^{ens} was calculated using tissue level Green strain tensor $\mathbf{E}$:

$$\varepsilon^{ens} = \mathbf{N}^T \mathbf{E} \mathbf{N} \tag{4}$$

where

$$\mathbf{E} = \frac{1}{2}\left(\mathbf{F}^T\mathbf{F} - 1\right) \quad (5)$$

with $\mathbf{F}$ being the deformation gradient tensor.

To estimate the unknown parameters d_1, d_2, μ, and σ, biaxial mechanical tests were performed on the excised ovine MV anterior leaflet. The parameters were calculated by fitting the experimental results to the constitutive model using MATLAB lsqcurvefit function.

The *in-vivo* leaflet deformation was obtained via transducer implantation in a male Dorsett sheep with four transducers sutured on the anterior leaflet midsection. Sonomicrometry array localization was used to determine the 3D coordinates of each transducer every 5 ms throughout the cardiac cycle [6]. The leaflet deformation gradient were computed based on previously detailed methods [6] via a finite element-based surface interpolation technique using a convective, in-surface coordinate system. The *in-vivo* deformation gradient was subsequently multiplied by *ex-vivo*-to-*in-vivo* deformation gradient to obtain a same reference frame for both *in-vivo* sonomicrometry data and *ex-vivo* mechanical tests. Finally, the *in-vivo* stress was calculated from the *in-vivo* deformation using equations (1-6) and fitted material parameters.

3. RESULTS

Figure 1 shows the results of a typical biaxial test. For a set of three-protocol experiments (S11 = S22, S11 = 0.75 * S22, and S22 = 0.75 * S11), the fitted parameters d_1, d_2, μ, and σ were 0.0538 kPa, 34.45, 15.48°, and 3.031°, respectively. As shown in Fig. 1, the model fitted the experimental data reasonably well (R^2 = 0.93 in the circumferential (11) and R^2 = 0.97 in the radial (22) directions).

Figure 2 shows the *in-vivo* stress and strain values during three cardiac cycles. The peak stress value was 355 kPa and 302 kPa in the circumferential and radial directions, respectively (Fig. 2a). The strain in the circumferential direction was smaller than the circumferential direction (Fig. 2b). In both directions, the stress value was fairly unchanged from one cardiac cycle to the next. As shown in Fig. 2c, the circumferential and radial stress values were maximized roughly at the peak left ventricular pressure.

4. CONCLUSIONS

We calculated the leaflet stress from the dynamic *in-vivo* deformation data. Using a nonlinear constitutive structural model provided a better estimation of the leaflet stress in comparison to previous isotropic and orthotropic linear models (e.g. [7, 8]). Our dynamic *in-vivo* stress calculation could provide a framework to evaluate the accuracy of our future structurally and anatomically accurate MV finite-element models.

Our method could also be employed in obtaining *in-vivo* leaflet stress following numerous MV repair tourniquets. A fundamental aspect of MV repair is the relation between leaflet geometry, tissue stress and homeostasis. The long-term goal in our laboratory includes further investigating the etiology of MV repair failure and studying how changes in leaflet tissue stress affect MV interstitial cell biosynthetic abilities, and how these changes in-turn affect MV repair durability.

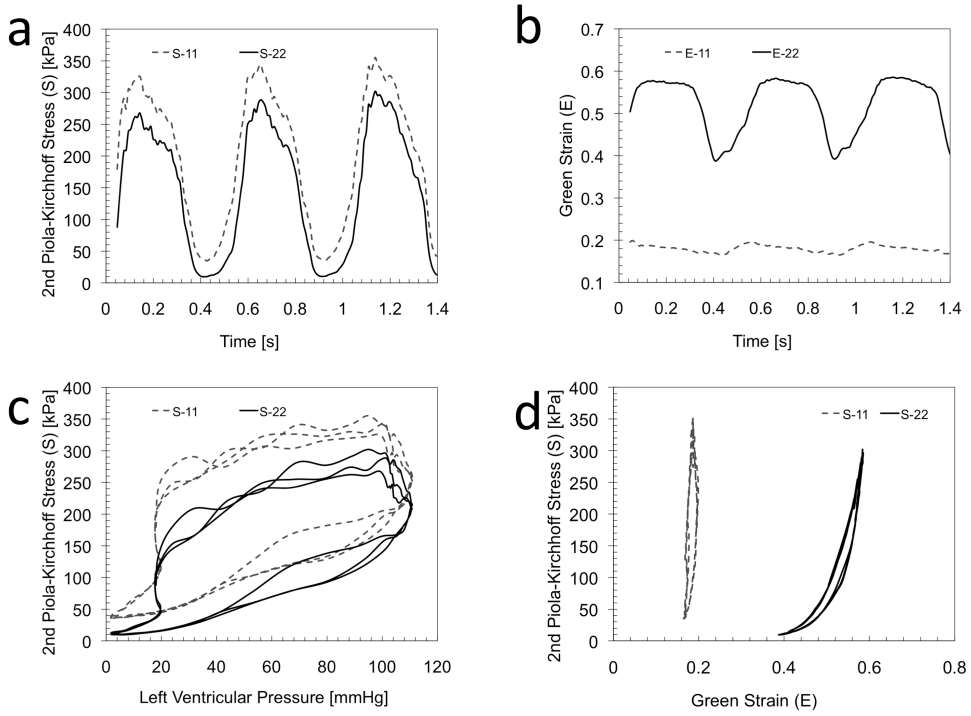

Figure 2. Dynamic circumferential (11 direction) and radial (22 direction) strain and stress values during three cardiac cycles: (a) Second Piola-Kirchhoff stress versus time, (b) Green strain versus time (c) Second Piola-Kirchhoff stress versus left ventricular pressure (d) Second Piola-Kirchhoff stress versus Green strain

REFERENCES

[1] D. H. Adams*, et al.*, Degenerative mitral valve regurgitation: best practice revolution, *Eur Heart J,* vol. 31, pp. 1958-66, Aug 2010.

[2] A. Carpentier, Cardiac valve surgery--the "French correction", *J Thorac Cardiovasc Surg,* vol. 86, pp. 323-37, Sep 1983.

[3] M. S. Sacks*, et al.*, Surface strains in the anterior leaflet of the functioning mitral valve, *Annals of Biomedical Engineering,* vol. 30, pp. 1281-90, Nov-Dec 2002.

[4] C. E. Eckert*, et al.*, In vivo dynamic deformation of the mitral valve annulus, *Ann Biomed Eng,* vol. 37, pp. 1757-71, Sep 2009.

[5] K. L. Billiar and M. S. Sacks, Biaxial mechanical properties of the native and glutaraldehyde-treated aortic valve cusp: Part II--A structural constitutive model, *J Biomech Eng,* vol. 122, pp. 327-35, Aug 2000.

[6] M. S. Sacks*, et al.*, In-vivo dynamic deformation of the mitral valve anterior leaflet, *Ann Thorac Surg,* vol. 82, pp. 1369-77, Oct 2006.

[7] G. Krishnamurthy*, et al.*, Stress-strain behavior of mitral valve leaflets in the beating ovine heart, *J Biomech,* vol. 42, pp. 1909-16, Aug 25 2009.

[8] G. Krishnamurthy*, et al.*, Regional stiffening of the mitral valve anterior leaflet in the beating ovine heart, *J Biomech,* vol. 42, pp. 2697-701, Dec 11 2009.

2nd International Conference on Mathematical and Computational Biomedical Engineering - CMBE2011
March 30 - April 1, 2011, Washington D.C, USA
P. Nithiarasu and R. Löhner (Eds.)

Imaging-based Cardiac Valve Lagrangian-FSI in LS-DYNA

Facundo Del Pin*, Daniel R. Einstein, Andrew P. Kuprat**, Xiangmin Jiao,***, James P. Carson** and Karyn S. Kunzelman*****

*Livermore Software Technology Corp., 7374 Las Positas Road, Livermore, CA 94551, fdelpin@lstc.com

**Pacific Northwest National Laboratory, 902 Battelle Blvd., P.O. Box 999; MSIN P7-58, Richland, WA 99352, {andrew.kuprat, daniel.einstein, james.carson}@pnl.gov

***Department of Applied Mathematics & Statistics, Stony Brook University, Stony Brook, NY 11794, xjiao@sunysb.edu

****University of Maine, Department of Mechanical Engineering, 219 Boardman Hall, Orono, Maine 04469, kunzelka@msn.com

SUMMARY

Imaging-based computational fluid-structure interaction (FSI) analysis of cardiac valve mechanics is an important step toward patient-specific analysis. In addition, a Lagrangian-FSI analysis of imaging based cardiac analysis holds the promise for robustly investigating the role of interfacial shear stresses on valve mechanics in health and disease. In this study, we present a survey of our evolving methods for performing robust Lagrangian-FSI simulations of imaging based cardiac valve geometries in LS-DYNA, as well as outline outstanding challenges shared by the valve modeling community. Topics include 1) development of a parallel Lagrangian incompressible FSI solver; 2) implementation of a unified passive/active large-deformation, anisotropic, nearly incompressible constitutive model; 3) topologically correct image processing; 4) 3D fiber mapping; 5) grid adaptivity; 6) a novel computational mesh dynamics formulation that supports contact; 7) and automatic prismatic boundary-layer generation. This work was in part supported by National Institutes of Health (NIH) Research R01HL092926-01A2 (Karyn S. Kunzelman, PI)

Key Words: *cardiac valves, fluid-structure interaction, imaging.*

1 LAGRANGIAN-FSI IN LS-DYNA

The new FSI solver in LS-DYNA, is a finite element - rather than finite volume - Lagrangian method in that all interfaces are boundary fitted with the immersed structure. Internal nodes, however, are treated in an arbitrary Lagrangian-Eulerian (ALE) manner. A summary of the method is given in [1].

Recent developments include

1. parallel support for the solution of the equations of motion
2. automatic grid remeshing - if necessary - including, edge flips, edge-collapase and edge-bisection
3. a robust node repositioning scheme based on Gradient Weighted Moving Finite Elements that supports immersed contact

Results on an idealized imaging based geometry are shown in Figure 1.

2 CARDIAC TISSUE CONSTITUTIVE MODEL IN LS-DYNA

In [2], we proposed a three-dimensional splay invariant, based on a computationally efficient approximation of a three-dimensional Gaussian distribution of fibers. Herein, we briefly describe the implementation of an extension of that constitutive model as a standard material option available in LS-DYNA. The implementation includes two innovations of note for imaging-derived cardiac valve FSI. First, an active term for accounting for myofibers based on the same splay invariant is included. Second, we included a mechanism for directly incorporating either diffusion tensor data, or mapped fiber data from other sources, such as histology. We briefly describe these developments below. In terms of the 2^{nd} Piola-Kirchhoff stress, the model is:

Figure 1: Lagrangian-FSI simulation of turbulent flow through an idealized imaging-based aortic valve and root.

$$\mathbf{S} = \kappa J\left(J-1\right)\mathbf{C}^{-1} + \mu J^{-2/3}\mathbf{DEV}\left[\frac{1}{4}\left(I-\overline{\mathbf{C}}^{-2}\right)\right] + \sum_{i=1}^{n}\sigma_i\left(\lambda_i\right)J^{-2/3}\mathbf{DEV}\left[\mathbf{K}_i\right] + \sum_{i=1}^{n}\epsilon\left(\lambda_i\right)J^{-2/3}\mathbf{DEV}\left[\mathbf{K}_i\right] \quad (1)$$

where S is the second Piola–Kirchhoff stress, J is the Jacobian and κ is the bulk modulus; σ_i is the passive fiber stress–strain rule for the i^{th} (1 or 2) fiber population. Similarly, ϵ is the active fiber stress-strain rule, and DEV is the deviatoric projection operator, and $\mathbf{C}$ is the right-Cauchy deformation. The dispersed fourth invariant is:

$$\lambda_i^2 = tr\left[\mathbf{K}\overline{\mathbf{C}}\right] \quad (2)$$

where $\overline{\mathbf{C}}$ is the isochoric part of the right Cauchy deformation. Note that, λ is not a stretch in a classical sense, as $\mathbf{K}$ embodies the concept of dispersion. $\mathbf{K}$ is called the dispersion tensor or anisotropy tensor and is given in global coordinates. The passive (σ) and active (ϵ) fiber models are defined in the fiber coordinate system. In effect, $\mathbf{K}$ rotates and weights these 1D models, such that they are both three-dimensional and in the Cartesian frame.

In the case where, the splay parameters described in [2] are specified, $\mathbf{K}$ is given by:

$$\mathbf{K}_i = \mathbf{Q}_i k_i \mathbf{Q}_i^T \quad (3)$$

$$\mathbf{K_i} = \mathbf{Q}_i\begin{bmatrix} \frac{1}{2}\left(1+e^{-2\varsigma_i^2}\right) & 0 & 0 \\ 0 & \frac{f_i}{2}\left(1-e^{-2\varsigma_i^2}\right) & 0 \\ 0 & 0 & \frac{1-f_i}{2}\left(1-e^{-2\varsigma_i^2}\right) \end{bmatrix}\mathbf{Q}_i^T \quad (4)$$

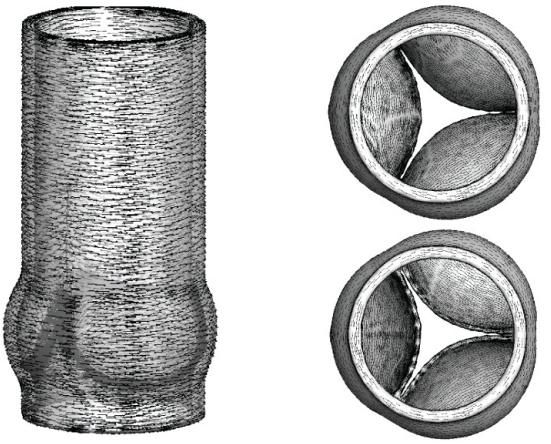

Figure 2: Computation of valvular collagen orientation based on notions of fiber synthesis.

where Q_i is the transformation tensor that rotates k_i from local coordinates to global Cartesian coordinates. In this case

However, in the case where diffusion tensor data is available, $\mathbf{K}$ is given by:

$$\mathbf{K}_i = \mathbf{Q^T}_i k_i \mathbf{Q}_i \tag{5}$$

$$\mathbf{K_i} = \mathbf{Q^T}_i \begin{bmatrix} \chi_1 & 0 & 0 \\ 0 & \chi_2 & 0 \\ 0 & 0 & \chi_3 \end{bmatrix} \mathbf{Q}_i, \tag{6}$$

where the χ are the DTI eigenvalues. Note that in this case the transformation goes the other way since the χ values are given in a global not local coordinate system.

These developments are important since they enable, for example in the case of the mitral valve, a single unified approach to modeling valve leaflets, chordae, papillary muscles and myocardium. They also enable modeling the recently discovered active behavior of valvular tissue.

3 3D FIBER MAPPING AND COMPUTATION

While the above formulation enables the direct incorporation of DTI data (or histology data), such data are unfortunately unavailable for valve leaflets, chordae which are finer then current DTI resolution.

To initialize these regions, we have derived a geometric result (Figure 2) which has its roots in an understanding of collagen synthesis and valvular mechanics. The gist of the method is that we have some certainty with respect to some areas of alignment. For example, we know that the fiber orientation is mostly aligned with the axis of the chordae, and the free edges of the leaflets. In addition, we know that the fiber field to be mechanically optimal must be slowly varying.

Let Ω be the volume over which fiber orientations need be determined, and S be the set of seed points where the fiber directions $\hat{\mathbf{d}}$ are known. We solve Laplace's equation for the 3x3 matrix $\mathbf{M}$ over Ω with Dirichlet boundary data constructed from $\hat{\mathbf{d}}$:

$$\begin{aligned} \nabla^2 \mathbf{M}(\mathbf{x}) &= 0, \quad \mathbf{x} \in \Omega \setminus S \\ \mathbf{M}(\mathbf{x}) &= \hat{\mathbf{d}}\hat{\mathbf{d}}^T, \quad \mathbf{x} \in S. \end{aligned}$$

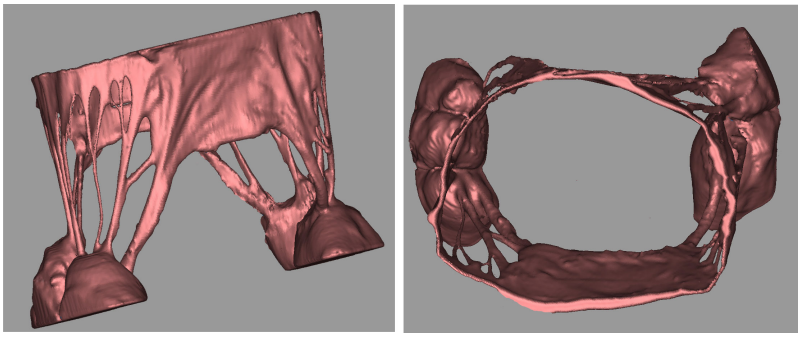

Figure 3: Segmented imaging-based mitral valve: lateral view (left) and ventricular view (right).

The solution $\mathbf{M}(\mathbf{x})$ over $\Omega \setminus S$ is then decomposed into an eigenvalue decomposition:

$$\mathbf{M} = \mathbf{E} \begin{pmatrix} \lambda_1 & 0 & 0 \\ 0 & \lambda_2 & 0 \\ 0 & 0 & \lambda_3 \end{pmatrix} \mathbf{E}^T, \tag{7}$$

with $\lambda_1 \geq \lambda_2 \geq \lambda_3 \geq 0$. The first (orthonormal) column vector $\mathbf{e}_1$ in E is taken to be the fiber direction at each point $\mathbf{x}$ in $\Omega \setminus S$.

For completeness, it should be mentioned that the mapped fiber direction is a mean fiber direction. Mesh segmentation algorithms must be applied to differentiate ontologies corresponding to 'vessel', 'leaflet' or 'chordae' to correctly assign material behavior to each region.

4 SEMI-AUTOMATIC SEGMENTATION OF COMPLEX VALVULAR GEOMETRIES

We have developed an adaptive semi-automated segmentation approach that faithfully captures the complexities of valvular geometry while preserving correct topology. Figure 3 illustrates this approach applied to the mitral valve.

5 CONCLUSIONS

Imaging-based analysis of cardiac valve presents some formidable challenges. We have present some of our recent developments in LS-DYNA to meet these challenges.

REFERENCES

[1] DR-Einstein, F Del Pin, K Kunzelman, J Xiangmin, AP Kuprat, JP Carson, JM Guccione, and MB Ratcliffe. Fluid-Structure Interactions of the Mitral Valve and Left Heart: Comprehensive Strategies, Past, Present and Future, *Com. Numer. Meth. Eng.* 26, 348-380, 2010.

[2] AD-Freed, DR-Einstein, I-Vesely. Invariant formulation for dispersed transverse isotropy in aortic heart valves: an efficient means for modeling fiber splay. *Biomech Model Mechanobiol*. 4, 100-17, 2005.

2nd International Conference on Mathematical and Computational Biomedical Engineering – CMBE2011
March 30 – April 1, 2011, Washington D.C., USA
P. Nithiarasu and R. Löhner (eds)

Optimal Unloaded Leaflet Shape for the Ovine Pulmonary Valve Single Leaflet Replacement Surgery

Rong Fan[1], Christopher M. Hobson[1], Ahmed Bayoumi[3], John E. Mayer[3], William R. Wagner[2], Michael S. Sacks[1,*]
[1]Department of Bioengineering and the McGowan Institute for Regenerative Medicine
[2]Departments of Surgery, Bioengineering, and Chemical Engineering
University of Pittsburgh, Pittsburgh, PA United States
[3]Department of Cardiac Surgery and Children's Hospital of Boston
Harvard Medical School, Boston, MA United States
*Email: msacks@pitt.edu

SUMMARY

Pulmonary valve (PV) replacement surgery is one treatment option for infants born with congenital pulmonary valve defects. The unloaded shape of leaflet for replacement is essential to the normal function of PV after replacement surgery. In this study, an approach for optimal leaflet shape design based on finite element (FE) simulation of tissue engineered pulmonary valve (TEPV) is presented. The mechanical properties of the material for leaflet replacement are measured by biaxial tension testing and flexural testing. The material is modelled as transversely isotropic hyperelastic material using generalized Fung-type constitutive model for FE simulation. The optimal shape of leaflet is determined by minimizing the error between the deformed leaflet shapes obtained from FE simulation of TEPV and microCT scan of a native ovine PV. This study aims to provide a guide on designing the shape of leaflet for PV replacement surgery.

Key Words: *Tissue engineering, constitutive modeling, finite element, biomechanics.*

1. INTRODUCTION

The pulmonary valve (PV) is located between the right ventricle and pulmonary artery. The normal pulmonary valve has three leaflets. The three leaflets open to permit the blood to flow into the pulmonary artery during ventricular systole, and close to prevent the blood backflow into the right ventricle at the end of systole. The movement of the three leaflets is critical to the function of the pulmonary valve. PV replacement surgery is one treatment option for infants born with pulmonary valve defects. Tissue engineered pulmonary valve (TEPV) is one approach that has the potential to serve as a replacement pediatric heart valve with the potential for somatic growth. In TEPV development, single leaflet replacements can assist in developing candidate biomaterials and modelling their responses to in-vivo function. However, the unloaded shape of leaflet is usually determined by experience, which may result in abnormal valve function due to incomplete coaptation of leaflets. The mechanical response of PV leaflet under transvalvular pressure is determined mainly by several key factors: mechanical properties of material, leaflet shape and thickness. Electrospun poly (ester urethane) ureas (ES-PEUU) biomaterials exhibit mechanical properties similar to the native PV material [1]. In this work we present an approach to determine the optimal leaflet shape utilizing a single sheet of ES-PEUU for single leaflet replacement surgery via finite element (FE) simulation. The material properties of ES-PEUU

scaffold for leaflet replacement are obtained from biaxial in-plane tension test and three-point bending flexural test. By perturbing the initial shape of leaflet and simulating its quasi-static deformation under PV diastolic loading, the optimal shape of unloaded leaflet is determined by comparing the deformed shape of leaflet obtained from simulation of TEPV with the one from microCT scan of a native ovine PV.

2. METHODS

2.1 Mechanical testing. Both biaxial in-plane tension testing and three-point bending flexural testing are conducted to measure the mechanical properties of ES-PEUU. For details of the testing procedure see our previous work in [2, 3].

2.2 Material constitutive modelling. Generalized Fung-type hyperelastic model [4] is utilized in this study. The strain energy U is defined as:

$$U = \frac{c}{2}(\exp(Q) - 1)$$

where $Q = E_{ij}a_{ijkl}E_{kl}$ with c and a_{ijkl} being material parameters and E_{ij} being the Green-Lagrange strain tensor. The second Piola-Kirchhoff stress tensor S_{ij} is defined as:

$$S_{ij} = \frac{\partial U}{\partial E_{ij}}$$

2.3 Material parameter estimation. Both biaxial testing and flexural testing data are used to estimate the material parameter c and a_{ijkl}. For fully anisotropic material, there are 21 independent components a_{ijkl}. In our study, we assume the material is transversely isotropic and the number of independent components is reduced to 5. For the case of plane stress, the stress-strain relationship can be written as:

$$\begin{Bmatrix} S_{11} \\ S_{22} \\ S_{12} \end{Bmatrix} = c * exp(Q) \begin{bmatrix} a_{1111} - \frac{a_{1122}^2}{a_{2222}} & a_{1122} - \frac{a_{1122} * a_{2233}}{a_{2222}} & 0 \\ a_{1122} - \frac{a_{1122} * a_{2233}}{a_{2222}} & a_{2222} - \frac{a_{2233}^2}{a_{2222}} & 0 \\ 0 & 0 & 2a_{1212} \end{bmatrix} \begin{Bmatrix} E_{11} \\ E_{22} \\ E_{12} \end{Bmatrix}$$

$$= c * exp(Q) \begin{bmatrix} b_{1111} & b_{1122} & 0 \\ b_{1122} & b_{2222} & 0 \\ 0 & 0 & 2b_{1212} \end{bmatrix} \begin{Bmatrix} E_{11} \\ E_{22} \\ E_{12} \end{Bmatrix}$$

By fitting biaxial tension experimental data, we can obtain the material parameter c and 4 independent coefficients of b_{ijkl}. The five independent components of a_{ijkl} can be obtained by FE simulation to match the bending moment-curvature data from three-point bending testing.

2.4 Leaflet geometry. The same design parameters used for aortic leaflet design are used in this study since the shape of pulmonary valve is similar to aortic valve. For a normal three-leaflet pulmonary valve, the geometry model of a single leaflet can be constructed in terms of five parameters [5] as shown in Figure 1.

2.5 Finite element modelling. To simulate the quasi-static deformation of ES-PEUU leaflet under 18 mmHg transvalvular pressure, the commercial finite element software package ABAQUS (Dassault Systèmes Simulia Corporation, Providence, RI) is used. Assuming that the three-leaflet pulmonary valve is perfect symmetric, only one leaflet for replacement is modelled. The contact of the leaflet with the other two leaflets is assumed to be rigid. Except the free edge of leaflet, fixed boundary conditions are imposed on all the other leaflet edges. A uniform

pressure is applied on the leaflet surface and remains vertical to the surface as the leaflet deforms. The ES-PEUU material is modelled as transversely isotropic hyperelastic material using built-in generalized Fung-type form in ABAQUS/Explicit.

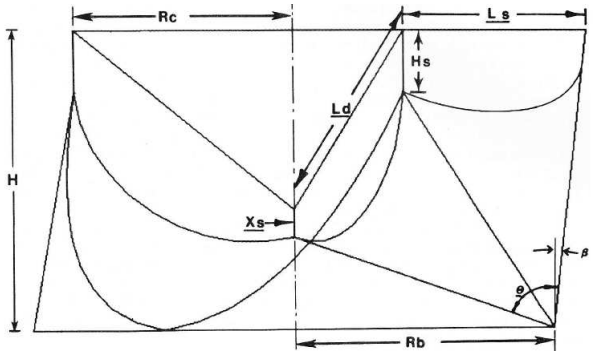

Rb: radius of base
Rc: radius of commissures
H: leaflet height
Hs: height of commissures
β: angle of open leaflet

Figure 1: Design parameters of open leaflet model [5].

2.6 Error estimation. The deformed shape of ES-PEUU leaflet from FE simulation is compared with the shape of native leaflet obtained from microCT scan. The error *E* between the two shapes is defined to be

$$E(S_1, S_2) = \frac{1}{|S_1|}\int_{S_1} d(p, S_2)ds$$

where S_1 is the surface of leaflet from FE simulation, S_2 is the surface of leaflet from microCT scan, and $d(p, S_2)$ is the distance between a point p in S_1 and the surface S_2. This method has been implemented into the software Metro [6].

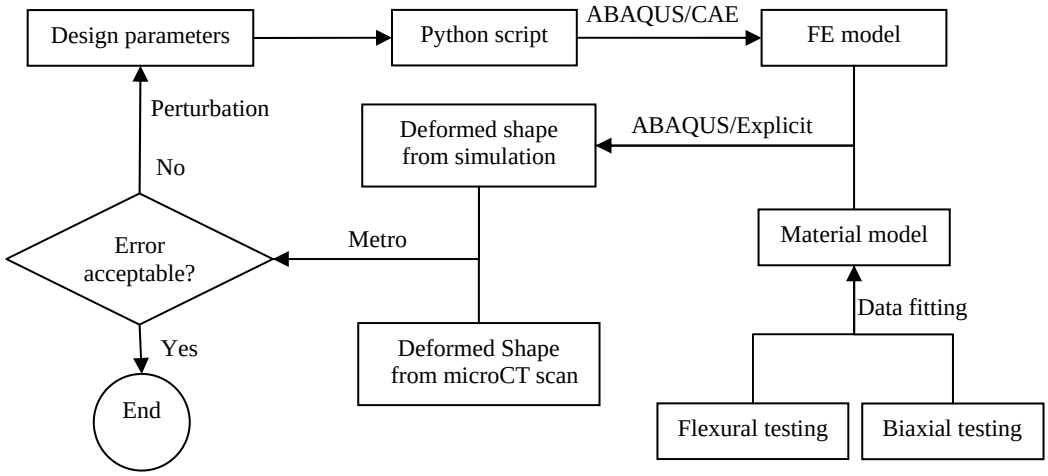

Figure 2: Design flowchart for optimal leaflet shape.

2.7 Design flowchart. A process flow for optimal leaflet shape was developed (Figure 2). Starting with the initial design parameters that describe the shape of open leaflet, these parameters were then passed to a Python script. The Python script is used in ABAQUS/CAE scripting interface to create the finite element model of leaflet automatically. Once the finite element model is available, the quasi-static deformation of leaflet under transvalvular pressure is simulated using ABAQUS/Explicit. With Metro, the deformed shape of leaflet from simulation is then compared with the deformed shape from microCT scan. If the error between the two shapes is not acceptable, we perturb the design parameters of the initial shape of leaflet and repeat the above steps until the optimal shape is obtained.

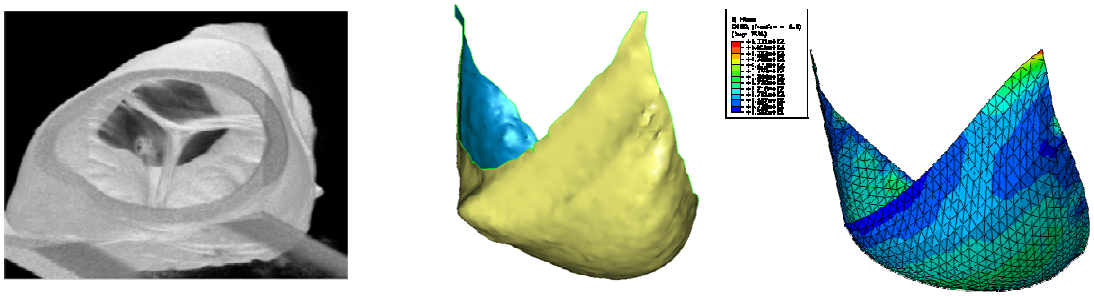

(a) MicroCT image of pulmonary valve

(b) Segmented image of single leaflet

(c) Von-Mises stress contour of leaflet

Figure 3: Leaflet images from microCT scan and FE simulation.

2.8 Results. High resolution image of a native ovine pulmonary valve and the segmented image of single leaflet are shown in Figure 3(a) and 3(b), respectively. The deformed shape and Von-Mises stress contour of TEPV leaflet under 18 mmHg transvalvular pressure are shown in Figure 3(c). It can be seen that the deformed shape of leaflet from FE simulation is very close to the shape of native leaflet obtained from microCT scan. In the present study, the simulation results are obtained from ABAQUS/Explicit, which uses an explicit time integration method. The total kinetic energy of the whole FE model is less than 1% of total strain energy, which means that the deformation can be considered to be quasi-static and the numerical results are acceptable.

3. CONCLUSIONS

A design approach of TEPV leaflet shape for single leaflet replacement surgery has been developed by incorporating experimental testing with FE simulation. The optimal shape of TEPV leaflet is obtained. This approach can guide the design of the leaflet shape for PV replacement surgery. In future studies, structural constitutive model [1] will be implemented and applied to analyze the mechanical behaviour of native and engineered soft tissues.

REFERENCES

1. Courtney, T., et al., *Design and analysis of tissue engineering scaffolds that mimic soft tissue mechanical anisotropy.* Biomaterials, 2006. **27**(19): p. 3631-8.
2. Sacks, M.S., *A method for planar biaxial testing that includes in-plane shear.* Journal of Biomechanical Engineering, 1999. **121**: p. 551-555.
3. Gloeckner, D.C., K.L. Billiar, and M.S. Sacks, *Effects of mechanical fatigue on the bending properties of the porcine bioprosthetic heart valve.* Asaio J, 1999. **45**(1): p. 59-63.
4. Fung, Y.C., *Biomechanics: Mechanical Properties of Living Tissues*. 2nd ed. 1993, New York: Springer Verlag. 568.
5. Thubrikar, M., *The Aortic Valve*. 1990, Boca Raton: CRC. 221.
6. Cignoni, P., C. Rocchini, and R. Scopigno, *Metro: Measuring error on simplified surfaces.* Computer Graphics Forum, 1998. **17**(2): p. 167-174.

2nd International Conference on Mathematical and Computational Biomedical Engineering – CMBE2011
March 30 – April 1, 2011, Washington D.C., USA
P. Nithiarasu and R. Löhner (eds)

Breast Linear and Nonlinear Real-time Ultrasound Elastography

Abbas Samani[1,2,3], Shadi Shavakh[2], Mohammadhosein Amooshahi[2] and Seyed Reza Mousavi[2]

[1]Dept. Medical Biophysics, University of Western Ontario, London, Ontario, Canada
[2]Dept. Electrical & Computer Eng., University of Western Ontario, London, ON, Canada
[3]Robarts Research Institute, London, Ontario, Canada

SUMMARY

Two breast elastography techniques are presented. One technique uses tissue displacement and surface force data to reconstruct the Young's modulus of tumor and normal tissues. The other uses tissue displacement data to reconstruct the tissue hyperelastic parameters. These techniques employ a constrained reconstruction approach that lead to an iterative algorithm. Each iteration involves a finite element analysis for tissue stress calculation. To speed up the reconstruction, a very fast statistical finite element technique was incorporated in the algorithm paving the way for real-time reconstruction. *In silico* and breast tissue mimicking phantoms indicated that real-time and reasonably accurate reconstruction of the tissue absolute Young's modulus and relative hyperelastic properties is possible.

Key Words: *breast cancer, elastography, real-time, hyperelasticity, reconstruction algorithm*

1. INTRODUCTION

Among cancer related deaths, breast cancer is ranked second worldwide. During lifetime 1 out of each 8 women develop breast cancer. In the USA it is estimated that ~40,000 women will die from breast cancer in 2010 [1]. Early detection of breast cancer is key to its successful treatment. Breast cancer screening or diagnostic techniques such as manual palpation, X-ray mammography, ultrasound (US) and MRI have known weaknesses. These include low sensitivity and specificity, ionizing radiation or high cost [2]. Elastography is an alternative imaging technique developed with aim of addressing some of the these drawbacks [3,4,5]. Elastography reconstruction techniques can be formulated as inverse problems. Depending on the accuracy of modeling tissue stress distribution inverse problems may lead to straight forward or complex computational problems. In strain imaging the stress is assumed to be uniform leading to very fast estimation of the relative Young's modulus (YM). While suitable for real-time imaging, this technique suffers from producing significant artifacts [3]. Other techniques employ continuum mechanics equations to develop inverse problem formulations for image reconstruction. While they provide accurate images of relative elastic modulus, the computation involved in their reconstruction process is highly demanding. Such techniques are, therefore, not suitable for real-time applications such as breast needle biopsy guidance. To address the shortcomings of these techniques, we developed a highly accurate and yet fast breast US elastography method [6]. This method uses tissue displacement and surface force data to image the absolute (YM) of breast tumour in real-time fashion.

Under small deformation breast tissues exhibit linear response; hence elastography reconstruction algorithms based on linear elasticity are sufficient. If breast tissue stimulation involves large compression, such algorithms become less reliable as the tissue deviates from linear elasticity. In such cases, more accurate reconstruction techniques can be developed based on inverse problem formulations with tissue hyperelastic models as their forward models. In such techniques hyperelastic parameters can be reconstructed. There are several advantages to this approach including achieving high signal-to-noise ratio (SNR), reconstructing hyperelastic parameters which are independent of the amount of the compression, and obtaining more valuable diagnostic information [7]. In this article, we present a novel technique to reconstruct breast tissue hyperelastic parameters. Here, we use the Veronda-Westman hyperelastic model which has been recently used by other researchers [8]. Unlike other nonlinear elastography techniques, this technique does not involve optimization or regularization, hence it is more efficient.

The presented techniques involve iterative linear and nonlinear finite element (FE) analysis, respectively. To accelerate the parameter reconstruction we employed a statistical FE method [9]. For the linear elastography technique multi-focal tumor cases are also investigated. *In silico* and tissue mimicking phantom studies have demonstrated the feasibility of accurate absolute YM or hyperelastic parameter reconstruction in real-time fashion.

2. Methods and Results

2. 1. Linear Elastography Methods

The linear elastography system is capable of reconstructing the absolute YM. This system involves a Sonix RP ultrasound machine (Ultrasonix Medical Corporation, BC, Canada) for B-mode and axial strain image acquisition. It also involves a surface force data acquisition system attached to the ultrasound probe that facilitates imaging the absolute YM. This investigation involves *in silico* breast phantoms with single or multiple inclusions simulating multi-focal breast cancers. In US elastography the FOV is limited to a portion of the breast. Part of this research was dedicated to a numerical study to assess the impact of using approximated breast shape in FE modeling. In this numerical study a trapezoidal area was used to construct an approximate breast FE model. A gelatin-agar phantom with a single stiff inclusion mimicking breast cancer was also studied. The reconstruction algorithm follows the constrained elastography concept proposed by [10]. This algorithm takes advantage of the US image information to determine the tumor area. The algorithm assumes that the YM variations within the tumor and normal tissue areas are insignificant. This leads to an iterative YM reconstruction procedure which involves YM updating using Hooke's law followed by stress field calculation. While FEM is highly accurate for stress calculation, its computational procedure is highly involved; hence it precludes real-time YM reconstruction. To make real-time reconstruction possible, we developed a statistical finite element method (SFEM) which is capable of stress estimation in a split of a second [9]. This method establishes a relationship between shape space of an organ (e.g. breast) while undergoing a given loading (e.g. US probe compression) with its corresponding stress field. The premise of this method is that, under a given loading, there is a high degree of similarity between the organ's shape space and its stress field. The SFEM process involves two steps. The first is conducting FE analysis of a large number of 2D block-shaped or trapezoidal numerical phantoms with different tumor geometry, location, and randomly generated YM values of background and tumor. These phantoms undergo linear loading pertaining to US probe pressure. In this step we establish a relationship between shape space and FE space by using an optimized Neural Network (NN). In the second step, we use the NN to find the stress field for the actual phantom by inputting its shape parameters. By combining the computed stress field with the strain field acquired by the US system via Hooke's law, we are able to reconstruct the inclusion and background tissue's absolute YM.

2. 2. Nonlinear Elastography Methods

Similar to the linear system, this nonlinear elastography system also involves a Sonix RP ultrasound machine for B-mode and strain image acquisition. As a typical elastography technique, the core of this technique is its inverse problem of tissue hyperelastic parameters reconstruction. The inverse problem in this technique is based on the constitutive relationship of incompressible hyperelastic materials, which has the following general form:

$$S = \frac{2}{J} DEV\left[\left(\frac{\partial U}{\partial \bar{I}_1} + \frac{\bar{I}_1 \partial U}{\partial \bar{I}_2}\right)\bar{B} - \frac{\partial U}{\partial \bar{I}_2}\overline{BB}\right] \qquad (1)$$

In this equation S is the deviatoric stress, DEV indicates the deviatoric part, and U is a strain energy function chosen by the user. $\bar{I}_1$, $\bar{I}_2$, $\bar{I}_3$, $\bar{B}$ and $\overline{BB}$ are functions of displacements, hence they can be calculated using the acquired displacement data. In this work, the Veronda-Westman strain energy function is employed which uses three parameters (C_1, C_2 and C_3) to describe tissue nonlinear behavior:

$$U = C_1\left[e^{C_3(\bar{I}_1 - 3)} - 1\right] + C_2(\bar{I}_2 - 3) \qquad (2)$$

To formulate the inverse equations the Veronda-Westman function in Eqn. (2) is substituted in Eqn. (1) leading to:

$$S = \frac{2}{J} DEV\left[\left(C_1 C_3 e^{(C_3(\bar{I}_1 - 3))} - C_2\bar{I}_1\right)\bar{B} + C_2\overline{BB}\right] \qquad (3)$$

Since this equation is nonlinear in terms of C_1 and C_3, a simple matrix-based equation system inversion cannot be employed. One possible way to determine the C hyperelatic parameters is via nonlinear optimization. Such approach is computational time demanding and prone to issues such as lack of a unique solution. As an alternate approach, we developed a novel technique to determine the hyperelastic parameters. The main idea of this technique is to use a mathematical approximation to the exponential term of the Veronda-Westman energy function. For this purpose MATLAB's *ployfit* function approximation was used, which is the closest Polynomial approximation using the Least Squared errors measure. With this approximation, a change of variables scheme was used to change the system of equations into an equivalent linear system of equations. Hence, this linear system was solved for the new variables. Finally, the unknown C_1, C_2 and C_3 parameters are determined using the calculated new variables. The whole procedure consists of three steps. In each step, one of the unknown parameters of C_2, C_3 and C_1 is reconstructed. Similar to linear elastography, the iterative constrained reconstruction concept was used. Again, each iteration involves updating the C_1, C_2 and C_3 hyperelastic parameter values for each tissue region by averaging the values over its volume followed by stress calculation. Convergence occurs when the difference of tumours' hyperelastic parameters values obtained in two consecutive iterations is less than a preset value. To accelerate the reconstruction process, the SFEM technique was used to analyze the stress of the nonlinear model. Note that Eqn. (3) involves both of the two displacements components in 2D problems. As the Sonix RP system provides the axial displacements only, we developed an Optical Flow (OF) based technique that incorporates the acquired axial displacements into the OF governing equations. This research involves *in silico* and a Poly Vinyl Alcohol (PVA) breast phantoms with a single inclusion. To achieve tissue nonlinear behavior, the PVA phantom layers were subjected to variable freeze-thaw procedures. The hyperelastic parameters of each tissue mimicking layer in the phantom was measured independently using a uniaxial test.

2. 3. Linear Elastography Results

The proposed method was evaluated using 1000 FE numerical phantom models with two inclusions. The first 800 generated FE models were fed into the NN for training. To tune up the neural network, 100 models from the generated dataset were used as a validation set during training. The remaining 100 generated dataset were used to test the NN function. YM reconstruction errors are given in Table 1. This reconstruction took only 0.36 sec on a regular desktop computer with 2.66 GHz Intel CPU. These results indicate that using the proposed method for developing a highly accurate real-time US elastography of multi-focal breast cancer is feasible.

Table 1: Percentage average errors of YM reconstruction

Geometry / Tissue type	Phantoms with single tumour	Phantoms with two tumours in two sections	Phantoms with two tumours in one section
Background	0.37 ± 0.23%	0.04 ± 0.025%	1.46 ± 0.09%
Tumour	4.16 ± 1.58%	5.31 ± 1.96%	3.73 ±2 .7%

Simulation with the approximate trapezoidal breast model led to a maximum tumor YM reconstruction of up to 20%. YM reconstruction of the gelatine-agar phantom indicated errors of less than 6%.

2. 4. Nonlinear Elastography Results

True values of the PVA phantom layers, which are obtained by uniaxial testing, are given in Table 2. This table includes the corresponding reconstruction results. These results indicate that fast hyeprelatic parameter tissue reconstruction with high accuracy is feasible.

Table 2. True Parameters and Constructed Parameters (C_1 and C_2 are in kPa , C_3 is unitless)

Parameter	Adipose	Fibroglandular	Tumor	Reconstruc -ted value	Error (%)
C_1	4.3	6.6	9.1	9.9	8.8
C_2	-0.6	-3.0	-1.7	-1.9	11.8
C_3	1.56	2.00	2.59	2.76	6.6

3. CONCLUSIONS

The obtained results are promising and indicate that the developed system is capable of conducting real-time linear and nonlinear elastography with sufficient accuracy. Errors due to US limited FOV in breast elastography may lead to significant errors of up to 20%. This shortcoming can be addressed by incorporating a surface shape measurement module into the elastography system.

REFERENCES

[1] American Cancer Society: http://www.cancer.org/
[2] Zhi, H, *et al*, 2007, J Ultrasound Med; **26**:807–815.
[3] Ophir, J., *et al* 1991, Ultrason. Imag., vol. **13**, pp. 111–134.
[4] Doyley, M, *et al*, 2001, Ultrasound Med. Biol., vol. **27**, no. 10, pp. 1347–1357.
[5] Konig, K., *et al*, 2005, J Urol; **174**:115–117.
[6] Karimi, H., *et al*, 2009, "A real-time method for breast cancer diagnosis using optical flow," SPIE Medical Imaging.
[7] Sinkus, R., *et al*, 2002, Proceedings of the 10th Annual Meeting of ISMRM.
[8] Gokhale, N. H., *et al*, *Inverse Problems*, vol. 24, 2008.
[9] Khalaji, I., *et al*, 2008, 30th Annual International IEEE EMBS Conf., Vancouver, BC, Canada.
[10] Samani, A., *et al*, IEEE Trans. Med. Imag., vol. **20**, no. 9, pp. 877-885, 2001.

2nd International Conference on Mathematical and Computational Biomedical Engineering – CMBE2011
March 30 – April 1, 2011, Washington D.C., USA
P. Nithiarasu and R. Löhner (eds)

AN ERROR IN CONSTITUTIVE EQUATIONS APPROACH FOR ELASTICITY IMAGING

Wilkins Aquino*and Marc Bonnet**
*School of Civil and Environmental Engineering, Cornell University, Ithaca, NY, wa27@cornell.edu
** Laboratoire de Mécanique des Solides (UMR CNRS 7649), Ecole Polytechnique, 91128 Palaiseau Cedex, France.
bonnet@lms.polytechnique.fr

SUMMARY

In this work, we present an inverse problem methodology based on an error in constitutive equations (ECE) for the identification of elastic properties. The basic premise in the ECE approach is that, given an over-determined set of boundary or internal data (e.g. displacements and tractions), and a set of kinematically admissible displacements and statically admissible stresses, a cost functional is defined based on the error in the constitutive equations that connect these sets of stresses and strains. This cost functional has been shown to be convex for elliptic problems, and presents significant advantages for elasticity imaging problems. This work demonstrates that ECE approaches can yield faster convergence and better accuracy than approaches based on the minimization of the L2 norm.

Key Words: *Error in constitutive equations, elasticity imaging, energy functionals, inverse problems.*

1. INTRODUCTION

The mechanical properties of soft biological tissue are closely related to pathology. Thus, the identification of elastic and viscoelastic material properties has sown significant promise for disease diagnosis [1,2]. For instance, elastic and viscoelastic properties can significantly increase specificity in differentiating malignant and benign tumors [1]. Yet, the direct measurement of material properties in-vivo is very difficult, if not impossible. However, indirect measurements in the form of solutions to inverse problems have been promising. In this work, we present an inverse problem methodology based on an error in constitutive equations (ECE) for the identification of elastic properties from static displacement fields.

2. MAIN BODY

The basic premise in the ECE approach is that, given an over-determined set of boundary or internal data (e.g. displacements and tractions), and a set of kinematically admissible displacements and statically admissible stresses, a cost functional is defined based on the error in the constitutive equations that connect these sets of stresses and strains. This cost functional has the important property of being zero for the exact constitutive equations and strictly positive and otherwise. For example, ECE-based identification strategies for transient and materially nonlinear problems have been recently proposed in [3], while other aspects of ECE are surveyed in [4].

Figure 1 shows the results of an inverse reconstruction of the shear modulus of hard inclusions embedded in a soft matrix. The figures contrast the results obtained using a conventional L2

minimization using a LBFGS algorithm versus the results obtained with the proposed ECE approach.

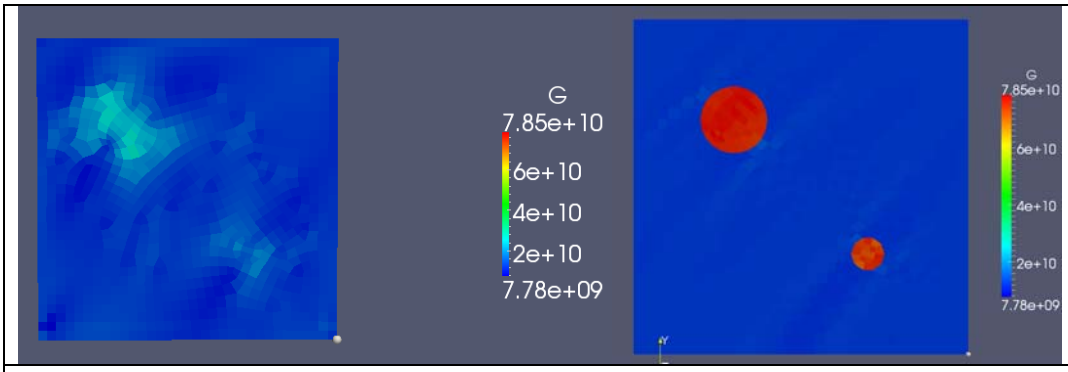

Figure 1. Comparison between L2 minimization and ECE method for the reconstruction of the shear modulus distribution from a static test. Left picture shows the solution obtained using the adjoint method and a LBFGS algorithm. The right picture shows the results obtained using ECE. Both algorithms were run for 20 iterations.

3. CONCLUSIONS

Our results demonstrate that cost functionals based on ECE present several advantages over conventional L2 functionals for inverse problems that involve the identification of distributed material parameters. Some of these advantages include faster convergence and improved accuracy over their L2 counterpart.

REFERENCES

[1] Sinkus, R., Siegmann, K., Xydeas, T., Tanter, M., Claussen, C., and Fink, M., MR elastography of breast lesions: Understanding the solid/liquid duality can improve the specificity of contrast-enhanced MR mammography. Magnetic Resonance in Medicine, Vol. 58, No. 6, 2007, pp. 1135-1144

[2] Sridhar, M., Liu, J., and Insana, M.F., Viscoelasticity imaging using ultrasound: parameters and error analysis. Physics in Medicine and Biology, Vol. 52, No. 9, 2007, pp. 2425-2443.

[3] Nguyen, H-M., Allix, O., Feissel, P., A robust identification strategy for rate-dependent models in dynamics. Inverse Problems, 2008, 24:R1-R50.

[4] Bonnet, M., Constantinescu, A., Inverse problems in elasticity. Inverse Problems, 2005, 21:R1-R50 (topical review article).

2nd International Conference on Mathematical and Computational Biomedical Engineering - CMBE2011
March 30 - April 1, 2011, Washington D.C, USA
P. Nithiarasu and R. Löhner (Eds.)

CORRELATION OF BIOMECHANICS TO TISSUE REACTION IN AORTIC ANEURYSMS ASSESSED BY FEM AND FDG-PET-CT

M.W. Gee*, W.A. Wall*, A. Maier*, C. Reeps and M. Essler*****
*Institute for Comp. Mechanics, TU Munich, Germany, [gee,wall]@lnm.mw.tum.de
**Clinic for Vascular Surgery, Klinikum rechts der Isar, TU Munich, Germany
***Clinic for Nuclear Medicine, Klinikum rechts der Isar, TU Munich, Germany

SUMMARY

It is a widely accepted hypothesis that mechanobiological transduction plays a central role in pathogenesis of aortic aneurysm (AA). While stresses and strains acting in AA wall can be assessed by computational finite element analyses (FEM) [1,2], assessment of material properties and their spatial distribution involves inverse analysis methods and/or advanced medical imaging techniques. Here, we present an advanced forward computational model of aortic aneurysm based on statistically representative material properties and combine results with [18F]flourodeoxyglucose positron emission tomography/CT (FDG-PET-CT). FDG-PET-CT provides a quantitative assesment of metabolic activity and therefore the hyphothesis of mechanobiological interaction can be tested. It has been reported that glycolytic activity in AA wall non-invasively assessed by FDG-PET-CT is associated with increased proteolytic activity, structure-protein-degradation, AA progression and consequently AA wall instability as well as rupture risk [3]. FEM stresses and strains and FDG-PET-CT were compared *qualitatively* by our research group in an individual AA patient in [4] as well as by other groups in [6] and [7]. Here, the correlation of computational biomechanics with metabolic activity assessed by FDG-PET-CT is analyzed in a larger patient cohort (n=18) in a quantitative manner for the first time [5].

Key Words: *aortic aneurysm, mechanotransduction, flourodeoxyglucose.*

1 METHODS

FDG-PET-CT data sets of 18 AA patients with notably increased FDG uptake in AA wall were studied. For further analyses detailed 3-D geometry of each AA including thrombus was reconstructed from angio-CT in 3mm-slices. FEM analysis including thrombus material and considering a pre-stressed state of the imaged AA geometry was performed using non-linear material and geometrical model assumptions as described in [1]. Subsequently, wall stresses, strains and their distributions were obtained and visualized as exemplarily shown in Fig. 1 b) and c). Further, FDG-PET clouds were anatomically fitted, reduced to FDG activity in AA wall, mathematically processed (Gauss-filter, 85% Rank-order-filter) and superimposed to the 3-D AA geometry (Fig. 1a). For correlations of maximum FDG uptake with maximum stresses and strains from FEM analyses, the maximum standardized uptake value of FDG (SUVmax) was determined by conventional analyses. Additionally, spatial distribution of FDG-uptake of each AA was qualitatively and quantitatively correlated to wall stress and strain spatial distributions. Visual analyses were performed in anterior, posterior and left or right lateral views as shown in Fig. 1. For quantitative analyses the 33% of the AA wall with highest FDG uptake, highest wall stress and strain was

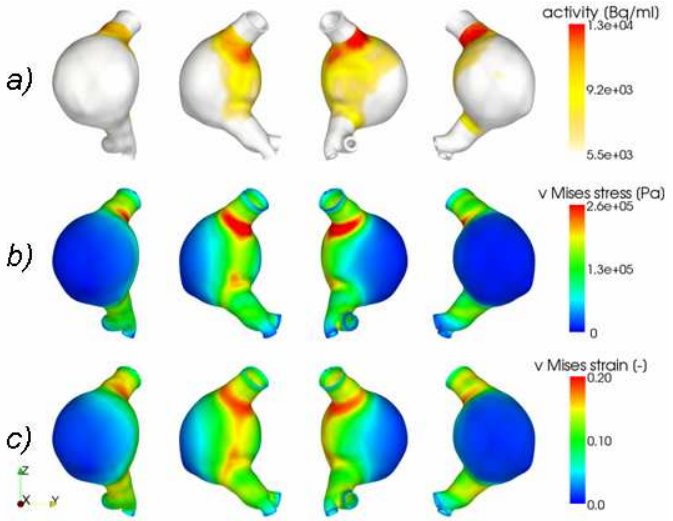

Figure 1: Abdominal AA in anterior, left lateral, posterior and right lateral view with high spatial correlation of a) regional metabolic activity (FDG-uptake; [Bq/ml]) and b) computed peak wall stress (von Mises stress; [kPa]) and c) strain distribution ([-]) in AA wall; Color indicates FDG-uptake (a), wall stress (b) and strain levels (c).

determined. Consecutively the overlap of these portions was quantified. A spatial overlap of 33% among such regions has to be considered as random for methodical reasons while higher or lower overlap were seen as indicative for correlation or miscorrelation, respectively.

2 RESULTS

SUVmax varied from $1.3 - 4.6$ (average SUVmax 3.3 ± 0.9) and average stress and strain were $38.2\,N/cm^2 \pm 13.7\,N/cm^2$ (range: $10.0 - 64.0\,N/cm^2$) and 0.22 ± 0.02 (range: $0.19 - 0.26$), respectively. Quantity of SUVmax was significantly correlated to PWS and maximum strain (SUVmax vs. PWS: $R2 = 0.60$, $p = 0.008$ and SUVmax vs. maximum strain: $R2 = 0.66$, $p = 0.004$; Fig. 2a) and b). In all but 3 AA, areas with increased FDG-uptake showed well and visible spatial correlation to areas with increased stresses and strains while areas with low stress and strain showed negligible FDG-uptake. Spatial overlap varied from 41% to 78% (average $56.3\% \pm 11$) without consideration of qualitative similarities such as shape [5].

3 DISCUSSION

Our results indicate that biomechanical stress or strain may be causative for regionally increased FDG-uptake and therefore inflammatory activity in AA wall. Thereby, inflammatory reaction is correlated quantitatively and spatially to levels of stress and strain respectively. These results strongly support the commonly accepted hypothesis that biomechanical conditions are highly relevant for pathogenesis and formation of AA in vivo. The biological and biochemical mechanisms leading to increased AA wall inflammation due to increased biomechanical stress and strain levels still have to be elucidated in detail. It can be hypothesized that cyclic stresses and strains exerted by blood pressure acting in AA wall may cause pro-inflammatory cytokine liberation by vascular smooth muscle cells in aortic wall media [8,9], followed by macrophage infiltration and therefore increased FDG-uptake. However, stress independent metabolic activity was found also

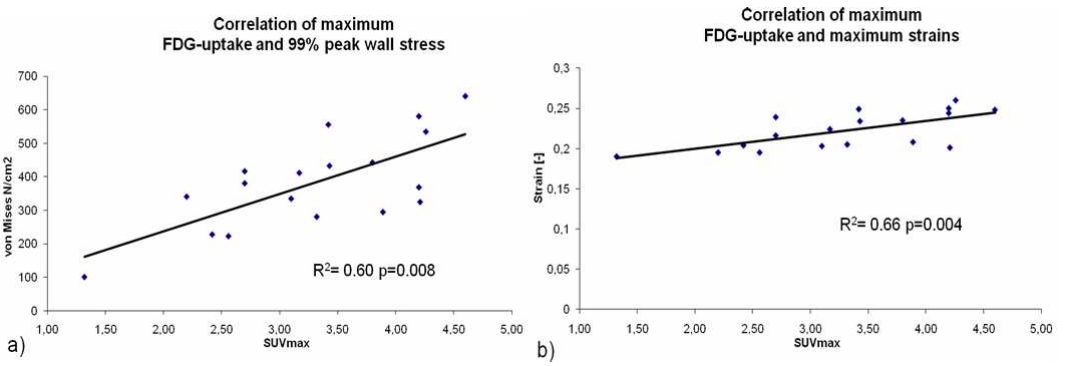

Figure 2: Quantitative correlation of SUVmax with corresponding peak wall stresses (a) and strains (b); R^2: Spearman's ρ correlation coefficient; SUVmax: maximum standardized uptake value of F18-Flourodeoxyglucose.

indicating additional autochthon inflammatory biological activity. Therefore, larger studies will be performed to confirm these results and to gain further insight in pathogenesis of AA.

REFERENCES

[1] Reeps, C., Gee, M.W., Maier, A., Gurdan, M., Wall, W.A., Eckstein, H.H. (2010): The impact of model assumptions on results of computational mechanics in abdominal aortic aneurysm, Journal of Vascular Surgery, 51, 679-688.

[2] Gee, M.W., Reeps, C., Eckstein, H.H., Wall, W.A. (2009): Prestressing in finite deformation abdominal aortic aneurysm simulation, Journal of Biomechanics, 42, 1732-1739

[3] Reeps C, Essler M, Pelisek J, Seidl S, Eckstein HH, Krause BJ. Increased 18F-fluorodeoxyglucose uptake in abdominal aortic aneurysms in positron emission/computed tomography is associated with inflammation, aortic wall instability, and acute symptoms. Journal of Vascular Surgery, 2008; 48(2):417-23.

[4] Reeps, C., Gee, M.W., Maier, A., Pelisek, J., Gurdan, M., Wall, W.A., Mariss, J., Eckstein, H.H., Essler, M. (2009): The glucose metabolism in the vessel wall correlates with mechanical instability and inflammatory changes in a patient with a growing aneurysm of the abdominal aorta, Circulation: Cardiovascular Imaging, 2, 507-509.

[5] Reeps, C., Maier, A., Gee, M.W., Baust, M., Zimmermann, A., Ockert, S., Pongratz, J., Navab, N., Wall, W.A., Eckstein, H.-H., Essler, M. (2010): Correlation of Biomechanics to Tissue Reaction in Aortic Aneurysm Assessed by Finite Elements and 18F-Fluordeoxyglucose-PET/CT, Circulation Cardiovascular Imaging, submitted.

[6] Xu X.Y., Borghi A., Nchimi A., Leung J., Gomez P., Cheng Z., Defraigne J.O., Sakalihasan N., High levels of 18F-FDG uptake in aortic aneurysm wall are associated with high wall stress. Eur J Vasc Endovasc Surg. 2010; 39:295-301.

[7] Truijers M., Kurvers H.A., Bredie S.J., Oyen W.J., Blankensteijn J.D. (2008) In vivo imaging of abdominal aortic aneurysms: increased FDG uptake suggests inflammation in the aneurysm wall. J Endovasc. Ther. 15(4):462-467.

[8] Guest T.M., Vlastos G., Alameddine F.M., Taylor W.R. Mechanoregulation of monocyte chemoattractant protein-1 expression in rat vascular smooth muscle cells. Antioxid Redox Signal. 2006, 8(9-10):1461-71.

[9] Birukov K.G. Cyclic stretch, reactive oxygen species and vascular remodeling. Antioxid Redox Signal. 2009. (published online ahead of print)

2nd International Conference on Mathematical and Computational Biomedical Engineering - CMBE2011
March 30 - April 1, 2011, Washington D.C, USA
P. Nithiarasu and R. Löhner (Eds.)

4D IMAGE-BASED CFD OF A COMPLIANT VESSEL

Eldad Haber*, Lucia Mirabella, Tiziano Passerini***, Marina Piccinelli*** and Alessandro Veneziani*****

*University of British Columbia, Vancouver, Canada, haber@math.ubc.ca
**WH Coulter Department of Biomechanical Engineering, GA Tech, Atlanta (GA) USA
lucia@bme.gatech.edu
***Department of Mathematics and Computer Science, Emory University, Atlanta (GA), USA
{tiziano,marina,ale}@mathcs.emory.edu

SUMMARY

In patient-specific simulations numerical modeling of the vascular structure and its interaction with the blood flow requires parameter identification difficult to accomplish and time consuming computational procedures. New imaging devices provide time sequences of the moving vessel of interest within a few heart beats. When one is interested only in the blood dynamics in the compliant vessel, a possible alternative to the full fluid-structure interaction simulation is to track the vessel displacement from the images and then to solve the fluid problem in the moving domain reconstructed accordingly. In this talk, we present an example of this image-based technique. We describe in detail the steps necessary for this approach (image acquisition and 3D geometric reconstruction, motion tracking, numerical simulation) and present some results for validating the proposed technique vs. a traditional fluid-structure interaction simulation in a carotid bifurcation. This approach dramatically reduces the CPU time since the dynamics of the structure is retrieved from the images instead of being numerically computed. Moving from this approach, solution of a suitable inverse problem can then be carried out for estimating the structural properties of the tissue at hand. This work moves into the direction of a strong integration between data (images/measures) and simulations that is likely to introduce a significant improvement in the reliability of cardiovascular numerical mathematics.

Key Words: *image-based numerical hemodynamics, fluid-structure interaction, image registration, inverse problems.*

1 INTRODUCTION

An emerging research line in Cardiovascular Mathematics is the integration of simulation and data made available by new imaging and measurements devices, so to improve both the knowledge extracted from data and the reliability of numerical results. Integrating observed data into a numerical model, also referred to as *data assimilation*, is common in fields such as weather prediction and ground water flow. It is natural to use similar techniques in cardiovascular mathematics and medical imaging. In particular, recent imaging devices allow the acquisition of images in time (4D) of vessels of interest within a few heart beats. This allows to track the wall motion from images rather than retrieving it from a numerical simulation, by means of a proper *registration* procedure. The latter is a methodology for aligning images acquired from different sources or different viewpoints. With the same approach it is actually possible to register images taken at

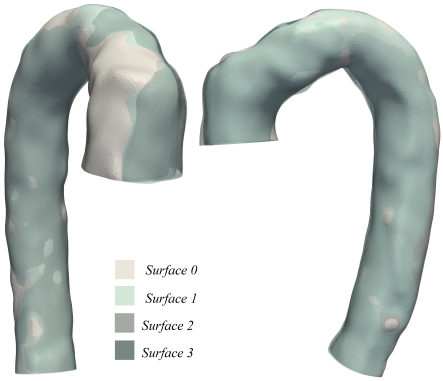

Figure 1: Synoptic representation of the first four surfaces (out of ten) reconstructed from a human aorta.

different time instants for estimating the motion of the structure of interest. Once the vessel motion has been retrieved, fluid dynamics can be computed in the moving domain. In this way, the computational cost is reduced and the structure modeling is waived by the registration procedure (see [1]).

The computation of blood flow is therefore carried out following three steps.

1. *Segmentation of a 4D image (space+time) and reconstruction for each time frame of the 3D surface that identifies the vessel of interest.*

2. *Tracking in time of the position of vessel wall surfaces by means of a 3D surface registration algorithm.*

3. *Moving domain simulation.*

Numerical results show that the proposed 4D Inage-Based (4DIB) approach is consistent with traditional fluid-structure interaction (FSI) solvers. Moreover, it yields a significant reduction of the computational costs with respect to more standard approaches to the modeling of FSI.

2 WORKFLOW

2.1 SEGMENTATION

The boundary of the region of interest (ROI) is identified on the images by means of a *level set approach*. This means that the boundary in 3D is regarded as the zero-level isosurface of a function solving a proper advection-diffusion nonlinear problem. At the end of this step, for each time frame a mathematical representation of the inner surface of the lumen is given as a triangulated mesh. The segmentation has been performed with the *Vascular Modeling ToolKit* (available at http://www.vmtk.org).

2.2 TRACKING

Given $M+1$ time frames, the tracking process consists of performing M registration steps between two consecutive frames; within each registration stage, points of one mesh are mapped to points of the surface extracted from the subsequent time frame and the displacement field is computed; the new positions of the points are used as initial condition for the registration to the subsequent time

frame. At the end of the whole tracking procedure M surface displacement fields are available describing the motion of the vessel wall at the instants of the image acquisition. There are many different strategies for performing image and surface registration. In this work we regard the registration as the computation of a map that minimizes a suitable distance between the two images. In particular, we resort to a *non-parametric map* implicitly defined with a collocation approach by the position of the nodes on the reference image. The coordinates of the vertexes, computed by the minimization process, implicitly define the map point-wise. The map is then extended to the entire template surface by a piecewise linear interpolation of the values of the vertexes. The distance between the starting (template) image $\mathcal{S}_T$ and the final (reference) one $\mathcal{S}_R$ can be defined as

$$\mathcal{D}(\mathcal{S}_T, \mathcal{S}_R) := \left(\frac{1}{|\mathcal{S}_T|} \int_{\mathcal{S}_T} (\mathrm{dist}(\mathbf{x}, \mathcal{S}_R))^2 \; d\mathcal{S}_T(\mathbf{x}) \right)^{1/2} \tag{1}$$

where $|\mathcal{S}_T| := \int_{\mathcal{S}_T} d\mathcal{S}$ is a normalization factor and $\mathrm{dist}(x, S_R) = \inf\{\|\mathbf{x} - \mathbf{y}\| \; : \; \mathbf{y} \in \mathcal{S}_R\}$ is the usual distance of a point to a surface. This definition of distance can be regarded as a modification of the well known *Iterative Closest Point* functional, which however features poor regularity properties that affect the minimization. In order to force better mathematical properties to the functional to be minimized, we add a Tikhonov-like regularizing term based on a simplified physical model of the vascular wall at hand. In particular, we describe vascular walls as elastic thin membranes, and use the membrane energy as regularizing term. In this way, the deformations that feature large membrane energy are heavily penalized whilst deformations that do not increase the energy of the surface are allowed. Finally, in order to prevent "flips" of triangles we add this as a constraint to the mathematical formulation, by forcing explicitly that the area of the mapped triangles is positive (see [3] for more details).

Minimization is numerically performed with a classical BFGS method. In Fig. 1 we illustrate the results of the registration of 4 frames of a human aorta.

2.3 SIMULATION

From the sequence of maps describing the motion of the surface points from one time frame to the subsequent one, the velocity of the boundary of the moving domain is computed at the image acquisition times. Since the set of all the time instants where the fluid equations will be solved is typically larger than the set of time instants where the images are acquired, an interpolation procedure is required to define the velocity of the boundary at each time instant in the CFD simulation. This interpolation procedure needs to guarantee regularity to the computed velocity/acceleration, so we resort to a cubic spline interpolation. Once the wall motion is available, incompressible Navier-Stokes equations can be written in the *Arbitrary Lagrangian Eulerian* (ALE) formulation to be numerically solved. This step requires the computation of the lifting of the boundary velocity in the vessel lumen, typically attained by the solution of a Laplace problem (for which fast solvers are usually available). Numerical results presented are obtained with a software based on the C++ object oriented finite element library `LifeV` (available at http://www.lifev.org).

3 RESULTS

We report two sets of numerical simulations. In the former (Fig. 2 left) we present the comparison of the simulation obtained with a traditional FSI approach vs the 4DIB results applied to the same displacement field. Results show that the image-based approach is consistent with the traditional approach. Computational cost is however significantly lower. In the second test case, we apply the approach to a real data set of a human aorta, retrieved from images provided by a SOMATOM

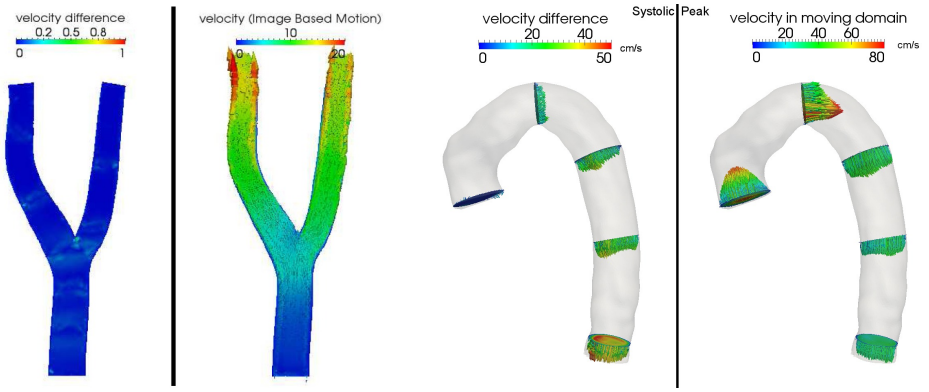

Figure 2: Left: comparison of a 4DIB and a traditional FSI simulations. The two approaches yield comparable results (left panel: difference between the two results, right panel: velocity computed by the 4DIB approach). Right: 4DIB simulations in a human aorta point out the relevance of the moving domain on the numerical results. (Left panel: difference of 4DIB and rigid simulations. Right panel: velocity computed in the moving domain with the 4DIB approach.)

Definition Flash Dual-Source CT Scanner ©(10 time frames per cardiac cycle). The original 4D computed tomography angiography set refers to a 72 years old male patient. The results (Fig. 2 right) point out the relevance of the aorta movement on the wall shear stress map.

4 CONCLUSION

Availability of new imaging techniques and data raises new challenges for numerical Cardiovascular Mathematics. Assimilation of these data with numerical simulations is expected to bring a mutual advantage to the quality of data and accuracy/efficiency of numerical simulations, as it is in geophysical a metereological applications. The significant time reduction of the computations is certainly a valid motivation for pursuing the 4DIB approach for fluid-structure interaction. In the talk, we will address also recent advances in using the same approach for evaluating vessels paramaters such as the Young modulus, by solving an inverse fluid-structure interaction problem (see [2]).

Analysis of the impact of the noise in measurements and errors in registration on the accuracy of the numerical simulations is still an open problem. For more details, see [3].

REFERENCES

[1] D. M. Sforza, R. Lohner, C. Putman, and J. Cebral. Hemodynamic analysis of intracranial aneurysms with moving parent arteries: Basilar tip aneurysms. *International Journal for Numerical Methods in Biomedical Engineering*, 26:1219–1227, 2010.

[2] M. Perego, A. Veneziani, and C. Vergara. A variational approach for estimating the compliance of the cardiovascular tissue: An inverse fluid-structure interaction problem. Technical Report 18, Dept Math & CS, Emory Univ, www.mathcs.emory.edu, 2010.

[3] M. Piccinelli, L. Mirabella, T. Passerini, E. Haber and A. Veneziani. 4D Image-Based CFD Simulation of a Compliant Blood Vessel In preparation, 2010.

2nd International Conference on Mathematical and Computational Biomedical Engineering - CMBE2011
March 30 - April 1, 2011, Washington D.C, USA
P. Nithiarasu and R. Löhner (Eds.)

4D Image-Based approach for CFD in compliant blood vessels

Lucia Mirabella*, Marina Piccinelli, Tiziano Passerini**, Maria Restrepo*, Eldad Haber***, Ajit P. Yoganathan*, Alessandro Veneziani****

* Wallace H. Coulter Department of Biomedical Engineering, Georgia Institute of Technology, 315 Ferst Dr., Atlanta 30332, GA, USA, {lucia.mirabella, ajit.yoganathan}@bme.gatech.edu, mrestrepo3@gatech.edu

**Department of Mathematics and Computer Science, Emory University, 400 Dowman Dr. Suite W401, Atlanta, GA, 30322, USA,{tiziano, marina, ale}@mathcs.emory.edu

***Department of Mathematics, University of British Columbia, 1984 Mathematics Road Vancouver, B.C. Canada V6T 1Z2, haber@math.ubc.ca

SUMMARY

One of challenging aspects of computational hemodynamics is the numerical simulation of blood flow in a compliant vascular wall. In this work we study an alternative approach (with respect to the more standard fluid-structure interaction algorithm) to perform numerical simulations of blood flow in compliant vessels. More precisely, we aim at exploiting the availability of accurate time resolved medical images to obtain information on the motion of the vascular structure. The details of the proposed algorithm are discussed and preliminary results are presented on an aorta and a carotid geometry. Ongoing work includes the study of the effect of the motion on the blood flow features that are relevant for the success of the Total Cavopulmonary Connection, the current procedure of choice for surgical palliation of single ventricle congenital heart diseases, where more accurate CFD simulations could improve surgical decisions.

Key Words: *4D medical images, compliant vessels, registration, ALE formulation, total cavopulmonary connection.*

1 INTRODUCTION

Every physical phenomenon occurring in the cardiovascular system involves the interaction of different biological tissues, each featuring peculiar mechanical properties. For example, blood flow in arteries and veins interacts mechanically with the vessel tissue, where the pressure exerted by the fluid on the wall contributes to generate its displacement and in turn the vessel motion influences the fluid dynamics.

As a result of the mechanical forces involved, the tissue in the cardiovascular system experiences detectable deformation during the cardiac cycle. These evidences suggest that the motion effects are non-negligible if precise reproduction of the local flow features is desired.

The standard approach to simulate the coupling between fluid and solid structures is to develop mathematical models for each medium as well as for the coupling conditions describing their interaction. However this strategy raises issues from the modeling and numerical point of view, as the accuracy of the mechanical model employed (in particular in presence of diseases) and the computational costs of the simulation, which are generally high both with segregated or monolithic approaches [1].

We present here an alternative strategy to include the motion of the domain of interest in the simulation of blood flow in compliant blood vessels, where the tissue displacement is computed at each time step from 4D medical images (3D space plus time) and the computational domain is moved accordingly. The main advantage of this strategy is that it maintains a tight link between numerical simulations and patient specific data, including intrinsically the mechanical features of the structure and of the surrounding tissues, with a limited additional computational cost with respect to the fixed geometry case. A similar technique has been proposed in [2,3] where the authors apply the image-based motion approach to intra-cranial aneurysms and coronary arteries, respectively, implementing however different strategies for the single steps of the algorithm.

2 DESCRIPTION OF THE METHODOLOGY

The starting point of the procedure is the acquisition of a time sequence of 3D medical images, as computed tomography (CT) or magnetic resonance imaging (MRI), whose space and time resolution is enough to provide a proper reconstruction of the moving domain. The 4D Image-Based (4DIB) approach can then be decomposed in the following steps:

2.1 Image segmentation The boundary of the region of interest is identified on the phasic images by means of a *level set approach* [4]. At the end of this step, a mathematical representation of the 3D surfaces that identifies the interface between the fluid and the vessel wall is given as a triangulated mesh. In this work the segmentation has been performed using the *Vascular Modeling ToolKit* (www.vmtk.org).

2.2 Motion tracking To take into account the motion of the domain in the simulation, it is necessary to track the movement of each point of the computational grid. This *registration* process can be accomplished by means of various techniques [5]. Given $M + 1$ time frames, the tracking process consists of performing M registration steps between two consecutive frames. At the end of the whole tracking procedure M surface displacement fields are available describing the motion of the vessel wall at the instants of the image acquisition. We have adopted a 3D surface registration algorithm based on a minimization approach, where the functional to be minimized is the sum of a distance function and a regularization term which is added to overcome the ill-posedness of the minimization problem and filter out non physical solutions. This step is performed by using an in-house Matlab (The MathWorks Inc., Natick, MA) code.

2.3 Formulation in moving domain From the sequence of maps describing the motion of the surface points from one time frame to the subsequent one, the velocity of the boundary of the moving domain is estimated at the image acquisition times and it is then interpolated to define the velocity of the boundary at each time instant in the CFD simulation. To ensure the continuity of the derivative of the points position, a cubic spline interpolation has been chosen. The displacement and velocity of the whole domain are found as the harmonic extension of the boundary fields, computed for each time step of the simulation. Once the domain motion is available, incompressible Navier-Stokes equations for a Newtonian fluid can be written in the *Arbitrary Lagrangian Eulerian* (ALE) formulation (ALE-NS) [6] to be numerically solved. On the wall boundary a Dirichlet condition on the fluid velocity is prescribed equal to the boundary velocity, while inflow and outflow boundary data can be retrieved by measures or designed to reproduce a physiological or pathological behavior. In the next Section, details on the numerical approach adopted will be provided.

This algorithm can be enriched in case more information on the patient is acquired, like PC-MRI images from which the blood velocity in selected sections of the domain can be reconstructed and used as boundary conditions in the CFD simulation.

3 RESULTS

To discretize the ALE-NS system, we have chosen a first-order time advancing scheme and a finite element approximation for the space dependence ($\mathbb{P}_1$ for the pressure and $\mathbb{P}_1$bubble for the fluid velocity). Numerical results are obtained with a software based on the C++ object oriented finite element library *LifeV* (www.lifev.org). Numerical tests have been run to evaluate the difference between the velocity and wall shear stress (WSS) fields computed with the 4DIB approach and those computed on a rigid domain simulation, the latter being the standard assumption chosen in the literature when no information on the structural dynamics is available. The domain of interest for this case is representative of an ascending and thoracic aorta, whose geometry in time is reconstructed from a set of CT images. On the considered domain of interest, the motion is significant. Accordingly, both the velocity and the WSS fields exhibit a considerable difference with respect to the rigid domain case, as shown in Figure 1, left and middle panels. In particular, the relative norm of the difference between the 4DIB fields and the rigid domain fields has an average over the cardiac cycle of 84.52% for the velocity and 52.26% for the WSS. We also performed an *in-silico*

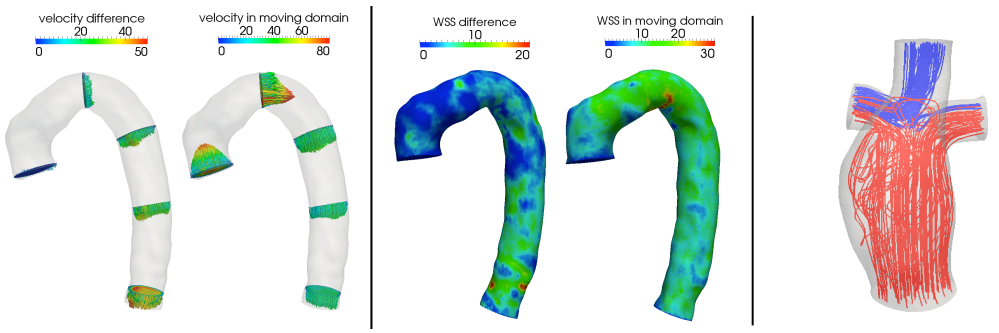

Figure 1: Left panel: difference between the fluid velocity computed in the rigid domain simulation and the one computed in the 4DIB simulation (left) and velocity computed with the 4DIB approach (right), at peak systole (in cm/s). Middle panel: difference between the WSS computed in the rigid domain simulation and the one computed in the 4DIB simulation (left) and WSS computed with the 4DIB approach (right), at peak systole (in dyne/cm^2). Right panel: inferior vena cava (red) and superior vena cava (blue) flow split between right and left pulmonary arteries.

validation of the 4DIB approach with respect to a FSI simulation, considered as benchmark. In particular we have first run a FSI simulation, obtaining the fluid velocity and pressure fields and the displacement in the vessel wall. We have then used this displacement to run a 4DIB simulation, with the same inflow/outflow boundary conditions and fluid properties as in the FSI case, obtaining 4DIB velocity and pressure fields. The comparison of the results obtained with the two approaches has shown a good agreement (below 1% of relative difference, on both velocity and WSS), while the computational time required by the 4DIB simulation is by far smaller than the one required by the FSI simulation, confirming the validity of the approach.

The ongoing work we are performing to complement this study is twofold. On one side we are investigating the sensitivity of the results on the entity of the motion. The hypothesis we test is that the inclusion of the motion data in the model and simulation is worthwhile only if the motion experienced by the tissue is large enough. On the other side we are evaluating the application of this approach on a clinically relevant case. In particular we are considering the case of a post-operative configuration after a Total Cavopulmonary Connection (TCPC) has been implemented [7], to bypass the right side of the heart in patients with single ventricle congenital defects (occurring in 2 over 1000 children). The interest of performing CFD simulations for studying the hemodynamics

in these cases is very high, since single ventricle patients are still subject to numerous long-term complications, despite improvements in the outcome obtained with this surgical procedure. Since the hemodynamics have been related to the patient-specific anatomies (see e.g. [8]), a CFD study may lead to better surgical decisions and better patient outcome. In this respect, the inclusion of more realistic features such as the measured domain motion (both due to the blood-wall interaction and to the respiration) could provide more realistic results and improve the accuracy of the quantity of interest evaluated (e.g. energy loss across the artificially created connection or hepatic flow split between the pulmonary arteries, see Figure 1). Moreover in the TCPC case FSI simulations would be particularly challenging due to the heterogeneous mechanical properties of the connection (made of veins, arteries and artificial baffle), while a prescribed motion approach could overcome the problem. Preliminary results on these extensions of the work will be presented.

4 CONCLUSIONS

We point out the advantages of the 4DIB methodology proposed. It provides more realistic simulations where the motion is relevant, avoiding the use of complex mechanical models, sometimes not well established (e.g. for the diseased arterial wall). It also reduces the computational time for the numerical simulations with respect to FSI simulations and allows to take into account the motion due to extra-vessel forces (e.g. action of surrounding tissues, respiration), which would be otherwise difficult to be considered. Finally, this approach is applicable to every flow phenomenon occurring in a moving structure (not only blood flow in vessels, or even biological tissue), as long as the motion can be accurately recorded by imaging devices. The main limitation is the intrinsic impossibility to evaluate the effect of the flow on the wall mechanics. Therefore it should be used only when the focus of the study is the on the flow features alone.

REFERENCES

[1]L. Formaggia, A. Quarteroni, and A. Veneziani. *Cardiovascular mathematics: modeling and simulation of the circulatory system*,. Springer, 2009.

[2]D. M. Sforza, R. Löhner, C. Putman, J. R. Cebral. *Hemodynamic analysis of intracranial aneurysms with moving parent arteries: Basilar tip aneurysms*. International Journal for Numerical Methods in Biomedical Engineering, 26 (10):1219-1227, 2010.

[3]R. Torii, J. Keegan, N. B. Wood, A. W. Dowsey, A. D. Hughes, G. Yang, D. N. Firmin, S. A. McG. Thom and X. Y. Xu *MR Image-Based geometric and hemodynamic investigation of the right coronary artery with dynamic vessel motion*. Annals of Biomedical Engineering, 38 (8):2606-2620, 2010.

[4]J. Sethian. *Level set methods and fast marching methods*. Cambridge University Press, Cambridge, 1999.

[5]J. A. Maintz and M. Viergever. *A survey of medical image registration*. Medical Image Analysis, 2(1):1-37, 1998.

[6]J. Donea, S. Giuliani, and J. Halleux. *An arbitrary lagrangian-eulerian finite element method for transient dynamic fluid-structure interactions*. Computer Methods in Applied Mechanics and Engineering, 33(1-3):689-723, 1982.

[7]F. Fontan, E. Baudet. *Surgical repair of tricuspid atresia*. Thorax, 26:240-248, 1971.

[8]K. Pekkan, D. de Zelicourt, L. Ge, F. Sotiropoulos, D. Frakes, M. A. Fogel, et al. *Physics-driven CFD modeling of complex anatomical cardiovascular flows - a TCPC case study*. Annals of Biomedical Engineering, 33(3):284-300, 2005.

2nd International Conference on Mathematical and Computational Biomedical Engineering - CMBE2011
March 30 - April 1, 2011, Washington D.C, USA
P. Nithiarasu and R. Löhner (Eds.)

MICROCRACK LOCAL STRESS FIELD IN HUMAN HAVERSIAN CORTICAL BONE

E. Budyn*, J. Jonvaux* and T. Hoc**
*University of Illinois at Chicago, Department of Mechanical Engineering, 842 West Taylor Street, Chicago, IL 60607 USA, ebudyn@uic.edu, jjonva2@uic.edu
**Ecole Centrale Lyon, Department of Mechanical Engineering - LTDS UMR 5513, 36 avenue Guy de Collongue, 69134 Ecully Cedex FRANCE, Thierry.Hoc@ec-lyon.fr

SUMMARY

Osteocytes are bone cells located throughout the mineralized tissue that are mechano-sensitive and can sense mechanical stimulation, to which they respond by adapting their internal biology to the changes of their mechanical environment. Osteoporosis is an aging pathology often following a hormonal decrease where a cell activity imbalance produces an overly porous tissue. The effect of a modified mechanical microenvironment on the cells is not precisely quantified. To perform stress field visualization near cells, a Physical Imaging procedure is presented where microcracks in human Haversian cortical bone are imaged and tracked using Light Microscopy during either tension or compression tests. The tissue morphology is acquired by digital imaging and the tissue elastic moduli are measured by Back Scattered Electron Microscopy (BSEM) and nanoindentation. The displacements are measured at grid points by Digital Image cross-Correlation (DIC) to provide the boundary conditions of a polyphase finite element model. Based on the strain energy balance, as the crack growth is considered quasi-static and in a brittle material, the stress intensity factors of the microcracks are calculated using the reconstructed micro stress field. Concomitantly, the stress intensity factors are also derived from variation of the global energy using the macroscopic load deflection curve of the sample in order to identify bone fracture law.

Key Words: *bone, fracture, stress intensity factors.*

1 INTRODUCTION

Microcracks in bone are usually associated with the remodelling process of the tissue [1, 2]. Osteocytes are the mechano-sensing cells present throughout bone tissue that are suspected to detect microcracks through their interconnections within micron scale canals called caniliculi. Precise measurement of the stress field and its modifications near the cells can improve the understanding of the remodeling stimuli. During daily exercise, bones undergo cyclic fatigue loading that alternates between tension and compression. The presented model proposes a method to determine the stress field near bone microcracks during their growth in tension and compression micro tests. The cracks are imaged and tracked under light microscopy in millimetric specimens of female human cortical bone harvested from fresh cadaveric posterior femur mid-diaphysis.

2 MATERIAL AND METHOD

To study bone microcracks, a miniaturized tension/compression machine to test millimetric bone

beam samples is placed under a light microscope in Figure 2(1). The beam specimen of cortical bone of square cross-section of 2 mm width measured 5 mm in length. For tensile tests, the specimens are precracked by a 600 μm notch. The tests are performed along the longitudinal, tranverse and anti-plane longitudinal directions of the osteons. In compression the samples do not require any initial notch.

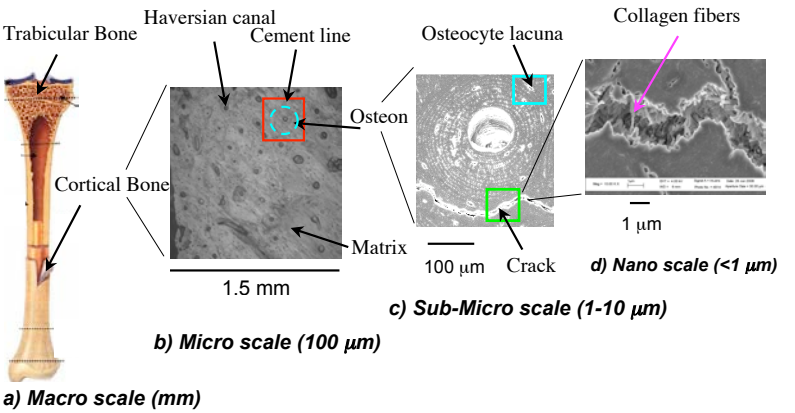

Figure 1: (a) Microscopic illustration of a long bone, (b) Light Microscopy of human Haversian cortical bone, (c) BSEM (Back-Scattered Electron Microscopy) of human cortical bone, (d) BSEM zoom inside a micro-crack in human cortical bone.

The light microscope lens is equipped with a high-resolution camera providing digital images with a 2048×2048 pixel resolution in Figure 1(b). The cortical bone polyphased morphology is surveyed by a digital imaging processing technique [3] in Back Scattered Electron Microscopy (BSEM) in Figure 1(c). To construct the physical stress field at the micro scale, the model includes the osteons, the cement lines around them, distinct secondary osteons remnants inside the interstitial bone phase [4,5] as viewed in Figure 2(2). The Haversian canals are represented as free boundaries inside active osteons, where *in vivo* cytoplasmic fluid flows freely and replaced by saline solution in the experiment. The crack topologies are also explicitly surveyed.

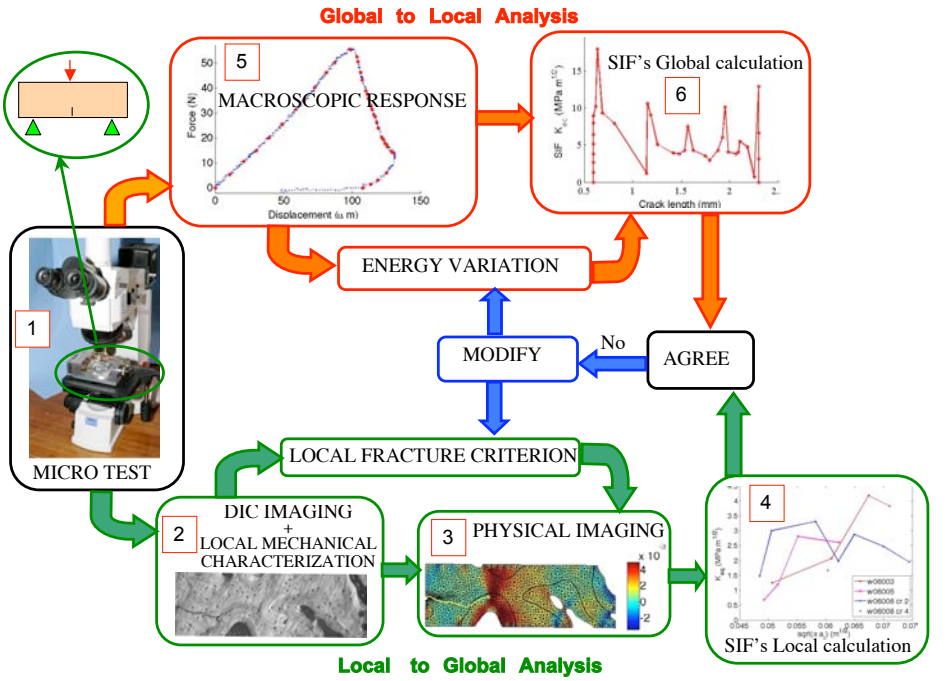

Figure 2: Osteocyte stress field assessment: (1) experimental setting, (2) Light Microscopy observation of fresh human cortical bone, (3) strain field under tension, (4) stress intensity factor calculations at the micro scale, (5) macroscopic load deflection curve, (6) stress intensity factor calculations based on energy variation.

The local elastic moduli are scaled to the mineralisation levels that are correlated to the grey scale levels in the BSEM observations, and calibrated by nanoindentation measurements. The local Poisson ratios are extrapolated using the osteonal strain fields. Small windows of observation of up to approximately $900 \times 900\ \mu m$ are studied in the vicinity of the cracks.

The experimental displacements are registered between the different stages of crack growth at grid points laid over the observation window using cross-correlation [6,7] where the domain of correlation includes polyphase and fracture partition. These displacements provide the boundary conditions of the model. The correlation and numerical model domains are homeomorph. The finite element model is discretised using non-structured triangles [8].

In the microstructural model, the impenetrability condition of the crack edges under compression is enforced by penalty forces [9] with frictional contact [10], while a cohesive law is applied in the wake of the crack tip to model the progressive rupture of the collagen fibrils in Figure 1(d). Due to its high content of hydroxyapatite cortical bone is quite brittle and the crack growth is considered quasi-static. The model is under plane stress condition as the surface of the sample is observed. The dominant strain energy can be measured given reliable local mechanical properties. The stress field obtained [11] provide the basis to calculate the local stress intensity factors at the micro scale [12] in Figure 2(4). At the macroscopic level, the internal energy stored in the sample as microcracks grow balances the energy of the external applied force. A concomitant global energy variation of the macroscopic sample response (F, u) makes it possible to calculate the energy release rate at each crack growth in Figure 2(6). The values obtained for different direction of loading are in agreement with the literature [13]. The macroscopic calculations using the appropriate traction separation law along the cracks edge can be applied to identify the microscopic fracture law.

3 CONCLUSIONS

A procedure to image and reconstruct the physical field of microcracks in human cortical bone makes it possible to visualize the stress field in the vicinity of the cracks near osteocytes. The method is driven by the identification of bone micro fracture law using concomitant micro and macro analyses. The present study shows the significant local influence of the Haversian porosity on the evolving values of the stress intensity factors and therefore show for the first time the fluctuations of the stress field produces by growing cracks as they approach the canals.

REFERENCES

[1] R.K. Nalla, J.H. Kinney and R.O. Ritchie, Mechanistic fracture criteria for the failure of human cortical bone,*Nature Materials, 2, 164-168,2003.*

[2] P. Fratzl, When the cracks begin to show, *Nature Materials, 7, 610-612, 2008.*

[3] R. Smith, *Plot Digitixer User's Manual, Plot Digitizer, Version* 2.4.1*,* $http$: $//plotdigitizer.sourceforge.net$ USA, 2007.

[4] E. Budyn and T. Hoc, Multiple scale modeling of cortical bone fracture in tension using X-FEM, *Revue Européenne de Mécanique Numérique (European Journal of Computational Mechanics), 16, 213-236, 2007.*

[5] E. Budyn and T. Hoc, Fracture strength assessment and aging signs detection in human cortical bone using an X-FEM multiple scale approach, *Computational Mechanics, 42(4), 579-591, 2008.*

[6] P. Doumalin, M. Bornert and J Crépin, Characterization of the strain distribution in heterogeneous materials, *Méc Ind, 4, 607-617, 2003.*

[7] T. Bretheau and J. Crepin and P. Doumalin and M. Bornert M, Microextensometry: a tool for the mechanics of materials, *Revue de Métallurgie - Cahiers dInformations Techniques, 100(5), 567-, 2003.*

[8] C. Geuzaine and J.F. Remacle, *GMSH User's Manual, GMSH, Version* 62*, Geuzaine* & *Remacle, Cleveland USA* & *Louvain Belgium, 2006.*

[9] A.R. Mijar and J.S. Arora, An augmented Lagrangian optimization method for contact analysis problems, 1: formulation and algorithm, *Structural and Multidisciplinary Optimization, 28, 99-112, 2004.*

[10] A. Dorogoy and L. Banks-Still, Shear loaded interface crack under the influence of friction: a finite difference solution, *International Journal of Numerical methods in Engineering, 59, 1749-1780, 2004.*

[11] E. Héripré, M. Dexet, J. Crépin, L. Gélébart, A. Roos, M. Bornert and D. Caldemaison, Coupling between experimental measurements and polycrystal finite element calculations for micromechanical study of metallic materials, *Journal of Plasticity, 23, 1512-1539, 2007.*

[12] E. Budyn and T. Hoc. Analysis of micro fracture in human haversian cortical bone under transverse tension using extended physical imaging. *International Journal of Numerical Methods in Engineering, 82(8):940-965, 2010.*

[13] K.J. Koester, J.W. Ager and R.O. Ritchie, The true toughness of human cortical bone measured with realistically short cracks, *Nature Materials, 7, 676-677, 2008.*

2nd International Conference on Mathematical and Computational Biomedical Engineering - CMBE2011
March 30 - April 1, 2011, Washington D.C, USA
P. Nithiarasu and R. Löhner (Eds.)

MOTION TRACKING STRATEGIES FOR BIOMECHANICAL IMAGING

Timothy J. Hall and Jingfeng Jiang
Medical Physics Department, University of Wisconsin, 1005 Wisconsin Institutes for Medical Research, 1111 Highland Avenue, Madison, WI 53705 USA, tjhall@wisc.edu

SUMMARY

We are developing algorithms for tracking motion among pairs of ultrasound echo signal fields. Radiofrequency data are recorded while imaging with standard clinical ultrasound imaging systems and custom software estimates the local displacement that can be displayed as either displacement images, strain images, shear strain images, or used as input to an elastic modulus reconstruction algorithm to display a modulus image. Increasing sophistication in these algorithms has provided more robust displacement fields when motion is complex. Improved algorithms have also allowed tracking larger single-step and accumulated displacements. This report will highlight our progress in real-time elasticity imaging and providing input for modulus reconstruction algorithms. Although these methods began with $2D$ data fields and motion tracking algorithms, current methods have been extended to $3D$ echo data, motion tracking, strain fields and modulus images. New technologies on the horizon are expected to further improve our results.

Key Words: *ultrasound, elastography, motion tracking, displacement, strain, modulus, reconstruction*

1 INTRODUCTION

Breast biopsy is the current standard of practice for diagnosing solid breast lesions at many institutions. However, in more than 75% of these cases a benign condition is found. In addition, biopsy is the single most expensive component of the breast cancer screening protocol. So there is great motivation to improve the confidence of clinicians when viewing breast images to allow a reduction in the rate of referral for biopsy and to increase both the positive predictive value and negative predictive value of breast imaging.

Elasticity imaging has demonstrated great promise toward that goal [1–4]. Several of the clinical ultrasound imaging system manufacturers provide some type of elasticity imaging as an optional product on their systems. As the availability of these products increases, the range of applications and the expertise also increases. However, most of these systems provide images of small-deformation axial (along the acoustic beam axis) strain, Since strain is a relative property, and there is often little or no control over initial conditions, results can be highly variable even when high quality data are acquired.

Elastic modulus reconstructions are the obvious solutions to this ambiguity. When displacement estimates are sufficiently accurate and low noise, direct inversion techniques can provide acceptable results [5]. More often, iterative reconstruction techniques are required [6]. In this case, it is especially important to provide unbiased displacement estimates.

This overview will highlight the progression of our work that has allowed consistent high quality motion tracking for *in vivo* breast imaging and to describe the current challenges and some potential solutions.

2 METHODS

Ultrasound radiofrequency echo signals for breast imaging typically have center frequencies of 10MHz or higher and fractional bandwidths of about 80%. With these characteristics, correlation-based algorithms are a reasonable choice since the signal phase is highly sensitive to motion. The simplest approach for motion tracking is to use a block-matching algorithm. It is common to use the cross correlation coefficient as the metric for choosing the best match between the kernel of data in the 'reference image' and the location of the 'best match' in the search region of the 'post-deformation image'. Historically cross correlation was in many cases too time consuming given the large number of image points to track, so surrogates for cross correlation, such as the sum-absolute-difference or sum-squared-difference, were used. Unfortunately, there are several drawbacks to the simple block-matching approach. First, since the data are typically acquired with freehand scanning, the underlying motion is unknown and potentially large compared to a wavelength of the echo signal, the search regions need to be large. The large search region increases the computational cost of the search algorithm. Second, if the signal to noise ratio for the echo signal is too low, and the search range is larger than a wavelength, there is a high probability of integer-wavelength ("peak hopping") displacement errors that severely degrade the motion tracking accuracy.

In an attempt to reduce the computational load of motion tracking for real-time elasticity imaging, we developed a "guided search" block-matching strategy [5]. The underlying concept was that, since adjacent echo signal samples occur at physically close proximity to their immediate neighbors (small distances compared to the acoustic pulse dimension), accurate displacement estimates at one location provide a good initial guess for displacement estimates in the immediate neighborhood. That initial guess was used to vastly reduce the search region in block matching with a corresponding significant reduction in the computational cost of the algorithm. The initial method used continuity among axial displacement estimates in a row (constant depth) to suggest "reliable" displacement estimates, and used those estimates to predict displacement in the row below (and so on). Errors in displacement estimates, used to predict the displacement at the next row below, were thus propagated axially (with increasing depth) and an extensive error detection and correction scheme was needed. An example of this axial error propagation is shown if Fig. 1b. The vertical streaks of similar gray shade are the result of displacement estimate errors propagating in the direction of displacement prediction. Error detection and correction routines find these errors, stop their further propagation, and 'fix' them to a limited extent.

The frequent occurrence of propagating errors and the complexity of the error detection and correction schemes led to an alternate approach for guided search block matching. The echo signals decorrelate more rapidly in the axial direction than perpendicular to the acoustic beam. Therefore, there is a higher chance that a decorrelated echo signal is used to predict motion with axial guidance than with lateral guidance. The lateral guidance block matching algorithm [7] is more robust when motion is complex and can naturally be split into multiprocessing tasks. An example is shown in Fig. 1c. However, this approach retains the requirement that a sequence of consecutive displacement estimates are used for guiding the block matching algorithm at adjacent locations.

A novel improvement on the guided search concept was reported [8]. The general approach randomly selects a set of initial locations to estimate motion, again using a correlation-based block

matching algorithm. Some metric is used to decide which among these is the "best" displacement estimate (such as that with the highest cross correlation coefficient), and a list ranking the highest to lowest measure of "best" displacement estimate is created. The displacement estimate corresponding to the top of the list is used to guide displacement estimates in its immediate neighborhood. The metric for each of these displacement estimates are entered into the ranking list, the displacement estimate corresponding to the top of the updated list is used to guide displacement estimates in its immediate neighborhood, and the process continues until displacements are estimated throughout the desired field. An improvement on this approach [9] tests the reliability of each of the initial displacement estimates prior to forming the list of potential guidance candidates and thereby measurably improves the reliability of motion tracking. An example is shown in Fig. 1d.

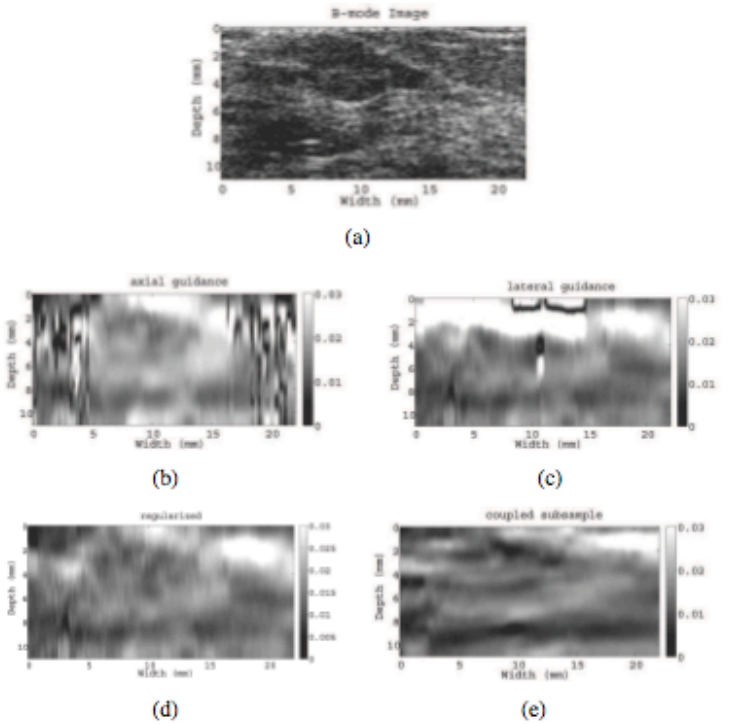

Figure 1: B-mode and axial strain images of a breast fibroadenoma which is the most commonly occurring solid breast tumor — a fiboradenoma — which is a benign disease. A typical finding in strain images of fibroadenoma is the similarity in the size of the tumor seem in the two image types. Unlike benign disease, strain images of cancers typically appear significantly larger in strain images than in B-mode images.

The methods described above provide displacement estimates at integer multiples the spacing of the echo signals which is too coarse for strain imaging or modulus reconstruction — subsample accuracy is required. A typical approach to obtain subsample displacement estimates is to interpolate the correlation function to find its peak. Typical interpolation techniques, such as quadratic or cosine, introduce bias that is undesirable. Many alternative methods have been reported, but among them is a new approach [10] that couples the lateral and axial subsample displacement estimates in an effort to substantially improve the lateral displacement estimates while maintaining high quality axial displacement estimates. An example is shown in Fig. 1e.

These methods are used to provide high quality $1D$, $2D$ and $3D$ displacement estimates for linear and nonlinear modulus reconstructions with promising results.

3 CONCLUSIONS

Current displacement estimation strategies provide very good results for single-step deformations as large as 5% in phantoms and about 2% in tissues. Displacements can be accumulated up to at least 20% strain with $2D$ tracking and this limit will likely be exceeded with $3D$ data and $3D$ tracking.

4 ACKNOWLEDGEMENTS

We are grateful for funding from NIH/NCI grants R21CA133488 and R01CA140271 and technical support from Siemens Healthcare Ultrasound Division.

References

[1] E. S. Burnside, T. J. Hall, A. M. Sommer, G. K. Hesley, G. A. Sisney, W. E. Svensson, and N. J. Hangiandreou, "Ultrasound strain imaging to improve the decision to biopsy solid breast masses," *Radiology*, vol. 245, no. 2, pp. 401–410, 2007.

[2] G. Scaperrotta, C. Ferranti, C. Costa, L. Mariani, M. Marchesini, L. Suman, C. Folini, and S. Bergonzi, "Role of sonoelastography in non-palpable breast lesions," *European Radiology*, vol. 18, no. 11, pp. 2381–2389, 2008, 0938-7994.

[3] Y.-M. Sohn, M. J. Kim, E.-K. Kim, J. Y. Kwak, H. J. Moon, and S. J. Kim, "Sonographic elastography combined with conventional sonography: how much is it helpful for diagnostic performance?" *Journal of Ultrasound in Medicine*, vol. 28, no. 4, pp. 413–420, 2009.

[4] F. K. W. Schaefer, I. Heer, P. J. Schaefer, C. Mundhenke, S. Osterholz, B. M. Order, N. Hofheinz, J. Hedderich, M. Heller, W. Jonat, and I. Schreer, "Breast ultrasound elastography–results of 193 breast lesions in a prospective study with histopathologic correlation," *European Journal of Radiology*, In press.

[5] Y. Zhu, T. J. Hall, and J. Jiang, "A finite element approach for young's modulus reconstruction," *IEEE Trans Med Imag*, vol. 22, no. 7, pp. 890–901, 2003.

[6] A. A. Oberai, N. H. Gokhale, S. Goenezen, P. E. Barbone, T. J. Hall, A. M. Sommer, and J. Jiang, "Linear and nonlinear elasticity imaging of soft tissue in vivo: demonstration of feasibility," *Phys Med Biol*, vol. 54, no. 5, pp. 1191–1207, 2009.

[7] J. Jiang and T. J. Hall, "A parallelizable real-time motion tracking algorithm with applications to ultrasonic strain imaging," *Physics in Medicine and Biology*, vol. 52, no. 13, pp. 3773–3790, 2007.

[8] L. Chen, G. M. Treece, J. E. Lindop, A. H. Gee, and R. W. Prager, "A quality-guided displacement tracking algorithm for ultrasonic elasticity imaging," *Med Image Anal*, pp. 286–296, 2009.

[9] J. Jiang and T. J. Hall, "A fast hybrid algorithm combining regularized motion tracking and predictive search for reducing the occurrence of large displacement errors," *IEEE Trans Ultrason, Ferroelec, Freq Cont*, submitted 2010.

[10] ——, "A coupled subsample displacement estimation method for ultrasound-based elasticity imaging," *IEEE Trans Med Imag*, submitted 2010.

2nd International Conference on Mathematical and Computational Biomedical Engineering - CMBE2011
March 30 - April 1, 2011, Washington D.C, USA
P. Nithiarasu and R. Löhner (Eds.)

MODELING SHEAR WAVES IN SOFT TISSUE RESULTING FROM ACOUSTIC RADIATION FORCE EXCITATION

Kristen H. F. Lee* and Antoinette M. Maniatty*
*Department of Mechanical, Aerospace, and Nuclear Engineering, Rensselaer Polytechnic Institute, 110 8th Street, Troy, NY 12180-3590, leek2@rpi.edu and maniaa@rpi.edu

SUMMARY

A simulation capability has been developed that links model predictions of ultrasound intensity in an acoustic radiation force used to excite soft tissue to the resulting viscoelastic response in order to model how shear waves are created and travel through the tissue.

Key Words: *elastography, viscoelasticity, shear waves, acoustic radiation force.*

1 INTRODUCTION

The overall goal of this work is to develop a new method to image shear wave velocity in tissue for cancer diagnosis, where the shear waves are generated with an acoustic radiation force. Focused acoustical energy may be used to induce localized tissue deformation deep within soft tissue. This effectively allows palpation of interior tissue. With the same transducer used to generate the acoustic force, it is also possible to track the tissue motion using pulse-echo techniques [1, 2, 3]. If only a single wave is generated, it is not possible to image the wave in real time with conventional ultrasound scanners. Bercoff et al. [3] have overcome this limitation by developing an ultrafast, ultrasound scanner, and Wu et al. [4] have developed a novel technique to use interfering shear waves to generate a slowly propagating interference pattern that can be imaged using conventional ultrasound. Since the wave motion depends on the mechanical properties of the soft-tissue, it is possible to apply inverse problem algorithms to recover some of those properties [5,6]. Since the mechanical properties of soft tissue depend on the underlying structure, the mechanical properties are strongly influenced by pathological changes in the tissue. The development of the experiments and inverse algorithms to reconstruct mechanical properties for disease diagnosis continues to be an important research area.

In this work, simulation tools for modeling the shear waves resulting from an acoustic radiation force excitation are developed. The goals of the simulations described here are to: (a) aid in experimental design by developing a predictive capability that will provide a means of easily trying out different experimental conditions, (b) help provide insight into the sources of experimental observations, and (c) provide data for testing inverse algorithms for reconstructing viscoelastic properties. The simulations can be used to predict how different pushing sequences and types of pushes (level of focus and beam steering) will create shear waves and how they will propagate, spread, and decay. This can be used to define what sort of pushes should be used in the experiment. Furthermore, in the simulations, the displacements at all times are computed, so the data can be down-sampled and the spectral variance computed to see what the experiment is measuring and how that data may be interpreted in the context of recovering shear wave speed. Finally, the data can be used to test the shear wave speed reconstruction algorithms as the experiment is further refined and developed.

2 MAIN BODY

The modelling of the acoustic field and resulting intensity is coupled to a viscoelastic finite element model of soft tissue to model the mechanical response of soft tissue to an acoustic radiation pulse. In most simulations of waves generated by acoustic radiation forces, the force is treated as an internal point source, see for example Bercoff et al [7]. In this work, the full field of the acoustic force is modelled and compared against results for a point source. The work presented here relies on two software packages, the freely available Field II developed by Jensen [8], which simulates the fields generated by an ultrasonic transducer, and Abaqus [9], which is a commercial finite element code that can be used to solve a wide variety of problems in solid mechanics. Software was developed for interpreting the Field II results and generating the associated input files for Abaqus.

The analysis procedure involves several steps. First, a finite element discretization of the geometry of interest is created and the location of the integration points within the elements are identified. Then, using Field II modules with the transducer properties and settings defined for creating an acoustic radiation force, the intensity field resulting from the focused ultrasound pulse is computed at the finite element integration points throughout the domain. The intensity is proportional to the resulting body force transmitted to the medium from the focused ultrasound pulse. Thus, the body force distribution, at the integration points, is computed. That body force distribution is then input into Abaqus, and using a viscoelastic model for soft tissue, the displacement response is computed as a function of time. A Prony series, generalized viscoelastic model is used for modelling the soft tissue. The effect of the material parameters and number of terms in the Prony series is explored. The effect of the size of the radiation field considered by thresh-holding is also investigated as well as a comparison of the results to that from a point source. Results are compared to experimental data from the literature too.

A sample of some results simulating an experiment conducted on a tissue-mimicking phantom at the University of Rochester in K. Parker's research group is shown below. Figure 1(a) shows a diagram of the experimental set up. The phantom has a 6 mm cylindrical inclusion that is stiffer than the surrounding material. The transducer is focused at a point about 9 mm to the left and 3 mm above the center of the inclusion, with a focal depth of 25 mm and an f-number of 1. Figure 1(b) shows the computed intensity field on the center plane of the transducer, where the color scale is the logarithm of the intensity field. Note, only one half of the domain is imaged, and the domain is approximated as symmetric, which is reasonable as long as reflected waves from the inclusion either do not have time or are dissipated before arriving back to the centerplane. Figure 1(c) shows the displacement field computed in the finite element model of the phantom a short time after the pulse. Note, a quarter model is used, again making use of symmetry.

3 CONCLUSIONS

A simulation approach and tools have been created for modeling the mechanical response of viscoelastic soft tissue to a acoustic radiation force, where the induced force is treated as a body force proportional to the intensity field rather than a point source. It is found that while the intensity is highly focused, the field away from the focus has a significant effect on the resulting dynamic displacement field, and thus, the point source approximation is not adequate.

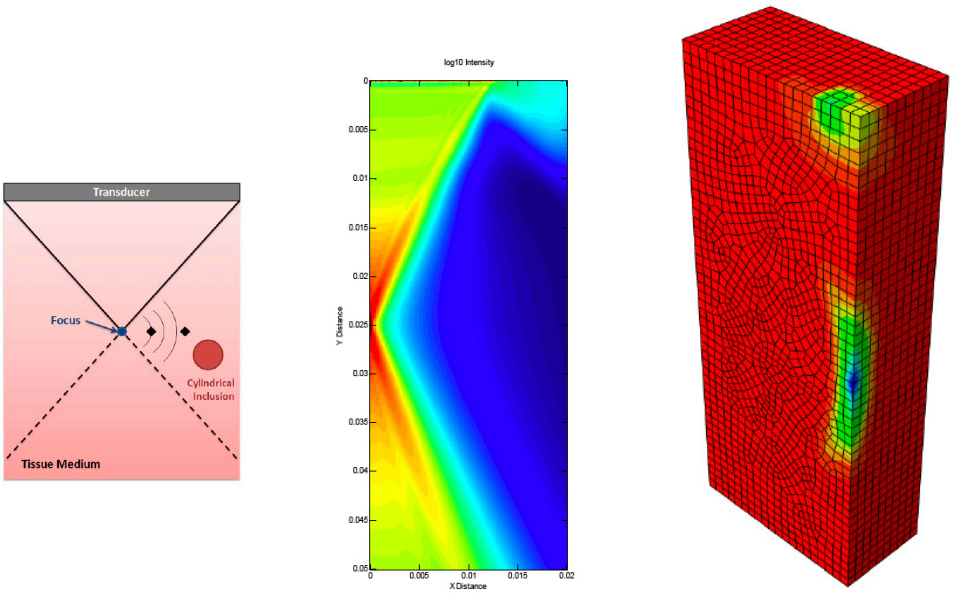

(a) (b) (c)

Figure 1: Misorientation distribution on a 2D slice: (a) VT model and (b) ST model. Horizontal is along RD and vertical is along ND.

4 ACKNOWLEDGEMENTS

This work has been supported by NIH (5R01AG29804-3) in partnership with University of Rochester and General Electric Medical Imaging. The authors also acknowledge the very useful discussions with A. Oberai and J. R. McLaughlin at Rensselaer, K. Parker and his research group at the University of Rochester and C. Hazard at General Electric Global Research.

REFERENCES

[1] K. R. Nightingale, M. L. Palmeri, R. W. Nightingale, and G. Trahey, On the feasibility of remote palpation using acoustic radiation force, *J Acoust Soc Am*, 110, 625-634, 2001.

[2] F. Lizzi, R. Muratore, C. X. Deng, J. Ketterling, K. Alam, S. Mikaelian, and A. Kalisz, Radiation-force technique to monitor lesions during ultrasound therapy, *Ultrasound Med Biol*, 29, 1593-1605, 2003.

[3] J. Bercoff, M. Tanter, and M. Fink, Supersonic shear imaging: A new technique for soft tissue elasticity imaging, *IEE Trans Ultrason, Ferroelec, Freq Contr*, 51, 396-409, 2004.

[4] Z. Wu, L. S. Taylor, D. J. Rubens, K. J. Parker, Sonoelastographic imaging of interference patterns for estimation of the shear velocity of homogeneous biomaterials, *Phys Med Biol*, 49, 911-922, 2004.

[5] J. R. McLaughlin and D. Renzi, Using level set based inversion of arrival times to recover shear wavespeed in transient elastography and supersonic imaging, *Inverse Problems*, 22, 707-725, 2006.

[6] E. Park and A. M. Maniatty, Finite element formulation for shear modulus reconstruction in transient elastography, *Inverse Problems Science Engng*, 17, 605-626, 2009.

[7] J. Bercoff, M. Tanter, M. Muller, and M. Fink, The role of viscosity in the impulse diffraction field of elastic waves induced by the acoustic radiation force, *IEEE Trans Ultrason, Ferroelec, Freq Contr*, 51, 1523-1536, 2004.

[8] J. A. Jensen and N. B. Svendsen, Calculation of pressure fields from arbitrarily shaped, apodized, and excited ultrasound transducers, *IEEE Trans Ultrason, Ferroelec, Freq Contr*, 39, 262-267, 1992.

[9] *Abaqus Analysis Users Manual, Version 6.9*, Dassault Systemes Simulia Corp. Providence, RI, 2009.

2nd International Conference on Mathematical and Computational Biomedical Engineering - CMBE2011
March 30 - April 1, 2011, Washington D.C, USA
P. Nithiarasu and R. Löhner (Eds.)

FSI analysis of a diseased human trachea before and after prosthesis implantation

M. Malvè*, A. Pérez del Palomar*, S. Chandra, J.L. López-Villalobos***, E. Finol**, A. Ginel*** and M. Doblaré***

*Group of Structural Mechanics and Materials Modeling, Aragón Institute of Engineering Research (I3A), Universidad de Zaragoza (Spain), C/María de Luna 3, E-50018 Zaragoza
Centro de Investigación Biomédica en Red en Bioingeniería Biomateriales y Nanomedicina (CIBER-BBN), C/Poeta Mariano Esquillor s/n, E-50018 Zaragoza,
mmalve@unizar.es

**Institute for Complex Engineered Systems (ICES), Carnegie Mellon University, 5000 Forbes Avenue, Pittsburgh, PA 15213, USA

***Hospital Virgen del Rocío, Department of Thoracic Surgery, Avenida de Manuel Siurot s/n, E-41013 Seville, Spain

SUMMARY

Endotracheal stenting technique is the common treatment for tracheal disorders as stenosis, chronic cough or dispnoea episodes. Medical treatment and surgical technique are still challenging due to the difficulties to overcome potential prosthesis complications. In this work we analysed the response of a stenotic trachea after a stent implantation. A finite element model of a diseased and stented trachea was developed starting from patient specific computerized tomography (CT) scan. Tracheal wall was modelled as a fiber reinforced hyperelastic material introducing the anisotropy due to the orientation of the collagen fibers. Deformations of the tracheal cartilage rings and of the muscle membrane, as well as the maximum principal stresses, are analysed with FSI approach. As boundary conditions, impedance-based pressure waveforms were computed, modelling the non reconstructed lung vessels as binary fractal network. The results showed that, the presence of the stent prevents tracheal muscle deflections and evidenced possible mucous plugging. The present work gives a new insight in clinical procedures predicting the mechanical consequences of a prosthesis implantation. This tool could be used in the future as a preoperative planning software to help the thoracic surgeons in deciding the optimal stent type as well as its size and positioning.

Key Words: *Fluid Structure Interaction, impedance method, fiber reinforced material, trachea, stenosis, stent.*

1 INTRODUCTION

Tracheal stenosis, which is the most common tracheal injury, is usually caused by a tracheotomy intubation with unsuitable pressure. Prolonged ischemia and infection causes necrosis of the tracheal wall and deterioration of the cartilaginous structure through the formation of granulation tissue. This granulation may lead to the collapse of the tracheal wall. Many methods are available to deal with tracheal stenosis as tracheal dilation, excision of stricture and anastomosis (end-to-end joining after resection of a tracheal part) or reconstruction but, after treatment, the stenosis may reappear especially in case of serious injuries. A clear understanding of how the implantation of

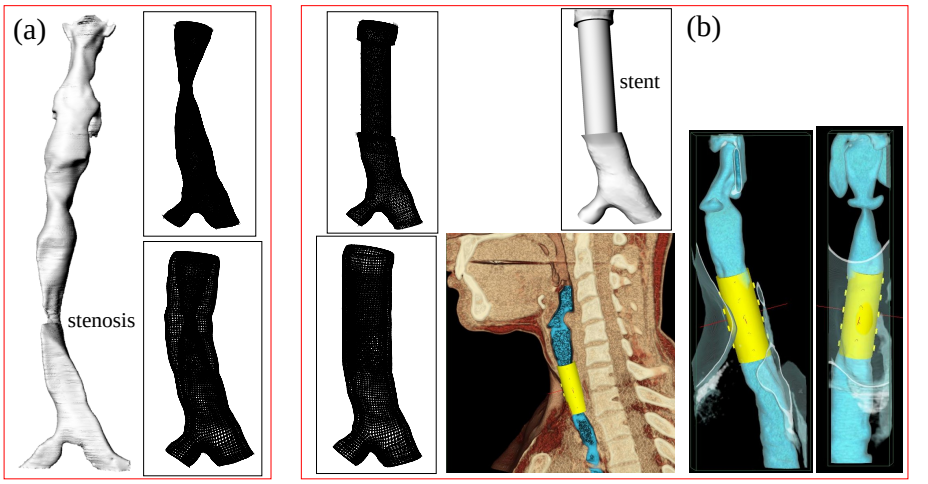

Figure 1: Geometry and computational grid of the diseased (a) and stented (b) CT-reconstructed trachea.

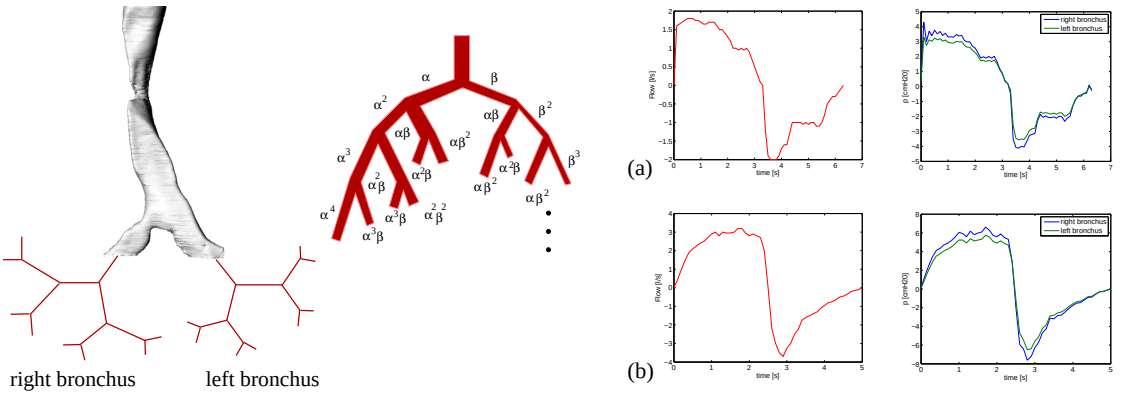

Figure 2: Fractal network (left) and impedance-based outflow conditions (right) for stenotic (a) and stented (b) trachea.

a prosthesis affects the response of the trachea is challenging. The analysis of these aspects using computational approach may improve surgical outcomes studying a more convenient prosthesis design, and/or determine the stent positioning before surgery. In fact, although after prosthesis implantation, patients gain around 50% of breathing capability, other problems may take place, because of the increased rigidity of the tracheal wall due to the presence of the prosthesis [1], such as coughing difficulties, stent migration, inflammatory granulation tissue, and, formation, and obstruction secondary to the interference with mucociliary clearance [1]. While most of the published works, analysed airflow patterns using idealized or approximated airways geometries [2,3,4] and only a few were based on accurate airways geometries obtained from medical images, more recently, fluid structure interaction studies in lower healthy airways were performed for simplified models/geometries, tracheal tube and single or multiple bifurcations [5,6]. The aim of this study is the analysis of the impact of a prosthesis on the tracheal walls, especially on the muscle deflections. In this sense, this could be considered a first step to create a tool for analysing pre- and post-operatory tracheas in order to help surgical decisions.

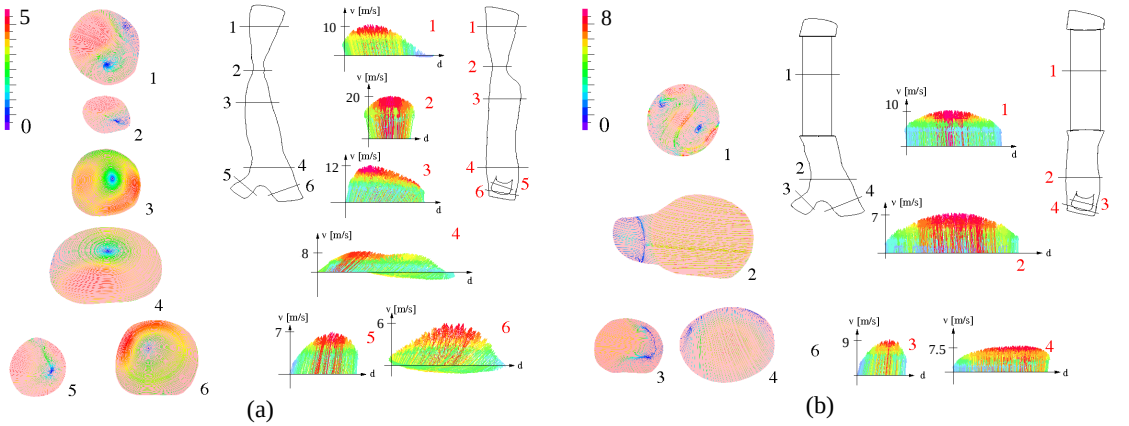

Figure 3: Streamlines of the stenotic (a) and stented (b) trachea during forced expiration.

2 MATERIAL AND METHODS

The finite element model of the human trachea was made based on a CT scan performed to a 56 years old diseased patient before and after prosthesis implantation. A full hexahedral mesh of the trachea was made using ABAQUS (Figure 1). Regarding the fluid domain, a tetrahedral-based fluid grid was generated filling the tracheal channel using the commercial software IcemCFD (ANSYS Software). The final mesh was then imported in the software package ADINA $R\&D$ Inc. where the fluid-structure interaction analysis was performed. Cartilage rings and membrane muscle, in which we considered the preferential orientations due to the collagen fibers, were characterized using a constitutive model described in previous works [11,6]. Airflow was assumed turbulent (the $k-\omega$ model was used). As boundary conditions, impedance pressure waveforms were computed starting from a patient specific spirometry performed before and after the surgery (Figure 2). The impedance method is well known in literature for cardiovascular [7,8,9] and pulmonary system [10].

3 RESULTS

Expiration, which is crucial for stenting migration during breathing and coughing was analyzed. The exhalation flow is regulated from the two daughters airways. In the trachea, a swirl-flow develops, a cause of the asymmetric flow divider: the swirl-flow coming from the right bronchus joins those coming from the left with indentation of the skewed velocity profiles of both main bronchi. This flow type, visible also in the section 3 of Figure 3 (a), induces a typical swirl-flow in the upper section of the trachea (Figure 3 (a), section 1) resulting in a skewed profile with reversed velocity components caused by the stenotic geometry. The flow through the stent is axial, strongly flattened by the turbulence regime and by the geometry of the stent, as shown in the Figure 3 (b). No secondary flow was found in the main bronchi. While normal breathing and coughing are characterized by an important movement of the muscular membrane which increases the section of the trachea during inhalation and decreases it during expiration [6] contributing to the pressure-balance inside the lungs, the stent implantation massively affect the tracheal behaviour. In particular, the muscle deflection which is prevented by the stenotic fibrous cap in the diseased trachea, is still prevented by the prostheses after surgery. This is especially relevant during coughing since the muscle deflection are more important than during breathing [6]. Finally, we observed that the high velocity jet crossing the stent causes a recirculation at the top of the prosthesis, near

the tracheal wall, which, as documented in literature [1] is a region predisposed to mucous deposition. This work confirms that after a surgical stent implantation, even the patient acquires part of the lost pulmonary capacity (compare Figure 2 (a) and (b)), the fluid flow seems to be cause of well known post-operatory problems.

4 CONCLUSIONS

We presented a detailed approach to simulate pre- and post-operatory human trachea under impedance outflow conditions. In particular we analysed the expiratory flow. To correctly evaluate tracheal wall stresses, strains and muscle deflections, we applied the impedance method which allows the computation of pressure waveforms at the outlet of the 3D domain, modelling the non-imageable vessels of the lungs as a binary network. We found that during exhalation, the mechanical response of the tracheal muscle is prevented by the presence of the stent and the flow patterns show a recirculation which can cause mucous plugging. Quantification of flow patterns inside different airway geometries due to different prostheses could be performed before a surgery in order to help the surgical technique and the choice of stent type. In the future, this may help clinical outcomes.

REFERENCES

[1] F. Sun, J. Uson, J. Ezquerra, V. Crisostomo, L. Luis and M. Maynar, Endotracheal stenting therapy in dogs with tracheal collapse, *The Veterinary Journal*, 175, 186-193, 2008.

[2] R.K. Calay, J. Kurujareon and A.E. Holdo, Numerical simulation of respiratory flow patterns within human lungs, *Respiratory Physiology and Neurobiology*, 130, 201-221, 2002.

[3] T. Gemci, V. Ponyavin, Y. Chen, H. Chen and R. Collins, Computational model of airflow in upper 17 generations of human respiratory tract, *Journal of Biomechanics*, 41, 2047-2054, 2008.

[4] B. Ma, K.R. Lutchen, An anatomically based hybrid computational model of the human lung and its application to low frequency oscillatory mechanics. *Annals of Biomedical Engineering*, 34(11), 1691-704, 2006.

[5] W.A. Wall and T. Rabczuk, Fluid-structure Interaction in lower airways of CT-based lung geometries. *International Journal for Numerical Methods in Fluids*, 57, 653-675, 2008.

[6] M. Malvè, A. Pérez del Palomar, J.L. López-Villalobos, A. Ginel, M. Doblaré, FSI analysis of the coughing mechanism in a human trachea. *Annals of Biomedical Engineering*, 38(4), 1556-1565, 2010.

[7] M.S. Olufsen, A structured tree outflow condition for blood flow in larger systemic arteries, *American Journal of Physiology - Heart and Circulatory Physiology*, 276, H257-H268, 1999.

[8] M.S. Olufsen, C.S. Peskins, W.Y. Kim, E.M. Pedersen, A. Nadim and J. Larsen, Numerical simulation and experimental validation of blood flow in arteries with structured tree outflow conditions, *Annals of Biomedical Engineering*, 28, 1281-1299, 2000.

[9] B.N. Steele, M.S. Olufsen and C.A. Taylor, Fractal network model for simulating abdominal and lower extremity blood flow during resting and exercise conditions, *Computer Methods in Biomechanics and Biomededical Engineering*, 10(1), 37-51, 2007.

[10] A. Comerford, C. Foerster W.A. Wall, Structured Tree Impedance Outflow Boundary Conditions for 3D Lung Simulations, *Journal of Biomechanical Engineering*, 132, 081002-1/10, 2010.

[11] O. Trabelsi, A. Pérez del Palomar, J.L. Lopez-Villalobos, A. Ginel, M. Doblaré, Experimental characterization and consitutive modelling of the mechanical behaviour of the human trachea, *Medical Engineering and Physics*, 32, 76-82, 2010.

2nd International Conference on Mathematical and Computational Biomedical Engineering CMBE2011
March 30 - April 1, 2011, Washington D.C, USA
P. Nithiarasu and R. Löhner (eds)

VALIDATION AND COMPARISON OF DIFFERENT FLUID-STRUCTURE INTERACTION SCHEMES IN HAEMODYNAMIC APPLICATIONS

Fabio Nobile [†], **Matteo Pozzoli** [†], **Cristian Vergara** [♯]

[†] MOX-Dipartimento di Matematica, Politecnico di Milano,
Piazza Leonardo da Vinci 32, 20133 Milan, Italy
fabio.nobile@polimi.it,
matteo1.pozzoli@mail.polimi.it

[♯] Dept. of Information Technology and Mathematical Methods,
Università degli Studi di Bergamo, Viale Marconi 5, 24044 Dalmine (BG), Italy
christian.vergara@unibg.it

SUMMARY

In this work we focus on particular topics for the numerical solution of the Fluid-Structure Interaction problem in the haemodynamics context.

Key Words: *Fluid-Structure Interaction, partitioned schemes, temporal schemes.*

1 INTRODUCTION

In this work we focus on the numerical solution of the Fluid-Structure Interaction (FSI) problem in the context of haemodynamics applications. In particular, we investigate and apply some numerical strategies for different topic, such as i) the prescription of suitable clinical boundary conditions, ii) the comparison between schemes that treat in an implicit or in an explicit way the interface position, based on the introduction of a new test with analytical solution for the FSI problem, iii) the comparison between the convergence properties of the Robin-Robin algorithm varying the temporal schemes both for the fluid and for the structure problem.

2 MAIN BODY

In this work we focus in the modeling and in the numerical simulation of the Fluid-Structure Interaction (FSI) problem in vascular dynamics. The blood is modelled as an incompressible Newtonian fluid and the vessel as a linear elastic structure in a truncated computational domain.

A difficult task in hemodynamic simulations concerns the prescription of realistic boundary data on the artificial sections as, typically, only partial data are available. At the inlet

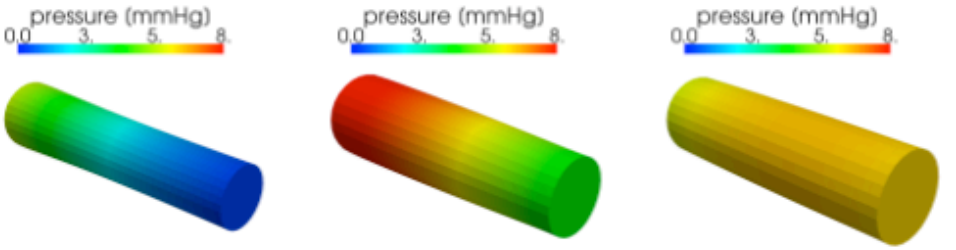

Figure 1: Fluid velocity at the time T = 0.005 s, T=0.010 s and T=0.015 s.

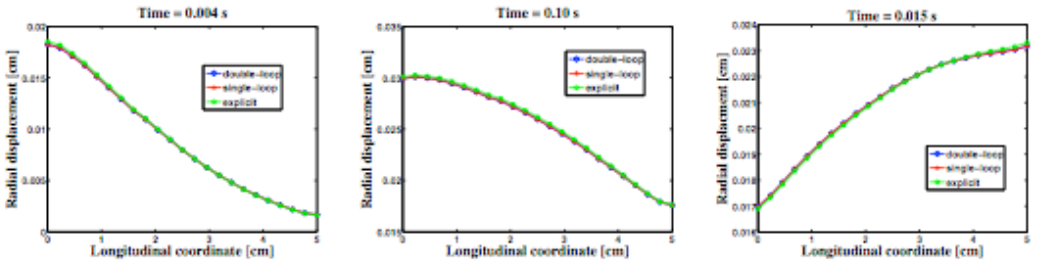

Figure 2: Radial displacement for three algorithms at the time T = 0.005 s, T=0.010 s and T=0.015 s.

For the comparison among different temporal schemes, we consider backward differential formulae (BDF) for fluid and structure, θ-method for the fluid, and Newmark and α-generalized methods for the structure. First of all, we observe in Figure 3 that all these shemes converge towards the analytical solution, with the expected convergence rate.

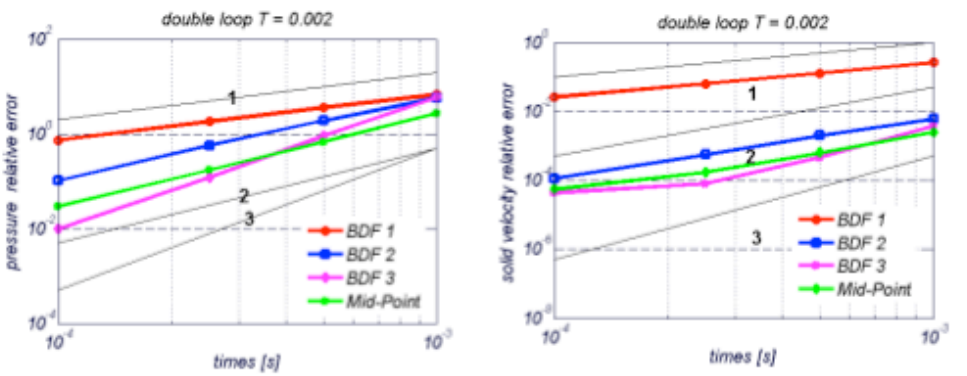

Figure 3: Convergence rate for different temporal schemes. Fluid pressure solution (left) and structure velocity solution (right). Time = $t = 0.002\,s$.

Finally, we study the convergence performance of Robin-Robin algorithm varying the temporal schemes. From the proposed theoretical analysis and from the numerical results, we observe that the temporal schemes influence the convergence of the algorithm.

we impose the flow rate by the Lagrange multiplier approach proposed in [4]. Moreover, to avoid spurious reflections of pressure waves, we introduce new *absorbing resistance boundary conditions*.

The numerical discretization of FSI problem requires the management of the *interface continuity conditions* and the treatment of the *interface position*. For the treatment of the interface position (and fluid convective term) we consider two possible treatments: explicit or implicit. In the explicit treatment, we extrapolate the interface position from previous time steps, whilst, in the implicit treatment, the interface position is an unknown of the problem, and it is necessary to solve a non-linear problem, introducing fixed-point iterations.

At each time step in the explicit treatment or at each fixed-point subiteration in the implicit treatment, we obtain a linearized FSI problem, where the satisfaction of the interface continuity conditions is mandatory. In this work, this is guaranteed by using *partitioned procedures*, where the fluid and the solid subproblems are solved separately until convergence and are coupled through transmission conditions. In particular, we consider the Robin-Robin (RR) scheme introduced in [1].

Where an implicit treatment of the interface position is considered, we distinguish two algorithms: i) A *single-loop* scheme, where just one loop is considered to update the interface position and the continuity conditions; ii) A *double-loop* scheme, where we introduce two loops, an external one for the update of the interface position, and an internal loop for the treatment of the interface continuity conditions. We provide a comparison among these three schemes, aiming at investigating which of them is effective in haemodynamics applications.

Then, we consider different temporal schemes for the discretization of the fluid and of the structure subproblems. The aim here is to check the global convergence rate of the time discretization of the FSI problem. To do this, we introduce a new test case where an analytical solution for the FSI problems is provided.

Finally, we would like to investigate the convergence properties of the Robin-Robin scheme when different temporal schemes are considered for the time discretization of the fluid and structure subproblems. Indeed, the coefficients of transmission conditions in the Robin bc depend on the temporal scheme. This fact influences the convergence velocity of the different temporal schemes. For the comparison, we propose a theoretical convergence analysis on a reduced FSI model for the different temporal schemes, extending the results obtained in [2], [1] and [3].

3 NUMERICAL RESULTS

We consider a cylindrical domain and we impose at the inlet a sinusoidal flow rate and at the outlet an absorbing resistance condition. In Figure 1 we show the fluid pressure at time $t = 0.005\,s$, $t = 0.010\,s$ and $t = 0.015\,s$. In Figure 2, we show the radial interface displacement obtained with the three algorithms. We observe that the solution obtained with implicit algorithms are the same, whilst the solution obtained with an explicit algorithm is slightly different.

Moreover, we observe that for the explicit algorithm, some temporal schemes result more stable than others. For example, when the mid-point scheme is used for the structure, the interface displacement features numerical oscillations in the phase of decompression. Otherwise, algorithms based on BDF schemes do not exhibit this phenomenon.

References

[1] S. Badia, F. Nobile, C. Vergara *Fluid-structure partitioned procedures based on Robin transmission conditions Journal of Computational Physics*, Volume 227, Issue 14, Pages 7027-7051, July 2008

[2] P. Causin, J-F. Gerbeau and F. Nobile,*Added-mass effect in the design of partitioned algorithms for fluid-structure problems*. Comput. Methods Appl. Mech. Engrg. 2005, vol. 194/42-44, pp. 45064527.

[3] L. Gerardo-Giorda, F. Nobile, and C. Vergara, *Analysis and optimization of Robin-Robin partitioned procedures in fluid-structure interaction problems*. SIAM J. Num. Anal. 2010

[4] L. Formaggia, A. Veneziani, C. Vergara *Flow rate boundary problems for an incompressible fluid in deformable domains: Formulations and solution methods*. Computer Methods in Applied Mechanics and Engineering, Volume 199, Issues 9-12, Pages 417-778 (15 January 2010)

2nd International Conference on Mathematical and Computational Biomedical Engineering - CMBE2011
March 30 - April 1, 2011, Washington D.C, USA
P. Nithiarasu and R. Löhner (Eds.)

FSI Analysis of a Human Carotid Bifurcation under Impedance-Based Boundary Conditions

M. Malvè[⋆], S. Chandra[⋆⋆], A. García[⋆], M.A. Martínez[⋆], E. Finol[⋆⋆] and M. Doblaré[⋆]
[⋆]Group of Structural Mechanics and Materials Modeling, Aragón Institute of Engineering Research (I3A), Universidad de Zaragoza (Spain), C/María de Luna 3, E-50018 Zaragoza, Spain
Centro de Investigación Biomédica en Red en Bioingeniería Biomateriales y Nanomedicina (CIBER-BBN), C/Poeta Mariano Esquillor s/n, E-50018 Zaragoza, Spain
mmalve@unizar.es
[⋆⋆]Institute for Complex Engineered Systems (ICES), Carnegie Mellon University, 5000 Forbes Avenue, Pittsburgh, PA 15213, USA
finol@andrew.cmu.edu

SUMMARY

In this study, we develop structured tree outflow boundary conditions for modeling the human carotid bifurcation hemodynamics. The model geometry was reconstructed through computerized tomography (CT) scan. Unsteady state CFD analyses were performed under different conditions using a commercial software package (ADINA $R\&D$ Inc.) in order to assess the impact of the boundary conditions on the flow variables. In particular, the results showed that the peripheral vessels significant impact the pressure while the flow is relatively unaffected. In addition, an unsteady FSI simulation was carried out using impedance-based conditions in order to evaluate the dependence of the wall shear stress (WSS) on the arterial wall compliance in the carotid bifurcation. For this reason, a comparison between FSI and rigid-wall models was conducted. Results showed that the wall shear stress distributions were substantially affected by the diameter variation of the arterial wall. In particular, even similar WSS distributions were found for both cases, the computed WSS values significantly varied.

Key Words: *Carotid bifurcation, CFD, FSI, impedance method, blood flow, wall shear stress.*

1 INTRODUCTION

It has been well accepted that low and oscillating flow shear stresses correlate positively with intimal thickening and atherosclerosis progression [4,5]. Even still debated in literature, this hypotesis considerably influenced the research in the atherogenesis field in recent years [5]. However, more recent studies often associated plaque progression and lumen narrowing in carotid bifurcation with high wall shear stress [4]. Carotid hemodynamics is very sensitive to geometrical factors as tortuosity, curvature ratio and bifurcation angle [3,6]. Recently, extensive studies were conducted on computational fluid dynamics (CFD) for healthy carotid providing statistical analyses of correlation between disturbed flow with bifurcation geometry of several patients [3,6]. Due to the interindividual variability of geometry and flow dynamics, this sensitivity is crucial and challanging for CFD models and fluid structure interactions (FSI) features. While most of the works on FSI are oriented to the statistical stress analysis of atheroscerotic plaque [4,7], others [2] try to validate the hypothesis that low or oscillatory shear and high maximum principle cyclic

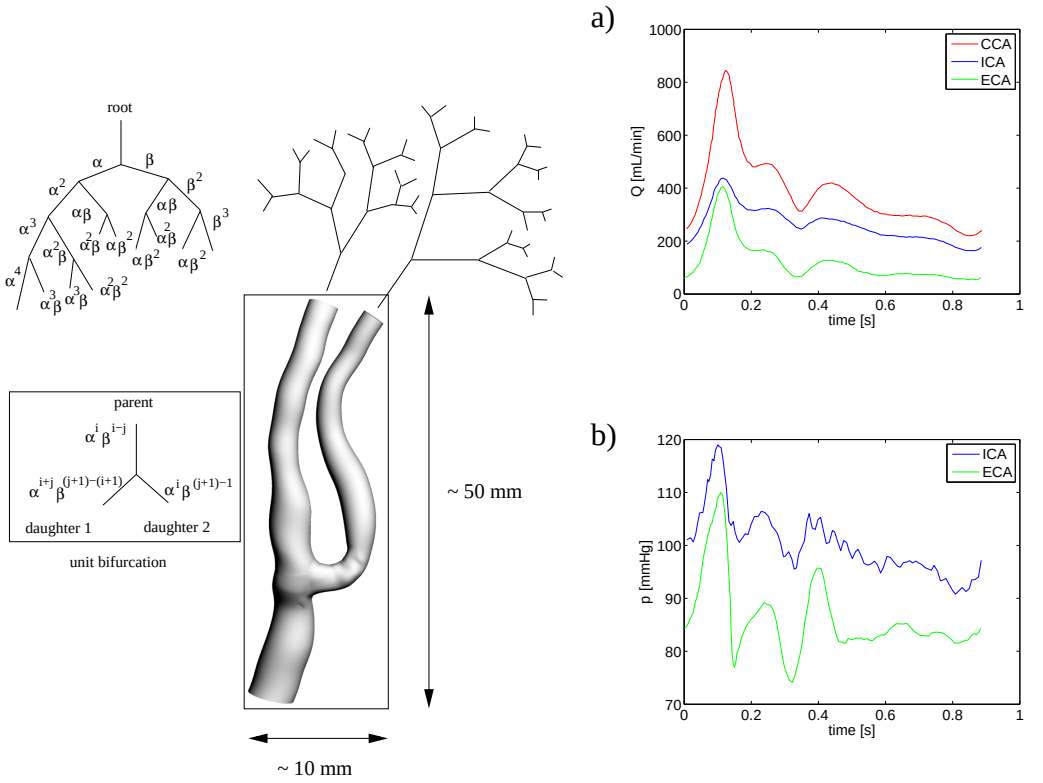

Figure 1: Geometry, fractal network and boundary conditions of the CT-reconstructed carotid bifurcation (inflow (a) and impedance-based outflow conditions (b)).

strain correlate with known inflammation sites in the carotid bifurcation. The aim of this work is to apply to a carotid bifurcation the impedance method in order to obtain physiological pressure boundary conditions as a function of the inflow and of the geometry of the artery. This method can be considered an attractive tool to compute physiological intravascular pressures when these are not available and/or considering the difficulties and the limitations to get these data *in vivo*. Moreover, to assess the importance of the FSI analysis (where pressure informations are necessary to compute the wall compliance), we applied the impedance-based conditions to evaluate how the wall compliance can affect the blood flow pattern and the WSS in a human carotid comparing fluid-structure interaction analysis with rigid wall simulation.

2 MATERIAL AND METHODS

The patient-specific carotid geometry was reconstructed using computed tomography (CT) scans at one time point of the cardiac cycle. The arterial tree considered in this study included the common carotid (CCA) and its principle branches: the internal (ICA) and the external (ECA). A fluid tetrahedral mesh of about 200000 elements was generated using the commercial software IcemCFD (Ansys Software Inc.) starting from the internal shell that represents the numerical fluid solid interface domain. For the solid grid, since no data were available from real images, a constant thickness was given to the arterial wall. A full hexahedral mesh of about 60000 elements was created using the meshing tool of the commercial software ABAQUS Inc. The geometry of the considered model is represented in Figure 1. The final mesh was imported into the software package ADINA $R\&D$ Inc. where the FSI and rigid wall simulations were performed. Blood rheology was assumed as Newtonian. In particular, according to literature, the blood density and the

blood viscosity were taken as 1067 Kg/m^3 and 0.0035 N/m^2 respectively. Since the Reynolds number based on the average arterial diameter was about $Re = 950$, the blood flow was assumed laminar and incompressible under unsteady flow conditions. The carotid wall was modeled as a hyperelastic incompressible isotropic and homogeneous material. For this preliminary study, the viscoelasticity, the active behavior of muscle fibers of the artery, and the intrinsic anisotropy, due to the preferencial directions of collagen and muscle fibers, were not considered. The carotid bifurcation was then characterized by the following strain energy function W:

$$W = \frac{a}{b}\left[exp\left(\frac{b}{2}(\overline{I}_1 - 3)\right) - 1\right] + U(J), \tag{1}$$

where $\overline{I}_1$ is the first invariant of the deviatoric right Cauchy-Green tensor $\overline{\mathbf{C}} = J^{-2/3}\mathbf{F}^T\mathbf{F}$, $J = det(\mathbf{F})$ is the Jacobian, $\mathbf{F}$ is the standard deformation gradient, U is the volumetric energy function and a, b are material constants. In particular we considered $a = 44.2\ kPa$ and $b = 16.7$ [1,2].

3 RESULTS

The importance of using impedance-based pressure conditions is assessed first comparing different outflow conditions (impedance-based pressures and simply traction free conditions) using the same geometry and the same approach (CFD). The results show that even similar pressure distributions are found, the time history of the pressure is completely different for the two scenarios (see Figure 2). From a physiological perspective the above is the major importance because the correct evaluation of the intravascular pressure plays an important role in the cardiovascular mechanics, especially in diseased patients. Moreover, intravascular pressure are crucial for evaluating arterial stress distributions which, as reported by [1,2] among others is recognized to play an important role in combination with the WSS distributions for initiation, develop and progression of atherosclerosis. WSS was computed and compared for FSI and rigid wall models. Its temporal history showed that significant differences can be found between the considered cases. The computed WSS distributions show higher values if computed with CFD simulation rather than FSI analysis in each carotid branches. The TAWSS was also analyzed for both FSI and CFD simulation, in order to assess the importance of FSI in determinig carotid hemodynamics. Its distribution resulted different for the two cases confirming that the wall compliance can be neglected only in first approximation while studying carotid hemodynamics. The wall stresses and strains were finally analyzed. The maximal stress is located at the side wall region of the intersection of the two branches and exhibits a low WSS distribution. This correlation between the low WSS with the maximal arterial wall stress in this location is consistent with that of previous investigators [2,5].

4 CONCLUSIONS

The proposed impedance method can be considered a very attractive tool to compute physiological pressures starting from blood flow measures. In fact, while intravascular flow can be obtained with standard techniques through non invasive measurements (as ultrasound Doppler for example), intravascular pressures required the use of invasive probes which can affect the overall blood flow during the measure. Comparison with standard outflow conditions demonstrated clear differences between the numerical results of the computed pressures. Moreover, while standard boundary conditions provide almost the same WSS distributions in comparison with those obtained with impedance-based conditions, these cannot be used to compute the wall stresses and strains which are important factors to take into account in atherogenesis. Comparison of computational results

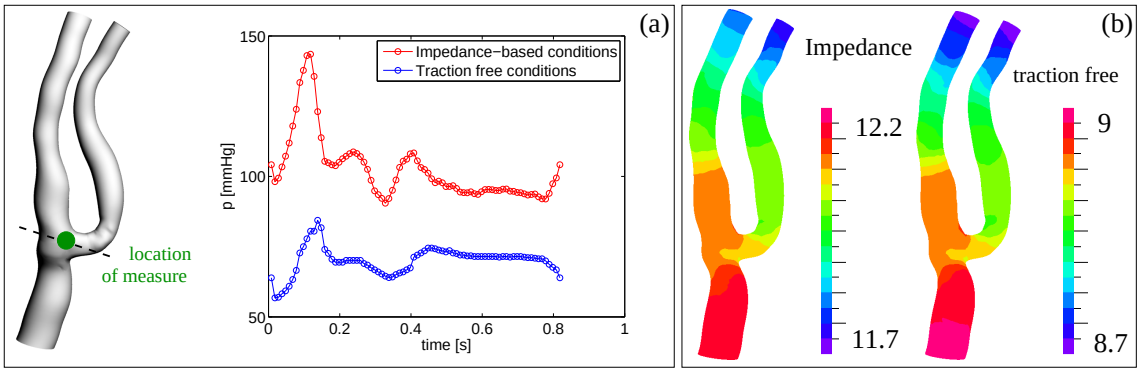

Figure 2: Comparison of the temporal intravascular pressure history (a) and of the diastolic pressure distribution (b) (in [kPa]) between impedance and traction free conditions.

between rigid and compliant arterial wall showed not only remarkable qualitative discrepances in the WSS distribution, but also relevant differences in the WSS temporal profiles. This confirms that to study the atherogenesis for carotid hemodynamics, arterial wall compliance can be neglected only in first approximation since, for an accurate WSS computation, wall displacements can play an important role. Computed wall stresses showed high values in correspondance to areas characterized by low wall shear stresses. As known, these zones are recognized to be subjected to high-risk of atherosclerosis. Identification of these areas could lead to future advance in the preventive medicine and from this point of view, numerical simulations should take into account the fluid and the structure in a coupled approach.

REFERENCES

[1] A. Delfino, N. Stergiopulos, J.E. Moore, J.J. Meister jr., Residual strain effect on the stress field in a thick wall finite element model of the human carotid bifurcation *Journal of Biomechanics*, 8, 777-786, 1997.

[2] H.F. Younis, M.R. Kaazempur-Mofrad, C. Chung, R.C. Chan, A.G. Isasi, D.P. Hinton, A.H. Chau, L.A. Kim, R.D. Kamm, Hemodynamics and wall mechanics in human carotid bifurcation and its consequences for atherogenesis: investigation of inter-individual variation, *Biomechanical Model Mechanobiology*, 3, 17-32, 2004.

[3] S.W. Lee, L. Antiga, J.D. Spence, D.A. Steinman, Geometry of the Carotid Bifurcation Predicts Its Exposure to Disturbed Flow. *Stroke* 39, 2341-2347, 2008.

[4] D. Tang, C. Yang, S. Mondal, F. Liu, G. Canton, T.S. Hatsukami, C. Yuan, A negative correlation between human carotid atherosclerosis plaque progression and plaque wall stress: *In vivo* MRI-based 2D/3D FSI models. *Journal of Biomechanics*, 41, 727-736, 2008.

[5] D.N. Ku, D.P. Giddens, C.K. Zarins, S. Glagov, Pulsatile Flow and Atherosclerosis in the Human Carotid Bifurcation: Positive Correlation Between Plaque Location and Low and Oscillating Shear Stress. *Arteriosclerosis*, 15, 293-302, 1985.

[6] J.B. Thomas, L. Antiga, S.L. Che, J.L. Milner, D.A. Hangan-Steinman, J.D. Spence, B.K. Rutt, D.A. Steinman, Variation in the carotid bifurcation geometry of young versus older adults: implications for geometric risk of atherosclerosis. *Stroke*, 36, 2450-2456, 2005.

[7] H. Gao, Q. Long, M. Graves, J.H. Gillard, Z.Y. Li, Carotid arterial plaque stress analysis using fluid-structure interactive simulation based on *in-vivo* magnetic resonance images of four patients. *Journal of Biomechanics*, 42, 1416-1423, 2009.

2nd International Conference on Mathematical and Computational Biomedical Engineering - CMBE2011
March 30 - April 1, 2011, Washington D.C, USA
P. Nithiarasu and R. Löhner (Eds.)

ADVANCED COMPUTATIONAL APPROACHES FOR FLUID-STRUCTURE INTERACTION IN HEMODYNAMICS

Wolfgang A. Wall, Michael W. Gee, Thomas Klöppel, Ulrich Küttler, Alexander Popp
Institute for Computational Mechanics, Technische Universität München
Boltzmannstr. 15, 85748 Garching b. München, Germany
e-mail: wall@lnm.mw.tum.de

SUMMARY

In this talk we will report on some novel computational approaches that we developed recently for challenging problems of fluid-structure interaction (FSI) in biomechanics and show their application to problems in hemodynamics on different scales. The focus will be on three new methods. First we will introduce a truly monolithic algebraic multigrid approach for fluid-structure interaction and show its advantageous performance for biomechanical FSI. In order to be able to treat non-conforming interfaces in an efficient and reliable way we have developed a dual mortar based strategy that is applicable to both monolithic and partitioned fluid-structure interaction approaches. And finally we will show how to treat 3D finite deformation contact in such FSI scenarios. We will apply a combination of our methods to problems like FSI for Abdominal Aortic Aneurysms, the simulation of red blood cells (in flow and through capillaries) and clamping of an aorta during surgery.

Key Words: *fluid-structure interaction, algebraic multigrid, dual mortar contact, non-conforming interfaces, AAA, red blood cells.*

1 METHODS

It is well known that biomechanical problems are often the most challenging multifield problems – not only from the point of view of modeling but also as far as computational techniques are concerned. One prominent class of multifield problems in bioengineering is fluid-structure interaction (FSI). Some of the challenges here come from the usually quite complex geometries – while already the initial geometry, usually obtained from medical imaging, is quite complex it sometimes even gets more complicated through changing topologies. Challenges also come from the complexity and special characteristics of the individual fields – complex nonlinear behavior and prestressing of soft tissue; complex, sometimes even turbulent, flows; etc. Another challenging fact for computational algorithms for FSI is that densities of fluid and tissue are in the same range which causes some coupling algorithms to diverge and some to converge very slowly. In order to meet these challenges we will introduce three novel computational approaches:

1.1 AMG(FSI) – Algebraic Multigrid Fluid-Structure Interaction

The first approach is concerned with the efficient solution of the coupled problem. In order to come up with an efficient solution strategy for this class of problems we are utilizing algebraic multigrid

principles. While multigrid methods have been excessively studied for single field phenomena, less attention has been given to the application of multigrid principles in complex multiphysics and multiscale simulations. In the presented approach, an AMG hierarchy for the nonsymmetric monolithic fluid, structure and mesh movement system of equations is constructed that considers a coarse representation of interfield off-diagonal coupling blocks in a variationally consistent way. This FSI multigrid preconditioner is based on a mixed smoothed aggregation and nonsymmetric smoothed aggregation approach that accounts for the hybrid nature of the monolithic FSI problem, where the underlying discretization is either conforming or non-conforming based on a dual mortar approach (see below). It limits the amount of artificial smearing of individual fields on coarse levels by construction and allows for field specific smoothers within its block oriented smoothing procedure.

1.2 DMFSI – Dual Mortar based Fluid-Structure Interaction

Because of the usually quite complex geometries involved and different meshing demands from the individual fields it is not always possible or advisable to use matching or conforming grids. Hence we present a novel approach to deal with non-matching grids in the context of fluid-structure interaction (FSI) simulations with the finite element method. The proposed method is based on the integration of a dual mortar method into the general FSI framework. The main focus is set on monolithic coupling algorithms for FSI as described above. In these cases the dual mortar approach allows for the elimination of the additional Lagrange multiplier degrees of freedom from the global system by condensation. The resulting system matrices have the same block structure as their counterparts for the conforming case and therefore permit the application of the above mentioned algebraic multigrid solver for monolithic FSI systems. For partitioned Dirichlet- Neumann coupling schemes it is shown that the dual mortar approach permits a numerically efficient mapping between fluid and structure quantities at the interface. Owing to its generality, the proposed method is not limited to any specific formulation neither for structure, fluid or ALE. The numerical and convergence behavior of state-of-the-art iterative solvers is shown to be comparable to standard simulations with conforming discretizations at the interface.

1.3 FSCI — Fluid-Structure-Contact Interaction

Many problems in biomechanics and more specifically in hemodynamics require the simulation of contact interaction of deformable solids embedded in fluid flow. Some examples are heart valves, synovial joints or capillary flow of red blood cells. Solving these types of systems requires powerful simulation approaches for both fluid-structure interaction (FSI) and finite deformation contact and poses several very challenging problems to state-of-the-art numerical methods and algorithms. First, the employed FSI scheme must be capable of dealing with large structural movements, rotations and deformations. Second, a contact formulation needs to be consistently integrated into the global FSI framework both in terms of its variational basis and its discretization. This second aspect requires special attention, since contact interaction by definition causes topology changes of the surrounding fluid domain. The proposed method for 3D fluid-structure-contact interaction combines a recently developed mortar contact formulation with a fixed-grid FSI approach based on the extended finite element method (XFEM). The derivation of a fully coupled discrete formulation as well as geometric aspects of how to accurately capture fluid-structure interfaces and contact regions will be addressed. Solution of the resulting linearized systems of equations is shown to be possible with either partitioned or monolithic fluid-structure coupling algorithms. Numerical examples demonstrate that flow patterns around approaching bodies close to contact

are resolved with high accuracy and in particular that dealing with the limit case of actual contact is straightforward within the proposed fixed-grid FSI framework.

2 CONCLUSIONS

Three novel computational techniques have been developed that allow high quality simulations of challenging fluid-structure interaction problems in hemodynamics. After introducing the methods and their advantages, combinations of these approaches have been applied to different FSI-problems in hemodynamics. The numerical examples range from FSI for Abdominal Aortic Aneurysms, the simulation of red blood cells (in flow and through capillaries) to the clamping of a human aorta during heart surgery. These examples demonstrate the versatility and efficiency of the proposed methods.

REFERENCES

[1] A. Gerstenberger, W.A. Wall, An eXtended Finite Element Method/Lagrange multiplier based approach for fluid-structure interaction. *Comp. Meth. in Appl. Mech. and Engng.*, 197:1699–1714, 2008.

[2] A. Gerstenberger, W.A. Wall, An embedded Dirichlet formulation for 3D continua, *Int. J. Numer. Meth. Eng.*, 82:537-563, 2010.

[3] M.W. Gee, U. Küttler, W.A. Wall, Truly monolithic algebraic multigrid for fluid-structure interaction. *Int. J. Numer. Meth. Eng.*, in press, DOI http://dx.doi.org/10.1002/nme.3001, 2010.

[4] T. Klöppel, A. Popp, U. Küttler, W.A. Wall, Fluid-structure interaction for non-conforming interfaces based on a dual mortar formulation. *Comput. Meth. Appl. Mech. Engrg.*, submitted, 2010.

[5] U. Küttler, M.W. Gee, Ch. Förster, A. Comerford, W.A. Wall, Coupling strategies for biomedical fluid-structure interaction problems. *Int. J. Numer. Meth. Biomed. Eng.*, 26:305–321, 2010.

[6] U.M. Mayer, A. Popp, A. Gerstenberger, W.A. Wall, 3D fluid-structure-contact interaction based on a combined XFEM FSI and dual mortar contact approach. *Comp. Mech.*, 46(1):53–67, 2010.

[7] A. Popp, M. Gitterle, M.W. Gee, W.A. Wall, A dual mortar approach for 3D finite deformation contact with consistent linearization. *Int. J. Numer. Meth. Eng.*, 83:1428-1465, 2010.

2nd International Conference on Mathematical and Computational Biomedical Engineering – CMBE2011
March 30 – April 1, 2011, Washington D.C., USA
P. Nithiarasu and R. Löhner (eds)

Morphogenesis: a multiphysics model for cell mechanics

D. Aubry*, R. Allena*
*Laboratoire MSSMat/CNRS UMR8579,
Ecole Centrale Paris, 92295 Chatenay-Malabry, France,
denis.aubry@ecp.fr, rachele.allena@ecp.fr

SUMMARY

Morphogenesis is the biological process that causes an organism to develop its shape. We describe here several particular aspects of its numerical modeling especially the coupling of morphogen concentration diffusion with mechanical strains. An inverse problem approach is finally considered to estimate several parameters which are currently out of reach of current measurements.

Key Words: *morphogenetic movements, active cell deformation, morphogen concentration diffusion-reaction, inverse problem.*

1 INTRODUCTION

Morphogenesis is the biological process that causes an organism to develop its shape. It can take place also in a mature organism, in cell culture or inside tumor cell masses. Modeling these movements is particularly interesting because it involves both cell and tissue behavior. Biologist scientists think furthermore that their understanding can also provide information on cell collective migration, which is fundamental to cancer metastatis development.

In embryogenesis, morphogenesis regulates the organized spatial distribution of cells and it involves a coordinated series of events that are triggered by a limited number of cellular processes such as migration, multiplication, stretching and folding of the epithelium. Tissues then undergo large deformations, including growth and contraction, so that their final configuration and the physical form of the organs are optimally designed to carry out their specialized functions.

Together with genetics and molecular biology, it has then become very important in the last decades to identify and better understand the mechanics of this space-time dependent process [5]. Several biological systems are observed to achieve this goal such as *Zebrafish*, *C. Elegans* or *Drosophila* embryos. The latter one has been the object of our research for the last few years and is illustrated here.

2 NEW MODELLING APPROACH OF ACTIVE CELL DEFORMATION INSIDE THE EPITHELIAL MEMBRANE

Very often in life sciences we find complex and irregular forms. The analytical description of their geometry represents a major issue when computer modeling is used to simulate their behavior. Furthermore, many biological systems such as tissues and membranes may deform themselves through a series of successive processes, so that their shape becomes more and more complicated. Even though recent new imaging techniques such as MRI (Magnetic Resonance Imaging) and CTI (Constant Time Imaging) together with several microscopy methods have played a significant role to provide digital images of living tissues, many fundamental parameters of the systems remain unknown. Therefore, for computer simulations drastic approximations of the real geometrical shapes are usually introduced. Such simplifications allow qualitatively describing elementary deformations, but still for highly idealized structures such as spheres, ellipsoids or other simple analytical geometries. Consequently, we have developed an intermediary technique, which lies at the middle line between an analytical approach for simplified biological structures and a digital segmentation of real complex living structures [2].

The key idea is to parametrize one of the coordinates of a general shell, specifically the thickness variable, using the electric potential, which is calculated by the classical Laplace's equation and to define then a curvilinear coordinates system, which enables to describe any type of three-dimensional geometry, even those showing irregularities or holes. Once the coordinate system has been defined, we are then able to introduce and model any type of elementary deformation occurring to the biological structure.

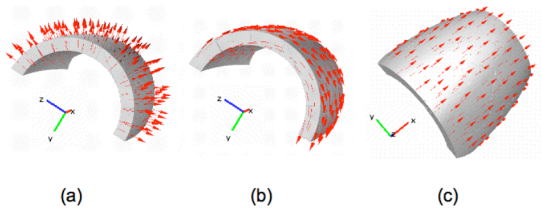

Fig. 1 Numerical computation of the curvilinear basis for a generic 3D structure using the *electrical* parametrization. (a) The normal vector $\boldsymbol{n}_0$. (b) and (c) The tangential vectors $\boldsymbol{V}_\theta$ and $\boldsymbol{V}_z$ respectively (for illustrative purpose only part of the 3D structure is represented).

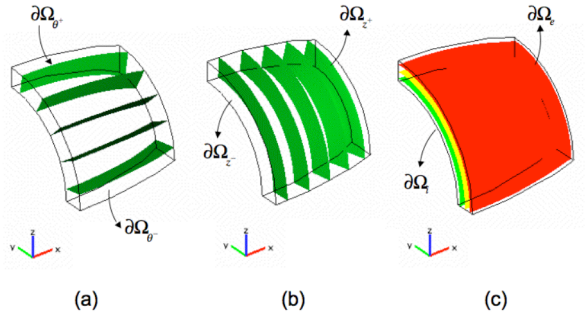

Fig. 2 Isovalues of the three potentials giving the coordinates system constituted by V_{ξ_1} (a), V_{ξ_2} (b) and V_{ξ_3} (c) (for illustrative purpose only part of the 3D structure is represented).

3 GRADIENT OF DEFORMATION DECOMPOSITION FOR TISSUE RESPONSE TO CELL DEFORMATION

As an example, a three-dimensional finite element model of the *Drosophila* embryo has been created in order to simulate three morphogenetic movements: ventral furrow invagination (VFI), cephalic furrow (CF) formation and germ band extension (GBE) [1]. The thin embryonic tissue modelled as a Saint-Venant material and a unilateral contact condition with the surrounding stiff vitelline membrane was implemented. The membrane encloses the yolk, not meshed here, which is considered to stay under uniform pressure implying a non-local pressure condition because of the volume conservation.
The large strains occurring to the cells are considered using a deformation gradient decomposition method. The total deformation $\boldsymbol{F}$ was split into two parts: an initial active deformation $\boldsymbol{F}_a^i$ which accounts for individual cell movements and a subsequent passive deformation $\boldsymbol{F}_m$ undergone by the adjacent tissues. Therefore we have

$$\boldsymbol{F} = \boldsymbol{F}_a^i \boldsymbol{F}_m \qquad (1)$$

The active deformations $\boldsymbol{F}_a^i$ change according to the morphogenetic movement considered. For the VFI (Fig. 3) and CF, apical constriction is implemented as the only active deformation responsible of the movement. Additionally, for the CF formation we have been able to reproduce the movements of the cells towards the anterior pole of the embryo, which, to our knowledge, has never been proposed in literature before. (Fig. 4) [3]. For GBE, we introduce an elongation along the antero-posterior axis of the embryo and a shortening along the dorsal-ventral axis, so that the convergent-extension movement of the tissues is simulated. Together with the individual simulations of the movements, we also proposed the concurrent simulation of the biological events.

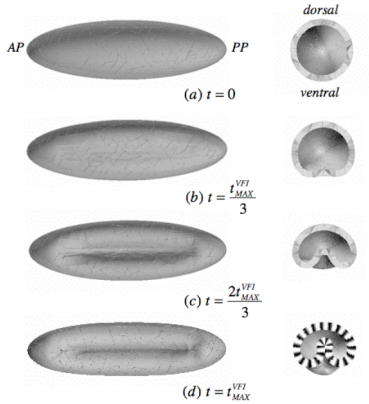

Fig. 3

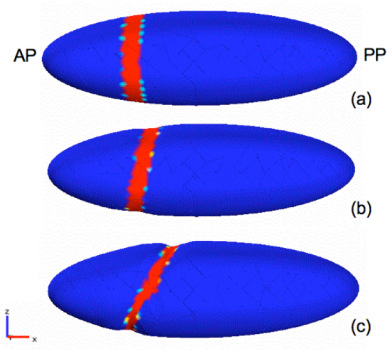

Fig. 4

Fig.3 Successive phases of VFI. On the left ventral views, on the right cross sections of the embryo (AP= anterior pole, PP= posterior pole). **Fig. 4** From (a) to (c), successive steps of the dynamic simulation of the CF tested for a hollow ellipsoidal geometry. In red the active region where the active deformation is introduced.

4 MECHANO-DIFFUSION OF MORPHOGEN

So far, the active deformations proper to each morphogenetic movements have been detected from experimental observations, therefore directly introduced in the model. The true link between mechanics, and the chemical and genetic activity remains less known. However recent biological experiments have shown that a diffusion phenomenon of

morphogen concentration, which is considered as an additional signaling parameter [4]. may drive and control these active celle deformations.
To couple the chemical and the mechanical fields, we introduce, on one hand, a simple linear relationship between the rate of the active deformation magnitude α and the actual concentration of morphogen per unit of deformed volume c as follows

$$\frac{d\alpha}{dt} = \beta \cdot c \qquad (2)$$

where β is a positive constant. On the other hand, the morphogen concentration c verifies the following diffusion-reaction equation in highly deforming media written in the initial configuration:

$$\frac{d(Jc)}{dt} = div_p\left(J\, k_D\, \boldsymbol{C}^{-1}\left(\nabla_p c\right)\right) + Jk_R c \quad (3)$$

with $J = \det \boldsymbol{F}$, k_D the diffusivity scalar constant, k_R the chemical reaction coefficient and $\boldsymbol{C} = \boldsymbol{F}^T \boldsymbol{F}$ is the Cauchy-Green deformation tensor.
By the individual simulations of three morphogenetic movements, we show that deformation patterns similar to those experimentally observed, can be modeled by properly combining the two phenomena.

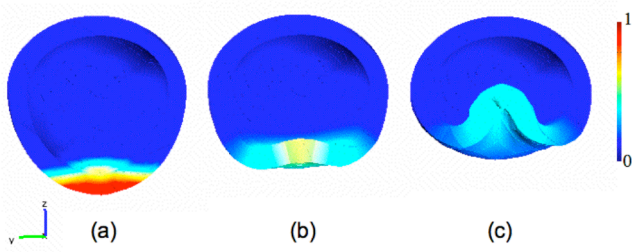

Fig.4 From (a) to (c) successive steps of the VFI simulation. As we can observe, the morphogen concentration c decreases as long as the active deformation increases so that the VFI occurs.

5 INVERSE PROBLEM APPROACH

Numerical simulation requires rather accurate quantification of material parameters, and geometries. In many areas this is a difficult issue to obtain experimentally such information but in morphogenesis this is particularly exacerbated.
Thus an inverse problem approach appears extremely valuable. We use a misfit function $J_{err,}$ which depends on parameters such as material properties, F_a the active deformations or even the internal shape of the embryo because often only the external boundary has been measured and identified.
The optimisation of the error function J_{err} is performed by computing the optimality equations for all the parameters via an adjoint state which allows to elegantly and efficiently compute its gradient. All the unknowns are finally computed using a Newton Scheme with unidirectional line search.
Several examples of such an approach applied to morphogenesis will be illustrated during the presentation.

6 CONCLUSIONS

We have discussed several aspects of morphogenesis simulation which couples individual cell movements with macroscopic tissue deformation. These peculiar cell deformations are activated by morphogen concentration, which satisfies a diffusion equation in deforming media. Results have been presented which shows how successful numerical simulation may be to understand complex phenomena such as invagination.

REFERENCES

[1] R. Allena, A. –S. Mouronval, D. Aubry, Simulation of multiple morphogenetic movements in Drosophila embryo by a single 3D Finite Element model, *JMBBM*, DOI 10.1016/j.jmbbm.2010.01.001, 2010.

[2] R. Allena and D. Aubry, A novel technique to parametrize shell-like deformations inside biological membranes, *Computational Mechanics*. DOI: 10.1007/s00466-010-0551-8, 2010.

[3] R. Allena and D. Aubry, An extensive numerical simulation of cephalic furrow formation in Drosophila embryo, *Computer methods in biomechanics and biomedical engineering*

[4] R. Allena, J. Muñoz, D. Aubry, Diffusion reaction model fro Drosophila embryo development. *To be published in Biomechanics and Modelling in Mechanobiology.*

[5] L.A. Taber Non linear elasticity: applications in biomechanics. World Scientific Publishing, Singapore.

2nd International Conference on Mathematical and Computational Biomedical Engineering - CMBE2011
March 30 - April 1, 2011, Washington D.C, USA
P. Nithiarasu and R. Löhner (Eds.)

MODELLING BLOOD FLOW THROUGH SUBJECT-SPECIFIC CAROTID BIFURCATIONS WITH PARTICULAR ATTENTION TO WALL SHEAR STRESS

R. L. T. Bevan*, P. Nithiarasu*, R. van Loon*, I. Sazonov* and H. Luckraz**
*Civil and Computational Engineering Centre, Swansea University, Swansea, SA2 8PP, UK.
P.Nithiarasu@Swansea.ac.uk
**Heart and Lung Centre, Royal Wolverhampton Hospital, Wolverhampton, UK.

SUMMARY

Blood flow modelling within a carotid artery bifurcation is of interest with regards to the genesis and diagnosis of atherosclerotic plaques. In the present study, the arterial geometries were reconstructed using AMIRA and an in-house meshing software. Boundary layer meshes were employed to accurately resolve high near-wall velocity gradients inside the artery. A locally conservative Galerkin (LCG) spatial discretisation was applied along with an artificial compressibility and characteristic based split (CBS) scheme to solve the 3D incompressible Navier-Stokes equations. The blood was modelled as a Newtonian fluid and a no-slip boundary condition was applied to the vessel wall. A Womersley profile was applied to the inflow and outflow boundaries. Turbulence was modelled using a Spalart-Allmaras one equation model in cases of severe stenosis. In order to analyse the transient flow within the carotids, haemodynamic wall parameters (HWPs) are utilised. Selected results have been presented in the current work, highlighting both the variations and conformities between inter-patient carotid haemodynamic wall parameter distributions.

Key Words: carotid bifurcation, patient-specific modelling, LCG, local flux conservation, CBS, wall shear stress

1 INTRODUCTION

Clinical observations have shown that atherosclerotic disease typically occur at regions of complex haemodynamics such as arterial bifurcations. Simulating the blood flow within the artery can provide understanding to the genesis and diagnosis of atherosclerotic plaques. Since cardiovascular disease is the principle cause of death in the United States, Europe and regions of Asia, this topic is of particular importance. Research has found that low or oscillatory wall shear stress is associated with atherogenesis and high oscillatory shear stresses have been shown to induce inflammatory pro-atherogenesis effects such as monocyte adhesion. Whereas high shear stresses have been linked to mechanical and/or chemical mechanisms that provide athero-protective effects. In the present work, six haemodynamic wall parameters from the literature are brought together and thoroughly investigated in order to assess atherosclerotic plaque formation [1].

In order to model the blood flow, the locally conservative Galerkin (LCG) method is employed within the characteristic based split (CBS) scheme. The technique was developed in order to rectify some of the inherent drawbacks of the discontinuous Galerkin (DG) methods while maintaining advantages such as explicit local and global conservation. Use of DG methods within

industry is often hampered by the large CPU and memory requirements, due to the need of storing multiple solutions at a node as well as solving for additional flux variables. To overcome these restrictions, the approach adopted within this work allows for the introduction of the interface flux into the continuous Galerkin framework [2, 3].

In this work we briefly outline the method used for flow simulation. In order to deal with domains including severe stenosis, turbulence modelling and Windkessel boundary conditions are introduced. The computational code developed in-house is described and its scalability discussed. It is then applied to study the fluid induced wall shear stress distributions on a number of patient-specific carotid bifurcation problems.

2 NUMERICAL SCHEME

2.1 Semi-discrete form of the characteristic based split (CBS) scheme

The present work couples the semi-discrete CBS scheme [4] with the LCG spatial discretisation [1, 3] procedure to obtain an element-wise solution strategy. The CBS approach adopted in this work, starts with a solution to an intermediate velocity field. This intermediate velocity field is then corrected, once the pressure field is obtained from a pressure (continuity) equation. Ignoring third and higher order terms, the three steps of the CBS scheme are defined respectively as:

$$u_i{}^{\dagger} = u_i{}^{n} - \Delta t \left(\frac{\partial u_j u_i}{\partial x_j} \right)^n + \Delta t \frac{\partial}{\partial x_j} \left(\frac{1}{Re} \frac{\partial u_i}{\partial x_j} \right)^n + \frac{\Delta t^2}{2} u_k \frac{\partial}{\partial x_k} \left(\frac{\partial u_j u_i}{\partial x_j} \right)^n \tag{1}$$

$$p^{n+1} = p^n - \beta^2 \Delta t \rho \frac{\partial}{\partial x_i} \left(u_i{}^{\dagger} - \Delta t \left(\frac{\partial p}{\partial x_i} \right)^n \right) \tag{2}$$

$$u_i{}^{n+1} = u_i{}^{\dagger} - \Delta t \left(\frac{\partial p}{\partial x_i} \right)^n + \frac{\Delta t^2}{2} u_k \frac{\partial}{\partial x_k} \left(\frac{\partial p}{\partial x_i} \right)^n \tag{3}$$

The artificial compressibility from of the CBS scheme is employed along with a dual-time stepping approach to recover the transient solution [4].

2.2 The Spalart-Allmaras turbulence model

If a stenosis is present within the domain, then the flow may experience transition from laminar to turbulent. If this is the case, a Spalart-Allmaras (SA) turbulence model is employed. It is a one equation model, which uses a single scalar equation and several constants to model turbulence. The SA model is applied as a fourth step to the CBS scheme. The SA model equation is given below

$$\underbrace{\frac{\partial \hat{\nu}}{\partial t} + \frac{\partial \hat{\nu} \bar{u}_i}{\partial x_i}}_{Convection} = \underbrace{\frac{1}{\sigma_{\hat{\nu}}} \left[\frac{\partial}{\partial x_i} (\nu + \hat{\nu}) \frac{\partial \hat{\nu}}{\partial x_i} + c_{b2} \left(\frac{\partial \hat{\nu}}{\partial x_i} \right)^2 \right]}_{Viscous\ \ diffusion} - \underbrace{c_{w1} f_w \left(\frac{\hat{\nu}}{d} \right)^2}_{Near-wall\ \ inviscid\ \ destruction} + \underbrace{c_{b1} \hat{S} \hat{\nu}}_{Production} \tag{4}$$

The reader is referred to [5] for further information on the SA model and the modifications required for Step 1 of the CBS scheme.

2.3 Boundary conditions

The blood dynamic viscosity and density are taken to be $\mu = 0.004$ kg/m s and $\rho = 1.0 \times 10^3$ kg/m^3 respectively. A no-slip boundary condition was applied to the vessel wall. The blood flow is assumed to be unsteady and fully developed with a Womersley profile being employed. Another alternative would be to use measured velocity profiles captured using MRI and phase contrast measurements. However, this was not possible in this case and thus a Womersley profile is used. Construction of the velocity profile, the harmonics used in waveform generation and the mapping procedure to map the the flow profile to a non-circular cross section can be found in [1, 6].

In order to simplify the boundary conditions, we have assumed an internal carotid artery (ICA) flow rate of 60% and an external carotid artery (ECA) flow rate 40% of the total common carotid artery (CCA) flow rate for healthy geometries.

3 MESH RECONSTRUCTION

Geometry was constructed from a set of CT images. The healthy right carotid from Patient 1 was constructed from a set of scans provided by Singleton Hospital, Swansea, UK. Further carotid geometries (left and right from each patient) were constructed from sets provided by Royal Wolverhampton Hospital, Wolverhampton, UK. At least one of the carotids in each of the Wolverhampton sets has been clinically diagnosed with a stenosis. The geometric reconstruction was undertaken using AMIRA. In order to improve the quality of the AMIRA surface mesh, surface coarsening and smoothing using the technique given by Saksono *et al* [7] was undertaken. Preparation of the surface mesh included introducing cuts to ensure the inlet and outlets were perpendicular relative to the arterial wall. To capture the high velocity gradient close to the wall boundary layers are required. They are constructed by projecting the surface points inward along the surface normal. A new surface mesh is constructed from these new points, with the same topology as the outer surface mesh. The two surface meshes are connected together and tetrahedra are formed by the subdivision of prismatic elements. Multiple boundary layers can be constructed through repetition of this technique. The volume mesh for the remainder of the domain is formed using a meshing solver based on the Delaunay method. The boundary layer mesh thickness exponentially decreases closer to the vessel wall [1, 7].

4 RESULTS

Six derived haemodynamic parameters were investigated in order to predict the locality of atherogenesis. These include time-averaged wall shear stress (WSS), oscillating shear index (OSI) and the wall shear stress angle deviation (WSSAD). Selected results of the time-averaged WSS are shown in the figure below. In the case of the right carotid of Patient 01 (PAT01R) and the left carotid of Patient 03 (PAT03L), the peak values occur at the stenosis proximal to the bifurcation. Low WSS is predicted along the outer wall of the ECA. Within the geometry of PAT03R, high WSS occurs near the flow divider. This is an athero-protected region. This is in good agreement with other reported work [8]. From PAT01R and PAT03L, high rather than low values of WSS are found at the stenosis. The low and oscillating wall shear stress hypothesis does not explain the continued growth of plaque, once sufficiently accumulated to alter the preceding shear stress distribution as seen in PAT01R and PAT03L. The predicted peak of 805 dyne/cm^2 in PAT03L is exceptionally high and damaging. This is greater than the 315 dyne/cm^2 that Holme *et al* [9] determined was sufficient to induce platelet activation and enhanced platelet thrombus formation.

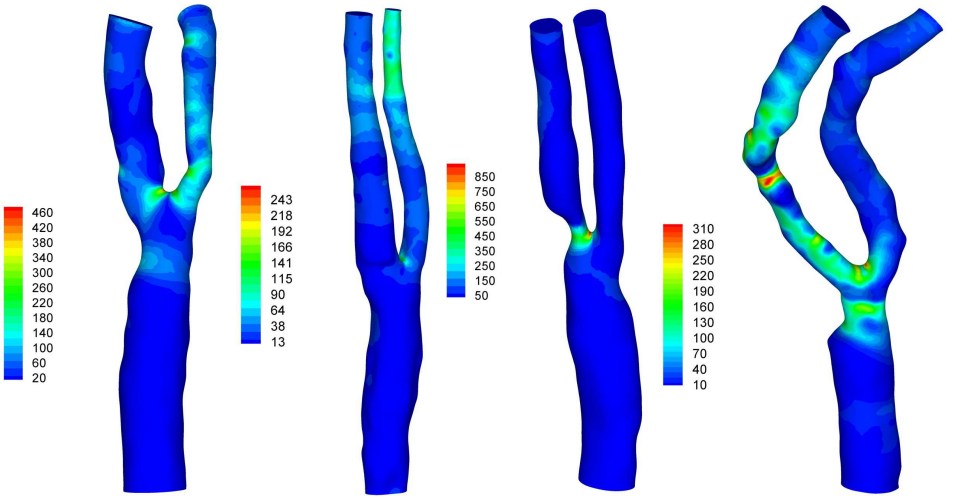

Figure 1: Figure showing the Time-Averaged Wall Shear Stress (dyne/cm^2) distribution for four carotids. (a) PAT01R (b) PAT03R (c) PAT03L (d) PAT04L

5 CONCLUSIONS AND FUTURE WORK

This short paper outlined a method of modelling blood flow and using haemodynamic wall parameters to analyse atherogenesis with the intention of geometrical classification. Work is ongoing in the analysis of further geometries and model refinement. Further research is certainly necessary both in terms of understanding the atherogenesis and classification of carotid stenoses.

References

[1] R.L.T. Bevan, P. Nithiarasu, R. Van Loon, I. Sazonov, H. Luckraz, and A. Garnham. Application of a locally conservative galerkin (lcg) method for modelling blood flow through a patient-specific carotid bifurcation. *International Journal for Numerical Methods in Fluids*, DOI: 10.1002/fld.2313.

[2] P. Nithiarasu. A simple locally conservative Galerkin (LCG) finite element method for transient conservation equations. *Numerical Heat Transfer, Part B Fundamentals*, 46:357–370, 2004.

[3] C. G. Thomas, P. Nithiarasu, and R. L. T. Bevan. The locally conservative Galerkin (LCG) method for solving incompressible Navier-Stokes equations. *International Journal For Numerical Methods in Fluids*, 57:1771–1792, 2008.

[4] P. Nithiarasu, R. Codina, and O. C. Zienkiewicz. The characteristic based split scheme - a unified approach to fluid dynamics. *International Journal for Numerical Methods in Engineering*, 66:1514–1546, 2006.

[5] P. Nithiarasu, C.-B. Liu, and N. Massarotti. Laminar and turbulent flow calculations through a model human upper airway using unstructured meshes. *Communications in Numerical Methods in Engineering*, 23:1057–1069, 2007.

[6] J. P. Mynard and P. Nithiarasu. A 1D arterial blood flow model incorporating ventricular pressure, aortic valve and regional coronary flow using the locally conservative galerkin (LCG) method. *Communications in Numerical Methods in Engineering*, 24:367–417, 2008.

[7] P. H. Saksono, P. Nithiarasu, and I. Sazonov. Computational flow studies in a subject-specific human upper airway using one-equation turbulence model. influence of the nasal cavity. *Int. J. Numer. Meth. Engng*, Submitted 2010.

[8] H. F. Younis, M. R. Kaazempur-Mofrad, R. C. Chan, A. G. Isasi, D. P. Hinton, A. H. Chau, L. A. Kim, and R. D. Kamm. Hemodynamics and wall mechanics in human carotid bifurcation and its consequences for atherogenesis - investigation of inter-individual variation. *Biomechanics and Modeling in Mechanobiology*, 3:17–32, 2004.

[9] P.A. Holme, U. Orvim, M.J.A.G Hamers, N.O. Solum, F.R.Brosstad, R.M Barstad, and K.S. Sakariassen. Shear-induced platelet activation and platelet microparticle formation at blood flow conditions as in arteries with a severe stenosis. *Arteriosclerosis Thrombosis and Vascular Biology*, 17:646–653, 1997.

2nd International Conference on Mathematical and Computational Biomedical Engineering – CMBE2011
March 30 – April 1, 2011, Washington D.C., USA
P. Nithiarasu and R. Löhner (eds)

NUMERICAL SIMULATION OF BLOOD FLOWS AROUND AORTIC VALVE LEAFLETS BY VIRTUAL FLUX METHOD

T. FUKUI* and K. Morinishi**
*Dept. of Mech. and Syst. Eng., Kyoto Inst. Tech,
Goshokaido-cho, Matsugasaki, Sakyo-ku, Kyoto 606-8585, Japan,
e-mail: fukui@kit.ac.jp
** Dept. of Mech. and Syst. Eng., Kyoto Inst. Tech,
Goshokaido-cho, Matsugasaki, Sakyo-ku, Kyoto 606-8585, Japan,
e-mail: morinisi@kit.ac.jp

SUMMARY

The heart pumps blood throughout the body efficiently owing to the heart valves operation. Aortic stenosis (AS) is one of the most common diseases related to dysfunction of the heart valves. In this study, we apply the virtual flux method to the 2D aortic valve leaflets, and consider the movements of the valve leaflets during cardiac cycle. The longitudinal length L and diameter D of the aorta are 200 mm and 20 mm. The shape of the sinus of Valsalva is approximated as a semi-ellipse. The Reynolds number Re at the peak velocity corresponds to 100. The aortic valves open due to pressure gradient and the blood flows toward the aorta. Vortices are obviously confirmed in the sinus of Valsalva, which are considered to help the aortic valves to close. We successfully reproduced the movements of the aortic valve leaflets during cardiac cycle by the virtual flux method.

Key Words: *Aortic valve, blood flow, sinus of Valsalva.*

1. INTRODUCTION

The aortic valve consists of three thin membranous cusps, which in the open position are displaced outward toward the aorta to eject blood in the left ventricle, and come together to seal the aortic orifice in the closed position. The heart pumps blood throughout the body efficiently owing to the heart valves operation. Aortic stenosis (AS) is one of the most common diseases related to dysfunction of the heart valves. The opening area of the valve decreases due to AS, which cause considerable reduction of amount of blood flow. Clinically, the severity of AS is evaluated by estimating the opening area of the valve. The opening area determined by using planimetry to trace manually at the level of the orifice usually includes some errors [1]. A modification of the Bernoulli equation is applied to determine the pressure gradient [2], however, there is a tendency for pressure gradients derived by echo data to be larger than those directly measured using invasive cardiac catheters. It is necessary to know blood flows around aortic valve and pressure drop changes due to AS in advance. Numerical simulation is expected to lead to a better understanding of AS and its dependence on flow parameters. In this study, we apply the virtual flux method (VFM) [3], which is a tool to describe stationary or moving body shapes, to the 2D aortic valve leaflets, and consider the movements of the valve leaflets during cardiac cycle.

2. METHODS
2.1. COMPUTATIONAL MODEL

Numerical simulation of blood flow in aorta with valve leaflets and sinus of Valsalva is performed. Figure 1 shows the schematic view of the 2-dimensional simulation model used in this study. The longitudinal length L and diameter D are set to 200 mm and 20 mm. The valve leaflets whose length is $D/2$ are placed at $2D$ from the inlet. The shape of the sinus of Valsalva is approximated as a semi-ellipse with the longitudinal length and depth are 20 mm and 10 mm, respectively.

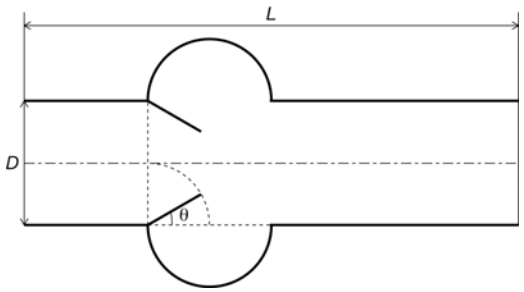

Figure 1. Schematic view of the computational model.

2.2. GOVERNING EQUATION

The lattice Boltzmann equation (LBE) with a 2D square lattice model with 9 velocities for incompressible fluid, which is proposed by He and Luo, is used as a governing equation.

$$p_\alpha(\boldsymbol{x}+\boldsymbol{e}_\alpha\Delta t, t+\Delta t) - p_\alpha(\boldsymbol{x},t) = -\frac{1}{\tau}\left\{p_\alpha(\boldsymbol{x},t) - p_\alpha^{(eq)}(\boldsymbol{x},t)\right\}, \tag{1}$$

where p_α is the distribution function, $p_\alpha^{(eq)}$ is the equilibrium distribution function, and τ is the relaxation time. It is shown that the Navier-Stokes equations can be derived from the LBE though a Chapman-Enskog expansion procedure in the incompressible limit with a relaxation time τ as,

$$\tau = \frac{3\nu}{c\delta x} + \frac{\delta t}{2}. \tag{2}$$

The most common choice for the equilibrium distribution function $f_\alpha^{(eq)}$ is the truncated form of the Maxwell distribution, which is a very good approximation for small Mach numbers.

$$p_\alpha^{(eq)} = \omega_\alpha\left[p + \rho_0\left(\left(\boldsymbol{e}_\alpha\cdot\boldsymbol{u}\right) + \frac{3}{2}\frac{\left(\boldsymbol{e}_\alpha\cdot\boldsymbol{u}\right)^2}{c^2} - \frac{1}{2}\boldsymbol{u}^2\right)\right], \tag{3}$$

where ω_α is the weight coefficients given as 4/9 (α = 0), 1/9 (α = 1 ~ 4), and 1/36 (α = 5 ~ 8). Macroscopic quantities such as pressure p and velocity $\boldsymbol{u}$ can be directory evaluated as,

$$p = \sum_\alpha p_\alpha, \tag{4}$$

$$\boldsymbol{u} = \frac{1}{\rho_0 c_s^2}\sum_\alpha p_\alpha \boldsymbol{e}_\alpha, \tag{5}$$

where c_s is the sound speed which is given by

$$c_s = \frac{c}{\sqrt{3}}. \tag{6}$$

The motion of the valve leaflets obeys following equation

$$T = I\ddot{\theta}, \tag{7}$$

where T is the torque, I is the moment of inertia, and θ is the angle of the valve leaflet. The range of the valve leaflet angle θ is 0 to $\pi/2$.

2.3. BOUNDARY CONDITIONS

Axial velocity u at the inlet and pressure p at the outlet are given as shown in Fig. 2. Other parameters are linearly extrapolated. No-slip conditions are assumed on the wall and valve leaflets. The Reynolds number Re at the peak velocity in Fig. 2 corresponds to 100.

2.4. VIRTUAL FLUX METHOD

Boundary conditions are taken to expand the distribution function. In case that boundary points are not located on the cell vertex, we apply the virtual flux method (VFM), which enables us to estimate flow field around arbitrary body shapes properly in a Cartesian grid [3]. Figure 3 shows an example of virtual flux boundary, where the virtual boundary point b is placed between cell vertexes 1 and 3. When the distribution function at vertex 1 is obtained, the distribution function at vertex 3, which includes the effect of the virtual boundary, is necessary, and vice versa. The macroscopic quantities on the virtual boundary point b are then determined to satisfy the boundary conditions. No-slip condition on the boundary, for example, is attained to assume zero pressure gradient (Eq. (8)) and zero velocity (Eq. (9)) on the boundary.

$$p_b = \frac{(1+r)^2 p_1 - r^2 p_2}{(1+r)^2 - r^2}, \tag{8}$$

$$\boldsymbol{u}_\mathrm{b} = \mathbf{0}, \tag{9}$$

where r is the distance between vertex 1 and virtual boundary point b. Next, the equilibrium distribution function $p_\alpha^{(eq)}$ and distribution function p_α at the virtual boundary point b are obtained through Eqs. (3) and (10).

$$p_{\alpha,\mathrm{b}} = p_\alpha^{(eq)}(\boldsymbol{u}_\mathrm{b}, p_\mathrm{b}) + \left(p_{\alpha 1} - p_{\alpha 1}^{(eq)}\right), \tag{10}$$

where $p_\alpha^{(eq)}(\boldsymbol{u}_\mathrm{b}, p_\mathrm{b})$ is the equilibrium distribution function, whose macroscopic quantities $\boldsymbol{u}_\mathrm{b}$ and p_b satisfy the boundary condition. The distribution function p_α at the vertex 3 is then estimated to extrapolate that at the virtual boundary point b.

$$p_{\alpha 3} = \frac{p_{\alpha,\mathrm{b}} - (1-r)p_{\alpha 1}}{r}, \tag{11}$$

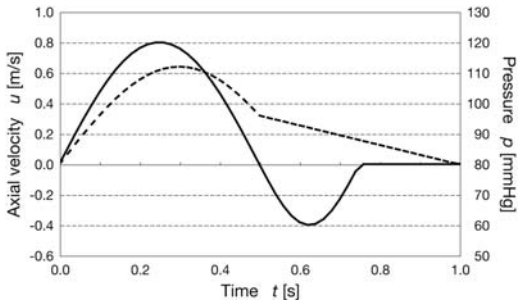

Figure 2. Axial velocity u and pressure p.

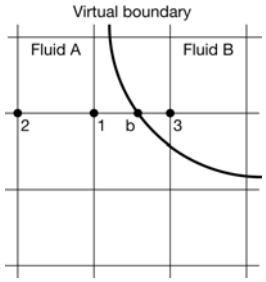

Figure 3. Virtual boundary.

3. RESULTS AND DISCUSSION

The pressure distribution around the aortic valve leaflets is shown in Fig. 4. The aortic valves open due to pressure gradient and the blood flows toward the aorta. Vortices are obviously confirmed in the sinus of Valsalva, which are considered to help the aortic valves to close. We successfully reproduced the movements of the aortic valve leaflets during cardiac cycle by the virtual flux method.

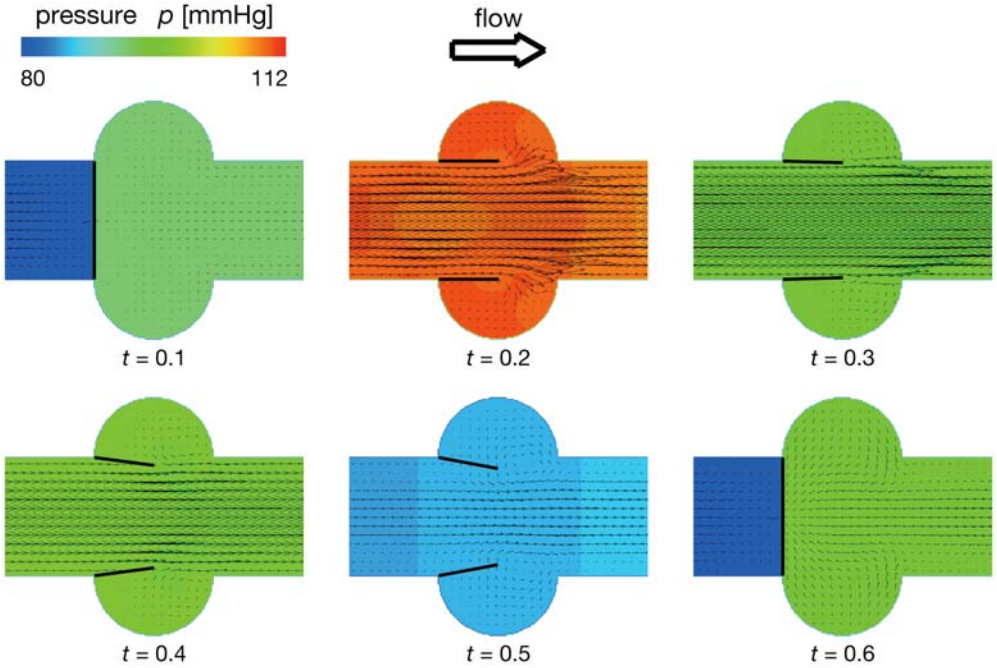

Figure 4. Pressure distribution and velocity vectors around the aortic valve leaflets.

REFERENCES

[1] A.D. Friedrich and P.S. Shekar, Interrogation of the aortic valve, *Crit. Care Med.*, 35(8 Suppl), S365-S371, 2007.

[2] B.A. Carabello, Aortic stenosis, *N. Engl. J. Med.*, 346(9), 677-682, 2002.

[3] I. Tanno, K. Morinishi, K. Matsuno, and H. Nishida, Validation of virtual flux method for forced convection flow, *JSME Int. J.*, B49(4), 1141-1148, 2006.

2nd International Conference on Mathematical and Computational Biomedical Engineering - CMBE2011
March 30 - April 1, 2011, Washington D.C, USA
P. Nithiarasu and R. Löhner (Eds.)

Simulation of the Blood Flow in the Left Ventricle Using A Finite Element Method With Moving Geometries Based on Ultrasound Measurements

J. H. Spühler[⋆], J. Hoffman[⋆], J. Jansson[⋆], U. Gustafsson[⋆⋆], M.Broomé[⋆⋆⋆], M.G. Larson[⋆⋆⋆⋆], P. Vesterlund[⋆⋆⋆⋆]

[⋆]Computational Technology Laboratory, School of Computer Science and Communication, KTH, SE-100044 Stockholm, (spuhler, jhoffman, jjan)@csc.kth.se

[⋆⋆]Department of Public Health and Clinical Medicine, Umeå University, SE-901 85 Umeå, ulf.gustafsson@medicin.umu.se

[⋆⋆⋆]School of Technology and Health, KTH, SE-100044 Stockholm, broom@kth.se and ECMO Center, Karolinska University Hospital, Karolinska Institutet, SE-171 76 Stockholm, Sweden

[⋆⋆⋆⋆]Computational Mathematics Laboratory, Department of Mathematics and Mathematical Statistics, Umeå University, SE-901 87 Umeå, (mats.larson, per.vesterlund)@math.umu.se

SUMMARY

Key Words: *Finite element methods, Arbitrary Lagrangian-Eulerian method, blood flow, left ventricle, heart failure*

1 INTRODUCTION

A functioning heart is a prerequisite for human life. It consists of 4 chambers, the two atria and two ventricles. The left ventricle (LV) pumps the oxygenated blood coming from the lungs into the whole body. Our research interest lies in developing a good and reliable model of the LV based on our knowledge in numerical analysis and high performance computing, in cooperation with medical expertise, aiming for a better understanding of cardiac function.
We model the blood flow in the left ventricle by a finite element method with a geometrical model based on ultrasound measurements during the four basic stages of the cardiac cycle; isovolumetric relaxation, diastole (filling), isovolumetric contraction and systole(emptying). The goal is to develop a model that can address clinical hypothesis about heart failure and its treatment. The simulations are based on the open source software Dolfin and Unicorn [2] which are part of the FEniCS platform.

2 MAIN BODY

2.1 The model

In our approach, blood flow in the LV is driven by the prescribed movement of the inner wall and the pressure difference between ventricular pressure and the exterior pressure in the aorta and atrium respectively, when the valves are open. For this purpose, the inner wall of the LV is sampled from one healthy person in different scan planes by ultrasound imaging and saved as data

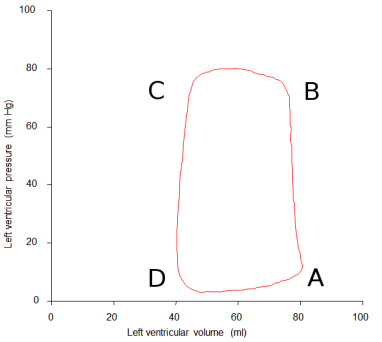

Figure 1: Left ventricle Pressure-Volume diagram

in form of a set of surface meshes [1]. Hermite interpolation is applied to interpolate the boundary movement, and the volume mesh is updated by Laplacian smoothing. The cardiac cycle in our model lasts for a period of 1.124 seconds, and is as a first step divided into the two basic stages of diastole and systole, see Fig.1 (DA) and (BC).
The two stages are modeled by prescribing boundary conditions at marked regions on the surface of the model of the LV, representing the mitral valve and the aortic valve. At the open valves the pressure is set to zero and at the closed valves a no-slip boundary condition is applied so that the blood has the same velocity as the wall. The calculation is started shortly before the systole and the initial velocity is set to zero. Thus the simulation has to be run over several cycles to get a flow simulation independent of the initial conditions.
At the moment we are working with modelling the full cardiac cycle with its four stages, including the isovolumetric relaxation (CD) and isovolumetric contraction (AB). With the heart cycle we are able to recreate the full pressure-volume diagram. Differences compared to the reduced model will be studied, and the model of the full heart cycle will also be validated against experimental data.

2.2 Discretization

Our mathematical approach to describe the blood velocity is the incompressible Navier-Stokes equations formulated as an Arbitrary Lagrangian-Eulerian method (ALE) taking into consideration that the boundary is moving. We choose a standard stabilized cG(1)cG(1) finite element method [3] with piecewise continuous linear trial functions in time and space, and test functions piecewise constant in time. The heart model is based on software components suitable for high performance parallel computing [4], and development is now under way to port the model onto high performance computer architectures.

2.3 Evaluation of the model

To validate the model, simulations were performed on a three times uniformly refined mesh, where we compare the velocity profile to available medical data. We find that the form of the velocity profiles at the inflow and outflow matches well with medical data from ultra sound measurements although the amplitude of the velocity differs in this very crude model (see Fig.2 and 3). The second phase in the outflow profile which can't be observed clinically is a result of not including the valves and a sample volume at some distance from the outflow.
A first test application of our model was to study heart failure characterized by a dilated heart. We modified the geometry in such a way that the stroke volume is retained and we examined the ef-

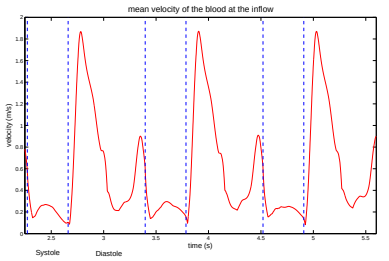

(a) Simulation

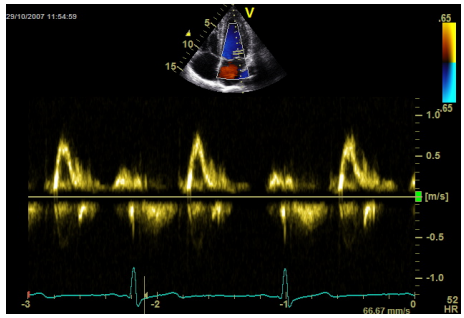

(b) Medical data

Figure 2: Flow Velocity at the inflow for a healthy heart.

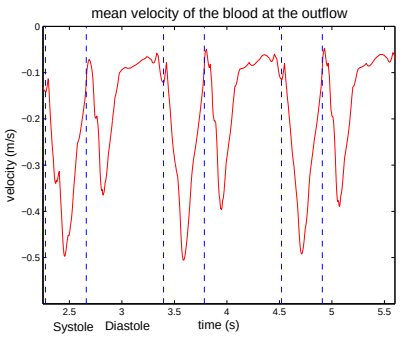

(a) Simulation

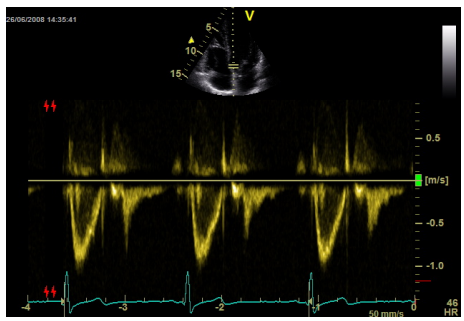

(b) Medical data

Figure 3: Flow Velocity at the outflow for a healthy heart.

fects of this state on the blood flow pattern. The results in Fig.4 are gained from a ventricle where the volume was enlarged by a scale of 1.5 in x and y direction (but not in the length direction z). We find a significant difference in flow patterns, with in particular a large region of stagnating flow near the apex in the dilated heart, which in clinical medicine is associated with risk of clot formation.

3 CONCLUSIONS

Based on ultrasound measurements and the Navier Stokes equations discretized by a standard finite element method we were able to simulate the blood flow in the left ventricle. In our simulation the movement of the inner wall is interpolated with boundary positions measured in ultrasound measurements which makes it possible to render a realistic representation of the real heartbeat. Future work will be forward on enhancing the model geometrically and numerically. We have started to build a platform with research groups in human-computer interaction, to develop a multi-model interface, including haptic interaction. To secure, develop and make our model applicable the discussions, dialogue, feedbacks and inputs from physicians are of high importance, and we are in contact with medical researchers and clinical doctors from the Umeå University and the Karolinska Institutet.

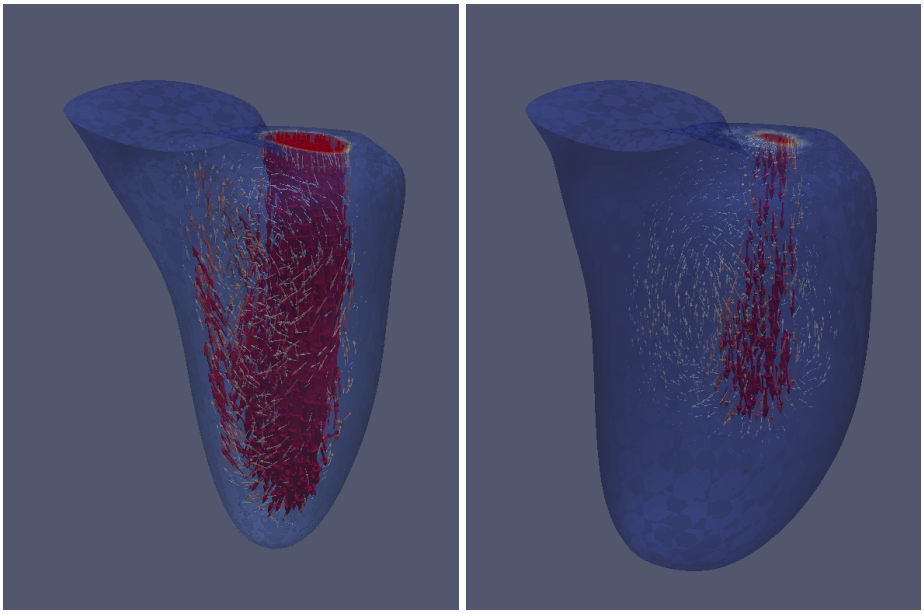

(a) Velocity in a healthy heart (b) Velocity in a dilated heart

Figure 4: Velocity at time t=0.6s.

References

[1] Matthias Aechtner. Arbitrary lagrangian-eulerian finite element modelling of the human heart. *http://www.nada.kth.se/utbildning/grukth/exjobb/rapportlistor/2009/rapporter09/aechtner_matthias_09022*

[2] FEniCS. Fenics project. `http://www.fenicsproject.org`, 2003.

[3] Johan Hoffman and Claes Johnson. *Computational Turbulent Incompressible Flow: Applied Mathematics Body and Soul Vol 4*. Springer-Verlag Publishing, 2006.

[4] Niclas Jansson, Johan Hoffman, and Johan Jansson. Parallel Adaptive FEM CFD. Technical Report KTH-CTL-4008, Computational Technology Laboratory, 2010. http://www.publ.kth.se/trita/ctl-4/008/.

2nd International Conference on Mathematical and Computational Biomedical Engineering - CMBE2011
March 30 - April 1, 2011, Washington D.C, USA
P. Nithiarasu and R. Löhner (Eds.)

RUNNING HAEMODYNAMIC SIMULATIONS ON GPUS

Rainald Löhner[⋆], Andrew Corrigan[⋆⋆], Fernando Camelli[⋆], Fernando Mut[⋆] and Juan Cebral[⋆]

[⋆] CFD Center, Dept. of Computational and Data Science
M.S. 6A2, College of Sciences, George Mason University
Fairfax, VA 22030-4444, USA
[⋆⋆] Center for Reactive Flow & Dynamical Systems
Laboratory for Computational Physics and Fluid Dynamics
Naval Research Laboratory, Washington, DC 20375, USA

SUMMARY

Haemodynamic calculations are carried out on GPUs. Speedups in the range of 1:3-1:4 are achieved.

Key Words: *GPU, CFD, blood flow, aneurysm.*

1 INTRODUCTION

Over the last years, graphics processing units (GPUs) have increased tremendously in performance, and continue to do so at a much faster pace than CPUs. As an example, the latest Fermi architecture from The NVIDIA Tesla C2050 now achieves more than 0.5 Teraflops of peak double-precision performance with a peak memory bandwidth of 144 GB/s. The consumer-market oriented GeForce GTX 480 achieves more than 1.25 Teraflops of peak single-precision performance with a peak memory bandwidth of 177.4 GB/s [Nvi10,Nvi09]. Furthermoe, the appearance of general-purpose programming interfaces such as CUDA [Nvi10] and OpenCL [Khr09] have made them accessible to scientific computing applications. It is therefore not surprising that running computational fluid dynamics (CFD) simulations on GPUs has received considerable attention recently, mainly for aerodynamic applications [Owe07, Bra08, Leg08, Coh09, Cor09, Jac09, Jes09, Göd09, Koc09, Phi09, Ant10, Aso10, Cor10, Kam10].

Given that most medical visualization devices have, at their core, powerful graphical processing units (GPUs), and that almost any PC or laptop today has at least one powerful GPU, it is obvious that running CPU-intensive applications, such as haemodynamic [Ceb02, Ceb05, Mut10] and aelodynamic (i.e. fluid dynamics) simulations on GPUs offers an extremely attractive way to increase turnaround times without having to migrate the applications to off-side supercomuting centers.

2 FEFLO-TO-GPU

The starting point for the endeavour followed here was FEFLO, typical adaptive, edge-based finite element code for the solution of compressible and incompressible flow. It consists (like so many

so-called legacy codes) of nearly one million lines of primarily Fortran 77 code, and is optimized for many types of parallel architectures.

While GPUs offer high performance, arbitrary code cannot simply be recompiled and expected to run efficiently on GPUs. Instead GPUs require that code be re-written using interfaces such as CUDA [Nvi10] or OpenCL [Khr09]. While writing new code in CUDA or OpenCL is not intrinsically difficult, the manual translation of a code on the scale of FEFLO necessarily introduces a large number of bugs, and would involve an overwhelming amount of tedious work. There are more than 10,000 parallel loops in FEFLO to be translated. Translating loops is actually relatively simple compared to handling the intricate bookkeeping required to properly track arrays across the subroutine call graph in order to ensure their consistent placement into either the GPU or CPU memory space, deducing sub-array semantics, and correctly calling data transfer subroutines when necessary. Just translating the code in its current state would be a formidable task. Furthermore, FEFLO remains under continuous development, and therefore a manual approach would result in a perpetual translation process and necessitate the creation of two separate codebases.

Another issue is that of choosing the right interface to access GPU hardware. CUDA has the disadvantage of being proprietary, while OpenCL is an open standard. However CUDA is more mature and has extensive C++ support. Both of these factors have contributed to the availability of libraries such as Thrust [Hob09], which are used extensively in the GPU version of FEFLO. A similar library, with such a breadth of generic, data parallel algorithms, does not appear to be available for OpenCL. In addition, even if a GPU code is written in OpenCL, it still needs to be optimized to satisfy the performance requirements of different hardware. Therefore, an approach is needed which can be rapidly adapted to new combinations of hardware and software.

Due to these issues, an automatic translator is used in this work, which avoids most issues plaguing manual translation, and is flexible enough to satisfy future hardware and software requirements. Automatic approaches often compromise on performance, which contradicts the ultimate purpose of porting codes such as FEFLO to GPUs. That is not the case here, since the translator was specialized to generate the same code that would be written via a manual translation. As a result, the purpose of this script is not to automatically parallelize any arbitrary code, or even translate any arbitrary OpenMP-parallelized code. Rather its purpose is to enable the main developers of FEFLO to continue development in Fortran, with certain additional necessary restrictions. Most of the script, however, is general-purpose, and as a side benefit, it is entirely conceivable that this translator could be adapted to also translate other codes automatically by adapting to the coding style used.

In summary, the resulting translator is just a few thousand lines of Python code, which automatically:

- Converts simple OpenMP loops to CUDA kernels, with support for arbitrary reduction operations;
- Exposes finer-grained parallelism in coarse-grained OpenMP loops using FEFLO-specific logic;
- Detects GPU arrays and enforces consistency across the subroutine call graph;
- Tracks physical array sizes of subarrays across subroutine calls;
- Uses a transposed array layout appropriate for meeting coalescing requirements;
- Handles GPU array I/O and memory transfer;

- Allows ‘difficult’ subroutines to be ignored and left on the CPU, or overridden with custom implementations, usually based on Thrust [Hob09]; and
- Integrates with pure CPU code, including MPI code.

A more detailed description of the translator may be found in [Cor10].

3 AN EXAMPLE

This example considers the laminar steady flow in an aneurysm. The incompressible Navier-Stokes equations are solved using an explicit integrator for the advection terms, implicit integration of the viscous terms, and a projection technique for pressure increments [Loh06, Loh08]. Therefore, a large portion of the compute time is consumed by the diagonally preconditioned conjugate solvers of the velocity and pressure increments. Figure 1 shows a typical result obtained.

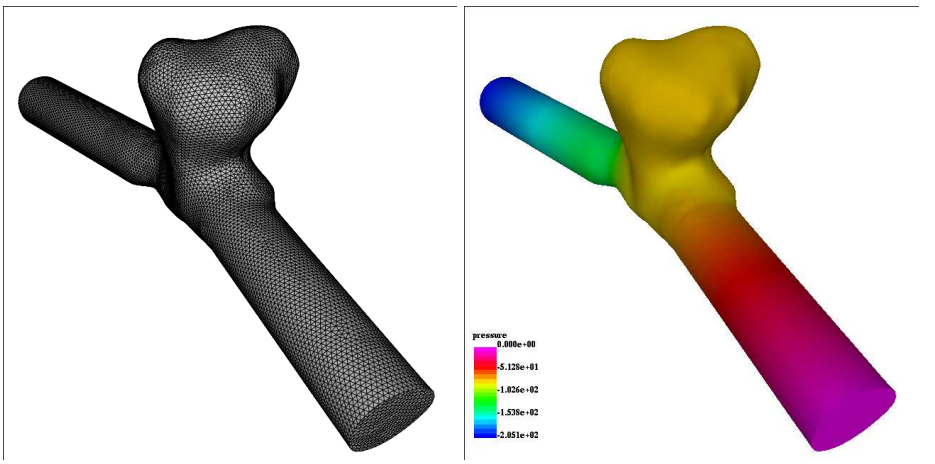

Figure 1 Aneurysm

The timing studies were carried out with the following set of parameters: Incompressible Navier-Stokes, Advection: RK3, Roe, nlimi=2, Pressure: Poisson (Projection, DPCG), Steady State, Local Timestepping, 0.5 Mels, Run for 200 Steps

`nelem`	CPU/GPU	`mvecl`	Time [sec]
0.5 Mels	Xeon i7 (1)	32	352
0.5 Mels	GTX 285	12,600	114

Table 1: Aneurysm

REFERENCES

[Ant10] A.S. Antoniou, K.I. Karantasis, E.D. Polychronopoulos and J.A. Ekaterinaris - Acceleration of a Finite Diffence WENO Scheme for Large-Scale Simulations on Many-Core Architectures; *AIAA*-2010-0525 (2010).

[Bra08] T. Brandvik and G. Pullan - Acceleration of a 3D Euler Solver Using Commodity Graphics Hardware; *AIAA*-2008-607 (2008).

[Ceb02] J.R. Cebral, P.J. Yim, R. Löhner, O. Soto and P.L. Choyke - Blood Flow Modeling in Carotid Arteries with Computational Fluid Dynamics and MR Imaging; *Academic Radiology* 9, 11, 1286-1299 (2002).

[Ceb05] J.R. Cebral and R. Löhner - Efficient Simulation of Blood Flow Past Complex Endovascular Devices Using an Adaptive Embedding Technique; *IEEE Transactions on Medical Imaging* 24, 4, 468-476 (2005).

[Cor09] A. Corrigan, F.E. Camelli, R. Löhner and J. Wallin - Running Unstructured Grid-Based CFD Solvers on Modern Graphics Hardware; *AIAA*-2009-4001 (2009).

[Cor10] A. Corrigan, F. Camelli, R. Löhner and F. Mut - Porting of FEFLO to to Multi-GPU Clusters; *Proc. ECCOMAS-CFD Conf.* , Lisbon, June (2010).

[Göd09] D. Göddeke, S.H.M. Buijssen, H. Wobker and S. Turek - GPU Acceleration of an Unmodified Parallel Finite Element Navier-Stokes Solver; in *High Performance Computing & Simulation* , 12-21 (2009).

[Hob09] J. Hoberock and N. Bell - Thrust: A Parallel Template Library, Version 1.2 (2009).

[Jac09] D. Jacobsen, J. Thibault, and I. Senocak. An MPI-CUDA Implementation for Massively Parallel Incompressible Flow Computations on Multi-GPU Clusters; *AIAA*-2010-522 (2009).

[Khr09] Khronos OpenCL Working Group - The OpenCL Specification: Version 1.0 Rev. 48 (2009).

[Koc09] A. Kockner, T. Warburton, J. Bridge, and J. S. Hesthaven - Nodal Discontinuous Galerkin Methods on Graphics Processors; *J. Comp. Phys.* 228, 7863-7882 (2009).

[LeG08] P. LeGresley, E. Elsen and E. Darve - Large Calculation of the Flow Over a Hypersonic Vehicle Using a GPU; *J. Comp. Phys.* 227, 10148-10161 (2008).

[Löh06] R. Löhner, Chi Yang, J.R. Cebral, F. Camelli, O. Soto and J. Waltz - Improving the Speed and Accuracy of Projection-Type Incompressible Flow Solvers; *Comp. Meth. Appl. Mech. Eng.* 195, 23-24, 3087-3109 (2006).

[Löh08] R. Löhner - *Applied CFD Techniques*; J. Wiley & Sons (2008).

[Mut10] F. Mut, R. Aubry, R. Löhner and J.R. Cebral - Fast Numerical Solutions to Patient-Specific Blood Flows in 3D Arterial Systems; *Int. J. Num. Meth. Biomed. Eng.* 26, 73-85 (2010).

[NVI09] NVIDIA Corporation. Fermi Compute Architecture White Paper (2009).

[NVI10] NVIDIA Corporation. NVIDIA CUDA 3.1 Best Practices Guide (2010).

[NVI10] NVIDIA Corporation. NVIDIA CUDA 3.1 Programming Guide (2010).

[Pet09] P. Peterson - F2PY: A Tool for Connecting Fortran and Python Programs; *Int. J. Comp. Science and Engineering* 4, 296-305 (2009).

[Phi09] E.H. Phillips, Y. Zhang, R.L. Davis and J.D. Owens - Rapid Aerodynamic Performance Prediction on a Cluster of Graphics Processing Units; *AIAA*-2009-565 (2009).

2nd International Conference on Mathematical and Computational Biomedical Engineering – CMBE2011
March 30 – April 1, 2011, Washington D.C., USA
P. Nithiarasu and R. Löhner (eds)

Fluid-structure interaction finite element analysis on the relationship between left ventricular pump function and fiber structure within the wall

Hiroshi Watanabe*, Seiryo Sugiura* and Toshiaki Hisada*

* Graduate School of Frontier Sciences, The University of Tokyo,
5-1-5 Kashiwanoha, Kashiwa, Chiba, Japan 277-8563,
nabe@sml.k.u-tokyo.ac.jp, sugiura@k.u-tokyo.ac.jp, hisada@mech.t.u-tokyo.ac.jp

SUMMARY

In this study, a 3D finite element based simulation program incorporating the propagation of excitation and excitation-contraction coupling mechanisms developed by us was modified to reproduce the more realistic ventricular wall structure. FE model of LV consists of six layers of muscle bundles and the fiber direction of the inner-most layer was longitudinal. Although the detailed modeling did not influence the global pump function of the LV appreciably, we could successfully identify the functional significance of longitudinal fibers as pointed out by clinical observations. Furthermore, we also changed the heart structure drastically to elucidate the functional significance of the fiber structure. The results suggest that the double-helical structure the heart has developed through the evolutionary process can be an optimal design for a blood pump.

Key Words: *computer modeling, fluid-structure interaction analysis, blood flow, hemodynamics, biomechanics.*

1. INTRODUCTION

It is well recognized that computational science is now becoming an indispensable disciplines for understanding the complex scenario of living systems resulting from the dynamic interactions among proteins, cells and organs. In this filed, the heart is a challenging target for the researchers because modeling of this organ requires the integration of multi-physics and multi-level phenomena and many investigators have tried to simulate the various aspect of cardiac function under both normal and diseased conditions. We have already reported a fluid-structure analysis of the left ventricle based on the propagation of excitation in the wall and the excitation-contraction coupling mechanism in each cardiac cell [1]. In this simulation, the ventricular wall was divided into six layers from endocardial (the inner-most layer facing the cavity) to epicardial (the outer-most layer facing outside), the fiber orientations of which were varied from –60 to 60 degrees. Although experimental studies unanimously showed a continuous change in fiber direction from endocardial to epicardial layer, there is some discrepancy in result about the inner-most layer. Streeter et al.(2)-(3) reported that the fiber orientation ranges from − 60 (endocardial layer) to 60 degrees (epicardial layer). But some researchers claimed the functional significance of the inner-most fibers running almost longitudinally (-90 degrees)(4). This fiber population, mainly consisting of trabeculae, constitutes only a small portion of the entire ventricular wall, but its functional role has attracted the interest of cardiac physiologists and clinicians. Reduction of ventricular cavity volume during ejection is brought about not only by the shortening of the minor axis but also, although to a lesser degree, by the shortening of the long axis. In normal hearts, the long axis shortening begins during the isovolumic contraction period to make the ventricle more spherical. Because myocardial

excitation spreads from the endocardial layer to epicardial layer, this initial shortening in the long axis may be caused by the endocardial longitudinal fibers. On the other hand, as most diseased process including ischemia insults the endocardial layer first, impairment of the long axis shortening is suggested to serve as an initial sign of global cardiac dysfunction. However, as the obliquely running fibers incorporated in our previous model did reproduce the long axis shortening, the relationship between the pump function of the left ventricle and its fiber structure in the wall needs more detailed analysis from both medical and mechanical points of view.

Accordingly, the purpose of this study was two-fold. First, by modifying the fiber structure in the ventricular wall including the inner-most one running longitudinally, the effect of detailed modeling on the predictability and accuracy of the simulation were examined based on the comparison with the clinical data reported in the literature. Second, by varying the fiber structure (orientation) of ventricular wall in multiple combinations, we tried to gain an insight into the significance of heart structure on its pump function. The results clearly indicated that 1) the detailed modeling is surely helpful in accurately reproducing the clinical observation, and 2) the double-helical structure the heart has developed through the evolutionary process is close to optimal design for a blood pump.

2. METHODS

The present simulation is based on the finite element method (FEM). The model of the left ventricle consists of 9792 elements divided into 6 layers from the endocardium to the epicardium (see Fig. 1). The fiber orientations of the model were –90, -60, -30, 0, 30 and 60 degrees respectively. Hereafter this model is referred as 6-layered model or physiological model. To compare the effect of the fiber structure, we constructed hearts with various fiber angle among those including the physiological model: 1) single layer with various fiber angle, e.g. the fiber orientations of single-layered 30 degree model were –30, -30, -30, -30, -30 and -30 degrees respectively, 2) two layers also with various angles, e.g. the fiber orientations of two-layered 30 degree model were –30, -30, -30, 30, 30 and 30 degrees respectively. Also made was the six-layered model without the fiber direction of inner-most layer running longitudinally, i.e., the fiber orientations of this model were –60, -30, 0, 0, 30 and 60 degrees respectively. In response to electrical stimulation applied to the endocardium, the excitation propagates towards the epicardium to induce the contraction/relaxation cycle of each element, representing the myocytes. In this simulation, the FitzHugh-Nagumo (FHN) model was coupled with the monodomain propagation model to reproduce the excitation and its propagation in the ventricular wall tissue. Upon excitation, a series of sub-cellular events lead to a transient increase in intracellular calcium concentration [Ca^{2+}], which in turn controls the interaction of the contractile proteins, actin and myosin, (cross-bridge kinetics) resulting in the development of a force. To describe the dynamic relationship between [Ca^{2+}] and cross-bridge kinetics, a four-state model proposed by Peterson et al. was employed. To connect the membrane depolarization (FHN) model and the four-state model for E-C coupling, an FHN model was used to give a trigger (timing) for the phasic change in Ca^{2+} ion concentration (Ca^{2+}-transient). To characterize the properties of cardiac muscles, we adopted the Lin-Yin model, which is based on hyperelastic material theory, for the constitutive equation. In this model, the strain energy potential (W) is divided into two components, a passive (W_{pass}), and an active (W_{act}) component. As the E-C coupling model provides active force (F) of the muscles depending on the calculated population of the attached cross-bridges, we can consider the coefficients for the active components in the Lin-Yin model to be a function of F, whereas those for the passive components are constant. Because we did not model the conduction system, we applied the stimulation signal to all the elements on the endocardial surface to initiate the excitation.

3. RESULTS

Figure 2(a) shows the length change in long axis direction of 6-layered model (–90, –60, –30, 0, 30 and 60 degrees) and 3-layered model (–60, –60, 0, 0, 60 and 60 degrees). The results obtained by

the two models look similar, but reveals important difference as follows. In the very beginning of contraction (0 to 0.1 sec), 6-layered model (100%) showed an abrupt shortening followed by a smaller gradient interval (0.1 to 0.15 sec), whereas 3-layered model shortens monotonously throughout this phase. In addition, when the performance of the inner-most layer was reduced, the shortening of the 6-layered model (60%) virtually disappeared thus showing clear contrast to the 3-layered model in which long axis shortening takes place similarly to the control. Recently, tissue-Doppler technique is widely applied in clinical cardiology to report an important finding about the shape change in long axis of the LV; the velocity of mitral ring in the long axis direction during systole (equivalent to the time-derivative of long axis length) consists of two distinct peaks and the first one decreases its amplitude at the early stage of heart disease when global ejection fraction is well maintained. The abrupt shortening in our 6-layered model coincides with this first peak of Doppler signals and accurately reproduced the clinical observation. Time derivative of the ventricular pressure (dP/dt) is often used as an index of cardiac contractility and reaches its peak during the isovolumic contraction phase when only the inner layer is activated. In both 6- and 3-layerd models, the reduction in performance of the inner-most layer decreased the maximum dP/dt by about 20%.

Figure 2(b) shows the series of P-V loops produced by models with various fiber structures. Most of the 1-layered models showed severely impaired pump function except for the 0 degree one in which all the fibers run circumferentially. In contrast, the functions of 2-layered models are better than physiological model (6-layered with longitudinal fiber) except for the 60 degree one. As is easily expected, 1-layered model twist greatly in one direction showing clear contrast to the 2-layered model and physiological model which rotates in both directions during the cardiac cycle. Despite their high degree of torsional deformation, most of 1-layered models show poor pump function. In addition, judging from the fact that 1-layer (0 degree) model with virtually no rotation can achieve very good pump function, twisting motion of the ventricle is not an important factor for ejection of blood. The length change in long axis is dependent on the angle rather than the number of layers. In general, the models with larger angles relative to the equatorial plane tend to shorten more. Only exception is the 1 layer (0 degree) model which lengthens greatly. We also note that length change in long axis did not correlate with the global pump function.

4. CONCLUSIONS

To analyze the left ventricular pump function, the comprehensive simulation program was developed. Using the FE model of LV whose ventricular wall is divided into six layers with the fiber direction of inner-most layer running longitudinally, we could successfully reproduced the initial abrupt shortening of long axis. Furthermore, through the analyses of various kinds of the heart structure, we could reveal the functional significance of the fiber structure. The results show that the double-helical structure the heart has developed through the evolutionary process is close to optimal design for a blood pump.

REFERENCES

[1] H. Watanabe, et al, Multi-physics simulation of left ventricular filling dynamics using fluid-structure interaction finite element method, *Biophys J.*, 87, 2074-2085, 2004.

[2] D. D. Streeter Jr. et al, Engineering Mechanics for Successive States in Canine Left Ventricular Myocardium, I. Cavity and Wall Geometry, *Circ. Res.*, 33, 639-655, 1973.

[3] D. D. Streeter Jr. et al, Engineering Mechanics for Successive States in Canine Left Ventricular Myocardium, II. Fiber Angle and Sarcomere Length, *Circ. Res.*, 33, 656-664, 1973.

[4] R.A. Greenbaum, et al, Left Ventricular Fibre Architecture in Man, *Br. Heart J.*, 45, .248-263, 1981.

Figure 1. Diagram of the macroscopic model.
FEM meshes for solid (ventricular wall with its fiber direction) and fluid (blood) elements are shown with electrical analogs of the after-load (systemic arterial tree) and pre-load (pulmonary circulation with active left atrium). R_1, characteristic impedance; R_2; peripheral resistance; C, capacitance; P_V, pulmonary source pressure; R_V, source resistance; C_P, pulmonary venous capacitance; R_P, pulmonary resistance; L_P, pulmonary inertance; R_{AV}, atrioventricular resistance; L_{AV}, atrioventricular inertance; E_{LA}, time-varying elastance of the left atrium. Red arrow: inflow angle of the physiological model. Blue arrow: inflow angle of the non-physiological model.

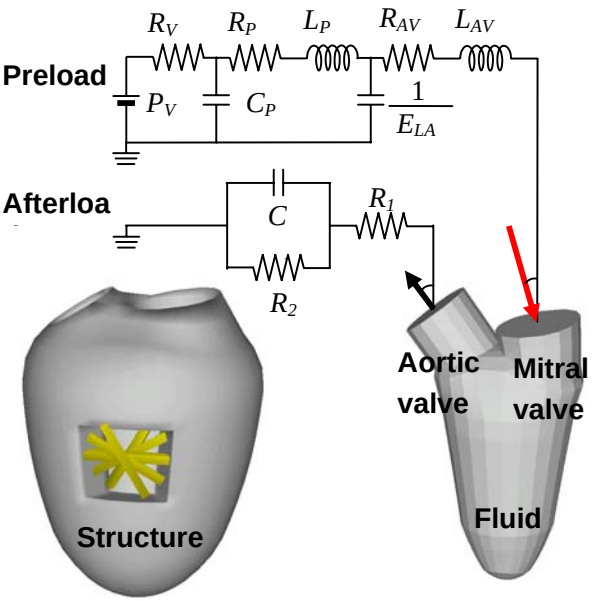

Figure 2 Vertical displacement histories and Pressure-volume loop

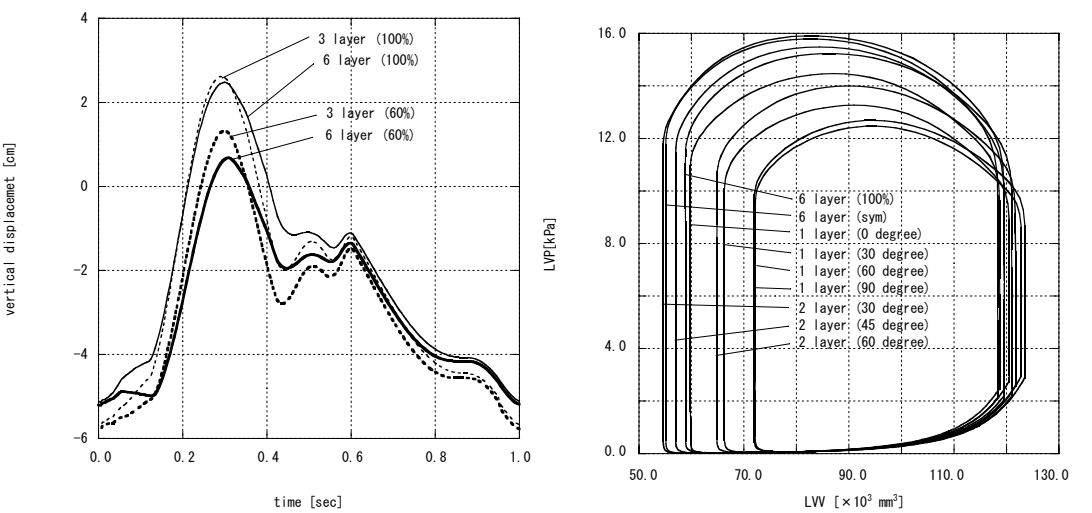

(a) (b)

2nd International Conference on Mathematical and Computational Biomedical Engineering - CMBE2011
March 30 - April 1, 2011, Washington D.C, USA
P. Nithiarasu and R. Löhner (Eds.)

Parallel Computational Electrophysiology in NVIDIA GPUs

F. Rubio, M. Hanzich, R. Arís, M. Vázquez and G. Houzeaux

Barcelona Supercomputing Center, Campus Nord UPC, Barcelona, Spain, felix.rubio@bsc.es

SUMMARY

In a previous paper we show how a HPC platform, such as Cell/B.E., could be used to simulate electrophysiology models that include diffusion and non-linear terms. In the present work we make one step further in the research for performance by using an NVIDIA GPUs to solve the same problem, paying attention to the differences in development effort and performance when compared to the other HPC platforms. Our simulator uses a Finite Differences method explicitly advanced in time, using a first order stencil. By means of a performance-driven desing process, we have developed a simulator that includes several techniques to improve the memory access and the arithmetics involved in the simulation. Thus, we have enhanced the efficiency of the overall simulation to a maximum.

Key Words: *Computational Electrophysiology, Excitable Media, High Performance Computing, NVIDIA GPU*

1 INTRODUCTION

Even considering that Graphical Processor Units were developed in the '70s, only in the past decade they are facing a golden age. Despite of its design as a pure graphics processors, their potential to be used as computing accelerators for commodity processors has arised. Nonetheless, with the aparition of first NVIDIA's CUDA release (2007), scientific computing has experienced an speed-up of one order of magnitude order. Taking into account that a 1 Teraflop GPU can be less than €300.00, almost everybody is able to have a small supercomputer to boost its research with a humble investment. Furthermore, CUDA design allows the developer to work without the need of having in mind the specific GPU architecture he is programing for. Following their philosophy, if more computational power is needed it is enough to change the GPU, without making any changes (at most recompiling) to the code.
After having seen how fast the accelerator market is evolving, we have designed a modular software platform able to incorporate any new number crunching machine that appeared. Hence, only the accelerator parts must be rewritten, while reusing all the common parts, that are not optimized and run in any general purpouse processor.

2 HPC ELECTROPHYSIOLOGY

In this paper, the Physiological model of the excitable media is based on the Hodgkin-Huxley theory. As a first approach, we implemented the FitzHugh - Nagumo (FHN) [1] model,

$$C_m \frac{\partial \phi}{\partial t} = \frac{\partial}{\partial x_i} \left(\frac{D_{ij}}{S_v} \frac{\partial \phi}{\partial x_j} \right) + I_{\text{ion}}, \tag{1}$$

where C_m and S_v are constants of the model, the membrane capacitance ($\mu F\, cm^{-2}$) and the surface to volume ratio respectively. The total membrane ionic current is I_{ion} ($\mu A\, cm^{-2}$). In this model, to the ionic current definition, a gate potential W equation is added:

$$\begin{aligned} I_{\text{ion}} &= c_1 \phi(\phi - c_3)(\phi - 1) + c_2 W \\ \frac{\partial W}{\partial t} &= \varepsilon\,(\phi - \gamma W). \end{aligned} \tag{2}$$

W is called recovery potential. Constants c_1, c_2 and c_3 define the shape of the propagation wave and ε and γ control the recovery potential evolution.

The numerical discretization used for implementing the stated equations, is based on the Finite Differences Method (FDM) [2], explicitly advanced in time. The presented scheme is a proof of concept, based on the following points:

- The computational domain is a paralelepipedal structured mesh.
- The Physiological model is simple: the FHN.
- The model does not includes fiber orientation information.

The pseudo-code shown in Algorithm 1, implement the equations using FDM. The body of the algorithm is a loop in time that applies the equations for each and every point in the input potential model (lines 1 and 2). For each point, the algorithm computes the laplacian (Equation 1), which is the most time consuming part of the algorithm due to the low operation/memory access ratio. This situation encourage us to optimize the laplacian calculation in order to get the maximum efficiency from the algorithm.

Potential propagation

input: model, spatial and time discretization, source
output: potential field

```
1: for all time steps do
2:     for all model points do
3:         compute the laplacian
4:         compute the free term
5:         do time integration
6:         compute the coupled equation
7:     end for
8: end for
```

Figure 1: The potential propagation algorithm

Our focus in this work is to map Algorithm 1 on an NVIDIA GTX280, that, without being a high-end GPU system (compared to Tesla and Fermi), has a considerable 1 TFlop peak performance and a bandwidth of 142 GBytes/s from GPU to GPU memory. As we show in our last work [3], our algorithm is memory bounded. Because of the memory characteristics of our accelerator, we have reached an application performance of 101.3 Gflops (10.85 % of the peak).

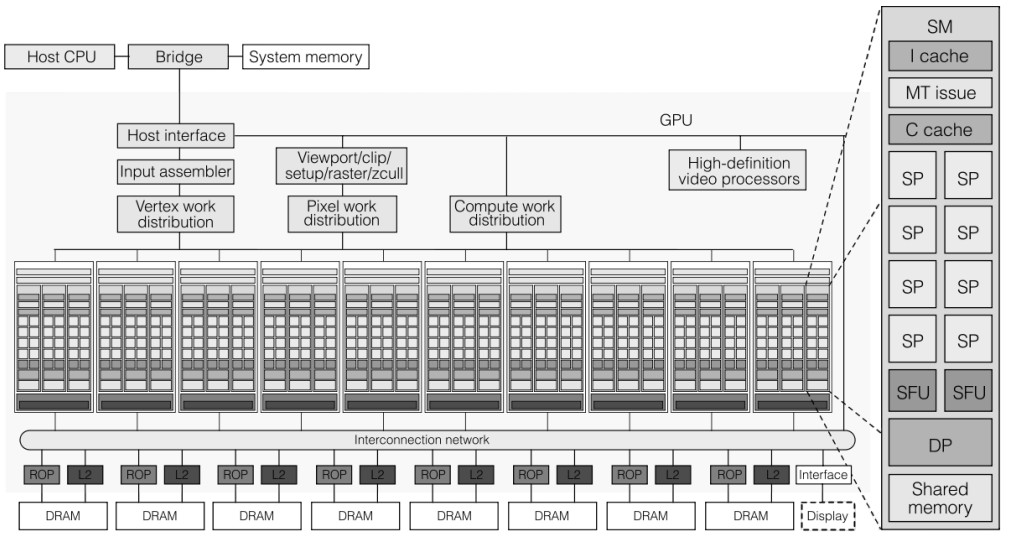

Figure 2: Tesla unified graphics and computing architecture of a GeForce GTX 280 or Tesla C1060 GPU with 240 SP functional units, organized in 30 SM multi-threaded multi-processors. Each SM can handle up to 768 concurrent threads; the GPU executes up to 30,720 concurrent threads [4]

Figure 2 show the general GPU architecture for NVIDIA GTX 280. It is important to remark that modern 3D graphics processing units (GPUs) are designed to take advantage of the data-parallel characteristics found in image generation algorithms. They contain hundreds of functional units that can operate in parallel when accessing different data elements (SM in figure 2). The computing power of these devices easily exceeds that of general purpose multi-core CPUs. Thus, some GPU manufacturers like ATI and NVIDIA have generalized the design of the processors to allow them execute general purpose programs using C-like programming languages.

3 CONCLUSIONS

The current work presents the FHN equations implemented on an NVIDIA GTX280. Today we have obtained 101.3 Gflops using a FD numerical scheme. Consequently, we can run simulations of sizes that we could only imagine some years ago. In the future we want to enhance the complexity of the model while mantaining the performance.

References

[1] Fitzhugh, R. *Biophys. J.* **Vol. 1**, 445–466 (1961).

[2] Cohen, G. C. *Higher-Order Numerical Methods for Transient Wave Equations*. Springer, (2002).

[3] Rubio, F., Hanzich, M., Aris, R., Houzeaux, G., and Vazquez, M. In *1st International Conference on Mathematical and Computational Biomedical Engineering,* Perumal Nithiarasu, Rainald Löhner, R. v. L., editor, volume 1, 273–275. Swansea University, June (2009).

[4] Garland, M., Grand, S. L., and et al. *IEEE MICRO* **Vol. 28**(4), 13–27 (2008).

2nd International Conference on Mathematical and Computational Biomedical Engineering – CMBE2011
March 30 – April 1, 2011, Washington D.C., USA
P. Nithiarasu and R. Löhner (eds)

STRATEGIES FOR HIGH PERFORMANCE COMPUTATION OF HEMODYNAMICS IN CEREBRAL ANEURYSMS

Rainald Löhner*, Fernando Mut*, Fernando Camelli*, and Juan R. Cebral*
*Center for Computational Fluid Dynamics, George Mason University,
4400 University Drive, Fairfax, VA 22030, USA, jcebral@gmu.edu

SUMMARY

The clinical application of image-based computational fluid dynamics models of blood flows in cerebral aneurysms requires efficient incompressible flow solvers for the following purposes: a) quick analysis of aneurysmal flow patterns for risk evaluation and treatment planning, b) analysis of large complex problems involving endovascular devices, and c) study of large numbers of cases for statistical analysis. This paper summarizes different strategies recently incorporated to our flow solver that allow us to reduce the computational time of hemodynamics calculations.

Key Words: *cerebral aneurysm, hemodynamics, high performance computing.*

1. INTRODUCTION

Over the past decade a variety of techniques have been developed and used to compute blood flows in a wide range of biomedical applications. These include explicit and implicit schemes for incompressible flows, embedded and immersed boundary methods, adaptive and moving meshes, volume of fluid methods, and fluid-structure interaction. Implementation of these techniques on different high performance computing hardware and architectures is important for both clinical and basic science studies. The purpose of this paper is to describe a number of strategies for accelerating numerical simulations of blood flows in realistic arterial geometries of different complexities, and to illustrate the speedups obtained in a variety of patient-specific cerebral aneurysm models.

2. METHODS

The following strategies and techniques have been adopted to improve the speed of incompressible flow solvers and in particular for their application to hemodynamics:

- Efficient Solution Schemes [1]: implicit flow solvers, edge-based finite element formulations and renumbering algorithms to reduce bandwidth and indirect addressing.
- Deflated preconditioned conjugate gradients algorithm (DPCGA) [2]: to accelerate the convergence of the pressure Poisson equation in elongated or tubular domains.
- Parallelization for shared memory computers [3]: implementation in OpenMP, coloring algorithms to avoid memory contingencies and dirty cache lines.
- Parallelization for distributed memory computers [3]: implementation in MPI, mesh splitting algorithms for minimization of communications and load balancing (coded in OpenMP), assembly of result files, immersed/embedded and moving grids techniques, parallel DPCGA.
- Graphic Processor Units (GPUs) [4]: code translation using python scripts (possible due to uniform style coding), gradual porting of code parts, renumbering strategies to minimize transfers to/from main memory access.

3. RESULTS

Deflated Conjugate Gradients Algorithm

The first set of examples shows the increased speed of hemodynamic calculations in patient-specific arterial and aneurysmal models using the preconditioned deflated conjugate gradients algorithm to accelerate the convergence of the pressure Poisson equation in the pressure projection algorithm for incompressible flows. This approach takes advantage of the tubular or elongated nature of the vascular domains to build groups of elements along the vessels and eliminate the largest eigenmodes of the pressure equation and accelerate the convergence. The results show that this technique yields speedups between 3 to 5 with respect to the normal conjugate gradients algorithm running on a single processor (see Figure 1).

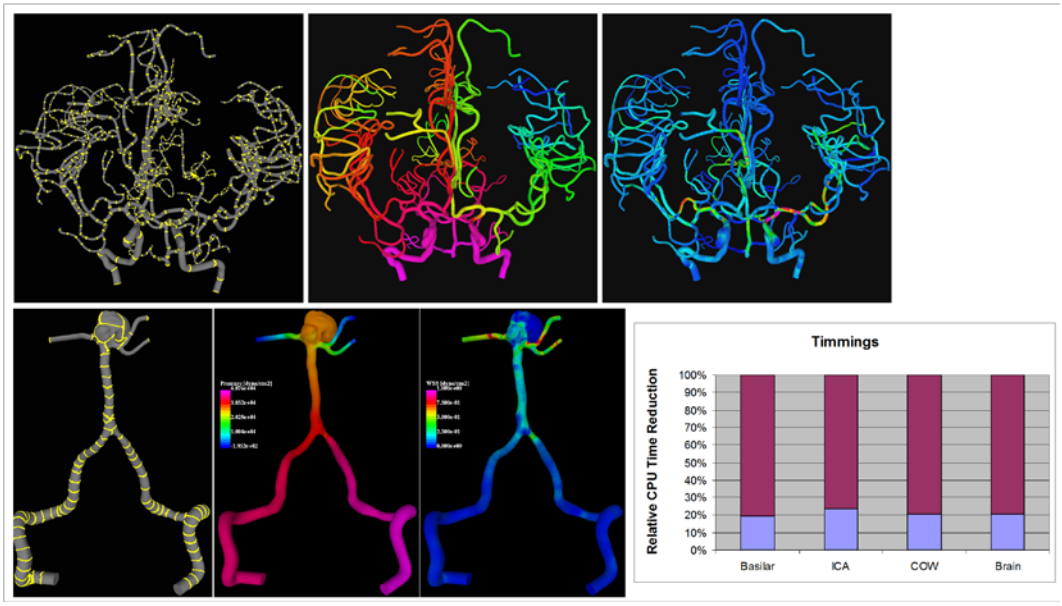

Figure 1: Time reductions of blood flow calculations in cerebral arteries and aneurysms using a DPCGA for the pressure Poisson equation. The frames show (left to right) domain subdivision into groups along vessels, pressure and WSS distributions, and CPU time reductions relative to the normal CGA.

Parallel Hemodynamic Calculations

This example shows parallel calculations of the steady blood flow in a patient-specific aneurysm model after implantation of a flow diverting stent. This case was run with an implicit finite element solver that uses an LU-SGS algorithm for the advection operator and the preconditioned deflated conjugate gradients algorithm described before for the pressure equation as well as an immersed boundary technique to model the stent wires. All these algorithms work in parallel using OpenMP for shared memory computers and MPI for distributed memory architectures. In order to obtain a mesh convergent result, the computational grid was adaptively refined a number of times around the stent wires. The resulting grids with different levels of refinement had 14M, 64M and 128M elements. Speedups obtained with the 64M element mesh running in parallel on a Silicon Graphics ICE computer are presented in Figure 2. The first point in the speedup curve corresponds to a shared memory run using OpenMP on 4 processors on the same computer. These results demonstrate good speedups of this combination of algorithms for up to 256 processors.

Graphic Processors

The last example illustrates the calculation of the hemodynamics in a cerebral aneurysm on a GPU. In order to fit the problem on a relatively small graphic card, the geometry of the parent

artery was simplified and the corresponding mesh consisted only in about 500K elements. In this case, the steady flow solution was obtained using an explicit finite element scheme. The reduction of the compute and elapsed times obtained are presented in Figure 3.

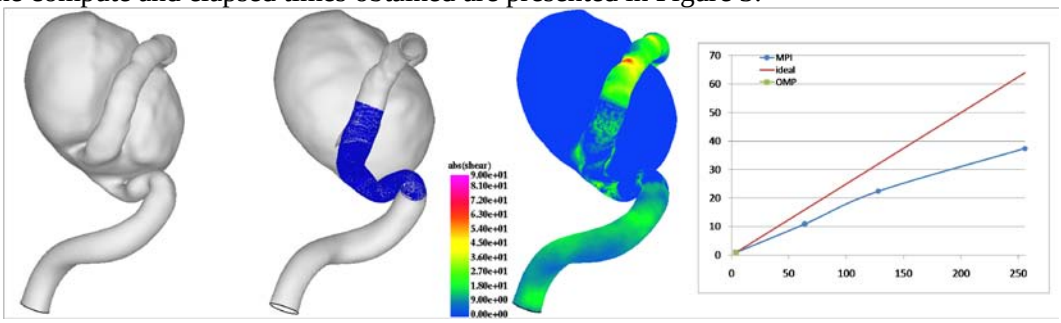

Figure 2: Example of speedups obtained in the parallel calculation of the blood flow in a stented aneurysm model using an implicit finite element solver and immersed boundary method to model the stent wires. Left to right: vascular model, implanted stent, WSS distribution, speedup curves using MPI up to 256 processors.

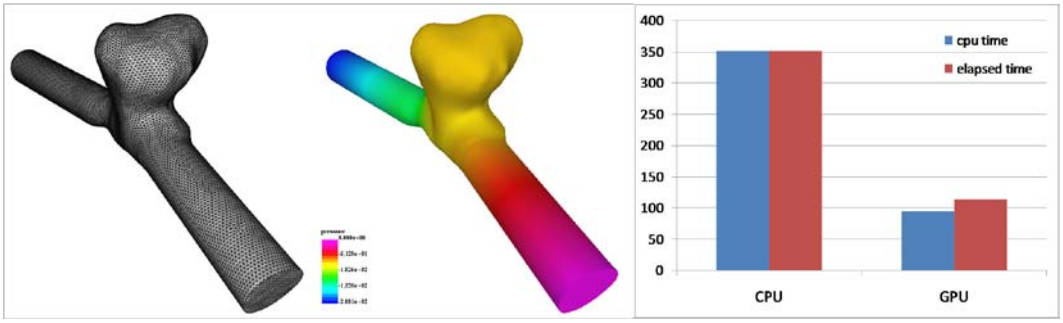

Figure 3: Reduction of the execution times obtained in the calculation of the steady blood flow in a simple aneurysm model (approximately 500K element mesh) using the graphic processor. Left to right: mesh, pressure distribution, CPU and elapsed times.

4. CONCLUSIONS

A variety of strategies for accelerating the computation of blood flows in realistic vascular geometries have been described and illustrated with representative examples. Some of the strategies were specifically designed to accelerate vascular hemodynamic simulations, while others were designed to accelerate the numerical solution of incompressible flow equations in general. These techniques and their combination are important for making larger more complex problems practical, for large throughput studies involving many simulations, and for implementing simulation tools for routine clinical use.

REFERENCES

1. Löhner, R., *Cache-efficient renumbering for vectorization.* Int J Biomedical Eng, 2010. **26**(5): p. 628-636.
2. Mut, F., et al., *Fast numerical solutions in patient-specific simulations of arterial models.* Comm Num Meth Eng, 2009. **DOI 10.1002/cnm.1235**.
3. Camelli, F., R. Löhner, and E. Mestreau, *Timings of an unstructured-grid CFD code on common hardware platforms and compilers*, in *46th AIAA Aerospace Sciences Meeting*. 2008: Reno, Nevada. p. AIAA-08-0477.
4. Corrigan, A., F. Camelli, and R. Löhner, *Porting of an edge-based CFD solver to GPUs*, in *49th AIAA Aerospace Science Meeting*. 2010: Orlando, Florida. p. AIAA-10-0523.

2nd International Conference on Mathematical and Computational Biomedical Engineering - CMBE2011
March 30 - April 1, 2011, Washington D.C., USA
P. Nithiarasu and R. Löhner (Eds.)

Quality meshing algorithms for accurate and efficient cardiovascular simulations

E. Marchandise, **E. Sauvage**, **J.-F. Remacle**,
Université catholique de Louvain, 1348 Louvain-la-Neuve, Belgium.
C. Geuzaine
Department of Electrical Engineering and Computer Science, Université de Liège, Belgium.

Key Words: *surface remeshing, STL triangulation, mesh quality, mesh convergence, cardiovascular.*

PROPOSAL

In the cardiovascular numerical simulation community, the fluid volume meshes are often based on the lumen surface triangulation and composed of unstructured isotropic tetrahedral meshes. Most of the time, a mesh sensitivity analysis is undertaken with different isotropic meshes with a grid refinement factor using for example the Grid Convergence Index (GCI) method. This mesh convergence study is mostly performed on fluid quantities such as flow rate, velocity or pressure while the discussions and conclusions of the blood flow simulations (performed on the converged mesh) are often driven by analysis of derived quantities such as wall shear stresses (WSS). Those derived quantities however do not converge with the same rate as the velocity and pressure do and hence might not be captured accurately with the chosen mesh. Moreover, they might show spurious fluctuations for fully unstructured meshes. In order to capture those WSS while keeping for efficiency purposes a reasonable number of mesh elements, it is desirable to build a CFD boundary layer mesh by extruding the lumen surface mesh in the inward direction.

As far as the vascular wall mesh is concerned, most of the numerical studies create the wall mesh by extruding the lumen surface mesh in the outward direction with either a constant wall thickness or a thickness proportional to the local lumen radius. One of the major problems with surface extrusion is that in case of vascular geometries with small angles between the arterial branches, the extruded surfaces may have intersecting triangles.

This work presents two meshing algorithms for cardiovascular simulations implemented in the open source mesh generator Gmsh. The first algorithm is a surface remeshing method based on a finite element harmonic parametrization [1, 2] and the second is volume meshing algorithm with a robust mesh boundary layer generation technique. We present mesh quality statistics for cardiovascular meshes generated with the presented algorithms. Finally simulation results are given that provide information about the mesh requirements for cardiovascular simulations. In particular, we aim at studying the effects of the mesh resolution upon the simulations in order to find the best trade-off between simulation accuracy and speed.

REFERENCES

[1] J-F. Remacle, C. Geuzaine, G. Compère, and E. Marchandise. High quality surface remeshing using harmonic maps. International Journal for Numerical Methods in Engineering, 83(403-425), 2010.

[2] E. Marchandise, C. Carton de Wiart, W.G. Vos, and C. Geuzaine and J-F. Remacle, High quality surface remeshing using harmonic maps. part ii: Surfaces with high genus and of large aspect ratio. International Journal for Numerical Methods in Engineering, accepted, 2010.

2nd International Conference on Mathematical and Computational Biomedical Engineering – CMBE2011
March 30 – April 1, 2011, Washington D.C., USA
P. Nithiarasu and R. Löhner (eds)

MESHING CHALLENGES FOR PATIENT-SPECIFIC CARDIOVASCULAR SYSTEMS

Yongjie (Jessica) Zhang
Assistant Professor in Mechanical Engineering,
Courtesy Appointment in Biomedical Engineering,
Carnegie Mellon University, Pittsburgh, PA, USA, jessicaz@andrew.cmu.edu

SUMMARY

The development of cardiovascular biomechanics has increased the need for high-fidelity geometric model construction from volumetric imaging data. Although there have been tremendous progresses in the area of surface reconstruction and 3D geometric modeling, it still remains a challenging process to generate desirable models in various application projects. In this talk, I will present meshing challenges in biomedical applications, as well as details of our octree-based meshing algorithms to extract adaptive and quality 2D/3D finite element meshes for patient-specific cardiovascular systems, conforming to boundaries defined as level sets of a scalar function in the domain. A meshing software package named LBIE-Mesher (Level Set Boundary Interior and Exterior Mesher) has been developed. Besides piecewise-linear element meshes, a skeleton-based sweeping method was developed to construct hexahedral solid NURBS and cubic Hermite from imaging data. Furthermore, I will also talk about one novel method we recently developed to convert any unstructured quadrilateral meshes into T-Spline surfaces. The constructed solid NURBS have been successfully used in isogeometric analysis of arterial blood flow, and the constructed cubic Hermite models have been used in electronic activity analysis of the human heart.

Key Words: *Geometric modeling, mesh generation, cardiovascular system, NURBS, T-Spline, Cubic Hermite.*

REFERENCES

[1] Y. Zhang, C. Bajaj and B-S. Sohn. 3D Finite Element Meshing from Imaging Data. *Computer Methods in Applied Mechanics and Engineering*, 194(48-49):5083-5106, 2005.

[2] Y. Zhang and C. Bajaj. Adaptive and Quality Quadrilateral/Hexahedral Meshing from Volumetric Data. *Computer Methods in Applied Mechanics and Engineering*, 195(9-12):942-960, 2006.

[3] Y. Zhang, Y. Bazilevs, S. Goswami, C. Bajaj and T. J.R. Hughes. Patient-Specific Vascular NURBS Modeling for Isogeometric Analysis of Blood Flow. *Computer Methods in Applied Mechanics and Engineering*, 196(29-30):2943-2959, 2007.

[4] Y. Zhang, C. Bajaj, G. Xu. Surface Smoothing and Quality Improvement of Quadrilateral/ Hexahedral Meshes with Geometric Flow. *Journal Communications in Numerical Methods in Engineering*, 25(1):1-18, 2009.

2nd International Conference on Mathematical and Computational Biomedical Engineering – CMBE2011
March 30 – April 1, 2011, Washington D.C., USA
P. Nithiarasu and R. Löhner (eds)

Hexahedral mesh generation for image-based computational fluid dynamic investigation of vascular districts

Gianluca De Santis*, Matthieu De Beule*, Patrick Segers*, Pascal Verdonck* and Benedict Verhegghe*
*IBiTech-bioMMeda, Ghent University, De Pintelaan 185, Gent, Belgium
Gianluca.DeSantis@UGent.be

SUMMARY

Mesh generation is a critical step in image-based computational fluid dynamic investigation of vascular districts. While structured hexahedral meshes are known to be superior to unstructured meshes for CFD/FEA simulations, their use has been very limited due to the complex and non-automated generation procedure. We propose a new meshing strategy to generate structured conformal hexahedral meshes inside a realistic vascular lumen by combining synthetic descriptors of vascular topology (centerlines and radii of the maximal inscribed spheres) available in *vmtk* with powerful geometrical tools implemented in *pyFormex,* both open source software packages. The final volume mesh closely matches the original surface and can be classified as optimal following usual cell-quality metrics, thus suitable for accurate CFD applications.

Key Words: *mesh, hexahedral, computational fluid dynamics (CFD), artery, pyFormex.*

1. INTRODUCTION

Accessing high temporal and spatial resolution flow data in vascular districts of a patient is becoming reality thanks to the image-based computational fluid dynamics. This approach requires a number of serial steps: medical imaging (CT, MRI, US) and flow measurements at the boundaries of the region of interest, vessel geometry segmentation, computational mesh generation, integration of the Navier-Stokes equations, and post-processing to extract the indices of interest. Among the others, the mesh generation is a critical issue, mainly because the geometry is not build in a bottom-up process (like in manufacturing industry), but appears all together in its complexity after the segmentation. Automatic meshing schemes are widely preferred in patient-specific CFD, typically using unstructured tetrahedral meshes with near-wall prismatic layer, while structured hexahedral meshes are rarely adopted. In a recent study we have compared the performance of unstructured and structured meshes in solving the flow equations with a commercial software (*Fluent, Ansys*) in a coronary artery district and, as expected, we found that unstructured meshes needed much higher resolution than structured meshes to reach mesh independency, with higher computational costs (computational time and memory). Interestingly, the wall shear stress (WSS, a differential quantity) did plateau with structured meshes but did not exhibit a clear converging trend with unstructured meshes [1]. Other sources support such a difference in performance, and attribute it to the high numerical diffusion errors associated with unstructured meshes [2]. As mainly differential quantities (e.g. TAWSS, OSI) are of interest in vascular domains, the CFD results need to have high accuracy. Thus, meshing the

volume domain with hexahedral cells would not only simplify the computational side but also improve the reliability of the calculated values.
In this paper, we present a novel structured hexahedral meshing methodology suitable for vascular districts, which has been implemented in pyFormex, a python-based open-source software under development at Ghent University dedicated to create and to handle large geometrical models [E1].

2. METHODS

A vascular surface (generally in a stereolithography format, STL) needs to be subdivided into simpler domains suitable for structured meshing. Thus, a different strategy is adopted for no/single bifurcating vessels (sweeping case, which represent a simplified case), and for generally branched vessels (mapping case).

2.1 Sweeping case - Single bifurcating vessels (e.g. carotid artery) can be oriented on a plane parallel to the bifurcation axis, which allows drawing some 2D lines around the vessels. Such lines can be used to guide a number of cutting planes which slice the vessel in semi-circular sections aligned longitudinally along the three branches. Then, a sweeping operation can be performed to generate a volume mesh [Figure 1-top].

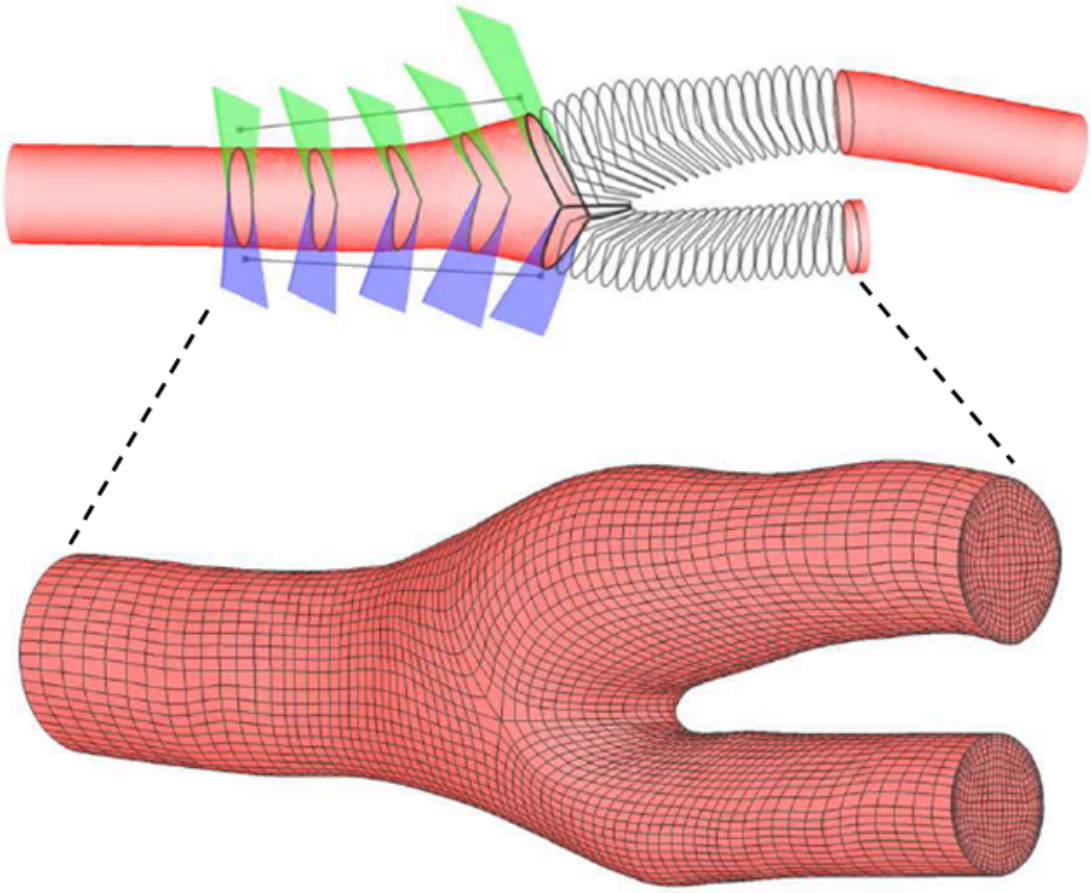

Figure 1: Meshing of a carotid artery by means of three sweeping operations. Top: subdivision of the bifurcation into three branches, which are then sliced into semi-circular sections. Bottom: conformal structured hexahedral mesh of the carotid lumen.

2.2 Mapping case - For more complex districts, such as mice and human aorta, synthetic descriptors of the vascular topology, like centerlines and radii of the maximal inscribed spheres, are needed. An open-source software package (i.e. the "vascular modelling toolkit, *vmtk*", E2) provides automated generation of these descriptors (Figure 2-left). Centerlines and radii can be imported in pyFormex in order to design a series of blocks around the vessel surface, including regions of branching (bif-, tri- or n-furcations, Figure 2-center). In each of these blocks, it is trivial to generate a structured hexahedral mesh and its resolution can be adapted parametrically. Projecting the mesh nodes of the lateral surface of these blocks on the vessel surface provides a one-to-one correspondence between block surface (source) and vessel surface (target). The source-to-target correspondence can be then used to map the volume mesh of each block inside the vessel lumen, by means of an isoparametric transformation. A human aorta is shown as example and the equiangle skew [1] and the scaled Jacobian at all cell nodes [3] are taken as metrics of mesh quality (optimal values are 0 for the equiangle skew and one for the scaled Jacobian).

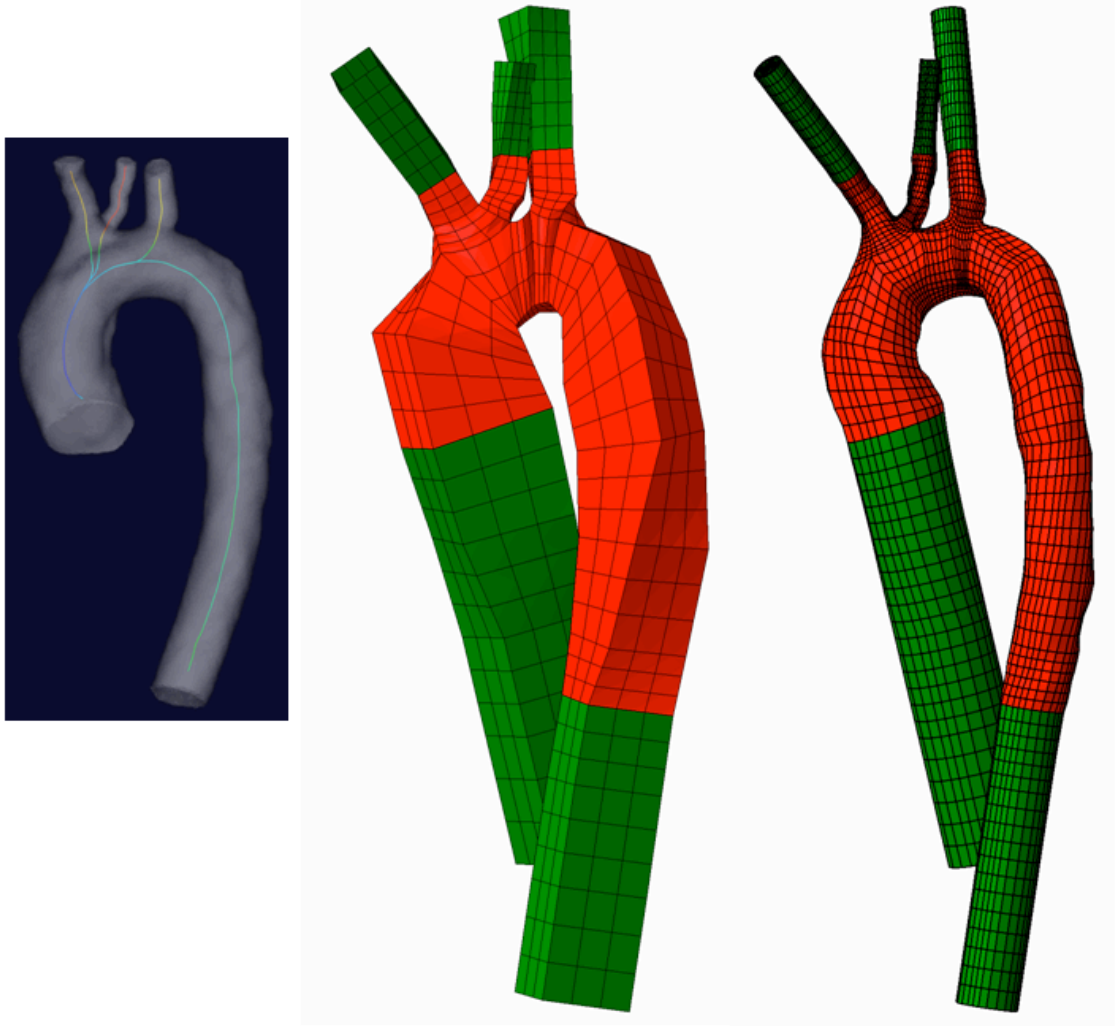

Figure 2: Meshing of a human aorta. Left: centerlines coloured by radius (vmtk). Center: series of blocks around the vessel surface (pyFormex). Right: lumen mesh, with real domain (red) separated from flow extensions (green). The equiangle skew is in average 0.21 and max 0.77; the scaled Jacobian is 0.90 on average, and the minimal value is 0.23.

3. RESULT AND DISCUSSION

3.1 Sweeping case - A carotid artery can be meshed using a Graphical User Interface in a matter of seconds [4, E3]. The mild stenosis present on the ICA does not produce distortion of the cells, as the cross-sections still resemble a nearly circumferential contour (Figure 1-bottom).

3.2 Mapping case -The cells of the aortic computational domain can be divided into two groups, in order to separate the real flow domain from the flow extensions (added with vmtk to apply correct boundary conditions), so that the post-processing can be performed only on the real domain (Figure 2-right). The elements are finer near the wall, to provide higher accuracy for near-wall quantities, and are globally aligned with the flow. Average equiangle skew is below 0.25, which is classified as optimal [E4] and the scaled Jacobian in all cells is positive (valid cells) and higher than 0.2 [3].

4. FUTURE WORK

Current development is aiming at conformal refinement of hexahedral meshes and generation of vessel wall around the lumen from image data (external wall surface) or, alternatively, from anatomical scaling data (variable wall thickness as percentage of lumen radius).

REFERENCES

[1] De Santis G, Mortier P, De Beule M, Segers P, Verdonck P, Verhegghe B (2010). Patient-specific computational fluid dynamics: structured mesh generation from coronary angiography. Med Biol Eng Comput, 48, 4:371-80.

[2] Vinchurkar S, Longest PW (2008). Evaluation of hexahedral, prismatic and hybrid mesh styles for simulating respiratory aerosol dynamics. Comput Fluids 37:317.

[3] Knupp P (2000). Achieving finite element mesh quality via optimization of the Jacobian matrix norm and associated quantities. Part II: A framework for volume mesh optimization. Internat J Numer Methods Engrg, 48, 1165-1185.

[4] De Santis, G, De Beule, M, Segers, P, Verdonck, P, Verhegghe, B, Patient-specific computational hemodynamics: generation of structured and conformal hexahedral meshes from triangulated surfaces of vascular bifurcations. Comput Meth Biomech Biomed Eng, in Press.

ELECTRONIC REFERENCES

(available on 22/10/2010)

[E1] www.pyFormex.org

[E2] www.vmtk.org

[E3] http://www.youtube.com/watch?v=T1pVFCzrmGI

[E4] www.fluentusers.com

2nd International Conference on Mathematical and Computational Biomedical Engineering - CMBE2011
March 30 - April 1, 2011, Washington D.C, USA
P. Nithiarasu and R. Löhner (Eds.)

High-order meshing and flow simulation of the rabbit arterial system

A. Plata*, J. Peiró*, S.J. Sherwin* and V. Peiffer*
*Department of Aeronautics, Imperial College London,
South Kensington Campus, London SW7 2AZ, UK,
{a.plata-garcia07,j.peiro,s.sherwin,v.peiffer09}@imperial.ac.uk

SUMMARY

We discuss a methodology developed to produce high-order subject-specific computational flow simulations of the three-dimensional flow of blood within the rabbit arterial system.

A very detailed geometrical description of the arterial tree is obtained from high-resolution CT scan data of a resin corrosion cast. Standard segmentation techniques are then used to produce a triangulation of the vessel surface, which is subsequently smoothed to improve mesh quality. This triangulation is used to generate a volume mesh of straight-sided elements.

The curvilinear mesh required for the high-order incompressible solver Nektar++ is generated by projecting the additional nodes onto a piecewise smooth high-order representation of the surface which is obtained via interpolation of spherigon patches.

Finally, we will present flow simulations obtained for this geometry and briefly discuss the effect of geometry on the distribution of wall shear stresses (WSS) for flows at Reynolds numbers of 50, 300 and 1300.

Key Words: *p-meshing, subject-specific reconstruction, high-order flow simulation.*

1 Introduction

Subject-specific computational flow simulations of the three-dimensional flow of blood within the rabbit arterial system are useful to characterise flow patterns, to determine the spatial distribution of wall shear stresses (WSS) to and analyse the effect geometrical features on the distribution of atheroesclerosis.

Atherosclerosis is known to occur in a spatially non-uniform fashion within the arterial system that might correlate with the WSS patterns. The distribution of vascular wall shear stress (WSS) has been shown to depend strongly on subject-specific geometric features [1]. Therefore, generating a detailed and faithful computational definition of the vascular geometry is necessary in order to accurately model blood flow within the arterial system. Here, blood flow is modelled in a highly realistic representation of the rabbit aorta using the high-order flow solver Nektar++. This will require the generation of high-order meshes for the geometry of the aortic arch from a set of CT images. This procedure is described in the following.

2 Geometrical definition

A corrosion cast of a male New Zealand White rabbit aged 18 months and weighing 3.25 kg was obtained in accordance with the protocols described in [2] and it is shown in Fig. 1. The cast was

scanned at a resolution of 55.2μm using a micro-CT scanner from which $2000 \times 2000 \times 2000$ voxels of DICOM data were obtained. The image resolution is such that 100 voxels span the root of the aorta.

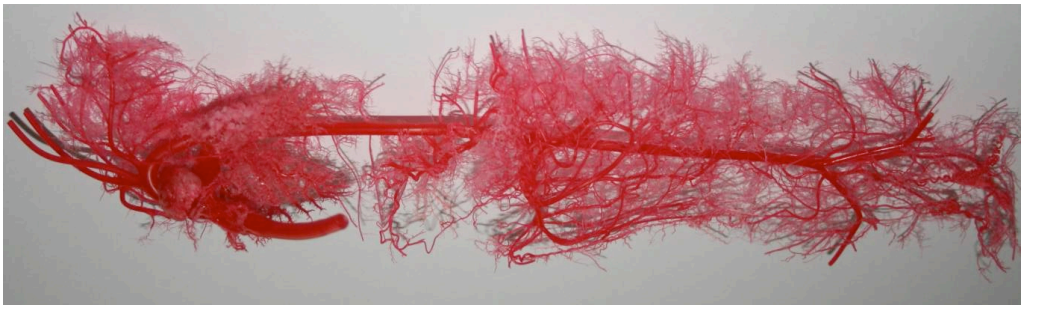

Figure 1: Cast of the main arteries of the arterial tree of a male New Zealand White rabbit.

An intensity iso-surface was segmented from the micro-CT scan data using Amira (Visage Imaging, Inc.). Further processing was carried out using the open-source software VMTK (www.vmtk.org). Firstly the surface was cropped in order to remove unwanted arteries and bound the computational domain. Then flow extensions were extruded form each outflow vessel to allow the imposition of boundary conditions sufficiently far from the domain of interest. Finally, the surface was smoothed to remove any artifacts introduced during the scan and segmentation process whilst preserving all small-scale geometrical features.

Images of the final surface definition are shown in Fig. 2. Note that the geometry includes the vessels emanating from the aortic arch, followed to at least their second branching generation, and five pair of intercostal arteries.

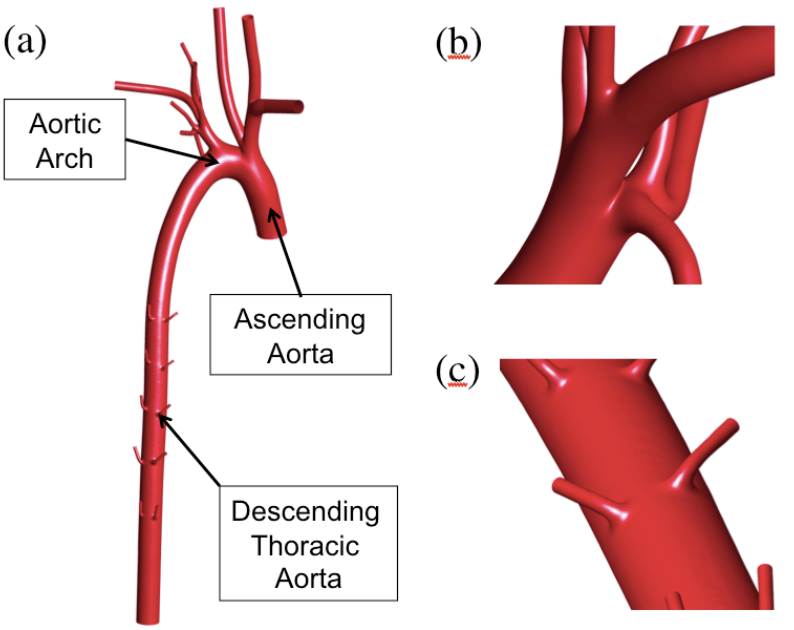

Figure 2: Views of the reconstructed aortic geometry: (a) global view of the geometry, (b) enlargement near the carotid artery; and (c) enlargement of the descending thoracic aorta showing some of the intercostal arteries.

3 High-order mesh generation

The high-order continuous Galerkin finite element method Nektar++ [3] is used to simulate the flow of blood as a Newtonian incompressible fluid. This requires that the computational domain is subdivided into elements, within which the solution is represented by a high-order polynomial expansion [4].

A mesh of straight-sided elements was generated first as follows. An initial surface triangulation was constructed with Gambit 2.4.6 (ANSYS, Inc). The size of the elements was based on the curvature of the surface definition, such that smaller elements were position in areas of greater curvature. The volume mesh was generated with Tgrid 4.0.24 (ANSYS, Inc). A prismatic boundary layer of variable thickness (based on the curvature) was defined first. An interior mesh of linear tetrahedral elements was then generated.

Subsequently, to generate a high-order mesh, the external faces of the prismatic boundary elements were curved using spherigon patches [5] following the approach described in [6]. The resulting volume mesh shown in Fig. 3 contains 25,498 prismatic and 79,847 tetrahedral elements (i.e. 105,345 elements in total).

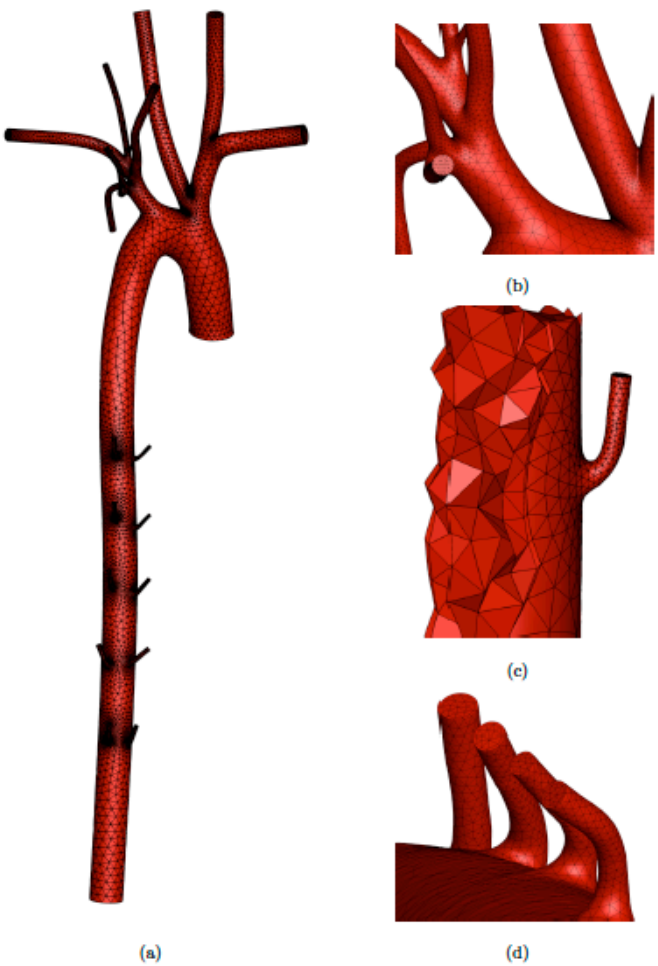

Figure 3: High-order mesh containing 25,498 prismatic and 79,847 tetrahedral elements. Note that only the (curved) edges of the high-order elements are shown. The images show: (a) whole computational mesh, (b) an enlargement of the mesh at the quadfurcation of the left subclavian artery, (c) an axial section of the descending aorta, and (d) four intercostal arteries.

4 High-order flow solution

The flow of blood in the aortic arch is modelled using the steady-state incompressible Navier-Stokes equations for a Newtonian flow. The numerical simulation is performed using the high-order solver Nektar++ [3] that employs a spatial discretization of finite elements with spectral basis and a fractional step integration in time.

An inflow boundary condition is imposed at the root of the aorta where a flat velocity profile is assumed. Three values of inflow velocity magnitude were considered that led to values of the Reynolds' number, Re, of 50, 300 and 1300. Outflow boundary conditions were set to achieve a flow rate split consistent with Murrays law. The motion of the wall was neglected in the simulations.

A p-convergence analysis established that adequate accuracy could be obtained using a 5th order polynomial expansion to represent the flow solution. The results obtained on the high-order mesh (Fig. 3) with $p = 5$ are shown in Fig. 4. The computed WSS distribution in the descending aorta depends significantly on Re. For a given vascular geometry, the skewness of the axial velocity dictate the location of the low and high WSS streaks, and hence the macroscale WSS distribution. In particular, an increase in Reynolds number is associate with enhanced swirling of the blood flow, resulting in greater rotation of the axial velocity (and hence the WSS streaks) about the streamwise axis. The distribution of these streaks matches well the distribution described in [7].

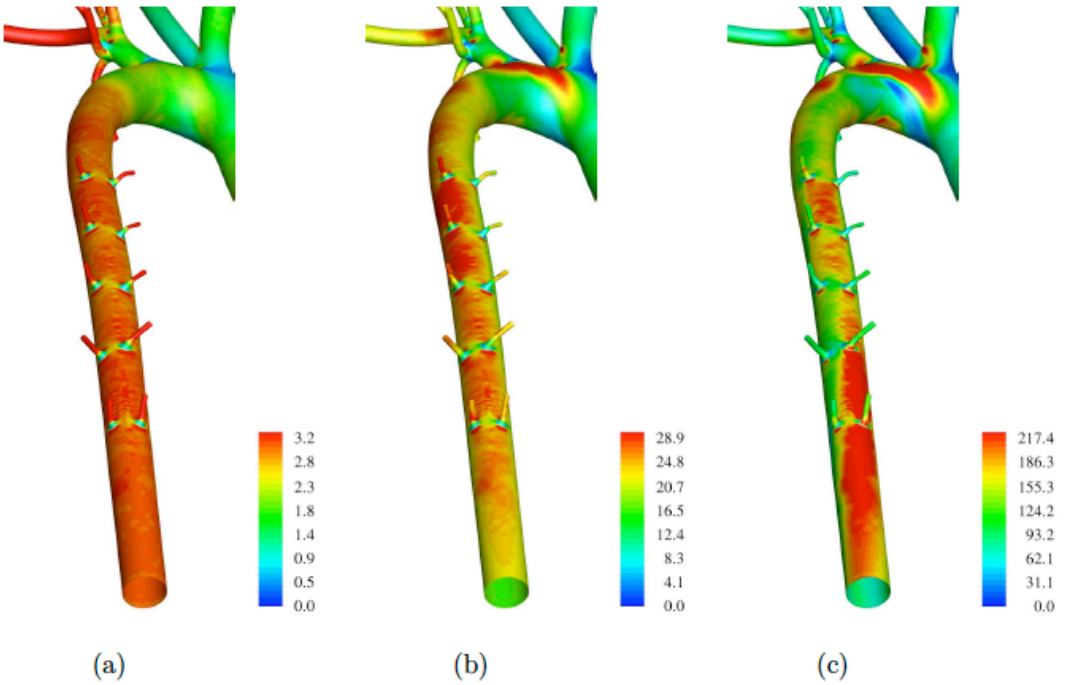

Figure 4: Colour maps of WSS (dynes/cm^2) at the proximal descending thoracic aorta, viewed dorsal-ventral: (a) Re=50, (b) Re=300, and (c) Re=1300.

5 CONCLUSIONS

A high-order continuous Galerkin finite element method has been used to simulate steady Newtonian blood flow within a realistic representation of the rabbit aortic arch and descending thoracic aorta, which was assumed to have rigid and stationary walls.

The computed distribution of endothelial WSS in the region near the inter-costal arteries was found to exhibit a distribution very similar to the lesion patterns in the proximal thoracic aorta in mature rabbits reported in [7]. This result certainly suggests that blood flow, and in particular WSS, plays a significant role in regulating the onset of the disease. However, further computational work is required to confirm such an effect of geometrical features on blood flow.

Acknowledgements

The authors would like to thank Peter Weinberg and Tony Hunt for providing the rabbit's cast. We would also like to acknowledge the contribution of Peter Vincent, who designed the protocol for reconstructing vascular geometries from CT scan data sets.

REFERENCES

[1] A.M. Shaaban and A.J. Duerinckx, Wall shear stress and early atherosclerosis: a review, *Am J Roentgenol* **174**, 1657 (2000).

[2] P.D. Weinberg et al., Characteristics of the pulse waveform durin altered nitric oxide synthsis in the rabbit, *Brit. J. Pharm.*, **133**, 161 (2001).

[3] S.J. Sherwin and R.M. Kirby, Nektar++ distribution, *www.nektar.info* (last accessed December 2010).

[4] G.E. Karniadakis and S.J. Sherwin, *Spectral/hp element methods for computational fluid dynamics*, Oxford Scientific Publications, 2nd edition, (2005).

[5] P. Volino and N. Magnenat-Thalmann, The Spherigon: a simple polygon patch for smoothing quickly your polygonal meshes, in Proceedings of the Computer Animation, 72 (1998).

[6] L. Grinberg, T. Anor, J.R. Madsen, A. Yakhot, and G.E. Karniadakis, Large-scale simulation of the human arterial tree, *Clin. Exp. Pharmacol.* **36**, 194 (2009).

[7] S.E. Barnes and P.D. Weinberg, Contrasting patterns of spontaneous aortic disease in young and old rabbits, *Arterioscl. Throm. Vas.* **18**, 300 (1998).

2nd International Conference on Mathematical and Computational Biomedical Engineering - CMBE2011
March 30 - April 1, 2011, Washington D.C, USA
P. Nithiarasu and R. Löhner (Eds.)

SEMI-AUTOMATIC MESH GENERATION AND COSMETICS FOR SUBJECT-SPECIFIC BIOMEDICAL GEOMETRIES

Igor Sazonov⋆ and Perumal Nithiarasu⋆⋆
⋆College of Engineering, Swansea University, Singleton Park, Swansea, SA2 8PP, U.K.
i.sazonov@swansea.ac.uk
⋆⋆College of Engineering, Swansea University, Singleton Park, Swansea, SA2 8PP, U.K.
p.nithiarasu@swansea.ac.uk

SUMMARY

Surface and volume mesh generation techniques are presented for subject-specific medical geometries. The applications of interest are hemodynamics in blood vessels and air flow in upper human respiratory systems. The methods described are designed to minimize distortion to a given domain boundary. They are also designed to generate a triangular surface mesh first and then volumetric tetrahedrons with high quality surface and volume elements. A simple procedure to generate boundary layer mesh is also presented. The methods described here are semi-automatic in nature due to the fact that the geometries are complex and full automation of the procedures is possible only if high quality scan can be obtained.

Key Words: *mesh generation, surface mesh cosmetics, Marching Cubes.*

1 INTRODUCTION

Subject-specific numerical modelling of blood and air flow through arteries and respiratory systems includes several stages: (a) Segmentation of 3D scans; (b) Generation of a 3D mesh (both surface and volume) with a smooth surface that is as close to the original geometry as possible; (c) Numerical flow solution.

The performance of a solution scheme depends significantly on the mesh quality: the elements should be of proper size, quality and shape. In this work, we concentrate on the second stage in which mesh generation and relevant cosmetics are carried out. We apply a combination of some standard methods and their improvements.

At present, powerful mesh generation methods (surface and volume) exist for traditional engineering applications such as aerospace and process engineering when the object boundaries can be defined and described analytically or piecewise analytically (for example, by the NURBS patch method). In subject-specific biomedical geometries, the surfaces are not well-defined and analytical description is not easy.

Hence, generation of mesh in such objects needs different approaches (mainly in generating the surface mesh). In extending standard methods to medical applications, the surface is divided by pathes first and NURBS approximation [1] or harmonic mapping technique [2] is then applied for every patch.

Here we develop a meshing approach in which the surface is not divided into patches. This method is based on surface preserving mesh cosmetics applied to the surface mesh.

2 OBTAINING AN INITIAL MESH

Result of segmentation in most the cases is represented as a binary image. Then the simplest way to build a consistent surface mesh is the Marching Cube (MC) method. If the boundary of segmented object is represented by a smooth level set function (changing its sign at the boundary) then the Advanced Marching Cube method [3] can be applied. The Advanced MC gives a smoother mesh that the standard MC method.

If the object geometry is complicated, containing many parts and passages of lengthscales comparable to the voxel size (for example, nasal cavity, system of small blood vessels, lungs, etc.), then the mesh can contain many nodes and/or edges belonging simultaneously to different parts of the mesh. If such nodes or edges are rare and separated from each other, it is handled by some simple correction methods: for example, to remove all elements containing a node or an edge belonging to different parts of the mesh and triangulate the formed gaps. If many such edges are connected, then an artificial increase of resolution of the image can help: the binary entries are interpolated onto a finer grid which is double of original size. This gives a smoother level set function field with values that include fractions. Then the mesh built by the advanced MC method contains much smaller number of such edges and nodes and therefore can be easily "healed".

3 CROPPING THE OBJECT

When dealing with modelling blood flow or air flow through subject-specific geometries, the patient scans are often not clean and may contain much larger domain than that is required. It is also currently not possible to segment the human arteries or airways down to smallest capillaries or the tiniest bronchi and alveoli. In such cases, it is necessary to crop the geometry to specify boundary conditions at the inlets and outlets of blood vessels or airways. It is easy to crop the image to a required size but the inlets and exits may not be orthogonal to the inlet or exit axis. The slanted inlet and exit thus obtained can cause difficulties in imposing boundary condition during the numerical simulation. Thus, it is important to crop objects at the required locations and as orthogonal as possible to the anticipated flow direction.

In cropping an object, a useful stage is skeletonisation which preserves the object topology. It is easy to indicate a point on a skeleton line (for example by mouse) or develop automatic method determining such point: to set a certain distance along the blood vessel axis from a blood vessel bifurcation, stenosis, aneurysm, and other peculiarity.

The skeletonisation consists of following stages: (i) voxel thinning, (ii) skeleton line analyzing, (iii) skeleton line smoothing.

The direction of cropping plane is set by a tangent to a smoothed skeleton line. A procedure is developed to correct this direction in case of complicated geometry of the blood vessel or air passage in the vicinity of the cropping point.

After determination of cropping planes for every inlet/outlet (set by a point on a skeleton line and the direction), the initial surface mesh is trimmed, and an unclosed mesh is obtained. For cosmetics purposes, it is necessary to triangulate the open inlet/outlets by a plane mesh.

Note that after cropping, we obtain different sort of mesh faces: wall faces and inlet/outlet faces. Edge containing both sort of faces is a ridge edge and its endpoints are ridges points.

4 SURFACE MESH COSMETICS

The mesh obtained by the marching cube method is not smooth; always contains a number of ill-shaped elements(triangles with the small aspect ratio); and the triangular element size is usually smaller or larger than that required for flow solution scheme. Therefore, the mesh needs some mesh cosmetics which improves the quality of the mesh. There are essentially three procedures used here to improve the mesh quality: (i) Mesh smoothing; (ii) Edge swapping; (iii) Edge. splitting/contraction.

(i) During the mesh smoothing, the points are moved along the surface in order to enhance quality of surface triangles without changing the mesh topology. Here Taubin smoothing is used [4] to minimize distortion of the surface. Note, that the Taubin smoothing protects very well the shape of ball-like objects, but too many iteration steps can modify essentially the surface of cylinder-like objects such as blood vessels. Also, it can easily make dramatic changes to the mesh in vicinity of saddle points formed in a bifurcation of blood vessels or airways if not carried out carefully. Therefore the number of smoothing steps should be minimized. In smoothing the initial mesh, it is useful to restrict displacement of the nodes from their initial positions by half of the voxel size. At inlet/outlet the Laplace smoothing can be applied. The most care is needed for the ridge nodes.

(ii) We apply the topology based edge swapping [5]. Then, the beneficial effect on the mesh triangle quality appears after the smoothing procedure. In this procedure the cumulative difference of the nodal index from the perfect value of 6 is minimized. Slightly different procedure is used for the so-called near ridge edges. Ridge edges should never be swapped.

(iii) If the mesh contains a significant number of very short or/and very long edges and the average edge length is not sufficiently close to some predefined reference length as required by the numerical integration scheme, then edge splitting and contraction [6] are very useful procedures. After every splitting or contraction of edges, edge swapping and then the Taubin smoothing are locally applied. Note that after splitting or contraction a new point appears and this new part should be located on the surface. A simple method is derived for determining the position of this new point.

In complicated geometries such as a nasal cavity, where width of the air passages is comparable to the scan resolution, the noise in the scans may result in a significant number of narrow tunnels in the initial mesh. This sponge-like geometry need special care as a contraction of some edges can make the mesh inconsistent. Methods of removing such narrow tunnels, caused by noise, are developed.

5 BUILDING VOLUMETRIC MESH

To resolve the viscous boundary layer in flow studies, a special structure of the near-wall volumetric mesh is required. The elements built in the direction of inward normal to the wall should be essentially smaller than the element size in the inner volume of a domain. The short edge of a near-boundary tetrahedra should be directed normal to the wall. Special procedure of building the boundary layer tetrahedron mesh is developed. The thickness of the boundary layer mesh is adjusted to the local diameter of the blood vessel or to the width of air passage.

To generate a volumetric mesh in the inner domain, we use an in-house developed code [7] based on a Delaunay triangulation to insert the points to generate a 3D volume mesh of tetrahedrons. Subsequently, 3D mesh cosmetics based on 3D swapping, and smoothing is applied. As mentioned, the quality of the 3D mesh depends on the quality of the surface mesh. In all carotid arteries that we have reconstructed so far, the smallest tetrahedral aspect ratio for a specific geometry lies between 0.01 and 0.1.

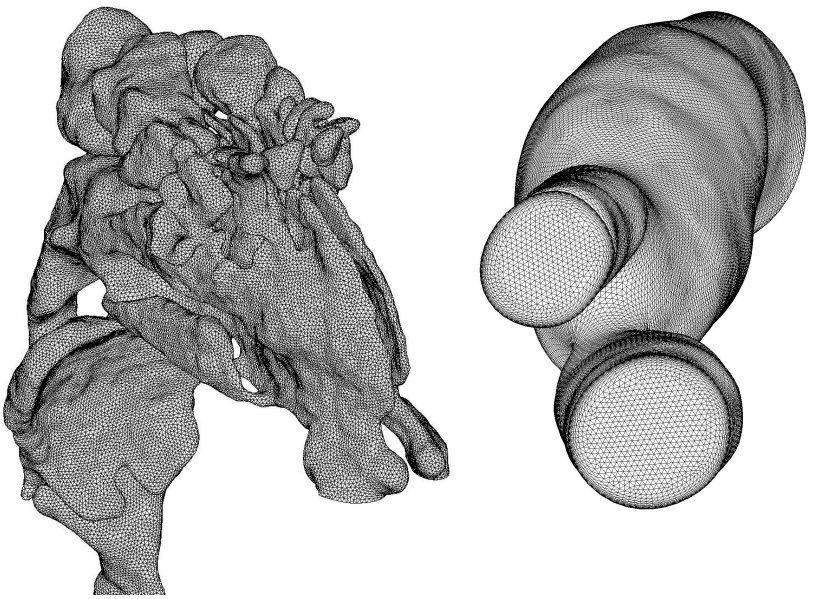

Left: Nasal part of the upper airways. Right: Carotid with triangulated outlets

REFERENCES

[1] Y. Zhang, Y. Bazilevs, S. Goswamia, C. Bajaj, and T. Hughes, Patient-specific vascular NURBS modeling for isogeometric analysis of blood flow, *Computer Methods in Applied Mechanics and Engineering*, 196(2930), 2943-2959, 2007.

[2] E. Marchandise, G. Compère, M. Willemet, G. Bricteux, C. Geuzaine, and J.-F. Remacle, Quality meshing based on STL triangulations for biomedical simulations, *Communications in Numerical Methods in Engineering*, to appear, 2010.

[3] W. H. Frey and D. A. Field, Mesh relaxation: a new technique for improving triangulation, *Int. J. Numer. Meth. in Engineering*, 31, 1121-1133, 1991.

[4] E. V. Chernyaev, *Marching cubes 33: Construction of topologically correct isosurfaces*, Technical report Cern CN 95-17, CERN, 1995.

[5] G. Taubing, A signal approach to fair surface design, in *Procedding of SIG- GRAPH (August 1995)*, 351-358, 1995.

[6] D. Wang, O. Hassan, K. Morgan, and N. P. Weatherill, Enhanced remeshing from STL foles with applications to surface grid generation, *Communications in Numeriacal Methods in Engineering*, 23, 227-239, 2007.

[7] N. Weatherill and O. Hassan, Efficient three-dimensional Delaunay triangulation with automatic point creation and imposed boundary constraints, *International Journal for Numerical Methods in Engineering*, 37, 2005-2039, 1994.

2nd International Conference on Mathematical and Computational Biomedical Engineering - CMBE2011
March 30 - April 1, 2011, Washington D.C, USA
P. Nithiarasu and R. Löhner (Eds.)

GENERATING SMOOTH SURFACE MESHES FROM LABELLED MEDICAL DATA SETS

V. d'Otreppe[⋆,⋆⋆]**, R. Boman**[⋆⋆] **and J.P. Ponthot**[⋆⋆]
[⋆]F.R.S.-FNRS Research Fellow, vdotreppe@ulg.ac.be
[⋆⋆] Aerospace and Mechanical Engineering Department, University of Liege, Belgium

SUMMARY

In this article, an innovative procedure to create high quality triangular meshes from medical scans is proposed. The approach is based on an enhanced Marching Tetrahedra algorithm that extracts a consistent multiple region surface mesh from a labelled volume data set; coupled with a surface reconstruction method to avoid typical staircase artifacts. Mesh smoothing and decimation algorithms are also revised to conform to the multiple material nature of the system as well as to adhere to the underlying volume data. The proposed method is well suited for subsequent volume mesh generation and finite element simulations.

Key Words: *Biomechanics, Mesh Generation, Finite Element Method.*

1 INTRODUCTION

The finite element (FE) method is commonly used in biomedical applications for the simulation of the behaviour of biological structures. A key component in FE simulation is the creation of a finite element mesh. In medical applications, the meshes should be directly generated from the medical scans. Moreover, biological structures are usually composed of several inner regions that need to be separately segmented, labelled and meshed to be able to apply different material properties in the finite element model. The mesh is generally created in two steps. First, the boundaries of the labelled regions are extracted as a set of triangular meshes. Then this multiple region surface mesh is extended to the third dimension using one or another volume mesh generator [10].

This article addresses the problem of surface mesh generation from a multi-valued volume data set. Following properties are guaranteed:

- The generated mesh consists of a set of non manifold triangle meshes that separate each connected component in the labelled data set. These interface meshes join each other consistently along their boundaries, i.e., no T junctions nor gaps may appear.
- The surface mesh is a geometrically accurate representation of the data represented in the medical scans. However, it is not be tainted by the typical aliasing and staircase artifacts that are due to the discrete nature of the voxels.

2 APPROACH OVERVIEW

The problem of generating a multi-domain mesh from labelled scans has been addressed several times in the literature [3,6,8,10]. The simplest methods generalize the Marching Cubes algorithm

to domains containing several regions [11]. However, these approaches are often confounded by ambiguity problems and inconsistent meshes. Solutions to these ambiguity problems have been proposed in [1,9]. An alternative solution is to use the Marching Tetrahedra algorithm instead of the Marching Cubes [5]. In the Marching Tetrahedra algorithm, the binary input data set is divided into tetrahedra, and each tetrahedron is processed in turn. Depending on the voxel values evaluated at its vertices, a triangulation approximating the boundary surface of the segmented region in the tetrahedron is created. This simplest algorithm may be generalised to a multi-label data set by defining new triangulation patterns [7]. These new triangulation patterns give the polygonalisation of a tetrahedron when its vertices are located in three or four distinct material regions. This multi-material Marching Tetrahedra algorithm is well adapted to the generation of meshes from images containing many labels, as the computation time does not depend on the number of labels present in the image. However, since the meshes are directly generated from the segmented data, they are tainted with aliasing or staircase artifacts [3]. Mesh smoothing approaches may eventually be used to suppress the ridges in the mesh. However, these approaches cannot guarantee that the result is an accurate representation of the initial volume [2].

The use of a surface reconstruction method prior to mesh generation is the best way to avoid aliasing artifacts whilst preserving geometric accuracy. The problem of reconstructing a continuous 3D implicit model from a set of points in the Euclidean space has been studied by many authors [2]. One of the first implicit reconstruction methods has been proposed by Hoppe [6]: a signed distance function is obtained from a set of unorganized points in $\Re^3$ by taking the distance to the tangent plane evaluated at the closest input point. Other methods have then been developed based on moving least squares, level sets, radial basis functions and finally, by using multi-level partition of unity (MPU) models [8]. In the latter, an approximation of the distance function to the surface is given by a set of overlapping local approximation functions that are blended together, summing to one (partition of unity). The authors show that the MPU implicit function is a reasonable approximation to the Euclidean distance field near the zero isosurface and that the geometric approximation error is user-controlled and bounded. The approach is extremely well adapted to the large data sets encountered in medical imaging as it uses a recursive octree subdivision in order to adapt to local surface details. Hence, computational time rather depends on surface complexity instead of image size. Developed in the context of Computer Graphics, MPU implicit models have already been used to create a smooth closed surface from a set of parallel contours [2]. Two main issues need to be solved to further extend this method to multi-label three-dimensional images. First, the original algorithm only generates closed surfaces and is, a priori, not adapted to define surfaces composed of several material domains. Second, a procedure to extract the input sets of points and corresponding normals from a segmented volume need to be determined.

The first issue is solved by using constructive solid geometry operations to define the domain of validity of each interface surface composing the structure. In other words, from a multi-label volume image containing N connected components, N interface surfaces are defined, corresponding to the N boundaries existing between two distinct labels. In opposition to the classical algorithm, these surfaces may either be open or closed. Open surfaces are always bounded by another surface. In the present algorithm, the information about the surfaces relative position is initially extracted from the input volume. A property of the MPU implicit function is that, for an open set of points, the function extends the surface at its boundaries. Thanks to this property, the intersection between the different interface surfaces is well defined, whatever their relative angle and position are.

Each MPU function requires a set of points and corresponding normals to be extracted from the segmented volume. In the proposed approach, boundary points are obtained for each interface surface $s_n$separating two different labels $[\lambda_1, \lambda_2]$, by taking each voxel $v_{i,j,k}$ in turn and evaluating its neighbourhood. If voxel $v_{i,j,k}$ equals λ_2 and if λ_1 is in the neighbourhood of the voxel $v_{i,j,k}$ then a new point p with the position of the voxel is added to the set of points corresponding to surface

s_n. The same neighbourhood is used to evaluate the corresponding normal. The input normals are subsequently normalised and smoothed to augment the efficiency of the MPU approach. Also, the input points are translated by 0.5 times the image spacing in the direction of its normal.

The use of a surface reconstruction method prior to mesh extraction inherently removes the problems of staircase artifacts in the mesh. An additional advantage is that the sampling grid used in the polygonalisation method is decoupled from the image spacing and may thus be adjusted according to the minimum feature size that should be preserved. However, the problem is often the opposite: the image resolution is too low to capture all details (e.g., teeth appear attached to each other in a classical CT of the mandible and should be separated in the FE model). In this case, it may be useful to integrate the user's knowledge about the topology. This option is easily introduced in the present algorithm.

Finally, mesh simplification and mesh smoothing algorithms are also introduced and adapted to the multiple material nature of the system. Indeed, grid based methods as the Marching Tetrahedra always generate too many triangles for a given sampling resolution. In the proposed approach, a vertex decimation scheme is integrated to the mesh extraction algorithm to eliminate unnecessary triangles directly and reduce the memory footprint of the algorithm. An enhanced Laplacian smoothing algorithm that preserves the mesh integrity as well as its geometric accuracy is also proposed. The method consists of a traditional Laplacian smoothing algorithm, in which the nodes are subsequently projected at the zero level of their respective distance functions, using the Newton-Raphson method.

3 RESULTS

The procedure has been tested on several of data sets of different modality and anisotropy. In each case, the geometric approximation error ϵ and mesh quality q have been measured. The error ϵ is evaluated at each mesh node as its distance to the nearest input point, normalised by the image in-plane spacing. The mesh quality is evaluated by computing the shape quality q of each triangle composing the surface mesh [4].

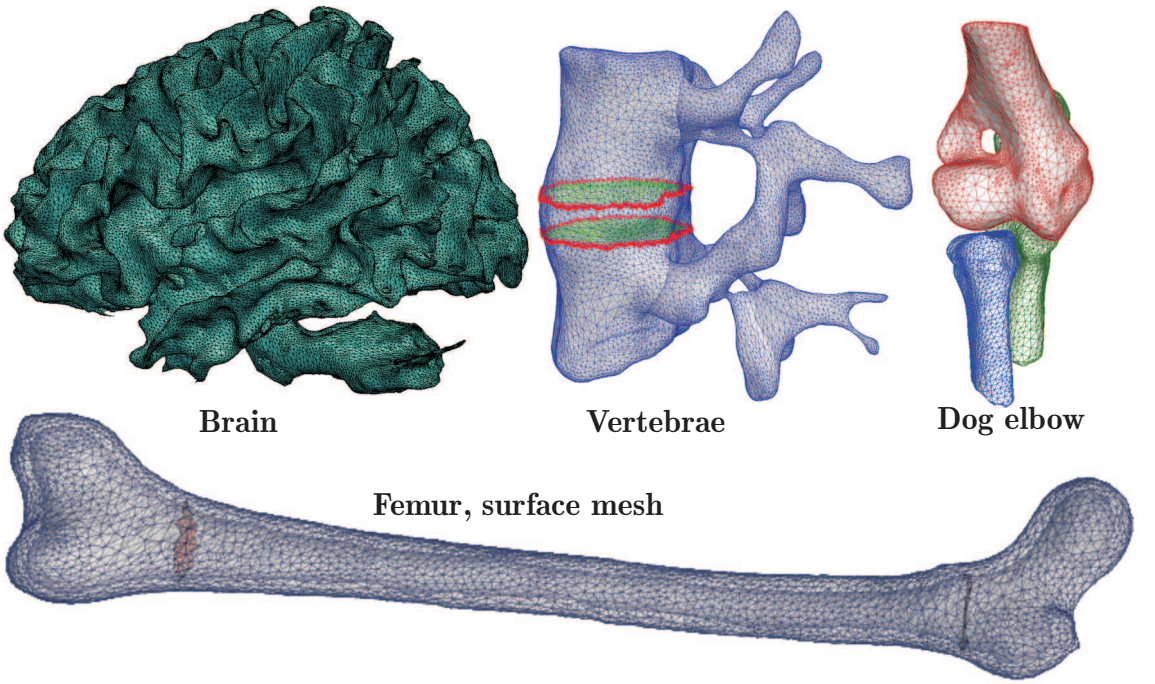

Results indicate that more than 90% of the mesh nodes are located at a maximum of half a voxel distance of the input points. Table [1] also shows that generated surface meshes are of good quality, well suited for further volume mesh generation and finite element simulation.

	Source	# Labels	# Cells	# Nodes	CPU time	$\bar{\epsilon}$	$\bar{q}$
Brain	MRI	3	390264	193812	2h36m50s	0.053	0.76
Dog elbow	CT	4	127798	63819	45m30s	0.137	0.77
Vertebrae	CT	3	33720	16641	3m6s	0.196	0.75
Mandible	CT	14	555760	276666	36m25s	0.422	0.78
Aluminium foam	μ-CT	1	141768	70580	1h56m44s	0.116	0.75
Femur	CT	4	44014	21928	3m45s	1.018	0.75

Table 1: *Results obtained on a number of data sets.*

4 CONCLUSIONS

A novel approach to generate smooth multi-region surface meshes has been proposed. Results, based on a broad range of data sets, show that the procedure is extremely robust. The generated multi-material meshes are consistent, topologically correct and geometrically accurate. They are of good quality and well adapted to FE simulations.

REFERENCES

[1] J. Bloomenthal and K. Ferguson. Polygonization of non-manifold implicit surfaces. In *Proceedings of the 22nd annual conference on Computer graphics and interactive techniques*, pages 309-316, ACM, 1995.

[2] I. Braude, J. Marker, K. Museth, J. Nissanov and D. Breen. Contour-based surface reconstruction using mpu implicit models. *Graphical Models*, 69(2):139-157, 2007.

[3] S. Dillard, J. Bingert, D. Thoma and B. Hamann. Construction of simplified boundary surfaces from serial-sectioned metal micrographs. *IEEE Transactions on Visualization and Computer Graphics*, pages 1528-1535, 2007.

[4] P.L. George and H. Borouchaki. Delaunay triangulation and meshing: application to finite elements. *HERMES*, Paris, 1998.

[5] A. Gueziec and R. Hummel. Exploiting triangulated surface extraction using tetrahedral decomposition. *IEEE Transactions on visualization and computer graphics*, 1(4):328-342, 1995.

[6] H. Hoppe. Surface reconstruction from unorganized points. *PhD thesis*, University of Washington, 1994.

[7] H. Müller. Boundary extraction for rasterized motion planning. *Modelling and Planning for Sensor Based Intelligent Robot Systems*, pages 41-50, 1994.

[8] Y. Ohtake, A. Belyaev, M. Alexa, G. Turk and H.-P. Seidel. Multi-level partition of unity implicits. In *ACM SIGGRAPH 2005 Courses*, Los Angeles, California, 2005.

[9] B. Reitinger, A. Bornik, and R. Beichel. Constructing smooth non-manifold meshes of multi-labeled volumetric datasets. *WSCG (Full Papers)*, pages 227-234, 2005.

[10] H. Si. a quality tetrahedral mesh generator and three-dimensional delaunay triangulator. *Weierstrass Institute for Applied Analysis and Stochastic*, Berlin, Germany, 2006.

[11] Z. Wu and J.M. Sullivan Jr. Multiple material marching cubes algorithm. *International Journal for Numerical Methods in Engineering*, 58(2):189-207, 2003.

2nd International Conference on Mathematical and Computational Biomedical Engineering - CMBE2011
March 30 - April 1, 2011, Washington D.C, USA
P. Nithiarasu and R. Löhner (Eds.)

Robust Medial Curve Computation for Biomedical Geometries

V. Dyedov*, D. Einstein and X. Jiao***
* Department of Applied Mathematics and Statistics, Stony Brook University, Stony Brook, NY 11794 (vladimir@ams.sunysb.edu, jiao@ams.sunysb.edu)
** Biological Monitoring and Modeling, Pacific Northwest National Laboratory, Richland, WA 99354 (daniel.einstein@pnl.gov)

SUMMARY

One-dimensional representation (commonly known as the curve skeleton or medial curve) of a three-dimensional object has a wide range of applications in biomedical engineering, such as morphometry and computer assisted surgery. The computation of medial curves poses significant challenges, in terms of both theoretical analysis and practical efficiency and reliability. We propose a definition and analysis of medial curves and also describe an efficient and robust method called *local orthogonal cutting* for computing medial curves. Our approach is based on three key concepts: a local orthogonal decomposition of objects into substructures, a differential geometry concept called the interior center of curvature, and integrated stability and consistency tests. We illustrate the effectiveness and robustness of our approach with some highly complex, large-scale, noisy biomedical geometries derived from medical images, including lung airways and blood vessels. We also present comparisons of our method with some existing methods. This work was in part supported by National Institutes of Health (NIH) Research Grant R01HL073598

Key Words: *curves and surfaces, medial curves, orthogonal decomposition, interior center of curvature, stability.*

1 INTRODUCTION

Medial curves and other curve skeletons have a wide range of applications in geometric modeling and analysis, such as shape matching and shape retrieval, which are surveyed thoroughly in [1]. We primarily focused on identifying medial curves for tubular structures. Though this class seems narrow, it actually addresses a wide range of biomedical needs, e.g biological trees, such as lung airways and blood vessels. Aslo for these objects the medial curve is mathematically well-defined. The motivating applications for this work are multiscale modeling [2], morphometry [3, 4], physiology [5], image analysis [6], and computer assisted surgery [7]. For example, the medial curves can form the basis of a morphometric analysis of tree-structured airways in the lung [3] or coronary vessels in the heart [8], by providing statistics for segment length, diameter, and bifurcation angle. Since the medial curves embed the topology of the tree and distill its geometry, these data can then be analyzed for fractal relationships that reveal genetic decision making in morphogeneis, pathological remodeling or anatomic variation. The medial curve is also useful for reconstructing NURBS models from patient-specific imaging data for isogeometric analysis of blood flow [9]. It can also be used for automatic identification of the outlets in biological geometries for imposing boundary conditions in numerical simulations [10].

These applications pose the following requirements for the medial curve:

- Topological and structural correctness: The medial curve should be homotopic to the object, and should represent the structure of the object by correctly labeling the ends and branches.
- Smoothness: The medial curve should be smooth except at branches and distinct sharp turns.
- Centeredness: The medial curve should be near the center of the object.

In addition, an algorithm for computing medial curves must satisfy the following requirements.

- Robustness: algorithm must handle complex geometries with tens of thousands of branches without user intervention.
- Noise resistance: algorithm should tolerate moderate levels of noise, which are unavoidable in image-derived geometries.
- Efficiency: algorithm must be fast and have a small memory footprint (i.e. have close to linear complexity in time and space) to handle large datasets with millions of triangles.

Our objective is to define the medial curve and construct algorithms that satisfy the above requirements. We focus on imaging-derived biomedical geometries. However, the above requirements also apply to some other application areas (such as virtual navigation), to which our methodology will also apply. We assume the input geometry is given by a surface triangulation, such as that obtained by an isosurfacing algorithm (see [11] for a survey of such algorithms).

2 MAIN BODY

We take a novel perspective on defining and computing medial curves, and propose an algorithm for robust computation. We first propose a concept called the interior center of curvature (ICC) of surfaces. For canonical shapes (such as spheres, cylinders and tori) and more generally the canal surfaces [12, Sec. 20.2], the ICCs of the surface give precisely their medial curves. For general surfaces, we define the average interior center of curvature (AICC) as approximations of ICC with improved noise resistance, and use AICCs as a starting point for finding the medial curves. Secondly, we define the medial curve based on a *local orthogonal decomposition* of the object into tips, segments, and junctions. We define this decomposition based on geometric quantities (including AICC and orthogonality) and topological invariance (the Euler characteristic). The medial curve is then the graph connecting the centers of these substructures and of the cutting planes between them. In practical applications medial curve defined this way behaves much more stable and noise resistant than conventionally defined skeleton. Thirdly, we propose a new algorithm for the computation of medial curves, called local orthogonal cutting (LOC).

LOC is designed to facilitate local orthogonal decomposition for geometries that can be well approximated by canal surfaces. It identifies tips, segments and junctions and constucts medial curve following the definition. Figure 1 shows a simplified control flow of our algorithm. In order to efficiently detect substructures that comprise geometry, LOC simultaneosly processes local patches of surface mesh. To insure robustness, each patch is classified as tip, junction of segment only when its topologically stable. Substructures are bounded and separated from each other by planes, approximately orthogonal to surface (hence the name of the method). Tips, which are closely related to outlets, are identified first, and segments and junctions are identified later. Because of this order algorithm is useful for outlet truncation as well, making it applicable to any geometry with outlets.

Our algorithm is robust and resistant to noise, and it has nearly linear time and space complexities. We demonstrate the effectiveness of our method for complex biomedical geometries derived from

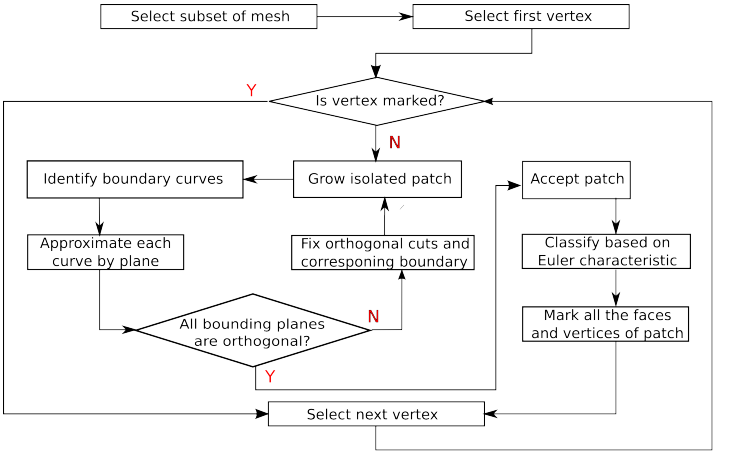

Figure 1: Simplified flowchart of the algorithm.

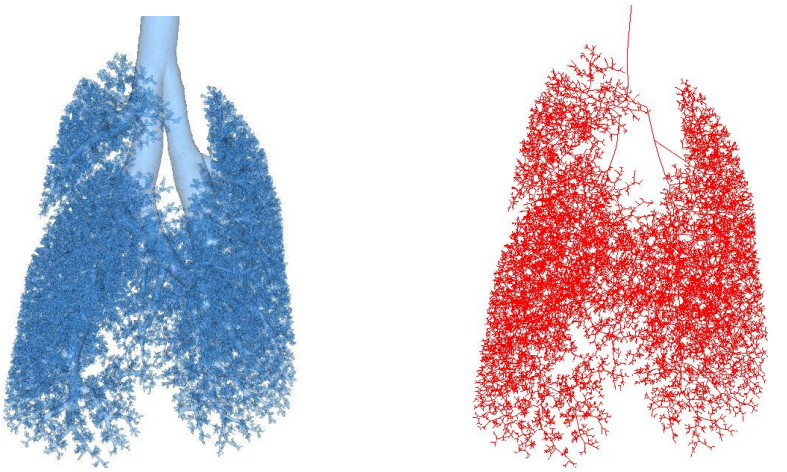

Figure 2: Monkey lung with 4 million vertices. Surface on the left, medial curve on the right.

medical images, including lung airways and blood vessels, and present comparisons of our method with some existing methods. To assess the robustness and noise resistance, we have conducted experiments on raw, unsmoothed surface meshes from isosurfacing, as well as smoothed meshes. We will present results for complex biomedical geometries, including mouse coronary artery network, a monkey pulmonary airway tree, and a rat pulmonary airway tree. Figure 2 shows the medial curve for the noisy monkey lung airways, which is challenging as the noise in the dataset has a magnitude of up to one voxel. An inspection of sampled areas indicates that the medial curve fully agreed with the intuition of a trained biologist. This result shows that our method is relatively insensitive to noise. In addition, our algorithm is highly efficient, and it took less than one minute for this case on a Linux computer with a 2.4GHz Intel Duo Core processor and 4GB memory.

3 CONCLUSIONS

We have developed new method for computing the medial curves of surface meshes. Effectiveness and robustness of our approach is illustrated with some highly complex, large-scale, noisy

biomedical geometries derived from medical images, and present a qualitative comparison of our method with some existing methods. Our method is not without limitations. As mentioned earlier, we have primarily focused on objects composed of string-like sub-structures, and omitted objects with intrinsic ambiguities and disk-like sub-structures. However, our approach, in particular the concept of the interior centers of curvature, should be useful in identifying the boundary of medial surfaces of disk-like sub-structures.

REFERENCES

[1] N. D. Cornea, D.Silver and P. Min, Curve-skeleton properties, applications, and algorithms. *IEEE Trans. Vis. Comput. Graph.*, 13, pp. 530548, 2007.

[2] Y. Huo and G.S. Kassab, A hybrid one-dimensional/Womersley model of pulsatile blood flow in the entire coronary arterial tree. *Am J Physiol Heart Circ Physiol.*, 292(6), pp. 262333, 2007.

[3] D. R.Einstein, B. Neradilak, N. Pollisar, K.R. Minard, C. Wallis, M. Fanucchi, J.P. Carson, A.P. Kuprat, S. Kabilan, R.E. Jacob and R.A. Corley, An automated self-similarity analysis of the pulmonary tree of the sprague-dawley rat. *Anat Rec*, 291(12), pp. 162848, 2008.

[4] T. Wischgoll, J.S. Choy, E.L. Ritman and G.S. Kassab, Validation of image-based method for extraction of coronary morphometry. *Ann Biomed Eng*, 36(3), pp. 35668. 2008.

[5] R.C. Molthen, K.L. Karau and C.A. Dawson, Quantitative models of the rat pulmonary arterial tree morphometry applied to hypoxia-induced arterial remodeling. *J Appl Physiol*, 97(6), pp. 237284, 2004.

[6] M. Maddah, A. Afzali-Kusha and H. Soltanian-Zadeh, Efficient center-line extraction for quantification of vessels in confocal microscopy images. *Med Phys*, 30(2), pp. 20411, 2003.

[7] D. R. Whittaker, J. Dwyer and M. F. Fillinger, Prediction of altered endograft path during endovascular abdominal aortic aneurysm repair with the gore excluder. *J Vasc Surg.*, 41(4), pp. 57583, 2005.

[8] Y. Huo and G. S. Kassab, A scaling law of vascular volume. *Biophys J.*, 96(2), pp. 34753. 2009.

[9] Y. Zhang, Y. Bazilevs, S. Goswami, C. Bajaj and T. J. Hughes, Patient-specific vascular NURBS modeling for isogeometric analysis of blood flow. *Comput. Meth. Appl. Mech. Engrg.*, 196, pp. 29432959, 2007.

[10] X. Jiao, D.R. Einstein, V. Dyedov and J.P. Carson, Automatic identification and truncation of boundary outlets in complex imaging-derived biomedical geometries. *Med. Bio. Engrg. Comput.*, 47, pp. 989999, 2009.

[11] T. Newman and H. Yi, A survey of the marching cubes algorithm. *Computers and Graphics*, 30, pp. 854879, 2006.

[12] A. Gray, E. Abbena and S. Salamon, *Modern Differential Geometry of Curves and Surfaces with Mathematica*, 3rd ed. Chapman and Hall/CRC.

[13] X. Jiao, D.R. Einstein and V. Dyedov, Local Orthogonal Cutting Method for Computing Medial Curves and Its Biomedical Applications. *SIAM Journal on Scientific Computing*, Vol. **32**, 2, pp.947-969, 2010.

2nd International Conference on Mathematical and Computational Biomedical Engineering - CMBE2011
March 30 - April 1, 2011, Washington D.C, USA
P. Nithiarasu and R. Löhner (Eds.)

MESH GENERATION TECHNOLOGY FOR DOMAINS WITH SMALL STRUCTURAL ELEMENTS

Alexander A. Danilov⋆ and Yuri V. Vassilevski⋆⋆
⋆Institute of Numerical Mathematics, Gubkina 8, Moscow, Russian Federation,
a.a.danilov@gmail.com
⋆⋆Institute of Numerical Mathematics, Gubkina 8, Moscow, Russian Federation,
yuri.vassilevski@gmail.com

SUMMARY

We present a robust mesh generation technology for objects with small structural elements. This technology is a combination of boundary discretization methods, an advancing front technique and a Delaunay-based tetrahedral mesh generation technique, triangular surface mesh and tetrahedral mesh cosmetics. Two biomedical problems are used for illustration of these methods: modelling of bioimpedance analysis for body composition problems and modelling of interferon distribution in secondary lymphoid organs.

Key Words: *tetrahedral meshes, surface meshes, bioimpedance analysis, immune processes.*

1 INTRODUCTION

Unstructured tetrahedral meshes are widely used in mathematical modelling due to their simplicity and ability to represent complex domains. A tetrahedral mesh is called conformal, if each its two tetrahedra have one common vertex, one entire common edge, or one entire common face, or do not have any common points. The similar definition applies to conformal triangulations. Mesh conformity is an important and desirable property.

Tetrahedral mesh generation process consists of two stages: surface meshing and volume meshing. At the first stage we construct a surface conformal triangular mesh. The surface mesh can be produced in several different ways. At the second stage we mesh the volume inside the domain into tetrahedra while preserving given surface triangular mesh on the boundary.

There exist two main approaches for tetrahedral mesh generation: methods based on Delaunay triangulations (DT), and advancing front technique (AFT). The Delaunay triangulation approach does not guarantee the boundary conformity. Several techniques are proposed to match the boundary: local mesh transformations, mesh refinement, and constrained Delaunay triangulations (CDT). On the other hand, the advancing front technique does not have issues with boundary recovery since it starts from the given surface mesh. However, AFT methods have difficulties in successfully closing up their fronts. Our volume mesh generation method is a combination of a conventional AFT, a DT based fallback method and a metric-based adaptation mesh cosmetics method [1].

The presented technology of tetrahedral mesh generation is implemented as a part of Ani3D package [3], the successor of Ani2D package [2]. Both packages provide tools for unstructured mesh

generation, anisotropic metric-based adaptation, finite element discretization, and linear system solving. These packages are publicly available.

In section 2 we present a brief overview of mesh generation methods. In section 3 we illustrate an application of these methods for bioimpedance analysis modelling. In section 4 we present another application for modelling of interferon distribution in secondary lymphoid organs. We make concluding remarks in section 5.

2 OVERVIEW OF MESH GENERATION ALGORITHMS

We employ the advancing front technique (AFT) for initial mesh generation. We define the initial front as a set of oriented triangular faces forming a closed conformal surface mesh. The idea of the AFT is to construct new tetrahedra by advancing this front inside the computational domain. The front actually divides the domain into two parts: already meshed one and the remaining part. At each step, a new tetrahedron is constructed and the front is advanced.

By design, majority of tetrahedra produced by the AFT have high-quality provided that the initial front consists of high-quality triangles. A good surface mesh is the key to successful mesh generation. If the initial front contains low-quality triangles, we start with improving their quality. In [4] we introduced a new technique for surface mesh modification which is implemented in the Ani3D package.

The AFT algorithm implemented in the Ani3D package allows the user to provide a size function $h(x)$ to control the local size of mesh elements. The size function can be defined on the basis of a posteriori error estimates. It must be bounded from below to avoid an infinite refinement loop.

The major advantage of the AFT is its low cost. For quasi-uniform tetrahedral meshes, the cost of the AFT is roughly $N \log(H/h)$, where N is the total number of constructed tetrahedra, H is the characteristic size of the computational domain, and h is the mesh size. The logarithmic complexity is achieved by using an octree-based search tree for searching faces in the three-dimensional space.

The major drawback of the AFT is lack of robustness. It may fail to construct a mesh for the entire computational domain. The unmeshed volume is usually less than 1% of the domain volume.

If the AFT fails to mesh the entire domain, we launch the Delaunay triangulation (DT) method to mesh the remaining lacunas and to preserve their boundary faces. The general idea of this method has been proposed in [5]. Here, we discuss main features of the DT method and its necessary modifications.

By design, the DT method tends to produce high-quality tetrahedra provided that the mesh vertices are appropriately placed. The appearance of slivers is usually induced by irregular distribution of mesh nodes at the boundaries of lacunas.

We improve the mesh quality using a sequence of local changes of mesh topology. The local topological operations provide a robust way to adapt the mesh to the problem solution and to gain additional accuracy for the same number of mesh elements. The general idea of the metric-based adaptation (MBA) is described in [6].

Local changes of the mesh topology is the key to the method robustness. The package Ani3D has seven local topological operations including edge-face swapping, generalized edge-faces swapping, node deletion, node insertion, edge collapse, and node movement. Complete mesh regeneration may require 5-15 sweeps of the MBA operations through the mesh, which makes it rather costly.

3 BIOIMPEDANCE ANALYSIS

In this section we describe an application of proposed mesh generation techniques for the modelling of bioimpedance processes. The bioelectrical properties of various tissues of the human body are different. In order to represent this discontinuity we construct the final mesh with several subdomains. We start from the simple domain representations. The first mesh is created based on the parametric representation of the human body, the lungs and the heart. The anisotropic skin layer with several electrodes is created on the surface. The mesh is automatically refined near the electrodes, where the solution has big gradients.

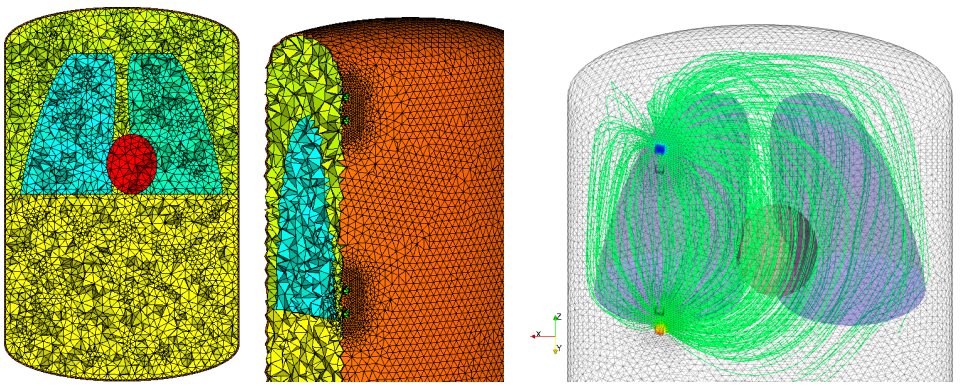

Figure 1: A cut through the volume mesh of a simplified body, and the current lines inside the body.

The next goal for the mesh generation is processing of actual medical images for generation of accurate volume mesh. The boundaries of the main human organs may be obtained from the binary representation of a segmented CT image. In this case the surface triangular mesh is first created using a marching cubes technique and then re-meshed using our surface mesh modification algorithm.

4 INTERFERON DISTRIBUTION IN LYMPHOID ORGANS

In this section we describe an application of proposed mesh generation techniques for the modelling of interferon distribution in secondary lymphoid organs [7].

Secondary lymphoid organs have highly elaborate structure and organization to facilitate the interaction between the immune cells and the lymph-borne pathogens derived from distant tissues. Functionally the lymph node (domain Ω) consists of three major subdomains: an outer antigen-sampling zone (subcapsular sinus, trabecular sinuses, conduit tubes), referred to as subdomain Ω_1; B-cell follicules which make subdomian Ω_2; T-cell zone (cortext and paracortex) denoted as subdomain Ω_3.

Conduits represent an important system of distribution channels for small soluble antigens and immune modulators They extend from subcapsular sinus floor through the T-cell zone and form a contigous lumen with fluid channels around the high emdothelial venules, thus making a network highly connected with the cappillaries and venules of the cortex. The paradigmatic lymph node domain Ω is schematically described in Fig.2 using a constructive solid geometry representation via combining three subdomains $\Omega_i, i = 1, 2, 3$. Each subdomain is made of composition of geometric primitives, such as spheres and cylinders differing in their sizes and orientation.

The OpenCASCADE technology (see http://www.opencascade.org) was used to construct the 3D geometric model of a paradigmatic lymph node.

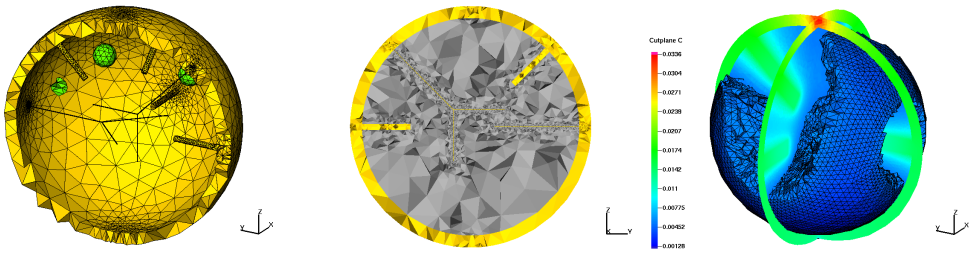

Figure 2: A cut through the volume mesh of a lymph node, and the computed concentration of interferon.

The final OpenCascade-based 3D geometric model of the lymph node consists of 50 vertices, 62 curved edges and 30 curved faces. The solid geometry model and its mesh approximation are presented in Fig.2. This geometry requires resolution of multiple length scales for the representation of the conduits and the overall major domains. Notice that the mesh is fine-grained closer to conduits in order to represent properly the structure of conduits, whose diameter is three order of magnitude smaller than the one of the lymph node.

5 CONCLUSIONS

We presented an approach to generation of tetrahedral meshes. The initial mesh generation employs robust combination of the advancing front technique and the Delaunay triangulation. The metric based mesh re-generation method provides essential improvement of the mesh quality in complex biomedical models. Two biomedical applications are presented for illustration of the proposed methods.

REFERENCES

[1] A.A. Danilov, Unstructured tetrahedral mesh generation technology, *Comp. Math. and Math. Phys.*, 50, 139–156, 2010.

[2] 2D generator of anisotropic meshes. `http://sourceforge.net/projects/ani2d/`

[3] 3D generator of anisotropic meshes. `http://sourceforge.net/projects/ani3d/`

[4] Yu.V. Vassilevski, A.V. Vershinin, A.A. Danilov, A.V. Plenkin, Tetrahedral mesh generation in domains defined in CAD systems, *Proc. of the Institute of Numerical Mathematics*, Moscow, 21–32, 2005.

[5] P.-L. George, H. Borouchaki, E. Saltel, Ultimate robustness in meshing an arbitrary polyhedron, *Int. J. for Num. Meth. in Engnr.*, 58, 1061–1089, 2003.

[6] Y. Vassilevski, K. Lipnikov, Adaptive algorithm for generation of quasi-optimal meshes, *Comp. Math. and Math. Phys.*, 39, 1532–1551, 1999.

[7] G.A. Bocharov, A.A. Danilov, Yu.V. Vassilevski, G.I. Marchuk, V.A. Chereshnev and B. Ludewig, Reaction diffusion modelling of interferon distribution in secondary lymphoid organs, *Math. Model. Nat. Phenom.*, in press.

2nd International Conference on Mathematical and Computational Biomedical Engineering – CMBE2011
March 30 – April 1, 2011, Washington D.C., USA
P. Nithiarasu and R. Löhner (eds)

Evaluation of Mesh Morphing and Mapping Techniques in Patient Specific Modeling of the Human Pelvis

Salo, Zoryana*†; Whyne, Cari*†
*Orthopaedic Biomechanics Laboratory, Sunnybrook Research Institute
†Institute of Biomaterials and Biomedical Engineering, University of Toronto
2075 Bayview Avenue, UB19, Toronto, Ontario, M4N 3M5
cari.whyne@sunnybrook.ca

SUMMARY

The objective of this study was to develop and apply mesh morphing and mapping techniques to facilitate and automate the creation and structural analysis of multiple specimen-specific FE models of the pelvis. A source mesh, generated using a traditional user intensive meshing scheme and experimentally validated, was initially morphed using a landmarked based approach and subsequently mapped, onto a target surface generated from a CT scan of a second pelvis. Morphing consisted of movement of individual exterior source nodes to target surface vertices. Mapping functioned to simultaneously shift groups of selected nodes directly onto the surfaces of the target model. Morphing and mapping techniques were effectively applied to generate geometrically complex specimen-specific pelvic FE model and recreate strain distributions as found in the target pelvis FE model.

Key Words: *Mesh morphing and mapping, specimen-specific model, source mesh.*

1. INTRODUCTION

The complex geometric, material property and loading conditions of the pelvis require advanced computational modeling techniques to accurately describe its behaviour. Parametric models based on averaged anatomic data can be challenging to build, but allow for single factor alterations to consider the effects of individual geometries, materials and their combinations. Specimen-specific finite element (FE) models, generated using 3D medical imaging data allow for highly inhomogeneous material property distributions and geometries, but can be limited in their ability for parametric assessment. Due to the complexities of model development, many studies consider results from single specimen-specific models, limiting the clinical relevance of findings. The development of robust automated morphing techniques for multifaceted skeletal structures would both allow parametric assessment of specimen-specific FE models and the streamlining of the generation of multiple FE models from different specimens/patients. Mesh morphing techniques have been investigated to allow robust and efficient specimen-specific meshing and parametric FE analysis. [1, 2] The objective of this study was to develop and evaluate mesh morphing and mapping techniques to facilitate and automate the creation and structural analysis of multiple specimen-specific FE models of the pelvis.

2. METHODS

A single, specimen-specific pelvic, tetrahedral, first-order FE model (source mesh) was generated from a cadaveric CT scan utilizing highly labour-intensive meshing methods. The source mesh was morphed onto a target surface generated from a CT scan of an additional pelvis using a landmarked based approach employing a combination of 3D image analysis, finite element and programming software (AmiraDEV5.2, Visage Imaging, FR; Hyperworks®, Altair®, US; Matlab, Mathworks, US; ABAQUS, HBK, US) (Figure 1a) [1,2]. Specifically, the location of the target surface vertices and the exterior nodes on the source mesh were identified (Figure 1b). Exterior source nodes were shifted to the target surface vertices (Figure 1c). A smoothing algorithm was used to regulate the nodes in the centre of the source mesh to improve element quality. The source surface was then morphed along with the source mesh. The process was repeated using an iterative approach. The success of the morphing technique was quantified by comparing morphed and target surfaces and evaluating the resultant morphed mesh quality.

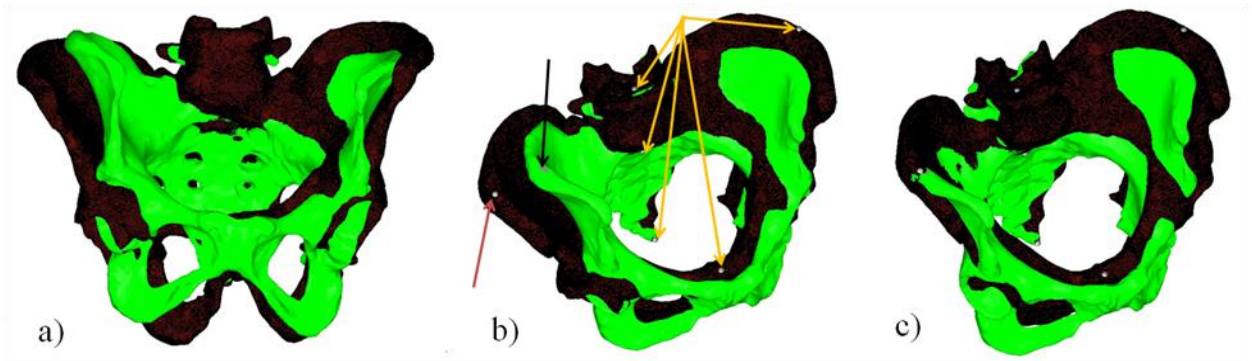

Figure 1: a) Source mesh (red) target surface (green). b) Target surface vertex (black arrow), an exterior node on the source mesh (red arrow), and fixed nodes on the source mesh (yellow arrows). c) Exterior source node shifted to the target surface vertex.

A copy of the morphed model was further refined through mesh mapping. Surface nodes of the initial morphed model were selected in patches and mapped onto the surfaces of the target model. A smoothing algorithm regulated the nodes in the centre of the mesh to improve element quality. Elements, which could not be smoothed with the algorithm, were isolated along with some adjacent elements and automatically remeshed. The process was repeated in patches until the model was fully mapped. Areas, where the distance from the mesh to the target surfaces was very large causing the elements to become highly distorted, were remorphed and subsequently remapped. The elements in the mapped mesh were then automatically cleaned to ensure even element size. Distorted surface elements were manually repaired.

BONEMAT III [3] integrated with Matlab code was used to assign CT density based material properties to the models. First-order tetrahedral elements in all models were changed to second-order tetrahedral elements for analysis. The source, target, morphed and mapped models were loaded through the fifth lumbar vertebra to 125 N in axial compression and the centre of each acetabular surface was fully constrained. The four FE models (target, source, morphed and meshed) were solved using linear static FE analysis in Abaqus Standard 6.6-1 (HBK, Pawtucket, Rhode Island) and their strain distributions evaluated.

3. RESULTS

All of the elements in the source, target, the morphed and the mapped meshes had sufficient quality for analysis (Table 1). CT density based material properties were distributed comparably in the target, source and mapped meshes, but were patchier in the morphed model. Morphed and mapped FE models effectively simulated the ability of such techniques to create specimen-specific models and their ability to recreate the target strain distributions in the pelvis. Figure 2 shows the maximum principal strain patterns in the morphed, mapped and target FE models. Qualitatively and quantitatively, the mapped model was most comparable to the target model. Smaller differences in maximum principal strains (based on the selected iliac region of interest – red highlight) were found between the target (38.6 μs) and mapped (41.6 μs) models as compared to the morphed model (35.4 μs). Similarly, in considering maximum principal strains in the supra-acetabular region (yellow highlight), the mapped model (91 μs) was able to more closely approximate the target model (104.4 μs) as compared to the morphed model (80.3 μs).

Table 1: Quality assessment of the source, morphed, mapped and target meshes. For each element quality parameter the minimum value found in the mesh is reported for each model. The percent of elements that failed each set quality criteria is also reported (red brackets).

Quality parameter	Source	Morphed	Mapped	Target
Aspect ratio > 5	3.82 (0%)	4.97 (0%)	4.99 (0%)	3.63 (0%)
Skew > 60	81.72 (0%)	81.4 (0%)	75.99 (0%)	64.42 (0%)
Jacobian < 0.7	1 (0%)	1 (0%)	0.26 (0.0007%)	1 (0%)
Volume aspect ratio > 5	75.4 (0.001%)	83.31 (0.2%)	19.56 (0.3%)	6.14 (0.001%)
Minimum angle < 20^o	5.18 (0.002%)	5.77 (0.3%)	10.03 (0.5%)	14.82 (0.002%)
Maximum angle > 120^o	159.83 (0.002%)	166.07 (0.5%)	158.44 (0.7%)	126.08 (0.005%)

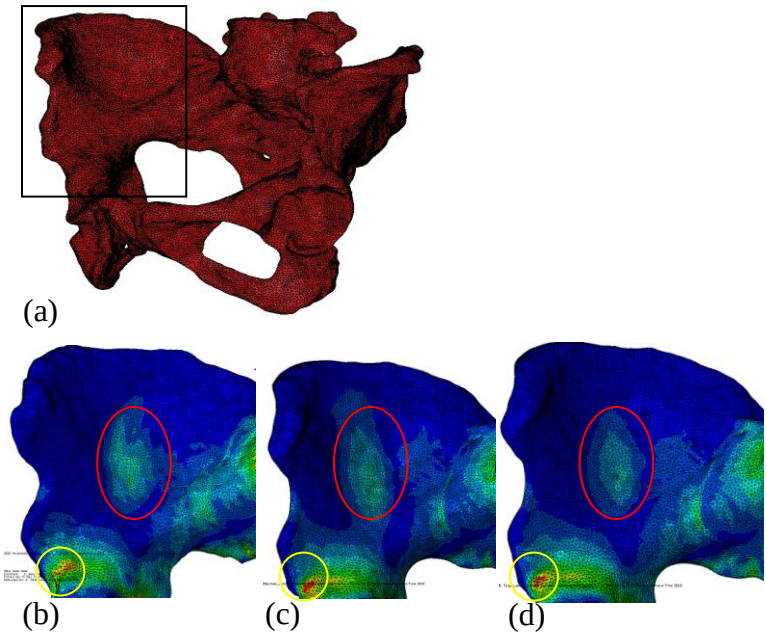

Figure 2: (a) Specimen-specific target mesh. Maximum principal strain patterns for the (b) morphed model, (c) mapped model and (d) target model.

4. DISCUSSION

A mesh morphing and mapping method combining 3D image analysis, finite element and programming software was successfully used to geometrically reconfigure a specimen-specific pelvic source mesh onto a new target surface to generate a new specimen-specific FE model. This morphing and mapping method was performed manually, morphing one landmark at a time, to explore the ability of such a method to generate a quality mesh for a complex structure such as the pelvis. Manual morphing and mapping is a time consuming process, but provides the justification for automation of the technique to standardize and speed up the procedure. In particular, during morphing, some element distortion occurred which was irreparable using the smoothing algorithm alone. As such, after several (5 to 6) morphs, the quality of the mesh was examined and clusters surrounding the isolated failed elements were remeshed to ensure mesh stability. Morphing alone was unable to represent the patterns of strain; the addition of mapping yielded improved qualitative and quantitative results. Ongoing work is focused on automating the morphing and mapping techniques to speed up the model creation process. The proposed morph/mesh process is sufficiently robust to generate new target models and may further allow parametric evaluation of geometric changes within given target models. The development of robust automated morphing and mapping techniques for complex skeletal structures will greatly enhance the ability of specimen-specific FE models to yield clinically relevant information addressing normal biomechanical behaviour, pathological conditions and the optimization of repair and reconstruction strategies in the pelvis and other complex skeletal structures.

5. CONCLUSIONS

A combination of mesh morphing and mapping was successfully employed to reconfigure a source pelvic FE mesh onto a target surface generated from a distinct pelvis, yielding similar strain patterns to a traditionally generated target pelvic FE model. These results provide motivation for future automation of this process to enable the generation of multiple complex FE models necessary to better understand patient specific differences, population norms and the implications of skeletal pathologies in the pelvis.

REFERENCES

[1] I.A. Sigal, M.R. Hardisty and C.M. Whyne, Mesh-morphing algorithms for specimen-specific finite element modeling, *Journal of Biomechanics*, 41, 1381 – 1389, 2008.

[2] M.A. O'Reilly and C.M. Whyne, Comparison of computed tomography based parametric and patient-specific finite element models of the healthy and metastatic spine using a mesh-morphing algorithm, *Spine*, 33 (17), 1976 – 1881, 2008.

[3] C. Zannoni, R. Mantovani and M. Viceconti M, Material properties assignment to finite element models of bone structures: a new method, *Medical Engineering Physics*, 20, 735–40, 1998.

2nd International Conference on Mathematical and Computational Biomedical Engineering - CMBE2011
March 30 - April 1, 2011, Washington D.C, USA
P. Nithiarasu and R. Löhner (Eds.)

VARIATIONAL GENERATION OF HYBRID PRISM-TETRAHEDRON MESHES FOR BIOMEDICAL APPLICATIONS

Daniel R. Einstein*, Vladimir Dyedov, Andrew P. Kuprat*, Navamita Ray** and Xiangmin Jiao****

*Biological Monitoring & Modeling, Pacific Northwest National Laboratory, Richland, WA.
Email: {daniel.einstein,andrew.kuprat}@pnl.gov

**Department of Applied Mathematics & Statistics, Stony Brook University, Stony Brook, NY.
Email: {vladimir,nray,jiao}@ams.sunysb.edu

SUMMARY

Prismatic boundary-layer meshes are attractive for computational fluid dynamics and fluid-structure interaction simulations. However, generating these meshes is difficult for complex biological geometries. Recently, we developed a variational method for generating hybrid meshes with prismatic boundary layers and a tetrahedral interior. Our method generated the boundary layer by propagating the triangulated surface using the face-offsetting method, guided by the feature size of the geometry. Following propagation, the interior tetrahedral mesh was constructed using constrained Delaunay tetrahedralization. Herein, we extend our previous method by simultaneously deforming an input tetrahedral mesh while generating the prismatic boundary layer. This latter enhancement enables us to effectively add prismatic layers to any valid tetrahedral mesh and improve the quality of the tetrahedral core for very complex geometries. In addition, the new approach can accommodate an anisotropic tetrahedral core. This work was in part supported by National Institutes of Health (NIH) Research Grants R01HL073598 and R01HL092926

Key Words: *boundary-layer meshes, blood flow, wall shear stress.*

1 INTRODUCTION

Layered hybrid prismatic-tetrahedral meshes are attractive in a variety of imaging-based biomedical computations, for example where fluid-boundary layers need to be accurately resolved, where tissue structures are inherently layered or where collapse and/or contact occurs in a fluid-structure interaction simulation.

We introduce an important extension to our previous method [1] which contributes to both versatility and improved mesh quality. The main limitation of our previous method in [1] was that the tetrahedral core had to be generated by a constrained tetrahedralization, which prohibits the addition of Steiner points on the surface. As a result, both the quality and the character of the resulting tetrahedral mesh was limited. To overcome this limitation, we propose an alternative strategy.

2 VARIATIONAL GENERATION OF HYBRID MESH

Like our previous method in [1], the new method takes some specification of the mesh sizes as input, in particular the *gradient-limited feature sizes* (*GLFS*), which we have found to be well

suited for biomedical applications [2]. The method has four key steps: 1) propagate an initial thin-layer of prisms; 2) shrink the tetrahedral core; 3) further expand prisms and shrink tetrahedra by variational smoothing.

2.1 STEP 1: PROPAGATE INITIAL THIN-LAYER

We propagate the boundary surface inwards by solving the Lagrangian evolution equation $\frac{\partial \boldsymbol{x}}{\partial t} = f(\boldsymbol{x}, t)\hat{\boldsymbol{n}}$, where t denotes time, $\hat{\boldsymbol{n}}$ denotes unit surface normal, and $f(\boldsymbol{x}, t)$ denotes the speed function, for which we use the GLFS. Rather than propagating vertices, we apply the face-offsetting method (FOM), which propagates the faces and then reconstructs vertices based on a weighted least squares approximation [1, 3]. For efficiency, we compute the GLFS only at the beginning, and reuse it throughout the propagation.

After computing all the vertex displacements, we check the positivity of the Jacobian of each prism, and reduce the time step if the Jacobian is negative anywhere in the mesh. Thereafter, we further optimize the prisms using a variational smoothing procedure, which minimizes the sum of two energies to improve the shapes of the triangles and the orthogonality of the side edges, respectively.

Overall, the initial propagation proceeds as follows:

1. compute vertex displacements for Δt using face offsetting with GLFS as speed function;
2. check positivity of Jacobian of the prisms and reduce Δt to prevent mesh folding;
3. apply variational smoothing to optimize triangle shapes and side-edge orthogonality;
4. if it has propagated sufficiently (say 50% of the desired depth of the prisms) or the time step was reduced to some too small value, then stop; otherwise return to step 1.

2.2 STEP 2: SHRINK TETRAHEDRAL CORE

After a thin boundary layer has been generated, we deform the tetrahedral mesh using a variational smoothing procedure:

1. add displacements computed from the initial propagation to boundary vertices; if the displacements cause tetrahedral elements to fold, scale back the displacements;
2. smooth the interior tetrahedral with fixed boundary;
3. if displacements were scaled back, go back to step 1 and repeat step 1 and 2, until all displacements have been applied or the displacements are scaled back to nearly zero.

We smooth the tetrahedra using a modified algorithm of that in [4]. In particular, we define an energy for each tetrahedron with respect to some "ideal" reference tetrahedron.

The energy $E_\theta(\tau)$ for a tetrahedron τ is

$$E_\theta = \frac{1}{V^{2/3}} \sum_{i=1}^{3} \left(\alpha_i \|\boldsymbol{l}_i\|^2 + \beta_i \|\boldsymbol{r}_i\|^2 \right), \tag{1}$$

where $\boldsymbol{l}_i$ and $\boldsymbol{r}_i$ are edge vectors and α and β are 'shape' parameters of the original mesh. Since the input mesh may be graded or layered, we try to preserve the shapes of the initial tetrahedra. Thus, the shape parameters α and β are computed directly from the reference mesh.

2.3 STEP 3: FURTHER EXPAND PRISMS AND SHRINK TETRAHEDRA

The previous step generated and smoothed prisms and tetrahedra independently of each other. During the process, if some tetrahedra have very large aspect ratios, the propagation of the prismatic boundary layers would terminate prematurely. We address the issue in this step by smoothing the prisms and tetrahedra simultaneously. Our goals are twofold: 1) to propagate the prisms further while continuing to shrink the tetrahedra, and 2) to allow local adaptation of prism heights based on the overall mesh quality. We assume that the input surface triangulation has a reasonable quality, and we do not move the vertices on the boundary, except for those on the outlet walls, which must slide along the walls.

To define the energy for a prism, for simplicity we sample a tetrahedron at each vertex of the prism, and use the corresponding vertices in the actual and target prisms as the actual and reference tetrahedra. For each pair of actual and reference tetrahedra, we substitute them into Equation (1) to compute its energy, and the energy for the prism is the sum of the energy of the six tetrahedra. We refer to this energy as the height energy of the prism, denoted by E_h, as its main objective is to control the height of the prisms.

In addition to the height energy, we also would like to optimize the orthogonality of the side edges of prisms. Orthogonality is important for producing smoother boundary layer meshes and for more accurately capturing the boundary layer effects in simulations. Note that the height energy also penalizes edges that are far from orthogonal, but it is not strong enough to enforce orthogonality. We use the same energy defined in [1].

Given these elemental energy, our overall prism expansion algorithm computes the total energy E as a weighted sum of the height energy E_h of the prisms, the orthogonality energy $E_\perp$, and the shape energy E_t of the interior tetrahedra, i.e., $E = w_t \sum E_t + \sum (w_h E_h + w_\perp E_\perp)$, where w denotes the corresponding weights. We set the weights to $w_h = 4$ and $w_\perp = w_t = 1$, where the higher weights for E_h allows more substantial growth of the prisms. We minimize this energy similarly as for tetrahedra, as summarized by the following procedure:

1. Loop through the interior tetrahedra, and for each tetrahedron compute the gradient and Hessian of E_t with respect to its vertex coordinates, and add them to the corresponding vertex values;
2. Loop through the prisms, and for each prism compute the gradient and Hessian of E_h and $E_\perp$ with respect to its vertex coordinates, and add them to the corresponding vertex values;
3. Loop through all vertices to divide the gradient by the Hessian to obtain a displacement; for vertices on the outlet walls, constrain the displacement within the wall or along the ridge;
4. Scale back displacements to avoid folding; if any vertex is scaled back, recompute the gradient and Hessian of its surrounding elements and compute its displacement;
5. Repeat steps 1 through 4 for a few times.

3 RESULTS

The figure below shows the addition of four layers of prisms added to the blood domain of idealized human heart model, originally from the NYU Medical Center. We started with a triangulation of the model in [5] and then adapted it to be commensurate with the GLFS. A layered tetrahedral mesh was then generated from that surface [2]. Four layers of scale-invariant prisms were then added to this anisotropic grid, following the procedure described above. The table below reports the element statistics and execution time for shrinking the tetrahedral grid and adding the prisms.

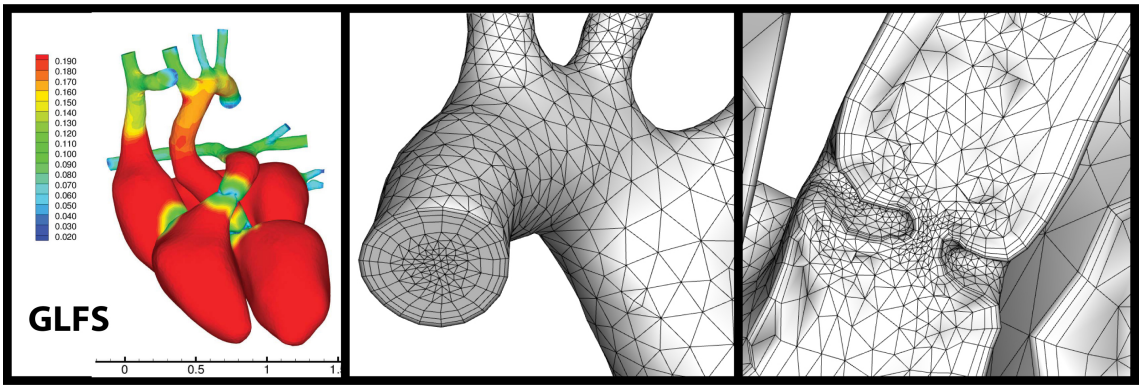

Figure 1: Hybrid prism-tet mesh. **A** GLFS defined on the blood domain of the triangulated surface. **B** Detail of an outlet, showing the graded prism layers. **C** Cros-section though the aortic valve.

	min vol	max vol	worst χ	worst α	worst ψ	worst f_x	ExecutionTime
Hybrid mesh	1.2E-10	6.3E-05	0.21	62.8	0.750	0.143	356 sec

Table 1: Statistics for hybrid prism-tet mesh of the human heart. The minimum surface edge length was 0.001. All units are dimensionless. χ is the aspect ratio, and α, ψ and f_x are the hybrid face orthogonality, skewness and uniformity, respectively. Execution time refers to prism generation only.

4 CONCLUSIONS

We have presented a simple and effective strategy for adding high quality prismatic boundary layers to tetrahedral grids derived from biomedical imaging data. In contrast with our previous work, the input tetrahedral grid can be isotropic, anisotropic or layered.

REFERENCES

[1] V. Dyedov, D.R. Einstein, X. Jiao, A.P. Kuprat, J.P. Carson and F. del Pin, Variational Generation of Prismatic Boundary-Layer Meshes for Biomedical Computing, *Int. J Numerical Methods in Engineering*, 79, 907-945, 2009.

[2] A.P. Kuprat and D.R. Einstein, An anisotropic scale-invariant unstructured mesh generator suitable for volumetric imaging data, *J. Comput. Phys.*, 228, 619-640, 2009.

[3] X. Jiao, Face Offsetting: A Unified Approach for Explicit Moving Interfaces, *J. Comput. Phys.*, 220, 612-625, 2007.

[4] X. Jiao, D. Wang and H. Zha, Simple and Effective Variational Optimization of Surface and Volume Triangulations, in *Proc. 17th Int. Meshing Roundtable*, 315-332, 2008.

[5] Y. Zhang, C. Bajaj and B-S. Sohn, 3D Finite Element Meshing from Imaging Data, *Comput. Meth. Appl. Mech. Engrg.* 194, 5083-5106, 2005.

2nd International Conference on Mathematical and Computational Biomedical Engineering - CMBE2011
March 30 - April 1, 2011, Washington D.C, USA
P. Nithiarasu and R. Löhner (Eds.)

LOCAL PHASE BASED AUTOMATIC IVUS MEDIA-ADVENTITIA BORDER DETECTION

Ehab Essa*, Xianghua Xie*, Igor Sazonov, and Perumal Nithiarasu****
*Department of Computer Science, Swansea University, UK
**College of Engineering, Swansea University, UK

ABSTRACT

We present a fully automatic segmentation method to extract media-adventitia border in IVUS images. We use a double-interface automatic graph cut technique to prevent the extraction of media-adventitia border from being distracted by those image features. Novel cost functions are derived from using a combination of symmetric and asymmetric local phase features with complementary texture features. Comparative studies on manual labeled data show promising performance of the proposed method.

Key Words: *IVUS, media-adventitia border, local phase, optimal interface segmentation.*

1 INTRODUCTION

Intra-vascular Ultrasound (IVUS) is a catheter-based technology where an ultrasound probe is moving inside the artery, transmitting signals and receiving the backscattered one from the inside and outside the artery that help to diagnosis of atherosclerosis diseases. Media-adventitia border is the outer side of the artery wall which can be used to measure the circumference, radius and 3D reconstruction of the artery. The appearance and visibility of the media-adventitia border are affected by artery diseases, and acoustic shadow artifacts.

Many techniques have been used in IVUS segmentation such as active contour and level set [1,2] and Graph search [3,4], which one based on minimizing a cost function that is derived from image features and possibly combined with shape prior to refine the segmentation. This approach is also adapted in [5] to deal with 3D volumetric segmentation using s-t cut algorithm to find the minimum closed graph.

Local phase features have shown to be an effective alternative to intensity derived features to deal with inhomogeneity, low image quality, and acoustic shadow that are common in ultrasound images. For example, in [6] it is used to find acoustic boundaries in echocardiography images. Two features can be extracted from local phase analysis: feature symmetry and feature asymmetry. Feature symmetry highlights the location of high congruency between objects in images. Since the media layer has generally uniform characteristics it can be detected by its symmetric feature, whileas feature asymmetry responds to edge-like feature and it can detect potential borders.

This paper presents a fully automated segmentation of media-adventitia border in 2D IVUS images. Double interface segmentation is introduced to obtain the media-adventitia border by combining image driven features with geometric constrains in well defined graph construction to overcome the impediments such as stents, calcification or plaque. The first interface removes any

distraction existed above the media-adventitia border and the second interface finds the border based on the characteristics of media layer.

2 PROPOSED METHOD

Briefly, the IVUS images are first transformed from Cartesian coordinates to polar coordinates, height field like, then removing catheter-ring down artifact. Two node-weighed directed graph are then constructed so that the border extraction is considered as computing a minimum closed set graph by using s-t cut algorithm. The extracted media adventitia border from the second graph is smoothed using radial basis function (RBF).

2.1 Graph construction

In [7], the authors proposed a novel graph construction method, which transforms the surface segmentation in 3D into computing a minimum closed set in a directed graph. We adapt this method to a 2D segmentation, which can carry out double-interface segmentation simultaneously in low order polynomial time complexity and does not require user initialization. For each desired interface, construct a graph $G = \langle V, E \rangle$, where each node $V(x, y)$ corresponds to a pixel in 2D image $I(x, y)$. Along each column in graph, each node is connected to the precedence node in the same column, and then connected to other node in different column to construct the closed graph. After constructing the graph for each of the two interfaces, taking into account interrelations between them is necessary and this is achieved by setting up another set of arcs to connect them. Geometrical constraints can be imposed by setting minimum δ_{min} and maximum δ_{max} separation distances. The two interfaces thus will not intersect or overlap.

2.2 Feature extraction

Local phase features – Two types of features can be extracted from phase congruency: feature asymmetry $FA(x, y)$ and feature symmetry $FS(x, y)$. Feature asymmetry highlights step-like image patterns, and is defined as [6]:

$$FA(x,y) = \sum_m \frac{\lfloor [|o_m(x,y)| - |e_m(x,y)|] - T_m \rfloor}{A_m(x,y) + \varepsilon} \tag{1}$$

where m denotes filter orientation,$o_m(x, y)$ and $e_m(x, y)$ are odd and even symmetric Log Gabor filter, ε is a small constant, T_m is an orientation-dependent noise threshold, $A_m(x, y) = \sqrt{e_m^2(x, y) + o_m^2(x, y)}$ and $\lfloor . \rfloor$ denotes zeroing negative values. Feature symmetry favors bar-like image patterns, which is useful in extracting the thin media layer. We modify the feature symmetry equation in [6] to focus only on the dark polarity (minimum intensity) symmetry by:

$$FS(x,y) = \sum_m \frac{\lfloor [-|e_m(x,y)| - |o_m(x,y)|] - T_m \rfloor}{A_m(x,y) + \varepsilon} \tag{2}$$

First order derivative of Gaussian – This set of filters is designed to highlight the intensity difference between media and adventitia. Four different orientations are used.

Band-pass log-Gabor – Log Gabor is used as a bandpass filter in three scales to enhance the border and to reduce speckles and other image artifacts. This process is carried out in coarser scales, i.e. in the 3rd, 4th and 5th scales. Hence, these features particularly show dominant edges.

2.3 Cost function

For the media-adventitia border, all the three types of features described in Sect. 2.3 are used. It takes the following form:

$$C_1(x,y) = C_d(x,y) + \alpha_1 G(x,y) + \alpha_2(1 - FS(x,y)) \tag{3}$$

where C_d denotes the term for derivative of Gaussian features,C_G is for log-Gabor, and α_1 and α_2 are constants. C_G can be obtained by cascading the filtering responses across scales. However, more weight can be assigned to coarser scale features so that it presence the connectivity of media-adventitia border at the existence of acoustic shadow, e.g. $C_G = G^{(3)} + G^{(4)} + 1.5G^{(5)}$ as used here and $G^{(i)}$ denotes ith scale. Feature symmetry FS is useful in enhancing the thin layer of media. It is normalized beforehand, and since the middle of the layer has larger values $1-FS$ is used in the cost function so that the interface between media and adventitia is highlighted. Note that each of the term in the cost function is normalized. For the auxiliary interface that is above media-adventitia, we use a combination of log- Gabor feature and feature asymmetry:

$$C_2(x,y) = C_G(x,y) + \alpha_3(1 - FA(x,y)) \tag{4}$$

where α_3 is a constant. The combination of those two types of features leads the cost function to favor linking globally dominant image features, which very often is distractive for media-adventitia border segmentation.

2.4 Compute the minimum closed set

Each graph node is weighted by a value represents its rank to be selected in the minimum closed set graph where the arc costs between graph nodes are infinitive. The weight assignment is carried out according to $w(x,y) = C(x,y) - C(x,y-1)$ where C denotes the cost function and w is the weight for each node in the directed graph, which serves as the base for dividing the nodes into non-negative and negative sets. The $s-t$ cut method can then be used to find the minimum closed set. The source s is connected to each negative node and every non-negative node is connected to the sink t, both through a directed arc that carries the absolute value of the cost node itself.

2.5 Post-processing

The segmented media-adventitia may still contain local oscillations. Smoothing based post-processing can be adopted to eliminate such oscillations. Here, RBF interpolation using thin plate base function is used to effectively obtain the final interface.

3 EXPERMENTAIL RESULTS

A total of 95 IVUS images from 4 acquisitions of 2 patients are used to evaluate the proposed method. These images contain various forms of soft and fibrous plaque, calcification, stent, and acoustic shadow. In most of the images, For all the tested images, ground-truth via manual labeling is available for quantitative analysis. All the parameters are fixed: distance between two surfaces are set as $\delta_{min} = 5$, $\delta_{max} = 140$, and cost function weightings are set as $\alpha_1 = 0.7$, $\alpha_2 = 0.5$, and $\alpha_3 = 0.5$.

The proposed method was compared against the single-interface segmentation with the cost function in (3). The cost function for the media-adventitia was kept the same. Fig. 1 The single-interface segmentation gave partial media-adventitia border, as shown in first row (b). However,

Table 1: comparison between single-interface and double-interface segmentation results. AD: area difference in percentage; AMD: absolute mean difference in pixel compared to ground-truth.

	Single interface		Double-interface AD AMD	
	AD	AMD	AD	AMD
Mean	9.99	12.55	5.84	6.99
Std.	11.06	11.45	4.53	4.13
Min	1.60	1.76	1.47	1.75
Max	57.08	54.70	25.04	24.42

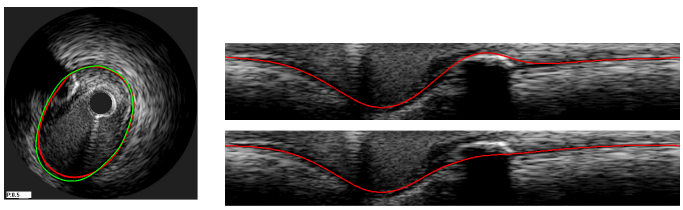

(a) (b)

Figure 1: (a) Comparison between groun-truth (green) and the proposed method (red), (b) first row shows single-interface result, and second row shows the proposed method.

its performance degraded when there were interfering image structures. Table 1 provides the quantitative comparison between single-interface approach and the proposed method. The proposed method achieved better accuracy and consistency.

4 CONCLUSION

We presented an automatic double-interface segmentation method, whose cost functions combine local and global image features and its geometric constrain is integrated in graph construction. Qualitative and quantitative comparison showed superior performance of the proposed method.

REFERENCES

[1] E. Brusseau et al., "Fully automatic luminal contour segmentation in intracoronary ultrasound imaging-a statistical approach," IEEE Trans Med Imaging. vol. 23 No. 5, pp. 554-66, 2004.

[2] M. Plissiti et al., "An Automated Method for Lumen and Media-Adventitia Border Detection in a Sequence of IVUS Frames," IEEE Trans Inf Technol Biomed, Vol. 8, No. 2, pp. 131-141, 2004.

[3] M. Sonka et al., "Segmentation of intravascular ultrasound images: A knowledge-based approach," T-MI, vol. 14, No. 4, pp. 719–732, 1995.

[4] A. Takagi et al., "Automated contour detection for high frequency intravascular ultrasound imaging: A technique with blood noise reduction for edge enhancement," Ultrasound Med. Biol., vol. 26, pp. 1033–1041, 2000.

[5] A. Wahle et al., "Plaque development, vessel curvature, and wall shear stress in coronary arteries assessed by X-ray angiography and intravascular ultrasound," Medical image analysis, vol. 10, no. 4, pp. 615–31, 2006.

[6] M.Mulet-Parada and J.Noble, "2D + T acoustic boundary detection in echocardiography," Medical Image Analysis, vol. 4, no. 1, pp. 21–30, 2000.

[7] K.Li, et al., "Optimal surface segmentation in volumetric images-a graph-theoretic approach," T-PAMI, vol. 28, no. 1, pp. 119–34, 2006.

2nd International Conference on Mathematical and Computational Biomedical Engineering – CMBE2011
March 30 – April 1, 2011, Washington D.C., USA
P. Nithiarasu and R. Löhner (eds)

Learning Patient-specific Motion based on Decomposing a Multilinear Shape Model

Yipeng Hu and Dean Barratt
Centre for Medical Image Computing, University College London, Gower Street, London, WC1E 6BT, UK, {yipeng.hu, d.barratt}@ucl.ac.uk

SUMMARY

In this study, we investigate the feasibility of using a multilinear statistical shape model (MSSM) to predict patient-specific prostate gland motion due to the placement of a transrectal ultrasound (TRUS) probe. A MSSM was trained using synthesized shape data, generated by modelling gland motion using a nonlinear finite-element model of the prostate and surrounding anatomy, which was in turn derived from an MR image for each patient. Once generated, the MSSM was used to predict the probe-induced prostate motion for a new patient given unseen information on gland shape and size, derived from an MR image. A set of deformed gland shapes, predicted by this model, was then used as training data for a linear SSM for the new patient, constructed using principal component analysis, which approximates the shape variation expected during a TRUS-guided surgical procedure for this particular patient. We assess the feasibility of this approach by computing the error when using the final patient-specific SSM to model biomechanically simulated gland deformations for 14 patient datasets.

Key Words: multilinear shape model, organ motion, prostate cancer, minimally-invasive interventions

1. INTRODUCTION

Linear statistical shape analysis techniques, such as principal component analysis (PCA), based on image training data have been widely investigated for describing the variations in organ shape across a population, as well as variations in shape due to physiological motion [1]. In principle, this approach can also be applied to enable shape changes due to external forces, such as surgical instruments, but acquiring sufficient (image) training data to learn patient-specific motion is often impractical because reproducing the conditions that give rise to shape changes is usually not possible. One solution to this problem is to *simulate* training data using a patient-specific biomechanical model [2, 3].

In our recent work, we have developed a novel "model-to-image" approach for non-rigidly registering a pre-operative magnetic resonance (MR) image to 3D transrectal ultrasound (TRUS) images obtained during minimally-invasive biopsy and ablative therapies, such as high-intensity focused ultrasound ablation [4-6]. In this method, a patient-specific linear statistical shape model (SSM) of the prostate gland is fitted automatically to features (the gland capsule surface in this case) extracted from the target TRUS image. Training data for the model are generated using patient-specific finite element (FE) simulations of the gland and the surrounding pelvic anatomy, derived from a (T2-weighted) MR image, and represent the variation in prostate shape due to different TRUS probe poses and assumed tissue mechanical properties. By analysing the FE mesh node displacements, all the simulated shapes are decomposed into a "landmark" subspace and a motion subspace, wherein "landmarks" correspond to mesh node co-ordinates. Applying PCA enables the motion subspace to be projected into a lower dimension space, typically described by 10-20 modes. The linear SSM of the prostate gland deforms in a highly constrained but physically plausible manner. These properties make it very well-suited to constraining

deformable image registration algorithms, particularly when one of the images to be registered is of poor quality or contains sparse information on organ geometry.

This approach has yielded excellent results in our early work, with MR-TRUS registration errors around 2-3mm, based on image-visible landmarks within the gland [5,6]. However, the requirement for a patient-specific model places a significant burden on the clinical workflow, since accurate segmentation of the prostate and surrounding anatomy in an MR image currently requires manual contouring, which is both time-consuming and labour-intensive. Generating a FE mesh and performing the training simulations also requires special-purpose software and can introduce errors. To overcome these limitations, in this paper we propose: 1) employing a *multilinear* statistical shape model (MSSM) [7-9] that takes into account prostate shape variability *both* between different patients and within each individual patient; and 2) building a patient-specific linear model from the data predicted by the MSSM, given limited geometric information derived from an unseen MR image for a patient. The aim of this study was to investigate the feasibility of this approach.

2. METHODS

2.1 Multilinear Statistical Shape Model

2.1.1 Training Data Generation

Simulated training data for the MSSM was generated for 14 prostate cancer patients undergoing transperineal, template-guided biopsy or HIFU therapy procedures at UCL Hospital, London. For each patient, a pre-operative T2-weighted MR image was available, and the following tasks were carried out: 1) The MR image was manually segmented. The central and peripheral zones of the gland were delineated along with the pelvic bone, bladder, and rectum; 2) The segmented structures were meshed into 50-60,000 tetrahedron elements using meshing tool provided in the ANSYS FEA software (ANSYS Europe Ltd., Oxfordshire, UK); 3) Five-hundred FE simulations of gland motion due to different TRUS probe positions and tissue material properties were performed using a non-linear FE solver running on a GPU [10]. During each simulation, different material properties were randomly assigned to all the regions, and different boundary conditions were defined by different positions and orientations of the TRUS probe. Further details of the segmentation and FE modelling technique used in this study can be found in [5] and].

2.1.2 Point Correspondence

Because each training dataset was generated by simulating the physical deformation of a common FE model of the prostate gland (and surrounding soft-tissue), point correspondence between different training shapes for each patient is determined implicitly. The point correspondences *between* different patients (across the landmark subspace) were computed by groupwise non-rigid registration of the MR-derived prostate shapes using a landmark-guided coherent point drift algorithm [11]. The approximate locations of the base and apex of the gland were used as landmarks to aid the registration. The groupwise registration scheme updates the mean shape of the registered segmentations until the iterations converge. The final point correspondence was then propagated across the simulated data by interpolating the FE meshes.

2.1.3 Multilinear Model Generation

Following registrations and spatial interpolation, the point correspondences across the patient, motion and landmark spaces are known. Using the tensor multiplication, the MSSM is given by:

$$D = S \times_{\mathbf{1}} \mathbf{U}^{patient} \times_2 \mathbf{U}^{motion} \times_3 \mathbf{U}^{landmark} \quad (1)$$

where D is a 3-mode tensor ($D \in \Re^{I \times J \times K}$) that assembles K mean subtracted landmarks sampled from each of J datasets (see Figure 1); the first dataset corresponds to the original MR segmentation, whereas, for each of the I patient data, the j^{th} dataset ($j=2,\ldots,J$) corresponds to the deformed mesh produced by the FE simulations. The core tensor $S \in \Re^{I \times J \times K}$, computed by a high order singular value decomposition [7], represents the interactions of the patient, motion and

landmark subspaces, contained in matrices $\mathbf{U}^{patient} \in \Re^{I \times I}$, $\mathbf{U}^{motion} \in \Re^{J \times J}$ and $\mathbf{U}^{landmark} \in \Re^{K \times K}$ respectively. Thus, a new shape may be reconstructed by:

$$\mathbf{d} = S \times_1 \mathbf{u}^{patient} \times_2 \mathbf{u}^{motion} \times_3 \mathbf{U}^{landmark} \quad (2)$$

where $\mathbf{u}^{patient} \in \Re^{I}$ and $\mathbf{u}^{motion} \in \Re^{J}$ are patient and motion vectors, respectively. Therefore, given a new patient vector, $\hat{\mathbf{u}}^{patient}$, the shape for this patient, at the n^{th} point in motion subspace, can be predicted by back projection onto the original landmark subspace:

$$\mathbf{d}_n = S \times_1 \hat{\mathbf{u}}^{patient} \times_2 \mathbf{u}_n^{motion} \times_3 \mathbf{U}^{landmark} \quad (3)$$

Now, the shape vector $\mathbf{d}_1$ can be determined from the segmentation of the new patient MR data and projected to obtain the corresponding patient vector, $\hat{\mathbf{u}}^{patient}$, using the relation:

$$\hat{\mathbf{u}}^{patient} = B \times_2 \mathbf{d}_1, \text{ where, } \mathbf{B} = (S \times_2 \mathbf{u}_1^{motion} \times_3 \mathbf{U}^{landmark})^{-T} \quad (4)$$

2.2 A Patient-specific Statistical Model of Ultrasound-probe-induced Prostate Motion

Given a new patient vector, $\hat{\mathbf{u}}^{patient}$, obtained by registering a set of surface points identified in an unseen MR image to the mean shape of the all the segmentations in the training data (first column in Figure 1), *patient-specific* training data for a conventional PCA-based model of prostate deformation can be generated using the MSSM *without requiring a FE solver*. Furthermore, the number of surface points is small so that a complete segmentation of the (unseen) MR image is no longer required (In this study, ~100 points were re-sampled from 4 manually drawn contours). Using PCA, the resulting linear SSM that describes the variation in prostate shape for each patient from MSSM-generated data is given by:

$$\mathbf{x}_{\text{def}} \approx \mathbf{x}_0 + \bar{\mathbf{d}} + \sum_{i=1}^{L \le J} b_i \mathbf{e}_i = \mathbf{x}_0 + \bar{\mathbf{d}} + \mathbf{P}\mathbf{b} \quad (5)$$

where $\mathbf{x}_0$ is a 3N vector contains the node co-ordinates of the (undeformed), MR-derived shape; $\bar{\mathbf{d}}$ is the mean mesh node displacement vector; $\mathbf{e}_i$ is the i^{th} eigenvector of the covariance matrix formed from the set of training displacement vectors; J is the size of training data, including derived segmentation and predicted shapes; $\mathbf{b} = [b_1, b_2, ..., b_L]^{\mathrm{T}}$ is a weight vector; and $\mathbf{P}$ is a $3N$ by L matrix with columns that contain eigenvectors ordered so that the corresponding eigenvalue λ_i decreases in magnitude as i increases.

2.3 Model Validation

The new SSM generation method was validated by comparing the model generalisation ability (GA) and specificity [12] with those of a model generated using training data simulated by a biomechanical model. The GA measures the ability of a model to describe unseen data by computing the root mean square error (RMSE) of the distance between an SSM and the (ground truth) shape (see Figure 1). Model specificity measures the ability to reject abnormal data by computing the RMSE between the randomly sampled instances from the SSM and the ground truth. Here, biomechanically simulated shapes were used as the ground-truth. Patient-specific prostate SSMs were built for each patient with L modes of variation, chosen so that the accumulated variance covered 99% of the total variances. In each case, a MSSM was constructed using training data generated for the remaining 13 patients. The GAs and specificities were computed for each SSM.

3. RESULTS AND CONCLUSIONS

The GA and specificity for each SSM are plotted in Figure 2. The results demonstrate that the proposed modelling approach can usefully describe the simulated data by projecting the segmentation. The projection and prediction operations are very computationally efficient.

Furthermore, we have shown that a MSSM-generated SSM is able to reconstruct unseen deformation with an average reconstruction error (GAs) of 2.42 mm without the need to explicitly generate a finite element model from MR images or the need to perform finite element simulations. The performance of the method to constrain a non-rigid registration algorithm using real patient data is the subject of future work.

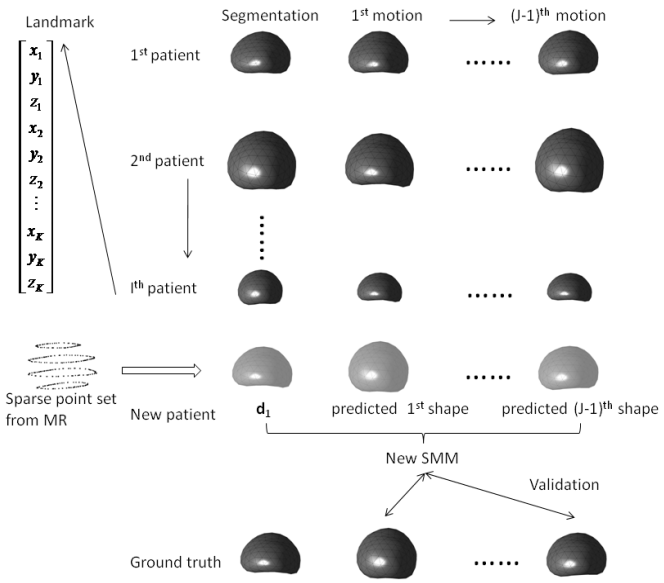

Figure 1. Illustration of the tensor *D* and the predicted training data given an MR segmentation, $\mathbf{d}_1$.

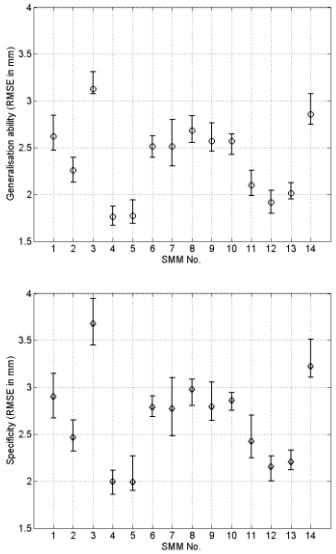

Figure 2. Plots of the GA (upper) and specificity (lower), computed from the leave-one-out test for the 14 SMMs. The error bars indicate the 10th /90th percentiles of the RMSEs.

REFERENCES

[1] T. Heimann and H.P. Meinzer (2009), Statistical shape models for 3D medical image segmentation: A review. Med. Imag. Anal. 13, 543-563

[2] C. Davatzikos, et al (2001), A Framework for predictive Modeling of Anatomical Deformations. IEEE. Trans. Med. Imaging 20(8), 836-843

[3] A. Mohamed, et al (2002), A Combined Statistical and Biomechanical Model for Estimation of Intra-operative Prostate Deformation. MICCAI 2002, LNCS 2489, 452-460

[4] Y. Hu, et al (2008), A Statistical Motion Model based on Biomechanical Simulations for Data Fusion during Image-guided Prostate Interventions. MICCAI 2008, LNCS 5241, 737-744

[5] Y. Hu, et al (2009), MR to Ultrasound Image Registration for Guiding Prostate Biopsy and Interventions. MICCAI 2009, LNCS 5761, 787-794

[6] Y. Hu, et al (2010), MR to Ultrasound Registration for Image-guided Prostate Interventions. Med. Imag. Anal., *in press*

[7] L.D. Lathauwer, et al (2000), A multilinear Singular Value Decomposition. SIAM J. Matrix Anal. Appl. 21(4), 1253-1278

[8] M. Alex, et al (2002), Multilinear Analysis of Image Ensembles: TensorFaces. ECCV 2002, LNCS 2350, 447-460

[9] Y. Zhu, et al (2010), Segmentation of the Left Ventricle from Cardiac MR Images using a Subject-Specific Dynamical Model. IEEE Trans. Med. Imaging 29(3), 669-687

[10] Z.A. Taylor, et al (2008), High-speed Nonlinear Finite Element Analysis for Surgical Simulation using Graphics Processing Units. IEEE Trans. Med. Imaging 27(5), 650-663

[11] Y. Hu, et al (2010), Deformable Vessel-based Registration using Landmark-guided Coherent Point Drift. MIAR 2010, LNCS 6326, 60-69

[12] Y. Hu, et al (2010), A Comparison of the Accuracy of Statistical Models of Prostate Motion Trained using Data from Biomechanical Simulations. Prog. Biophys. Mol. Biol., 103 (2010) 262-272

2nd International Conference on Mathematical and Computational Biomedical Engineering - CMBE2011
March 30 - April 1, 2011, Washington D.C, USA
P. Nithiarasu and R. Löhner (Eds.)

VARIATIONAL LEVEL SET SEGMENTATION USING SHAPE PRIOR

S. Y. Yeo*, X. Xie, I. Sazonov* and P. Nithiarasu***
*College of Engineering, Swansea University, Swansea SA2 8PP, U. K.,
{465186, i.sazonov, p.nithiarasu}@swansea.ac.uk
**Department of Computer Science, Swansea University, Swansea SA2 8PP, U.K.,
x.xie@swansea.ac.uk

SUMMARY

We proposed a new level set segmentation model with statistical shape prior using a variational approach. The image attraction force is derived from the interactions of gradient vectors across the whole image domain. This gives the active contour a global representation of the geometric configuration, making it more robust to image noise, weak edges and initial configurations. Statistical shape information is incorporated by using a nonparametric technique to model the shape distribution, which allows the model to handle relatively large shape variations.

Key Words: *level set, segmentation, shape prior.*

1 INTRODUCTION

Image segmentation is an important area in image processing and has a wide range of applications such as biomedical image analysis. Several approaches have been proposed for automatic object segmentation. Some of the main challenges include the extraction of object boundaries or regions from images with noise and intensity inhomogeneity. Other factors such as weak object edges, low resolution, and complex geometries can also affect the accuracy and efficiency of the shape extraction process.

Active contours provide an effective framework for object segmentation as they can easily adapt to shape variations. Various types of information can also be incorporated to regularize the smoothness and shape of the contour. Active contour models usually take the form of image gradient based approaches [1] and region based approaches [2, 3]. As conventional edge based methods are driven by external energies derived from local image information, they are often affected by local minima such as image noise, and have difficulties dealing with weak object edges. Region based methods make use of regional statistics such as means and variances to derive the external energies or forces, and are thus more robust to noise interference. However, as region based models [2, 3] are often based on the assumption that image objects consist of distinct regional statistics, they cannot deal with intensity inhomogeneity in images. Various groups have also incorporated shape prior information into their models. Many of these techniques are based on statistical assumptions, i.e. the training shapes are constrained to a Gaussian distribution. This can easily restrict the range of applications as real world objects can often take on complex shape variations.

In this paper, we propose a new variational level set model for efficient segmentation of images. The proposed method uses an image based energy derived from the global interaction of image

gradient vectors [4] to attract the active contour towards object boundaries. This image based energy greatly improves the performance of the active contour in handling weak edges, image noise and arbitrary cross-boundary initializations. We also incorporate statistical shape prior information into the variational segmentation model using nonparametric shape density distribution [5, 6]. By using kernel density estimation (KDE) to the space of shapes, the shape prior can model arbitrary shape distributions, and can be applied to segment various shapes from occluded or noisy images.

2 PROPOSED METHOD

The proposed variational model consists of an image attraction force which propagate contours towards object boundaries, and a global shape force which draws the model towards similar shapes represented in the training set. In this section, we formulate the variational segmentation model using Bayesian inference. Therefore, the segmentation of an image I can be considered as minimizing the following energy functional:

$$E(\phi) = -\log(p(I|\phi)) - \log(p(\phi)) = E_{\text{image}}(\phi) + \alpha E_{\text{shape}}(\phi) \tag{1}$$

where $E_{\text{image}}(\phi)$ represents the image based term, $E_{\text{shape}}(\phi)$ represents the shape prior and α is a constant weighting term.

We recently proposed a new image attraction force based on hypothesized gradient vector interactions [4] for contour evolution. Here, we formulate the image attraction force in a variational framework so that statistical prior information can be conveniently incoporated into the model. The proposed image based energy functional takes the following form:

$$E_{\text{image}}(\phi) = \nu \int_{\Omega} g(\mathbf{x})|\nabla H_{\epsilon}(\phi)|d\mathbf{x} + \int_{\Omega} G(\mathbf{x})H_{\epsilon}(\phi)d\mathbf{x} \tag{2}$$

where ν is a constant parameter, $g(\mathbf{x}) = 1/|1 + \nabla I|$, and H_{ϵ} is the regularized Heaviside function [2]. $G(\mathbf{x})$ represents the gradient vector interaction field given as:

$$G(\mathbf{x}) = \int_{\Omega} \frac{\hat{\mathbf{r}}_{\mathbf{x}\mathbf{x}'}}{r^{k}_{\mathbf{x}\mathbf{x}'}} \cdot \nabla I(\mathbf{x})d\mathbf{x} \tag{3}$$

where $\hat{\mathbf{r}}_{\mathbf{x}\mathbf{x}'}$ is the unit vector from pixel location $\mathbf{x}$ to $\mathbf{x}'$ and $r_{\mathbf{x}\mathbf{x}'}$ is the distance between the pixels. k is a constant which is set to the dimension of the image data (i.e. $k = 2$ for 2D image). $G(\mathbf{x})$ can be computed efficiently as a vector convolution using fast Fourier transform (FFT), and some effects caused by spurious edges can be removed by not considering pixels with edge magnitude smaller or greater than a certain percentage of the maximum magnitude. The first term in (2) induces the segmentation model to favour minimal length and smooths the contour, while the second term attracts the active contour towards image object boundaries.

The gradient vector interaction field $G(\mathbf{x})$ utilizes image pixels or voxels across the whole image domain, and thus gives a global representation of the geometric configuration. This provides the active contour with a high invariancy to initializations and a large attraction range. It also increases the robustness of the active contour against image noise and weak edges.

The shape based energy functional is defined using a shape distance measure [5] as:

$$E_{\text{shape}}(\phi) = D^2(\phi, \phi_i) = \int_{\Omega} (H(\phi(\mathbf{x} + \mu_{\phi}) - H(\phi_i))^2 d\mathbf{x} \tag{4}$$

where $\{\phi_i\}_{i=1...N}$ is a set of training shapes, and μ_ϕ is the center of gravity of the shape ϕ. The shape distance provides a dissimilarity measure which is invariant to translation of the shape ϕ. Intrinsic alignments with respect to scale and rotation can also be incorporated in the model [5]. Here, we use the nonparametric technique of kernel density estimation (KDE) to model the statistical shape distribution:

$$p(\phi) \propto \frac{1}{N}\sum_{i=1}^{N} \exp\left(-\frac{1}{2\sigma^2} D^2(\phi, \phi_i)\right) \tag{5}$$

where σ is the kernel width, and is set to the mean nearest-neighbor distance.

The minimization of the energy functional in (1) can be performed using calculus of variation, and the gradient descent with respect to the shape ϕ is derived as:

$$\frac{\partial \phi}{\partial t} = -\frac{\delta E_{\text{image}}(\phi)}{\delta \phi} - \alpha \frac{\delta E_{\text{shape}}(\phi)}{\delta \phi} \tag{6}$$

The gradient flow of the image based energy is given as:

$$\frac{\delta E_{\text{image}}(\phi)}{\delta \phi} = \nu g(\mathbf{x}) \nabla \cdot \Big(\frac{\nabla \phi(\mathbf{x})}{|\phi(\mathbf{x})|}\Big) \delta_\epsilon(\phi(\mathbf{x})) - G(\mathbf{x}) \delta_\epsilon(\phi(\mathbf{x})) \tag{7}$$

where δ_ϵ is the regularized version of the Dirac delta function, i.e. the derivative of H_ϵ, and the gradient flow of the shape based energy is defined as:

$$\frac{\delta E_{\text{shape}}(\phi)}{\delta \phi} = \frac{\sum_i w_i \frac{\partial D^2(\phi, \phi_i)}{\partial \phi}}{2\sigma^2 \sum_i w_i} \quad \text{where } w_i = \exp\Big(-\frac{1}{2\sigma^2} D^2(\phi, \phi_i)\Big) \tag{8}$$

The shape derivative with respect to ϕ is given as:

$$\begin{aligned} \frac{\delta D^2(\phi, \phi_i)}{\delta \phi} = 2\delta_\epsilon(\phi(\mathbf{x}))\Big((H_\epsilon(\phi(\mathbf{x})) - H_\epsilon(\phi_i(\mathbf{x} - \mu_\phi)) + \frac{(\mathbf{x} - \mu_\phi)^T}{\int\limits_\Omega H_\epsilon(\phi) d\mathbf{x}} \\ \times \int (H_\epsilon(\phi(\mathbf{x}') - H_\epsilon(\phi_i(\mathbf{x}' - \mu_\phi)\, \delta_\epsilon(\phi(\mathbf{x}'))\nabla \phi(\mathbf{x}')\, d\mathbf{x}'\Big) \end{aligned} \tag{9}$$

The proposed variational model therefore simultaneously attracts the active contour towards image object boundaries and similar shapes represented in the statistical shape distribution.

3 RESULTS

In this section, we show that the proposed method can be applied efficiently for image object segmentation. Figure 1 shows the segmentation of multiple annular-like objects from an image with 70% noise, occlusions and intensity variation. The training set consist of 20 images with annular-like objects of varying shapes. It is shown that the proposed active contour with shape prior can extract the shapes from the occluded and noisy image efficiently.

Figure 2 depicts the segmentation of carotid from computed tomography (CT) images. In this example, 20 training shapes are manually generated to model the shape distribution. Note that the image data consist of various structures such as adjacent vessels and bones, and image regions representing the carotid often contain diffused edges and intensity inhomogeneity. Therefore, careful initializations are often required for purely image based segmentation model to delineate the shape of the structure. As shown in the figure, the proposed active contour with image and shape based energy can be applied to segment the carotid structure efficiently.

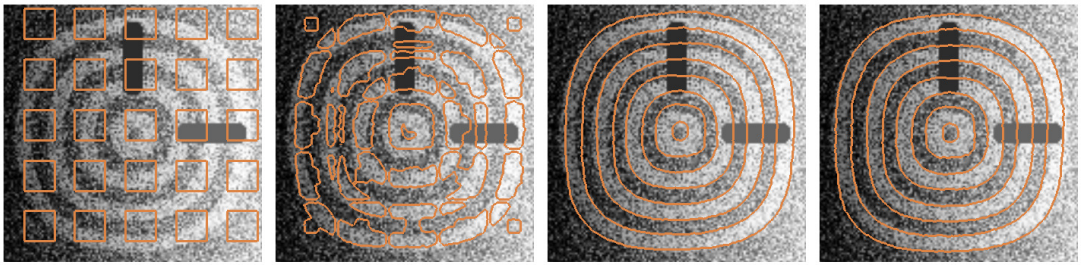

Figure 1: Segmentation of annular-like shapes using the proposed method.

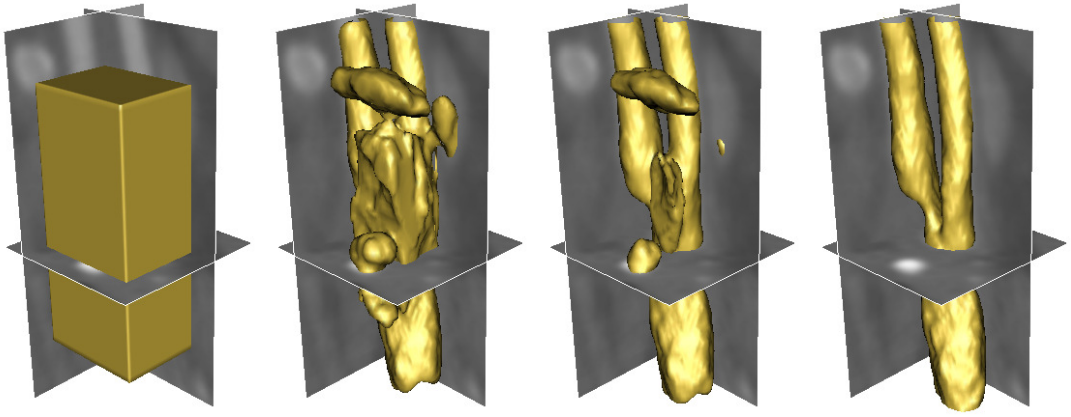

Figure 2: Segmentation of carotid from CT image using the proposed method.

4 CONCLUSIONS

We have presented a new level set segmentation model with statistical shape prior using a variational approach. The image based energy is derived from the global interaction of gradient vectors. The active contour model is thus more robust to image noise and weak edges, and has a strong initialization invariancy. By using kernel density estimation, the incorporated shape prior can model arbitrary shape distributions. The proposed model can thus be applied to segment complex shapes from images of various modalities efficiently.

References

[1] V. Caselles, R. Kimmel, and G. Sapiro. Geodesic active contour. *IJCV*, 22(1):61–79, 1997.

[2] T. Chan and L. Vese. Active contours without edges. *IEEE T-IP*, 10(2):266–277, 2001.

[3] N. Paragios and R. Deriche. Geodesic active regions and level set methods for supervised texture segmentation. *IJCV*, 46(3):223–247, 2002.

[4] S. Y. Yeo, X. Xie, I. Sazonov, and P. Nithiarasu. Geometrically induced force interaction for three-dimensional deformable models. *IEEE T-IP*, in press, 2011.

[5] D. Cremers, S. Osher, and S. Soatto. Kernel density estimation and intrinsic alignment for shape priors in level set segmentation. *IJCV*, 69(3):335–351, 2006.

[6] J. Kim, M. Cetin, and Wilsky A. S. Nonparametric shape priors for active contour-based image segmentation. *Signal Processing*, 87(12):3021–3044, 2007.

2nd International Conference on Mathematical and Computational Biomedical Engineering - CMBE2011
March 30 - April 1, 2011, Washington D.C, USA
P. Nithiarasu and R. Löhner (Eds.)

Using 4D Phase-Contrasts MRI to determinate blood flow patterns in the aortic diseases

Eduardo Soudah*, Jorge S. Ronda*, Marcelino Rodriguez, Herkel Hervilla**, Francesc Carreras*** and Eugenio Oñate***

*International Center for Numerical Methods in Engineering, Barcelona, 08034, Spain
**Universidad Central Marta Abreu, Las Villas, Cuba
***Departamento de Cardiologa del Hospital de la Santa Creu i Sant Pau., Calle Cant Antoni Maria Claret 167. 08025,Barcelona, Spain

SUMMARY

The effect of blood flow on arterial wall remodelling and the investigation of vascular hemodynamic within the vascular vessels are of great interest, for example in the aorta coarctation or Thoracic Aortic Aneurysms(TAA). The underlying causes for the formation of TAAs can be either inherited (related to Marfan's Syndrome) or acquired, with risk factors including smoking, hypertension and atherosclerosis. The identification of patients with aortic disease requires a detailed understanding of the link between vascular malformation and altered hemodynamic, and how is the relationship between the blood flow and the aortic wall; it has the potential to greatly enhance the understanding of the pathogenesis and progression of vascular diseases and to aid in the decision of whether treatment is warranted. If left untreated, TAAs tend to grow at a rate of 0.10 cm per year and may rupture or dissect upon reaching a fit diameter, at this stage, it is likely that the arterial wall will no longer withstand the blood pressure, and surgical intervention will be needed. In this perspective, 4D Phase-Contrast non-invasive magnetic resonance imaging (MRI), with its intrinsic sensitivity to blood flow, offers the unique possibility to simultaneously acquire morphology and spatially co-registered hemodynamic information non-invasively. The purpose of this study was to visualize and determinate the 3D blood flow patterns in the aorta obtained by 4D phase-contrast magnetic resonance and to use it as boundary condition for the computational fluid dynamics(CFD) in order to obtain other relevant parameters, as shear stress over the arterial wall.

Key Words: *blood flow, phase-contrast MRI, vascular hemodynamics, velocity mapping.*

1 INTRODUCTION

Mean aortic flow velocity is probably of greater use as a trend indicator of cardiovascular diseases, aorta coarctation or Thoracic Aortic Aneurysms(TAA) as a result of the recirculating flow or the wall shear stresses at the inner wall. Knowledge of the in vivo hemodynamics in aorta is important to better understand the underlying mechanisms of initiation and progression of these aortic diseases. Thanks to the new medical imaging techniques, such as MRI and CT scanning, we are able to get a lot of information non-invasively and to visualize complex geometry of the patients. In this work, we have developed a tool, DiPPo, able to integrate the velocity profile determined by 4D phase-contrast magnetic resonance in computational fluid dynamics. To date, these techniques have largely been applied to compute meshes for numerical simulations, but with DiPPo, we will use the blood velocity profile from the MR scan, in particular for deformable registration of 4D

MRI images, 3D morphologic and 3-directional blood flow data to calculate the shear stress over the arterial wall. Furthermore, DiPPo is focus in the medical image processing in the biomechanical research field to generating meshes from the medical images, to apply in Computational Fluid Dynamics (CFD) or structural mechanics(stress analysis).

2 METHODOLOGY

2.1 Magnetic Resonance

Measurements were carried out using a 3 T MR system (Magnetom TRIO; Siemens, Erlangen, Germany) time-resolved, 3-dimensional MR velocity mapping based on an RF-spoiled, gradient-echo sequence with interleaved 3-directional velocity encoding (predefined fixed velocity sensitivity = 150 cm/s for all measurements). Data were acquired in a sagittal-oblique, 3-dimensional volume that included the entire thoracic aorta and the proximal parts of the supra aortic branches. Each 3-dimensional volume was carefully planned and adapted to the individual anatomy (spatial resolution, 2.1 x 3.2-3.5 x 3.5-5 mm^3).In the in vivo situation, measurements may be compromised by the active cyclic motion of the heart (cardiac contraction and dilation) and the passive motion of the heart due to respiration. These motion components may lead to image artifacts and uncertainties about the exact measurement site in the aorta. Only if the breathing state was within a predefined window data was accepted for the geometrical reconstruction. To resolve the temporal evolution of vascular geometry and blood flow, measurements were synchronized with the cardiac cycle. The velocity data was recorder in intervals of Temporal Resolution(TeR) throughout the cardiac starting after the R-wave of the ECG. The initial delay after R-wave detection was required for execution of the navigator pulse and processing of the navigator signal. Two-fold acquisition (k-space segmentation factor = 2) of reference and 3-directional velocity sensitive scans for each cine time frame resulted in a temporal resolution of 8 repetition time = 45 to 49 milliseconds. To minimize breathing artifacts and image blurring, respiration control was performed based on combined adaptive k-space reordering and navigator gating. Further imaging parameters were as follows: rectangular field of view = 400x(267-300) mm^2, flip angle = 15 degrees, time to echo = 3.5 to 3.7 milliseconds, repetition time = 5.6 to 6.1 milliseconds, and bandwidth = 480 to 650 Hz per pixel. Velocity measurements a voluntary healthy, male subject underwent MR examinations; written informed consent was obtained from the subject.

2.1.1 Blood flow velocity decoding

Blood flow velocity in each voxel depends on acquisition velocity sensitivity and gray scale. In general the velocities are encoded in the phase difference images such that there is a linear relationship between the gray scale value and the underlying velocity. Velocity in cm/sec = ((PixelValue - GrayScale)/GrayScale)*Venc; where venc is the velocity sensitivity in cm/sec(in our case venc=150 cm/s), GrayScale depends of the DICOM(in our case 2048) and PixelValue is the value of the gray color of the phase contrast image (see 2.1).

2.2 Segmentation

An n-phase 4D (spatio-temporal) image can be viewed as a discrete set of n volumetric images defined at n different time instants. The 4D aortic surface can be also viewed as a sequence sequence of surfaces. During the segmentation stage, the 4D segmentation algorithm consists of the following steps according to [13]

- Aortic surface pre-segmentation: A 4D fast marching level set method simultaneously yields approximate 4D aortic surfaces [3]
- Centerline extraction: Aortic centerlines are determined from each approximate surface by skeletonization.
- Accurate aortic surface segmentation: Accurate 4D aortic surface is obtained simultaneously with the application of a novel 4D optimal surface detection algorithm.

In order to achieve an accurate and improve the aorta segmentation, a new step has been added. This new step consists to introduce an optimization of Dijkstra's shortest path algorithm. Thanks to this algorithm, the region of interest is more precise, the tubular structures[3] are improved and it is possible to select the branches of the aorta according to some values.

2.3 Meshing

The development of computational simulations in medicine, molecular biology and engineering has increased the need for quality finite element meshes[1]. For the segmentation procedure DiPPo includes a variety of ITK[8] filters, which are used interactively by the clinicians to determinate the volume of interest of the problem. After aorta segmentation(2.2), we end with a file with the image data and the value of the isosurface value defining the boundary of the volume of interest. The imaging data V is given in the form of sampled function values on rectilinear grids,

$$V = F(x_i, y_j, z_k) | 0 \leq i \leq n_x, 0 \leq j \leq n_y, 0 \leq k \leq n_z; \tag{1}$$

We assume a continuous function F is constructed through the trilinear interpolation of sampled values for each cubic cell in the volume. The format used to read the medical data is VTK[12] structured point as it is agreed in [7]. The description of this format can be found in [7]. The image in this format can also be rendered as a volume and manipulated with ITK[8]. Given an isosurface value defining the boundary of the volume of interest we can extract a geometric model of it. We are interested in creating a distcretization of the volume suitable for finite element computation. The following methods are able to generate a finite element meshes that can be used in the computational analysis; 1) Dual contouring, 2) Marching cubes, 3) Advancing front [6], and 4) Isosurface stuffing[5]. All of them has been integrated into DiPPo.

2.4 Numerical Simulation

In this work, blood is assumed as three-dimensional, steady, incompressible, homogeneous, Newtonian fluid with no external forces applied on it, while the arterial wall is comprised from non-elastic and impermeable material. The newtonian approximation is acceptable in large arteries[11]. Mathematically a newtonian fluid can be expressed as symmetric stress tensor by the follow constitutive equation:

$$\rho = -p\mathbf{I} + 2\mu\varepsilon(\mathbf{u}) \tag{2a}$$

$$\varepsilon(\mathbf{u}) = \frac{1}{2}\left(\nabla\mathbf{u} + \nabla\mathbf{u}^{\mathbf{T}}\right) \tag{2b}$$

where p is the fluid pressure, $\mathbf{I}$ is the unit tensor, μ denotes the apparent fluid viscosity and $\varepsilon(u)$ is the rate-of-strain tensor (2b). Therefore, according to this, blood flow is simulated with average

blood properties: fluid viscosity μ=0.0035 Pa·s and density ρ=1050 kg/m^3. Considering a fluid domain(large artery) Ω based on the arbitrary Lagrangian method [2] and adopting the following notation: $\Omega(0,t)$ is a three-dimensional arterial region, and x=(x_1, x_2, x_3) is an arbitrary point of Ω. For x ε Ω and t>0 the conservation of momentum and continuity in the compact form are described by the following equations:

$$\rho \cdot \left(\frac{\partial \mathbf{u}}{\partial \mathbf{t}} + (\mathbf{u} \cdot \bigtriangledown \mathbf{u}) \right) + \nabla \mathbf{p} - \nabla \cdot (\mu \bigtriangleup \mathbf{u}) = \rho \cdot \mathbf{f} \quad (3a)$$

$$\nabla u = 0 \quad (3b)$$

where **u** = **u** (x, t) denotes the velocity vector, **p** = **p** (x, t) the pressure field, ρ density, μ the dynamic viscosity of the fluid and f the volumetric acceleration. It is now possible to recast the Navier-Stokes equations that are used to describe the pulsatile blood flow in large arteries on the time-dependent domain Ω with appropriate boundary conditions. The boundary conditions of system (3) are prescribed velocities on the walls and inflow boundaries, as well as prescribed pressure P on the outflow boundary. The volumetric forces($\rho \cdot \mathbf{f}$) are not taken in to account in the present analysis. Due to the highly convective flow in the ascending aorta and in the general in the cardiovascular system, the numerical scheme requires a stabilization technique in order to avoid oscillations in the numerical solution. In this study an innovative stabilization method based on the Finite Increment Calculus(FIC) concept [9] [10] is applied that preserves the consistency of the scheme. Convergence was achieved when all mass, velocity component and energy changes, from iteration to iteration, were less than 10^8. The stabilized Navier-Stokes equations are solved numerically by means of a finite-element method, and its implementation was done in Tdyn [4] a fluid dynamics and multi-physics simulation environment.

3 CONCLUSIONS

The presented work allows easily combine medical imaging with computational fluid dynamics in a medical environment for a better understanding of aortic diseases. This environment may allow the extraction of novel quantitative trends describing static and dynamic properties of the normal and diseased aorta. The clinical role of imaging in this population is to identify patients who need aortic surgery before they suffer a major complication, such as dissection or aortic rupture. Nowadays, the clinicians only measures the aortic diameter to determinate the severity of the aortic diseases, but thanks to this environment we can provide to the clinicians more accurate static and dynamics measurements to identify patients in a high risk of disease. One of the main applications of DiPPo is to work directly with 4D-MRI images, allowing in a unique user-interface: filtering, segmented, meshing and visualizes a real blood flood profiles. Regarding the aorta segmentation, we have proposed a modifications of the procedure of Zhao [13] in order to reduce the computation time and automatize the segmentation process. Furthermore, DiPPo is designed to be integrated easily in other simulation programs. Other visualization and segmentation tools will be implemented according to the clinician's requirements. Future works will include advanced techniques in image processing, meshing and also improvements in the fitting techniques of the velocity encoding parameters.

References

[1] J.R. Cebral and R. Löhner, *From medical images to cfd meshes*, Proc. 8th Int. Meshing Roundtable, South Lake Tahoe, 1999, pp. 321–331.

[2] Quarteroni A. VenezianiA. Formaggia L., Nobile F., *Multiscale modelling of the circulatory system: a preliminary analysis.*, Comput.Visual.Sci **2** (1999), 75–83.

[3] Alejandro F. Frangi, Wiro J. Niessen, Koen L. Vincken, and Max A. Viergever, *Multiscale vessel enhancement filtering*, Medical Image Computing and Computer-Assisted Interventation MICCAI98 (William Wells, Alan Colchester, and Scott Delp, eds.), Lecture Notes in Computer Science, vol. 1496, Springer Berlin / Heidelberg, 1998, pp. 130–137.

[4] E. Oñate J. García, S.R. Idelsohn, and F. Del Pin, *Finite calculus formulations for finite element analysis of incompressible flows. eulerian, ale and lagrangian approaches*, Computer Methods in Applied Mechanics and Engineering **195** (2006), no. 23-24, 3001 – 3037, Incompressible CFD.

[5] Franois Labelle and Jonathan Richard Shewchuk, *Isosurface stuffing: fast tetrahedral meshes with good dihedral angles.*, ACM Trans. Graph. **26** (2007), no. 3, 57.

[6] Rainald Löhner and Juan R. Cebral, *Parallel advancing front grid generation*, in International Meshing Roundtable, Sandia National Labs, 1999, pp. 67–74.

[7] William E. Lorensen and Harvey E. Cline, *Marching cubes: A high resolution 3d surface construction algorithm*, SIGGRAPH Comput. Graph. **21** (1987), 163–169.

[8] L. Iba nez, W. Schroeder, L. Ng, J. Cates, t. Consortium, and R. Hamming, *The itk software guide*, (2003).

[9] E. Oñate, A. Valls, and J. García, *Fic/fem formulation with matrix stabilizing terms for incompressible flows at low and high reynolds numbers*, Computational Mechanics **38** (2006), 440–455.

[10] Eugenio Oñate, Aleix Valls, and Julio García, *Modeling incompressible flows at low and high reynolds numbers via a finite calculus-finite element approach*, J. Comput. Phys. **224** (2007), 332–351.

[11] Rappitsch G. Perktold K, *Computer simulation of local blood flow and vessel mechanics in a compliant carotid artery bifurcation model.*, J. Biomech. (1995), no. 28, 84556.

[12] Will Schroeder, Ken Martin, and Bill Lorensen, *Visualization Toolkit: An Object-Oriented Approach to 3D Graphics, 4th Edition*, Kitware, December 2006.

[13] Fei Zhao, Honghai Zhang, Andreas Wahle, Matthew T. Thomas, Alan H. Stolpen, Thomas D. Scholz, and Milan Sonka, *Congenital aortic disease: 4d magnetic resonance segmentation and quantitative analysis*, Medical Image Analysis **13** (2009), no. 3, 483 – 493.

2nd International Conference on Mathematical and Computational Biomedical Engineering – CMBE2011
March 30 – April 1, 2011, Washington D.C., USA
P. Nithiarasu and R. Löhner (eds)

A VARIATIONAL APPROACH FOR ESTIMATING THE COMPLIANCE OF CARDIOVASCULAR TISSUES

Mauro Perego*, Alessandro Veneziani and Christian Vergara*****

*Department of Scientific Computing, Florida State University,
400 Dirac Science Library, Tallahassee, FL, 32306, USA, mperego@fsu.edu
**Department of Mathematics and Computer Science, Emory University,400 Dowman Dr, Atlanta, GA 30322, USA, ale@mathcs.emory.edu
***Department of Information Engineering and Mathematical Methods, University of Bergamo, Viale Marconi 5, 24044, Dalmine (BG), Italy, christian.vergara@unibg.it

SUMMARY

The estimation of the rigidity of vascular tissues *in vivo* is a major issue in the clinical practice, but it is still a challenging problem. Here we propose a new method based on the solution of an inverse Fluid-Structure Interaction problem, starting from the knowledge of the displacement of the vessels from medical images.

Key Words: *Parameter estimation, Inverse problems, Fluid-structure interaction*.

1. INTRODUCTION

Estimation of the stiffness of a biological soft tissue is useful for the detection of pathologies such as tumors or atherosclerotic plaques. Elastography is a method based on the comparison between two images before and after a forced deformation of the tissue of interest. An inverse elasticity problem is then solved for the Young modulus estimation. In the case of arteries, no forced deformation is required, since vessels naturally move under the action of blood. Young modulus can be therefore estimated by solving a coupled inverse fluid-structure interaction (IFSI) problem. In this paper we focus on the mathematical properties of the IFSI problem and its numerical solution. We give some well posedness analysis and some preliminary results based on a synthetic data-set, i.e. test cases where the exact Young modulus is known and the displacement dataset is numerically generated by solving a forward fluid-structure interaction problem.
We address the problem of the presence of the noise in the measured displacement and of the proper sampling of images for obtaining reliable estimates.

2. MAIN BODY

The term compliance in physiology is referred to the tendency of a vessel or more in general a hollow organ to resist recoil toward its original dimension when a distending or compressing force is removed. A practical definition of compliance is the ratio between

the volume variation in a vessel and the corresponding pressure variation. Nevertheless, there are different definitions of compliance, mainly dependent on the different methods for measuring it. This parameter is supposed to have a role in different cardiovascular pathologies, so its estimation is a major issue in clinical diagnosis and therapy. For example, low compliance of artery vessel could be an indicator of atherosclerosis or hypertension. Moreover, an increase of the stiffness of the left ventricle wall is a clear marker of diastolic dysfunction, i.e. a clinical condition leading to an increase of the end diastolic left ventricle pressure, that may be the primum movens of heart failure. More in general, the deformability of soft tissues is an important index for the detection of anomalies or diseases such as tumors. For all these reasons, an accurate estimation of this parameter in vivo has a great relevance for diagnostic purposes and however it is difficult for many reasons. Among the techniques specifically devised for the vascular compliance, we mention 1) Methods based on the simultaneous measures of pressure and cross-sectional area at different points and times; 2) Methods based on measuring the rate of propagation of flow waves coming from the heart (pulse wave velocity). The former has a major drawback in its invasivity. The latter requires a specific attention in handling pressure wave reflections and relies upon the assumption of cylindrical vessels, which is not true in general. Other methods were proposed for more general purposes, in particular for the detection of tumors in a soft tissue. In particular, *elastography* is an approach where tissue elasticity (or stiffness) is inferred by the analysis of images of the tissue before and after the application of a proper deformation. Images are in general acquired with ultrasound or magnetic resonance. Basic steps of this approach are:

a) First acquisition of the specimen in the original configuration;

b) Application of a deformation to the specimen and second acquisition;

c) Tracking of the displacement from the comparison between the two images;

d) Estimation of the rigidity of the tissue.

Both steps (iii) and (iv) require the solution of inverse problems. Step (iii) is actually an image registration step for retrieving the displacement field. Step (iv) entails the solution of what has been called the *inverse elasticity problem*. The shear modulus or the Young modulus of the tissue, assumed to be linearly elastic, is estimated by minimizing the mismatch between the measures (displacement field) and the solution of an appropriate elasticity problem.

The present work follows a similar approach specifically devised for vessel compliance. As a matter of fact, the specificity of vessels is that they do not need an externally forced deformation, since blood pulsatility naturally induces vessel motion. The latter can be retrieved from time frames of the vessel of interest and proper measurements of blood velocity and pressure, once a routine 4D scan of the patient is available. The methodological drawback here is that the deformation is not known a priori but it is induced by blood. For this reason, the inverse problem to be solved for the parameter estimation is not simply an elasticity model, but a fully coupled fluid-structure interaction (FSI) system. In summary, our approach for estimating compliance is as follows (see Fig. 1).

1) *Retrieval of the vessel displacement by image registration procedures* on time frames of the vessel of interest. Registration entails by itself the solution of an inverse problem for tracking the vessel displacement from a sequence of time frames suitably reconstructed ion 3D (see e.g. [2]).

2) *Minimization of the difference between the vessel displacement and the displacement* computed by solving the coupled 3D blood-vessel problem, to estimate the Young modulus. Simulations include the available data of pressure and/or velocity on the boundaries.

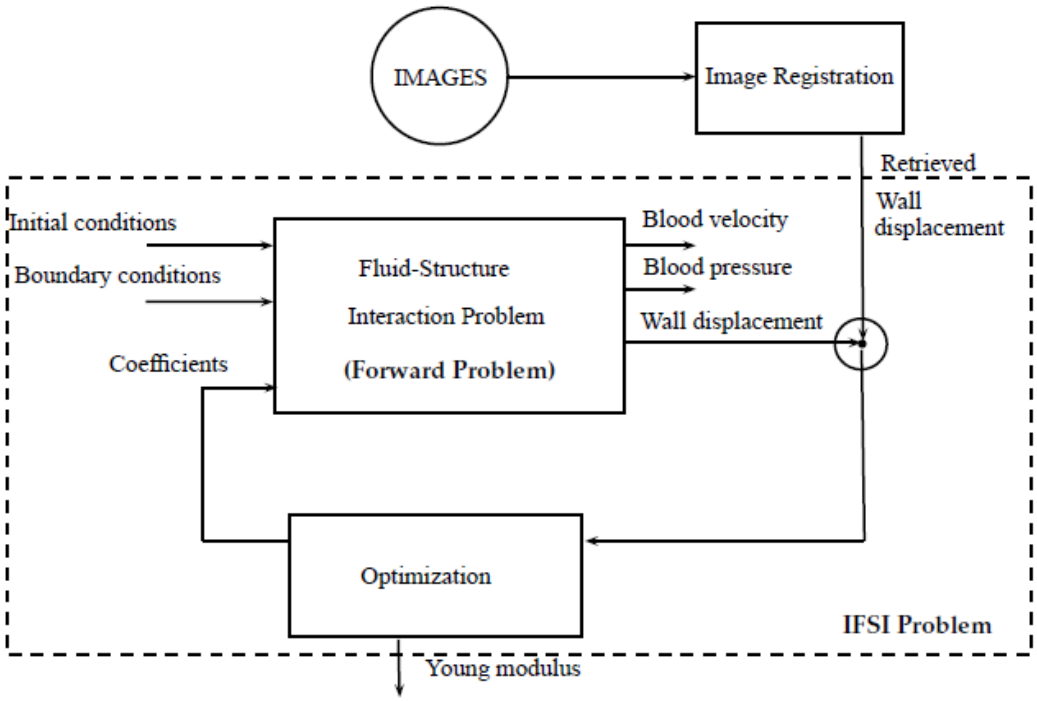

Figure 1: Scheme of the proposed approach for estimating the Young modulus.

In this talk we focus on the second step. The corresponding forward mathematical problem, the 3D fluid-structure interaction (FSI) system, has been considered in numerical haemodynamics simulations since many years. The purpose of this talk is to present a preliminary analysis of the IFSI problem when the structure is assumed to be linearly elastic and the only parameter to be estimated is the Young modulus. In particular, we discuss different approaches for tackling with IFSI problem. This is a 4D optimization problem. Different strategies can be followed for its solution depending on the order of the optimization and discretization steps. We focus on an approach where the original problem is first discretized in time, then the optimization step is performed. The well posedness of the resulting IFSI problem is analyzed. In particular, we have proved in [1] that a suitable formulation of the minimization process admits a solution that can be computed by solving the Karush-Kuhn-Tucker (KKT) system, under the assumption of a piecewise constant or linear in space Young modulus.

Possible numerical methods for the solution are then introduced. In this first work, numerical results presented refer to 2D and 2D axisymmetric test cases, where synthetic data (that is obtained by a forward FSI problem) are considered, aiming at a general assessment of the methodology. An example is presented in Figure 2, for a 2D carotid bifurcation.

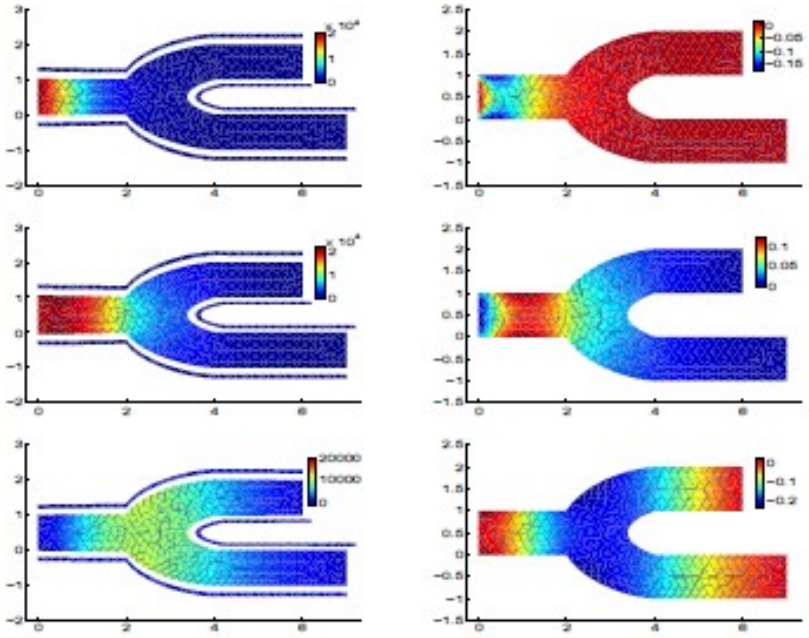

Figure 2 – Solution of the forward fluid-structure interaction problem (left) and comparison with the IFSI problem solved by identification of the Young modulus (right) in a carotid bifurcation.

3. CONCLUSIONS

We present a new method for the estimation of the rigidity of vascular tissues. This is based an an inverse FSI problem and it is not invasive. For this reason it could be an effective technique also in the clinical practice. More in general, the approach can be generalized to any structural parameter related to the cardiovascular tissue and the blood flow.

REFERENCES

[1] M.Perego, A.Veneziani, and C.Vergara. A variational approach for estimating the compliance of the cardiovascular tissue: An inverse fluid-structure interaction problem. Technical Report 18, Dept Math & CS, Emory Univ, www.mathcs.emory.edu, 2010.

[2] M. Piccinelli, L. Mirabella, T. Passerini, E. Haber, A. Veneziani, 4D Image Based simulation of blood flow in a compliant vessel, in preparation (2010).

2nd International Conference on Mathematical and Computational Biomedical Engineering – CMBE2011
March 30 – April 1, 2011, Washington D.C., USA
P. Nithiarasu and R. Löhner (eds)

Inverse stress analysis in AAA considering thrombus

Shouhua Hu, Jia Lu
Department of Mechanical and Industrial Engineering, Center for Computer Aided Design,
The University of Iowa, Iowa City, IA 52242-1527, USA
jia-lu@uiowa.edu

SUMMARY

This work investigates the influence of thrombus on abdominal aortic aneurysm wall stress predictions in inverse approach of stress analysis. By inverse stress analysis, we mean taking a pressurized geometric data as input to determine the wall stress. The advantage of inverse method is of two folds: one is that it can take into account the unknown pre-deformation; and two, the method can maximally capitalize on the property of static-determinacy, therefore allowing a more reliable stress prediction for applications where one does not have patient-specific tissue properties. The second feature will be compromised by the presence of thrombus. As such, it is of interest to know the influence of thrombus on inverse stress predictions. An image-based AAA model is considered. The wall stress at 80mmHg blood pressure is computed both forwardly and inversely. The sensitivity of stress solution over a certain range of material parameter variation is reported. It is found that the inverse stress results are less sensitive to material parameters within the given range of variation.

Key Words: *AAA, inverse elastostatics, wall stress, thrombus.*

1. INTRODUCTION

Abdominal aortic aneurysm (AAA) is a pathological expansion of the aorta due to gradual wall weakening. AAA represents permanent localized expansions of the aorta that form between the renal arteries and the iliac bifurcation. Their prevalence increases with age, and progressive AAA growth will lead to eventual rupture. Current clinical practice is to evaluate the likelihood of rupture only on the basis of the maximum transverse bulge diameter, ignoring all other factors that contribute to failure. From a biomechanical standpoint, internal stress is the physical factor that causes wall failure. Rupture is expected to be increasingly likely as the wall stresses generated by blood pressure approach or exceed the strength of the diseased wall. Based on this, the wall stresses distribution in AAA was submitted as an important indicator of rapture[1]. Early studies commonly ignored the intraluminal thrombus (ILT) inside into consideration [1, 2]. Recent investigations show that intraluminal thrombus in AAAs can reduce the peak wall stresses to some extent, acting like an elastic cushion [3, 4].

Recently, the authors' group utilized the inverse elastostatic method to compute AAA wall stress [5, 6]. This method has some advantages for patient-specific studies: For one, it can pointedly address the issue of unknown stress-free geometry; and two, the stress solution was found to be massively insensitive to the tissue properties. The second property is shown in saccular aneurysms [7]. This property is very important for patient-specific studies, because truly patient-specific tissue property data are unavailable,

and analysis has to be based on reported population mean properties. A high insensitivity to material properties means a more reliable stress prediction. The goal of this work is to numerically investigate the sensitivity of inverse stress solution at the presence of ILT. Particularly, we are interested in the range of stress variation over the 95% confidence interval of the reported material parameters, and how the stress variation compares with the forward solution.

2. METHOD AND RESULTS

The AAA model was reconstructed from the abdominal CT images. The vessel wall was assumed to have a uniform thickness of 1.9mm. The ILT was generated using our own algorithm, assuming it fills the space between the luminal surface visible from CT images and a hypothetic outer wall surface. The AAA wall was described as an elastic shell, modeled by the inverse shell element reported in [6]. The ILT is described by 3D continuum element. The shell element is based on the stress-resultant description that contains a separate rotation field [8]. Consequently, a three-D continuum element can be directly connected to the shell element without compatibility issue. Inverse algorithms for the continuum and shell elements were contained in [6, 9]. In the FE model, the nodes at the top and bottom cross sections are fixed in x, y, z directions. We assume that the reconstructed AAA with ILT model is the deformed state at the 80mmHg mean aortic pressure; we predicted the stress-free geometry and the stress in this state.

The stress resultant shell describes the in-plane stretch and the flexure bending separately. The in-plane response is characterized a 2D version the constitutive equation specifically for AAA model is employed in the study:

$$W = \alpha(I_1 - 2logJ - 2) + \beta(I_1 - 2)^2 \qquad (1)$$

where W is the strain-energy density, $I_1 = tr(F^T F)$, $J = detF$, and (α,β,k) are material constants. For the bending model we use $M = \frac{t^3}{12}\mathbb{D}$, where t is the shell thickness, and $\mathbb{D} = 4\frac{\partial^2 W}{\partial C \partial C}\Big|_{C=I}$, where $\boldsymbol{C}$ is the Cauchy-Green tensor. For ILT, the strain energy function was taken as [9, 10]:

$$W = c_1(I_1 - 2logJ - 3) + c_2(I_1 - 3)^2 \qquad (2)$$

where c_1 , c_2 are material parameters for the ILT. This function is slightly modified from the one in [11], We set the material model (1) with the population mean material parameters $\alpha = 17.39N/cm^2$, $\beta = 188.08N/cm^2$, and $c_1 = 2.6N/cm^2$, $c_2 = 2.6N/cm^2$ for the material model(2), the penalty parameter was set to $k = 100000N/cm^2$.

Fig 1 and Fig 2 show von Mises stresses at 80 mmHg arterial pressures for AAA with and without ILT in the image geometry by using inverse approach. The existence of ILT reduces the wall stress of AAA in nearby regions, consistently with the Wang's studies. To investigate the variation of wall stress within a realistic range of material parameter variation, we performed the same analyses by changing the parameters α and β within the reported 95% confidence interval[10]. We also performed repetitive analyses using the conventional forward analysis for comparison. We assigned α to the upper and lower limits in the confidence domain while keeping β fixed at the population mean, and vice versa. We calculated the average percentage differences in von Mises stress for both inverse and forward approach. Fig 3 and Fig 4 show point wise percentage differences between the first and third sets of parameters in Table1, by using inverse approach and forward approach individually. The average differences of von

Mises stresses for five sets parameters are listed in Table 1. The stress differences vary within the reported 95% confidence interval are less than 2% by using inverse method, while the difference are more than 10% for the conventional forward method.

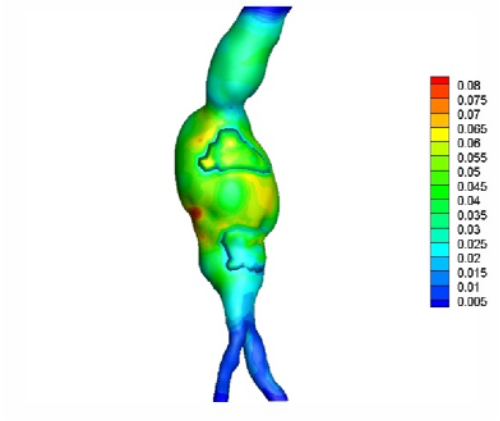

Fig 1 von Mises stress for AAA with ILT in the image geometry

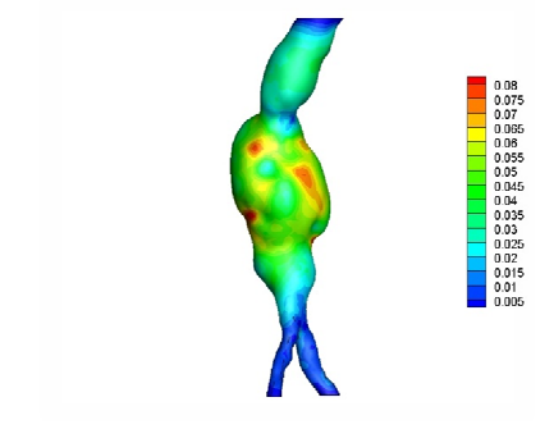

Fig

Fig 2 von Mises stress for AAA without ILT in the image geometry

Table 1 Comparison the maximum and mean differences ($\frac{\sum_1^n differ_i}{n}$)of von Mises stress with the variation of material parameters

(α, β)	σ_{max} **(Inverse)**	Mean differ %**(Inverse)**	σ_{max}**(Forward)**	Mean differ %**(Forward)**
(14.4, 188.08)	0.0847	1.58	0.0767	10.6
(20.4, 188.08)	0.0788	1.27	0.071	3.28
(17.4, 188.08)*	0.0812	—	0.0719	—
(17.4, 115.20)	0.0798	0.63	0.0705	12.7
(17.4, 261.00)	0.0823	0.48	0.0731	7.17

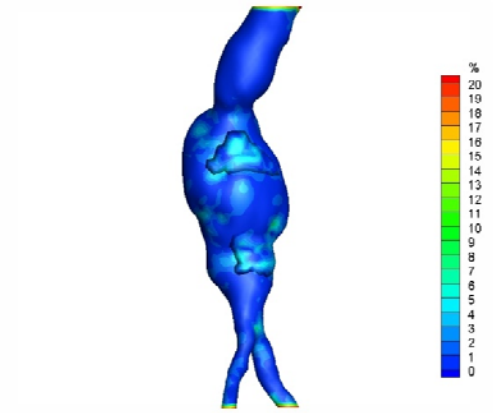

Fig 3 von Mises stress differences by inverse approach (%)

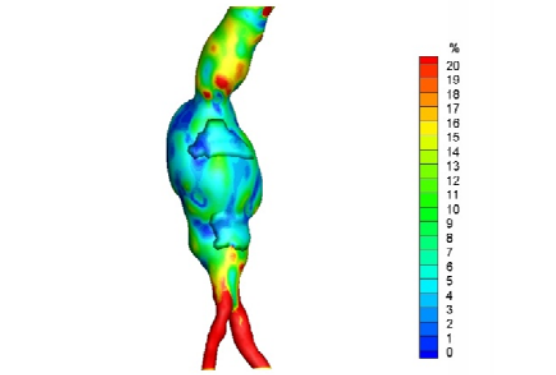

Fig 4 von Mises stress differences by forward approach (%)

In conclusion, we examined the influence of ILT on AAA wall stress magnitude and distribution. The inverse approach was shown to give more reliable prediction of stress distribution of AAA in the sense that the stress solution is less sensitive to the material parameter variations.

REFERENCES

1. Raghavan, M.L., et al., *Wall stress distribution on three-dimensionally reconstructed models of human abdominal aortic aneurysm.* Journal of Vascular Surgery, 2000. **31**(4): p. 760-769.
2. Mower, W.R., L.J. Baraff, and J. Sneyd, *Stress Distributions in Vascular Aneurysms - Factors Affecting Risk of Aneurysm Rupture.* Journal of Surgical Research, 1993. **55**(2): p. 155-161.
3. Wang, D.H.J., et al., *Effect of intraluminal thrombus on wall stress in patient-specific models of abdominal aortic aneurysm.* Journal of Vascular Surgery, 2002. **36**(3): p. 598-604.
4. Speelman, L., et al., *The mechanical role of thrombus on the growth rate of an abdominal aortic aneurysm.* Journal of Vascular Surgery, 2010. **51**(1): p. 19-26.
5. Lu, J., X.L. Zhou, and M.L. Raghavan, *Inverse elastostatic stress analysis in pre-deformed biological structures: Demonstration using abdominal aortic aneurysms.* Journal of Biomechanics, 2007. **40**(3): p. 693-696.
6. Zhou, X.L. and J. Lu, *Inverse formulation for geometrically exact stress resultant shells.* International Journal for Numerical Methods in Engineering, 2008. **74**(8): p. 1278-1302.
7. Lu, J., X.L. Zhou, and M.L. Raghavan, *Inverse method of stress analysis for cerebral aneurysms.* Biomechanics and Modeling in Mechanobiology, 2008. **7**(6): p. 477-486.
8. Simo, J.C. and D.D. Fox, *On a Stress Resultant Geometrically Exact Shell-Model .1. Formulation and Optimal Parametrization.* Computer Methods in Applied Mechanics and Engineering, 1989. **72**(3): p. 267-304.
9. Lu, J., X.L. Zhou, and M.L. Raghavan, *Computational method of inverse elastostatics for anisotropic hyperelastic solids.* International Journal for Numerical Methods in Engineering, 2007. **69**(6): p. 1239-1261.
10. Raghavan, M.L. and D.A. Vorp, *Toward a biomechanical tool to evaluate rupture potential of abdominal aortic aneurysm: identification of a finite strain constitutive model and evaluation of its applicability.* Journal of Biomechanics, 2000. **33**(4): p. 475-482.

2nd International Conference on Mathematical and Computational Biomedical Engineering - CMBE2011
March 30 - April 1, 2011, Washington D.C, USA
P. Nithiarasu and R. Löhner (Eds.)

NON-INVASIVE AND INVERSE PROPERTY ESTIMATION OF ARTERIAL WALLS

Amarpal S. Kapoor*, Perumal Nithiarasu* and Raoul van Loon*
*Swansea University, College of Engineering, Singleton Park, Swansea SA2 8PP, UK
A.S.Kapoor.568964@swansea.ac.uk

SUMMARY

An inverse procedure is developed to estimate the arterial wall properties using the Levenberg-Marquardt optimization algorithm. A 1D fluid-structure interaction code is employed to test the inverse procedure. Results clearly show that the developed algorithm is able to accurately predict arterial properties.

Key Words: *arterial elasticity, blood flow, non-invasive, inverse property estimation.*

1 INTRODUCTION

A fluid-structure interaction (FSI) based methodology is proposed for the estimation of arterial wall elasticity. It has been long discovered that there is a direct relationship between the stiffness of arteries and risk of cardiovascular events [1, 2, 3]. A prior knowledge of arterial wall elasticity can thus prove to be very important.

2 METHODOLOGY

The methodology employed for the arterial property estimation algorithm is broadly classified into the following stages as shown in figure 1.

Figure 1: *Proposed methodology for arterial elasticity estimation.*

Stage 0 deals with the real-time data acquisition via dynamic MRI (if applicable), which captures the displacement of arteries due to distending pressure as the blood flows. Data

acquired here acts as a benchmark against which the results of the CFD model are compared. This stage is not included in the current work but is essential in establishing the link between the human body and the CFD model.

Stage 1 constitutes the solution for the forward problem, which employs an explicit scheme to solve the governing 1D Navier-Stokes equations applied to flow over compliant tubes. The arterial deformation in response to the cardiac output of the heart is artificially obtained here by the blood-flow model in terms of the nodal area. The solution procedure also results in the nodal velocity of blood and the nodal pressure is finally evaluated using the area and velocity values. The Locally Conservative Taylor-Galerkin method (LCG) [4, 5] that is employed in the solution scheme helps reduce the computational effort as it prevents the need to invert huge matrices originating from the conventional assembly process by treating each element as a separate sub-domain with its own boundaries.

It should be noted that for the solution of the forward problem in stage 1, arterial stiffness was assumed to be known, but in real life problems the stiffness is actually not known a *priori* and its estimation is the hallmark of this work. Even though the forward problem solution is obtained only after using stiffness as an user input, inverse property estimation can be employed to yield the actual stiffness of arteries by making comparisons between the model predicted and experimental data. The Levenberg Marquardt (LM) optimization is used here. It is an iterative technique that locates a local minimum of a multivariate function that is expressed as the sum of squares of several non-linear, real-valued functions. It has been adopted in various data-fitting applications and has become a standard technique for non-linear least squares problems.

As a starting point, an objective function incorporating just nodal areas is considered. It is the least square error between the actual and model predicted area (nodal basis). The objective function is expressed as,

$$f = \sum_{j=1}^{n} (A_j - \overline{\overline{A}}_j)^2 \tag{1}$$

where, A_j is the actual area, $\overline{\overline{A}}_j$ is the model predicted area and j corresponds the number of nodes.

The LM algorithm operates by minimizing this objective function which in a physical sense is equivalent to repeating the forward run in an intelligent manner until the measured displacements equal the model predicted displacements, which would be indicative of the fact that the current stiffness equals the actual stiffness. It must also be noted that the experimental data here is generated by surrogate means and that no patient data is used for the purpose of this work. The LM algorithm also requires computation of the Jacobian and Hessian matrices (first and second order partial derivatives of area with respect to stiffness respectively) for incrementing/decrementing β (function of Young's Modulus) in every iteration depending on the errors in the current and previous iteration. Analytical evaluation is not possible and hence a numerical finite difference approximation is resorted for, by exploiting the method of perturbations. At every iteration the stiffness values are perturbed slightly (1% of current value) and a forward run is then executed at this value to generate the input arguments required in the forward difference approximation.

3 RESULTS

The proposed methodology is demonstrated to be working very well for 1D simulations considered here. Various meshes, indicative of several healthy and diseased states of the artery, are considered for the simulations and the errors in the actual and model predicted nodal stiffness are found to be less than 1%. The variations of the objective function (e_lm) and β with iteration number are illustrated for two cases in the figures 2 and 3.

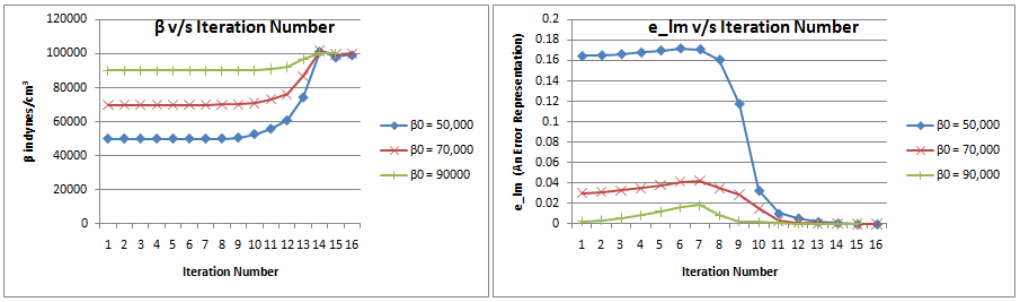

Figure 2: *Results for an open artery with different starting values for β .*

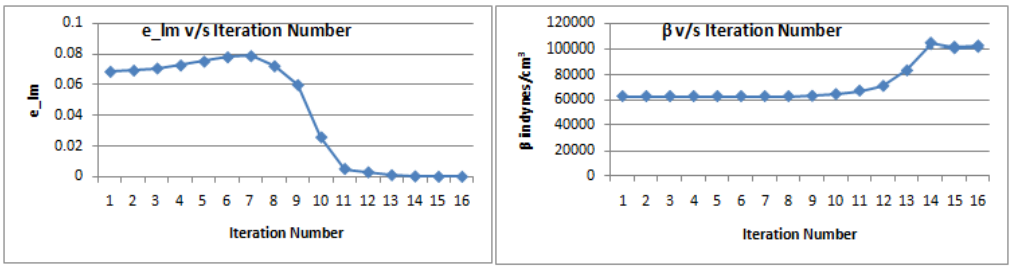

Figure 3: *Results for an open artery with linearly distributed values for β .*

4 CONCLUSIONS

The following conclusions were derived from the current work:

- Inverse parameter optimization is a feasible technique for material-parameter estimation of human arteries.
- Non-invasive procedures can be successfully employed for determining the arterial material properties.
- A high degree of agreement was observed between the generated data and model predicted values obtained from the Levenberg-Marquardt optimization routine and the error in most cases was found to be less than 1%.
- This study provides the motivation to implement non-invasive and patient-specific arterial material property estimation in multi-dimensions (up to 4D).

References

[1] M. O. Rourke, Arterial stiffness, systolic blood pressure, and logical treatment of arterial hypertension, *Hypertension*, 15, 339-347, 1990

[2] M. Persson, A. Eriksson, H. W. Persson and K. Lindström, Estimation of arterial pulse wave velocity with a new improved Tissue Doppler method, *23rd Annual International Conference of the IEEE Engineering in Medicine and Biology Society*, October 2001.

[3] Séverine Durier, Céline Fassot, Stéphane Laurent, Pierre Boutouyrie, Jean-Paul Couetil, Erika Fine, Patrick Lacolley, Victor J. Dzau and Richard E. Pratt, Physiological Genomics of Human Arteries: Quantitative Relationship Between Gene Expression and Arterial Stiffness, *Circulation*, 108, 1845-1851, 2003.

[4] C. G. Thomas and P. Nithiarasu, An element-wise, locally conservative galerkin (LCG) method for solving diffusion and convection-diffusion problems, *International Journal for Numerical Methods in Engineering*, 73, 642-664, 2008.

[5] J.P. Mynard and P. Nithiarasu, A 1D arterial blood flow model incorporating ventricular pressure, aortic valve and regional coronary flow using the locally conservative Galerkin (LCG) method, *Communications in Numerical Methods in Engineering*, 24, 367 - 417, 2008.

[6] Sam Roweis, Levenberg-Marquardt Optimization, In http://www.LS.nyu.edu/ roweis/notes/lm.pdf, Accessed on Aug. 17, 2010

[7] Michael J. Moulton, Lawrence L. Creswell, Ricardo L. Actis, Kent W. Myers, Michael W. Vannier, Barna A. szab and Michael K. Pasque, An inverse approach to determining myocardial material properties, *Journal of Biomechanics*, 28(8), 935-948, 1995.

2nd International Conference on Mathematical and Computational Biomedical Engineering – CMBE2011
March 30 – April 1, 2011, Washington D.C., USA
P. Nithiarasu and R. Löhner (eds)

INTEGRATION OF ULTRASOUND COLOR DOPPLER IMAGING AND NUMERICAL SIMULATION

Kenichi Funamoto*, Takaumi Kato* and Toshiyuki Hayase*
*Institute of Fluid Science, Tohoku University, 2-1-1 Katahira, Aoba-ku, Sendai 980-8577 Japan, funamoto@reynolds.ifs.tohoku.ac.jp

SUMMARY

Ultrasonic-measurement-integrated (UMI) simulation, in which feedback signals are applied to the governing equations based on errors between ultrasound Doppler measurement and numerical simulation, has been investigated to reproduce hemodynamics. In this study, feasibility of UMI simulation of blood flows in carotid arteries was examined for advanced diagnosis of circulatory diseases. Feedback of errors between measured and computed Doppler velocities made the computational result of the UMI simulation approach the measurement data, showing complicated color Doppler images with velocity profiles. Hemodynamic parameters can be accurately evaluated by the result of UMI simulation.

Key Words: *Hemodynamics, measurement-integrated simulation, ultrasonic measurement.*

1. INTRODUCTION

Hemodynamic stresses of wall shear stress (WSS) and pressure are the major factors for development and progression of circulatory diseases. Hence, accurate and detailed information of hemodynamics are necessary for advanced diagnosis of the diseases. Among methods to measure blood flow field, ultrasonic measurement is characterized by noninvasive, real-time visualization of hemodynamics as well as blood vessel configuration by means of color Doppler imaging. However, the information of blood flow in color Doppler images is limited to the one-directional component of the velocity vectors along the ultrasonic beam (Doppler velocity), and hemodynamic stresses cannot be directly obtained with the method. On the other hand, numerical simulation of blood flow provides information on hemodynamic stresses as well as on the blood flow field. Recently, fluid-structure interaction simulation enables investigation of the blood flow field considering blood vessel wall motion due to its elasticity. Though numerical simulation essentially depends on boundary and initial conditions, it is difficult to precisely set these conditions in the numerical simulation of *in vivo* complicated unsteady blood flow, resulting in a computational result which may be different from the real blood flow.
Measurement-integrated (MI) simulation or flow observer, which integrates measurement and numerical simulation, has been proposed as a methodology to overcome individual limitations in measurement and computation [1]. As medical applications of MI simulation, the authors have proposed integration of medical measurement (ultrasonic measurement or MRI) of blood flow velocity and a numerical simulation to reproduce the blood flow field [2, 3]. Ultrasonic-measurement-integrated (UMI) simulation feeds back errors between measured and computed Doppler velocities to the numerical simulation to make the computational result converge to the real flow (see Fig. 1). In our previous numerical experiments of UMI simulation [2], the

efficiency of the UMI simulation was revealed, and the transient and steady characteristics of the method were investigated.
In this study, feasibility of UMI simulation was examined by dealing with various clinical data of carotid arteries with/without atherosclerosis.

2. METHODS

Governing equations of UMI simulation of blood flow are the Navier-Stokes equations and the pressure equation for incompressible and viscous fluid flow,

$$\rho\left(\frac{\partial \mathbf{u}}{\partial t}+(\mathbf{u}\cdot\nabla)\mathbf{u}\right)=\mu\Delta\mathbf{u}-\nabla p+\mathbf{f}, \tag{1}$$

$$\Delta p=-\nabla\cdot\rho(\mathbf{u}\cdot\nabla)\mathbf{u}+\nabla\cdot\mathbf{f}, \tag{2}$$

where $\mathbf{u} = (u, v, w)$ is the velocity vector, p is the pressure, t is time, ρ is the density, and μ is the viscosity. $\mathbf{f}$ denotes the feedback signal at each feedback point, and it is described by the following equation.

$$\mathbf{f}=-K_v^*\frac{\Phi_d(\mathbf{u}_c-\mathbf{u}_s)}{U}\left(\frac{\rho U^2}{L}\right) \tag{3}$$

where K_v* is the feedback gain (nondimensional), U is the characteristic velocity, L is the characteristic length (the entrance diameter of the blood vessel), $\mathbf{u}_c$ and $\mathbf{u}_s$ are velocity vectors of the computational result and the real flow, respectively, and $\mathbf{\Phi}_d$ (d = 1, 2, 3) is a projection function of a three-dimensional vector to the d-dimensional subspace generated by the vectors of the ultrasonic beam directions. Note that the special case with K_v* = 0 is an ordinary numerical simulation without feedback. The acquisition of Doppler velocity by projecting a velocity vector in the direction of the ultrasonic beam corresponds to the case of d = 1. For detailed descriptions of the projection function, $\mathbf{\Phi}_d$, and discretization, see our previous study [2]. All parameters are nondimensionalized with the characteristic values, and the above governing equations were solved with an original program based on an algorithm similar to the SIMPLER method.
Computational conditions influence the result of numerical simulation. Since the exact boundary conditions are usually unknown, UMI simulation are carried out with simple boundary conditions: zero velocity on the wall, an unsteady parallel flow with a uniform/parabolic velocity profile at the inlet, and a free flow condition ($\partial/\partial n$ = 0, n: coordinate normal to the boundary) at the outlet. In UMI simulation, the error due to incorrect boundary conditions is expected to be reduced with the aid of the above-mentioned feedback algorithm. However, in case that an inaccurate flow rate is applied, the numerical simulation should lead to wrong flow field even with the feedback process. Hence, flow rate is estimated by golden section method so as to minimize the summation of the absolute value of the difference of measured and computed Doppler velocities in the feedback domain.
In the UMI simulation, the boundary conditions except for flow rate are not modified during the computation. By solving the above governing equations with feedback signals, the continuity equation is satisfied, but the adverse effect of the feedback appears in the pressure field. Therefore, correction of pressure field is necessary after convergence of each time step: values derived from the second term on the right-hand side of Eq. (2) are subtracted from the pressure field.
Blood vessel shape of each carotid artery was

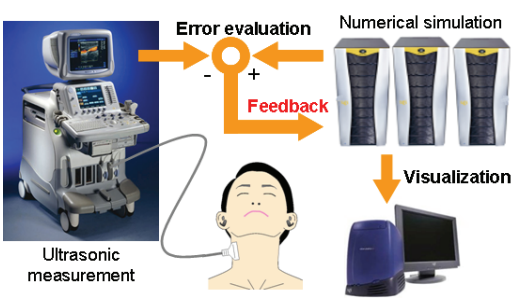

Fig. 1. Schematic diagram of UMI simulation system.

extracted with the following process. Ultrasound color Doppler images and B-mode images were averaged in the measurement period, respectively. Moreover, and edge detection was applied for the time-averaged B-mode image in the vertical direction with a differentiation filter. Then, the two time-averaged images were superimposed and binarized. After rotating the extracted blood vessel shape to make the main direction of blood flow correspond to the x-direction, the computational grid was generated. The approximate resolutions of the computational grid was Δx = 280 μm and Δy = 170 μm, and computational time increment (time resolution of ultrasound color Doppler imaging) was Δt = 0.061 s though they change by measurement data. Feedback domain was set from 1/8 to 7/8 of the computational domain from the upstream, and feedback signals were added at each computational grid point in the feedback domain. Here, ultrasound color Doppler imaging inherently includes several measurement errors, namely, aliasing, wall filter, and lack of data. To prevent the computational accuracy of UMI simulation from deteriorating by those effects, significantly large feedback signals were detected as a sign of aliasing, and feedback signals were not added at feedback points where measured Doppler velocities were considered to be aliased or zero. The feedback gain, K_v^*, was increased as by 10 from 0 to 100, and then set at 200, 500, and 1000.

Objectives were blood flows in 67 carotid arteries with/without moderate atherosclerosis obtained from 13 patients. Color Doppler images were acquired with ultrasound diagnostic imaging equipment (LOGIQ 7, GE Healthcare Japan Corp., Japan).

For evaluation of computational accuracy, error norm of Doppler velocity, V, was defined as follows:

$$\bar{e}_{MT^*}(\mathbf{u}) = \frac{1}{T^*}\int_{T^*}\left(\frac{1}{N}\sum_{n}\frac{|V_{cn}(t)-V_{sn}(t)|}{U}\right)dt \tag{4}$$

where T^* is five cardiac cycles in the measurement period, n and N are the index and the total number of monitoring points in the feedback domain M, respectively, and subscrips c and s respectively indicate the result of the UMI simulation and the standard solution.

3. RESULTS AND DISCUSSION

With the feedback gain of $K_v^* \leq 1000$, the convergent results were obtained for all objectives. Variations of error norm of velocity vector with feedback gain in UMI simulation of blood flow in six representative carotid arteries are show in Fig. 2. In each case, the error rapidly decreases with feedback gain, and then, converges to some constant value. On the other hand, as increasing feedback gain, computational time monotonically increased. Compromising the computational accuracy and computational time, practical results are obtained with feedback gain of about 100 in the following UMI simulations.

Figure 3 compares examples of an ultrasound color Doppler image and computational results of UMI simulation at K_v^* = 100 and ordinary simulation without feedback (K_v^* = 0) of a carotid artery. Conventional ultrasound color Doppler imaging provides color Doppler image, in which *in vivo* tissues are displayed with gray scale and flow dynamics are indicated with color based on Doppler velocities (see Fig. 3(a)). Since the Doppler velocity is one-directional velocity component of velocity vector, it does not show the complete flow dynamics. Actually, the image indicates that blood flows from left to right

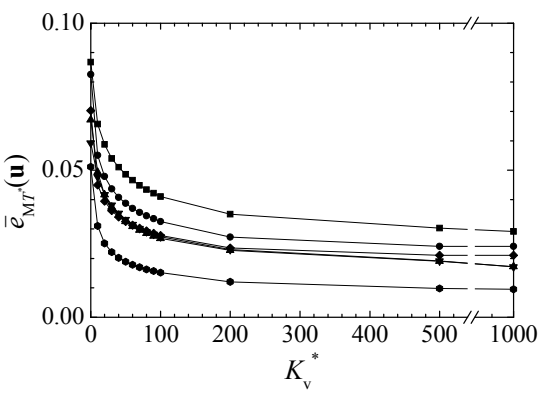

Fig. 2. Variation of error norm of Doppler velocity with feedback gain.

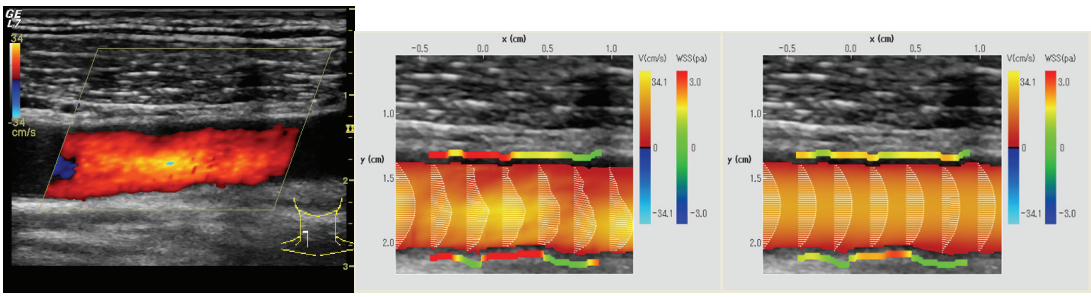

(a) (b) (c)

Fig. 3. Comparison of results among (a) conventional ultrasound color Doppler imaging, (b) UMI simulation ($K_v^* = 100$), and (c) ordinary simulation ($K_v^* = 0$).

with warm color. The corresponding results by UMI simulation and the ordinary simulation are shown in Fig. 3(b) and (c), respectively. The Doppler velocities were displayed with contour on measured B-mode image, and the computed velocity and WSS were displayed with vectors and with color bars along the vessel walls. In UMI simulation, though inaccurate velocity profile was applied at the upstream boundary, computational result in the feedback domain approaches the real blood flow owing to the feedback; computed color Doppler image becomes similar to the measured one for the sake of feedback (see Fig. 2(b)). Consequently, UMI simulation shows more complicated velocity profiles and WSS distributions than the ordinary simulation.

With the results of UMI simulation of 67 carotid arteries, the relationship between hemodynamic parameters, such WSS and oscillatory shear index (OSI), and pathology was investigated. As the result, there exist some threshold values to distinguish healthy and diseased carotid arteries based on the hemodynamic parameters (results are not shown).

For clinical use, it is desirable that UMI simulation can be performed with a computer mounted in ultrasonic diagnostic equipment. By optimizing the criteria of residuals for convergence with compromising between time and accuracy, the UMI simulation could simulate one cardiac cycle within several minutes with a high end PC (CPU: Intel Core2 Quad Q2450 @ 2.66 GHz 2.66 GHz, Memory: 4.00GB, 32bit operating system). Additionally, a method to display hemodynamic information is being developed for better comprehension of hemodynamics.

4. CONCLUSIONS

The feasibility study of UMI simulation was conducted to achieve advanced diagnosis of circulatory diseases dealing with color Doppler images of various carotid arteries. UMI simulation has potential to correctly visualize hemodynamic stresses as well as blood flow field.

REFERENCES

[1] T. Hayase and S. Hayashi, State estimator of flow as an integrated computational method with the feedback of online experimental measurement, *Journal of Fluids Engineering*, 119, 814-822, 1997.

[2] K. Funamoto, T. Hayase, T. Yambe and Y. Saijo, Numerical experiment for ultrasonic-measurement-integrated simulation of three-dimensional unsteady blood flow, *Annals of Biomedical Engineering*, 36, 1383-1397, 2008.

[3] K. Funamoto, Y. Suzuki, T. Hayase, T. Kosugi and H. Isoda, Numerical validation of MR-Measurement-Integrated Simulation of Blood Flow in a Cerebral Aneurysm, *Annals of Biomedical Engineering*, 37, 1105-1116, 2009.

2nd International Conference on Mathematical and Computational Biomedical Engineering - CMBE2011
March 30 - April 1, 2011, Washington D.C, USA
P. Nithiarasu and R. Löhner (Eds.)

REDUCED ORDER MODELLING FOR INVERSE PROBLEMS IN HAEMODYNAMICS

Andrea Manzoni, Alfio Quarteroni, Gianluigi Rozza
MATHICSE-CMCS, École Polytechnique Fédérale de Lausanne,
Station 8, CH-1015 Lausanne, Switzerland

The efficient solution of optimal control and/or shape optimization problems is an open problem in cardiovascular modelling. Since the recursive evaluation of the flow solution is required for many possible cardiovascular configurations, strategies able to reduce the dimensionality of the problem and the associated computational complexity need to be devised. Moreover, the possibility to develop predictive surgery stems from numerical blood flow simulations performed in a rapid and reliable way, often on patient-dependent geometries [1].

Efficient numerical schemes for many-query (e.g. optimization, control) and real-time (e.g. rapid simulation, parameter identification) problems dealing with flows across domains of complex and/or variable shape [2] are proposed. They combine a suitable low-dimensional parametrization of the cardiovascular geometry (yielding a geometrical complexity reduction) with numerical approximation schemes based on reduced basis methods (allowing a reduction of computational complexity).

Among existing model order reduction strategies, the reduced basis method [3, 4] represents a very efficient tool for simulating flows in parametrized geometries, as well as for solving shape optimization and more general inverse problems. An implementation of the reduced basis method for viscous flows modelled by (Navier)-Stokes equations will be presented, by considering some flexible shape parametrization techniques (such as free-form deformations [2], radial basis functions, transfinite mappings) in order to deal efficiently with complex shapes. Our analysis will focus on haemodynamics applications – such as the shape optimization of aorto-coronaric bypass grafts [2] and the blood flow simulations in carotid artery bifurcations – and highlight suitability and effectiveness of these model reduction techniques.

REFERENCES

[1] L. Formaggia, A. Quarteroni and A. Veneziani. *Cardiovascular Mathematics: Modeling and simulation of the circulatory system*, Springer, Series MS&A, Vol. 1, 2009.

[2] A. Manzoni, A. Quarteroni and G. Rozza, Shape optimization for viscous flows by reduced basis methods and free-form deformation, *Journal of Computational Physics*, submitted, 2010.

[3] G. Rozza, D.B.P. Huynh and A. Manzoni, Reduced basis approximation and a posteriori error estimation for Stokes flows in parametrized geometries: roles of the inf-sup stability constants, *Numerische Mathematik*, submitted, 2010.

[4] G. Rozza, D.B.P. Huynh and A.T. Patera, Reduced basis approximation and a posteriori error estimation for affinely parametrized elliptic coercive partial differential equations, *Arch. Comput. Methods Engrg.*, 15:229–275, 2008.

2nd International Conference on Mathematical and Computational Biomedical Engineering - CMBE2011
March 30 - April 1, 2011, Washington D.C, USA
P. Nithiarasu and R. Löhner (Eds.)

INVERSE IDENTIFICATION OF THE IN VIVO ARTERIAL WALL THICKNESS AND ANISOTROPY

S. Zeinali-Davarani[⋆], L. G. Raguin[⋆⋆], D. A. Vorp[⋆⋆⋆] and S. Baek[⋆]
[⋆]Department of Mechanical Engineering, Michigan State University, 2555 Engineering Builing, East Lansing, MI 48824, sbaek@egr.msu.edu
[⋆⋆]Departments of Mechanical Engineering and Radiology, Michigan State University, 2555 Engineering Building, East Lansing, MI 48824, raguin@msu.edu
[⋆⋆⋆]Departments of Surgery and Bioengineering, Center for Vascular Remodeling and Regeneration, University of Pittsburgh, vorpda@upmc.edu

SUMMARY

Patient-specific modeling of vascular growth and remodeling (G&R) is subject to new challenges. First, the assumption of the existence of vascular homeostasis in normal vessels, is not easy to implement in a vessel model built from medical images. Second, subjecting the vessel wall model to the normal pressure often makes the configuration deviate from the original geometry obtained from medical images. We propose a two-step optimization approach to address those issues; first, we estimate constitutive parameters of a healthy human aorta intrinsic to the material by using biaxial test data and a weighted nonlinear least-squares parameter estimation method; second, we estimate the distributions of wall thickness and anisotropy using a 2-D parametrization of the vessel wall surface and a global approximation scheme integrated within an optimization routine. The numerical optimization method results in a considerable improvement in both satisfying homeostatic condition and minimizing the deviation of geometry from the original shape based on *in vivo* images.

Key Words: *homeostasis, growth and remodeling, optimization, parameter estimation, patient-specific modeling.*

1 INTRODUCTION

Computational modeling of vascular adaptation using medical image-based geometries is an important step in diagnoses and treatments of vascular diseases on a patient-specific basis. However, there are technical challenges associated with patient-specific modeling of vascular diseases. First, a key assumption in theory of G&R is the existence of mechanical homeostasis, whereas it is not a trivial task to prescribe the *in vivo* material and structural parameters (i.e. wall thickness and fiber orientation) such that the condition of a homeostatic state is met throughout the wall. The second challenge stems from the fact that the *in vivo* image is obtained under the pressure and the stress-free configuration is not available. We address those issues by defining an inverse optimization problem where the *in vivo* material parameters are estimated in two steps. First, we estimate the constitutive parameters intrinsic to the material by fitting the *ex vivo* biaxial mechanical test data of a healthy human aorta. Second, we solve an optimization problem to estimate the distributions of the wall thickness and anisotropy such that the homeostasis is maintained while the geometry deviates minimally from the *in vivo* configuration. The optimization problem is solved for a more complex domain obtained from a healthy internal iliac artery.

2 MAIN BODY

2.1 ESTIMATION OF CONSTITUTIVE PARAMETERS

First we estimate the constitutive parameters by fitting biaxial mechanical test data of a healthy human aorta [1] using a weighted nonlinear least squares method described in [2]. More details about the constitutive relations, prescribed and estimated constitutive parameters can be found in [3]. Figure 1 shows the biaxial test profile of a healthy human aorta as well as the fitted profiles using the estimated parameters.

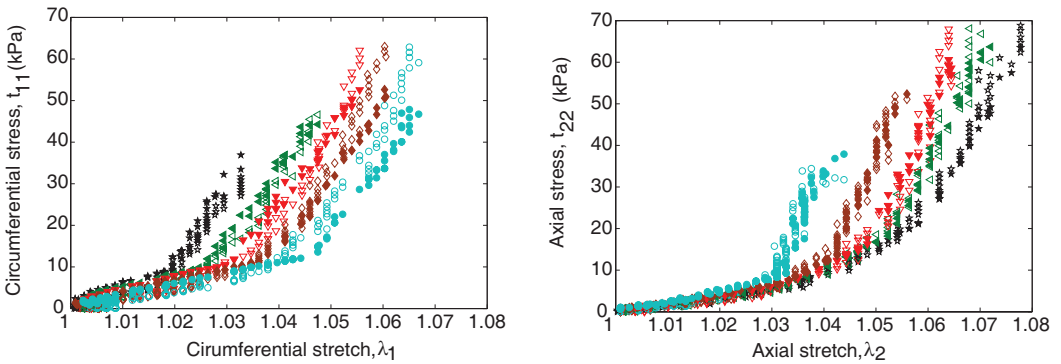

Figure 1: Stress versus stretch plots in both directions. Data (empty markers) and fitted values (filled markers) using the estimated parameters. Different markers correspond to a different ratios of tension in both directions.

2.2 AN INVERSE OPTIMIZATION PROBLEM

Next, we estimate the distributions of wall thickness and material anisotropy using an inverse optimization method where both the deviation of geometry from the *in vivo* configuration and the deviation of stress from the homeostatic value are minimized. The objective function to minimize is,

$$W = \frac{\int_\Omega ||\mathbf{x}(h,\alpha^k) - \mathbf{X}_{image}||^2 dA}{\int_\Omega ||\mathbf{X}_{image} - \bar{\mathbf{X}}||^2 dA} + \xi \sum_i \frac{\nu^i \int_\Omega (\sigma^i(h,\alpha^k) - \sigma_h^i)^2 dA}{\int_\Omega (\sigma_h^i)^2 dA} \tag{1}$$

where $i = m, 1, ..., k$ and $\mathbf{x}$ is the finite element (FE) solution for position vector and $\mathbf{X}_{image}$ is the position vector from medical image and $\bar{\mathbf{X}}$ is the geometric center of the artery. σ^i is a scalar measure of stress in the direction of the constituent i obtained from the FE analysis (See [4] for detailed explanation of the image-based FE model of the arterial wall). σ_h^i and ν^i are the homeostatic stress and mass fraction for the constituent i. (h, α^k) are the unknown wall thickness and anisotropy, i.e. orientation of the collagen fiber k.

As a practical approach, thickness and anisotropy distributions can be approximated with a smaller (I) number of unknown variables with associated base functions as

$$h(x,y,z) = \sum_{j=1}^{I} \{\beta_j^h \phi_j(x,y,z)\}, \qquad \alpha^k(x,y,z) = \sum_{j=1}^{I} \{\beta_j^k \psi_j(x,y,z)\}, \tag{2}$$

where (β_j^h, β_j^k) are variables for thickness and anisotropy associated with the approximation point j. $\phi_j(x,y,z)$ and $\psi_j(x,y,z)$ are basis/approximation functions defined on the computational domain Ω. To facilitate the approximation, the computational domain (the mid-surface of the vessel

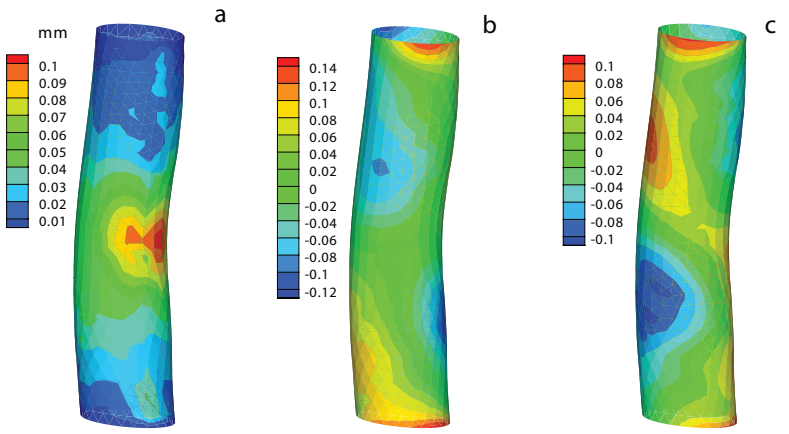

Figure 2: Deviation of the geometry from the *in vivo* geometry (a) ($||\mathbf{x} - \mathbf{X}_{image}||$) and the deviation of the stress ($(\sigma^k - \sigma_h^k)/\sigma_h^k$) from the target homeostatic stress in two helical fiber families (b, c) using optimized distributions of thickness and anisotropy for a healthy human aorta.

wall) is parameterized by two spatial variables s and θ (the longitudinal distance and azimuthal position) on the arterial wall (See [3] for details of the parametrization technique). Also, as a global approximation, products of Legendre polynomials (P_m) and periodic functions (F_n) are considered, respectively, for longitudinal and azimuthal directions as

$$h(s,\theta) = \sum_{m,n=0}^{m=M-1,n=N-1} \beta_{mn}^h P_m(s) F_n(\theta), \quad \alpha^k(s,\theta) = \sum_{m,n=0}^{m=M-1,n=N-1} \beta_{mn}^k P_m(s) F_n(\theta), \quad (3)$$

where M and N are, respectively, the total number of Legendre polynomials and periodic functions (i.e. $I = M \times N$). Towards solving the optimization problem Eq.(1), values of β_{mn}^h and β_{mn}^k are initially estimated such that they approximate a homogenous field of thickness and anisotropy. Subsequently, the Nelder-Mead Simplex, as a direct search method, is utilized to minimize the objective function until a proper stopping criterion is met. According to our parametric study, variation of ξ can have an impact on minimizing Eq.(1) by shifting the weight between its first and second additive parts. The optimal value appears to be $\xi = 0.01$ such that both parts can be minimized simultaneously [3]. Then, we prescribe $\xi = 0.01$ and consider $M = 6$ and $N = 3$ for the approximation.

2.3 RESULTS

Figure 2 shows the resulting deviation from the *in vivo*/image geometry ($||\mathbf{x} - \mathbf{X}_{image}||$) and the normalized deviation of stress from the homeostatic value ($(\sigma^k - \sigma_h^k)/\sigma_h^k$) in the direction of helical fiber families. The consequent distributions of wall thickness and anisotropy are depicted in Figure 3. The resulting spatial variation of anisotropy is not large although thickness considerably varied especially on the convex and concave regions with higher values on the concave side and lower values on the convex side. Figure 4 illustrates the resulting deviation of the geometry from the *in vivo* configuration and the distributions of the wall thickness for the internal iliac artery.

3 CONCLUSIONS

This study focuses on the *in vivo* configuration and estimation of the associated material and geometric parameters of healthy human arteries using an inverse optimization method such that the

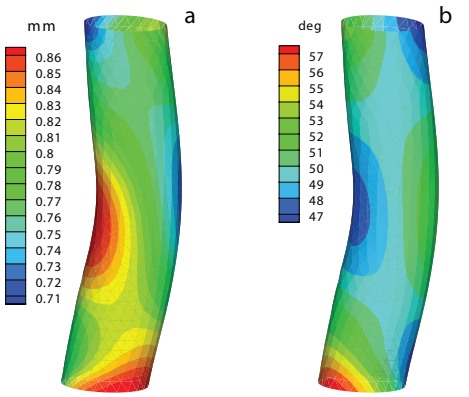

Figure 3: Distributions of thickness (a) and anisotropy (b) obtained from the optimization results for a healthy human aorta.

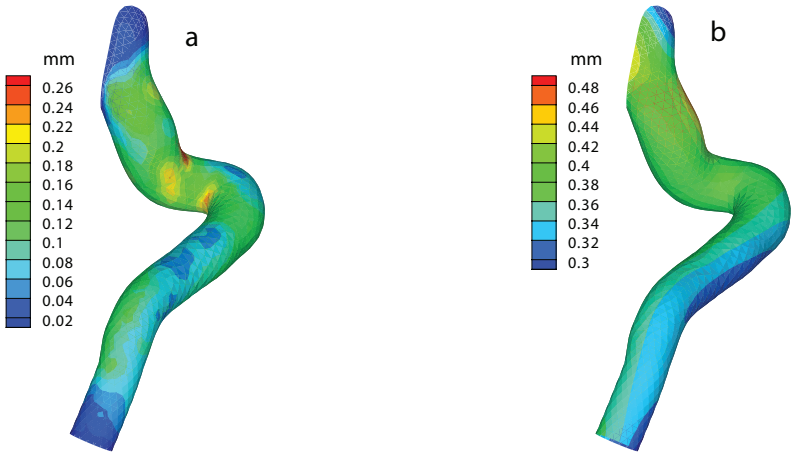

Figure 4: Deviation of the geometry from the *in vivo* configuration (a) and distribution of thickness (b) obtained from the optimization results for a healthy human internal iliac artery.

homeostatic condition is maintained while the deviation of geometry from the original *in vivo* configuration is minimized. The results are promising to the development of patient-specific G&R simulations especially when more experimental data as well as more accurate boundary condition are available. Particularly, in the current method the homeostasis assumption is based on stress whereas other hypothesis based on strain, cyclic strain, etc. can be tested provided that experimental validations become available.

REFERENCES

[1] J.P. Vande Geest and M.S. Sacks and D.A. Vorp, Age dependency of the biaxial biomechanical behavior of human abdominal aorta, *J Biomech Eng*, 126, 815-822, 2004.

[2] S. Zeinali-Davarani and J. Choi and S. Baek, On parameter estimation for biaxial mechanical behavior of arteries, *J Biomech*, 42, 524-530, 2009.

[3] S. Zeinali-Davarani and L.G. Raguin and D.A. Vorp and S. Baek, Identification of *in vivo* Material and Geometric Parameters of a Human Aorta: Towards Patient-Specific Modeling of Abdominal Aortic Aneurysm, *Biomech Model Mechanobiol*, in print, 2010.

[4] S. Zeinali-Davarani and A. Sheidaei and S. Baek, A finite element model of stress-mediated vascular adaptation: application to abdominal aortic aneurysms, *Comput Methods Biomech Biomed Eng*, in print, 2010.

2nd International Conference on Mathematical and Computational Biomedical Engineering - CMBE2011
March 30 - April 1, 2011, Washington D.C, USA
P. Nithiarasu and R. Löhner (Eds.)

A data assimilation procedure for including noisy measurements of blood velocity into hemodynamics simulations

M. D'Elia*, M. Perego ** and A. Veneziani***
*Emory University, 400 Dowman Dr. Atlanta, GA 30322, mdelia2@mathcs.emory.edu
**Florida State University, 400 Dirac Science Library, Tallahassee, FL 32306-4120, mperego@fsu.edu
***Emory University, 400 Dowman Dr. Atlanta, GA 30322, ale@mathcs.emory.edu

SUMMARY

We present a data assimilation technique for including noisy measurements of blood flow in the simulation of the Navier-Stokes equations. The procedure is formulated as an inverse problem where the control variable is the pressure drop between the inflow and outflow sections of the vessel. Numerical results prove the noise filtering properties in recovering blood velocity and flow-related variables of medical interest.

Key Words: *Computational Fluid Dynamics, Hemodynamics, Data Assimilation, Inverse Problems.*

1 INTRODUCTION

Including data into numerical simulations has always been an issue of relevance in the prediction of fluid geophysics phenomena. On the other hand, numerical methods for incompressible fluid dynamics have recently received strong impulse from applications to the cardiovascular system. A strong integration of data and numerical modeling is expected to bring a great benefit to the development of mathematical and computational tools with a clinical impact. Due to advanced and efficient techniques in biomedical imaging we can now collect a huge amount of data for the cardiovascular system (see Figure 1) [2]; this fact enhances the integration process and opens new challenges. Our goal is to use these - in general noisy and sparse - data to get an accurate approximation of the blood flow in vessels of interest in order to predict physical quantities of medical relevance. This integration process is known in literature as Data Assimilation (DA).

In this work we propose a DA technique for including noisy measurements of the blood velocity into the simulation of the Navier-Stokes equations (NSE), which are widely accepted as a reliable description of blood flow in large and medium sized arteries. In particular, the technique we present is formulated as an inverse problem where we use a Discretize-then-Optimize approach to minimize the misfit between the recovered velocity field and the data, subject to the partial differential equations (PDE) of the state variable. The proposed procedure for the solution of this optimization problem is a combination of two approaches: the well-known Newton linearization of the NSE and a DA procedure for the linear Oseen problem. We present conditions on the location of velocity measurements that guarantee the existence of a unique minimizer. Moreover, we consider the presence of the noise on 2D non-trivial geometries, representing vessels of interest, and its impact on non-primitive variables of medical interest such as the wall shear stress (WSS).

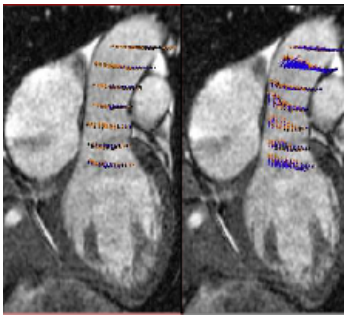

Figure 1: View of blood measured velocities in an MRI of the ascending aorta [2].

2 FORMULATION AND MAIN RESULTS

Formulation of the problem We consider the domain Ω in $\mathbb{R}^d$ ($d = 2,\ 3$) with inflow boundary Γ_{in}, outflow boundary Γ_{out} and physical wall of the vessel Γ_{wall}. Variables of interest are velocity $\mathbf{u}(\mathbf{x})$ and pressure $p(\mathbf{x})$ which are assumed to obey the NSE in Ω. Also, we assume to have velocity measures $\mathbf{d}$ available at some sites $\mathbf{x}_i^m \in \Omega$. We formulate the DA problem as an inverse problem of the form

$$\begin{aligned} &\min_{\mathbf{h}} \mathcal{J}(\mathbf{u},\, \mathbf{h}) = dist(f(\mathbf{u}(\mathbf{h})),\, \mathbf{d}) + \mathcal{R}(\mathbf{h}) \\ &\text{s.t.} \quad \begin{cases} -\nabla \cdot (\nu \nabla \mathbf{u}) + (\mathbf{u} \cdot \nabla)\mathbf{u} + \nabla p = \mathbf{s} \ \text{ and } \ \nabla \cdot \mathbf{u} = 0 \ \text{ in } \ \Omega \\ \mathbf{u} = \mathbf{0} \ \text{ on } \ \Gamma_{wall}, \ \ -\nu \frac{\partial \mathbf{u}}{\partial \mathbf{n}} + p \cdot \mathbf{n} = \mathbf{h} \ \text{ on } \ \Gamma_{in}, \ \ -\nu \frac{\partial \mathbf{u}}{\partial \mathbf{n}} + p \cdot \mathbf{n} = \mathbf{g} \ \text{ on } \ \Gamma_{out} \end{cases} \end{aligned} \tag{1}$$

where, $dist(\cdot,\, \cdot)$ is a proper measure of the discrepancy; $\mathcal{R}(\cdot)$ is a regularization term and the function f computes the numerical velocity in the measurements sites. Here, the boundary function $\mathbf{h}$ acts as control variable; in fact, we aim at finding the optimal pressure drop such that some distance between velocity and data is minimized. Starting from the formulation for the linearized NSE (where nonlinear convection term $(\mathbf{u} \cdot \nabla)\mathbf{u}$ is replaced by $(\boldsymbol{\beta} \cdot \nabla)\mathbf{u}$, being $\boldsymbol{\beta}$ is a known advection field), we present the technique for the nonlinear formulation.

Following a Discretize-then-Optimize approach (using Finite Element (FE) discretization) we solve the following algebraic optimization problem:

$$\begin{aligned} &\min_{\mathbf{H}} \mathcal{J}(\mathbf{V},\, \mathbf{H}) = \tfrac{1}{2}\|\mathrm{D}\mathbf{V}(\mathbf{H}) - \mathbf{d}\|_2^2 + \tfrac{a}{2}\|\mathrm{L}\mathbf{H}\|_2^2 \\ &\text{s.t.} \ \ \mathrm{S}\mathbf{V} = \mathrm{R}_{in}^{\mathrm{T}}\mathrm{M}_{in}\mathbf{H} + \mathbf{F}. \end{aligned} \tag{2}$$

Here,

$$\mathrm{S} = \begin{bmatrix} \mathrm{C} + \mathrm{A}^{\beta} & \mathrm{B}^{\mathrm{T}} \\ \mathrm{B} & \mathrm{O} \end{bmatrix} \tag{3}$$

The term $\frac{a}{2}\|\mathrm{L}\mathbf{H}\|_2^2$ is the discrete regularization, where L is the discretized gradient; $\mathbf{H}$ is the discretization of the control variable. Also, $\mathbf{V} = [\mathbf{U} \ \ \mathbf{P}]^{\mathrm{T}}$, where $\mathbf{U}$ and $\mathbf{P}$ are the discretization of velocity and pressure. $\mathrm{D} = [\mathrm{Q} \ \ \mathrm{O}]$, where Q is the discrete operator corresponding to f in (1); R_{in} is a *restriction matrix* which selects the degrees of freedom (DOF) of the velocity on Γ_{in}. M_{in} is the discretization of the mass operator restricted to inlet boundary nodes. Finally, C, A^{β} and B are the discretization of the diffusion, advection and divergence operators.
For the solution of problem (2), we use the Reduced Hessian method to solve the system necessary conditions for optimality induced by the Lagrangian

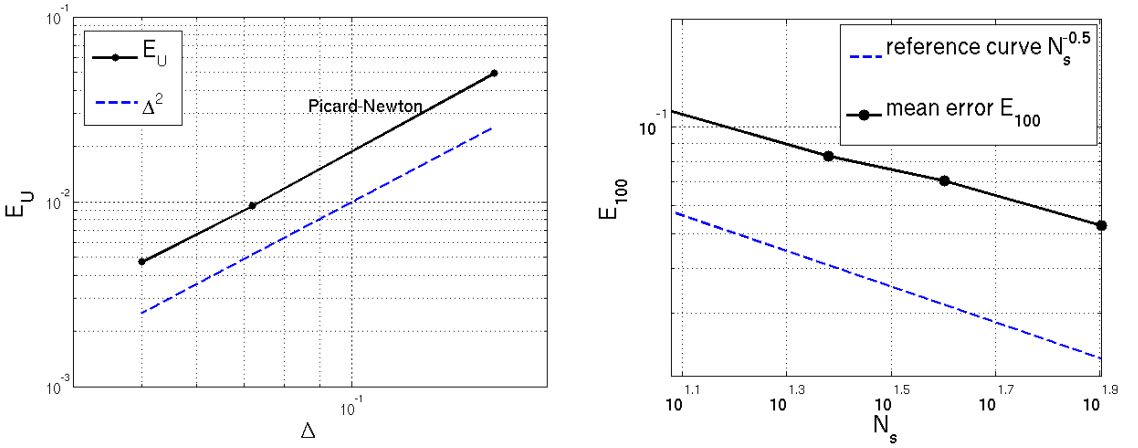

Figure 2: On the left, relative error versus discretization step with noise free data. On the right, relative error versus number of noisy data.

$$\mathcal{L}(\mathbf{V},\mathbf{H},\mathbf{\Lambda}) = \frac{1}{2}\|\mathrm{D}\mathbf{V}-\mathbf{d}\|_2^2 + \frac{a}{2}\,\|\mathrm{L}\mathbf{H}\|_2^2 + \mathbf{\Lambda}^{\mathrm{T}}(\mathrm{S}\mathbf{V} - \mathrm{R}_{in}^{\mathrm{T}}\mathrm{M}_{in}\mathbf{H} - \mathbf{F}); \tag{4}$$

where $\mathbf{\Lambda}$ is the discrete Lagrangian multiplier. By defining $\mathrm{Z}{=}\mathrm{D}\mathrm{S}^{-1}\mathrm{R}_{in}^{\mathrm{T}}\mathrm{M}_{in}$ and $\mathrm{H}_r = \mathrm{Z}^{\mathrm{T}}\mathrm{Z} + a\,\mathrm{L}^{\mathrm{T}}\mathrm{L}$ the reduced system reads: $\mathrm{H}_r\mathbf{H} = \mathrm{Z}^{\mathrm{T}}(\mathbf{d} - \mathrm{D}\mathrm{S}^{-1}\mathbf{F})$. It is possible to prove that, in absence of regularization, the well-posedness of the problem is guaranteed if enough measurements are collected on the inflow boundary (in case of FE spaces P1bubble-P1, one site per DOF is required). Since, in general, this is not verified we propose to extend available data on DOF in Γ_{in} using interpolation (see [1]).

We extend the present technique to the NSE, using an iterative procedure that exploits the one presented for the liner case. Given a guess for the velocity field at iteration $k+1$, say $\mathbf{U}_k$, we iteratively solve

$$\begin{aligned} &\min_{\mathbf{H}} \tfrac{1}{2}\|\mathrm{D}\mathbf{V}_{k+1}(\mathbf{H}_{k+1}) - \mathbf{d}\|_2^2 + \tfrac{a}{2}\|\mathrm{L}\mathbf{H}_{k+1}\|_2^2 \\ &\text{s.t.}\quad \mathrm{S}_k\mathbf{V}_{k+1} = \mathrm{R}_{in}^{\mathrm{T}}\mathrm{M}_{in}\mathbf{H}_{k+1} + \mathbf{F}_k \end{aligned} \tag{5}$$

until $\|\mathbf{U}_k - \mathbf{U}_{k+1}\| < \delta$ (a user defined tolerance). Here, S_k and $\mathbf{F}_k$ depend on $\mathbf{U}_k$, which plays the role of a known advection field.

Numerical results Several numerical tests cases conducted on analytical solutions validate our procedure as a consistent DA method in case of noise free data and as a noise filtering procedure in case of noisy data. In particular, assimilating non-noisy data we recover the FE solution for the NSE; this is confirmed by convergence tests of the discretization error with respect to the discretization step (see [1] and Figure 2, left). In case of noisy data, the analysis of the discretization error highlights the filtering properties. The error decreases as more data are available (see [1] and Figure 2, right) and the sample mean of the computed velocities for increasing realizations of noise converges to the noise free solution. Also, the interpolation technique proves to be competitive with the common Tikhonov regularization in terms of accuracy and to be much cheaper in terms of computational time.

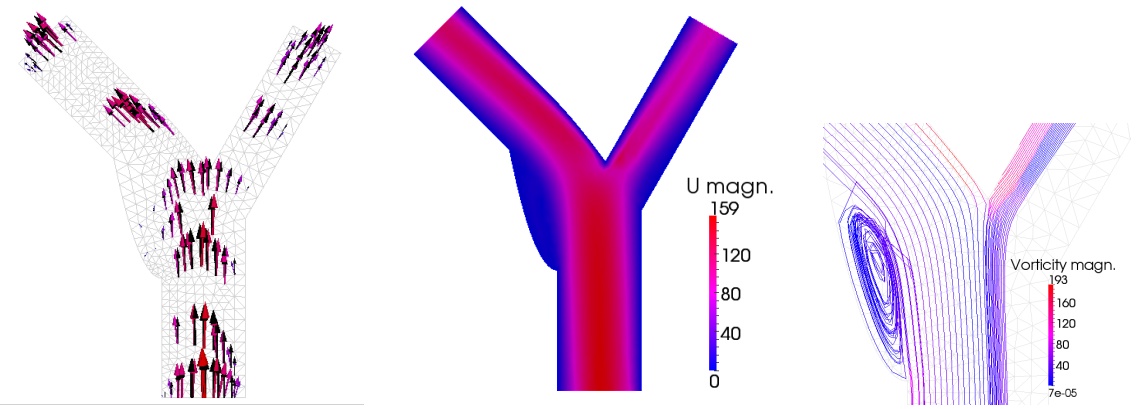

Figure 3: Left: actual data used in the DA process (original, in black, and interpolated). Center: magnitude of the velocity vector field. Right: detail of the vorticity map.

Performing DA on 2D geometries approximating vessels of interest allows to recover accurate velocity fields and flow related variables of medical interest such as the WSS. In Figure 3 we report the results of the assimilation procedure performed on a 2D approximation of a carotid artery. Velocity data, on the left, are generated adding noise to an available reference solution; sparse data on the inflow boundary (not satisfying well-posedness conditions) are interpolated using a piece-wise linear interpolating function. We also report the velocity profile (center) and the vorticity map (right), the latter features the typical vortexes in the carotid bulb, the region medical doctors are mostly interested in. A comparison of the recovered WSS with a reference solution highlights the filtering properties of the present procedure as opposed to current clinical methods of WSS estimation. Such methods compute the WSS from noisy data only, getting inaccurate results, not suitable for guiding early intervention.

3 CONCLUSIONS

On the basis of a DA procedure for linear problems we developed an efficient algorithm for the integration of noisy data and the numerical simulation of the steady NSE. As expected, the noise affects both the accuracy of the solution and the efficiency of the procedure. Also, data location plays a fundamental role in the well-conditioning of the formulation: numerical tests proved that both regularization and a suitable measurements distribution might improve the spectral properties of the problem. From these promising results, a natural extension of the formulation to the unsteady case is anticipated to be of great relevance in the accuracy of computations and data acquisition in time.

REFERENCES

[2] M. D'Elia, M. Perego, A. Veneziani, *A variational data assimilation procedure for the incompressible Navier-Stokes equations in hemodynamics*, submitted, Technical Report http://www.mathcs.emory.edu/technical-reports/techrep-00201.pdf.

[1] P. van der Velden, D. Sallee, E. Zaaijer, W. J. Parks, S. Ramamurthy, T. Q. Robbie, J. Huckaby, S. Chochua, and M. E. Brummer, *Systolic flow jet is an indicator of aortic root dilation for bicuspid aortic valves*, 2008.

2nd International Conference on Mathematical and Computational Biomedical Engineering - CMBE2011
March 30 - April 1, 2011, Washington D.C, USA
P. Nithiarasu and R. Löhner (Eds.)

Design of state estimators in fluid-structure interaction for data assimilation in large arteries

Cristóbal Bertoglio*, Dominique Chapelle, Miguel Fernández*, Jean-Frédéric Gerbeau* and Philippe Moireau****

*INRIA Reo team, 78153 Le Chesnay Cedex, France,
{cristobal.bertoglio,miguel.fernandez,jean-frederic.gerbeau}@inria.fr
**INRIA Macs team, 78153 Le Chesnay Cedex, France,
{dominique.chapelle,philippe.moireau}@inria.fr

SUMMARY

Medical imaging data is increasingly getting interest not only for patient specific geometry generation, but also for estimating uncertain parameters of the governing equations. However, parameter estimation in dynamical systems coming, e.g., from the discretization of partial differential equations requires not only efficient numerical methods but also to reduce other uncertainties coming from the modeling and discretization errors and initial condition. This is called in the literature *state estimation* [1].

A popular fashion to perform state estimation is by means of sequential approaches, e.g. optimal Kalman filters. Even though we can formulate fully-discrete fluid-structure interaction problems in a Kalman filter way, it becomes intractable on large distributed parameter systems. Therefore, we also apply and analyze the performance of physical filters (e.g., Luenberger observers [2]) - successfully applied in solid mechanics [3,4,5] - in the fluid-structure system under physiological conditions. We will also discuss the inclusion of velocity and pressure measurements in the fluid in improve the estimation results.

Key Words: *fluid-structure interaction, medical imaging, data assimilation, Luenberger observers*

REFERENCES

[1] D. Simon, Optimal State Estimation: Kalman, H-infinity, and Nonlinear Approaches, *John Wiley & Sons*, 2006.

[2] D. G. Luenberger. An introduction to observers, *IEEE Transactions on Automatic Control*, 16:596-602, 1971.

[3] P. Moireau, D. Chapelle, P. Le Tallec, Joint state and parameter estimation for distributed mechanical systems, *Comput. Methods Appl. Mech. Engrg.*, 197:659677, 2008.

[4] P. Moireau, D. Chapelle, P. Le Tallec, Filtering for distributed mechanical systems using position measurements: perspectives in medical imaging, *Inverse Problems*, 25, 2009.

[5] P. Moireau, D. Chapelle, Reduced-order Unscented Kalman Filtering with application to parameter identification in large-dimensional systems, *COCV*, Published online, 2010.

2nd International Conference on Mathematical and Computational Biomedical Engineering – CMBE2011
March 30 – April 1, 2011, Washington D.C., USA
P. Nithiarasu and R. Löhner (eds)

SOLVING PULMONARY HEMODYNAMIC INVERSE PROBLEMS BY TUNING MODELS WITH MULTIPLE LEVELS OF DETAIL

Ryan L. Spilker*, Jeffrey A. Feinstein, and Charles A. Taylor*****
Stanford University, Stanford, CA 94305
*Department of Radiology, 1201 Welch Road, Room PS055,
Lucas Center for Imaging, MC 5488, rspilker@alum.rpi.edu
**Department of Pediatrics, jaf@stanford.edu
***Department of Bioengineering, taylorca@stanford.edu

SUMMARY

A strategy for solving hemodynamic inverse problems was developed and applied to pulmonary arterial models with unilateral stenoses. Parameter values in four-element windkessel outflow boundary conditions were related to the impedance spectra of morphometry-based pulmonary arterial networks with linearized wave propagation solutions. Three-dimensional models with increasing mesh densities were approximated by their intrinsic impedances in lumped-parameter models. These surrogates were used in the tuning process. Preliminary results showed reasonable agreement with previous one-dimensional models.

Key Words: *Blood flow, patient-specific, optimization, inverse problems, morphometry, impedance.*

1. INTRODUCTION

Computational models utilized for studies of the cardiovascular system must be able to reproduce characteristics of measured hemodynamics prior to biomechanical analysis and prediction of treatment outcomes. The prohibitive computational expense of realistic simulations has motivated efforts to develop efficient methods to solve the related inverse problems. We have previously described iterative procedures for tuning morphometry-based arterial networks downstream of nonlinear one-dimensional patient-specific pulmonary arterial models to match measured mean pressure and flow.[1] We have more recently described tuning of three-dimensional models coupled to lumped-parameter models.[2] Both of these studies relied on quasi-Newton methods, which iteratively update affine approximations of the objective residuals to find parameter values for which these residuals vanish. In the present study, we instead updated a reduced-order model to be consistent with the results of the most recent multidomain simulation by determining the intrinsic impedances of the flow pathways through the three-dimensional model.[3] This surrogate for the more detailed model was then tuned to find the next approximation to the inverse problem's solution.

2. MAIN BODY

Geometric models of the pulmonary arteries of a pig and a patient with repaired tetralogy of Fallot were generated from magnetic resonance angiograms using custom software.[4]

Simulations of blood flow were performed by solving the unsteady Navier-Stokes equations governing flow of an incompressible, Newtonian fluid using a stabilized finite element method with linear, tetrahedral elements.[5,6] The arterial walls for these three-dimensional models were assumed to be rigid. Velocities were prescribed at the inlet of the model based on Womersley's analytical solution for periodic, fully-developed flow in rigid, circular cylinders and flow waveforms from phase-contrast MR velocimetry measurements. Convolution-based impedance boundary conditions were applied at the outlets using a coupled multidomain method.[6] Sets of possible hemodynamic impedance spectra were determined by constructing morphometry-based arterial networks to represent possible downstream vasculature[1,8] and calculating impedance through linearized wave propagation analysis based on Womersley's analytical solution for periodic, fully-developed flow in elastic, longitudinally-constrained tubes[9]. Four-element windkessel models were then fit to the impedance spectra to characterize the wave propagation solution. A study of the relationship between diameters and resistances of morphometry-based tree vessels revealed a trend of resistance being approximately proportional to the diameter raised to the power -2.50. Exponents for such trends in the remaining windkessel parameter values were also determined. The choice of morphometry-based trees for the outlets of the image-based model were made based on their cross-sectional area and the solution of the inverse problem of producing the measured mean values of flows to each lung and main pulmonary arterial pressure. It was initially assumed that the image-based arterial domain would present no impedance, reducing the surrogate model to the outflow boundary conditions in parallel. A coarse mesh was used for the initial multidomain model. The results of each simulation yielded intrinsic impedance spectra for the pathways from the inlet of the image-based model to each outlet. These intrinsic impedances were then placed in series with the outflow boundary conditions in updated reduced-order surrogate models. The inverse problem was solved with each updated surrogate by finding morphometry-based windkessel outflow boundary conditions for the multidomain model based on an adjustment of the constant in the resistance vs. diameter trend mentioned previously. Through this iterative process, the reduced-order surrogates increasingly approximated the behavior of the multidomain models near the solution of the inverse problem. When a solution was reached within given tolerances for a computational mesh, the mesh was refined to capture more detailed flow features. In an effort to rapidly achieve a steady state in the multidomain simulation, the reduced-order surrogates were also used to help choose a time point in the cardiac cycle when an initiating steady flow simulation would best approximate the pulsatile solution.

A pig experiment was conducted in which a stenosis was surgically created in the right pulmonary artery for one flow state and absent for the other measurement. For the model with the stenosis, the regions of complex flow were more highly resolved than other regions, but the meshes were fairly coarse, so the results reported here should be considered preliminary. The numbers of elements were 150,445 for the first mesh, 302,169 for the second mesh, and 415,613 for the final mesh. For the model without the stenosis, less refinement was used in the region of the stenosis. The numbers of elements for this model were 86,629 for the first mesh, 168,080 for the second mesh, and 372,192 for the final mesh. Updating the intrinsic impedance within the reduced-order surrogate model and adjusting the morphometry-based four-element windkessels successfully tuned the mean pressure in the main pulmonary artery and the flow split. The initial reduced-order model's assumption of no intrinsic impedance led to an initial mean pressure in the main pulmonary artery on the coarsest mesh that was 8.25 mmHg higher than measured and a flow fraction to the stenotic lung of 10.8%, which was lower than the measured 14.9%. A total of 4 simulations on the first stenotic mesh, 3 simulations on the second, and 2 simulations on the final mesh were needed to satisfy the tolerances of 0.1 mmHg for the mean pressure and 0.5% for the flow split.

When the anatomic model was updated to match the measured arterial geometry without the stenosis, the mean pressure in the main pulmonary artery dropped to 22.4 mmHg, closer to the measured 23.9 mmHg than the 20.6 mmHg found previously with a 1D multidomain model[1]. The flow fraction to the lung with the stenosis removed was 34.5% in the present model, only slightly more distant from the measured 42.5% than the predicted 36.4% of the 1D model.

The geometry of the patient with repaired tetralogy of Fallot was also compared to a previous 1D model. The 3D model was tuned such that the mean pressure in the main pulmonary artery matched that of the 1D model. For the 3D model with the patient-specific stenotic arterial geometry, the numbers of elements were 144,612 for the first mesh, 251,555 for the second mesh, and 639,507 for the final mesh. Tolerances were loose enough that the intrinsic impedances of the first simulations on each of the first and second meshes were used to determine the intrinsic impedances for their following meshes. The final stenotic mesh had a mean pressure that was 0.03 mmHg below the 1D simulation's. For a modified model simulating a surgical repair, the numbers of elements for this model were 143,509 for the first mesh, 253,326 for the second mesh, and 644,072 for the final mesh. The simulated surgical repair for the 3D model lowered the mean pressure in the main pulmonary artery by 0.24 mmHg and increased the flow fraction in the repaired lung from 28.5% to 30.2%, and these are similar to previous 1D model results[1].

3. CONCLUSIONS

These multidomain pulmonary hemodynamic simulations demonstrate a novel tuning approach using a reduced-order surrogate model that approximates the behavior of the entire multidomain model to match measured mean pulmonary arterial pressure and flow split. This tuning approach converged to a fixed point at which the intrinsic impedance of the 3D portion of the multidomain model was approximated within the surrogate. Results from this model showed reasonable agreement with previous 1D models, which had several important limitations. An empirical model for the energy losses due to stenoses was used in the 1D multidomain model; the data set for this model was collected using steady flow and idealized geometry, neither of which have been fully validated for approximation of pulsatile flow in patient-specific stenotic geometries. The results of these examples demonstrate the potential clinical value of treatment outcome predictions. Future work will focus on application of the strategy demonstrated here for solving hemodynamic inverse problems to models incorporating more cardiovascular characteristics.

REFERENCES

[1] R.L. Spilker, J.A. Feinstein, D.W. Parker, V.M. Reddy, and C.A. Taylor, Morphometry-based impedance boundary conditions for patient-specific modeling of blood flow in pulmonary arteries, *Annals of Biomedical Engineering*, 35, 546-559, 2007.

[2] R.L. Spilker and C.A. Taylor, Tuning multidomain hemodynamic simulations to match physiological measurements, *Annals of Biomedical Engineering*, 38, 2635-2648, 2010.

[3] R.L. Spilker. *Computational analysis of blood flow in arteries incorporating reduced-order models of the downstream vasculature*, Ph. D. Thesis, Stanford University, 2009.

[4] N.M. Wilson, K.C. Wang, R.W. Dutton, and C.A. Taylor, A software framework for creating patient specific geometric models from medical imaging data for simulation based medical planning of vascular surgery, *Lecture Notes in Computer Science*, 2208, 449-456, 2001.

[5] C.A. Taylor, T.J.R. Hughes, and C.K. Zarins, Finite element modeling of blood flow in arteries, *Computer Methods in Applied Mechanics and Engineering*, 158, 155-196, 1998.

[6] C.H. Whiting and K.E. Jansen, A stabilized finite element method for the incompressible Navier-Stokes equations using a hierarchical basis, *Computer Methods in Applied Mechanics and Engineering*, 35, 93-116, 2001.

[7] I.E. Vignon-Clementel, C.A. Figueroa, K.E. Jansen, and C.A. Taylor, Outflow boundary conditions for three-dimensional finite element modeling of blood flow and pressure in arteries, *Computer Methods in Applied Mechanics and Engineering*, 195, 3776-3796, 2006.

[8] W. Huang, R.T. Yen, M. McLaurine, and G. Bledsoe, Morphometry of the human pulmonary vasculature, *Journal of Applied Physiology*, 81, 2123-2133, 1996.

[9] J.R. Womersley, Oscillatory flow in arteries: The constrained elastic tube as a model of arterial flow and pulse transmission, *Physics in Medicine and Biology*, 2, 178-187, 1957.

2nd International Conference on Mathematical and Computational Biomedical Engineering - CMBE2011
March 30 - April 1, 2011, Washington D.C, USA
P. Nithiarasu and R. Löhner (Eds.)

Biomechanical Imaging: Inferring Tissue Microstructure and Pathology

Assad A. Oberai[⋆], Paul E. Barbone[⋆⋆], Ricardo Leiderman[⋆⋆⋆], Sevan Goenezen[⋆] and Jean-Francois Dord[⋆]
[⋆]Mechanical, Aerospace and Nuclear Engineering, Rensselaer Polytechnic Institute, Troy, NY, USA. oberaa@rpi.edu, goenes@rpi.edu,dordj@rpi.edu
[⋆⋆]Mechanical Engineering, Boston University, Boston, MA, USA. barbone@bu.edu
[⋆⋆⋆]Ciencia da Computacao, Universidade Federal Fluminense, Rio de Janeiro, Brazil. leider@ic.uff.br

Key Words: *biomechanical imaging, inverse problems, tissue microstructure.*

1 INTRODUCTION

By Biomechanical Imaging (BMI) we refer to all techniques and algorithms that go into generating images of mechanical properties of tissue in-vivo [1]. The resolution of these images is of the order of a millimeter and their size is a few centimeters.

2 MAIN BODY

Tissue pathology directly influences its microstructure and the microstructure in turn determines the macroscopic properties of tissue. By imaging these macroscopic properties in-vivo, biomechanical imaging offers a window into both tissue microstructure and tissue biology. This makes it useful in differentiating types of tissue and in aiding studies in mechanobiology. Current applications of BMI include detection, diagnosis and treatment monitoring of breast and prostate cancer, liver cirrhosis, atherosclerosis and thrombosis, and surgical planning.

Most approaches (and there are many) include the following steps: (1) image the tissue using standard imaging modality such as ultrasound; (2) deform the tissue, using gentle compression for example; (3) acquire another image in this deformed state; (4) using undeformed and deformed images determine the intervening displacement field everywhere in the imaging volume; (5) using the measured displacement field solve an inverse problem to create images of mechanical properties everywhere in the imaging volume.

We have developed novel, robust and efficient algorithms to solve the inverse problem of determining distributions of mechanical properties from displacement measurements. We have also developed macroscopic mechanical models of tissue that are informed by its microstructure. In this talk I will focus on algorithms for creating images of linear and nonlinear elastic and poroelastic properties. The former provide information about the arrangement of collagen fiber bundles in breast tissue, while the latter provide information about the leakiness and the density of the microvasculature. Both have the potential of being used to detect diagnose and monitor the progression/regression of breast cancer.

REFERENCES

[1] P.E. Barbone and A.A. Oberai, A Review of the Mathematical and Computational Foundations of Biomechanical Imaging, *Computational Modeling in Biomechanics*, 375–408, Springer, 2010.

2nd International Conference on Mathematical and Computational Biomedical Engineering – CMBE2011
March 30 – April 1, 2011, Washington D.C., USA
P. Nithiarasu and R. Löhner (eds)

REGISTRATION OF PLANTAR PRESSURE IMAGES

Francisco P. M. Oliveira, João Manuel R. S. Tavares
Faculdade de Engenharia da Universidade do Porto (FEUP) / Instituto de Engenharia Mecânica e Gestão Industrial (INEGI), Rua Dr. Roberto Frias, 4200-465 Porto, Portugal, {francisco.oliveira, tavares}@fe.up.pt

SUMMARY

We present an analysis of four different algorithms used to register plantar pressure images: a first one based on the matching of the external contours of the feet, a second algorithm based on the technique of phase correlation, a third one based on the direct optimization of the cross-correlation (CC) and using the Fourier transform, and a fourth and last algorithm that is based on the iterative optimization of an intensity (dis)similarity measure. In terms of accuracy, the later algorithm achieved the best registration results; on the other hand, the algorithm based on the matching of contours was the fastest, but its accuracy was inferior to the accuracy of the remaining algorithms.

Key Words: *Pedobarography, Matching, Optimization, Cross-correlation, Fourier transform.*

1. INTRODUCTION

Plantar pressure distribution provides significant information for clinicians and researchers about the structure and function of the foot and general mechanics of gait. It is, therefore, extremely helpful in the diagnosis of foot complaints, development of footwear [1] and to obtain useful information for gait analysis, just to mention some few examples. In fact, plantar pressure distribution allows the comparison of the loads in the limb, either between injured and non-injured or pre- and post-traumatic or -operative states, enables the comparisons between patients and control groups and provides detailed and specific information on each region of contact [2]. There are a number of different techniques to access the relevant pressure distribution, and, in the major part of them, the pedobarographic data can be converted into a discrete rectangular array. Therefore, techniques of image processing and analysis can be directly used on the converted data to aid both clinicians and researchers in order to obtain pertinent clinical information.

Image registration, the process of optimally aligning homologous structures represented in images, is demanded by clinicians and researchers, as some usual clinical tasks such as, cases comparison, identification of the main plantar pressure areas and classification of the foot type, can be easier attained. In addition, pedobarographic image registration supports pixel-level statistics, which makes possible the extraction of biomechanically-relevant information more effectively than traditional regional techniques [3].

Several studies on the registration of pedobarographic images have been developed; for example, using principal axes transformation [4], modal matching [5, 6], principal axes combined with steepest descent gradient search [7], optimization with evolutionary algorithms [8], based on foot size and progression angle [9], contours matching [10], optimization of the cross-correlation (CC) computed in the frequency domain [11], phase correlation [11], and optimization of an image

(dis)similarity measure using an iterative scheme [12]. In this work, the later four methodologies are studied; thus, their fundamentals are introduced and a discussion about their results is presented.

2. METHODS

2.1 *Registration based on the matching of contours' points*

The registration algorithm presented in [10] is based on the matching of the external contours of the feet represented in the input images, and can be described in the following steps (Figure 1): 1) extraction of the external contours; 2) computation of an affinity matrix between the contours' points; 3) searching for the best matching by minimizing the sum of the affinities; 4) computation of the geometric transformation that best register the matched points; 5) registration of the input images considering the transformation computed.

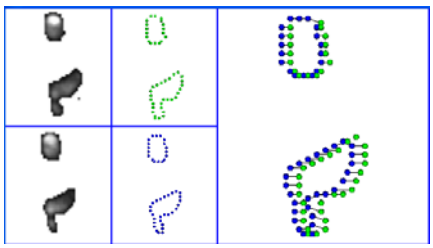

Figure 1: Matching the contours of two input images: on the left, two images to be registered; on the middle, extracted contours after a sampling process; and on the right, the matching found.

2.2 *Registration based on the technique of phase correlation*

The technique of phase correlation is based on the shift property of the Fourier transform; that is, a shift of a function in the space domain is represented by a shift on its phase when the function is represented in the frequency domain.

Let us consider two images, *f* and *g*, and their Fourier transforms, *F* and *G*, respectively, and suppose that $g(x,y) = f(x - x_0, y - y_0)$; thus, according to the shift property [13], we can get:

$$G(u,v) = F(u,v)e^{-2\pi i(ux_0 + vy_0)}. \quad (1)$$

Then, by computing the cross-power, we have:

$$\frac{F(u,v)G^*(u,v)}{|F(u,v)G^*(u,v)|} = e^{-2\pi i(ux_0 + vy_0)}, \quad (2)$$

where G^* represents the complex conjugate of *G*.

By computing the inverse of the Fourier transform of the cross-power, a Dirac δ-distribution centered at (x_0, y_0) is achieved. Therefore, the coordinates of the Dirac pulse indicate the optimal integer shift.

The aforementioned procedure allows the determination of the shift, but requires that the scale and rotation are known. To obtain the required values, first the spectrums of both images are built and converted into the log-polar coordinate system. Then, by determining the shift between the log-polar spectrums using the phase correlation, the scale and rotation can be known [11].

2.3 *Registration based on the optimization of an image intensity (dis)similarity measure*

This family of registration methodologies is based on the optimization of an image (dis)similarity measure related to the pixels' intensities. Thus, the geometric transformation that optimizes the (dis)similarity measure considered is then used to register the input images.

A two-step approach is considered in [12] to optimize the (dis)similarity measure adopted: in the begin, is determined a pre-registration; afterwards, in the second step, the optimization algorithm starts from the pre-registration solution searching iteratively for the geometric transformation that optimizes the adopted (dis)similarity measure. In that framework, for the pre-registration the user can choose the matching of the represented contours [10], the correlation of the images' phases or the cross-correlation of the input images [11]. Additionally, the Powell's method is adopted in the optimization process of the second step, taking into account one of the following (dis)similarity measures: the mean squared error (MSE), the mutual information (MI) or one based on the exclusive-or (XOR) [8].
In [12] the (dis)similarity measures are optimized using an iterative optimization algorithm. However, as shown in [11], for the CC and sum of the squared differences (SSD) (dis)similarity measures, the optimal integer shift, scaling and rotation values can be obtained directly by using the Fourier transform and convolution theorem. Let us consider two images, *f* and *g*, and their CC in function of a shift, *a*:

$$\mathrm{CC}_{fg}(a) = \sum_i f(i) g(i-a). \tag{3}$$

By the convolution definition, one have:

$$\mathrm{CC}_{fg}(a) = \sum_i f(i) \overline{g}(a-i) = \{f * \overline{g}\}(a), \tag{4}$$

where $\overline{g}(i) = g(-i)$ and $*$ represents the convolution. Then, from the convolution theorem, one can obtain:

$$\mathbf{F}\{f * \overline{g}\} = k \cdot \mathbf{F}\{f\} \cdot \mathbf{F}\{\overline{g}\}, \tag{5}$$

where $\mathbf{F}$ represents the Fourier transform and *k* is a constant that depends on the specific Fourier transform normalization.
Therefore, computing the inverse of the Fourier transform (using, for instance, the inverse fast Fourier transform (IFFT)) of the product in Equation (5), the correlation can be obtained for all shifts. Then, the coordinates of the point that has the higher value represents the desired integer optimal shift. On the other hand, to achieve the optimal scaling and rotation values, a procedure similar to the one refereed in section 2.2 can be used.
To directly obtain the similarity geometric transformation, that is, the scaling, rotation and shift values, which optimizes the SSD, a procedure similar to the one used to optimize the CC is employed [11].

3. DISCUSSION

All introduced algorithms were tested on a dataset consisting of 30 pairs of peak pressure images of 45×63 pixels, collected at 500 Hz using a 0.5 m Footscan system (RSscan, Olen, Belgium).
From the experimental results [10-12], we can point out the following conclusions. All algorithms revealed high accuracy, speed and noise robustness, being the most accurate the one presented in [12] that is based on a two-steps registration scheme and iterative optimization. This result was expected, since the second step of this algorithm starts from the pre-registration obtained by one of the remains algorithms.
In respect to the image (dis)similarity measure used in the algorithm presented in [12], when a known control geometric transformations were used to assess the registration accuracy, the best results were obtained by minimizing the MSE, being the associated residual error (RE) always inferior to 10^{-4} mm. However, very good results were also obtained when the MI was minimized (RE < 0.015 mm), and suitable results were obtained when the CC was directly maximized (0.041 mm) [12]. Considering the same known control geometric transformations, but after adding Gaussian noise, with a signal to noise ratio (SNR) between 1.5 and 3.5, to the images to be register, the maximum RE remained very low (< 0.4 mm) [12].

Finally, the processing time was always very low for the four algorithms, which were implemented in C++ and tested on a notebook PC with an AMD Turion64 2.0 GHz microprocessor and 1.0GB of RAM. The fastest algorithm was the one based on the matching of the represented contours (around 25 ms per image pair), and the slowest was the algorithm based on the two-steps registration scheme (around 70 ms) [12].

Acknowledgements

This work was partially done in the scope of the projects “Methodologies to Analyze Organs from Complex Medical Images – Applications to Female Pelvic Cavity”, “Aberrant Crypt Foci and Human Colorectal Polyps: mathematical modelling and endoscopic image processing” and “Cardiovascular Imaging Modeling and Simulation - SIMCARD”, with references, PTDC/EEA-CRO/103320/2008, UTAustin/MAT/0009/2008 and UTAustin/CA/0047/2008, respectively, financially supported by Fundação para a Ciência e a Tecnologia in Portugal.
The first author would like to thank Fundação Gulbenkian, in Portugal, for his PhD grant.

REFERENCES

[1] R. L. Actis*, et al.*, "Multi-plug insole design to reduce peak plantar pressure on the diabetic foot during walking," *Medical & Biological Engineering & Computing,* 46:363-371, 2008.
[2] D. Rosenbaum and H. Becker, "Plantar pressure distribution measurements. Technical background and clinical applications," *Foot and Ankle Surgery,* 3:1-14, 1997.
[3] T. C. Pataky*, et al.*, "New insights into the plantar pressure correlates of walking speed using pedobarographic statistical parametric mapping," *Journal of Biomechanics,* 41:1987-1994, 2008.
[4] A. J. Harrison and P. J. Hillard, "A moment-based technique for the automatic spatial alignment of plantar pressure data," *Proceedings of the Institution of Mechanical Engineers, Part H: Journal of Engineering in Medicine,* 214:257-264, 2000.
[5] L. F. Bastos and J. M. R. S. Tavares, "Improvement of modal matching image objects in dynamic pedobarography using optimization techniques," *Articulated Motion And Deformable Objects: Third International Workshop, Amdo 2004, Spain,* 39-50, 2004.
[6] R. R. Pinho and J. M. R. S. Tavares, "Dynamic pedobarography transitional objects by Lagrange's equation with FEM, modal matching and optimization techniques," *Image Analysis and Recognition: International Conference, ICIAR 2004, Portugal,* 92-99, 2004.
[7] T. C. Pataky and J. Y. Goulermas, "Pedobarographic statistical parametric mapping (pSPM): a pixel-level approach to foot pressure image analysis," *Journal of Biomechanics,* 41:2136-2143, 2008.
[8] T. C. Pataky*, et al.*, "A comparison of seven methods of within-subjects rigid-body pedobarographic image registration," *Journal of Biomechanics,* 41:3085-3089, 2008.
[9] N. L. W. Keijsers*, et al.*, "A new method to normalize plantar pressure measurements for foot size and foot progression angle," *Journal of Biomechanics,* 42:87-90, 2009.
[10] F. P. M. Oliveira*, et al.*, "Rapid pedobarographic image registration based on contour curvature and optimization," *Journal of Biomechanics,* 42:2620-2623, 2009.
[11] F. P. M. Oliveira*, et al.*, "Registration of pedobarographic image data in frequency domain," *Computer Methods in Biomechanics and Biomedical Engineering,* (in press).
[12] F. P. M. Oliveira and J. M. R. S. Tavares, "Novel framework for registration of pedobarographic image data," *Medical & Biological Engineering & Computing,* (in press).
[13] E. Castro and C. Morandi, "Registration of translated and rotated images using finite Fourier transforms," *IEEE Transactions on Pattern Analysis and Machine Intelligence,* 9:700-703, 1987.

2nd International Conference on Mathematical and Computational Biomedical Engineering – CMBE2011
March 30 – April 1, 2011, Washington D.C., USA
P. Nithiarasu and R. Löhner (eds)

FINITE ELEMENT COMPARISON OF DENTAL IMPLANTS WITH STANDARD AND PLATFORM SWITCHING PROSTHETIC COMPONENTS

M. A. Neto *, P. Nicolau, S. Rocha[3]* and R. P. Leal[4]***
,[3] Department of Mechanical Engineering, F.C.T U. C., Rua Luis Reis Santos, 3030-788 Coimbra, Portugal, * augusta.neto@dem.uc.pt; [4]* rogerio.leal@dem.uc.pt .
**, [3]* Department of Dentistry, Faculty of Medicine, University of Coimbra, Rua Larga, 3030- 504 Coimbra, Portugal, ** pgnicolau@mail.telepac.pt ;
[3]*salomaorocha@gmail.com

SUMMARY

Key Words: *Platform switching, dental implants, finite element.*

1. INTRODUCTION

Histologic and radiographic observations suggest that a biologic dimension of hard and soft tissues around dental implants extends apically from the implant-abutment interface [1]. The stress and strain distribution developed on this surrounding bone is the main mechanical reason for failure of many implants. In fact, although clinical studies have revealed that dental implants placed in the jawbone regions with lower density have higher chances of failing than the implants paced at regions with higher bone density [2], the process of bone remodeling is heavily influenced by the mechanical loading conditions.
From the clinical point of view, implant failures are mostly related to crestal bone loss [3] that is mainly contributed by two factors: the first is associated with peri-implantitis and the second one is related with the occlusal overload on the dental implant. Both factors can be affected by the design of the dental implant, as such as the implant diameter, length and shape [4]. In 1991, Implant Innovations introduced wide-diameter implants with matching wide-diameter platforms. When introduced, however, matching-diameter prosthetic components were not available, and many of the early 5.0- and 6.0-mm-wide implants received "standard"-diameter (4.1-mm) healing abutments and were restored with "standard"-diameter (4.1-mm) prosthetic components [1]. Long-term radiographic follow-up of these "platform-switched" (PS) restored wide-diameter dental implants have demonstrated a smaller than expected vertical change in the crestal bone height around these implants than is typically observed around implants restored conventionally with prosthetic components of matching diameters. The biomechanical rationale for this phenomena is addressed by Yashinobu et al. [5]. in a 3D finite element analysis, were they have concluded that PS abutment configuration has the biomechanical advantage of shifting the stress concentration area away from the cervical bone–implant interface. These models however were very simplified and did not consider the clinical situation on how marginal bone stability can be influenced by different bone qualities around implants restored with Standard or PS abutments. In this paper a special attention will be given to these clinical situations and the finite element models produced have the advantage of being validated with clinical data.

2. METHODOLOGY, RESULTS AND CONCLUSIONS

The use of the finite element method is the most common technique to represent the deformation of flexible bodies. Thus, several finite element models have been used to investigate the stress and strain distribution developed in the surrounding bone. In this paper a Camelog [ref.] dental implant is used to compare the strain and stress levels around the peri-implant region. Different material properties are used at the cortical and at the cancellous bones as well as at the bone implant interface. The finite element models of the standard and of the platform switched prosthetic components are different according the Camelog models. All the models are loaded assuming that the occlusal loads are applied to the teeth at a certain angle along both the sagittal and the coronal planes.

Some preliminary results show: 1) PS configuration has the biomechanical advantage of shifting the stress concentration area away from the cervical bone–implant interface.

2) •PS configuration did not influence Stress distribution on Peri-implant trabecular bone.

3)PS configuration may also be an advantage in implant sites with a reduced thickness of marginal cortical bone (Type III), than in sites of better bone quality (type II), according to the Lekhlom & Zarb, 1985, classification [6].

ACKNOWLEDGEMENTS

Co-financed by the Foundation for Science and Technology via project PTDC/SAU-BEB/108658/2008 and by FEDER via the «Programa Operacional Factores de Competitividade» of QREN with COMPETE reference: FCOMP-01-0124-FEDER-010961

REFERENCES

[1] R.J. Lazzara and SS. Porter, Platform switching: new concept on dentistry for controlling postrestorative crestal bone levels. *International Journal Periodontics Restorative Dental*, 26(1), 9-17, 2006.

[2] F. Genna, On the effects of cyclic transversal forces on osseointegrated dental implants: Experimental and finite element shakedown analyses. *Computer Methods in Biomechanics and Biomedical Engineering*, 6(2), 141-152, 2003.

[3] D.P. Callan, A. O´Mahony and CM. Cobb. Loss of crestal bone around dental implants: A retrospective study, *Implant Dentisitry*, 7, 258-265, 1998.

[4] C.M. Stanford and RA. Brand. Toward an understanding of implant occlusion and strain adaptive bone modeling and remodelling, *Journal of Prosthetic Dentistry*, 81(5), 553-561, 1999.

[5] Y. Maeda, J. Miura, I. Taki and M. Sogo. Biomechanical analysis on platform switching: is there any biomechanical rationale? *Clin. Oral Impl. Res*. 18, 581-584, 2007.

[6] U. Lekholm, G. Zarb. Patient selection and preparation. In: Branemark, P.-I., Zarb, G.A., Albrekts- son, T., (eds). Tissue integrated prostheses: osseointegration in clinical dentistry, 199-209. Chicago Quintessece, 199-209, 1985.

2nd International Conference on Mathematical and Computational Biomedical Engineering – CMBE2011
March 30 – April 1, 2011, Washington D.C., USA
P. Nithiarasu and R. Löhner (eds)

CHALLENGES IN IMAGE-BASED GEOMETRIC MODELING AND MESH GENERATION

Yongjie (Jessica) Zhang
Assistant Professor in Mechanical Engineering,
Courtesy Appointment in Biomedical Engineering,
Carnegie Mellon University, Pittsburgh, PA, USA, jessicaz@andrew.cmu.edu

SUMMARY

With finite element method and scanning technology seeing increased use in active research areas such as biomechanics, there is an emerging need for high-fidelity geometric modeling and quality mesh generation of the spatially realistic domains that are being studied. In images obtained from various scanning techniques like CT/MRI, the domain of focus often possesses heterogeneous materials and/or functionally different properties. For each of the partitioned material regions, high fidelity geometric models and quality meshes are needed, with meshes conforming at the material boundaries. Although there have been tremendous progresses in the area of surface reconstruction and 3D geometric modeling, it still remains a challenge to generate desirable models for such complicated domains.

I will present challenges in this research area along with details of meshing pipelines, especially octree-based algorithms to extract adaptive and quality 2D (triangular or quadrilateral) and 3D (tetrahedral or hexahedral) meshes of volumetric domains, conforming to boundaries defined as level sets of a scalar function on the domain. Guaranteed-quality all-quadrilateral meshing, feature preservation, and automatic meshing for multi-material domains will be discussed. Besides piecewise-linear element meshes, a skeleton-based sweeping method was developed to construct hexahedral solid NURBS for blood vessels from imaging data, then a wavelets-based scheme is used to simplify and fair the NURBS surface with continuity preservation, especially at the interface shared by multiple patches. Recently we also developed a novel method to convert any unstructured quadrilateral meshes to T-Spline surfaces. In this talk, I will additionally present several applications of our meshing schemes.

Key Words: *Geometric modeling, mesh generation, scanned images, heterogeneous domain.*

REFERENCES

[1] Y. Zhang, C. Bajaj and B-S. Sohn. 3D Finite Element Meshing from Imaging Data. *Computer Methods in Applied Mechanics and Engineering*, 194(48-49):5083-5106, 2005.

[2] Y. Zhang and C. Bajaj. Adaptive and Quality Quadrilateral/Hexahedral Meshing from Volumetric Data. *Computer Methods in Applied Mechanics and Engineering*, 195(9-12):942-960, 2006.

[3] Y. Zhang, T. J.R. Hughes, C. L. Bajaj. An Automatic 3D Mesh Generation Method for Domains with Multiple Materials. *Computer Methods in Applied Mechanics and Engineering*, 199(5-8):405-415, 2010.

[4] Y. Zhang, Y. Bazilevs, S. Goswami, C. Bajaj and T. J.R. Hughes. Patient-Specific Vascular NURBS Modeling for Isogeometric Analysis of Blood Flow. *Computer Methods in Applied Mechanics and Engineering*, 196(29-30):2943-2959, 2007.

[5] Y. Zhang, C. Bajaj, G. Xu. Surface Smoothing and Quality Improvement of Quadrilateral/ Hexahedral Meshes with Geometric Flow. *Journal Communications in Numerical Methods in* Engineering, 25(1):1-18, 2009.

[6] W. Wang, Y. Zhang. Wavelets-based NURBS Simplification and Fairing. *Computer Methods in Applied Mechanics and Engineering*, 199(5-8):290-300, 2010.

2nd International Conference on Mathematical and Computational Biomedical Engineering – CMBE2011
March 30 – April 1, 2011, Washington D.C., USA
P. Nithiarasu and R. Löhner (eds)

An Integrated Method for Intensity Inhomogeneity Correction and Local Image Enhancement of MRI Based on Curvelet Transform

Kunyu Tsai*, Jian Wu*, Datian Ye* and Jianwei Ma**
*Research Center of Biomedical Engineering, Graduate School at Shenzhen, Tsinghua University, Shenzhen, China, wuj@sz.tsinghua.edu.cn
** Program in Computational Science & Engineering, Florida State University, Tallahassee, Florida 32306, USA, jma2@fsu.edu

SUMMARY

Artifacts, such as intensity inhomogeneity (IIH), poor contrast and noise are often encountered in magnetic resonance imaging (MRI), which result in negative effects for automatic image segmentation and registration. In order to improve the quality of MRI, we propose an integrated preprocessing algorithm based on curvelet transform for IIH correction and local enhancement of edges. We decompose images by curvelet transform and then use the coarsest curvelet coefficients to reconstruct the images, which is treated as the estimation of bias field in IIH correction. In the phase of local image enhancement, we firstly compose feature vectors by curvelet coefficients and utilize Fuzzy C-means (FCM) clustering to classify pixels into three categories: edge, noise and smooth components. Then different enhancement strategies are implemented in different regions. The proposed method performs sharp edges between tissues and smoother within a particular tissue area, which is helpful to increase the accuracy of image segmentation or registration.

Key Words: *intensity inhomogeneity; local image enhancement; denoising; curvelet transform; feature extraction*

1. INTRODUCTION

MRI is usually accompanied with artifacts such as IIH, poor contrast and noise, which may hamper the accuracy of automatic segmentation and registration algorithm. IIH consists in slow nonanatomical intensity variations across images, which is generally considered as an interaction between IIH-free image and the multiplicative bias field. The most three popular mathematical models for IIH description are low-frequency model, hypersurface model and statistical model [1]. Lin et al. [2] successfully extended the low-frequency method by wavelet transform to remove IIH. Compared to hypersurface and statistical methods, wavelet-based methods have special advantages such as multi-resolution analysis and simplicity in computation. On the other hand, the quality of image can also be improved by enhancement. Methods for enhancement have been developed from hard or soft thresholding function with fixed threshold value in spatial domain to adaptive nonlinear thresholding functions in transform domain. Most of the methods apply uniform enhancement function to the whole image globally, which inevitably blurred the edge or magnified the noise. Thus, our motivation is to propose a new strategy for local enhancement to avoid this embarrassment, which will apply different enhancement functions in different regions to sharpen edges while depressing noise.

Curvelet transform proposed by Candès and Donoho [3], is one of geometric/directional wavelets which splits the whole frequency domain into multi-scales and multi-directions. Curvelet transform can represent edges more effective than wavelets. Detailed derivation and recent applications of curvelets can be found in [4]. In this paper, we propose an integrated preprocessing method based on the curvelet transform to correct IIH, extract features and implement the local image enhancement. The results show that the IIH artifact can be well removed and the feature extraction method is effective for classifying edges, noises and pixels in smooth area. The contrast can be increased by utilizing the local-enhancement method.

2. METHOD

IIH can be defined as $\mathbf{v}(x) = \mathbf{a}(x) \cdot \mathbf{u}(x) + \mathbf{n}(x)$ where $\mathbf{u}(x)$ is the original image, $\mathbf{a}(x)$ represents the bias field, $\mathbf{n}(x)$ is noise and $\mathbf{v}(x)$ is the IIH image. In the first phase of this paper, we focus on the estimation of $\mathbf{a}(x)$. We combine the method in [2] and curvelet transform to correct IIH. We apply an iterative procedure to estimate the bias field, which includes curvelet decomposition of IIH image, reconstructing an image by coefficients at the coarsest scale as the raw estimation of bias field and the most value projection (MVP) process to keep high gray value on the boundary [2]. The collected image is divided by the estimation of bias field to obtain the final IIH-free image. Here, for images with size of *m*n*, the level of curvelet decomposition is calculated by

$$s = \text{floor}[\log_2(\min\{m,n\})] - 1\,. \tag{1}$$

In the second phase, we construct feature vectors of pixels for classification. Considering boundaries have more obvious directional character than noises do, it can be supposed that boundaries present big curvelet coefficients in certain few directions and small coefficients in other directions. On the contrary, coefficients of noises at fine scales do not differ widely from direction to direction. In addition, energies of coefficients of edges and noises almost concentrate on fine scales and coefficients between scales of meaningful signals have high correlation. Based on the assumptions above, we utilize curvelet coefficients at the finest (s^{th}) and the second finest (s-1^{th}) scale to compose feature vectors. Let $\mathbf{x}_k \in \mathbb{R}^q$ denote the feature vector of k^{th} pixel in the image, where q is the dimension of the desired feature space. Here, q is defined as $q = d + d/2$, where d denotes the number of directions at s-1^{th} scale. Then the feature vectors can be constructed by two steps. 1) If s^{th} scale and s-1^{th} scale have the same number of directions, then t^{th} 'eigenvalue' of $\mathbf{x}_k$ can be calculated by

$$\lambda_{k,t} = |c_{k,s,t}| + |c_{k,s-1,t}|, t = 1,2, \dots, d \tag{2}$$

where $c_{k,s,t}$ is the corresponding curvelet coefficient of k^{th} pixel at s^{th} scale and t^{th} direction. Otherwise, if numbers of directions at two scales are different, the eigenvalue is calculated by

$$\lambda_{k,t} = \begin{cases} \frac{(|c_{k,s,2d}| + 2|c_{k,s,1}| + |c_{k,s,2}|)}{4} + |c_{k,s-1,1}| & , \quad t = 1 \\ \frac{(|c_{k,s,2t-2}| + 2|c_{k,s,2t-1}| + |c_{k,s,2t}|)}{4} + |c_{k,s-1,t}|, & \quad t = 2, \dots, d \end{cases} \tag{3}$$

Then reshape $\{\lambda_{k,1}, \dots, \lambda_{k,d}\} \subset \mathbf{x}_k$ in a descending order and apply the normalization to the front d eigenvalues of all pixles in the image as a whole. 2) In order to emphasis the gradients of the first d eigenvalues, we define the last $d/2$ eigenvalues as

$$\lambda_{k,d+i} = \lambda_{k,i+1} - \lambda_{k,i}, i = 1,2, \ldots, d/2. \quad (4)$$

Then we normalize the last $d/2$ eigenvalues of all pixles to construct the feature vectors. Finally FCM [5] is applied to classify the image into edge, noise and flat areas.

We locally utilize different enhancement strategies in different regions. At the s^{th} scale in curvelet domain, we apply soft thresholding to denoise in flat area. At the s-1^{th} scale, we apply adaptive enhancement method shown in Eq. 5 to edge area. At the 3^{rd} scale, Eq. 5 is used in flat area to increase the contrast between different tissues. In the experiments, we apply Otsu threshold [6] to judge the belonging of pixels in classification results of edge or flat areas, and then categorize the rest pixels into weak edge and noise group. The adaptive enhancement function is

$$\hat{c} = v\{sigm[u(c-T)/M] - sigm[-u(c+T)/M]\} \cdot M \quad (5)$$

where $v = 1/sigm[u(1-T/M)] - 1/sigm[-u(1+T/M)$, $sigm(x) = 1/(1+e^{-x})$, and $M = \mathrm{Max}\{|c_i||\forall c_i \in C\}$. C is the set of coefficients at certain scale and direction. u denotes the parameter for controlling the extent of enhancement which is generally between 5 to 20. The threshold T is defined by VisuShrink method [7]:

$$T = \sigma\sqrt{2log_2(N)} \quad (6)$$

where $\sigma = \mathrm{Median}\{|c_i||\forall c_i \in C\}/0.6745$ and N is the number of coefficients in C.

3. RESULT

The material is a T1-weighted abdominal cross section MRI, which is acquired in a Siemens MR scanner with the magnetic field strength of 1.5 Tesla. The size of the image is 384*384 with pixel's scale of 0.78*0.78 mm^2.

Figure 1 shows the results of IIH correction and local enhancement. With the correction of intensity distribution, the MRI image becomes more homogenous. Furthermore, the enhanced image shows less noises and sharper boundaries. Figure 2 shows the classification results. Generally, strong linear features in the image can easily be detected while some weak edges such as boundaries of the kidney and bowel are not able to be distinguished from noises. Figure 3 offers details of images. Through the gradient image, we can find out that the right image has much more bright pixels than the left on, which means the boundary becomes sharper after enhancement. In addition, within vertebra and kidney region, noises are well depressed by our method.

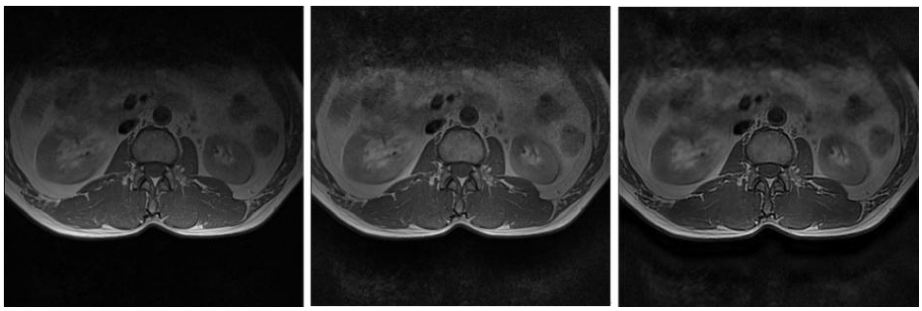

Figure 1. Original image (left), IIH corrected image (middle) and locally enhanced image (right).

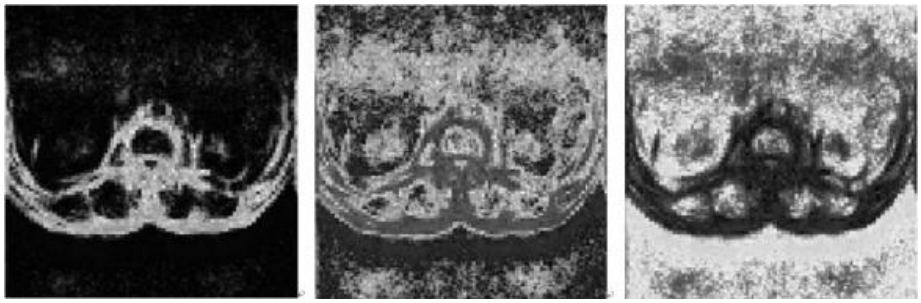

Figure 2. Classification results (from left to right: edge, noise and flat area).

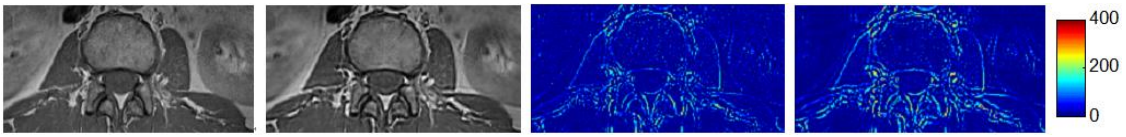

Figure 3. From left to right: closeup of Fig.1 (middle) and Fig.1 (right), and their gradient maps.

4. CONCLUSION

We present an integrated image preprocessing method based on curvelet transform for IIH correction and local enhancement. The results show good performance of the proposed method for recovery of IIH-free images with edge enhancement. In next work, we will apply the method to MRI image registration.

5. ACKNOWLEDGEMENT

The authors thank Tsinghua University-Siemens CKI project "Visualization of needle-knife of image segmentation and registration", as well as the Shenzhen City National 863 project matching funding support.

REFERENCES

[1] Z. Hou, A Review on MR Image Intensity Inhomogeneity Correction, *International Journal of Biomedical Imaging*, 2006: 1–11, 2006.

[2] F. Lin, Y. Chen, J. Belliveau and L. Wald, A Wavelet-Based Approximation of Surface Coil Sensitivity Profiles for Correction of Image Intensity Inhomogeneity and Parallel Imaging Reconstruction, *Human Brain Mapping*, 19 (2): 96-111, 2003.

[3] E. Candès, D. Donoho, "Curvelets—A surprisingly effective nonadaptive representation for objects with edges," in Curves and Surface Fitting: Saint-Malo 1999, A. Cohen, C. Rabut, and L. Schumaker, Eds. Nashville: Vanderbilt Univ. Press, 2000: 105–120.

[4] J. Ma, G. Plonka, The curvelet transform, *IEEE Signal Processing Magazine*, 27 (2): 118-133, 2010.

[5] J. Bezdek, Pattern Recognition with Fuzzy Objective Function Algoritm, Plenum Press, 1981.

[6] N. Otsu, A threshold selection method from gray-level histograms, *IEEE Trans. Systems, Man, and Cybernetics*, 9: 62-66, 1979.

[7] D. Donoho, J. Johnstone IM, Ideal spatial adaptation via wavelet shrinkage, *Biometrika*, 81(3): 425-455, 1994.

2nd International Conference on Mathematical and Computational Biomedical Engineering – CMBE2011
March 30 – April 1, 2011, Washington D.C., USA
P. Nithiarasu and R. Löhner (eds)

Image Registration for Tissue Biomechanics Imaging

Michael S Richards*, Paul E Barbone and Assad A. Oberai*****
* Department of Electrical and Computer Engineering, Hajim School of Engineering and Applied Sciences, University of Rochester, Rochester, NY 14627, USA, msr@ece.rochester.edu
** Department of Mechanical Engineering, Boston University, Boston MA, 02215, USA, barbone@bu.edu
*** Department of Mechanical, Aerospace and Nuclear Engineering, Rensselaer Polytechnic Institute, Troy NY, 12180, USA, oberaa@rpi.edu

SUMMARY

Key Words: *Image Registration, Biomechanical Imaging, Ultrasound Imaging, Speckle Tracking.*

1. Introduction

Fundamental to the process of elasticity imaging is the ability to measure physically accurate displacements from image sets of deforming tissues. For ultrasound (US) imaging, the high resolution of the images in the direction of sound propagation can yield very accurate estimates of the displacement component in that direction using standard cross correlation based, block-matching methods [1]. However, accurate estimates of the full displacement vector remain a challenge, due to the lower frequency image variation in both the lateral and elevational image dimensions. In an effort to improve the accuracy of the displacement vector field in US imaging, we propose utilizing *a priori* expectations of the measurements. To that end, we have framed the measurement problem as a global image registration problem. This also allows us to extend the use of the techniques of elasticity imaging to other imaging modalities.

The fundamental assumption of our technique is that the underlying tissue deformation between two or more images in a deformation sequence is equal to the warping that aligns the images. The registration is performed as an optimization where we minimize the integrated, squared intensity difference of image pairs as a function of that warping. The *a priori* information is included as additional penalty terms on the optimization functional. The functional of this minimization is:

$$\pi[\boldsymbol{u}(\boldsymbol{x})] = \frac{1}{2}\int_{\Omega} (I_1(\boldsymbol{x}) - I_2(\boldsymbol{x}+\boldsymbol{u}(\boldsymbol{x}))^2 d\Omega + R[\boldsymbol{u}(\boldsymbol{x})]. \quad \textbf{(1)}$$

Here, $\boldsymbol{u}(\boldsymbol{x})$ is the desired image warping, or deformation, I_1(x) and I_2(x) are the reference and post-deformation images of a sequence, respectively, and R is the term, or terms, used to penalize variations from our *a priori* expectations. The functional is minimized via Gauss-Newton's method.

The primary *a priori* information used in the reconstruction is that of smoothness in the displacement vector field. The R term that reflects this assumption is a regularization penalty on non-zero magnitudes of the displacement gradient tensor. The second type of *a priori* information considered is that of material incompressibility, which assumes that the divergence of

the deformation field is small. The use of this constraint is only relevant for applications of two dimensional plane strain and 3D problems (i.e. 3D image registration).

2. Methods and Results

In the algorithm described above, the displacement field is discretized with finite element, piece-wise linear shape functions. The images are interpolated using cubic interpolation. To avoid inaccuracies due to local minima, an accurate initial guess to the displacement field is often necessary and is evaluated using a gross estimate of the overall applied strain. The regularization term used in this work is as follows:

$$R[\boldsymbol{u}(\boldsymbol{x})] = \frac{\alpha}{2}\int_{\Omega} (\nabla \boldsymbol{u}(\boldsymbol{x}) : \nabla \boldsymbol{u}(\boldsymbol{x}))^2 d\Omega. \quad \textbf{(2)}$$

In this work, α is the relative strength of the penalty term. The incompressible penalty is used here is as follows:

$$R[\boldsymbol{u}(\boldsymbol{x})] = \frac{\alpha}{2}\int_{\Omega} (\nabla \cdot \boldsymbol{u}(\boldsymbol{x}))^2 d\Omega. \quad \textbf{(3)}$$

This equation penalizes non-zero divergences of the displacement field, which should be nearly zero for incompressible materials. The α parameter in either term is chosen such the R is approximately equal to the error in the image matching term at the converged solution ($\boldsymbol{u}$).

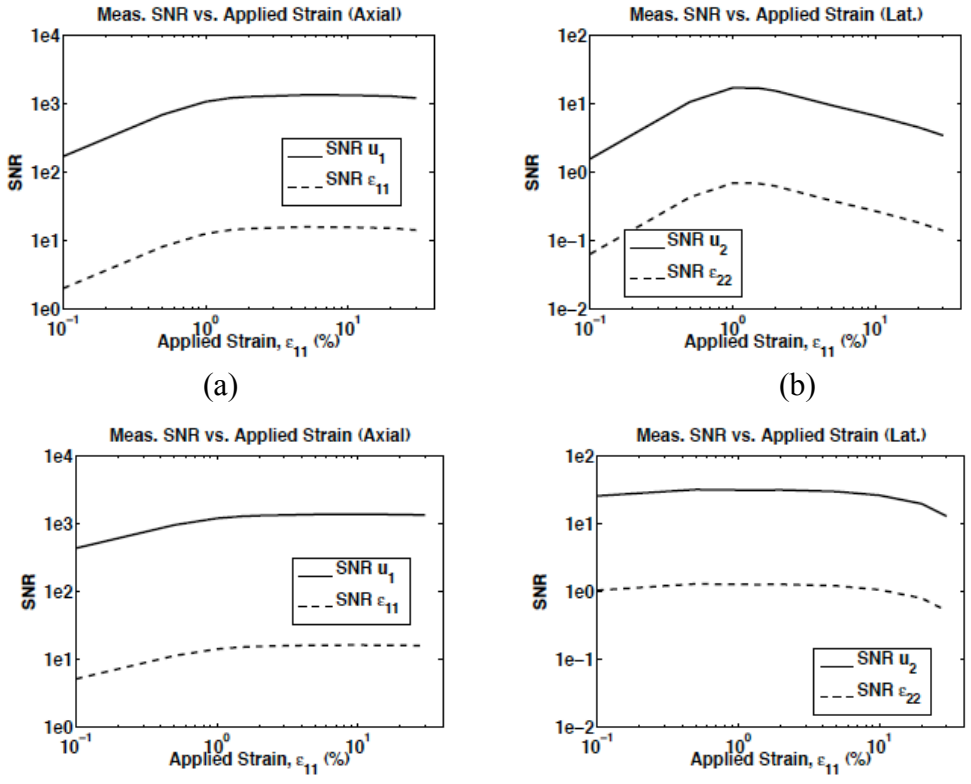

The accuracy of our algorithm was tested using simulated US images in one and two dimensions. Simulated US images were created from an analytical representation of a system point spread function (PSF) and the subsequent convolution of that PSF with point scatterers in an image field. Deforming the scatterers used in the reference image by some known displacement field and repeating the convolution yielded the post deformation images. The

displacement and strain (finite difference derivatives of the displacement field) values were quantified for their signal to noise ratios (*SNR*) and image matching quality.

Figure (a)-(d) show the SNR of the displacements and strain images for simulated 2D US images where the post-deformation image is created using a displacement field corresponding to an plane strain, axisymmetric deformation of a homogeneous block of incompressible material. That is, the deformation field has constant strain both axially and laterally at all image locations and $\nabla \cdot \boldsymbol{u}=0$. Figure (a) and (b) shows the displacement and strain SNR for the axial and lateral measurements, respectively, with no incompressibility used in the measurement. The axial strain SNR's reported here compare very well with those reported in previous work [1]. Figure (c) and (d) illustrates the improvement in SNR when the incompressibility term is utilized. Figures (e)-(g) shows an example set of two-dimensional strain images measured from experimental data of a gelatin phantom obtained using a SonixRP imaging system from Ultrasonix Inc. (Richmond, BC) and a L14-5/38 transducer. The applied strain was approximately 1.0% axially and only the regularization penalty was used in the measurement.

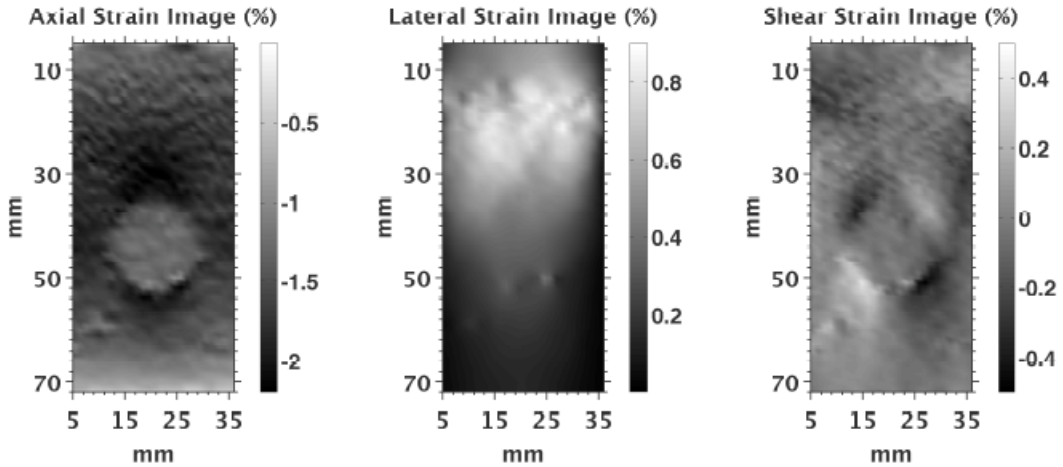

(e) (f) (g)

3. Conclusions

In this work we have developed an algorithm for the registration of images and measurement the subsequent deformation between those images. The use of physically relevant *a priori* knowledge of the displacement estimates can improve the accuracy of the full displacement vector when used as penalty terms in this algorithm.

REFERENCES

[1] J. Ophir, S.K. Alam, B. Garra, F. Kallel, E. Konofagou, T. Krouskop & T. Varghese, Elastography: ultrasonic estimation and imaging of the elastic properties of tissues, *Proceedings of the Institution of Mechanical Engineers,* 213, 203–233, 1999.

2nd International Conference on Mathematical and Computational Biomedical Engineering - CMBE2011
March 30 - April 1, 2011, Washington D.C, USA
P. Nithiarasu and R. Löhner (Eds.)

Geometric Analysis and Decomposition of 3-D Closed Surfaces for Applications in Diagnostic Medical Imaging

Jia Wu* and John C. Brigham*
*Department of Civil and Environmental Engineering, University of Pittsburgh, Pittsburgh, PA, USA, {jiw59,brigham}@pitt.edu

SUMMARY

A computational approach is presented for the quantitative comparison and statistical decomposition of three-dimensional (3-D) closed surfaces obtained from medical images. The framework relies on a novel combination of two fundamental techniques to analyze collections of surface point clouds that have been segmented from medical images. First, a mapping technique based on harmonic topological mapping is applied to uniquely redefine each surface as a continuous vector-valued function describing the shape with respect to a unified domain. A variation of the proper orthogonal decomposition method is then applied to the collection of shape functions to determine and rank the optimal set of modes (i.e., shape features) to represent the collection of surfaces. In addition to providing a unique and quantitative analysis, these methods benefit from tolerance to noise and independence from imaging modality and resolution. In the following, the computational methods are outlined and their capabilities displayed through an artificially generated data set.

Key Words: *harmonic mapping, proper orthogonal decomposition, medical imaging, shape decomposition.*

1 INTRODUCTION

There exist a multitude of pathologies that significantly and adversely affect human health and are well known to induce noticeable changes in the shape and/or mechanical behavior of certain organs or other biological structures. Medical imaging methods (such as CT, MRI, etc.) have long been aiding physicians in identifying these changes and using them to understand and diagnose pathology whenever possible. However, the shape and mechanical function of several biological structures (e.g., the right heart) continue to confound basic and clinical scientists alike. Furthermore, limitations remain in the ability to use imaging methods to noninvasively track motion and map kinematic behavior, and most importantly, there is currently no proven approach to quantitatively and arbitrarily (i.e., without *a priori* selection of simple geometric features or regions) compare multiple shapes, beyond bulk measures such as total volume or regional curvature.

To help overcome these challenges, a computational approach is proposed to analyze and compare a collection of anatomical surfaces segmented from medical images. The remaining sections are organized as follows. Section 2 provides the details of the approach, including a method for defining a unique mathematical representation of a given set of surface point clouds that allows for quantitative and arbitrary comparison between multiple surfaces, as well as a pattern recognition strategy to derive defining shape features from a collection of surfaces. Section 3 presents an example of the approach applied to a set of artificially generated shapes, followed by concluding remarks in Section 4.

2 APPROACH

The approach discussed herein assumes that 3-D, non-overlapping, closed surfaces have been previously obtained through some imaging and segmentation method, and this work deals solely with the analysis of a collection of n such surfaces. The k^{th} surface from the collection can be defined by a set of cartesian coordinates $\{\vec{x}_k\}$ (i.e., nodes) and the corresponding connectivity between the coordinates.

2.1 Surface Mapping

In order to quantitatively compare multiple surfaces, each surface must first be defined mathematically with respect to a common reference state (i.e., as a function defined over some fixed reference geometry, rather than a collection of points with respect to an arbitrary origin). Moreover, these representations should be uniquely obtained for subsequent comparisons to be meaningful and ideally require minimal user input (e.g., anatomically defined reference points). A harmonic mapping to the unit sphere is one such mapping that satisfies these constraints and has already been shown in several cases (see for example [1-3]) to provide consistently unique and non-overlapping surface representations for a wide variety of shapes. One minor limiting constraint on this approach is that it is only valid for genus-0 surfaces (due to the use of the sphere as the reference shape). However, there are several biological structures of clinical interest that are, or could be approximated as, closed genus-0 surfaces.

By definition, a harmonic mapping (i.e., change in coordinates) is simply a parameterization that satisfies Laplace's equation for each new parameter. As such, choosing the new parameters to be the spherical coordinates, ϕ (longitude) and θ (latitude), the spherical coordinates for each point on the given surface (i.e., location on the surface of the unit sphere) can be determined from the solution of the following:

$$\nabla^2\theta(\vec{x}) = 0 \quad \text{and} \quad \nabla^2\phi(\vec{x}) = 0 \quad in\ \Omega_k, \tag{1}$$

where Ω_k is the domain of the given surface (defined by $\{\vec{x}_k\}$). To uniquely define the mapping it is then only necessary to provide suitable boundary conditions for the spherical coordinates, which includes the north pole (Γ_n), the south pole (Γ_s), and the date line (Γ_d) as follows:

$$\theta = 0 \quad on\ \Gamma_n, \quad \theta = \pi \quad on\ \Gamma_s, \quad \phi = 0 \quad on\ \Gamma_d, \quad \text{and} \quad \phi = 2\pi \quad on\ \Gamma_d^o. \tag{2}$$

An important note is that the date line has a nonunique value (0 or 2π). Therefore, to produce a unique solution, the surface is separated at the date line (i.e., the date line is replicated to create Γ_d^o) with one side given the value of 0 and the other 2π.

The resulting boundary value problems described by Eqns (1) and (2) can be solved numerically for the spherical coordinates of each surface point (the present work relies on the Galerkin finite element method to solve these systems). Once mapped, each of the n surfaces can be described with respect to a common domain as $\vec{x}_k(\theta, \phi)\ \ in\ \ \theta \in (0, \pi), \phi \in (0, 2\pi)$.

2.2 Shape Mode Decomposition

Once a set of n surfaces is converted to a set of shape functions over the referential unit sphere domain, the application of a pattern recognition strategy to determine and rank the fundamental shape components that exist within the set is relatively straightforward. This work applies the method of proper orthogonal decomposition (POD), which has been used successfully in a variety of pattern recognition and reduced-order modeling applications (see [4] and the references

therein). POD is particularly beneficial to this work as it is well known to be tolerant to noise, and it can be formulated in a continuous form so that the set of shape functions can be analyzed without further processing regardless of mesh conformity (e.g., varying mesh density and/or node distribution throughout the set).

The main objective of POD is to identify the m basis functions $\{\vec{v}_i(\vec{X})\}_{i=1}^m$ that are optimal in the average sense for representing the given set of functions. Through several manipulations, including the application of the method of snapshots, this optimization problem to determine the modes can be solved through the following eigenvalue problem:

$$\frac{1}{n}\sum_{k=1}^{n} A_{jk}C_k^i = \lambda^i C_j^i, \quad A_{jk} = \int_0^{2\pi}\int_0^{\pi} \vec{y}_j \cdot \vec{y}_k d\theta d\phi, \quad C_k^i = \int_0^{2\pi}\int_0^{\pi} \vec{y}_k \cdot \vec{v}_i d\theta d\phi, \quad (3)$$

where $\vec{y}_k = \vec{x}_k - \vec{\bar{x}}$ and $\vec{\bar{x}}$ is the mean shape. The n-dimensional eigenvalue problem can then be solved to obtain at most n modes (i.e., fundamental shape components) as follows:

$$\vec{v}_i(\theta,\phi) = \frac{1}{\lambda^i n}\sum_{k=1}^{n} \vec{y}_k(\theta,\phi)C_k^i. \quad (4)$$

The corresponding eigenvalues (λ^i) relate to the relative importance of each mode, and the larger eigenvalues correspond to modes that are more significantly representative of the dataset.

3 EXAMPLE

To demonstrate the capabilities of the proposed approach, a collection of eight 3-D closed surfaces was artificially generated using three standard real-valued spherical harmonic functions as follows:

$$\vec{x}_k(\theta,\phi) = (\sum_{i=1}^{3} b_{ki}S_i(\theta,\phi))\vec{X}, \quad (5)$$

where $[S_1, S_2, S_3] = [\frac{1}{2}\sqrt{\frac{1}{\pi}}, \frac{1}{4}\sqrt{\frac{5}{\pi}}(-X_1^2 - X_2^2 + 2X_3^2), \frac{3}{16}\sqrt{\frac{1}{\pi}}(35X_3^4 - 30X_3^2 + 3)]$, b_{ki} are the randomly generated coefficients from a normal distribution, and $\vec{X} = [\sin(\theta)\cos(\phi), \sin(\theta)\sin(\phi), \cos(\theta)]^T$. To test the proposed method's ability to classify shape patterns within a set, the eight artificially generated shapes were divided into two groups of four shapes. The first group was generated only using S_1 and S_2, while the second group was generated only using S_1 and S_3.

Each shape was mapped to the unit sphere domain and then decomposed through POD to obtain a set of shape modes, as shown in the schematic in Figure 1. For this example, the eigenvalues of the first two POD modes totaled more than 99% of the sum of all eigenvalues. Therefore, the first two modes are sufficient to reconstruct the dataset and should represent the most significant features of the dataset. The two modes are then projected back onto each shape to obtain the set of modal coefficients defining the dataset. For comparison purposes the POD procedure (obtaining modes and then modal coefficients for the top two modes) was performed again for the dataset without applying the topological mapping procedure (Note: this is only possible because the dataset is artificially generated, and therefore has a known reference domain without mapping). Figure 2 shows the distribution of the modal coefficients for the two groups with and without mapping. As is expected from the method of generating the dataset, the two groups are clearly separable without mapping. More importantly, the modal coefficients after mapping are just as separable, if not more so, as without mapping.

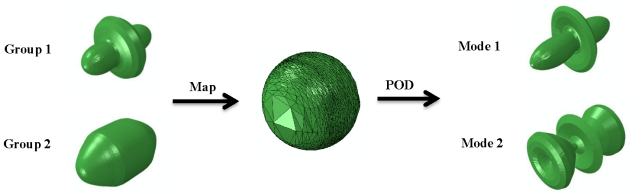

Figure 1: Mapping and POD process to obtain fundamental shape features from a set of images.

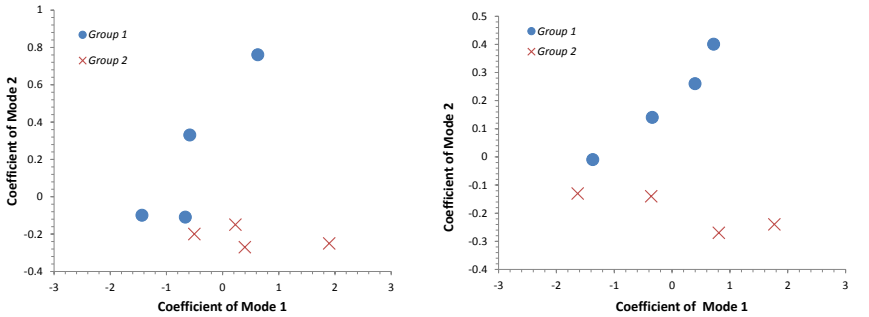

(a) (b)

Figure 2: Modal coefficients for each artificial shape (a) without mapping and (b) with mapping.

4 CONCLUSIONS

A computational framework was presented to quantitatively analyze 3-D, non-overlapping, closed surfaces, which can be used to effectively compare and analyze segmented medical images. This framework first applies a harmonic mapping technique to convert each surface into a function defined over a unified reference state, then applies the POD method to extract the fundamental modes from these functions, thereby defining the fundamental modes of the shapes themselves. These techniques are straightforward to implement and treat the data in the space of continuous functions without the need for compression to ensure preservation of all inherent shape features. Most importantly, they provide a unique and quantitative method to analyze shapes and shape changes of biological structures from medical images. The details of these methods were outlined and then demonstrated through a simple numerical example. Further comprehensive testing of this approach is currently underway, particularly with regards to the effect of imaging noise, and the long-term objective is to apply these methods to analyze and improve diagnostic procedures for right heart pathology.

REFERENCES

[1] L. Shen, J. Ford, F. Makedon, and A. Saykin, Hippocampal Shape Analysis: Surface-Based Representation and Classification, *Proceedings of SPIE - Medical Imaging*, 5032, 253-64, 2003.

[2] M.S. Floater and K. Hormann, Surface Parameterization: a Tutorial and Survey, *Advances in Multiresolution for Geometric Modelling*, IV, 157-86, 2005.

[3] C. Brechbuhler, G. Gerig, and O. Kubler, Parameterization of Closed Surfaces for 3-D Shape-Description, *Computer Vision and Image Understanding*, 61, 154-70, 1995.

[4] W. Aquino, An Object-Oriented Framework for Reduced-Order Models Using Proper Orthogonal Decomposition (POD), *Computer Methods in Applied Mechanics and Engineering*, 196, 4375-90, 2007.

2nd International Conference on Mathematical and Computational Biomedical Engineering – CMBE2011
March 30 – April 1, 2011, Washington D.C., USA
P. Nithiarasu and R. Löhner (eds)

Miniaturized Laser Speckle Contrast Imaging Microscope

Janaka Senarathna*, Kartikeya Murari*, Nan Li*, Ralph Etienne-Cummings ** and Nitish V. Thakor*

*Dept. of Biomedical Engineering, Johns Hopkins University, {dsenara1, kartik,nanli,nitish}@jhu.edu

**Dept. of Electrical and Computer Engineering, Johns Hopkins University, retienne@jhu.edu

SUMMARY

Miniaturizing image acquisition systems while retaining its original capabilities present several advantages. Specifically, adequate size reduction allows us to monitor the hemodynamic responses to natural behaviors in a rodent model. We present a novel rodent head mountable microscope architecture capable of performing both multi spectral reflectance imaging and laser speckle contrasted imaging. Housed in a 15mm diameter cylinder of 19mm height and weighting 7g it incorporates a custom built high sensitivity CMOS imager chip. Monte Carlo modeling is used to optimize and validate system design. The system was used to obtain images of the cortical vasculature of an anesthetized rat.

Key Words: Laser speckle contrasted imaging, multi-spectral reflectance imaging, Monte Carlo Modeling and rodent head-mountable microscope.

1. INTRODUCTION

Neurophysiology studies have classically employed techniques to image blood oxygenation and blood flow changes in response to functional stimulation in anesthetized animals [1]. However, the equipment associated with these methods includes bulky cooled CCD cameras and sophisticated optics. This severely limits the range of natural and realistic behaviors that can be monitored. Several prior attempts have been made to miniaturize the necessary imaging system [2, 3] but almost all of these rely upon optical fiber bundles to carry the light signals hence restraining the animal motion with a tether as well as limiting the spatial resolution. Our goal is to design and develop an integrated system capable of simultaneously performing both cerebral blood flow and oxygenation measurements in an untethered, unanesthetized animal. Blood oxygenation can be measured using multi spectral reflectance imaging (MSRI) whilst blood flow is measured using laser speckle contrast imaging (LSCI). Murari et al. [4] demonstrated a rodent head-mountable microscope for MSRI. Here, we expand on this work and present the details of optical assembly and preliminary results of a novel rodent head mountable microscope architecture that is capable of performing both MSRI and LSCI. Monte Carlo modeling of the cortical layers is undertaken to assess the capability and performance of our system.

2. SYSTEM DESCRIPTION

The optics is designed to accommodate as much miniaturization as possible. Fig. 1a shows an image of our microscope in comparison to a US quarter. We use a 670nm VCSEL (Vixar Inc, MN) cased in a 5mm diameter T046 package for laser illumination. A front surface mirror (Edmund Optics, NJ) facilitates an optical path for the laser beam to diverge and illuminate a 4mm diameter region of interest (ROI) in the target tissue. In addition a narrow bandwidth (half power full bandwidth of 25nm centred at 521nm) green LED (TT Electronics, UK) is included to serve as the second wavelength for MSRI. Light from the LED is provided an identical optical path as the laser, but along a perpendicular axis in the microscope tube cross-section. The entire assembly as shown in Fig.1b is the affixed to a rat's head to image the cortical surface through a thinned or exposed skull. LSCI is done by acquiring a stack of 80 sequential images under red laser illumination while for MSRI; the ROI is additionally imaged under green light. Time averaged raw laser speckle image is used as the other wavelength in this regard [1].

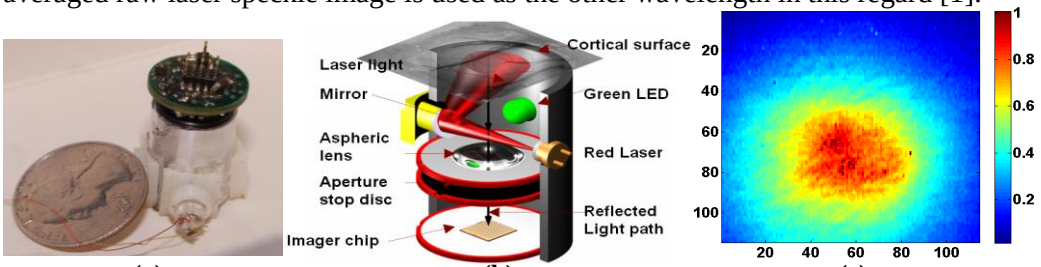

(a) **(b)** **(c)**

Figure1. The microscope architecture. (a) A photograph of the rodent head mountable microscope. (b) Detailed schematic of the imaging setup. (c) The beam profile of green LED on the focal plane with illumination intensity displayed in pseudo-color (laser profile is similar but grainier due to speckles). Each axis is marked with the number of pixels under unity magnification.

Illumination of the ROI follows a non uniform distribution as shown in Fig.1c necessitating proper normalization. Reflected light from the cortical surface is focused by a glass aspheric lens (Thorlabs, NJ) of focal length 4.6 mm and achieves a unity magnification. A lathed aperture stop of 0.375mm diameter allows the generation of speckles ~40µm in diameter ensuring optimal detection by the 20 µm [5] imager pixels .The power consumption of all light sources together is less than 4.5mW. A high sensitivity CMOS imager chip with performance comparable to a CCD camera at low light intensities [5], developed in house is utilized for the final photo-reception. It comprises a 132x124 array of 20µm pixels accessible via a pic24HJ64GP202 (Microchip Inc, AZ) microcontroller interface. The 12 bit analog to digital converter (ADC) module in the microcontroller is used to digitize the analog signals from the imager chip.

3. RESULTS

The head mountable integrated microscope was optimized and then, prototyped and tested. Design optimization involved the theoretical study of light absorption by tissue at various angles of incidence, and is described in the ensuing section.

3.1 Design optimization using Monte Carlo simulations.

Optical absorption and reflection was modelled using a Monte Carlo simulation with the dual purpose of optimizing the design as well as validating our observations. The exposed cortex was modelled as a semi-infinite homogeneous medium with scattering coefficient (μ_s) = 1 mm^{-1}, anisotropy (g) = 0.9 and refractive index (n) = 1.4 with total oxy and deoxy haemoglobin concentration as 0.085mM with a saturation level of 0.7 [6]. Absorption spectra for oxy and

deoxy haemoglobin by [7] were used. Figure 2 shows results of our simulation and tabulates the variation of two absorption properties, the absorption fraction and the absorption depth with increasing incident angle of light. Absorption fraction was defined as the ratio between the amount of light absorbed by the tissue in total and the incident amount of light. Average absorption depth was calculated by averaging the absorption over the total range of depths.

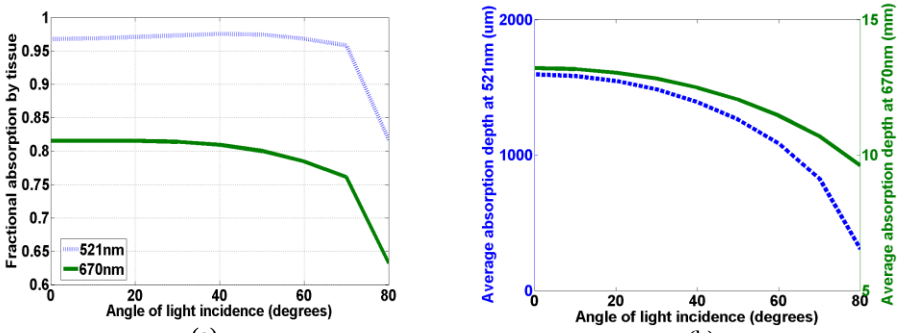

(a) (b)

Figure 2. (a) Fraction of light absorbed as a function of incident light angle. (b) Average depth of absorption as a function of incident light angle.

As displayed in Fig. 2a the angle of incidence does not critically alter the total amount of light absorption (within the majority of the range), hence allowing us the flexibility to tilt the incident light beam until an angle of 40^0 necessary due to the space constraints imposed by the physical size of optical elements within the microscope architecture. Fig. 2b demonstrates that the average depth of absorption for red light (670 nm) is an order of magnitude higher than the green light (521nm), owing to the largely reduced absorption coefficients of both oxy and deoxy haemoglobin within this region. This information allows us to estimate that green light will sufficiently penetrate (~1mm) the cortical surface at the currently utilized angle of ~40^0 and thus be capable of detecting the vasculature of interest. The higher depth of absorption of red light will inevitably introduce noise to the final MSRI calculations.

3.2 Imaging in animal experiments.

To test the feasibility and suitability of our integrated microscope for in vivo imaging, we performed experiments in an exposed skull model of the rat brain vasculature. Adult male Wistar rats were anesthetized and restrained in a stereotaxic frame following which our imager was affixed on their head as described by previously [4]. Figure 3a, b, c display a raw green light reflectance image and subsequently processed stages to enhance the structural detail. Laser speckle contrast is calculated as, $lsci(x,y) = \frac{\sigma(x,y)}{\mu(x,y)}$ with $\sigma = \sqrt{\frac{\sum_{k=1}^{N}(i(x,y,k)-\mu(x,y))^2}{N}}$ and

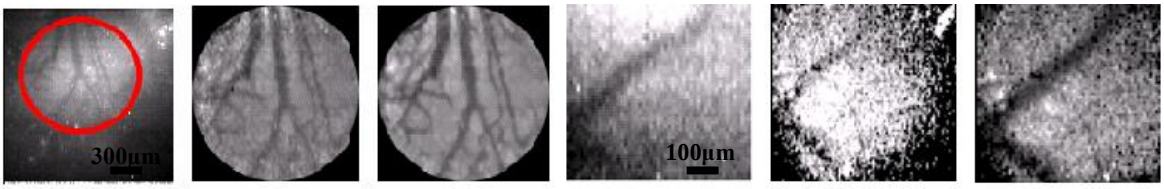

(a) (b) (c) (d) (e) (f)

Figure 3. In vivo imaging using our integrated microscope. (a) A green reflectance image with the ROI circled in red. (b) A 4X up-sampled and linear scaled image of the ROI. (c) Enhanced image of ROI obtainable through advanced offline image process techniques such as ridge detection. (d) A high magnification raw LED image of an isolated blood vessel. (e) A laser speckle contrasted image of the ROI. (f) A laser speckle contrasted enhanced offline.

$\mu = \frac{\sum_{k=1}^{N} i(x,y,k)}{N}$, where $i(x,y,k)$ refer to the intensity of (x,y) pixel in the k^{th} image frame and N is the number of frames used. Fig 3d shows a green reflectance image of an isolated blood vessel while Fig.3e, f display processed and enhanced LSCI. These results demonstrate our microscope's capability to perform both MSRI and LSCI.

4. CONCLUSIONS

We have described a first microscope architecture for acquiring both reflectance and laser speckle images in a very miniaturized head mountable footprint. System design and performance were justified by Monte Carlo simulations. Preliminary results of both green light and contrasted laser speckle images were shown. One concern is the quality of images limited by the noise floor of the ADC in the microcontroller. Further testing has shown that using a 16 bit dedicated ADC will allow for better results. Integration of the microscope with control and recording electronics in the form of a light weight backpack attachable on the rat is currently progressing. We believe that this will pave way to successfully demonstrate spectral and laser contrast imaging in awake and behaving animals for deeper understanding of neuronal behaviour withiin a realistic context.

ACKNOWLEDGEMENTS

The authors would like to thank Mr. A. Rege for valuable assistance and Mr. J. Burns for helping with the mechanical constructions. The work was supported by NIH grant R01AG029681.

REFERENCES

[1] N. Li, K. Murari, A. ReGe, P. Miao and N. Thakor, " Multifunction – laser speckle blood flow and deoxy-hemoglobin saturation – imaging of cerebrovascular response", *Proceedings of 4th International IEEE EMBS conference on Neural Engineering.* (May 2009)

[2] D. Rector, G. Poe, P. Redgrave, and R. Harper, "A miniature CCD video camera for high-sensitivity light measurements in freely behaving animals," *J. Neurosci. Methods*, vol. 78, pp. 85–91, Dec 1997.

[3] C. Engelbrecht, R. Johnston, E. Seibel, and F. Helmchen, "Ultracompact fiber-optic two-photon microscope for functional fluorescence imaging in vivo," *Opt. Express*, vol. 16, pp. 5556–5564, Apr 2008.

[4] K.Murari, E. Greenwald, R. Etienne-Cummings, G. Cauwenberghs and N.Thakor,"Design and Characterization of a miniaturized epi illuminated microscope**",** 31st Annual International Conference of the IEEE EMBS Minneapolis, Minnesota, USA, September 2-6, 2009

[5]K. Murari, R. Etienne Cummings, N. Thakor, G.Cauwenberghs, "A CMOS In-Pixel CTIA High Sensitivity Fluorescence Imager", IEEE Trans. Biomed. Circ. and Sys., accepted for publication, 2010

[6] M. Kohl, U. Lindaeur, G. Royl, M. Kuhl, L. Gold, A. Villringer and U. Dirnagl, "*Physical model for the spectroscopic analysis of cortical intrinsic optical signals*", In Phys. Med. Biol. 45 (2000) 3749 – 3764.

[7] Scot Prahl,"Tabulated Molar Extinction Coefficient for Hemoglobin in Water". (http://omlc.ogi.edu/spectra/hemoglobin/summary.html

2nd International Conference on Mathematical and Computational Biomedical Engineering – CMBE2011
March 30 – April 1, 2011, Washington D.C., USA
P. Nithiarasu and R. Löhner (eds)

Segmentation of Magnetic Resonance Images from Female Pelvic Cavity

Zhen Ma*, Renato Natal M. Jorge*, T. Mascarenhas and João Manuel R. S. Tavares***
*Faculty of Engineering, University of Porto
Rua Dr. Roberto Frias, s/n 4200-465 Porto - PORTUGAL
{zhen.ma, rnatal, tavares}@fe.up.pt
**São João Hospital and Faculty of Medicine, University of Porto
Al. Prof. Hernâni Monteiro 4200 - 319 Porto - PORTUGAL
tqc@sapo.pt

SUMMARY

Magnetic resonance imaging is currently one imaging modality for studying pelvic floor dysfunctions. In order to perform biomechanical analysis, the geometrical models of the concerned structures are needed, which implies that these structures should be segmented in the acquired image series. However, the appearances of the organs and muscles of female pelvic cavity can be easily distorted in the images by noise and partial volume effect, which leads to the failure of common segmentation algorithms. In this study, we propose algorithms to handle the segmentations of the pelvic organs and muscles in T2-weighted axial magnetic resonance images. The proposed algorithms are based on the imaging features of different structures, and use various image clues and prior knowledge for the segmentation. Implementation details and further issues are introduced and discussed. Additionally, numerical examples are included to demonstrate the effectiveness of the proposed algorithms.

Key Words: *image segmentation, pelvic floor, bladder, vagina, rectum, medical imaging, biomechanics.*

1. INTRODUCTION

Pelvic floor dysfunctions are a series of conditions that affect a large population of women. Numerous clinical studies have been done trying to unveil the causes of the symptoms [1]. However, the accurate biomechanical relationship between the pelvic organs and pelvic floor muscles remains unknown. Currently, clinical diagnosis has been considerably assisted by the use of magnetic resonance imaging (MRI) of female pelvic cavity [2]. The preprocessing of the acquired images needs a large amount of manual operations, and therefore makes the whole process very time-consuming. In order to improve the time efficiency and eliminate the intra/inter-observer errors, effective algorithms for segmentation and three-dimensional (3D) reconstruction are needed.

In this study, we focus on the segmentation algorithms. T2-weighted axial MRI was chosen as the imaging modality since the anatomy of different structures can be viewed clearly under this plane. The complex imaging background forms a big challenge for normal segmentation algorithms. Applying different types of algorithms have been discussed in [3], which concluded that effective algorithms should be based on the imaging appearances of the concerned structures.

Given the application background, the deformable models [3, 4] were chosen, mainly because of their flexibility to incorporate distinct segmentation clues. The used algorithms belong to the geometric deformable models, and use both image information and prior knowledge for the segmentation. To demonstrate the effectiveness of these algorithms, experimental examples are included and discussed in the present work.

2. METHODOLOGY

T2-weighted MRI has better imaging quality for soft tissues than other non-invasive imaging modalities. Nevertheless, the appearances of pelvic organs and pelvic floor muscles can be easily distorted in MR images by noise, or blurred by partial volume effect (PVE). Among the structures in female pelvic cavity, the levator ani (LA) muscle is the most difficult one to be successfully segmented. The LA muscle constitutes the main part of the pelvic floor muscles and usually appears as a "V" shape in the axial plane. Its large shape variance among imaging positions excludes the possibility to use prior shape knowledge, and its boundary may become discontinuous due to the influence of noise and partial volume effect. Given that the main biological function of the pelvic floor muscles is to support the pelvic organs, the status of the muscles is closely related with the status of pelvic organs. If the boundaries of pelvic organs are known, their locations and shapes can provide useful information to assist the segmentation of the LA muscle. Hence, the segmentation order adopted in this study is to first segment the pelvic organs and then the LA muscle.

2.1 Pelvic organs

Three pelvic organs are concerned in this study, which are the main structures involved in some of the pathologies related with pelvic cavity: bladder, vagina and rectum. The imaging appearances of the three pelvic organs are usually not stable and may suffer from noise influence, which makes the intensity gradient unreliable to be used in the segmentation approach. If the organs are to be segmented individually, considerable human intervention and post-processing are required in order to obtain satisfied results. Instead, our strategy is to combine the different imaging appearances of the three organs with prior shape knowledge on them, so that these organs can be segmented simultaneously. Thus, three deformable models are used: each model to segment one pelvic organ under consideration. The associated moving equations are derived based on the interactive information from the three moving contours. The main segmentation clue comes from the comparison between the intensities of the pelvic organs and the surrounding tissues. For example, the bladder lumen in T2-weighted images has high signal intensities because of the urines within it, while the bladder wall has low signal intensities. Both the vagina and the rectum have low signal intensities, while their intensity distributions are appreciably distinct. Additionally, the tissues that surround the pelvic organs have intermediate signal intensities, and their appearances are more similar to the bladder lumen than the vagina and rectum. With these clues, the region competition algorithm in [5] was modified and integrated in the used algorithms. As the boundary of the vagina can be easily blurred by noise and PVE, and the inner layer of the rectum can cause unwanted inner boundaries, prior shape knowledge of the two organs is used to handle these problems and further eliminate noise influence. The pelvic organs can be successfully segmented by the adopted coupling system that uses the intensity comparison as the main segmentation clue.

2.2 Levator ani muscle

Based on the spatial relationships between the pelvic organs and the levator ani muscle, the location of the muscle can be approximately identified to a region of interest (ROI). Normally, in

the ROI the levator ani muscle has the lowest signal intensity, and the segmentation of this muscle is a two-phase problem. However, due to the noise influence, some parts of the levator ani muscle may appear as pixel clusters. The intensity gradient again becomes unfeasible to be used in the segmentation process. To overcome this problem, the Chan-Vese model in [6] is chosen as the base model, which can segment objects whose boundaries cannot be defined through the intensity gradient. Nevertheless, due to the partial volume effect, the connective tissues between the rectum and the levator ani muscle can have a similar appearance as the muscle. Therefore, results of the C-V model tend to combine the boundaries of the two structures. A pushing force is needed to drive the upper contour to the correct position. As discussed before, no prior shape knowledge of the muscle is available because of its large shape variation. Given that the status of the rectum can reflect the deformation of the muscle, a shape influence field is defined using the boundary of the rectum [7], and is incorporated to the C-V model. The shape influence field can provide a pushing force when the upper contour is not at the correct position. The proper boundary of the levator ani muscle can then be effectively segmented by the shape guided C-V model.

3. RESULTS AND CONCLUSIONS

Two segmentation examples are illustrated in Fig. 1, in which the inhomogeneous intensity distributions of the pelvic organs, the thin appearances of the vagina, and the different layers of the rectum can be observed. One can see the boundaries of the pelvic organs were successfully segmented by the used algorithms. Furthermore, with the acquired rectum boundary, the levator ani muscles were correctly segmented.

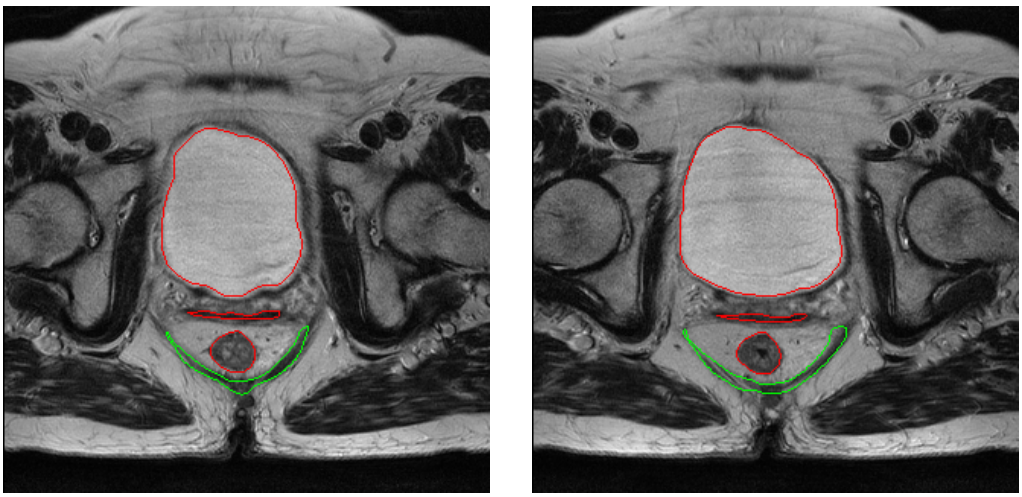

Fig. 1 Segmentation results of the used algorithms. Boundaries from up to down: bladder, vagina, rectum, and levator ani muscle.

The algorithms used in this study provide an efficient way to segment the organs and muscles in the female pelvic cavity. The three pelvic organs can be segmented simultaneously by the coupling system that consists of three deformable models. With the obtained rectum boundary, a shape influence field can be defined and incorporated into the C-V model in order to segment the boundary of the levator ani muscle successfully.

The used algorithms combine the interactive image information with prior knowledge to handle the segmentation, and their effectiveness has been verified through several case studies, with comparisons to the results obtained by manual segmentations.

4. ACKNOWLEDGEMENTS

This work was partially done in the scope of the projects “BIOPELVIC-Study of Female Pelvic Floor Disorders”, “Methodologies to Analyze Organs from Complex Medical Images – Applications to Female Pelvic Cavity”, “Aberrant Crypt Foci and Human Colorectal Polyps: mathematical modelling and endoscopic image processing” and “Cardiovascular Imaging Modeling and Simulation - SIMCARD”, with references PTDC/EEA-CRO/103320/2008, UTAustin/MAT/0009/2008 and UTAustin/CA/0047/2008, respectively, financially supported by FCT - Fundação para a Ciência e a Tecnologia in Portugal.
The first author would like to thank FCT for his PhD grant with reference SFRH/BD/43768/2008.

REFERENCES

[1] G. M. Buchsbaum, E. E. Duecy, L. A. Kerr, L. S. Huang, and D. S. Guzick, Urinary incontinence in nulliparous women and their parous sisters, Obstetrics & Gynecology, 106, 1253-1258, 2005.

[2] S. Paramasivam, A. Proietto, and M. Puvaneswary, Pelvic anatomy and MRI, Best Practice & Research in Clinical Obstetrics & Gynaecology, 20, 3-22, 2006.

[3] Z. Ma, J. M. R. S. Tavares, R. N. M. Jorge, and T. Mascarenhas, A review of algorithms for medical image segmentation and their applications to the female pelvic cavity, Computer Methods in Biomechanics and Biomedical Engineering, 13, 235-246, 2010.

[4] S. J. Osher and J. A. Sethian, Fronts propagating with curvature-dependent speed: algorithms based on Hamilton-Jacobi formulations, Journal of Computational Physics, 79, 12-49, 1988.

[5] T. Brox and J. Weickert, Level set segmentation with multiple regions, IEEE Transaction on Image Processing, 15, 3213-3218, 2006.

[6] T. F. Chan and L. A. Vese, Active contour without edges, IEEE Transaction on Image Processing, 10, 266-277, 2001.

[7] Z. Ma, R. N. M. Jorge, and J. M. R. S. Tavares, A shape guided C-V model to segment the levator ani muscle in axial magnetic resonance images, Medical Engineering & Physics, 32, 766-774, 2010.

2nd International Conference on Mathematical and Computational Biomedical Engineering - CMBE2011
March 30 - April 1, 2011, Washington D.C, USA
P. Nithiarasu and R. Löhner (Eds.)

INTEGRATING COMPUTATIONAL BIOMECHANICS AND ULTRASOUND SIMULATIONS TO IMPROVE ULTRASONIC VISUALIZATION AND QUANTIFICATION OF ARTERIAL MECHANICS

Abigail Swillens[⋆], Lasse Lovstakken[⋆⋆], Joris Degroote[⋆⋆⋆], Jan Vierendeels[⋆⋆⋆] and Patrick Segers[⋆]
[⋆]IBiTech-bioMMeda, Ghent University, Belgium, abigail.swillens@ugent.be
[⋆⋆]Department of medical imaging and simulation, NTNU, Trondheim, Norway
[⋆⋆⋆]Department of flow heat and combustion mechanics, Ghent University, Belgium

SUMMARY

Vascular imaging with ultrasound still shows severe limitations and further development of new imaging and signal-processing techniques is required. Since in-vitro or in-vivo setups do not offer sufficiently accurate information on the actually imaged blood vessel behavior, there is a need for a simulation tool where synthetic ultrasound (US) images can be validated towards a ground truth. We developed a simulation environment integrating computational biomechanics and US-simulations. First, CFD was coupled with US-simulations, which allowed to model US-images resulting from complex flow fields. This method is however limited by the absence of the moving vessel wall and therefore, we expanded the multiphysics tool by integrating fluid-structure interaction simulations with the US-simulator. An overview of the methodology to couple these different simulation strategies is given. The potential of these multiphysics simulations is demonstrated with the investigation of color flow imaging in a rigid and flexible blood vessel model.

Key Words: *CFD, FSI, ultrasound simulations, carotid artery.*

1 INTRODUCTION

In the context of early detection of cardiovascular diseases, ultrasonic imaging is often applied in clinical practice due to its non-invasive and radiation-free nature. Although today's ultrasound scanners are the result of numerous advances in several research areas, still many of the imaging goals are not fully achieved. Of note, vascular imaging shows several limitations: (i) only 1D blood flow measurements can be performed, visualizing the velocity component along the scanline, (ii) assessment of mechanical properties of arteries and plaques has only been investigated to a limited extent, with arterial distension estimation the most successful application so far. Hence, improved imaging and post-processing methods are needed.

2 METHODS AND APPLICATIONS

2.1 Overall modeling approach

Imaging development requires proper testing and validation, nowadays based on in-vitro and in-vivo setups. However, these do not allow proper validation of ultrasound (US) images, since the

imaged flow field and/or vessel wall deformation is not known and, other measurement techniques, also prone to errors, are necessary to reveal the true blood vessel behavior behind the US-image. A simulation environment which creates synthetic US-images from fully known hemodynamics and vessel wall mechanics would therefore be highly useful. An important tool in this context is Field II [1]. This software allows to model any linear imaging setup with advanced transducer geometries, scan sequencing and beam formation. The backscattered radiofrequent (RF) signals are obtained by modeling tissue as a distribution of point scatterers on which US-waves reflect. Hence, realistic US-images of arbitrary vessel behavior can be simulated, by moving the scatterers during the simulated scan according to realistic blood velocities and structural displacements. The total scatterer number is related to the imaging resolution and the scattering strength is modeled using a normal distribution of scattering amplitudes with mean and standard deviation adapted to the tissue properties.

However, because of the complex arterial geometries and vascular material properties, the scatterer movement cannot be obtained through analytical solution of the equations governing the blood flow and vascular wall behavior. Complex numerical techniques are required for this purpose. In a first phase, we studied ultrasonic blood flow imaging methods in a carotid artery, by deriving blood velocities from computational fluid dynamics (CFD) and using them as an input to Field II [2]. A realistic 3D vascular geometry and mesh was reconstructed from medical scans with the software Mimics (Materialise, Leuven, Belgium) and the CFD-problem was solved with Fluent 6.2 (Fluent Inc., Sheffield, UK).

This simulation strategy is however limited by the absence of the vessel wall. Therefore, we extended the computational phantom to allow for the simulation of the integral blood vessel behavior, by moving scatterers according to blood velocities and mechanical deformations obtained from fluid-structure interaction (FSI) simulations. FSI-modeling allows to simultaneously solve the blood flow and vessel wall deformation problem, by taking into account their mutual influence [3]. We used a partitioned FSI-approach, computing the flow and structural equations with a separate flow and structural solver. An in-house code 'Tango' was used to couple the flow solver Fluent and the structural solver Abaqus (Simulia, Inc., Providence, RI, USA). In particular, Dirichlet-Neumann partitioning was used (flow problem is solved for a given displacement; structural problem is solved for a stress boundary condition applied on wet side of the structure). To enhance convergence of the coupling, an Interface Quasi-Newton method was used, which replaces the complex fluid or solid solver on the interface by approaching the Jacobian of the solver on the interface [4]. For a complete overview on the applied methodology, we refer to fig. 1.

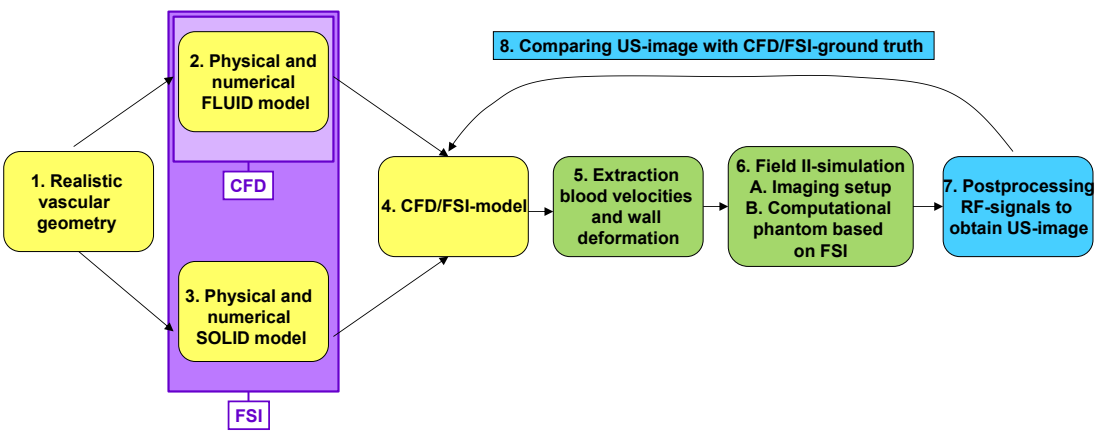

Figure 1: A flowchart illustrating the methodology of the ultrasound simulation environment

2.2 Rigid wall models

To couple the CFD-data to the positions of the point scatterers, 3D spatial interpolation of the CFD-velocities is executed in Matlab. Further, due to the large disparity in time scales between CFD (order ms) and US simulations (e.g. 0.067 ms for a frequency of the pulse excitations of 15 kHz), temporal interpolation of the CFD-velocities is necessary.

2.3 Distensible wall models

When integrating FSI and Field II, both the scatterer phantom of the blood pool and vessel wall require a more advanced approach. The fluid phantom in particular is highly challenging as straightforward interpolation techniques are no long applicable due to the changing fluid volume and the FSI-grid formulation (Arbitrary Lagrangian Eulerian method to match grid formulations for fluid and solid domain). Therefore, the scatterer displacement is approximated by updating scatterer velocities each FSI-timestep. To avoid that scatterers are displaced outside the fluid domain in a shrinking geometry or that voids are created in an expanding geometry, scatterers are displaced using the velocity vector from the subsequent FSI timestep, with the velocity vector extracted from an approximated mapped position at that timestep. This approach is justified due to the Backward Euler time discretization used by the flow solver. It provides correct displacements for scatterers at the fluid-structure interface, but it is an approximated approach within the flow field (cfr. fig.2).

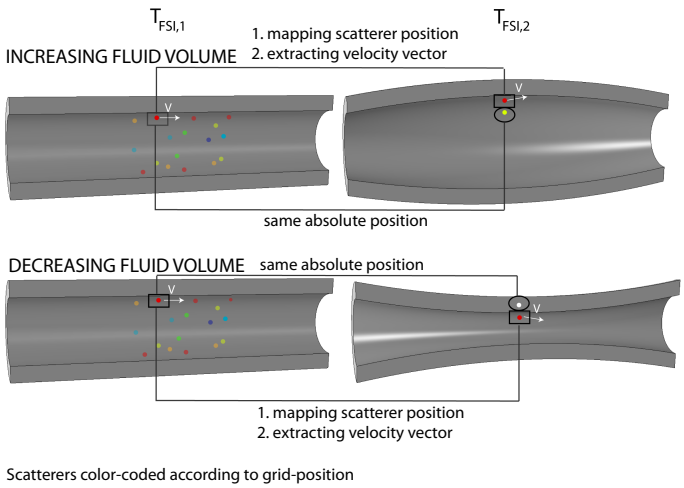

Figure 2: Principles behind the generation of the fluid phantom based on FSI-simulations

The structure phantom generation is less complex because the grid displacement corresponds with the material displacement and hence also with the scatterer displacement. However, the vessel wall needs more refined scatterer generation due to its complex composition, with flexibility of defining different scattering properties in different vessel regions. Besides these random scatterers, specular reflections at the transition regions between different tissue types (i.e. tissue/vessel wall and vessel wall/blood) are mimicked by placing scatterers at fixed distances along these interfaces.

2.4 Applications

Both with the distensible and rigid wall model, a commonly applied 1D blood flow estimator was investigated, i.e. color flow imaging (CFI). Panel A of fig.3 shows the comparison between CFI in the carotid artery during systolic deceleration and the true flow field known from CFD. Note that the CFD-data take into account the exact timing and positioning of the US-scanning sequence. It can be seen that CFI has difficulties capturing complex flow patterns. Panel B shows

a color M-mode image (color-coded velocities along a scanline during cardiac cycle) resulting from blood flow in a straight tube, representative of the common carotid artery. For this case, the US-simulations were based on FSI-data, as can be seen in the fluctuating blood flow domain (panel B).

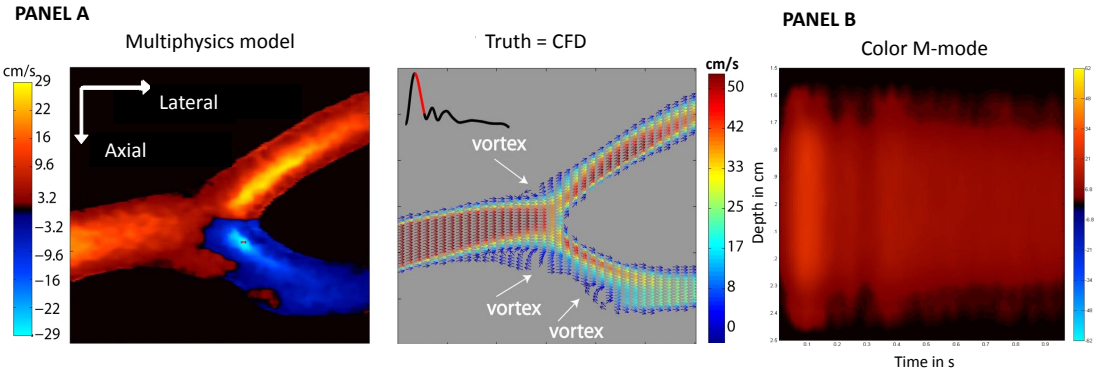

Figure 3: Panel A: comparison between color flow imaging and true flow field known from CFD. Panel B: Color M-mode image based on FSI-simulations in common carotid artery.

3 CONCLUSIONS

Coupling computational biomechanics and US-simulations provides realistic RF-signals from both tissue and blood which can be processed into US- images and measurements. Note, however, that simulations cannot include all the physical phenomena involved in the image formation process. Still, this simulation environment allows validation towards a gold standard, which is not possible for in-vitro or in-vivo testing, and as such this simulation tool has an important complimentary role to in-vitro/in-vivo validation.

REFERENCES

[1] Jensen JA (1996). Field: A program for simulating ultrasound systems. Med. Biol. Eng. Comput. 34, 351-353

[2] Swillens A, Lovstakken L, Kips J, Torp H and Segers P. (2009). Ultrasound Simulation of Complex Flow Velocity Fields Based on Computational Fluid Dynamics. IEEE TUFFC 56, 546-556.

[3] Swillens A, Degroote J, Vierendeels J, Lovstakken L, and Segers P (2010). A simulation environment for validating ultrasonic blood flow and vessel wall imaging based on fluidstructure interaction simulations: ultrasonic assessment of arterial distension and wall shear rate. Medical Physics 37(8), 43184330.

[4] Degroote J, Bathe KJ and Vierendeels J (2009). Performance of a new partitioned procedure versus a monolithic procedure in fluid-structure interaction. Computers and Structures 87, 793-801

2nd International Conference on Mathematical and Computational Biomedical Engineering – CMBE2011
March 30 – April 1, 2011, Washington D.C., USA
P. Nithiarasu and R. Löhner (eds)

IMAGE-BASED 3D SHAPE RECONSTRUCTION OF ABDOMINAL AORTIC ANEURYSM

Kenji Shimada

Carnegie Mellon University, Pittsburgh, PA 15213, U.S.A., shimada@cmu.edu

SUMMARY

This paper presents an effective computational method for reconstructing the three-dimensional shape of an abdominal aortic aneurysm (AAA) from a limited number of computed tomography (CT) images. The three-dimensional template geometry of a healthy abdominal aorta is used as a priori knowledge, and the template geometry is deformed by extended free-form deformation (EFFD) to generate a patient-specific AAA geometry. A two-step optimization scheme is devised to find an optimal set of deformation parameters that match the cross-section of the deformed template with the AAA contour shown in a CT image. The geometric continuity of the deformed model is maintained by raising the order of the polynomial function used in EFFD. Experimental results show that the proposed method creates the three-dimensional shape of AAA suitable for structural finite element analysis and computational fluid dynamics for medical diagnosis.

Key Words: *Shape reconstruction, free-form deformation, continuity control, abdominal aortic aneurysm*

1. INTRODUCTION

A patient-specific 3D AAA shape is the foundation for a biomechanical analysis of AAA to assess the risk of rupture. Recently, researchers have successfully performed computational fluid dynamics analyses, structural analyses, and fluid-structure interaction analyses using patient-specific AAA geometry. In these analyses, however, the generation of the patient-specific 3D AAA shape remains a time-consuming process that requires a considerable amount of manual intervention.

The conventional method of image-based 3D shape modelling consists of two steps: image segmentation and shape generation. Although there are effective algorithms available for the second step [1], the first step of image segmentation usually requires manual intervention and thus is time and labor intensive.

2. COMPUTATIONAL METHOD

In this study, an efficient computational technique for reconstructing a three-dimensional shape of AAA from a set of tomographic cross-sections is proposed [2, 3, 4]. The method enables automatic reconstruction of a patient-specific AAA shape from a limited number of CT images (see Figure 1(a)). The three-dimensional template geometry of a healthy abdominal aorta, as illustrated in Figure 1(b), is used as a priori information, and the template geometry is deformed by extended free-form deformation (EFFD) [5] as shown in Figure 1(c). A two-step optimization scheme is devised to locate an optimal set of EFFD parameters that match the cross-section of the

deformed template with the AAA contour shown in a CT image. The geometric continuity of the deformed model is achieved by raising the order of the polynomial function used in EFFD.

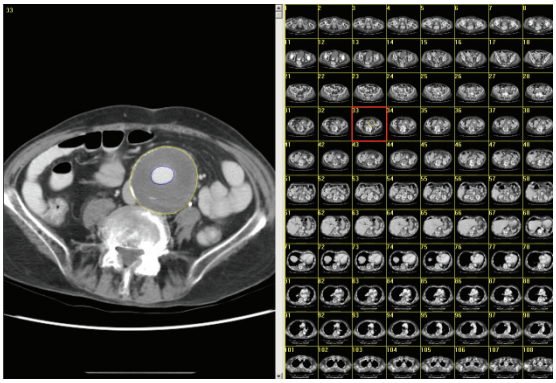

(a) Input CT images of an abdominal aortic aneurysm

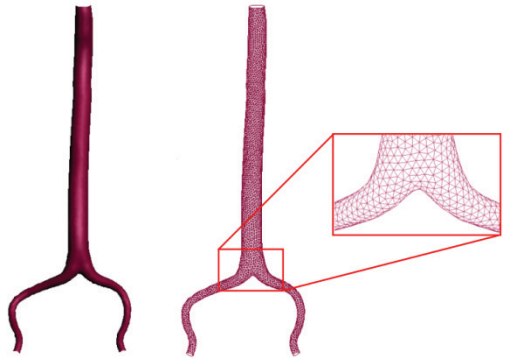

(b) 3D shape template of a healthy abdominal aorta

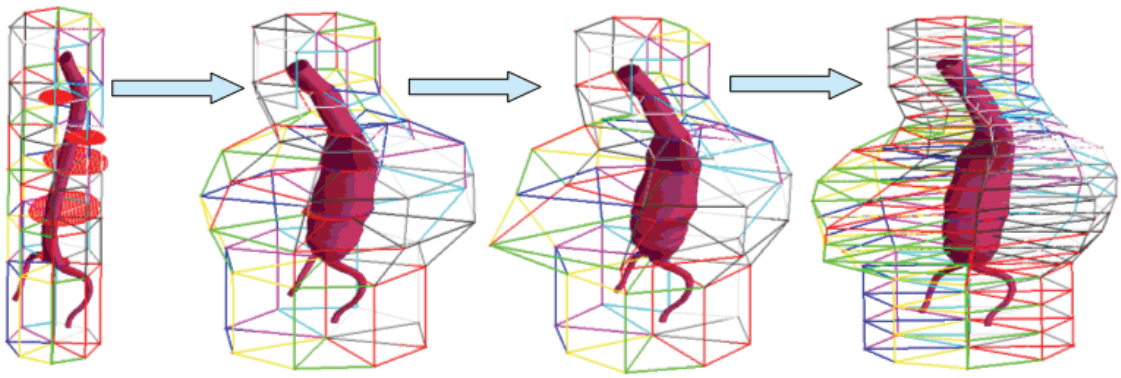

(c) The 3D shape template is deformed by the optimization of the control parameters of extended free-form deformation. The left-most image shows the template with four contour plots from input CT images

Figure 1. The proposed method takes as input CT images and a 3D shape template of a healthy abdominal aorta, and deforms the template until the cross-sectional shapes of the deformed model matches the input images.

The template is represented as a shell of a polygonal mesh, consisting of a set of vertices and a set of triangular faces. The triangular boundary representation of the template makes it easy to calculate a planar cross section. It is important that there be no gap or overlap between faces; any gap or overlap will make it difficult to create a quality mesh for structural finite element analyses or for computational fluid dynamics. The resolution of the template should be fine enough to maintain shape features after the template is deformed. Our current template polygonal model consists of 8,823 triangular polygons.

In order to solve the two-step optimization problem, we use the sequential quadratic programming (SQP) algorithm, one of the most effective methods for solving optimization problems with significant nonlinearity. Previously developed sequential quadratic programming code, CFSQP [6], is used in this study – this is a C implementation of a modified version of SQP that generates feasible iterations.

Five case studies have been performed to verify the effectiveness of the proposed method. The converging history and computational time were investigated in order to evaluate the performance of EFFD. Figure 2 shows the convergence of the external-wall shapes of an AAA

obtained from 10, 15, and 20 CT images. The shapes converge quickly in the initial EFFD process and slowly in the EFFD optimization process. In the initial EFFD process the distance between two contours was fitted by locating an optimal radius on each image via one-variable optimization. On the other hand, in the EFFD optimization process the distance between two contours was reduced gradually and iteratively by the CFSQP optimizer.

As illustrated in Figure 3, when 15 or more contours are given as input, the average area error is reduced to less than 5%, which is considered sufficient for structural finite element analysis and computational fluid dynamics analysis. This was the same in all the other case studies. The number of iterations required to optimize the deformation parameters using CFSQP is shown in Figure 4. The optimization process takes a couple of minutes for 15 input images.

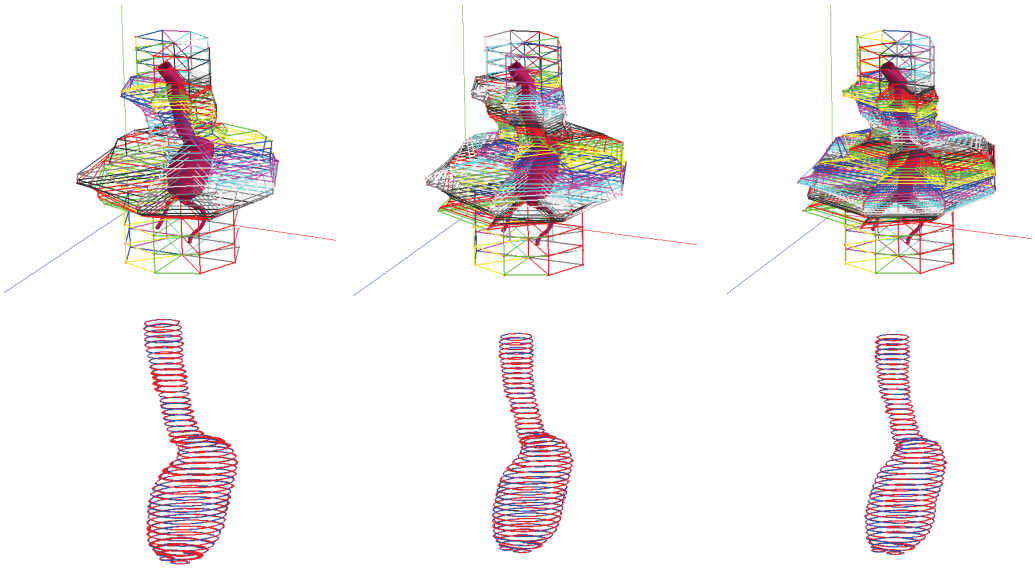

(a) 10 input images (b) 15 input images (c) 20 input images

Figure 2 3D shape reconstructed from different numbers of input images

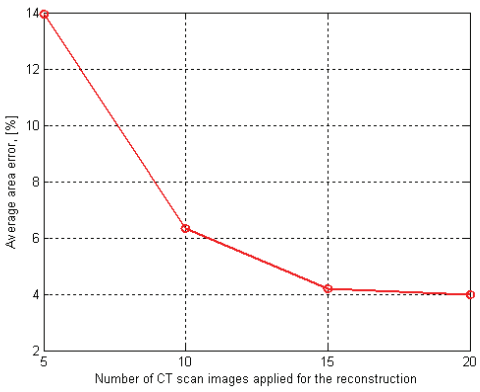

Figure 3 Convergence of the shape reconstruction error

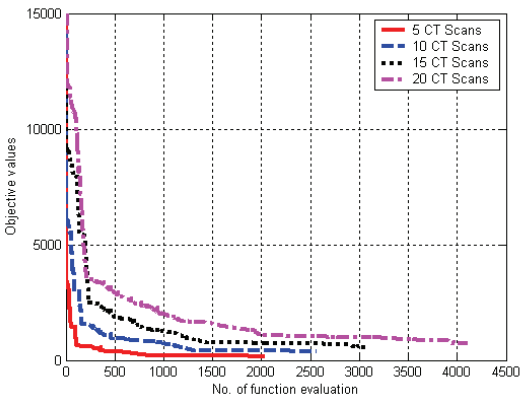

Figure 4 Number of iterations required in the optimization of the deformation parameters

3. CONCLUSIONS

The proposed method has two advantages: (1) the method reconstructs a patient-specific three-dimensional shape quickly, automatically and robustly by using a template geometry, and (2) the method always generates a topologically and geometrically valid shape for structural finite element analyses and computational fluid dynamics for medical diagnosis.

REFERENCES

[1] Bajaj, C.L., E.J. Coyle, K-N. Lin, "Arbitrary topology shape reconstruction from planar cross sections," Graphics Models and Image Processing, 58(6):524–43, 1996.

[2] Shimada, K., K. Krause K, R. Mendicino, L. Weiss, and T. Kanade, "Computer-aided bone distraction," US Patent, US6.701.174. 2004.

[3] Gunay, M., M. Shim, and K. Shimada, "Cost- and Time-effective Three-Dimensional Bone-Shape Reconstruction from X-ray Images," the International Journal of Medical Robotics and Computer Assisted Surgery, Vol. 3, Issue 4, pp.323-35, 2008.

[4] Shim, M., M. Gunay, and K. Shimada, "Three-dimensional shape reconstruction of an abdominal aortic aneurysm form computer tomography images using extended free-form deformation," Computer-Aided Design, Vol. 41, Issue 8, pp.555-565, 2009.

[5] Coquillart, S., "Extended free-form deformation: A sculpturing tool for 3D geometric modeling," ACM SIGGRAPH 24(4):187–96, 1990.

[6] C. Lawrance, et al.. "User's Guide for CFSQP Version 2.3: A C Code for solving (LargeScale) Constrained Nonlinear (minimax) Optimization Problems, Generating Iterates Satisfying All Inequality Constrains," Electrical Engineering Department and Institute for Systems Research, University of Maryland, College Park, MD, USA, 1994.

2nd International Conference on Mathematical and Computational Biomedical Engineering - CMBE2011
March 30 - April 1, 2011, Washington D.C, USA
P. Nithiarasu and R. Löhner (Eds.)

LARGE SCALE CONTINUUM ELECTROMECHANICAL CARDIAC SIMULATIONS

P. Lafortune*, R. Arís*, M. Vázquez*, G. Houzeaux*, and A. Jérusalem**
*Barcelona Supercomputing Center, Campus Nord UPC, Barcelona, Spain,
mariano.vazquez@bsc.es
**IMDEA Materials Institute, Madrid, Spain

SUMMARY

This paper describes an electromechanical simulation of the heart scalable to thousands of processors. The heart is a multiscale/multiphysics system, ranging from molecular (ion) up to organ level (muscle). Each system is governed by a set of partial differential equations, ultimately coupled together. Building on such approach, a multiscale massively parallel continuum model describing the activation potential propagation at the molecular level and its coupling with the mechanical deformation at the macroscopic level is proposed here. This model is implemented in Alya, a parallel computational mechanics platform developed at BSC.

Key Words: *electrophysiology, cardiac mechanics, parallelization, multiphysics, continuum model*

1 INTRODUCTION

This paper is the last of a set of conference contributions and articles [1,2,3,4,5] which describe a parallel computational model of the heart. The authors continue with the simulation tests of the electromechanical coupling.

The heart is a physical system integrating various models that have different time and length scales. In this study, the activation potential is coupled to the mechanical deformation via a simple equation describing the rise of intracellular calcium. Our methodology present two main advantages. Firstly, Alya assures the needed flexibility for developing the multiphysics model in the same framework. Secondly, the model is efficiently calculated in parallel on up to thousands of cores.

2 ELECTROMECHANICAL MODEL

The main elements of our scheme are:

- Electrophysiological model: FitzHugh-Nagumo and Fenton-Karma models [6]. Anisotropic fiber model. Finite elements, explicit in the case of monodomain and solved in non-structured meshes.
- Mechanical model: The total stress is the sum of a passive and an active contributions. The passive behavior is based on a law proposed by Holzapfel and Ogden [7]. The material is considered orthotropic and compressible. A local fiber-sheet-normal coordinate system is defined for every node of the mesh. The active part is transversely isotropic, with the active stress generated along the fiber direction.

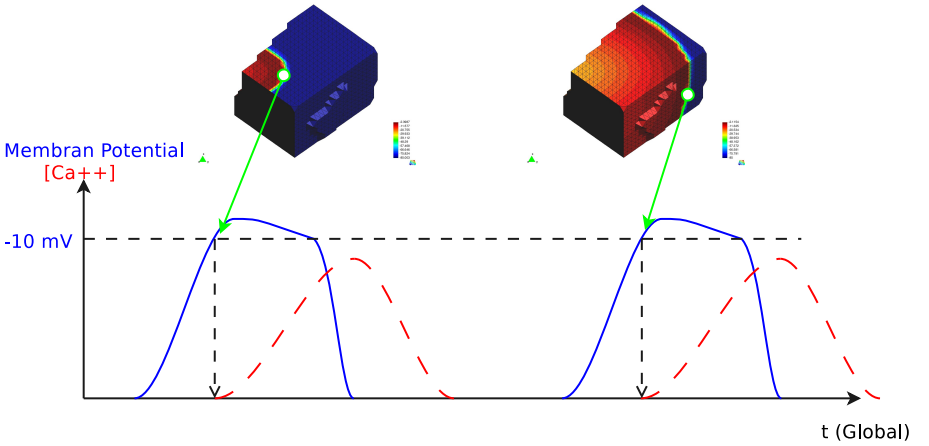

Figure 1: The temporal evolution of electromechanical coupling is shown on a small myocardium sample (top). The colors represent the activation potential. The electrical wave (continuous line) triggers the increase of the free calcium concentration (dash line).

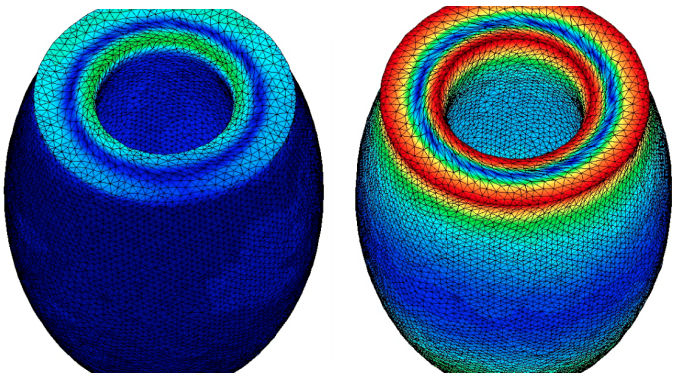

Figure 2: Simplified ventricular contraction and the effect of fibers, colored according to the displacement norm. Left: initial mesh. Right: final mesh.

- Coupling: As the wave propagates through the myocardium, a tensile force is created in the muscle cells (the *active contribution*). This force is function of the fiber's stretch and calcium concentration. This causes the myocardium to contract.
- Wall pressure: Windkessel model.

The model is programmed in Alya, the BSC in-house parallel platform. An explicit total Lagrangian finite element method accounting for large deformation is used. The model scalability has been tested on up to 5000 cores in the Marenostrum IBM blade center and in Blue Gene L and P clusters. Alya's parallelization is hybrid: MPI and automatic mesh partition with Metis and OpenMP directives for inner loops taking profit of local shared-memory multicores. This has allowed the authors to run cases with up to 40 million elements for a full contraction cycle (0.4 s) in $\sim$ 6 hours. The maximum amount of degrees of freedom for such coupled cases is of 400 M d.o.f.

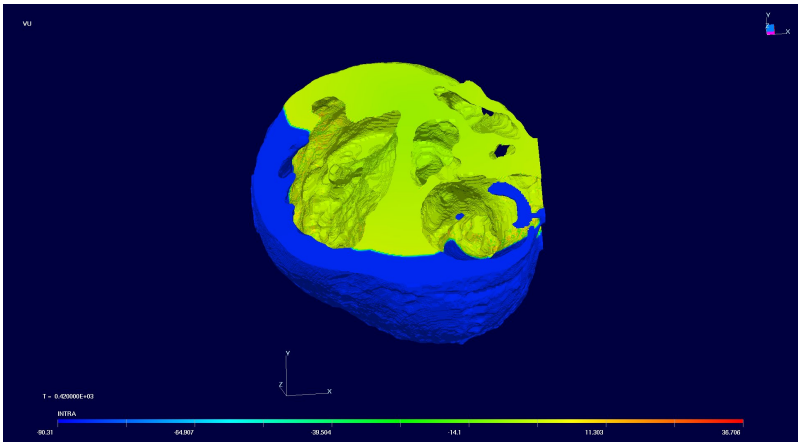

Figure 3: Activation potential on a 16M tetrahedra mesh heart (geometry provided by D. Gil and J. Garcia-Barnés, CVC, Spain).

3 CONCLUSIONS

The paper presents a coupled electromechanical simulation of the heart scalable to thousands of processors. The authors have tested the model through a set of benchmarks of increasing complexity, from a few elements up to millions of elements for a full heart.

REFERENCES

[1] M. Vázquez, R. Arís, A. Rosolen and G. Houzeaux. A High Performance Computational Electrophysiology Model Presented at the 8th. World Congress on Computational Mechanics (WCCM8) 5th European Congress on Computational Methods in Applied Sciences and Engineeering (ECCOMAS 2008). Venice, Italy. 2008

[2] D. Gil, J. Garcia-Barnes, M. Vázquez, R. Arís and G. Houzeaux Patient-Sensitive Anatomic and Functional 3D Model of the Left Ventricle. Presented at the 8th. World Congress on Computational Mechanics (WCCM8) 5th European Congress on Computational Methods in Applied Sciences and Engineeering (ECCOMAS 2008). Venice, Italy. 2008

[3] M. Vázquez, R. Arís, P. Lafortune, P. Villar, G. Houzeaux, D. Gil, J. García-Barnés, M. Ballester-Rodés and F. Carreras. Massively parallel electromechanical model of the heart. Presented at the 9th. International Symposium on Computer Methods in Biomechanics and Biomedical Engineering (CMBBE2010). Valencia, Spain. 2010.

[4] F. Rubio, M. Hanzich, R. Arís, G. Houzeaux and M. Vázquez. Parallel computational electrophysiology in Cell/B.E. Processors. Presented at the 1st. Computational and Mathematical Biomedical Engineering International Conference. (COMPBIOMED2010). Swansea, UK. 2009.

[5] M. Vázquez, R. Arís, G. Houzeaux, R. Aubry, P. Villar, J. García-Barnés, D. Gil and F. Carreras. A massively parallel computational electrophysiology model of the heart. Submitted to *Int. J. Num. Meth. Biomed. Eng.*, 2010.

[6] R. A. FitzHugh. Impulses and physiological states in theoretical models of nerve. *Membran Biophys J*, 1:445-466, 1961.

[7] G.A. Holzapfel and R.W. Ogden. Constitutive modelling of passive myocardium: a structurally based framework for material characterization. *Philosophical Transactions of the Royal Society*, 367(1902):3445-3475, 2009.

2nd International Conference on Mathematical and Computational Biomedical Engineering - CMBE2011
March 30 - April 1, 2011, Washington D.C, USA
P. Nithiarasu and R. Löhner (Eds.)

MODEL ADAPTIVE METHODS FOR THE BIDOMAIN EQUATIONS IN ELECTROCARDIOLOGY

Luca Gerardo Giorda[⋆], Lucia Mirabella[⋆⋆], Mauro Perego[⋆⋆⋆] and Alessandro Veneziani[⋆⋆⋆⋆]
[⋆] Department of Biology, Emory University, Atlanta (GA), USA, lgerard@emory.edu
[⋆⋆] WH Coulter Department of Biomedical Engineering, GA Tech, Atlanta (GA), USA, lucia@biomed.gatech.edu
[⋆⋆⋆] Department of Scientific Computing, Florida State University, Tallahassee (FL), USA, mperego@fsu.edu
[⋆⋆⋆⋆] Department of Mathematics & Computer Science, Emory University, Atlanta (GA), USA, ale@mathcs.emory.edu

SUMMARY

The Bidomain model is nowadays one of the most accurate mathematical descriptions of the action potential propagation in the heart. However, its numerical approximation is in general fairly expensive as a consequences of the mathematical features of this system. For this reason, a simplification of this model, called Monodomain problem is quite often adopted in order to reduce computational costs. Reliability of this model is however questionable, in particular in the presence of applied currents and in the regions where the upstroke or the late recovery of the action potential is occurring. In this talk we present some methods we have developed in the last years for solving numerically the Bidomain equations. We have investigated model-adaptive solvers, such that the Bidomain system is solved only in the critical regions that require high accuracy [2,3]. The *a-posteriori* error estimator and the mixed Bi-Monodomain domain-split problem will be discussed. Suitable boundary conditions for the matching between the Bidomain and the Monodomain models will be presented. Results both on idealized benchmarks and on real geometries retrieved from SPECT images show the effectiveness of the approach proposed.

Key Words: *Electrocardiology, Model adaptivity, Domain Decomposition, Time adaptivity* .

1 INTRODUCTION

Mathematical features of the Bidomain model for the propagation of the electric potential in the heart induce some numerical difficulties in its numerical approximation that lead to ill conditioned problems. For this reason many efforts have been devoted to the set up of efficient solvers and preconditioners, possibly based on parallel multigrid approaches or suitable approximations of the equations. Another approach has been aiming at a simplification of the original problem. In particular, under a simplifying assumption on the anisotropy in the intra and extra-cellular spaces, the two equations of the Bidomain system can be combined yielding a single nonlinear reaction-diffusion parabolic equation for the transmembrane potential. This is called Monodomain problem and it is clearly simpler to solve at the computational level. However, it has been pointed out that this model fails in capturing some remarkable features of the action potential propagation. Nevertheless, the Monodomain model can still be used for reducing the computational time (a) as a preconditioner for the Bidomain model (see [4]); (b) as a model to be used in non-critical zones of the

region of interest. In this talk, we explore the latter approach. In particular, we consider the possible matching conditions for a domain-split formulation of the coupled Bidomain/Monodomain solver. Selection of proper conditions is non-trivial because of the different nature of the two problems. Moreover, we consider a possible a-posteriori error estimator for the identification of the regions where the Bidomain model needs to be turned on. Results are presented on both academic test cases and on geometries retrieved from SPECT images.

2 THE BI-MONODOMAIN DOMAIN SPLIT PROBLEM

Let u_i and u_e be the intra and extra-cellular potential in the region $\Omega = \Omega_B \cup \Omega_M$. In Ω_B (Ω_M) we assume the Bidomain (Monodomain) system to hold, i.e. (using a non-symmetric formulation for the Bidomain system)

$$\text{in} \quad \Omega_B : \begin{cases} \chi C_m \dfrac{\partial u}{\partial t} - \nabla \cdot \left(\dfrac{\lambda \mathbf{D}_i}{1+\lambda} \nabla u \right) - \nabla \cdot \left(\dfrac{\lambda \mathbf{D}_i - \mathbf{D}_e}{1+\lambda} \nabla u_e \right) + \chi I_{ion}(u) = I^{app} \\ \\ -\nabla \cdot [\mathbf{D}_i \nabla u + (\mathbf{D}_i + \mathbf{D}_e) \nabla u_e] = \widetilde{I}^{app}, \end{cases} \tag{1}$$

and

$$\text{in} \quad \Omega_M : \chi C_m \frac{\partial u}{\partial t} - \nabla \cdot \mathbf{D}_M \nabla u + \chi I_{ion}(u) = I^{app}. \tag{2}$$

where $u = u_e - u_i$ is the transmembrane potential, χ, C_m are physical constants, λ is a numerical coefficient, $\mathbf{D}_{i,e}$ are the conductivity tensors, I_{ion} represents the ionic current (which is a non-linear function of the transmembrane potential depending on the selected ionic model), I^{app} and $\widetilde{I}^{app}$ are the forcing terms. In [2] we have investigated how to devise proper matching conditions to be prescribed at the interface between Ω_M and Ω_B. Starting from Robin-Robin conditions for a full Bidomain-Bidomain problem (see also [5]), we came up with the condition

$$\vec{n}_B^T \mathbf{D}_i \nabla u_i + \vec{n}_B^T \mathbf{D}_e \nabla u_e + \alpha\, u_i + \lambda \alpha\, u_e = \alpha u^{rest}, \tag{3}$$

where u^{rest} is the resting potential and α is a numerical parameter to be tuned. This condition is added to the classical (Robin-type) continuity of the transmembrane potential. A Fourier analysis of the problem allows to establish the optimal values of the numerical parameters in the framework of Optimized Schwarz Domain Decomposition schemes. In Fig. 1 we report a 2D test case where in the left half of a rectangular region we have the Bidomain system, while the Monodomain holds in the right half. The results compare the domain-split solution with a full Bidomain model, showing that the results are similar. The domain-split solver is however faster.

Similar results in 3D will be presented in the talk.

3 AN A-POSTERIORI ERROR ESTIMATOR

In [3] we have investigated a possible *a-posteriori* error estimator for selecting the region where to activate the Bidomain model, by introducing a *hybrid model* called "hybridomain", obtained by merging the Bidomain and a properly extended version of the Monodomain models. If $u_{e,H}$ denotes the hybrid solution, the error estimator reads

$$\eta^2_{\Omega_M}(u_{e,H}) \equiv \frac{1}{2} \int_{\Omega_M} \nabla u_{e,H}^T \mathbf{D}_\varepsilon^T (\mathbf{D}_i^{-1} + \mathbf{D}_e^{-1}) \mathbf{D}_\varepsilon \nabla u_{e,H}, \tag{4}$$

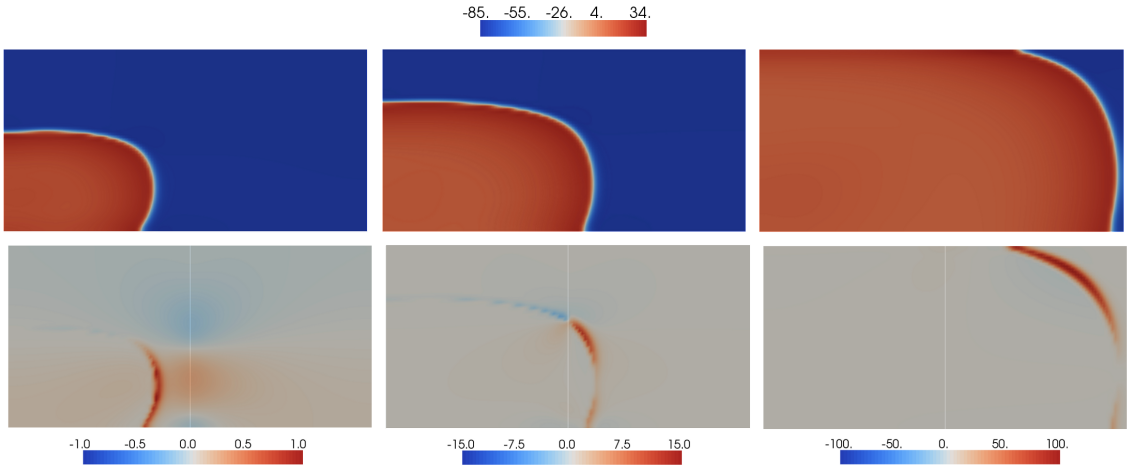

Figure 1: Membrane potential u_{Bido} (top) and error $u_{Bido} - u_{DD}$ with 2 Schwarz iterations at each time step (bottom) at different time levels (left to right $t = 9, 14, 26ms$): $\Omega_B = [0,1] \times [0,1]$, $\Omega_M = [1,2] \times [0,1]$.

where $\mathbf{D}_\varepsilon \equiv \frac{\mathbf{D}_e - \lambda \mathbf{D}_i}{1+\lambda}$. In the talk, the specific properties in terms of reliability and efficiency of this estimator will be addressed. Figure 2 highlights (in red) the distribution in space of the active Bidomain elements (region Ω_B) at three different time steps computed on a left ventricle reconstructed form SPECT images. Comparing the activation pattern with the Bidomain transmembrane potential pattern we stress that the adaptive strategy based on the estimator $\eta_{\Omega_M}(u_{e,H})$ successfully activates the Bidomain model in the area involved by the propagating front. This confirms the reliability of the a priori error estimator.

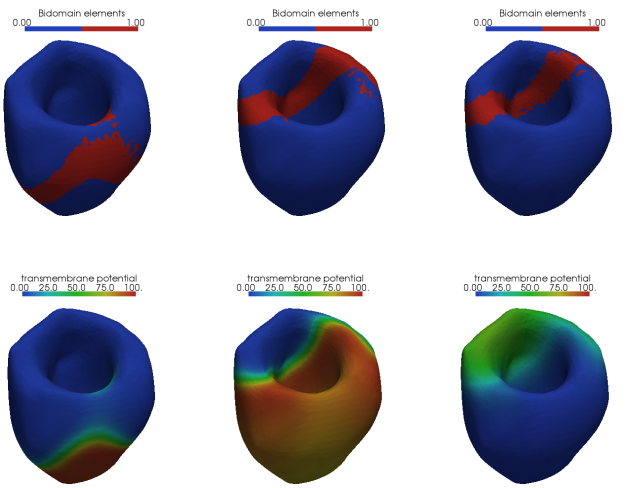

Figure 2: Top: Bidomain elements activated in Ω (Ω_B shown in red) for $t = 40, 80, 200$ ms. Bottom: Bidomain transmembrane potential at $t = 40, 80, 200$ ms.

We have tested also the case of an artificial scar on the ventricle wall tissue, still working on the same geometry as in the previous case. It is evident from Figure 3 that the propagating front predicted by the Hybridomain near the scar is more similar to the Bidomain front than the Monodomain pattern.

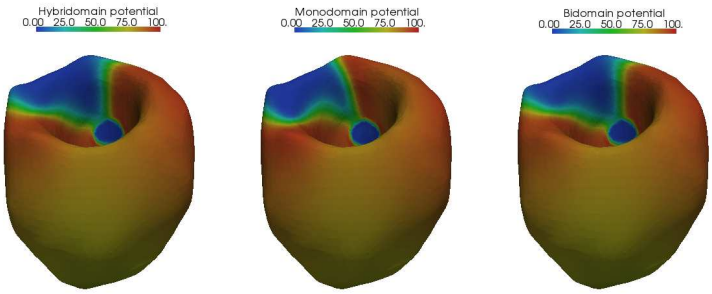

Figure 3: Comparison among Bidomain, Hybridomain and Monodomain solutions on a scarred ventricle at $t = 90$ ms. From the left to the right: Hybridomain transmembrane potential; Monodomain transmembrane potential; Bidomain transmembrane potential .

4 CONCLUSIONS

Model adaptivity is a viable strategy for reducing the computational cost in the investigation of the potential propagation in the heart, still maintaining high accuracy. The error estimator we have proposed works in a reliable and effective way in test cases based on real geometries. However this is still based on the extended version of the Monodomain problem, which reduces the computational improvement. Domain decomposition methods using Robin-Robin matching conditions (3) in the Optimized Schwarz framework actually refer to the original version of the Monodomain problem and seem therefore to be competitive for a further reduction of the computational cost. Implementation and numerical issues (including time-adaptivity, see [1]) of this approach will be discussed.

REFERENCES

[1] M. Perego, A. Veneziani, An Effcient Generalization of the Rush-Larsen Method for Solving Electro-Physiology Membrane Equations, ETNA *(Electronic Transaction in Numerical Analysis)*, 35, pp. 234-256 (2009)

[2] L. Gerardo Giorda, M. Perego, A. Veneziani, Optimized Schwartz coupling of bidomain and monodomain models in electrocardiology, to appear in M2AN, published online: 20 August 2010

[3] L. Mirabella, F. Nobile, A. Veneziani, An a posteriori error estimator for model adaptivity in electrocardiology , to appear in Comp Meth Appl Mech Engr, Available online 23 March 2010

[4] L. Gerardo Giorda, L. Mirabella, F. Nobile, M. Perego, A. Veneziani, A model preconditioner for the Bidomain problem in electrocardiology, *J. Comput. Phys.*, Vol. 228, pp. 3625- 3639 (2009)

[5] L. Gerardo Giorda, M. Perego, Optimized Schwarz Methods for the Bidomain system in electrocardiology, submitted (2010)

2nd International Conference on Mathematical and Computational Biomedical Engineering - CMBE2011
March 30 - April 1, 2011, Washington D.C, USA
P. Nithiarasu and R. Löhner (Eds.)

EFFICIENT PRECONDITIONERS FOR THE BIDOMAIN SYSTEM IN ELECTROCARDIOLOGY

Luca Gerardo-Giorda[⋆], Lucia Mirabella[⋆⋆], and Mauro Perego[⋆⋆⋆]
[⋆] Real Lab, Department of Biology, Emory University,
1510 Clifton Rd NE, Atlanta 30322, GA, USA, lgerard@emory.edu
[⋆⋆] Wallace H. Coulter Department of Biomedical Engineering, Georgia Institute of Technology,
315 Ferst Dr., Atlanta 30332, GA, USA, lucia.mirabella@bme.gatech.edu
[⋆⋆⋆] Department of Scientific Computing, Florida State University,
Tallahassee, FL, USA, mperego@fsu.edu

SUMMARY

We present here a preconditioner for the Bidomain system governing the action potential propagation in the myocardial tissue. The preconditioner is based on a suitable adaptation of the Monodomain model, a simplified version of the Bidomain one, which is easier to solve, but unable to capture significant features of physiological and pathological patterns. We show optimality of the preconditioner, as its performance is proven independent of the mesh size. In order to devise a parallel extension of the preconditioner, we introduce an Optimized Schwarz Method for the Bidomain system. We prove convergence for the method and we show numerical evidence of our findings.

Key Words: *Electrophysiology, Bidomain system, Preconditioning, Optimized Schwarz Methods*

1 INTRODUCTION

The electrical activation of the heart is the biological process that generates the contraction of the cardiac muscle, pumping the blood to the whole body. In physiological conditions, the pacemaker cells of the sinoatrial node generate an action potential, that is a sudden variation of the cell transmembrane potential $u = u_i - u_e$, namely the difference between the intracellular potential u_i and the extracellular one u_e. Following preferential conduction pathways, the electrical stimulus propagates throughout the heart wall and causes the contraction of the heart chambers. Due to this coupling between the electrophysiology and the mechanical behavior, when some anomalies occur in the action potential propagation, the proper function of the heart pump can be affected.
One of the most accurate model available in literature is the Bidomain model, a degenerate, quasi-linear, parabolic system, consisting of two non-linear partial differential equations governing the macroscopical dynamics of the intracellular and extracellular potential, coupled with a model for the ionic currents, flowing through the membrane of a single cell. Such model can be derived from a homogenization of the electrostatic laws for the potential in the intracellular and extracellular space. Its numerical solution is an intrinsically difficult task, due to the very nature of the system, yielding severe conditioning for the linear system associated with the discrete problem. We present in this talk a model-based block-triangular preconditioner [1,2], and an Optimized Schwarz Method [3] we investigated in the recent years for the solution of the Bidomain system, and we address some further developments.

2 A MODEL-BASED PRECONDITIONER

The Bidomain system can be reformulated in terms of the transmembrane and the extracellular potentials u and u_e

$$\begin{cases} \chi C_m \dfrac{\partial u}{\partial t} - \nabla \cdot \left[\frac{\lambda \mathbf{D}_i}{1+\lambda} \nabla u \right] - \nabla \cdot \left[\frac{\lambda \mathbf{D}_i - \mathbf{D}_e}{1+\lambda} \nabla u_e \right] + \chi I_{ion}(u) = I^{\text{app}} \\ -\nabla \cdot [\mathbf{D}_i \nabla u + (\mathbf{D}_i + \mathbf{D}_e) \nabla u_e] = \widetilde{I}^{\text{app}}. \end{cases} \tag{1}$$

The parameter λ in (1) is chosen between $\lambda_m = \min \left\{ \frac{\sigma_e^l}{\sigma_i^l}, \frac{\sigma_e^t}{\sigma_i^t} \right\}$ and $\lambda_M = \max \left\{ \frac{\sigma_e^l}{\sigma_i^l}, \frac{\sigma_e^t}{\sigma_i^t} \right\}$. An IMEX scheme in time and a finite element approximation in space of (1) result in solving, at each time step, the linear system

$$\begin{bmatrix} \mathbf{B}_{uu} & \mathbf{B}_{ue} \\ \mathbf{B}_{eu} & \mathbf{B}_{ee} \end{bmatrix} \begin{bmatrix} \mathbf{u} \\ \mathbf{u}_e \end{bmatrix}^{n+1} = \begin{bmatrix} \mathbf{f} \\ \mathbf{g} \end{bmatrix}. \tag{2}$$

We proposed to precondition (2) by a block-Gauss-Seidel strategy, relying on its lower block-triangular part

$$\mathbf{M} = \begin{bmatrix} \mathbf{B}_{uu} & \mathbf{0} \\ \mathbf{B}_{eu} & \mathbf{B}_{ee} \end{bmatrix},$$

that corresponds to the discretization of an *extended Monodomain* model with Neumann boundary conditions. We analyzed the proposed preconditioner from both the theoretical and the numerical viewpoint [1]. Numerical results confirm, for any value $\lambda \in [\lambda_m, \lambda_M]$, the predicted little dependence on the mesh size, for both a simple geometry and a real geometry reconstructed from SPECT imaging. A significant gain in CPU time has been obtained by using a Flexible GMRES with a coarse solution of the preconditioning step. A more accurate analysis on the conditioning of the preconditioned problem (based on singular values) as well as of the convergence properties (based on eigenvectors) of an associated Krylov method has been performed [2]. It turns out that minimizing the conditioning of the preconditioned problem is more effective than minimizing the conditioning of the eigenvectors matrix. As a consequence, a minimization of the upper bound for

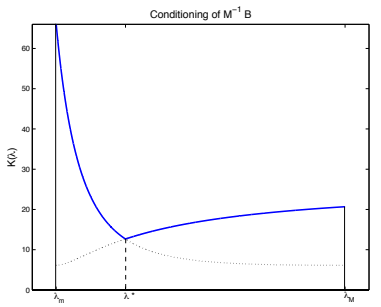

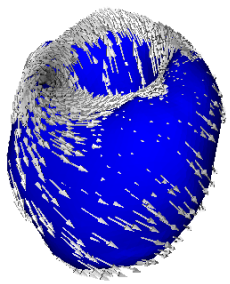

# nodes	iter
22,470	5.04
58,943	6.01
156,733	6.12
276,578	6.00
677,000	6.05

Figure 1: Left: upper bound on the conditioning of the preconditioned problem. Middle: SPECT reconstructed geometry. Right: Iteration counts for different values of the parameter λ

the conditioning of the preconditioned problem (see figure 1, left) yields the optimal parameter

$$\lambda^* = \frac{\lambda_m + \lambda_M + 2\lambda_m \lambda_M}{2 + \lambda_m + \lambda_M}, \tag{3}$$

depending only on the coefficients of the original problem. In figure 1 we plot the ventricular geometry recovered from SPECT imaging (middle) and report the iteration counts for different mesh sizes (right).

A way to parallelize the model-based preconditioner relies on domain decomposition techniques. Schwarz methods are a class of domain decomposition methods for the numerical solution of partial differential equations. The classical Schwarz algorithm, currently at the core of several parallel preconditioning strategies, is based on Dirichlet transmission conditions on the interfaces between subdomains, and features a rather slow convergence rate, that is very much dependent on the size of the subdomains overlap. Moreover, in general the classical Schwarz method is not convergent in the absence of overlap. To overcome these drawbacks, the class of Optimized Schwarz Methods (OSM) was developed in recent years, based on more effective transmission conditions than the classical Dirichlet ones, ensuring convergence also in the absence of overlap. OSM in general rely on parameters that are optimized by minimizing the convergence rate of the algorithm. We present an Optimized Schwarz Method for the Bidomain system, where the Robin-type interface coupling conditions are naturally derived from the non-symmetric formulation [3]: using Fourier analysis we prove that the OSM has better convergence properties than the Classical Schwarz one. Moreover, we devise optimal parameters by minimizing the convergence rate in both u and u_e. In figure 2 (left) we plot the convergence rate for both u (solid line) and u_e (dashed

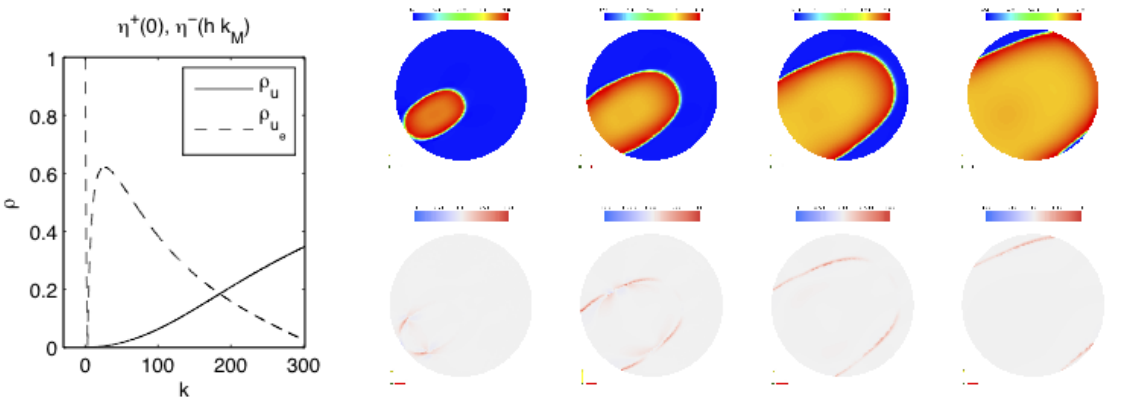

Figure 2: Left: convergence rate in u and u_e. Right: Action potential propagation in a Bidomain simulation u_{Bido} and error $u_{Bido} - u_{OS}$ along time (left to right, $t = 7, 13, 19, 25$): u_{OS} is computed with 2 iterations of the Optimized Schwarz algorithm. Top: action potential. Bottom: 1% error region.

line). It appears that the convergence in u is faster than the convergence in u_e, a feature confirmed by numerical experiments that will be presented. The great accuracy provided by the interface matching conditions can be appreciated in figure 2 (right), where we plot the 1% error region for a 2D test case, where only 2 iterations of the OSM are run per time step.
The performance of the algorithm can further be enhanced by solving the interface problem by a Krylov acceleration method where the OSM acts as a preconditioner, and the matrix-vector products require the solution of the subdomain subproblems. In figure 3 we plot the results for a 3D idealized geometry, where the Krylov method shows its reliability even with a coarse tolerance. Whatever the choice (OSM in iterative form or Krylov acceleration), the local subproblems can be solved in parallel, with the Monodomain-based preconditioner.

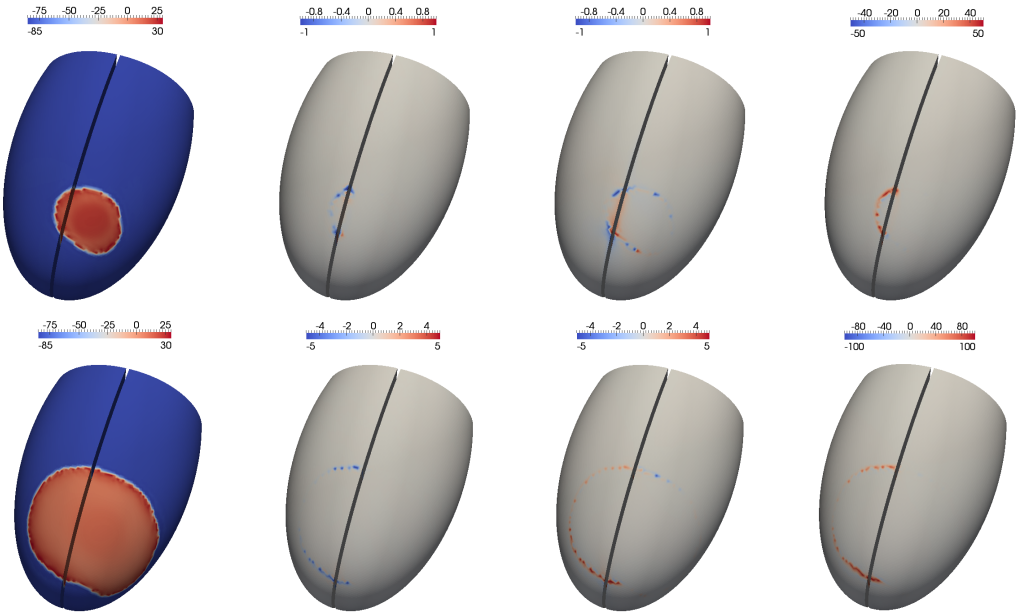

Figure 3: Action potential propagation in a Bidomain simulation u_{Bido} and errors $u_{Bido} - u_{OS}$ for different algorithms and stopping criteria to compute u_{OS}. Left to right: Krylov ($\varepsilon = 1e-3$); OSM ($\varepsilon = 1e-3$); OSM (4 iterations). Top: $t = 7\ ms$, bottom: $t = 25\ ms$.

4 CONCLUSIONS

The model-based preconditioner introduced in [1] proved to be effective in terms of both iteration counts and CPU time, and its performance is optimized by the parameter λ^* provided by the explicit formula (3) given in [2]. The preconditioner parallelization is currently under investigation, and in this direction, the Optimized Schwarz Method introduced in [3] proved to be very robust in terms of mesh size and fibers orientation. The latter can thus be the core of a parallelization strategy where the matching conditions on the interfaces between subdomains are given by the OSM, while the single subproblem is solved using the Monodomain-based preconditioner: numerical aspects of this approach will be discussed.

REFERENCES

[1] L. Gerardo-Giorda, L. Mirabella, F. Nobile, M. Perego and A. Veneziani. A model-based block-triangular preconditioner for the Bidomain system in electrocardiology, *J. Comp. Phys.*, 228:3625–3639, 2009.

[2] L. Gerardo-Giorda and L. Mirabella. Spectral analysis of a block-triangular preconditioner for the Bidomain system in electrocardiology, *Technical Report TR-2010-006*, Mathematics and Computer Science, Emory University, 2010 (in revision).

[3] L. Gerardo-Giorda and M. Perego. Optimized Schwarz Methods for the Bidomain system in electrocardiology, *Technical Report TR-2010-016*, Mathematics and Computer Science, Emory University, 2010 (in revision).

2nd International Conference on Mathematical and Computational Biomedical Engineering - CMBE2011
March 30 - April 1, 2011, Washington D.C, USA
P. Nithiarasu and R. Löhner (Eds.)

ON SOME NUMERICAL ASPECTS OF AN ACTIVE STRAIN FORMULATION IN CARDIAC MECHANICS

A. Quarteroni[†,‡], S. Rossi[†] and R. Ruiz-Baier[†]
[†]Modeling and Scientific Computing, MATHICSE, École Polytechnique Fédérale de Lausanne, CH-1015 Lausanne, Switzerland, {alfio.quarteroni, simone.rossi, ricardo.ruiz}@epfl.ch
[‡]MOX - Dipartimento di Matematica F. Brioschi, Politecnico di Milano, via Bonardi 9, 20133 Milano, Italy

SUMMARY

We are interested in analyzing a particular model in cardiac mechanics, where the material law consists in the Holzapfel-Ogden law accounting for the passive mechanical properties of the tissue, and the Euler-Lagrange equations for minimization of the total energy are written in terms of an active and a passive deformation factors, where the active part is supposed to depend internally at the microscopic level, on the electrodynamics and specific orientation of the cardiac cells. We have found that such formulation leads, in particular, to a naturally well-posed problem associated to a generic Newton iteration of the linearization process, and we further observe that the stability of the solution depends on the values assumed by the *active strain* function. Some numerical experiments illustrate the adequateness of the model along with the good properties of the proposed method.

Key Words: *Active strain formulation, cardiac electromechanical response, finite elements.*

1 Introduction

Studying living soft tissues presents several challenges ranging from anisotropy, nonlinearities of varied kinds, geometrical complexity, heterogeneities, and so on. From the viewpoint of the solid mechanics analysis, these can be viewed as anisotropic hyperelastic materials, since they can experience non-linear elastic large deformations both under normal physiological conditions and during injury. One of the most appealing subjects is without doubts the modeling of cardiac tissue. In order to obtain fairly reasonably results, the governing equations should be cast in the framework of nonlinear elasticity (no assumption of infinitesimal strain), using an anisotropic description of the collagen fibers compound that form the tissue. An additional assumption widely accepted in the vast majority of the related literature, is that the material can be considered as incompressible, given that the heart muscle is made mainly of connective tissue, cardiac cells, and extracellular matrix filled with fluid, that consist essentially of water.

2 Mathematical model for cardiac mechanical response

By $\boldsymbol{x}$ we denote the present position in Cartesian coordinates of a material particle (in a $d-$ dimensional bounded body $\mathcal{B}$) that was originally placed at $\mathbf{X}$ in the undeformed frame of reference $\Omega \subset \mathbb{R}^d$, $d = 2, 3$. The deformation of the elastic body is defined using the smooth one-to-one

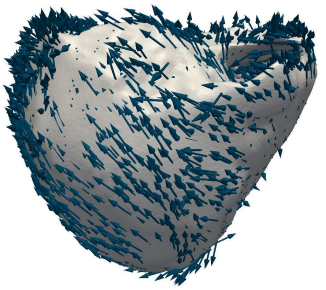

Figure 1: Bi-ventricular geometry with fibers' distribution.

map $\boldsymbol{\varphi} : \Omega \to \mathcal{B} \subset \mathbb{R}^d$, $\boldsymbol{\varphi}(\mathbf{X}) = \mathbf{X} + \boldsymbol{u}(\mathbf{X})$, where $\boldsymbol{u}$ denotes the displacement vector $\boldsymbol{u} = \boldsymbol{x} - \mathbf{X}$. The main measures of deformation, from which we start the derivation of re remaining strain measures, are the deformation gradient tensor $\mathbf{F}$, and the right and left Cauchy-Green stretch tensors $\mathbf{C}$, $\mathbf{B}$ defined as

$$\mathbf{F} = \mathbf{I} + \nabla \boldsymbol{u}, \quad \mathbf{C} = \mathbf{F}^T\mathbf{F}, \quad \mathbf{B} = \mathbf{F}\mathbf{F}^T, \tag{1}$$

where $\mathbf{I}$ is the second-order identity tensor, and ∇ stands for the gradient with respect to material coordinates. By $J = \det \mathbf{F}$ we denote the volume map.

2.1 Modeling of passive myocardium

We consider the material as hyperelastic, and hence the measures of stress are obtained by differentiating certain (material-dependent) elastic strain energy potential $\mathcal{W}$ with respect to strain. In principle, to assure incompressibility of the material (where only isochoric behavior is allowed), we follow the approach in which the strain energy is assumed to take the form $\mathcal{W}^{\text{iso}} = \mathcal{W}(\boldsymbol{u}) - p(J-1)$, where $p = p(\mathbf{X})$ is the Lagrange multiplier arising from the imposition of the incompressibility constraint $J = 1$ (conservation of mass), and which is usually interpreted as the hydrostatic pressure field. We focus our attention on a specific material law for the pericardium, proposed by Holzapfel and Ogden [3], which takes into account several notable features such as material orthotropy, invariant-based construction, and that generalizes other similar laws in the literature. We consider

$$\mathcal{W}(\boldsymbol{u}, p) = \frac{a}{2b}\exp(b[I_1 - d]) + \sum_{i=f,s}\frac{a_i}{2b_i}\left[\exp(b_i[I_{4,i} - 1]^2) - 1\right] + \frac{a_{fs}}{2b_{fs}}\exp(b_{fs}I_{8,fs}^2 - 1), \tag{2}$$

for which the subindexes f and s refer to the local fiber and sheets axes, $\boldsymbol{d}_{\text{f}}$ and $\boldsymbol{d}_{\text{s}}$, respectively. Moreover, quantities $a, a_{\text{f}}, a_{\text{s}}, b, b_{\text{f}}, b_{\text{s}}, a_{\text{fs}}, b_{\text{fs}}$ are experimentally fitted material parameters, and the terms $I_1, I_{4,\text{f}}, I_{4,\text{s}}, I_{8,\text{fs}}$ are invariants of the right Cauchy-Green tensor $\mathbf{C}$ and the fiber directions, and are defined as

$$I_1 := \text{tr}(\mathbf{C}),\ I_{4,\text{f}} := \mathbf{C} : (\boldsymbol{d}_{\text{f}} \otimes \boldsymbol{d}_{\text{f}}),\ I_{4,\text{s}} = \mathbf{C} : (\boldsymbol{d}_{\text{s}} \otimes \boldsymbol{d}_{\text{s}}),\ I_{8,\text{fs}} = \mathbf{C} : \text{sym}(\boldsymbol{d}_{\text{f}} \otimes \boldsymbol{d}_{\text{s}}).$$

Notice that the invariant I_1 is the usual first invariant for isotropic materials, whereas the remaining invariants take into account the contraction in the fiber and sheet directions, and the relative shear between them [2]. The Cauchy stress tensor then assumes the form

$$\begin{aligned}\mathbf{T} = {} & a\exp(b[\mathbf{I}_1 - d])\mathbf{B} - p\mathbf{I} + 2\sum_{\text{i=f,s}} a_i(I_{4,\text{i}} - 1)\exp(b_{\text{i}}[I_{4,\text{i}} - 1]^2)\boldsymbol{d}_{\text{i}} \otimes \boldsymbol{d}_{\text{i}} \\ & + 2a_{\text{fs}}I_{8,\text{fs}}\exp(b_{\text{fs}}I_{8,\text{fs}}^2)[\boldsymbol{d}_{\text{f}} \otimes \boldsymbol{d}_{\text{s}} + \boldsymbol{d}_{\text{s}} \otimes \boldsymbol{d}_{\text{f}}].\end{aligned}$$

The first Piola-Kirchoff stress tensor $\mathbf{P}(\boldsymbol{u}, p) = \frac{\partial \mathcal{W}}{\partial \mathbf{F}}$, represents the force measured per unit undeformed area acting on the deformed body $\mathcal{B}$. When $\mathcal{B}$ is under a given load $\boldsymbol{\ell}$ per unit volume in the reference configuration, according to the principle of stationary potential energy, the total energy satisfies

$$\int_\Omega \mathcal{W}(\boldsymbol{u}, p) = \int_\Omega \boldsymbol{\ell} \cdot \boldsymbol{u},$$

and hence the Euler-Lagrange equations (of finite elastostatics) written in a mixed variational form read

$$\begin{aligned} \int_\Omega \mathbf{P}(\boldsymbol{u}, p) : \nabla \boldsymbol{v} = \int_\Omega \boldsymbol{\ell} \cdot \boldsymbol{v} \quad \forall \boldsymbol{v} \in \boldsymbol{\mathcal{V}}, \\ \int_\Omega (J-1) q = 0 \quad \forall q \in Q, \end{aligned} \tag{3}$$

where $\boldsymbol{\mathcal{V}}$ and Q are admissible spaces for displacement and pressure fields, respectively.

2.2 The active strain formulation

Unlike the general approach outlined in the previous subsection, now we assume that that the deformation gradient $\mathbf{F}$ admits a factorization into a passive elastic part acting at a macroscale, and an active factor at the microscale

$$\mathbf{F} = \mathbf{F}_{\mathrm{p}} \mathbf{F}_{\mathrm{a}}. \tag{4}$$

Similar splitings of the deformation gradient have been proposed, for instance, in the context of finite elastoplasticity (see e.g. [6]). Notice, however that (4) is not to be confused with the decoupling of deviatoric and dilational responses $\mathbf{F} = \mathbf{F}_{vol} \tilde{\mathbf{F}}$, where $\det \tilde{\mathbf{F}} = 1$ and so the deformation induced by $\mathbf{F}_{vol}$ is the only one influencing the changes of volume in the material (see e.g. [6]). Note also that $\mathbf{F}$ is given by the gradient of a vector map, while $\mathbf{F}_{\mathrm{p}}, \mathbf{F}_{\mathrm{a}}$ are not, in general. We further stress that, for infinitesimal deformations, the active strain formulation and the one given in the previous subsection actually coincide (see e.g. [4]). The active part of the deformation is assumed to take the following form

$$\mathbf{F}_{\mathrm{a}} = \mathbf{I} + T_{\mathrm{a}}^{\mathrm{f}} \boldsymbol{d}_{\mathrm{f}} \otimes \boldsymbol{d}_{\mathrm{f}} + T_{\mathrm{a}}^{\mathrm{s}} \boldsymbol{d}_{\mathrm{s}} \otimes \boldsymbol{d}_{\mathrm{s}},$$

where $T_{\mathrm{a}}^{\mathrm{i}} = T_{\mathrm{a}}^{\mathrm{i}}(\mathbf{X})$, $\mathrm{i} = \mathrm{f}, \mathrm{s}$ denotes an *active strain* function that, in the context of a model coupling the cardiac elastostatics with the electrophysiology, carries the relevant information of the electrical propagation through the tissue (see [5]). Now, notice that decomposition represents that an intermediate configuration exists between the actual and the reference configurations. In such intermediate configuration, the stored energy function is transformed as

$$\widehat{\mathcal{W}}(\mathbf{F}) = J_{\mathrm{a}} \mathcal{W}(\mathbf{F}_{\mathrm{p}}) = J_{\mathrm{a}} \mathcal{W}(\mathbf{F} \mathbf{F}_{\mathrm{a}}^{-1}),$$

where J_{a} denotes the determinant of $\mathbf{F}_{\mathrm{a}}$. This transformation has the implication that the good properties of $\mathcal{W}$ (entirely invariant-based, orthotropic, polyconvex, and dependent on physically meaningful parameters [3]) are preserved in $\widehat{\mathcal{W}}$.

3 The linearized system

It is clear that for obtaining a numerical approximation of the nonlinear problem (3), a Newton (or Newton-like) linearization is required. Let us introduce the following linearized problem,

considered around a generic solution $(\hat{\boldsymbol{u}}, \hat{p})$: Find $\boldsymbol{u} \in \boldsymbol{\mathcal{V}}$, $p \in Q$ such that

$$\begin{aligned}
&\int_\Omega 2b\hat{\psi}(\hat{\mathbf{F}} : \nabla \boldsymbol{u})\hat{\mathbf{F}} : \nabla \boldsymbol{v} + \int_\Omega \hat{\psi}\nabla \boldsymbol{u} : \nabla \boldsymbol{v} - \int_\Omega p\hat{J}\hat{\mathbf{F}}^{-T} : \nabla \boldsymbol{v} - \int_\Omega \hat{p}\hat{J}(\hat{\mathbf{F}}^{-T} : \nabla \boldsymbol{u})\hat{\mathbf{F}}^{-T} : \nabla \boldsymbol{v} \\
&\quad + \int_\Omega \hat{p}\hat{J}(\hat{\mathbf{F}}^{-T}\nabla \boldsymbol{u}^T\hat{\mathbf{F}}^{-T}) : \nabla \boldsymbol{v} + \int_\Omega (T_{\mathrm{a}}^{\mathrm{f}}\nabla \boldsymbol{u}\boldsymbol{d}_{\mathrm{f}} \otimes \boldsymbol{d}_{\mathrm{f}} + T_{\mathrm{a}}^{\mathrm{s}}\nabla \boldsymbol{u}\boldsymbol{d}_{\mathrm{s}} \otimes \boldsymbol{d}_{\mathrm{s}}) : \nabla \boldsymbol{v} = R_{\boldsymbol{u}}(\hat{\boldsymbol{u}}, \hat{p}, \boldsymbol{w}), \qquad (5) \\
&\int_\Omega q\hat{J}\hat{\mathbf{F}}^{-T}\nabla \boldsymbol{u} = R_p(\hat{\boldsymbol{u}}, q),
\end{aligned}$$

for all $\boldsymbol{v} \in \boldsymbol{\mathcal{V}}$, $q \in Q$, and where $R_{\boldsymbol{u}}$ and R_p denote the Newton residuals

$$R_{\boldsymbol{u}}(\hat{\boldsymbol{u}}, \hat{p}, \boldsymbol{w}) = \int_\Omega \boldsymbol{\ell} \cdot \boldsymbol{v} - \int_\Omega \hat{\mathbf{P}} : \nabla \boldsymbol{v}, \quad R_p(\hat{\boldsymbol{u}}, q) = \int_\Omega q(\hat{J} - 1).$$

Problem (5) holds in particular for the state $(\hat{\boldsymbol{u}}, \hat{p}) = (\mathbf{0}, 0)$, and hence it can be recasted in the mixed form: Find $\boldsymbol{u} \in \boldsymbol{\mathcal{V}}$, $p \in Q$ such that

$$\begin{aligned}
a(\boldsymbol{u}, \boldsymbol{v}) + b(\boldsymbol{v}, p) &= F(\boldsymbol{v}) \quad \forall \boldsymbol{v} \in \boldsymbol{\mathcal{V}}, \\
b(\boldsymbol{u}, q) &= 0 \quad \forall q \in Q,
\end{aligned}$$

where the used forms are

$$\begin{aligned}
a(\boldsymbol{u}, \boldsymbol{v}) &:= 2ba \int_\Omega \nabla \cdot \boldsymbol{u}\nabla \cdot \boldsymbol{v} + a \int_\Omega \nabla \boldsymbol{u} : \nabla \boldsymbol{v} + \int_\Omega (T_{\mathrm{a}}^{\mathrm{f}}\nabla \boldsymbol{u}\boldsymbol{d}_{\mathrm{f}} \otimes \boldsymbol{d}_{\mathrm{f}} + T_{\mathrm{a}}^{\mathrm{s}}\nabla \boldsymbol{u}\boldsymbol{d}_{\mathrm{s}} \otimes \boldsymbol{d}_{\mathrm{s}}) : \nabla \boldsymbol{v}, \\
b(\boldsymbol{v}, q) &:= -\int_\Omega q\nabla \cdot \boldsymbol{v}, \qquad F(\boldsymbol{v}) := \int_\Omega \boldsymbol{\ell} \cdot \boldsymbol{v} - a \int_\Omega \nabla \cdot \boldsymbol{v},
\end{aligned}$$

for all $\boldsymbol{v} \in \boldsymbol{\mathcal{V}}$, $q \in Q$. From classical results we know that the conditions for well-posedness of this problem are continuity and coercivity of $a(\cdot, \cdot)$ in $\boldsymbol{\mathcal{V}}$, and the fullfilment of the inf-sup condition for $b(\cdot, \cdot)$:

$$\inf_{q \in Q} \sup_{\boldsymbol{v} \in \boldsymbol{\mathcal{V}}} \frac{b(\boldsymbol{v}, q)}{\|\boldsymbol{v}\| \, \|q\|} \geq C,$$

for some constant $C > 0$. Since in our case $b(\cdot, \cdot)$ is the usual operator associated to the divergence, this condition is known to be satisfied. Then, the following results provides the solvability of (5).

Lemma 3.1 *Assume that the active stress functions $T_{\mathrm{a}}^{\mathrm{f}}, T_{\mathrm{a}}^{\mathrm{s}}$ satisfy the condition*

$$T_{\mathrm{a}}^{\mathrm{f}}(\mathbf{X}) + T_{\mathrm{a}}^{\mathrm{s}}(\mathbf{X}) \geq -1, \text{ for a.e. } \mathbf{X} \in \Omega.$$

Then the linearized problem (5) *admits a unique solution $\boldsymbol{u} \in \boldsymbol{\mathcal{V}}$, $p \in Q$.*

REFERENCES

[1] F. Auricchio, L. Beirão da Veiga, C. Lovadina and A. Reali, A stability study of some mixed finite elements for large deformation elasticity problems, *Comput. Methods Appl. Mech. Engrg.* **194** (2005), 1075–1092.

[2] S. Göktepe, S.N.S. Acharya, J. Wong and E. Kuhl, Computational modeling of passive myocardium, *Int. J. Numer. Methods Biomed. Engrg.* (2010), to appear.

[3] G.A. Holzapfel and R.W. Ogden, Constitutive modelling of passive myocardium: a structurally based framework for material characterization, *Phil. Trans. R. Soc. A* **367** (2009), 3445–3475.

[4] P. Nardinocchi and L. Teresi, On the active response of soft living tissues, *J. Elast.* **88** (2007), 27–39.

[5] F. Nobile, A. Quarteroni and R. Ruiz-Baier, Numerical solution of an active strain formulation for the electromechanical activity in the heart, submitted.

[6] J.C. Simo and K.S. Pister, Remarks on rate constitutive equations for finite deformations, *Comp. Methods Appl. Mech. Engrg.* **46** (1984), 201–215.

Standard Sessions

2nd International Conference on Mathematical and Computational Biomedical Engineering - CMBE2011
March 30 - April 1, 2011, Washington D.C, USA
P. Nithiarasu and R. Löhner (Eds.)

TIME-DOMAIN ULTRASONIC WAVE PROPAGATION IN ANISOTROPIC POROELASTIC BONE PLATE

Vu-Hieu Nguyen, Salah Naili
Université Paris-Est, Laboratoire Modélisation et Simulation Multi Echelle,
MSME UMR 8208 CNRS, 61 avenue Général de Gaulle, 94010 Créteil cedex,
vu-hieu.nguyen@univ-paris-est.fr

SUMMARY

This paper deals with modeling of the ultrasound axial transmission technique for *in vivo* cortical long bone which is known as being a anisotropic solid medium with functionally graded porosity. The bone is modeled as an anisotropic poroelastic medium using the Biot's theory. We develop a hybrid finite element formulation to obtain the time-domain solution of ultrasonic waves propagating in a poroelastic plate immersed two fluid halfspaces. The numerical method is based on a combined Laplace-Fourier transform which solves the problem in the frequency-wavenumber domain. In the spectral domain, as radiation conditions may be exactly introduced in the infinite fluid halfspaces, only the heterogeneous solid layer needs to be analyzed using finite element method. Several numerical tests are presented showing very good performances of the proposed approach.

Key Words: *cortical bone, ultrasound, poroelastic, spectral finite element method.*

1 INTRODUCTION

In recent years, quantitative ultrasound (QUS) has demonstrated its promising potential in assessment of *in vivo* bone characteristics. For measuring *in vivo* properties of cortical long bones, a so-called "axial transmission" (AT) technique has been developed [1]. The axial transmission technique uses a set of ultrasonic transducers (transmitters and receivers) placed on a line in contact with the skin along the bone axial axis. The transmitter emits an ultrasound pulse wave (around 250 KHz-2 MHz) that propagates along the cortical layer of bone.

Mechanical modeling of this experiment deals with considering a model describing vibro-acoustic interactions of a solid waveguide (which represents the cortical bone) coupled with two fluid media (which represents soft tissues such as skin or marrow). The cortical bone may be described as plate-like or cylindrical-like structures. Bone is a strongly heterogeneous material with complex structures whose the architecture displays an organization at different hierarchical levels: the macrostructure (bone), the microstructure (harvesian system, osteon, interstitial tissues) and the other structures at lower scales. It has been shown that the microstructure of the bone has strong influence on characteristics of ultrasonic wave propagation. However, for modeling the guided ultrasonic waves propagating in cortical long bones, most of works has considered cortical bone as an equivalent linear (isotropic (see *e.g* [2]) or anisotropic (see *e.g* [3])) elastic medium.

In this paper, we propose to use a poroelastic model to represent the cortical bone in order to be able to describe the link between the bone microstructure (bone matrix properties as well as

porosity) and the time-domain response of ultrasonic wave propagation. For this purpose, we have developed a semi-analytical finite element method for simulating the transient ultrasonic waves propagating in cortical bones considered as an anisotropic poroelastic medium. The bone is assumed to be homogeneous in its axial direction but may be heterogenous in the radial direction.

2 METHOD

Geometrical description and governing equations. Long bone is modeled as 2D solid plate immersed in two fluid half-space as shown in Figure 1. The upper fluid presents soft tissues and the lower fluid represents the bone marrow. The thickness of bone player is denoted by h.

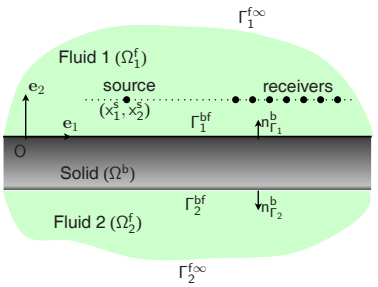

Figure 1: Geometrical configuration of the trilayer model for ultrasound axial transmission test

We use the Biot's theory of anisotropic poroelasticity to model bone's mechanical behavior. The bone layer is assumed to consist of a solid skeleton (of density ρ_s) and of a connected pore network saturated by a fluid (of density ρ_f). Its mixture density is denoted by ρ, with $\rho = \phi\,\rho_f + (1-\phi)\,\rho_s$ where ϕ is the porosity. The displacement vectors of the solid skeleton and of the fluid are denoted by $\boldsymbol{u}^s$ and $\boldsymbol{u}^f$, respectively; the displacement vector of the fluid relative to the solid frame (weighted by the porosity) is defined by $\boldsymbol{w} = \phi(\boldsymbol{u}^f - \boldsymbol{u}^s)$. The constitutive equations for the bone layer seen as an anisotropic linear poroelastic material may be stated as

$$\boldsymbol{\sigma} = \mathbb{C}\,\boldsymbol{\epsilon} - \boldsymbol{\alpha}\,p\,, \tag{1}$$

$$-\frac{1}{M}\,p = \nabla\cdot\boldsymbol{w} + \boldsymbol{\alpha} : \boldsymbol{\epsilon}\,, \tag{2}$$

where $\boldsymbol{\sigma}$ is the stress tensor and p is the interstitial pore pressure; $\mathbb{C}$ is the drained elasticity fourth-order tensor of the porous material, $\boldsymbol{\alpha}$ is called Biot effective stress tensor, which is a symmetric second-order tensor and M is the Biot scalar modulus. The infinitesimal strain tensor $\boldsymbol{\epsilon}$ is the symmetric part of the gradient of $\boldsymbol{u}^s$. Otherwise, both fluid media are supposed to be idealized acoustic fluids. The acoustic wave celeries in these domains are denoted by c_1 and c_2, respectively.

Neglecting the body forces (other than inertia), the equations describing the wave propagation in the described coupled system read

$$\frac{1}{c_1^2}\,\ddot{p}_1 - \nabla^2 p_1 = \dot{Q} \qquad \text{in } \Omega_1^f \tag{3}$$

$$\left.\begin{aligned} &\nabla\cdot\boldsymbol{\sigma} = \rho\,\ddot{\boldsymbol{u}}^s + \rho_f\ddot{\boldsymbol{w}}\,,\\ &-\nabla p = \rho_f\,\ddot{\boldsymbol{u}}^s + \boldsymbol{k}^{-1}\,\dot{\boldsymbol{w}} + \boldsymbol{b}\,\ddot{\boldsymbol{w}}\,, \end{aligned}\right\} \qquad \text{in } \Omega^b \tag{4}$$

$$\frac{1}{c_2^2}\,\ddot{p}_2 - \nabla^2 p_2 = 0 \qquad \text{in } \Omega_2^f\,, \tag{5}$$

where Q is the acoustic source; the two tensors $\boldsymbol{k}$ and $\boldsymbol{b}$ are symmetric second-order tensors; the first one is the anisotropic permeability tensor and the second one is determined from the tortuosity tensor $\boldsymbol{a}$ as $\boldsymbol{b} = (\rho_f/\phi)\,\boldsymbol{a}$.

At both solid-fluid interfaces, the continuity conditions of fluid pressure and normal stress as well as the fluid velocity read

$$\left.\begin{array}{l} p = p_i \\ \boldsymbol{\sigma}\boldsymbol{n}_i^{bf} = -p_i \boldsymbol{n}_i^{bf} \\ \left(\frac{1}{\rho_i}\nabla p_i + \ddot{\boldsymbol{w}} + \ddot{\boldsymbol{u}}^s\right)\cdot \boldsymbol{n}_i^{bf} = 0 \end{array}\right\} \quad \text{on } \Gamma_i^{bf} \text{ for } i = 1, 2\,, \tag{6}$$

Computation procedure using spectral finite element approach. The problem presented deals with solving a system of linear partial differential equations in which the coefficients are homogeneous in the longitudinal direction given by x_1-axis. Here, we propose to solve the system as follows: (i) the system of equations is firstly transformed into frequency-wavenumber domain by using a Fourier transform with respect to x_1 combined with a Laplace transform with respect to t; as a consequence, a one-dimensional system of PDEs with respect to x_1 can be established; (ii) in the frequency-wavenumber domain, the wave equations in two fluid domains (Ω_f^1 and Ω_2^f) are analytically solved providing impedance boundary conditions for the solid domain; (iii) the weak formulations have been then developed for poroelastic equations in the domain (Ω^b) to carry out finite element equations in (iv) the space-time solution is finally obtained by performing the inverse Fourier transform (using FFT technique) and the inverse Laplace transform (using the CQM technique). The described procedure has been successfully developed in Matlab and validated by comparing with results obtained by using standard finite element procedure [4].

3 NUMERICAL TESTS AND CONCLUSIONS

Using the proposed approach, we have conducted a parametric analysis in order to study to influence of the bone's porosity on the behavior of guided ultrasonic wave in long bones.

We assume that the solid phase of the bone material is transversely isotropic elastic medium which has $c_{11}^m = 28.7$ GPa, $c_{12}^m = 9.1$ GPa, $c_{22}^m = 23.6$ GPa, $c_{66}^m = 7.25$ GPa. The elastic stiffness ($\mathbb{C}$) and Biot's coefficients ($\boldsymbol{\alpha}$, M) are then determined by using a homogenization procedure in which the micropores are assumed to be cylindrical inclusions in the working direction of the biological bone cells (*i.e* $\boldsymbol{e}_1$-direction) [5]. The fluid phase in bone and both fluid domains are assumed to be water with the mass density $\rho_f = 1000$ kg.m^{-3} and the bulk modulus $K_f = 2.25$ GPa. The thickness of the bone plate is $h = 4\,mm$. The acoustic source excited at emitter (located at $(x_1^s, x_2^s) = (0, 2)\,mm$)) has the form: $Q(t) = P_0\, e^{-4(f_0 t-1)^2} \sin(2\pi f_0 t)$, where f_0 is the central frequency et P_0 is a constant. For this test, $f_0 = 1$ MHz and $P_0 = 1$ Pa. The response of the system is measured at 14 receivers located in the upper fluid domain (Ω_1^f). These 14 receivers are regularly spaced with a pitch of 0.8 mm and the distance from the emitter to the closest receiver equals to 11 mm.

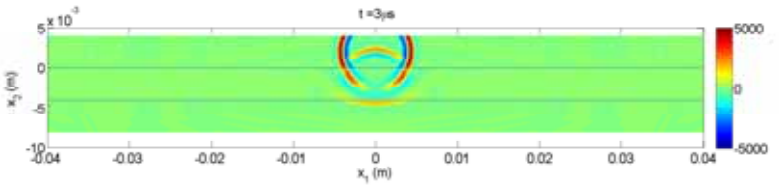

Figure 2: Snapshot of fluid pressures in the fluids and pore fluid pressure in the bone

In Fig. 2, we present a snapshot of fluid pressures field (p_1 for $\boldsymbol{x} \in \Omega_1^f$, p for $\boldsymbol{x} \in \Omega^b$, p_2 for $\boldsymbol{x} \in \Omega_2^f$). Figure 3 presents a comparison between the seismograms measured at the 14 receivers

in two cases of bone's porosity: $\phi = 5$ % and $\phi = 15\%$. This result shows that the change of the bone's porosity influences not only the FAS (First Arrival Signal) but also reflected and diffracted waves.

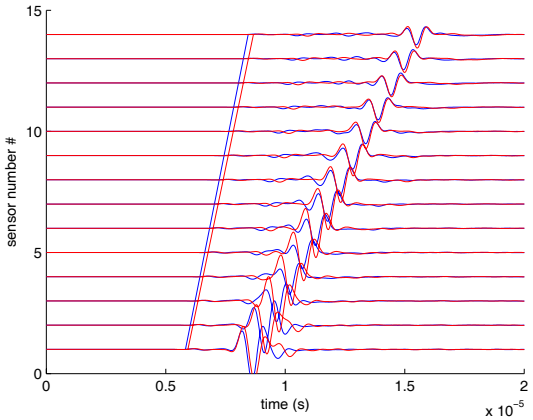

Figure 3: Normalized acoustic pressures captured at 14 sensors: porosity $\phi = 5\%$ (blue signals) and porosity $\phi = 15\%$ (red signals)

We note that the computation time required for each case presented in Fig. 3 is only about 300 seconds on a personal computer.

4 CONCLUSIONS

The present work shows a efficient numerical method based on the spectral finite element technique to simulate transient ultrasonic wave propagation in cortical long bones which is considered as an functionally graded anisotropic poroelastic medium. Such poroelastic model allows to investigate the influence of the bone porosity as well as of the bone matrix properties on the characteristics of ultrasonic wave propagation. As the method requires very low computation cost (even in high frequency domain), it is a powerful tool to carry a study when the solid is considered to have random material properties. Moreover, this method can be directly used to study the wave propagation in cancellous bones.

REFERENCES

[1] G. Lowet, G. Van der Perre. Ultrasound velocity measurements in long bones: measurement method and simulation of ultrasound wave propagation. *Journal of Biomechanics*, 29, 1255-1262, 1996.

[2] Q. Grimal, S. Naili. A theoretical analysis in the time-domain of wave reflection on a bone plate. *J. Sound Vib.*, 298, 12-29, 2006.

[3] G. Haiat, S. Naili, Q. Grimal, M. Talmant, C. Desceliers, C. Soize. Influence of a gradient of material properties on ultrasonic wave propagation in cortical bone: Application to axial transmission. *J. Acoust. Soc. Am.*, 125(6), 4043-4052, 2009.

[4] V.-H. Nguyen, S. Naili, V. Sansalone, Simulation of ultrasonic wave propagation in anisotropic cancellous bones immersed in fluid. *Wave Motion*, 47(2), 117-129, 2010.

[5] C. Hellmich, F.-J. Ulm, Microporodynamics of Bones: Prediction of "Frenkel-Biot" Slow Compresional Wave, *J. Engr. Mech.* 131(9), 918-926, 2005.

2nd International Conference on Mathematical and Computational Biomedical Engineering – CMBE2011
March 30 – April 1, 2011, Washington D.C., USA
P. Nithiarasu and R. Löhner (eds)

Acoustical Analysis of Swallowing Mechanism

Samaneh Sarraf Shirazi*, and Zahra Moussavi *
* Department of Electrical and Computer Engineering, University of Manitoba,
Winnipeg, MB R3T 5V6, Canada, umsarraf@ee.umanitoba.ca,
mousavi@ee.umanitoba.ca

SUMMARY

In this paper a mathematical representation of the swallowing sound generation and its application are discussed. A simple linear time invariant model was assumed to represent the pharyngeal wall and tissue which are excited by a train of impulses. It is assumed the pharyngeal response is the same for both groups of control and dysphagic subjects but the neural activities to initiate the swallow are different between the two groups. Thus, a wavelet basis function was chosen to represent the pharyngeal response and the neural impulses were assumed to be related to the wavelet coefficients at a specific level of decomposition. The results show the wavelet based model complied reasonably well with the physiological characteristics of swallowing mechanism, and provided a very strong discrimination between the swallowing sounds of the control and dysphagic groups of our study.
Key Words: *Swallowing sound, acoustical analysis, wavelet.*

1. INTRODUCTION

Swallowing is one of the most complicated mechanisms in human body. The timing and coordination of the swallowing events are important as any slight mismatch in the process may result in aspiration (the food drawing into the airway). In recent years, swallowing sound analysis has received considerable attention as a non-invasive monitoring tool for swallowing assessment [1-3], as well as gaining more insight about swallowing mechanism and its pattern of occurrence within the respiratory cycle in both control and dysphagic subjects at different age groups [4-6]. However, swallowing sound analysis is still at its infancy stage, and the exact source of swallowing sounds is unknown. This study attempts to derive a mathematical model for swallowing sound generation and transmission that may shed some light on the cause of the swallowing disorders.

To monitor and assess the factors contributing to swallowing disorders, different specialized assessment tools such as videofluoroscopy, fiber-optic endoscopic evaluation (FEES), electromyography, pharyngeal manometry, and auscultation are used. While videofluoroscopy study (VFSS) is considered as the current gold standard technique for swallowing evaluation, its application is limited. It can only be run for a short duration due to the radiation exposure. On the other hand, FEES has been reported to be a valid tool for detecting swallowing disorders such as aspiration, penetration and pharyngeal residue when compared with VFSS images [7, 8].

Meanwhile, acoustical monitoring and analysis of swallowing mechanism has received considerable attention as a non-invasive and convenient method for swallowing assessment [2-4,9-11]. The swallowing sound consists of two distinct segments [12]: initial discrete sound (IDS) and bolus transit sound (BTS). IDS occurs during the pharyngeal phase and are related to the opening of the upper esophageal sphincter, while BTS occurs during esophageal phase and are

the gurgle sounds associated with the peristaltic contraction that pushes the bolus into the esophagus.
While swallowing sounds analysis has been reported to classify the control and dysphagic groups with a relatively high accuracy [2,13,14], modeling of swallowing sound generation and transmission has not been addressed adequately. In one of our group's previous works [15] a model was introduced in an attempt to explain swallowing sound generation. In that model, swallowing sounds were assumed to be produced by exciting the pharyngeal wall structure and tissue with an impulse train coming from the pharynx. Having assumed the excitation source and the pharyngeal wall structure are independent, the model shown in Fig. 1 was proposed to represent the swallowing sound generation.

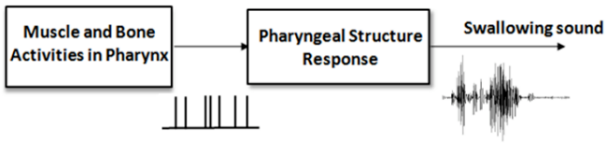

Fig. 1. Model of swallowing sound production (adopted from [15] with permission).

2. Method

2.1 Data

Swallowing sound recordings of 5 individuals as the control group were adopted from the previous study [15]. The swallowing sounds of 5 dysphagic subjects with swallowing disorders, as a result of either brain stroke or traumatic brain injury, were recorded at Riverview Health Center, Winnipeg, MB, Canada. All study subjects gave written consent and the study was approved by the Ethics Board of the University of Manitoba. As the FEES test was performed, the swallowing sounds along with the FEES video data were recorded simultaneously.
All subjects were fed juice by 5 ml spoon. The swallowing sounds of the control subjects were recorded by a Siemens (EMT25C) accelerometer placed over the suprasternal notch of the trachea and digitized at 44 kHz; the patients' data were recorded by a Sony ECM-88B microphone placed over the suprasternal notch of trachea and digitized at 44 kHz.

2.2 Modeling

The swallowing sound can be thought to be the output of a linear and time invariant (LTI) system representing the oropharynx muscle and tissue responses to the neural activities that initiate swallow, and are represented by an impulse train.
In the proposed modeling in this paper, it is assumed that the transfer function of the pharyngeal walls to the initiating neural pulses is the same for both normal and dysphagic swallows but it is the neural pulses, i.e. the input of the system that accounts for the difference between the two groups. Therefore, it was assumed that the pharyngeal response (the system transfer function) can be suitably represented by a wavelet basis function at a fixed pre-defined level. The selection of the type of the basis function is described later. To investigate the feasibility of the above modeling wavelet decomposition was applied to the IDS parts of the swallowing sounds of both groups.
The discrete wavelet approximation coefficients different levels of decomposition were examined. The Symlet wavelet of order 8 was chosen to be consistent with previous studies [15]. It is speculated that the average power of the coefficients at a specific level can mimic the impulses applying to the system. The average power is calculated as the sum of the square of magnitude over the length of the signal.
To find the level of decomposition that can best distinguish between the control and dysphagic swallows, a simple classification by setting a threshold were done. For each swallowing sound, the average power of the approximation coefficients was calculated at 8 levels of decomposition.

The best level was chosen according to the specificity and sensitivity of the classification calculated for each level. The classification results of using every one of the 8 levels of wavelet coefficient for classifying all the recorded swallows are shown in table I.

TABLE I. The classification results at 8 levels of decomposition.

level	Accuracy	Specificity	Sensitivity
1	89.69%	87.50%	92.68%
2	90.72%	89.09%	92.86%
3	92.78%	90.91%	95.24%
4	87.63%	82.26%	97.14%
5	86.60%	80.95%	97.06%
6	80.41%	77.97%	84.21%
7	71.13%	65.38%	94.74%
8	70.10%	64.56%	94.44%

As demonstrated in Table I, the 2nd and 3rd level can discriminate between the control and dysphagic swallows better than the other levels. To display the classification results for all subject swallows in the two groups, the average power of the 3rd level coefficients were plotted versus that of the 2nd level coefficients (Fig. 2). As it can be seen, these two features can serve as two characteristic biomarkers with 100% accuracy in distinguishing the two study groups. It should be noted that the accuracy values presented in Table I are when every swallow is considered as one individual case; however, in Fig. 2 the average values of the two biomarkers for the swallows of each subject are calculated and plotted, which resulted in 100% accuracy in separating the two groups.

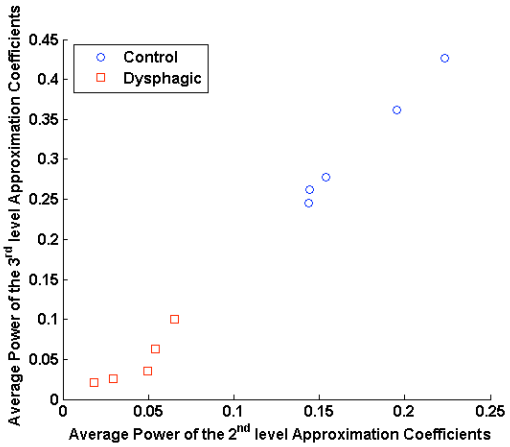

Fig. 2. The scatter plot of the average power of the control and dysphagic data at two levels of wavelet decomposition averaged among each subject's swallows..

3. CONCLUSIONS

In this study, the swallowing mechanism modeling was investigated using acoustical analysis of the swallowing sound. The proposed model benefits from the known relationship between the generated sounds during the swallow and the physiological events caused by the neural circuitry, by which the whole mechanism is governed. Therefore, it is assumed that swallowing sound is a result of a linear time invariant system (pharyngeal response) excited by a train of impulses (neural activities) that may be different between healthy and dysphagic swallows.

The patients participating in this study lack a controlled, coordinated swallow due to neuromotor impairments as a result of stroke or traumatic brain injury that may interfere with efficient food processing, delays in initiating swallows, and inefficient oropharyngeal clearance of the

swallowed material [4]. Therefore, the wavelet modeling seems to be an appropriate representation of the swallowing sound generation. The wavelet based model that takes into account the effect of the input is congruent with physiological cause of dysphagia that occurs in these patients.

The proposed linear time invariant model presented in this paper is the first attempt toward modeling the swallowing mechanism. The results of this study can be used for developing non-invasive and relatively simple diagnostic/screening tool.

ACKNOWLEDGMENT

The authors would like to acknowledge A. Meakin, C. Brooke, R. Daun, and L. Lentile at Riverview Health Center for their help in recruiting patients and collecting data.

REFERENCES

[1] J. E. Dempsey, F. L. Vice, J. F. Bosma, "Combination of cervical auscultation and videoradiography in evaluation of oral and pharyngeal dysphagia (abstract)," *Symposium on Dyspbagia*, Johns Hopkins Hospital, March, 1990.

[2] L. Lazareck and Z. Moussavi, "Classification of Normal and Dysphagic Swallowing Sounds by Acoustical Means", *IEEE Trans. Biomed. Eng.*, vol. 51, no. 12, pp. 2013-2112, 2004.

[3] M. Aboofazeli and Z. Moussavi, "Analysis of Temporal Pattern of Swallowing Mechanism," *Proc. IEEE EMBS*, Sept. 2006.

[4] G. Rempel and Z. Moussavi, "The Effect of Viscosity on the Breath Swallow Pattern of Young People with Cerebral Palsy," *Dysphagia*, vol. 20, no. 2, pp. 108-112, 2005.

[5] S. L. Hamlet, R. L. Patterson, S. M. Fleming, and L. A. Jones, "Sounds of Swallowing Following Total Laryngectomy," *Dysphagia*, vol. 7, no. 3, pp. 160-165, 2006.

[6] J. A. Logeman, *Evaluation and Treatment of Swallowing Disorders*, Austin, Tx, Pro-Ed, 1998.

[7] S. E. Langmore, K Schatz, and N. Olson, "Endoscopic and Videofluoroscopic Evaluations of Swallowing and Aspiration," *Ann Otol. Rhinol & Laryngol*, vol. 100, no. 8, pp. 678-681, 1991.

[8] S. E. Langmore, K. Schatz, and N. Olsen, "Fiberoptic Endoscopic Examination of Swallowing Safety: A New Procedure," *Dysphagia*, vol. 2, pp. 216-219, 1988.

[9] R. C. Mackowiak, H. S. Brenman, and M. H. F. Friedman, "Acoustic Profile of Deglutition," *Proc. Soc Exp Biol Med.*, vol. 125, pp. 1149-1152, 1967.

[10] S. L. Hamlet, R. J. Nelson, R. L. Patterson, and D. Michigan, "Interpreting the Sound of Swallowing: Fluid Flow through the Cricopharyngeus," *Ann Otol. Rhinol & Laryngol* 99, pp. 749-752, 1990.

[11] J. A. Y. Cichero, B. E. Murdoch, "Acoustic Signature of the Normal Swallow: Charecterization by Age, Gender, and Bolus Volume," *Ann. Otol. Rhinol. Laryngol* 111, pp. 623-632, 2002.

[12] F. L. Vice, J. M. Heinz, G. Giuriati, M. Hood, J. F. Bosma, "Cervical Auscultation of Suckle Feeding in Newborn Infants," *Dev Med Child Neurol*., vol. 32, no. 9, pp. 760-768, 1990.

[13] M. Aboofazeli and Z. Moussavi, "Analysis and Classification of Swallowing Sounds Using Reconstructed Phase Space Features," *Proc. IEEE ICASSP*, pp. 421-424, March 2005.

[14] A. Yadollahi and Z. Moussavi, "Feature Selection for Swallowing Sounds Classification," *29th IEEE EMBS Conf*., pp. 3172 – 3175, Aug. 2007.

[15] A. Yadollahi and Z. Moussavi "A Model for Normal Swallowing Sounds Generation Based on Wavelet Analysis," *Canadian Conference on Electrical and Computer Engineering, CCECE*, pp. 827–830, 2008.

2nd International Conference on Mathematical and Computational Biomedical Engineering – CMBE2011
March 30 – April 1, 2011, Washington D.C., USA
P. Nithiarasu and R. Löhner (eds)

Investigation of Cigarette-Smoke Droplet Evaporation, Transport and Deposition using Puffing-Inhalation for a Realistic Mouth-to-Lung Respiratory System

Yu Feng*, Clement Kleinstreuer*
* Department of Mechanical & Aerospace Engineering, North Carolina State University, Raleigh, NC 27695, USA

SUMMARY

In this paper, conventional cigarette-smoke droplet evaporation and deposition patterns in a transient air flow field of a realistic respiratory geometry were investigated by numerical simulation using both CFX 12.0 and FLUENT 12.0 (ANSYS Inc., Canonsburg, PA) with realistic puffing-waveform inlet condition. Additionally, comparisons between steady-state and transient flow fields are provided. Results are essential for the prediction of smoking health hazards in the respiratory system, i.e., from mouth to lung airway generation 9.

Key Words: *Mouth-to-lung, smoking puff inlet, transient, evaporation, deposition, cigarette.*

1. INTRODUCTION

Smokers inhale a mixture of more than 4000 varyingly toxic substances including carcinogens, heavy metals as well as gaseous health-damaging materials [1]. Cigarette-droplet evaporation and deposition patterns inside the human respiratory system are essential for the prediction of critical lung sites, potentially leading to health hazards. In this paper, such a topic is investigated numerically with realistic boundary conditions.

The human respiratory model, here from mouth to lung airway generation 9, is the combination of mouthpiece geometry (from Virginia Commonwealth University) and a lung airway geometry provided by the Technical University Munich (TUM). The 3-D oral cavity geometry was created based on CT data of a healthy adult, imaged using a multi-row helical scanner with a slice thickness of 1mm [2]. Image files were then converted to a solid body model using the software package MIMICS (Materialise, Ann Arbor, MI). The TUM lung airway geometry was segmented using again the commercially available segmentation software MIMICS, based on standard CT scans with a resolution of 0.7 mm [3].This allowed up to 9 generations of the bronchial tree to be realized. The whole geometry is shown in Fig. 1 with extended outlets and cigarette-shape inlet.

2. MESH GENERATION AND DEPENDENCY TEST

Meshes were generated with the commercial software ICEM CFD v. 12.0 (ANSYS Inc., Canonsburg, PA). The unstructured tetrahedral meshes consisted of tetrahedral elements and pyramids elements with prism layers near the wall. A mesh independence test was performed using steady flow simulations of air at 25 ^{o}C with an inlet volume flow rate Q_{in}=60ml/s, which is representative of mean flow conditions. Four different meshes were generated. The wall boundary conditions were set to be no-slip. The outlet boundary conditions are set to be uniform pressures. A specified solver RMS residual is defined as 1e-5. Simulations were performed on two local Intel 3.20 GHz processors (Dell Precision T 3500 Desktop) running 64bit Microsoft Windows XP with 12 GB memory. Considering four different meshes, the velocity profiles were examined at different locations in the human respiratory geometry. A representative comparison is shown

in Fig. 2, where Mesh 3 is the final mesh being used which can perfectly repeat the numerical results provided by Mesh 4. Specifically, Mesh 3 contains 12,181,689 elements and 3,264,028 nodes.

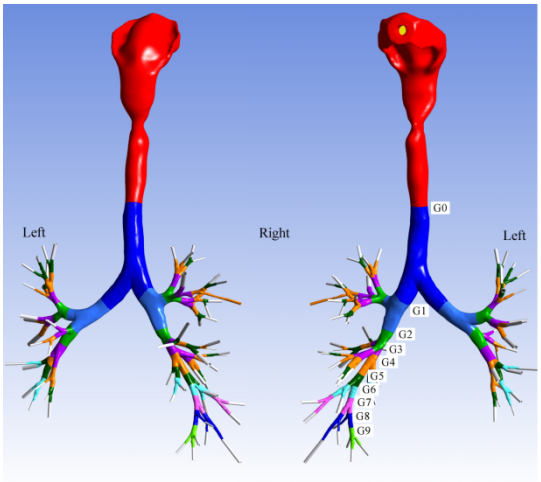

Fig. 1 The human respiratory mouth-to-G9 geometry

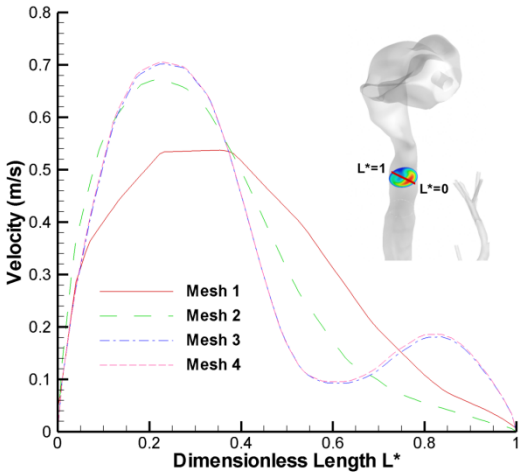

Fig. 2 Representative mesh independence test

3. TRANSIENT AIR FLOW IN THE RESPIRATORY SYSTEM

In order to obtain realistic evaporation results and deposition patterns of cigarette-smoke droplets, a realistic puffing waveform was used (see Fig. 3). The transient laminar air flow was numerically calculated with a maximum Reynolds number under 2000. The governing equations are provided in Ref. [4]. The resulting velocity contours at different cross sections of the respiratory system at t=0.6 s are shown in Fig. 4. In the oral cavity, i.e., from mouth inlet to vocal fold, the flow field is very complicated. For example, recirculating flow occurs near the inside bend of the pharynx as visualized in 3-D in Fig. 4. This region of recirculating flow is due to the sudden change of geometry and the inertia of the air flow. Also, jet flow is formed near the vocal fold because of the sudden reduction of the local cross sectional area. Additionally, secondary flows from mouth cavity to trachea can be observed (see Fig. 4).

The variation of the transient flow field inside the respiratory system are shown in Fig. 5 from t=0 s to t=1.75 s. Also, at peak flow, i.e., at=0.6s, the velocity field appears to be quite similar to the steady-state flow field with inlet condition Q_{in}=60ml/s. Thus, for a quick analysis one may just compute the steady-state flow instead of a transient flow field at the peak of the inlet waveform.

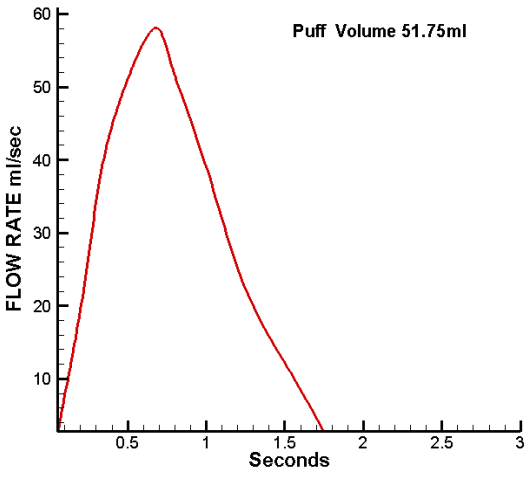

Fig. 3 Representative puffing waveform

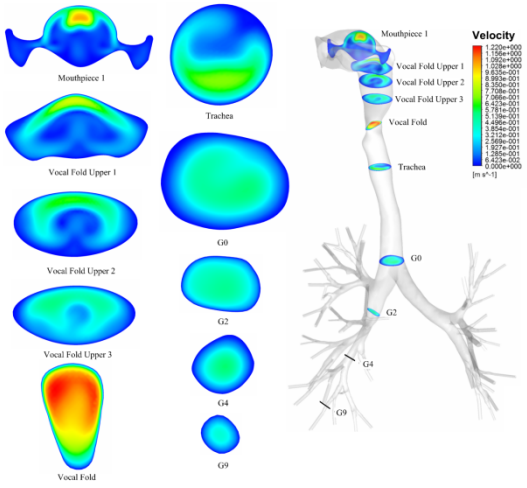

Fig. 4 Velocity contours at different cross secions of the respiratory system

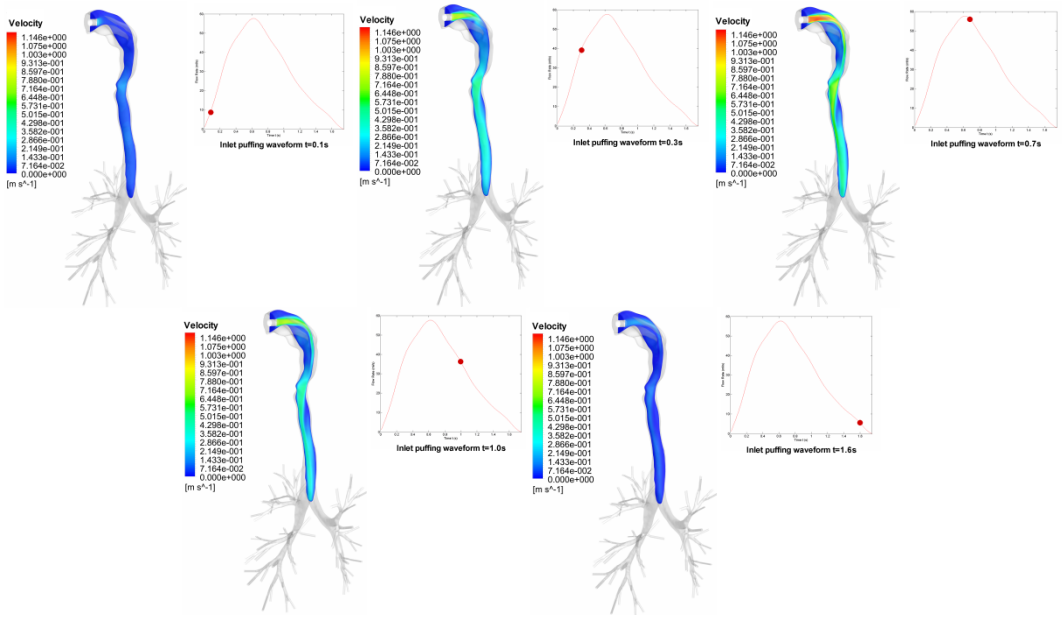

Fig. 5 Transient flow field inside the respiratory system

4. DROPLET EVAPORATION AND DEPOSITION ANALYSIS

Driven by the transient air flow field, cigarette-smoke droplet evaporation and deposition analysis will be performed using the ANSYS FLUENT 12.0 one-way coupled method. Discrete Phase Model (DPM) in FLUENT 12.0 is used to calculate droplet motion and change in diameter. Specifically,

$$\frac{d\overrightarrow{v_p}}{dt} = \overrightarrow{F_D} + \overrightarrow{F_g} + \overrightarrow{F_B} \tag{1}$$

where $\overrightarrow{F_g}$ is the gravity term which can be expressed as:

$$\overrightarrow{F_g} = \frac{\overrightarrow{g} \cdot \left(\rho_p - \rho_g\right)}{\rho_p} \tag{2}$$

and ρ_p and ρ_g are the densities of particle and gas (i.e. air), respectively. $\overrightarrow{F_D}$ is the Stokes drag force with Cunningham correction factor [5, 6]. $\overrightarrow{F_B}$ is the Brownian motion force modelled via a Gaussian white noise module in Fluent 12.0.

For droplet evaporation, the mass and heat transfer over the whole droplet surface is described in Ref. [7].

5. CONCLUSIONS AND FUTURE WORKS

The transient airflow field in a realistic human respiratory system from mouth to lung airway generation 9 was numerically calculated for typical puffing inhalation. Flow fields are visualized, i.e., secondary flows, inlet jet effect, etc. No significant difference between the transient air flow field at the peak of the inhalation waveform and a corresponding steady-state flow field for Q_{in}=60ml/s was observed.

Droplet evaporation and deposition analysis will be provided as part of the future work.

REFERENCES

[1] Haustein, K., Tobacco or Health? Physiological and Social Damages Caused by Tobacco Smoking, Springer, Berlin, Germany

[2] Xi, J., Longest, W. (2007), Transport and Deposition of Micro-Aerosols in Realistic and Simplified Models of the Oral Airway, Annals of Biomedical Engineering, Vol. 35, pp. 560-581

[3] Comerford, A., Bauer, G., Wall, W. A. (2010), Nanoparticle transport in a realistic model of the tracheobronchial region, International Journal for Numerical Methods in Biomedical Engineering, Vol. 26, pp. 904-914

[4] Steffens, J. (2010), Comparison of Particle Deposition for Realistic Adult and Adolescent Upper Airway Geometries Using Unsteady Computational Fluid Dynamics, Master Thesis, Department of Mechanical Engineering, Rochester Institute of Technology

[5] Ounis, H., Ahmadi, G., J.B., M. (1991), Brownian diffusion of sub-micrometer particles in the viscous sublayer, J. Colloid and Interface Science, Vol. 143, pp. 266-277

[6] Walters, D. K., Luke, W. H. (2011), Computational Fluid Dynamics Simulations of Particle Deposition in Large-Scale, Multigenerational Lung Models, Journal of Biomechanical Engineering, Vol. 133, pp. 011003-1-011003-8

[7] Zhang, Z., Kleinstreuer, C., Kim, C. S. (2006), Isotonic and Hypertonic Saline Droplet Deposition in a Human Upper Airway Model, Journal of Aerosol Medicine, Vol. 19, No. 2, pp. 184-198

2nd International Conference on Mathematical and Computational Biomedical Engineering - CMBE2011
March 30 - April 1, 2011, Washington D.C, USA
P. Nithiarasu and R. Löhner (Eds.)

COMPUTATIONAL MODEL OF TISSUES IN THE HUMAN UPPER AIRWAY

Jean-Paul V. Pelteret[⋆,1] **and B. Daya Reddy**[⋆,2]
[⋆]Centre for Research in Computational and Applied Mechanics,
University of Cape Town, Rondebosch 7701
[1]jppelteret.uct@gmail.com
[2]daya.reddy@uct.ac.za

ABSTRACT

This study presents a computational model of the tissues in the human upper airway. Anatomically and histologically correct data has been used to construct an accurate model of the hard, soft and fibrous tissues. An open-source finite element library has been used to create an incompressible quasi-static finite-strain model of the anatomy. Hyperelastic materials describe the behaviour of the materials. A Hill three-element model is used to represent the active skeletal muscle. A genetic algorithm has been used to control neural input to the model. Unsteady loading conditions are considered, and the predicted response of the genioglossus (GG) is compared to experimental data. Results indicate a good correlation between the predicted and measured response of the GG. A parametric study is performed to determine the influence of a number of factors on the response of the GG.

Key Words: Muscle modelling, upper airway anatomy, constitutive model, genetic algorithm

1 INTRODUCTION

Obstructive Sleep Apnoea (OSA) is a pathological disease that afflicts a large portion of the population. The condition involves a partial or complete blockage of the upper airway, resulting in a restless sleep and, ultimately, a multitude of severe and potentially life-threatening medical ailments for suffers. There are many mechanisms and factors involved [1], and computational modelling provides a unique insight into the causes of flow blockage.

Due to the histological and physiological complexity of the anatomy, describing the motion of the tongue is challenging. A complex interaction exists between the the soft-tissues of the upper airway and the airflow through the airway. Many of numerical models of varying complexity of the tongue have been created to date e.g. [2,3]. A major issue with using these models to study OSA is that they require a fixed contraction history for each muscle group which is defined *a priori*. OSA, by nature, occurs under varying conditions, which would be difficult to study with such a restrictive model. To circumvent this issue, Huang et al. [4], made assumptions that linked the genioglossus (GG) activation level to the pressure in the oropharynx, so that the response of the GG is not fixed but changes in response to the airway pressure.

The aim of this study is to understand the response of the GG, the main airway dilator muscle in the tongue, under various scenarios. To achieve this, an anatomically and physiologically realistic model of the human upper airway is reproduced. Additionally, a generic method of predicting the

neural response of the GG during time-dependent pressure of the tongue loading is developed and comparison of this response with experimental data is made.

2 DATA EXTRACTION AND GEOMETRY RECONSTRUCTION

Geometry from the female subject of the Visible Human Project [5] was extracted using commercial software. This data was used to reconstruct a three-dimensional model of the tongue, soft-palate and oropharynx. In addition to macroscopic structures, the underlying histology of each muscle group was extracted.

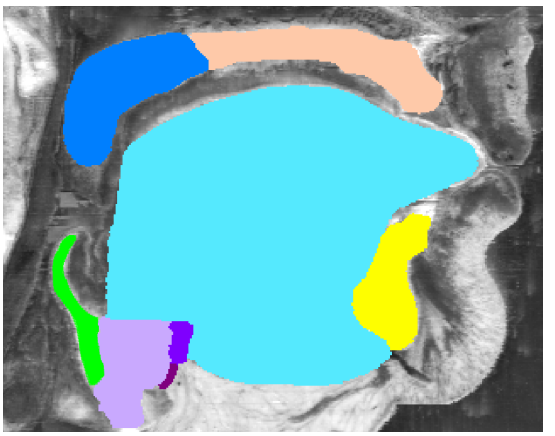

Figure 1: Anatomy extraction

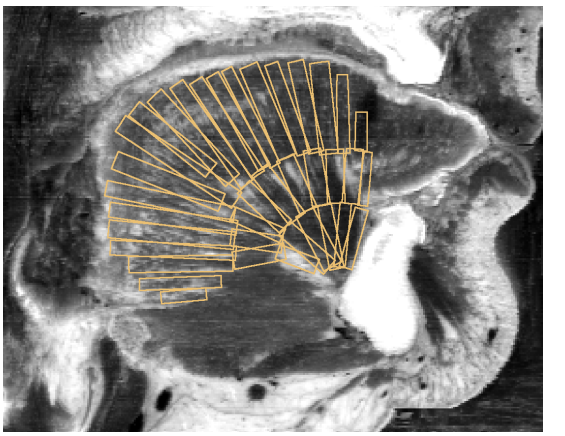

Figure 2: Microscopic histology extraction

A commercial meshing tool was used to reconstruct the geometry using a fully structured mesh. The tongue, epiglottis, uvula and surrounding hard and soft tissue were accurately represented.

3 COMPUTATIONAL METHODOLOGY

A fully non-linear quasi-static finite element model (FEM) was developed using deal.II, an open-source FEM library [6]. The incompressible nature of biological materials has been accounted for using an augmented Lagrange multiplier method, enforced using a Uzawa method [7]. A frictionless contact algorithm [8] has been included to model sliding contact between the tongue, hard-palate, epiglottis and uvula. The non-zero stress state [9] in the extracted geometry is accounted for by defining a new initial configuration (IC) from which the total deformation gradient in the current configuration is computed. The IC is defined in a simplistic manner by applying a body force to the bodies in the RC and recording this deformed state.

Representative models for each tissue type have been developed. A comprehensive Hill-type model for muscle tissue [10,11] that accounts for both the passive and active behaviour of muscles has been incorporated into the model. The complex and discontinuous force-length [12] and force-velocity [13] relationship of the contractile element have been accurately recreated using a mollifier function. Extrinsic muscle groups are included as external entities in order to reduce geometric complexity and contribute to the deformation of bodies through the addition of boundary terms.

A neural input model has been developed to compensate for the scarcity of experimental data [14,15,16] regarding the neural signals that control muscles in the HUA. The neural input model

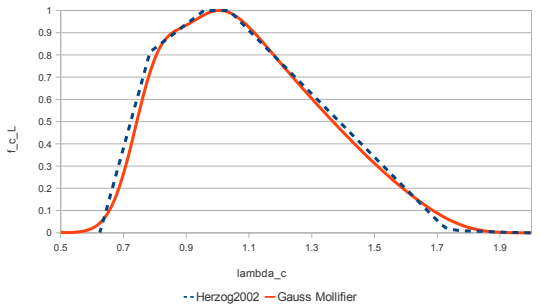

Figure 3: CE force-length relationship

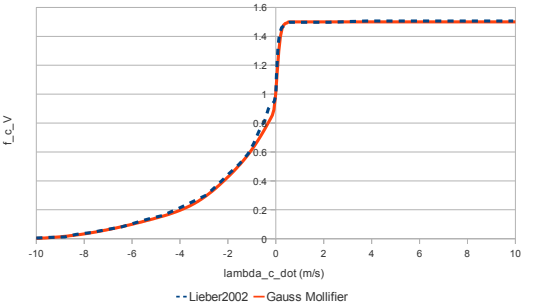

Figure 4: CE force-velocity relationship

uses an open-source genetic algorithm library [17,18,19] to control the level of activation of specific muscle groups based on pre-set criterion. The position of a net of points on the tongue as monitored and movement of the bodies is performed to minimise the distance of these control points from a specified position in space. As the the evaluation of the GA objective function is expensive, numerous techniques are employed to restrict the solution space and minimise the number of evaluations required to attain a optimum neural input.

4 RESULT OVERVIEW

The breathing cycle is emulated through the application of a sinusoidally oscillating pressure load on the surface of the bodies. Three cycles, with a peak pressure of 350Pa, are simulated. Using the GA, control over the time- and load-dependent position of a net of points on the tongue is achieved. Comparison between the case where position attainment and maintenance is required and when it is not indicates the effectiveness of the GA in controlling the movement of the tongue.

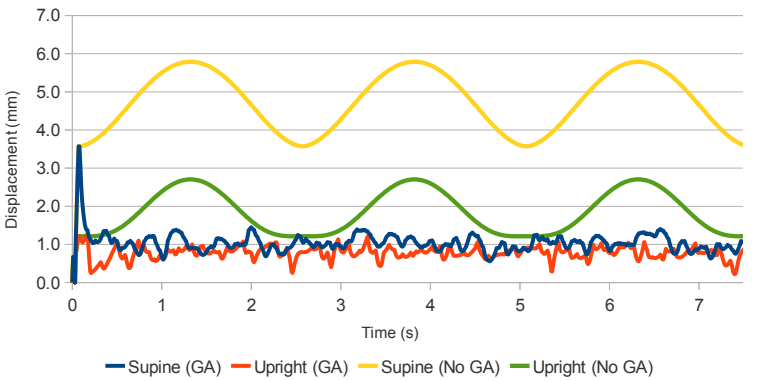

Figure 5: Goal position attainment and maintenance of rear surface of tongue

The GG activation history for the described case shows a good correlation to the experimental data. It is observed that the GG acts to prevent movement of the tongue due to the influence of the applied loading. The contraction level of the GG increases as the pressure load is increased, and vice versa. Additionally, it is observed that the GG activation history is different under varying gravitational orientations. This is primarily due to the body force working against the pressure force in the upright case, while in the supine case gravity and airway pressure both draw the tongue towards the posterior surface of the oropharynx.

Additional parametric studies involving different loading conditions and material parameters highlight the role of these factors in terms of their influencing the OSA condition.

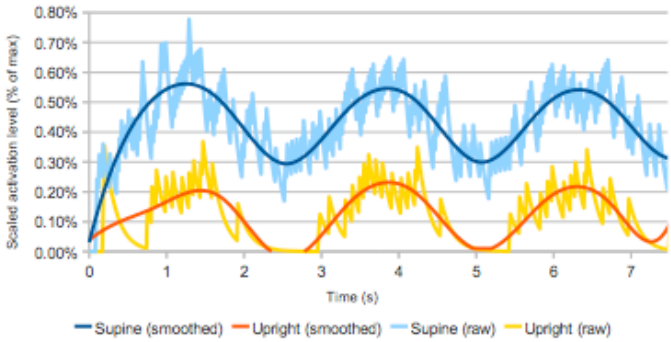

Figure 6: GG activation level history

5 REFERENCES

[1] A. Malhotra and D. P. White. Obstructive Sleep Apnoea. *The Lancet*, 360, 237–245, 2002.

[2] J-M. Gèrard et. al. A 3D dynamical biomechanical tongue model to study speech motor control. *Recent Research Developments in Biomechanics*. ,1 49–63, 2003.

[3] M.C. Wu et. al. Using Three-Dimensional Finite Element Models and Principles of Active Muscle Contraction to Analyse the Movement of the Tongue. *In Proceedings of 11th Australian International Conference on Speech Science & Technology*, 2006.

[4] Y. Huang and A. Malhotra and D.P. White. Computational simulation of human upper airway collapse using a pressure-/state-dependent model of genioglossal muscle contraction under laminar flow conditions. *Journal of Applied Physiology*, 99, 1138–1148, 2005.

[5] U.S. National Library of Medicine. The Visible Human Project ®. *http://www.nlm.nih.gov/research/visible/visible human.html*, August 2009.

[6] W. Bangerth, R. Hartmann, and G. Kanschat. deal.II a general-purpose object-oriented finite element library. *ACM Transactions on Mathematical Software*, 33, 2007.

[7] J.C. Simo and R.L. Taylor. Quasi-incompressible finite elasticity in principal stretches. Continuum basis and numerical algorithms. *Computer Methods in Applied Mechanics and Engineering*, 85, 273–310, 1991.

[8] Wriggers, P. *Computational Contact Mechanics*, 2nd. Edition. Springer-Verlag, 2006

[9] M. Gee, C.Forster, and W.A. Wall. A computational strategy for prestressing patient-specific biomechanical problems under finite deformation. *International Journal for Numerical Methods in Engineering*, 26, 52–72, 2010.

[10] J.A.C. Martins, E.B. Pires, R. Salvado, and P.B. Dinis. A numerical model of passive and active behaviour of skeletal muscles. *Computer Methods in Applied Mechanics and Engineering*, 151, 419–433, 1998.

[11] J.A.C. Martins, M.P.M. Pato, and E.B. Pires. A finite element model of skeletal muscles. *Virtual and Physical Prototyping*, 1, 159–170, 2006.

[12] W. Herzog and R. Ait-Haddou. Considerations on muscle contraction. *Journal of Electromyography and Kinesiology*, 12, 425–433, 2002.

[13] R.L. Lieber. *Skeletal Muscle Structure, Function and Plasticity: The Physiological Basis of Rehabilitation*, 2002.

[14] Malhotra, A. et al.. Genioglossal But Not Palatal Muscle Activity Relates Closely to Pharyngeal Pressure. *American Journal of Respiratory and Critical Care Medicine*, 162, 1058–1062, 2000.

[15] Stanchina, M. L. et al.. Genioglossus Muscle Responsiveness to Chemical and Mechanical Stimuli during Non-Rapid Eye Movement Sleep. *American Journal of Respiratory and Critical Care Medicine*, 165, 945–949, 2002.

[16] Pierce, R. et al.. Upper airway collapsibility, dilator muscle activation and resistance in sleep apnoea. *European Respiratory Journal*, 30, 345–353, 2007.

[17] Matthew Wall. GAlib: A C++ Library of Genetic Algorithm Components. *http://lancet.mit.edu/ga/*, July 2010

[18] Melanie Mitchell. *An Introduction to Genetic Algorithms*. MIT Press, 1999.

[19] B.S. Ibrahim et al.. Identification of Active Properties of Knee Joint using GA Optimization. *World Academy of Science, Engineering and Technology*, 55, 441–446, 2009.

2nd International Conference on Mathematical and Computational Biomedical Engineering - CMBE2011
March 30 - April 1, 2011, Washington D.C, USA
P. Nithiarasu and R. Löhner (Eds.)

A THREE-DIMENSIONAL DESCRIPTION OF ARTERIAL GROWTH AND REMODELING

Igor Karšaj*, Jurica Sorić* and Jay D Humphrey**
*Faculty of Mechanical Engineering and Naval Architecture, University of Zagreb, I.Lučića 5,
HR-1000 Zagreb, Croatia, E-mail: igor.karsaj@fsb.hr
**Biomedical Engineering, Yale University, New Haven, CT 06520 USA,
E-mail: jhumphrey@yale.edu

SUMMARY

This work describes a new method to model growth & remodelling (G&R) of the 3D arterial wall. The formulation describes all changes at the *in vivo* configuration. Each constituent (i.e. collagen, smooth muscle cells, and elastin) has its own stress free configuration but is constrained to deform with mixture. Illustrative results are shown for hypertensive remodeling and responses to flow.
Key Words: *constrained mixture model, adaptation, hypertension, growth and remodeling*

1 INTRODUCTION

In recent years, modeling of biological growth and remodeling (G&R) has attracted increased attention. Many questions concerning the formulation of constitutive models describing the biomechanical behaviour of soft tissue and particulary arteries remain open. Specifically, changes in blood pressure or flow from normal result in arterial adaptations via G&R processes. The earliest mathematical models of G&R were mostly focused on kinematical descriptions [1] or variations of these ideas [2]. Our model follows but extends ideas from [3] based on the concept of evolving configurations. G&R of arteries is thus described via the turnover of different constituents possessing different natural configurations and mechanical properties and exhibiting different rates of turnover that can change with mechanical stimuli [4]. The developed framework is restricted to elastostatics, but is able to describe 2-D or 3-D behaviours in general. The goal of this work is to extend prior developments to 3-D. We assume different rates of turnover of individual structurally significant constituents: elastin, collagen (4-fibre families), and smooth muscle cells, each of which can possess different natural configurations [4]. The production of the constituents is simulated by allowing normal stresses in the wall as well as shear stresses at the luminal surface of the artery control kinetic equations for each structurally significant constitutent [3], [5]. Indeed, a delicate balance between vasodilators (e.g. nitric oxid) and vasoconstrictors (endothelin-1) released by endothelial cells influence such turnover. The removal of the constituents is similarly assumed to be function of wall stress [3], [5]. Illustrative results are shown for cases of sustained reductions in flow or increase in pressure and compared to prior 2-D results. Close correspondence between the present 3-D formulation and well established 2-D formulations provide significant confidence in the extension of the present work to address diverse diseases of clinical importance.

2 KINEMATICS AND KINETICS

It proves convenient to define different deformation gradients for aspects of G&R. The theory of evolving natural configurations, as in [4], is used whereby individual constituents are stress-free only in the natural configuration associated with their time of production. Accordingly, $\mathbf{G}^k$ defines prestretch of the each constituent under which it is embedded in the wall during the G&R, Figure 1. The deformation gradient from the natural configuration giving the actual stretch of the constituent produced at the time τ observed at the instant s is $\mathbf{F}^k_{n(\tau)}$. Moreover, ${}^s_\tau\mathbf{F}$ quantifies mappings within mixture configurations between instants τ and s. The orientation of the constituents in the arterial wall is usually determined in the actual (*in vivo*) configuration at the time $\tau = 0$ and we denote it as $\mathbf{m}^k(0)$. Total mass $M(s)$ is a sum of mass of elastin and fibrous structures given by

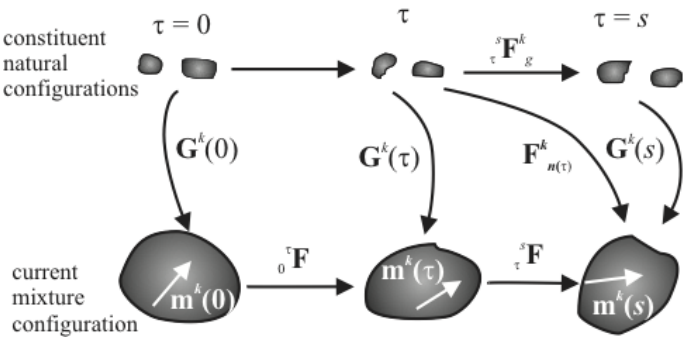

Figure 1: Schema of important configurations

$$M^k(s) = M^k(0)q^k(s) + \int_0^s m^k(\tau)q^k(s-\tau)\mathrm{d}\tau. \tag{1}$$

Herein, $m^k(\tau)$ is the production / removal term that is function of the change in stress within the wall and the change of shear stress on endothelial cells. The half-life time of each constituent is described by the function q^k which varies with stretches within fibrous structures.

3 G&R - CONSTITUTIVE RELATIONS

The elastic behaviour of the body is assumed to be characterized by a free stored energy function W given as a sum of that due to elastin, collagen, and SMC:

$$W = \frac{M^k(0)}{M(s)}q^k(s)\hat{W}^k(\mathbf{C}^k_{n(0)}) + \int_0^s \frac{m^k(\tau)}{M(s)}q^k(s-\tau)\hat{W}^k(\mathbf{C}^k_{n(\tau)})\mathrm{d}\tau. \tag{2}$$

The distribution of the Cauchy stress, $\mathbf{t}$, within the wall thus depends on three contributions:
1) stress in elastin

$$\mathbf{t}^e = 2\frac{M^e(0)}{M(s)}q^e(s)\mathbf{F}(s)\frac{\partial\hat{W}^e(\mathbf{C}^e_{n(0)})}{\partial\mathbf{C}}\mathbf{F}^T(s) + p\mathbf{I}, \tag{3}$$

2) stress in the fibrous structures (i.e. collagen and smooth muscle cells)

$$\mathbf{t}^k = 2\left(\frac{M^k(0)}{M(s)}q^k(s)\mathbf{F}(s)\frac{\partial\hat{W}^k(\mathbf{C}^k_{n(0)})}{\partial\mathbf{C}}\mathbf{F}^T(s) + \int_0^s \frac{m^k(\tau)}{M(s)}q^k(s)\mathbf{F}(s)\frac{\partial\hat{W}^k(\mathbf{C}^k_{n(\tau)})}{\partial\mathbf{C}}\mathbf{F}^T(s)\mathrm{d}\tau\right). \tag{4}$$

3) active responses of smooth muscle cells, contributing only in the circumferential direction,

$$t^{act} = T_M \phi^m(s)(1 - \mathrm{e}^{-C(t)^2})\lambda^m_{act}\left[1 - \left(\frac{\lambda_M - \lambda^m_{act}}{\lambda_M - \lambda_0}\right)^2\right] \tag{5}$$

where T_M is a scaling factor, $\phi^m(s)$ the mass fraction of SMC at time $t = s$, λ_M and λ_0 are stretches at which the force generating capacity is maximum and zero, respectively, $\lambda^m_{act} = r(s)/r^m_{act}(s)$ where $r^m_{act}(s)$ evolves via a first order rate equation.

4 GLOBAL EQUILIBRIUM EQUATION AND RESULTS

We restrict ourselves to an axisymmetric 3D cylinder. Unknowns appearing in the simulations of G&R are inner radius r_i, outer radius r_o or wall thickness h, and axial force L. For the solution, we thus need three equations of which two are equilibrium equations

$$P = \int_{r_i}^{r_o} (t_{\theta\theta} - t_{rr})\,\frac{\mathrm{d}r}{r}, \quad \text{and} \quad L = \pi \int_{r_i}^{r_o} (2t_{zz} - t_{rr} - t_{\theta\theta})\, r\mathrm{d}r, \tag{6}$$

and the third equation defines balance of the mass

$$r_o^2(\tau) - r_i^2(\tau) = \frac{J_m M(0)}{\rho(\tau)\pi l}. \tag{7}$$

Here, l is length of the deformed artery and $\rho(\tau)$ is the mass density of the wall, which is assumed to be constant during the G&R; t_{rr}, $t_{\theta\theta}$ and t_{zz} are radial, circumferential, and axial stress components, respectively.

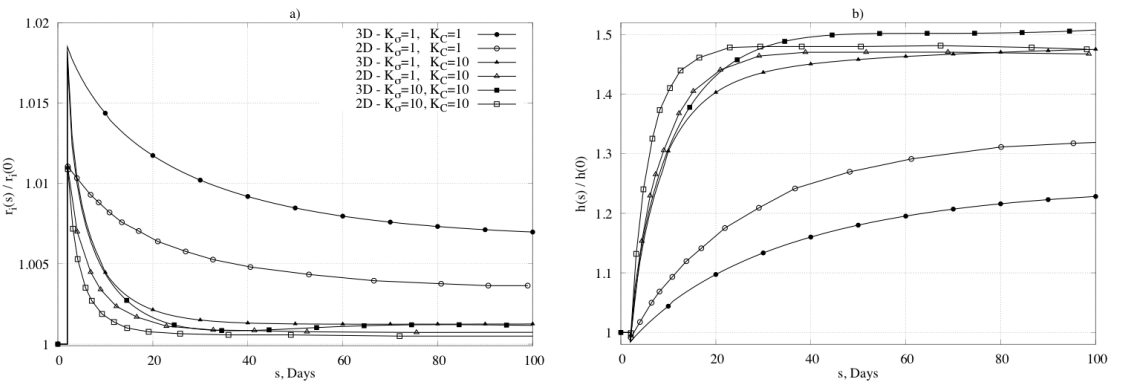

Figure 2: Geometric changes of the inner and outer radius in hypertension (50%)

To study the behavior of the model, we simulated G&R for a basilar artery, one of the key vessels supplying blood to the brain. Material parameters are taken from [7], or calculated to satisfy equilibrium and ensure normal tissue maintenance. As reported in [6], hypertension causes a thickening of the wall that tends to restore the circumferential stresses to its normal value. This long term adaptation is accompanied by an instantaneous increase in both inner and outer radius. As the G&R advances, however, the inner radius returns to initial value to restore the shear stress to normal. Results obtained with the present 3D model are compared those from a 2D model [7] in Fig. 2 for the case of a 50% increase in pressure, that is, hypertension with $P = 1.5P_h$. An advantage of a 3-D model is its capability to predict time courses for the unloaded or almost stress-free configurations (and the associated opening angles), which can be checked experimentally.

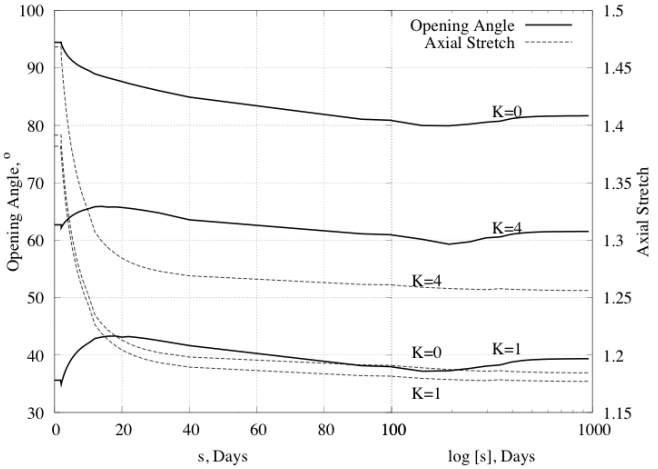

Figure 3: Time course of opening angle and axial stretches

Figure 3 shows changes in opening angle (solid lines) over time for different distributions of elastin prestretch through the wall (K=0 for constant, K=1 (linear), and K=4 for distribution). Similar to many reports in the literature, the opening angle first increased, then returned toward baseline. In addition, Figure 3 also shows the predicted evolution of the in vivo axial stretch (dashed line and right hand ordinate). As it can be seen, the model predicted dramatic decreases in the axial stretch (from 1.4 to 1.2). Such reductions in the in vivo axial stretch have also been reported for hypertension (Humphrey et al., 2009).

References

[1] R Skalak, G Dasgupta, M Moss, E Otten, P Dullumeijer, and H Vilmann. Analytical description of growth. *J Theor Biol*, 94(3):555–577, 1982.

[2] L A Taber and D W Eggers. Theoretical study of stress-modulated growth in the aorta. *J Theor Biol*, 180(4):343–357, 1996.

[3] J D Humphrey, S Baek, and L E Niklason. Biochemomechanics of cerebral vasospasm and its resolution: I. a new hypothesis and theoretical framework. *Ann Biomed Eng*, 35(9):1485–1497, 2007 Sep.

[4] J D Humphrey and K R Rajagopal. A constrained mixture model for arterial adaptations to a sustained step change in blood flow. *Biomech Model Mechanobiol*, 2(2):109–126, Nov 2003.

[5] S Baek, A Valentín, and J D Humphrey. Biochemomechanics of cerebral vasospasm and its resolution: II. constitutive relations and model simulations. *Ann Biomed Eng*, 35(9):1498–509, Sep 2007.

[6] P Fridez, M Zulliger, F Bobard, G Montorzi, H Miyazaki, K Hayashi, and N Stergiopulos. Geometrical, functional, and histomorphometric adaptation of rat carotid artery in induced hypertension. *J Biomech*, 36(5):671–680, 2003.

[7] A Valentín, L Cardamone, S Baek, and J D Humphrey. Complementary vasoactivity and matrix remodelling in arterial adaptations to altered flow and pressure. *J R Soc Interface*, 6(32):293–306, Mar 2009.

2nd International Conference on Mathematical and Computational Biomedical Engineering - CMBE2011
March 30 - April 1, 2011, Washington D.C, USA
P. Nithiarasu and R. Löhner (Eds.)

A non-linear homogeneous model for bone-like materials under compressive load.

M. Mengoni*, R. Voide, D. Toye***, A. Léonard***, G.H. van Lenthe** and J.P. Ponthot***
*University of Liège, LTAS - Non Linear Computational Mechanics, Liège, Belgium,
mmengoni@ulg.ac.be
**ETH Zurich, Institute for Biomechanics, Zurich, Switzerland
***University of Liège, Department of Applied Chemistry, Laboratory of Chemical Engineering, Liège, Belgium

SUMMARY

Using morphological data provided by computed tomography, finite element (FE) models can be used to compute the mechanical response of bone and bone-like materials without describing the complex local microarchitecture. A constitutive law is here developed and proposed for this purpose. It captures the non-linear structural behavior of bone-like materials through the use of fabric tensors. It also allows for irreversible strains using a plastic material model, allowing hardening of the yield parameters. These characteristics are expressed in a constitutive law based on the anisotropic continuum damage theory coupled with isotropic elastoplasticity in a finite strains framework. This law is implemented into Metafor, a non-linear FE software. Simulations of cylindrical samples undergoing stepwise compression are presented.

Key Words: *trabecular bone, constitutive law, plasticity, anisotropy, fabric.*

1 INTRODUCTION

Within the diverse approaches that have been adopted to model trabecular bone remodeling processes, most of them are qualified as phenomenological models. They are models whose goal is to predict the global mechanical behavior (displacement, strains and stresses) of a tissue or an organ, taking into account the applied loads, its microstructure and the constraints imposed at the boundaries. Most of these models assume the existence of a given mechanical stimulus (input) that produces bone apposition or resorption (output) in such a way that the stimulus tends to a physiological level in the long-term (homeostasis). These phenomenological models are therefore build on constitutive material laws linking non-local stresses to global strains with internal variables representative of the evolving local microstructure. These models therefore need not only to be validated against remodeling data but the global constitutive law itself needs to be validated as well.

The goal of this work is therefore to present a non-local constitutive law that can be used in bone remodeling simulations. The constitutive law therefore aims at describing the mechanical behavior of trabecular bone in the range of small to moderate compressive strains, considering accumulation of plastic deformation and possible low softening due to small buckling of the microstructure. Under compressive load, the mechanical behavior of trabecular bone shows characteristics of an elastoplastic cellular solid, hence, the proposed global mechanical behavior is to be validated against experimental data obtained for compressive tests of trabecular bone as well as materials with bone-like microstructure.

2 METHODS

The original remodeling law which is proposed is built on a damage/repair model, first proposed by Doblaré and co-workers [1]. It is enhanced to be coupled to an elastoviscoplastic material behavior in a finite strains framework. It can therefore capture permanent strains of the tissue beyond the ones due to the density variation. However, we present here only the purely mechanical part of the constitutive law, no damage variation due to remodeling is accounted for.

The bone tissue (global level) is considered as an anisotropic "organization" of elastoplastic trabeculae (local level). This "organization", as proposed in [1], is measured through a mean bone density and its anisotropy uses the concept of fabric tensor [2]. The continuum damage framework is used not to capture actual damage at the local level, i.e. micro-cracks of the trabeculae, but to represent the bone macroscopic porosity and therefore measure the volume fraction. In terms of morphological data provided by computed tomography, damage is therefore to be understood as a measure of the apparent density of the tissue ($\bar{\rho}$) while the anisotropy is measured by the fabric tensor (the fabric tensor $\hat{\boldsymbol{H}}$ is normalized in such a way that $\mathtt{tr}(\hat{\boldsymbol{H}}) = 1$). The undamaged material is therefore the ideal virtual situation of bone with null porosity and perfect isotropy. We use a tensor damage variable, $\boldsymbol{d}$, formulated so that it retrieves an isotropic definition as $d = 1 - E/E_0$, E being the Young's modulus of the bone tissue and E_0 the Young's modulus of the trabeculae and depends on the morphological parameters :

$$\boldsymbol{d} = \boldsymbol{I} - \bar{\rho}^{\beta} A \hat{\boldsymbol{H}}$$

where A is a calibration parameter to retrieve the damage definition in isotropy and β is defined so that the tissue young's modulus is related to the density as : $E(\rho) \propto \rho^{\beta}$

For an elasto-plastic material in an hypoelastic formulation, the basic assumption consists in an additive split of the strain rate into two parts : an elastic and reversible part $\boldsymbol{D}^e$ and an irreversible plastic part $\boldsymbol{D}^p$. The constitutive model defines an effective stress, $\tilde{\boldsymbol{\sigma}}$, acting on the effective area of the material. The effective stress rate is linked to the elastic strain rate by the generalized Hooke's law :

$$\overset{\bullet}{\tilde{\boldsymbol{\sigma}}} = \mathbb{C} : (\boldsymbol{D} - \boldsymbol{D}^p)$$

where $\mathbb{C}$ is the elastic stiffness tensor. The stress ($\boldsymbol{\sigma} = \boldsymbol{s} + p\boldsymbol{I}$) is obtained by taking into consideration the effect of the structural morphology represented by the damage tensor [3] :

$$\tilde{\boldsymbol{\sigma}} = \mathtt{dev}(\boldsymbol{H}\boldsymbol{s}\boldsymbol{H}) + \frac{p}{1 - \frac{\eta}{3} d_{kk}} \boldsymbol{I}$$

where, $\boldsymbol{H} = (\boldsymbol{I} - \boldsymbol{d})^{-1/2}$ and η is the degree of anisotropy. This reduces, when an isotropic fabric is considered, as $\tilde{\boldsymbol{\sigma}} = \boldsymbol{\sigma}/(1 - d)$.

The plastic part of the strain rate $\boldsymbol{D}^p$ can be calculated through the normality rule on the plastic criterion (associated plasticity) expressed in term of effective stress. This is therefore the plastic criterion one would get from a single trabeculea mechanical behavior. It is here assumed to be pressure independent and therefore a simple Von-Mises criterion is chosen, leading, when only isotropic hardening of the internal variable is allowed, to :

$$\boldsymbol{D}^{pl} = \frac{3}{2} \frac{\overset{\bullet}{\lambda}}{\tilde{\sigma}_{eq}} \mathtt{dev}(\boldsymbol{H}\tilde{\boldsymbol{s}}\boldsymbol{H})$$

where $\overset{\bullet}{\lambda}$ is the rate of plastic multiplier and $\tilde{\sigma}_{eq}$ is the equivalent stress used for the Von-Mises criterion.

The constitutive law is integrated in a finite element framework according to an iterative staggered scheme [4] and is implemented in Metafor [5], a in-house object-oriented finite element code.

3 RESULTS

This homogeneous formulation has been applied to several materials, all showing bone-like microstructure. For each type of material, cylindrical specimens were used. Images of the structure were acquired using a micro-tomographic imaging system. These images were analyzed to extract the morphological data needed to compute the parameters of the presented constitutive law. The samples were also compressed along their main axis in a mechanical testing device and load/displacement data were acquired.

The first material that has been tested is a porous aluminium alloy (Duocel 6101-T6, ERG, Oakland, CA). The specimen used (8 mm in diameter and 16 mm in height, with an apparent volume density of 11.8%) was arbitrarily chosen among 15 compressed and imaged specimens [6]. The compression was realized in a stepwise fashion from 0% to 16% apparent engineering strain. The second material is PLA (polylactic acid) foam, i.e. a polymeric foam based on biodegradable and biocompatible polyester (prepared by the CERM, University of Liège [7]). The specimen used (8.2 mm in diameter and 12.5 mm in height, with an apparent volume density of 15%) was compressed from 0% to 42% apparent engineering strain. The last material presented is cancellous tissue of a deer antler [8]. The specimen used (7.8 mm in diameter and 11.96 mm in height, with an apparent volume density of 18.7%) was compressed from 0% to 4.1% apparent engineering strain.

The experimental data (Figure 1(a) to (c) - dashed lines) shows that, within the testing range, both the aluminium foam and PLA foam specimens show apparent yield behavior. However, the trabecular antler bone only shows a stiffening of an apparent linear behavior. The three specimens described earlier were each modeled as cylinders with mechanical parameters (Young's modulus, yield stress) as found in the literature for their bulk material and morphological parameters (apparent density and fabric tensor) derived from the CT data. To represent the testing boundary conditions, a displacement was applied on one side of the cylinder (vertical displacement with free in plane movement) while the other side of the cylinder was modeled to be in contact (frictionless conditions) with a rigid plane. On the contact plane, one central node of the cylinder was constrained in the horizontal plane to prevent rigid body modes. The computed external force was finally compared to the experimental one. The morphological data was initially computed as a mean over the all volume of the specimen. However, such a model allows only for the representation of the linear apparent behavior and of the apparent yield stress value (Figure 1(a) and (b) - plain black line). When extracting morphological data on smaller regions of interest (ROI), the apparent yield strain is retrieved as well (colored plain lines on the same figures). When using up to 16 divisions per specimen, one can also retrieve the early post yield behavior showing apparent softening of the specimens. For the trabecular antler bone (Figure 1(c)), increasing the morphological accuracy allows a better representation of the out-of-linearity apparent behavior. While the simulations using a large number of ROI show promising results, some effort has still to be done on the convergence rate of these simulations as the softening is no well accounted for numerically.

4 CONCLUSIONS

We presented a homogeneous constitutive law based on morphological data acquisition. It provides a non-linear model of the mechanical response of bone-like materials, accounting for early post-yield behavior of the structure. This constitutive model has been applied to three materials presenting bone-like morphology undergoing stepwise compression. Using this model for morphological data extracted for regions of interests small enough, one can retrieve not only the linear behavior of the structure but also the apparent yield stress and strain and early post yield softening.

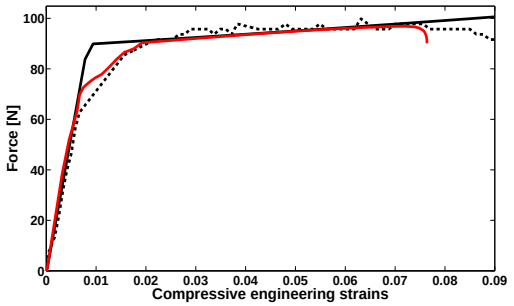

(a) Aluminium alloy

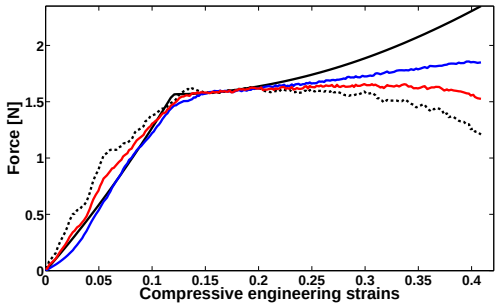

(b) PLA foam

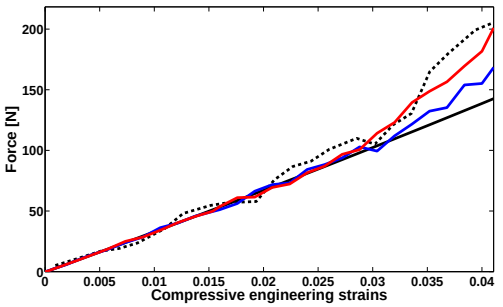

(c) Trabecular bone of deer antler

Figure 1: Computed (plain lines) and experimental (dashed lines) forces [N] vs. compressive engineering strains [-]. plain black : morphological data is computed for 1 ROI per sample ; plain blue : morphological data is computed for 8 ROI per sample ; plain red : morphological data is computed for 16 ROI per sample

REFERENCES

[1] M. Doblaré and J.M. García, Anisotropic bone remodelling model based on a continuum damage-repair theory, *J. Biomech.*, 35, 1-17, 2002.

[2] S.C. Cowin, R.T. Hart, J.R. Balser, and D.H. Kohn, Functional adaptation in long bones: establishing in vivo values for surface remodeling rate coefficients, *J. Biomech.*, 18, 665-684, 1985.

[3] J. Lemaitre and R. Desmorat, *Engineering Damage Mechanics: Ductile, Creep, Fatigue and Brittle Failures*, Springer, 2005.

[4] M. Mengoni and J.P. Ponthot, Isotropic continuum damage/repair model for alveolar bone remodeling, *J. Comp. App. Math.*, 234, 2036-2045, 2010

[5] Metafor, *A large strain finite element code*, LTAS-MN2L, University of Liège, http://metafor.ltas.ulg.ac.be/ , 2010.

[6] A. Nazarian and R. Müller, Time-lapsed microstructural imaging of bone failure behavior, *J. Biomech.*, 37, 55-65, 2004.

[7] V. Maquet, D. Martin, F. Scholtes, R. Franzen, J. Schoenen, G. Moonen, and R. Jérôme, Poly(D,L-lactide) foams modified by poly(ethylene oxide)-block-poly(D,L-lactide) copolymers and a-FGF : in vitro and in vivo evaluation for spinal cord regeneration, *Biomaterials*, 22, 11371146, 2001.

[8] Léonard, A., Guiot, L., Pirard, J. P., Crine, M., Balligand, M., and Blacher, S. Non-destructive characterization of deer antlers by X-ray microtomography coupled with image analysis, *J. Microscopy*, 225, 258263, 2007.

2nd International Conference on Mathematical and Computational Biomedical Engineering - CMBE2011
March 30 - April 1, 2011, Washington D.C, USA
P. Nithiarasu and R. Löhner (Eds.)

Tissue Length Dependence and Left Ventricular Blood flow in the Human Heart

David Nordsletten[†], Matt McCormick[‡], David Kay[‡] and Nicolas Smith[†]
[†] King's College London, St. Thomas Hospital, London SE1 7EH
[‡] Oxford University, Computing Laboratory, Wolfson Building OX1 3QD

SUMMARY

In this study, we extend our previous coupled fluid-solid ventricular models of the left ventricle to understand the influence of varied hemodynamics on tissue strain heterogeneity. As tissue contraction is strongly dependent on fiber strain via the Frank-Starling mechanism, the heterogeneity introduced by ventricular hemodynamics can significantly alter contractile behavior. In this paper, we investigate this effect by coupling our previous fluid-solid model of the heart to Windkessel models of the circulatory system. This integration is handled seamlessly through the introduction of Lagrange multipliers (LM). A novel plural cavity / pericardial model is also purposed based on a total heart volume constraint. The new model is then used to quantify the influence of length heterogeneity on cardiac contraction.

Key Words: *Blood flow, cardiac tissue mechanics, ALE Navier Stokes, fluid-solid coupling.*

1 INTRODUCTION

Cardiac pump function in the left ventricle involves a tight coupling between blood flow and tissue mechanics, where crossbridge cycling translates into tissue contraction and ventricular outflow. While the influence of tissue on blood flow is straightforward to see during systole – where tissue is actively squeezing blood into the systemic circulatory system – the influence of blood flow on tissue mechanics is less clear. In fact, traditional cardiac models often treat the influence of blood flow in the left ventricular chamber as a homogenous change in pressure [3].

While intraventricular fluid pressure does represent the dominant force transferred to the tissue, the pressure is seen to vary through the chamber during both diastole and systole. Moreover, the dynamic movement of blood yields local heterogeneities in tissue deformation during diastole, making the stretch observed in the heart wall inhomogeneous [6]. While this may have minor implications on the characteristics of diastole, the subsequent contraction of the tissue may be significantly impacted. This is due to the Frank-Starling mechanism, which adapts the strength of contraction to the volumetric load on the heart through length dependent cellular mechanisms.

In this paper, we investigate the influence ventricular flow and heterogeneity on systolic contraction and subsequent cardiac efficiency. To accomplish this, our ventricular model previously introduced in Nordsletten [6] is coupled to Windkessel models of the circulatory system, allowing multiple beat simulations with varied conditions. A novel plural cavity / pericardial model is also introduced to provide more accurate exterior constraints on the heart. With these added tools, we quantify the impact of blood flow on cardiac performance, considering different heart rates and flow conditions. Finally, these results are compared with classic solid mechanical simulations, providing insight into the mechanical impact of blood flow on tissue behavior.

2 METHODS

The dynamics of blood flow and tissue movement are governed by the conservation of mass and momentum, see equation (1), over the respective fluid and solid domains, denoted Ω_f and Ω_s (see cf. [5, 6] for further details). Here an arbitrary Lagrangian-Eulerian (ALE) approach is followed for the fluid and a Lagrangian approach for the solid, both of which relate the current physical domains $\Omega_f(t)$ and $\Omega_s(t)$ at a time t to reference domains, denoted Λ_f and Λ_s [2, 1, 4].

$$\begin{aligned} \rho\,\partial_t\left(\mathbf{v}\jmath_f\right) \;+\; \jmath_f\nabla_{\mathbf{x}}\cdot\left[\;\rho(\mathbf{v}-\mathbf{w})\mathbf{v} \;+\; p_f\mathbf{I} \;-\; \mu(\nabla_{\mathbf{x}}\mathbf{v}+\mathbf{v}\nabla_{\mathbf{x}})\;\right] &= \mathbf{0}, \quad \text{on } \Lambda_f, \quad (1a)\\ \jmath_f\nabla_{\mathbf{x}}\cdot\mathbf{v} &= 0, \quad \text{on } \Lambda_f, \quad (1b)\\ \jmath_s\nabla_{\mathbf{x}}\cdot\boldsymbol{\sigma}_s(\mathbf{u}) \;-\; \nabla_{\mathbf{x}}p_s &= \mathbf{0}, \quad \text{on } \Lambda_s, \quad (1c)\\ \partial_t(\jmath_s) &= 0, \quad \text{on } \Lambda_s, \quad (1d) \end{aligned}$$

Here ρ is the blood density, p_f the blood pressure, μ_f the blood viscosity, $\mathbf{v}$ the blood velocity, $\mathbf{w}$ the ALE domain velocity, $\jmath_f$ the determinant of the Jacobian mapping on Λ_f, $\boldsymbol{\sigma}_s(\mathbf{u})$ is the non-hydrostatic component of the tissue Cauchy stress, p_s is the hydrostatic pressure, and $\jmath_s$ the determinant of the Jacobian mapping on Λ_s.

Due to the relative dominance of fluid momentum and the large strains observed in heart tissue, the myocardial model used in this work followed the formulation of Nash and Hunter [3]. The non-hydrostatic Cauchy stress may be characterized by two tensor components, $\boldsymbol{\sigma}_s = \boldsymbol{\sigma}_p(\mathbf{u}) + \boldsymbol{\sigma}_a(\lambda_f)$, where $\boldsymbol{\sigma}_p$ denotes the passive tissue properties and $\boldsymbol{\sigma}_a$ the active contraction properties. Importantly, the behavior of $\boldsymbol{\sigma}_a$ depends upon the local length change along tissue fiber directions, λ_f (see Nordsletten [6]). This important link couples diastolic inflow to the subsequent systolic outflow.

The fluid and solid models were coupled along the endocardial boundary using the LM approach outlined in Nordsletten [5]. Briefly, this approach introduces a LM, $\boldsymbol{\lambda}$, along a common interface, Γ_I (see figure 1(a)). This variable acts to transfer force between domains while allowing the additional constraints of kinematic continuity to be included.

Windkessel Model of the Circulatory System

To incorporate the influence of the circulatory system, the left ventricular model was coupled to a Windkessel model based on the work of Shi [7]. This model relates flow rate in compartments of the vasculature to the drop in pressure using circuit analogues. To enable seemless linking to the ventricular system, the mitral and aortic boundaries of the model (seen in figure 1(a)) were constrained to match a velocity profile outlined in our previous work using an L^2-projection along the boundary [6], *i.e.*

$$\left(\,\phi_{mv},\,y\,\right)_{\Gamma_{mv}} = \left(\,v_{mv},\,y\,\right)_{\Gamma_{mv}}, \forall y\in\mathcal{V}^h, \qquad \left(\,\phi_{av},\,y\,\right)_{\Gamma_{av}} = \left(\,v_{av},\,y\,\right)_{\Gamma_{av}}, \forall y\in\mathcal{V}^h, \quad (2)$$

where ϕ_{mv} and ϕ_{av} denotes the mitral and aortic profiles, v_{mv} and v_{av} the profiles previously described [6], Γ_{mv} and Γ_{av} the respective mitral and aortic valve boundaries, and $\mathcal{V}^h$ the test space for each velocity component. The velocity is then constrained so that $\mathbf{v}|_{\Gamma_k} = \phi_k\mathbf{n}_k$ (for $k = mv, av$). While the profile was prescribed (with nodes prescribed as algebraic sums of their neighbors bar a single node left free), the magnitude (and thus the flow rate) of the profile was free. To link the mitral and aortic valves to the Windkessel model, two LMs were introduced, λ_{mv} and λ_{av}, which may be interpreted as pressures. These variables are introduced weakly at the boundary, *i.e.*

$$\left(\,\lambda_{mv}\mathbf{n}_{mv},\,\mathbf{y}\,\right)_{\Gamma_{mv}}, \qquad \left(\,\lambda_{av}\mathbf{n}_{av},\,\mathbf{y}\,\right)_{\Gamma_{av}}, \quad (3)$$

enabling the addition of constraints linking pressure and flow rate conditions to the Windkessel model,

$$\left(r,\ \partial_t[\mathbf{v}\cdot\mathbf{n}_{mv}] - \gamma_D[\lambda_{mv}+p_{la}] \right)_{\Gamma_{mv}}, \qquad \left(s,\ \partial_t[\mathbf{v}\cdot\mathbf{n}_{mv}] - \gamma_S[\lambda_{av}+p_a] \right)_{\Gamma_{av}}. \tag{4}$$

Here $(\lambda_{mv}, \lambda_{av}, r, s) \in \mathbb{R}$ are real constants in time, p_{la} is the left atrial pressure of the Windkessel Model, p_a the aortic pressure, γ_D is a constant relating the pressure-flow relation during diastole (and zero otherwise), and γ_S is a constant relating the pressure-flow relation during systole (and zero otherwise). Note that the integral of $\mathbf{v}\cdot\mathbf{n}_k$ across the valve plane is equivalently the flow rate.

Plural Cavity and Pericardial Model

A key constraint to the ventricle is the surrounding pericardial sac and plural cavity, both of which constrain free motion of the ventricle. The stiff constraint of the pericardium limits substantial increases in volume in the normal heart, while the surrounding tissues resist outward movement. To incorporate these effects, a LM was introduced, λ_E, along the epicardial boundary of the solid wall (denoted Γ_E, see figure 1(a)), *i.e.*

$$\left(\lambda_E \mathbf{n}_E,\ \mathbf{y} \right)_{\Gamma_E}, \tag{5}$$

enabling the addition of a constraint linking the volume of the heart chambers to that of the ventricular model,

$$\left(t,\ \mathbf{u}\cdot\mathbf{n} - V_h + V_o \right)_{\Gamma_E} = 0 \tag{6}$$

Here $(\lambda_E, t) \in \mathbb{R}$ are real constants in time, V_h is the summed volume of the atria and right ventricle (derived from the Windkessel model) and V_o is the reference volume. As a consequence, force on the ventricle is preferentially introduced as the heart wall deforms in the direction of the boundary normal.

Finite Element Formulation

The system is broken down using finite elements as outlined our previous work [5]. With the additional constraints, this involves finding $(\mathbf{v}, \mathbf{u}) \in \boldsymbol{\mathcal{V}}^h \times \boldsymbol{\mathcal{U}}^h$, $(p_f, p_s) \in \mathcal{W}_f^h \times \mathcal{W}_s^h$, $\boldsymbol{\lambda} \in \boldsymbol{\mathcal{M}}^h$, $(\lambda_{mv}, \lambda_{av}, \lambda_e) \in \mathbb{R}$ at each time step, such that,

$$\begin{aligned}
&\partial_t \left(\rho_f \mathbf{v},\ \mathbf{y} \right)_{\Omega_f} + \left(\nabla_{\mathbf{x}} \cdot \rho_f[\mathbf{v}-\mathbf{w}]\mathbf{v},\ \mathbf{y} \right)_{\Omega_f} + \left(\mu\mathbf{D},\ \nabla_{\mathbf{x}}\mathbf{y} \right)_{\Omega_f} - \left(p_f,\ \nabla_{\mathbf{x}}\cdot\mathbf{y} \right)_{\Omega_f} \\
&+ \left(q_f,\ \nabla_{\mathbf{x}}\cdot\mathbf{v} \right)_{\Omega_f} + \left(\boldsymbol{\lambda},\ \mathbf{y} \right)_{\Gamma_I} + \left(\lambda_{mv}\mathbf{n}_{mv},\ \mathbf{y} \right)_{\Gamma_{mv}} + \left(\lambda_{av}\mathbf{n}_{av},\ \mathbf{y} \right)_{\Gamma_{av}} \\
&+ \left(\boldsymbol{\sigma}_s(\mathbf{u}),\ \nabla_{\mathbf{x}}\mathbf{z} \right)_{\Omega_s} - \left(p_s,\ \nabla_{\mathbf{x}}\cdot\mathbf{z} \right)_{\Omega_s} + \left(q_s,\ \jmath_s - 1 \right)_{\Omega_s} - \left(\boldsymbol{\lambda},\ \mathbf{z} \right)_{\Gamma_I} \\
&+ \left(\lambda_E\mathbf{n}_E,\ \mathbf{z} \right)_{\Gamma_E} + \left(\boldsymbol{q},\ \mathbf{v} - \partial_t\mathbf{u} \right)_{\Gamma_I} + \left(r,\ \partial_t[\mathbf{v}\cdot\mathbf{n}_{mv}] - \gamma_D[\lambda_{mv}+p_{la}] \right)_{\Gamma_{mv}} \\
&+ \left(s,\ \partial_t[\mathbf{v}\cdot\mathbf{n}_{av}] - \gamma_S[\lambda_{av}+p_a] \right)_{\Gamma_{av}} + \left(t,\ \mathbf{u}\cdot\mathbf{n}_E - V_h + V_o \right)_{\Gamma_E} = 0,
\end{aligned} \tag{7}$$

for every $(\mathbf{y}, \mathbf{z}) \in \boldsymbol{\mathcal{V}}^h \times \boldsymbol{\mathcal{U}}^h$, $(q_f, q_s) \in \mathcal{W}_f^h \times \mathcal{W}_s^h$, $\boldsymbol{q} \in \boldsymbol{\mathcal{M}}^h$, and $(r, s, t) \in \mathbb{R}$, where $\boldsymbol{\mathcal{V}}^h$, $\boldsymbol{\mathcal{U}}^h$, $\mathcal{W}_f^h$, $\mathcal{W}_s^h$ and $\boldsymbol{\mathcal{M}}^h$ are appropriately selected spaces (see [5]). The governing system may be written in block matrix form, exhibiting classic saddle point structure. The system was solved using a preconditioned iterative solver which first solved for updates to the LM variables and, subsequently, updates to the kinematic variables $\mathbf{v}, \mathbf{u}$.

3 RESULTS & CONCLUSIONS

The fluid-solid coupled model outlined above enables novel investigations into the mechanics of the heart during diastole and systole, see figure 1(b). Most importantly, the model links hemodynamic effects to the ventricle, allowing the characterization of hemodynamic influences on cardiac

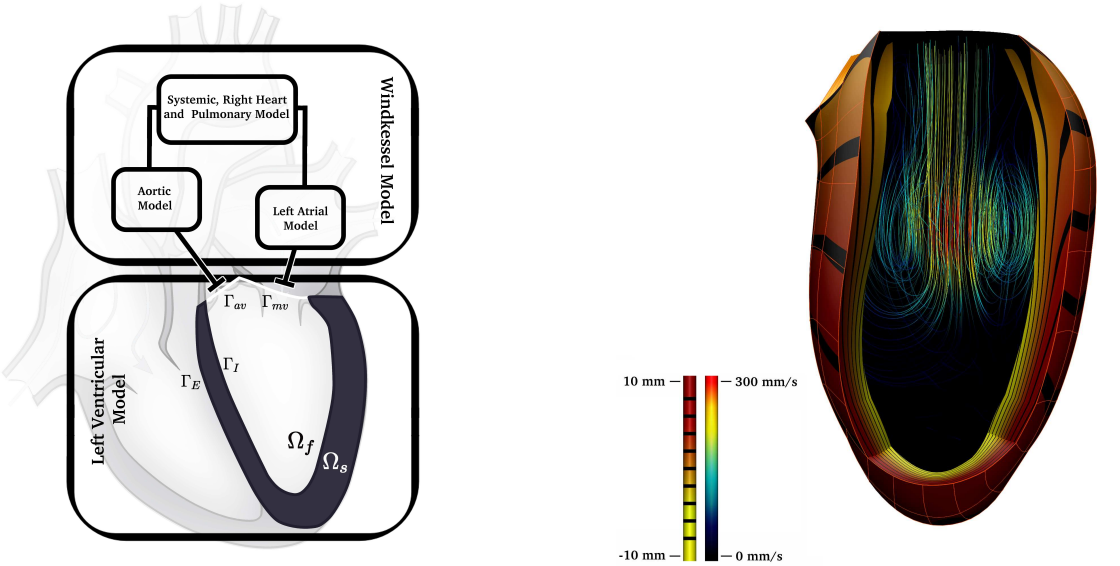

(a) Schematic of Coupled System.

(b) Simulation of Inflow.

Figure 1: (a) Schematic of the integrated 3D fluid-solid model with Windkessel model. Note the models are Linked both along the valve planes as well as the total volume constraint (6), (b) simulation of filling illustrating heterogenous deformations in the heart wall (colored according to λ_f) – fluid streamlines are colored according to velocity magnitude.

efficiency and function. In this study, we focused on understanding the influence of ventricular hemodynamics during diastole on contraction. Diastolic filling was seen to result in heterogeneous deformation of the heart wall, yielding spatial variations in active tension. These effects were investigated and quantified for various heart rates, illustrating the impact of hemodynamics on ventricular contraction and cardiac efficiency.

References

[1] TJR. Hughes, W. Liu, and TK. Zimmermann. Lagrangian-eulerian finite element formulation for incompressible viscous flows. *Comp. Meth. Appl. Mech. Engrg.*, 29:329–349, 1981.

[2] LE. Malvern. *Introduction to the mechanics of continuous medium*. Prentice-Hall, 1969.

[3] M. Nash and P. Hunter. Computational mechanics of the heart. *J. Elas*, 61:113–141, 2000.

[4] F. Nobile. *Numerical approximation of fluid-structure interaction problems with application to haemodynamics. Ph.D. Thesis*. École Polytechnique Fédérale de Lausanne, 2001.

[5] D. Nordsletten, D. Kay, and N. Smith. A non-conforming monolithic finite element method for problems of coupled mechanics. *J. Comp. Phys*, 229:7571 – 7593, 2010.

[6] D. Nordsletten, M. McCormick, P. Kilner, P. Hunter, D. Kay, and N. Smith. Fluid-solid coupling for the investigation of diastolic and systolic human left ventricular function. *Int. J. Num. Meths. Biomed. Engrg.*, DOI:10.1002/cnm.1405

[7] Y. Shi and T. Korakianitis. Numerical simulation of cardiovascular dynamics with left heart failure and in-series pulsatile ventricular assist device. *Art. Organs*, 30:929 – 948, 2006.

2nd International Conference on Mathematical and Computational Biomedical Engineering – CMBE2011
March 30 – April 1, 2011, Washington D.C., USA
P. Nithiarasu and R. Löhner (eds)

A MATHEMATICAL MODEL OF BIDIRECTIONAL GLENN HEMODYNAMICS WITH AN INCREMENT IN PULMONARY VASCULAR RESISTANCE

C.Vallecilla*, N. Sandoval and J. C. Briceño*,****
*Universidad de los Andes, Cra 1E # 19 A-40, c-vallec@uniandes.edu.co
**Fundación Cardioinfantil Instituto de Cardiología, Calle 163A # 13B-40

SUMMARY

Bi-directional Glenn (BDG) is one of the stages for Total Cavopulmonary Connection (TCPC), the palliative repair for single ventricle heart disease. Pulmonary Vascular Resistance (PVR), and blood oxygen saturation, are some important hemodynamic parameters that determine the outcome of BDG patients. The contribution of Superior Vena Cava flow to total Caval flow is determinant to identify ventricle overload in this patients. The aim of this work is to develop a mathematical model to understand hemodynamics of BDG with changes in PVR to identify if the contribution of SCV flow to total caval flow.

Mathematical analysis is performed according to PVR increments as a percentage from baseline. The model proposes an increment in PVR while total body oxygen consumption (VO_2) remains constant. At baseline conditions (normal PVR), the contribution of SVC flow to total flow is about 50%. Once PVR increases, SVC flow decreases in a rapid rate. For a PVR increase of 50%, ventricle overload will be 10%.

In this analysis an increment in PVR will produce a change in blood flow distribution, in order to maintain oxygen consumption constant in the upper and lower body. The model is being used to understand the effect of altitude on BDG's outcome.

Key Words: *Bidirectional Glenn, Pulmonary Vascular Resistance, Oxygen saturation.*

1. INTRODUCTION

In the normal heart, the systemic and pulmonary circulations are in series, each supported by a dedicated ventricle. In patients with a functionally single ventricle the systemic and pulmonary circulation are in parallel, with mixing of circulations within the heart [1]. The Total Cavopulmonary Connection (TCPC) [2,3] is the preferred surgical palliative repair for single ventricle heart disease [4]. The TCPC involves the three staged anastomosis of the venae cavae to the pulmonary arteries (PAs) such that the damaged side of the heart is bypassed to prevent the mixing of oxygenated and deoxygenated blood inside the heart [5,6]. The first surgery is the Norwood procedure which is a creation of a systemic to pulmonary fistula is known as SP1 (stage one palliation). The Bidirectional Glenn (BDG), known as SP2 palliation, consists on the anastomosis of the superior vena cava to the pulmonary artery to assure blood flow through the lungs to be oxygenated. If the patient's adaptation is adequate, the completion of SP3 palliation is the TCPC, performed to establish a circulation similar to normal circulation in series (figure 1).

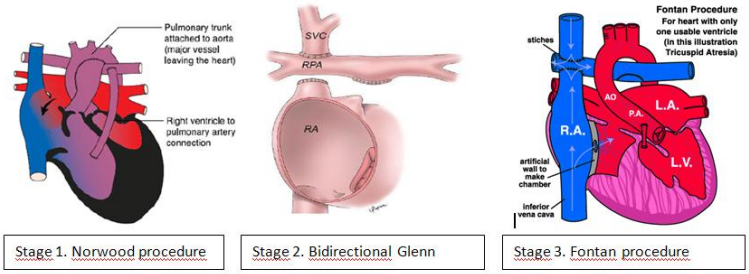

Figure1. Stages for the TCPC. SP1: Norwood procedure, SP2: Bidirectional Glenn (BDG), SP3: Total Cavopulmonary Connection (TCPC).

Although BDG is performed to reduce ventricle overload, because of persistent cyanosis, adequate systemic oxygen delivery requires an elevated cardiac output and that end-diastolic volume remains above normal levels [4]. In some cases as increment in PVR due to hypoxia or high altitude adaptation, ventricle overload can be a fatal condition for ventricular function. The contribution of Superior Vena Cava (SVC) flow to total Caval flow is a determinant parameter to identify ventricle overload in BDG patients. Ventricular function is one of important parameters to evaluate outcome of BDG procedure and is the risk to which the myocardium is exposed [4].

The objective of this study is to implement a mathematical model of BDG circulation to understand the effect of increased PVR in the contribution of Superior Vena Cava flow to total Caval flow.

2. MAIN BODY

A mathematical model is proposed where increments in PVR are set while oxygen consumption remains constant. Blood flow distribution is obtained for each increment in PVR to quantify the contribution of SCV flow to total caval flow. The hypothesis is that increment in PVR is going to change blood flow distribution, in order to maintain oxygen consumption (VO_2), instead of remaining constant as determined by body surface area (BSA) and age, as proposed in [7].

In figure 2 a circuit of a normal heart and a BDG repaired heart are shown.

Cardiac output is calculated using catheterism data from the patients, prior to BDG surgery and with equations using the s-factor for correction of numerical calculations for oxygen consumption [8].

Cardiac Output is calculated as follows:

$$(1) Q = \frac{VO_2}{(CaO_2 - CvO_2)\ x\ 10}\ [\text{l/min}]$$

Where VO_2 is the oxygen consumption in ml O_2/kg, C_aO_2 is the arterial oxygen content and C_vO_2 the venous oxygen content in ml O_2/100 ml blood.

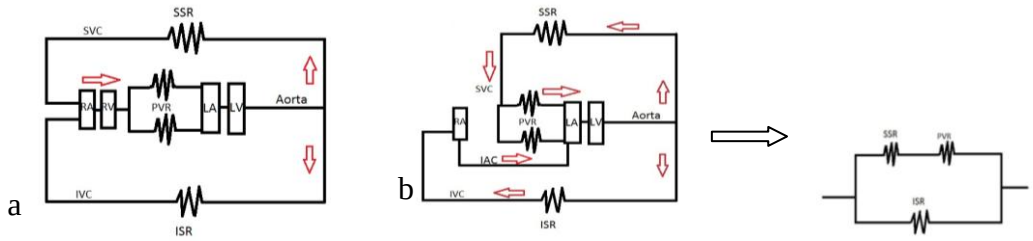

Fig 2. Circuit diagram of normal circulation (a) and BDG circulation (b). PVR: pulmonary vascular resistance, SSR=SVR: systemic vascular resistance for the inferior body, ISR=SVR_s: systemic vascular resistance for the superior body, RA: Right Atrium, LA: Left Atrium, LV: Left Ventricle, IVC: Inferior Vena Cava, SVC: Superior Vena Cava. Arrows indicate flow direction.

Resistances [HRU] within the circuit are calculated with the equations:

$$(2)\ PVR = \frac{P_{PA}-P_{LA}}{Q_p},\ (3)\ SVR_l = \frac{P_{Ao}-P_{LA}}{Q_{IVC}},\ (4)\ SVR_u = \frac{P_{Ao}-P_{LA}}{Q_{SVC}}$$

Where PVR is pulmonary vascular resistance, SVR_l: systemic vascular resistance for the lower body, SVR_u: systemic vascular resistance for the upper body, P_{PA}: Pressure in Pulmonary Artery, P_{LA}: Pressure in Left Atrium, P_{Ao}: Pressure in the Aorta, Q_{ivc}: Inferior Vena Cava flow, Q_{svc}: Superior Vena Cava flow and Q_p: pulmonary flow.

With a sensibility analysis flow split is determined through SVC and IVC depending on the increment in PVR as a percentage of SVR_l (figure 2a). SVC contribution to total caval flow and blood oxygen saturation are calculated for each PVR increment (figure 3).

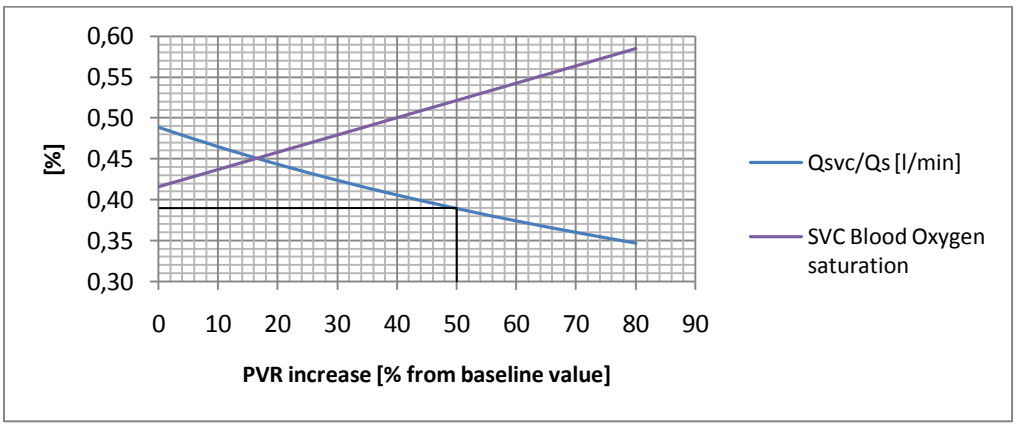

Fig 3. SVC flow and and Oxygen saturation with variation of superior resistance. Qsvc/Qs refer to superior vena caval flow of total caval flow.

At baseline conditions of PVR and blood oxygen saturation for a BDG patient, the contribution of SVC for to total flow is 50% (see figure 3 at 0% PVR increase). Once PVR increases, SVC flow starts to decrease in a rapid rate as shown in figure 3. In this stage for an increasing PVR of 50%, the caval flow would decrease in 10%.

3. CONCLUSIONS

At baseline conditions of PVR and blood oxygen saturation for a BDG patient, the contribution of SVC to total caval flow is 50%, which is the optimum percentage for a patient in these conditions to avoid ventricle overload and guarantee acceptable blood oxygen saturation. Once PVR increases, SVC flow starts to decrease at a rapid rate. With a PVR increase of 50%, SVC flow would decrease by 10%, resulting in an undesirable ventricle overload.

As a consequence an increment in PVR will produce a change in blood flow distribution, in order to maintain oxygen consumption constant in the upper and lower body.

To complement these results, a this mathematical model must be expanded to take into account changes in oxygen extraction rate (OER) and blood oxygen saturation (SO_2) with increases in PVR. It is believed that under these conditions, PVR will reach a point where oxygen consumption will be impeded due to extremely low mixed venous oxygen saturation.

This model is being used to understand the effect of altitude on individual BDG's outcome employing patient's specific data.

REFERENCES

References

[1] van Doorn, C. A. & de Leval, M. R. The Lateral Tunnel Fontan. *Operative Techniques in Thoracic and Cardiovascular Surgery,* 2006*, 11*, 105-122.

[2] Redington, A. The physiology of the Fontan circulation. *Progress in Pediatric Cardiology, 2*006*, 22*, 179-186.

[3] Gewillig M. The Fontan circulation. Biomedical Journal. Heart online. 2005, 91:839-846.

[4]Colan,S. D. Systolic and diastolic function of the univentricular heart. *Progress in Pediatric Cardiology*, 2002, 16, 79-87.

[5] Freedom, R. M. & Nykanen, D. The Physiology of the Bidirectional Cavopulmonary Connection. *Annals of Thoracic Surgery,* 1998*, 66*, 664-667

[6] de Leval M. The Fontan Circulation: a challenge to William Harvey? Nat. Clin. Pract. Cardiovascular. Med. 2005, 2: 202-208.

[7] Whitehead, K. K. & Sundareswaran, K. S. Blood flow distribution in a large series of patients having the Fontan operation: A cardiac magnetic resonance velocity mapping study. *The Journal of Thoracic and Cardiovascular Surgery,* 2009*, 138*, 96-102.

[8] Farrel, K. & Hill, A. Mathematical Modeling/Problem Solving in Global Oxygen Transport. *Journal of Surgical Research,* 2009*, 155*, 201-209.

2nd International Conference on Mathematical and Computational Biomedical Engineering - CMBE2011
March 30 - April 1, 2011, Washington D.C, USA
P. Nithiarasu and R. Löhner (Eds.)

Patient-specific Finite Element Analysis of Carotid Artery Stenting:
Impact of constitutive vessel modeling on vessel wall stress distribution

F. Auricchio[⋆], M. Conti[⋆◇], A. Ferrara[⋆], S. Morganti[⋆], A. Reali[⋆]
[⋆]Structural Mechanics Department, Università degli Studi di Pavia, Via Ferrata 1, 27100 Pavia, Italy
[◇]michele.conti@unipv.it

Key Words: *Finite Element Analysis (FEA), Carotid Artery Stenting (CAS), Patient-specific modeling.*

1 Introduction

Carotid artery stenting (CAS) is emerged as a safe and cost-effective treatment of carotid artery (CA) stenosis [1]. However the long-term efficacy of CAS is under clinical evaluation and, in particular, the role of in-stent restenosis (ISR) is not clear. More data and dedicated studies are necessary to elucidate the mechanisms of ISR and their relation with the novel carotid stent designs. Experimental evidence shows that ISR is related to vessel wall injury and numerical simulations can play a key role supporting the assessment of the vessel wall distribution after stent implant. In this scenario, the modeling of the vessel wall mechanics is an important issue which can influence the stress calculation. In this study, we evaluate the impact of constitutive vessel modeling on the vessel wall stress distribution computed through patient-specific finite element analysis (FEA).

2 Materials and Methods

2.1 CA Model

We base the CA model on DICOM images of a neck-head Computed Tomography-Angiography (CTA) performed on 70 years-old female patient. The CTA scan is performed at IRCCS San Matteo in Pavia, Italy, using a Somatom Sensation Dual Energy scanner (Siemens Medical Solutions, Forchheim, Germany). We elaborate the images using OsiriX (see figure 1-a); we focus on the left CA highlighting both the bifurcation lumen and the calcific plaque as shown in figure 1-b. We then export both lumen and plaque geometry as stereolithography (STL) file format. To create the CA finite element mesh, we follow a procedure, implemented by Matlab (Matlab, Mathworks Inc., Natick, MA) and characterized by three main steps: i) definition of vessel wall inner profile elaborating the lumen surface derived from the DICOM images; ii) definition of vessel wall outer profile enlarging, in an appropriate way, the inner profile; iii) generation of the mesh between the inner and outer profile; iv) inclusion of the plaque in the vessel wall model. In particular, through a dedicated subroutine implemented by Matlab, we create the plaque model by detecting the elements of the vessel wall mesh enclosed in the 3D surface of the plaque geometry obtained from the CTA.

2.2 Stent model

We consider a open-cell stent creating the corresponding finite element model from an high resolution micro-CT scan. The stent has a straight configuration with diameter of 9 mm and strut thickness 0.190 mm.

2.3 FEA of CAS

To investigate the interaction between the stent and the patient specific carotid artery model, we perform a two-step simulation procedure [2] where the stent deformation is driven by the change of configuration of the catheter. The simulation is performed using Abaqus/explicit (Dassault Systémes Simulia Corp., Providence, RI, USA) as finite element solver since the numerical analysis is characterised by non-linearity due to the material properties, large deformations and complex contact problems.

2.4 Constitutive modeling

To model the mechanical behaviour of the vessel wall, we choose two constitutive models, i.e. isotropic and anisotropic hyperlelastic. For the isotropic model, we use a second-order polynomial strain energy function (SEF):

$$U_I = \sum_{i+j=1}^{2} C_{ij}(\bar{I}_1 - 3)^i(\bar{I}_2 - 3)^j + \sum_{i=1}^{2} \frac{1}{D_i}(J^{el} - 1)^{2i} \tag{1}$$

where C_{ij} and D_i are material parameters; $\bar{I}_1$ and $\bar{I}_2$ are respectively the first and second deviatoric strain invariants; J^{el} is the elastic volume ratio.
For the anisotropic model, we use the SEF proposed by Holzapfel et al. [3] and Gasser et al. [4]:

$$U_A = C_{10}(\bar{I}_1 - 3) + \frac{1}{D}\left(\frac{(J^{el})^2 - 1}{2} - ln(J^{el})\right) + \frac{k_1}{2k_2}\sum_{\alpha=1}^{N}\left\{exp\left[k_2\left\langle \bar{E}_\alpha \right\rangle^2\right] - 1\right\} \tag{2}$$

where

$$\bar{E}_\alpha \equiv k(\bar{I}_1 - 3) + (1 - 3k)(\bar{I}_{4(\alpha\alpha)} - 1) \tag{3}$$

and C_{01},D,k_1,k_2 are material coefficients, while N is the number of families of fibers; in our case $N = 2$ as we assume two family of fibers; k represents the fiber dispersion, in our case we assume $k = 0$ which corresponds to a full anisotropic behaviour; $\bar{I}_1$ and $\bar{I}_{4(\alpha\alpha)}$ are invariants defined as specified in literature [3, 4]. Starting from the above described two SEFs, we consider the five model variants: 1) SEF U_I with the coefficients reported by Creane et al. [5] (model HI_1); ii) SEF U_I with the coefficients reported by Lally et al. [6] (model HI_2); iii) SEF U_A calibrated on data reported by Sommer et al. [7] for the intact wall (model HA_1). Both SEFs are already implemented in the material model library of Abaqus. In case of model HA_1, we implement in Matlab a procedure to define local coordinate system for each mesh element in order to assign fiber-orientation.

2.5 Post-processing

We evaluate the impact of stenting evaluating the von Mises stress distribution in the post-stenting vessel as a measure of potential injury induced by the stent apposition to the vessel wall. To

neglect peak values of von Mises stress, due to local concentration, we consider the 99 percentile with respect to the pre-stenting vessel volume (i.e. only 1% of the volume has stress above this value).

3 Results

The result of the CAS simulation for vessel model HA_1 is reported in figure 2-a, while in figure 2-b the von Mises stress (99 percentile) for each model is reported. It is possible to note that isotropic models HI_1 and HI_2 provide similar results while the use anisotropic model HA_1 provides a lower stress value.

4 Conclusions

The system under investigation is very complex; to simplify the analysis we neglect axial pre-stretch, residual stresses and arterial blood pressure. Keeping the highlighted limitations in mind, we believe that the present study represents a further step towards a quantitative assessment of the relation between the complex mechanical features of a given stent design and a given patient-specific anatomy, which could be useful for both procedure standardization and stent design evaluation. Clearly, the numerical analysis should be validated and integrated with clinical and biological considerations based also on the surgeon experience which plays a primary role for the optimal CAS outcomes.

5 Acknowledgments

This work is funded by PhD grant from MIUR (Ministero dell'Istruzione, dell'Università e della Ricerca, Italian Ministry of Education, University and Research). The authors would acknowledge: Dr. R. Dore, Prof. A. Odero and Dr. S. Pirrelli of IRCCS Policlinico S. Matteo, Pavia, Italy for support on medical aspects related to the present work; Eng. D. Van Loo of Ghent University (UGCT), Ghent, Belgium for micro-CT scanning of stent samples and Eng. C. Ferrazzano (Unipv) for medical image elaboration.

References

[1] CREST committee, Stenting versus endarterectomy for treatment of carotid-artery stenosis, New England Journal of Medicine 363 (2010) 11–24.

[2] F. Auricchio, M. Conti, M. De Beule, G. De Santis, B. Verhegghe, Carotid artery stenting simulation: from patient-specific images to finite element analysis, Medical Engineering & Physics, in press. DOI: 10.1016/j.medengphy.2010.10.011.

[3] G. Holzapfel, T. Gasser, R. Ogden, A new constitutive framework for arterial wall mechanics and a comparative study of material models, J Elast 61 (2000) 1–48.

[4] T. Gasser, R. Ogden, G. Holzapfel, Hyperelastic modelling of arterial layers with distributed collagen fibre orientations, Journal of the Royal Society Interface 3 (2006) 15–35.

[5] A. Creane, E. Maher, S. Sultan, N. Hynes, D. Kelly, C. Lally, Finite element modelling of diseased carotid bifurcations generated from in vivo computerised tomographic angiography, Computers in Biology and Medicine 40 (2010) 419–429.

[6] C. Lally, F. Dolan, P. Prendergast, Cardiovascular Stent Design and Vessel Stresses: a Finite Element Analysis, Journal of Biomechanics 38 (2005) 1574–1581.

[7] G. Sommer, P. Regitnig, L. Koltringer, G. Holzapfel, Biaxial mechanical properties of intact and layer-dissected human carotid arteries at physiological and supraphysiological loadings, Am J Physiol Heart Circ Physiol 298 (2009) H898–912.

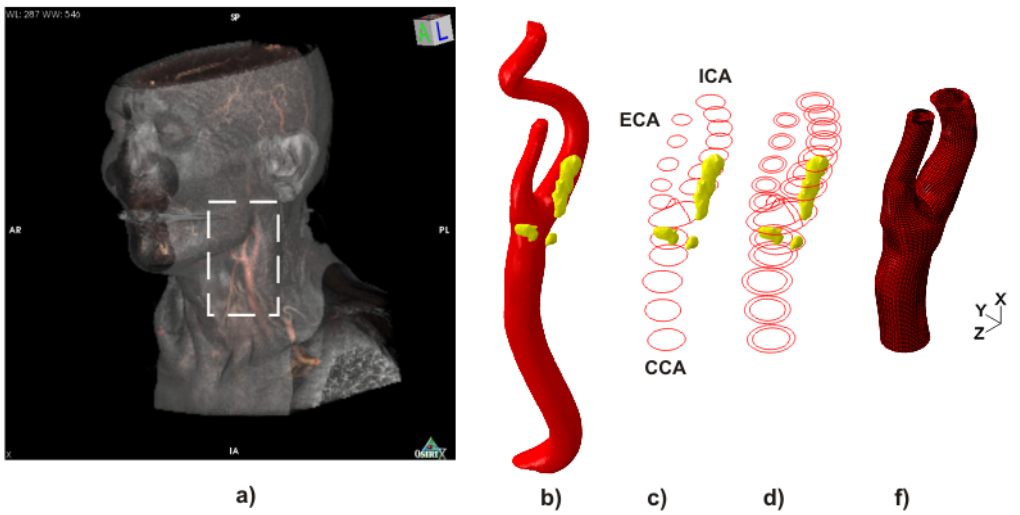

Figure 1: Elaboration of CTA DICOM images: a) whole 3D reconstruction of neck-head district highlighting the region of interest; b) 3D reconstruction of both lumen of left CA bifurcation and calcific plaque (depicted in white).

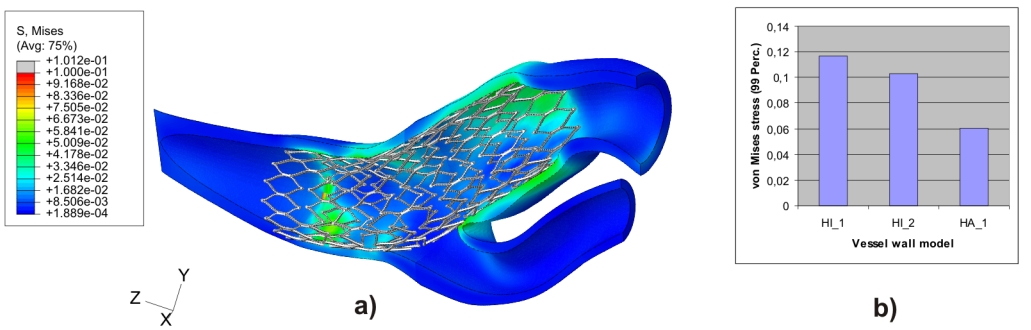

Figure 2: a) contour plot of the von Mises stress distribution in the CA wall after the stent apposition, the results refer to model HA_1; b) histograms depicting the maximum von Mises stress value (99 Perc.) as function of the vessel constitutive model. For both figures, MPa is the stress unit measure.

2nd International Conference on Mathematical and Computational Biomedical Engineering – CMBE2011
March 30 – April 1, 2011, Washington D.C., USA
P. Nithiarasu and R. Löhner (eds)

The mechanical response of the human coronary artery: simulation by high-order finite element analysis

E. Priel & Z. Yosibash

Computational Mechanics Laboratory, Mechanical Engineering Department, Ben-Gurion University of the Negev, Beer-Sheva, 84105, Israel. Email: prielel@bgu.ac.il

SUMMARY

High order (p-version) finite elements are utilized to study the mechanical response of a healthy human coronary artery. The arterial tissue is treated as a layered, anisotropic, nearly incompressible hyper-elastic material undergoing large deformations in the physiological pressure range. The effect of tissue compressibility, layer thickness ratio, and initial fiber orientation on the arterial mechanical response is investigated with emphasis on the reliability of the numerical simulations.

Key Words: *computational mechanics, p-version, arterial response.*

1. INTRODUCTION

The media and adventitia layer's passive mechanical response is investigated. These are represented by a hyperelastic constitutive model constructed as a homogenous isotropic nearly incompressible matrix embedded with two families of collagen fibers (see Figure 1). The strain energy density function is composed of three parts, an isochoric isotropic and a volumetric isotropic Neo-Hookean parts, and a transversely isotropic part representing the collagen fibers.

$$\psi(C) = \left[\psi_{isoch}(C) + \psi_{vol}(C)\right] + \psi_{fibers}(C) \tag{1}$$

The isotropic part of the SEDF is nearly incompressible:

Neo-Hookean SEDF:

$$\psi(C) = \underbrace{c_1\left(I_{c1}I_{c3}^{-\frac{1}{3}} - 3\right) + \frac{1}{D_1}\left(\sqrt{I_{c3}} - 1\right)^2}_{isotropic} \tag{2}$$

With I_{c1}, I_{c3} being the first and third invariants of the right Cauchy-Green tensor and $c_1 = \mu/2$, $D_1 = 2/\kappa$ represent the matrix shear and bulk modulus respectively.

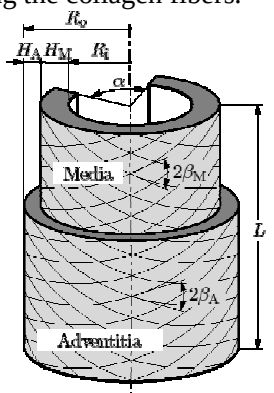

Figure 1: The arterial wall [1]

For the transversely-isotropic part of the SEDF two variations are considered [1,2]:

$$\psi(I_{c3}, I_{c4}, I_{c6}) = \underbrace{(k_1/2k_2)\sum_{i=4,6}\left\{\exp\left[k_2\left(I_{ci}I_{c3}^{-\frac{1}{3}} - 1\right)^2\right] - 1\right\}}_{anisotropic} \quad I_{4c}, I_{6c} \geq 1 \tag{3}$$

(4) $$\psi(I_{c4}, I_{c6}) = \underbrace{(k_1 / 2k_2) \sum_{i=4,6} \left\{ \exp\left[k_2 (I_{ci} - 1)^2\right] - 1 \right\}}_{anisotropic} \quad I_{4c}, I_{6c} \geq 1$$

With I_{c4}, I_{c6} representing the stretch in fiber direction for each fiber family.

For the incompressible limit case $I_{c3} \to 1$ one obtains the same transversely-isotropic SEDF but for the nearly incompressible case the two models may result in a different mechanical response. The difference between the two SEDF for the nearly incompressible case is investigated.

We will present several numerical simulations to study the human coronary artery, concentrating on different modeling issues. Both mono and multi layered models are presented. In Figure 2 the boundary conditions and material parameters used to simulate an artery-like structure are shown.

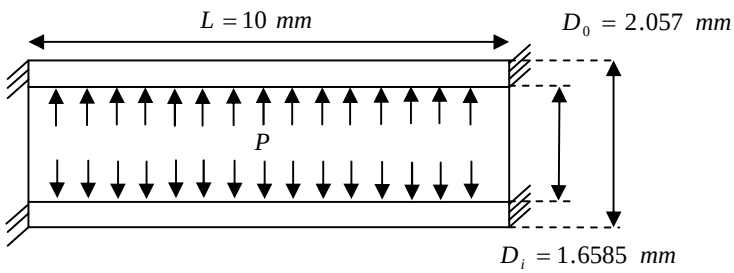

$C_{M1} = 27\ KPa \quad C_{A1} = 2.7\ KPa$
$D_{M1} = 0.01 \quad D_{A1} = 0.01$
$P = 5KPa$
$k_{M1} = 0.64\ KPa \quad k_{A1} = 5.1\ KPa$
$k_{M2} = 3.54 \quad k_{A2} = 15.4$
$\beta_M = 10^0 \quad \beta_A = 40^0$

Figure 2: Boundary conditions and dimensions for sample problem presented, material parameters taken from [5]

As an example the radial displacement across the media layer as a function of compressibility value for both models is shown in Figure 3.

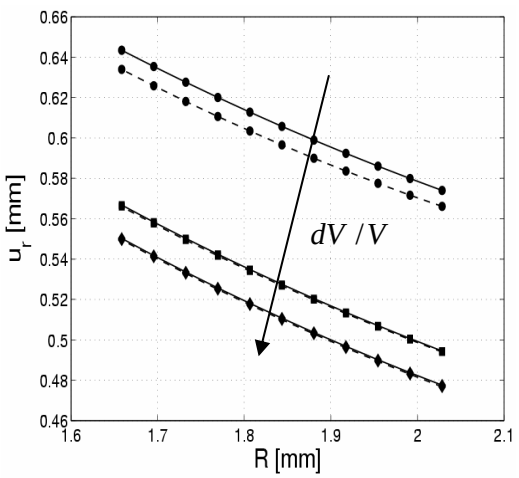

Figure 3: Radial displacement across the media layer of a coronary artery as a function of matrix compressibility (solid line: model (3) dashed line: model (4))

The p-FEM has significant advantages over the classical h-FEM, faster convergence rate, no limitation on element aspect ratio and the ability to accurately map the problem geometry. When nearly incompressible materials are addressed the p-FEM overcomes the well known locking

phenomenon with no special treatment required [3]. As an example the convergence in radial displacement and circumferential stress for the media layer of a pressurized human coronary artery is shown in Figure 4.

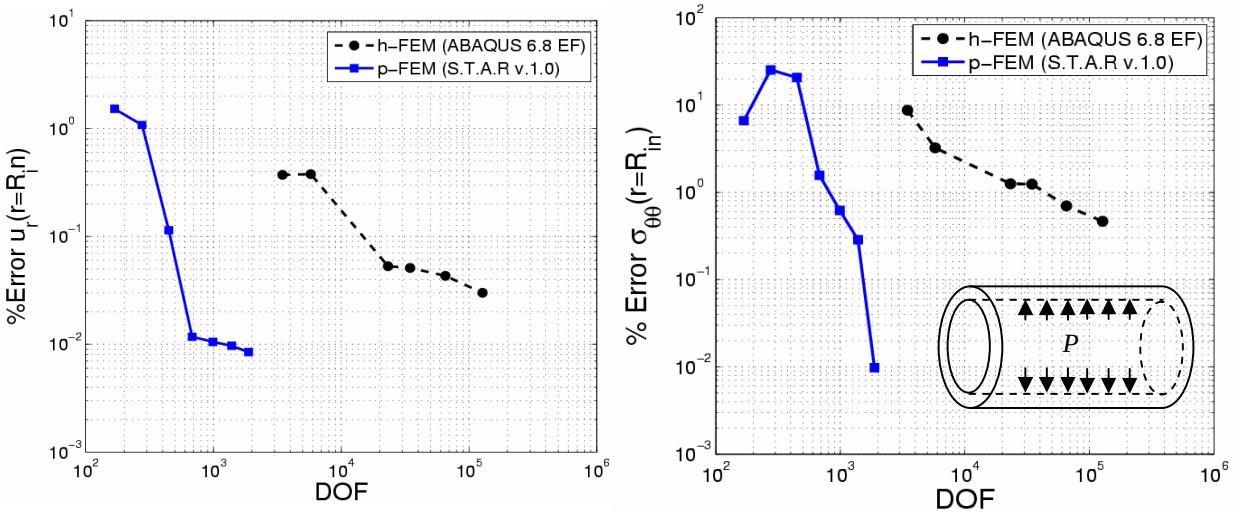

Figure 4: Convergence of radial displacement and circumferential stress (p-FEM and h-FEM)

Most studies model the arterial tissue as an incompressible material when in fact experimental observations [4] suggest slight arterial compressibility. The effect of tissue compressibility on the arterial response is investigated. As an example in Figure 5 the effect of compressibility on the radial displacement and circumferential stress across the media layer of the human coronary artery is shown.

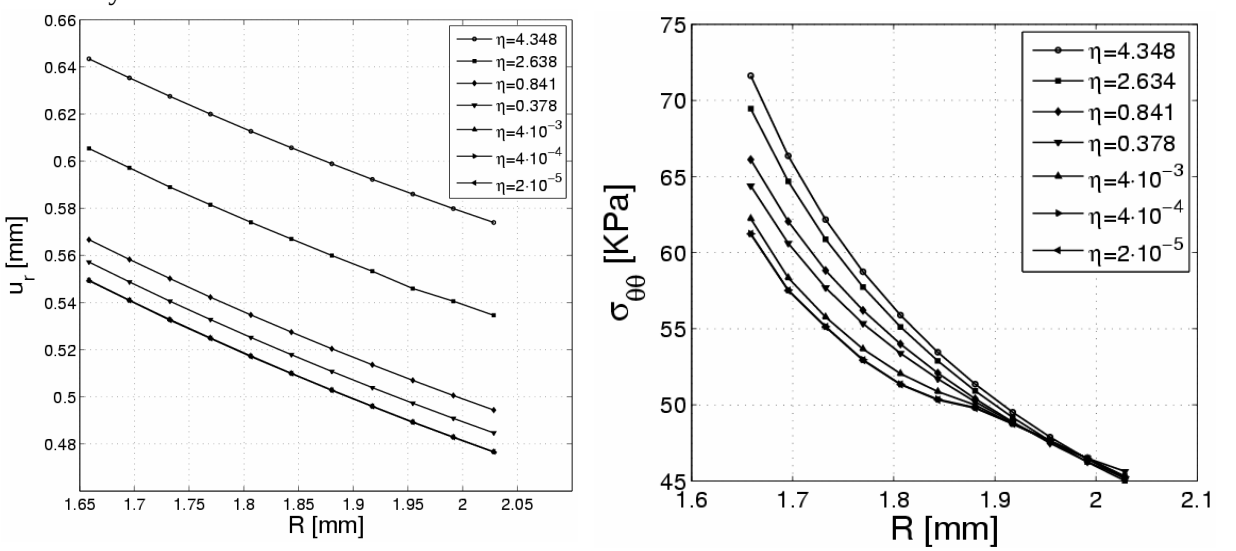

Figure 5: Radial displacement and circumferential stress across the media layer as a function of compressibility value $\eta = | V_{deformed} - V_{undeformed} / V_{undeformed} | \cdot 100\%$.

The media/adventitia layer thickness ratio is usually assumed to be about 0.666 [2,5]. The effect of small changes in thickness layer ratio on the global mechanical response is also studied. As an example in Figure 6 the effect of layer thickness ratio on the radial and circumferential stress across the media and adventitia layers of a human coronary artery is presented.

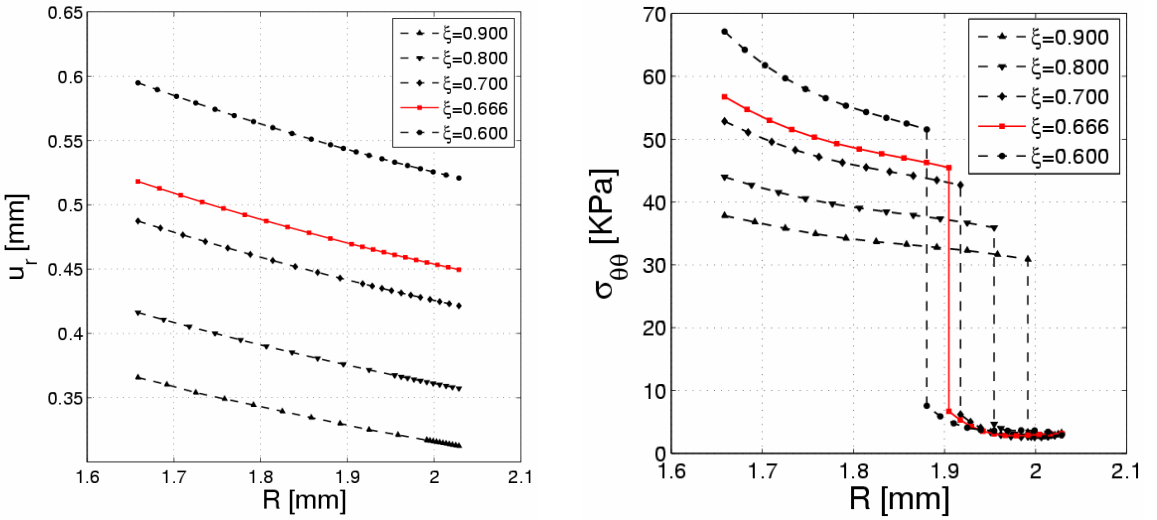

Figure 6: Radial displacement and circumferential stress across the media and adventitia layers as a function of layer thickness ratio $\xi = thickness_{Adventitia} / thickness_{Media}$.

The study has demonstrated the superiority of the p-FEM over the h-FEM when modeling arterial mechanical response. The numerical experiments conducted suggest that even a relatively small amount of compressibility (1-2%) has a non negligible effect on the displacement and stress fields in the arterial tissue and that the different SEDF's that yield similar results for the incompressible case differ in response when compressibility is considered. Structural parameters such as layer thickness ratio should be determined as accurately as possible when modeling the arterial response.

REFERENCES

[1] G. Holzapfel, C. Gasser and R. Ogden "A new constitutive framework for arterial wall mechanics and a comparative study of material models", *J. of Elasticity*, **61**, 1-48, 2000.

[2] G. Holzapfel, C. Gasser and R. Ogden " Comparison of a Multi-Layer Structural Model for Arterial Walls With a Fung-Type Model, and Issues of Material Stability", *J. of Biomedical Engineering*, **126**, 264-275, 2004.

[3] Z. Yosibash, S. Hartmann, U. Heisserer, A. Duester ,E. Rank and M. Szanto "Axisymmetric pressure boundary loading for finite deformation analysis using p-FEM", *Comp. Methods Appl. Mech Engrg.*, **196**, 1261-1277, 2007.

[4] C.J. Chuong and Y.C. Fung. "Compressibility and constitutive equation of arterial wall in radial compression experiments". *J. Biomechanics.*, **17** ,35-40, 1984.

[5] C. Gasser, A.J. Schulze-Bauer and G. Holzapfel, " A three dimensional finite element model for arterial clamping", *J. of Biomedical Engineering*, **124**, 355-363, 2002

2nd International Conference on Mathematical and Computational Biomedical Engineering - CMBE2011
March 30 - April 1, 2011, Washington D.C, USA
P. Nithiarasu and R. Löhner (Eds.)

Regional Differences in Mechanical Behavior of the Thoracic Aorta during Pressure-Induced Inflation

Jungsil Kim, Seungik Baek
Department of Mechanical Engineering, Michigan State University, East Lansing, MI 48824
kimjun40@egr.msu.edu, sbaek@egr.msu.edu

SUMMARY

We investigated aortic wall thickness and mechanical properties at four circumferentially different regions of the porcine thoracic aorta (anterior, left lateral, posterior, and right lateral sides) using the inflation test with a stereo vision tracking system. Our results showed that the anterior regions were significantly thicker but more compliant than the posterior regions. In addition, the mean circumferential stress was significantly higher at the posterior region in the physiological pressure range. There were, however, no significant differences in the mean stretch and pressure-strain elastic modulus among the local circumferential regions.

Key Words: *heterogeneous properties, mechanical homeostasis, vascular mechanics.*

1 INTRODUCTION

There have been significant advances in computational simulation of blood vessel wall dynamics, blood flow, and vascular growth and remodeling using medical image-based geometrical models. Most computational models, however, have assumed that the material properties of a vessel wall are homogeneous in the circumferential direction. There is a critical need for more experimental data and general understandings about regional mechanical properties of arterial walls, which can be used in the prescription of mechanical properties for a patient-specific arterial model. In this paper, we present our recent experimental study and analysis on circumferential variations in the thickness and mechanical properties of the porcine thoracic aorta during inflation tests with a fixed longitudinal stretch, and statistically test multiple hypotheses on mechanical homeostasis.

2 METHODS

Aorta Sample and Inflation Test

Seven porcine thoracic aortas were used for this study. After loose connective tissues around the aorta were removed and all aortic branches were tied, 550 μm-diameter spheres as markers were attached along the circumference at the proximal region, avoiding the surrounding region of aortic branches. The aorta was cannulated and then mounted vertically in a test chamber, which was filled with 0.9 $\%$ NaCl solution. Mechanical testing was performed using a biaxial extension-inflation test device equipped with a stereo vision system [1]. The aorta was preconditioned and then pressurized five times at a fixed longitudinal stretch ratio of 1.35 over 10 to 160 mmHg transmural pressure range. During the inflation test, digital images of the markers affixed on the sample were collected from two cameras and pressure values were recorded simultaneously. The

circumferential sides were identified as anterior, left lateral, posterior, and right lateral regions. The posterior region of a sample was determined by the vicinity of intercostal arteries, and its opposite side was the anterior region. The inflation tests were repeated for each local region of a sample. After the inflation test, the wall thickness was measured at every 45 degree along the circumference.

Data Analysis

The 3D positions of markers are reconstructed using series of stereo images at the load-free state and the deformed states during the inflation test, and they are converted to the cylindrical coordinate. The external wall surface of the sample is parameterized using two variables $\bar{\Theta}$ and $\bar{\mathrm{S}}$, which are convected to the wall surface. Here $\bar{\Theta}$ and $\bar{\mathrm{S}}$ are normalized values of the position of markers Θ and S in the reference configuration. Variables (Θ, S, R) in the reference configuration and (θ, s, r) in deformed configurations are expressed as functions of $\bar{\Theta}$ and $\bar{\mathrm{S}}$. Four variables R, s, θ and r are approximated by finite series of continuous base functions of $\bar{\Theta}$ and $\bar{\mathrm{S}}$

$$\hat{\Phi}(\bar{\Theta}, \bar{S}) = \sum_{j=1}^{n^u} \alpha_j \phi_j(\bar{\Theta}, \bar{S}) \tag{1}$$

where α_j are parameters and n^u is the number of degree of the base function ϕ_j, which are defined as combinations of Legendre Polynomials of $\bar{\Theta}$ and those of $\bar{S}$. Parameters α_n for each approximation function are estimated by the least squares optimization that minimizes the difference between the approximation and the experimental data.

In a convected curvilinear coordinate system, the 2D deformation gradient $\mathbf{F}$ of the surface is given by $\mathbf{F} = \mathbf{g}_i \otimes \mathbf{G}^i$ for i=1, 2, where $\otimes$ denotes the tensor product and the subscripts 1 and 2 denote circumferential and longitudinal directions, respectively. The components of the deformation gradient can be obtained by $F_{pq} = \hat{\mathbf{e}}_p \cdot \mathbf{F}\hat{\mathbf{E}}_q$, where $\hat{\mathbf{E}}_q$ and $\hat{\mathbf{e}}_p$ are the local orthonormal base vectors in the reference and deformed configurations, respectively. The wall thickness h during the inflation test is calculated by using the incompressibility condition ($(h/H_0)\mathrm{det}\mathbf{F} = 1$), and thus $h = H_0/(F_{11}F_{22} - F_{12}F_{21})$, where H_0 is the wall thickness in the load-free state. Stretch λ_i are calculated by $\lambda_i = \sqrt{\hat{\mathbf{E}}_i \cdot (\mathbf{F}^T\mathbf{F})\hat{\mathbf{E}}_i}$. During the inflation test, the mean radius of the curvature in the longitudinal direction is much larger than that of the circumferential direction. Therefore, the circumferential Cauchy stress σ_1 for each local region is estimated by

$$\sigma_1 = \frac{P(r_1 - h)}{h}. \tag{2}$$

where r_1 is the radius of the principal curvature of the vessel wall in the circumferential direction. The principal curvature is obtained by using the first and second fundamental forms of the surface in differential geometry. The stiffness $k(P_i)$, the tangent of the mean stress-stretch curve, for each local region is computed at the transmural pressure P_i by

$$k(P_i) = \frac{\partial \sigma_1}{\partial \lambda_1}|_{\lambda_1(P_i)} = \frac{\sigma_1\left(\lambda_1 + \triangle\lambda_1\right) - \sigma_1\left(\lambda_1 - \triangle\lambda_1\right)}{2\triangle\lambda_1}. \tag{3}$$

To estimate the structural stiffness during the cardiac cycle, pressure-strain elastic modulus E_p is calculated by

$$E_p = \frac{P_{sys} - P_{dia}}{\left(\lambda_{sys} - \lambda_{dia}\right)/\lambda_{dia}} \tag{4}$$

where subscript sys and dia denote the systolic and diastolic condition, respectively. We assume $P_{sys} = 114mm\mathrm{Hg}$ and $P_{dia} = 76mm\mathrm{Hg}$.

Statistical significances among the local circumferential regions and between each pair of two local regions were evaluated by ANOVA and two-sample t-test. The differences were considered significant if $p < 0.05$.

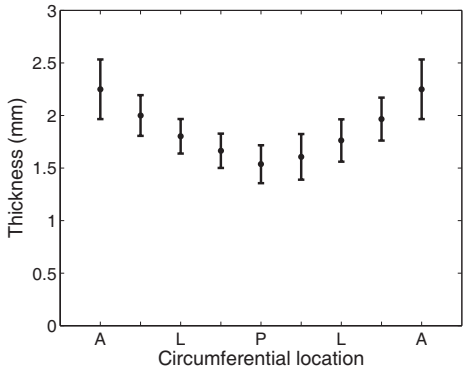

Figure 1: Variation in the thickness of the aortic wall. A: anterior region, L: left lateral region, P: posterior region, R: right lateral region

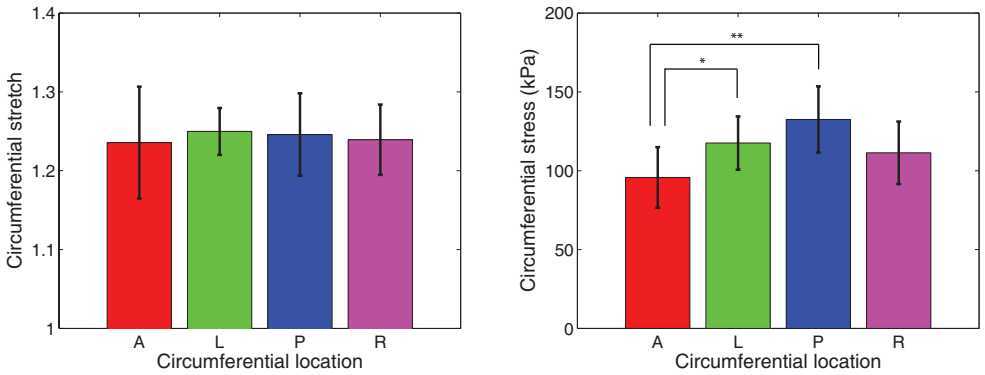

(a) Circumferential stretch

(b) Circumferential stress

Figure 2: Variations in the mean circumferential stretch (a) and mean circumferential stress (b) at the transmural pressure of 100 mmHg. Asterisks represent the significant differences (*: $p < 0.05$, **: $p < 0.01$)

3 RESULTS

The thickness of the aortic wall varied gradually along the circumference as shown in Fig. 1. For all samples, the anterior region was the thickest (2.3 $\pm$ 0.3 mm) and the posterior region was the thinnest (1.6 $\pm$ 0.2 mm). The ratio of the thickness of the anterior region to the posterior region was 1.5 $\pm$ 0.1.

The mean and standard deviation of circumferential stretches and Cauchy stresses of the aorta for each local circumferential region were calculated. At the transmural pressure of 100 mmHg, there was no significant difference in mean stretches among local regions in statistical analysis (Fig. 2a), but the mean stresses of the posterior region (132.52 $\pm$ 21.03 kPa) and left lateral region (117.56 $\pm$ 16.91 kPa) were significantly higher than the anterior region (95.73 $\pm$ 19.26 kPa) (Fig. 2b).

Likewise, the mean stiffness of the posterior region was the highest and that of the anterior region was the lowest, and the differences increased with the increase of the transmural pressure. At the transmural pressure of 100 mmHg, there were significant differences between the anterior (460.33 $\pm$ 132.14 kPa) and posterior (754.40 $\pm$ 114.79 kPa) regions, the posterior and right lateral (566.98 $\pm$ 79.99 kPa) regions, and the anterior and left lateral (625.28 $\pm$ 126.84 kPa) regions (Fig. 3a).

Under a physiological condition, the pressure-strain elastic modulus E_p was determined. There

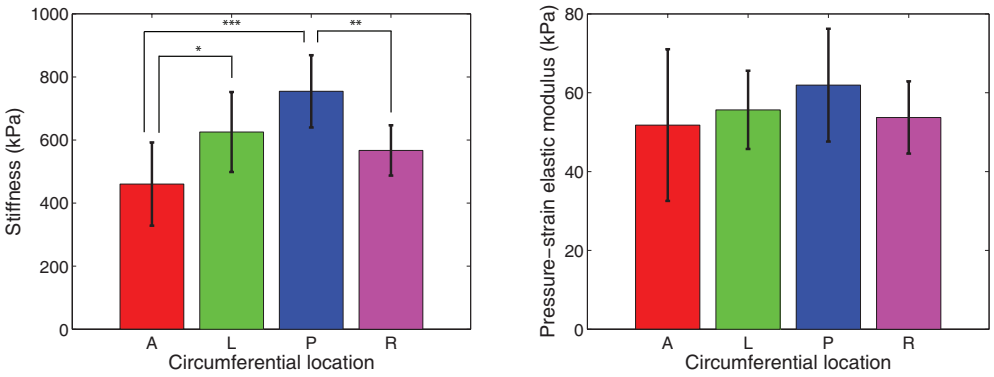

(a) Stiffness ($d\sigma/d\lambda$) (b) Pressure-strain elastic modulus

Figure 3: Variations in the mean circumferential stiffness ($d\sigma/d\lambda$) at the transmural pressure of 100 mmHg (a) and the mean pressure-strain elastic modulus E_p (b). Asterisks represent the significant differences (*: $p < 0.05$, **: $p < 0.005$, ***: $p < 0.001$)

was no significant difference among local regions, although there was a small variation as shown in Fig. 3b.

4 DISCUSSIONS

The present study found that there were significant differences in the thickness, mean stress, and material stiffness among the local circumferential regions, but no significant differences in the mean stretch and pressure-strain elastic modulus in the physiological pressure range. These results imply that the posterior region is thinner but stiffer than the anterior region, so that pressure-strain elastic modulus, which represents a structural stiffness during a cardiac cycle, becomes relatively uniform circumferentially.

Guo and Kassab [2] reported the relatively uniform strain along the porcine aorta compare to arteriole and suggested the existence of a homeostatic state of strain in the cardiovascular system. In addition, Lillie and Gosline [3] also suggested nearly constant physiological strain of the elastin along the porcine thoracic aorta. Consistent with those previous studies, our finding supports the hypothesis of strain homeostasis in the aortic wall.

REFERENCES

[1] J. Kim and S. Baek, Circumferential variations of mechanical behavior of the porcine thoracic aorta during the inflation test, *Journal of Biomechanics*, submitted.

[2] X. Guo and G.S. Kassab, Distribution of stress and strain along the porcine aorta and coronary arterial tree, *American Journal of Physiology, Heart & Circulatory Physiology*, 286, H2361 - H2368, 2004.

[3] M.A. Lillie and J.M. Gosline, Mechanical properties of elastin along the thoracic aorta in the pig, *Journal of Biomechanics*, 40, 2214-2221, 2007.

2nd International Conference on Mathematical and Computational Biomedical Engineering - CMBE2011
March 30 - April 1, 2011, Washington D.C, USA
P. Nithiarasu and R. Löhner (Eds.)

Computational study of blood flow within a multi-branched model of the rabbit thoracic aorta

A. M. Plata[1], P. E. Vincent[3], A. A. E. Hunt[2], S. J. Sherwin[1] and P. D. Weinberg[2]
[1]Department of Aeronautics, Imperial College London London, SW7 2AZ, UK
[2]Department of Bioengineering, Imperial College London London, SW7 2AZ, UK
[3]Department of Aeronautics, Stanford University Stanford, CA 94305, USA
aplataga@imperial.ac.uk

SUMMARY

Atherosclerosis is known to occur in a spatially non-uniform fashion within the arterial system. The patchy nature of the disease is thought to reflect spatial variation in the stresses exerted on the arterial wall by the flow of blood. Previous studies have highlighted the importance of geometrical accuracy when analysing flow metrics. This study investigates blood flow numerically within a realistic representation of the rabbit thoracic aorta and its branches. The vascular geometry was reconstructed using high resolution CT scan data of a vascular corrosion cast, representing a significant advance over previous geometric modelling efforts. This study aims to find correlations between flow and disease maps (previously obtained by associated experimental work), and hence to contribute to a greater understanding of atherogenesis.

This study investigates blood flow numerically using a spectral/hp element method. It is found that two Dean-type vortices (associated with a skewed velocity profile) form in the aortic arch and propagate along the descending thoracic aorta. This results in streaks of wall shear stress (WSS) similar in nature to the fatty streaks of early stage atherosclerosis observed in mature rabbits. Further, it is observed that the local WSS patterns in the vicinity of the intercostal arteries (produced by the blood entering the the vessels) are superimposed on the streaked macroscale WSS distribution. Such diverse range of WSS environment in which pairs reside may explain variation in disease reported between branch pairs.

Key Words: *blood flow, wall shear stress, atherosclerosis.*

1 Introduction

Approximately 40% of deaths in developed countries are due to cardiovascular diseases. Atherosclerosis is an extremely common form of cardiovascular disease characterised by the formation of lipid rich plaques within the intima of the arterial wall. Such plaques can lead to the stenosis of arteries, and may eventually rupture causing a heart attack or stroke.

Atherosclerosis is known to occur in a spatially non-uniform fashion within the arterial system. The patchy nature of the disease is thought to reflect spatial variation in the stresses exerted on the arterial wall by the flow of blood.

A great number of computational and mathematical studies have attempted to correlate areas of disease prevalence in arteries with various flow metrics such as WSS [1,2]. Most of these studies focused on the analysis of blood flow in a range of idealised vascular regions, primarily bends,

bifurcations and stenoses. Computational studies within such simplified geometries have been proved to be a useful tool to gain understanding of blood flow physics. However, flow metrics (in particular WSS [3]) have been shown to depend strongly on subject-specific geometrical features. Therefore, generating a detailed and faithful computational definition of the vascular geometry is necessary in order to accurately model blood flow within the arterial system. Here, blood flow in a highly realistic representation of the rabbit aorta is modelled in order to compare flow features with disease patterns.

2 Methods

Reconstruction of the vascular geometry

The vascular geometry was obtained from high resolution (55.2μM) CT scan data of a vascular corrosion cast (Fig. 1). Approximately 2000 DICOM images (9.2 GB) were obtained. There are over 100 voxels across the 6mm diameter of the aortic root.

An intensity isosurface was segmented from the CT scan data using Amira. (Visage Imaging, Inc.). Further processing (cropping unwanted arteries, adding flow extensions and surface smoothing) was carried out using VMTK (www.vmtk.org). A volume mesh was created using Gambit 2.4.6 and Tgrid 4.0.24 (ANSYS, Inc). SPHERIGON patches [4] were used in order to curve the external face of the volume elements. In terms of combined detail and extent, the resulting volume mesh shown in Fig. 2 represents a significant advance over previous geometric modelling efforts.

The computational domain comprises the ascending aorta, aortic arch and proximal descending thoracic aorta of a male New Zealand White rabbit. Vessels emanating from the aortic arch (followed to at least their second branching generation) and five pairs of intercostal arteries are also included.

Numerical methods

Steady state blood flow was modelled using the steady-state incompressible Navier-Stokes equations for a Newtonian flow. These equations were solved using the spectral/hp element Galerkin approximation [5].

Blood flow was computed for five different Reynolds numbers in order to simulate multiple time points in the cardiac cycle.

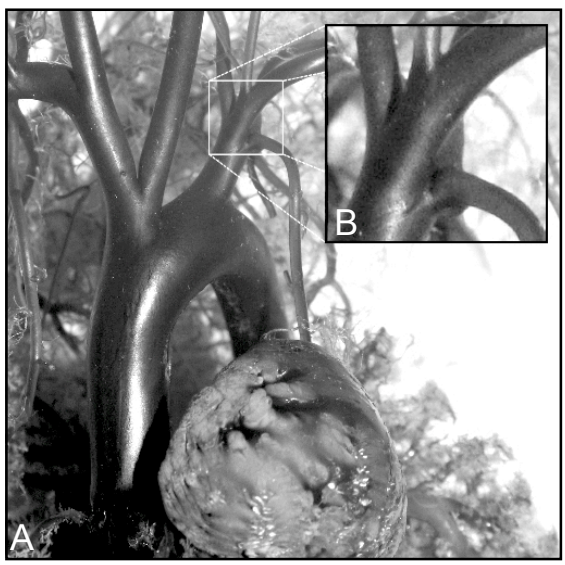

Figure 1: Images of the resin cast showing: (A) the aortic arch and (B) a quadfurcation of the left subclavian artery.

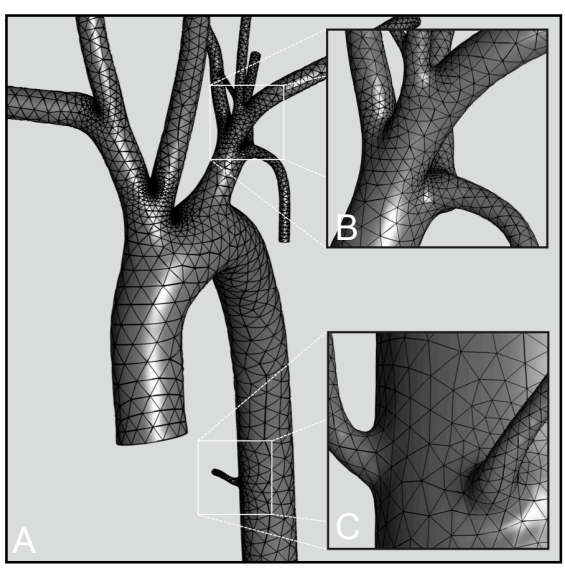

Figure 2: Images of the volume mesh showing: (A) the aortic arch, (B) quadfurcation of the left subclavian artery and (C) two intercostal arteries.

3 Results and conclusions

It is found that two Dean-type vortices (associated with a skewed velocity profile) form in the aortic arch and propagate along the descending thoracic aorta. The skewness of the axial velocity results in streaks of low and high WSS (Figs. 3a and 3b). Since atherosclerosis lesions are also streaked in the descending aorta in mature rabbits (Fig. 3c), the results of this study certainly support the hypothesis that flow (in particular WSS) mediates the onset of the disease. Further, it is observed that the local WSS patterns in the vicinity of the intercostal arteries (produced by the blood entering the the vessels) are superimposed on the streaked macroscale WSS distribution. Such diverse range of WSS environment in which pairs reside may explain variation in disease reported between branch pairs.

The results of this study emphasises the importance of geometrical accuracy when computing vascular WSS distribution. In particular it is showed that small-scale features, such as the cusp at the attachment site of the ligamentum arteriosum, cause deviations in the WSS of the same order of magnitude as flow-induced variations. Moreover, the vascular geometry (in particular the aortic torsion and tapering) may play a significant role in the formation and propagation of Dean vortices, and hence in determining the localisation of the WSS streaks.

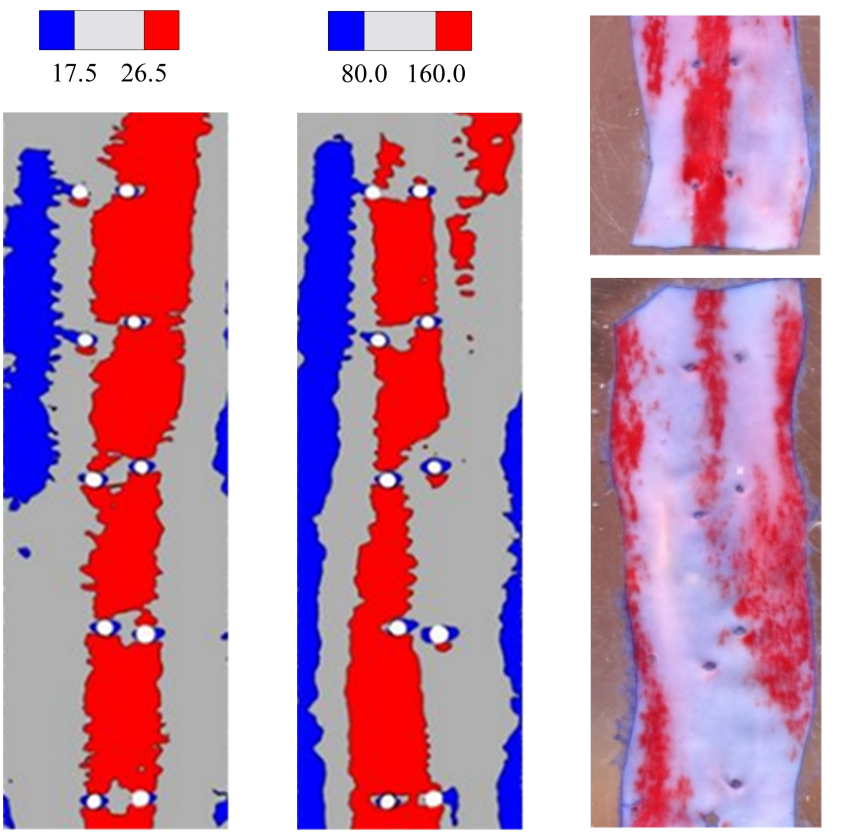

Figure 3: En face three tone colour maps of WSS (dynes cm^{-2}) in the descending aorta for Re=300 (a) and Re=1300 (b), and en face view sections from the descending aorta of a mature cholesterol-fed rabbit stained with oil red O dye to identify fatty streaks (c). All data are presented with the endothelial surface facing upwards. Blood flow is from top to bottom in all images. The disease maps are unpublished data courtesy of S. G. Cremers, S. J. Wolffram and P. D. Weinberg, obtained following an identical procedure to Weinberg *et. al.* [6].

REFERENCES

[1] J. Suo, D. E. Ferrara, D. Sorescu, R. E. Guldberg, W. R. Taylor, D. P. Giddens. Hemodynamic Shear Stresses in Mouse Aortas: Implications for Atherogenesis, *Arteriosclerosis, Thrombosis, and Vascular Biology*, 27, 346-351, 2007.

[2] Y. Huo, X. Guo and G. Kassab. The Flow Field along the Entire Length of Mouse Aorta and Primary Branches, *Annals of Biomedical Engineering*, 36, 685-699, 2008.

[3] J. G Myers, J. A. Moore, M. Ojha, K. W. Johnston and C. R. Ethier. Factors Influencing Blood Flow Patterns in the Human Right Coronary Artery, *Annals of Biomedical Engineering*, 29, 109-120, 2001.

[4] P. Volino and N. M. Thalmann. The SPHERIGON: a simple polygon patch for smoothing quickly your polygonal meshes, *Computer Animation 98. Proceedings*, 72-78, 1998.

[5] S. J. Sherwin and E. G. Karniakadis. *Spectral/hp Element Methods for Computational Fluid Dynamics*, Oxford University Press, 2005.

[6] S. E. Barnes and P. D. Weinberg. Contrasting patterns of spontaneous aortic disease in young and old rabbits *Arteriosclerosis, Thrombosis, and Vascular Biology*, 18(2), 300-308, 1998.

2nd International Conference on Mathematical and Computational Biomedical Engineering - CMBE2011
March 30 - April 1, 2011, Washington D.C, USA
P. Nithiarasu and R. Löhner (Eds.)

SwirlGraft versus conventional straight graft as vascular access: a full CFD-analysis

Koen Van Canneyt*, Gianluca De Santis*, Sunny Eloot, Patrick Segers* and Pascal Verdonck***

*Ghent University, IBiTech-bioMMeda, De Pintelaan 185, Gent, Belgium
Koen.VanCanneyt@UGent.be
**Dept. of Nephrology, Ghent University Hospital, De Pintelaan 185, Gent

SUMMARY

Two 3D models of an arterio-venous graft, a connection between an artery and a vein as vascular access for hemodialysis, were studied. One model of a conventional straight loop graft, the other of a graft with helical configuration (e.g. SwirlGraft (Veryan Medical, London, UK)). The statement that the helical design reduces Intimal Hyperplasia (IH) formation was studied by evaluating low wall shear stress and high oscillatory shear stress zones next to the helicity flow index. The IH-inducing zones were reduced but were not eliminated and the helicity of the flow was increased. The statement that the SwirlGraft avoids stenosis should however be considered with care in clinical practice.

Key Words: *arterio-venous graft, vascular access, CFD, shear stress, helicity.*

1 INTRODUCTION

Constructing an arterio-venous graft is one of the choices for long-term vascular access in patients on hemodialysis as renal replacement therapy. This alternative to an arterio-venous fistula (direct connection between artery and vein), mostly used in patients with low quality vessels, has however a high complication rate. Thrombosis due to underlying stenosis account for 80% of graft failure [1]. These stenoses mostly occur at the venous anastomosis or in the draining vein.
Stenoses at the venous anastomosis are originated from intimal hyperplasia (IH). The hemodynamic phenomenon of flow disturbance is known as an inducing factor [2]. This can be linked to low Wall Shear Stress (WSS), high oscillatory shear stress [3] or helicity of the bulk flow [4].
The SwirlGraft (Veryan Medical, London, UK) claims to reduce IH formation by adding a swirl to the conventional straight graft. This statement is assessed in a full Computational Fluid Dynamics (CFD) model, including artery, loop graft and vein.

2 MATERIAL AND METHODS

Two full 3D models were constructed in a parametric way, using pyFormex (pyformex.org):

- Straight conventional loop graft,
- SwirlGraft in loop configuration.

In both models (Figure 1), an artery with 4mm diameter and a vein of 6mm diameter, both 115 mm proximal and 45 mm distal length, were connected with a graft with a 45° anastomosis. The graft had in both cases a diameter of 6mm and a length of 300 mm. The SwirlGraft has a pitch of 70 mm and an amplitude of half the diameter.

Robust mesh sensitivity analysis was performed on the fully conformal structured hexahedral mesh to achieve results with less then 1% error on the WSS values. For the non-constant inlet case, a mesh of 1.3 million cells was used. The mesh was refined to a 3.3 million cell count to achieve reliable results for the non-constant inlet case. Both cases were calculated using Ansys Fluent 12 (ANSYS inc., Canonsburg, PA, USA), with double precision and unsteady (200Hz, even for the constant inflow).

With both models, two cases were calculated. One with a constant inflow of 600ml/min and one with a physiological relevant non-constant inflow (264-1500 ml/min, average 600ml/min, 60bpm), both with a parabolic inlet profile. The distal artery and distal vein outflow was set to 5% and the flow through the proximal vein was then the other 90%. A shear thinning viscosity model (Quemada) and a fluid density of 1054 kg/m^3 were used.

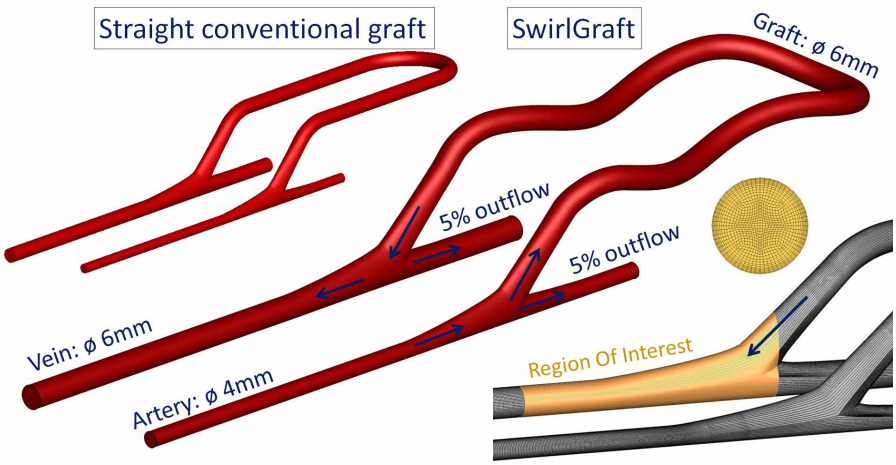

Figure 1: Overview: Two full 3D models, details of conformal hexahedral mesh and primary dimensions

The Region Of Interest (ROI) was defined at the venous anastomosis from 8 mm distal to 45 mm proximal to the center of the anastomosis, as shown in Figure 1. In this ROI, the average WSS (WSSavg) and the Oscillatory Shear Index (OSI) were calculated. The WSSavg was calculated from the constant inflow case:

$$WSSavg = \left|\overline{WSS}\right| \tag{1}$$

The OSI was calculated for the physiological inflow:

$$OSI = \frac{1}{2} \times \left(1 - \frac{\left| \int_0^T \overline{WSS} \cdot dt \right|}{\int_0^T \left|\overline{WSS}\right| \cdot dt} \right) \tag{2}$$

The areas with low WSSavg and high OSI were calculated in the ROI.

Next to these factors, the helicity (H) and the normalised helicity (ψ) of the flow were evaluated, calculated from the Velocity (V):

$$H = V.(\nabla \times V) \tag{3a}$$

$$\psi = \frac{H}{|V|.|\nabla \times V|} \tag{3b}$$

By calculating the Helicity Flow Index (HFI) [4], the helicity could be evaluated in a Lagrangian way:

$$HFI = \frac{1}{N_p}\sum_{i=1}^{N_p}\frac{1}{N_k}\sum_{j=1}^{N_k}|\psi_{ij}| \tag{4}$$

with N_p pathlines with each N_k points. In this study, the pathlines starting in the graft at 42 mm from the anastomosis side were used. For our analysis, 169 paths (N_p) with each 300 steps (N_k), covering the whole ROI, were used.

Post-processing was performed in Ansys Fluent 12, Matlab 7.8.0.347 (MathWorks inc.,Natick, MA, USA) and Tecplot 360 2010 (Tecplot inc., Bellevue, WA, USA).

3 RESULTS

Figure 2 shows the WSS (left) and the OSI (right) for the region of interest. Zones with low WSS and high OSI are located at the upper ceiling of the anastomosis and at the heel (entrance of distal artery) for both cases.

Areas of low WSS and high OSI are shown in Table 1 . A reduction of the area with low WSS and high OSI can be found comparing the SwirlGraft to the straight conventional graft. In Table 2, the results for the HFI are shown. A increase in the helicity can be found when a swirl is introduced in the graft design.

in ROI	Conventional graft	SwirlGraft	Area reduction
WSS $\leq$ 0.6 Pa	1.04 cm^2	0.77 cm^2	26 %
WSS $\leq$ 0.5 Pa	0.86 cm^2	0.60 cm^2	31 %
WSS $\leq$ 0.4 Pa	**0.67 cm^2**	**0.43 cm^2**	**35 %**
OSI $\geq$ 0.3	1.16 cm^2	0.84 cm^2	42 %
OSI $\geq$ 0.2	0.51 cm^2	0.39 cm^2	24 %
OSI $\geq$ 0.1	**0.25 cm^2**	**0.15 cm^2**	**28 %**

Table 1: Areas with low WSS and high OSI in ROI

	Conventional graft	SwirlGraft	Increase in Helicity
HFI	0.282	0.313	11 %

Table 2: Values for the Helicity Flow Index (HFI)

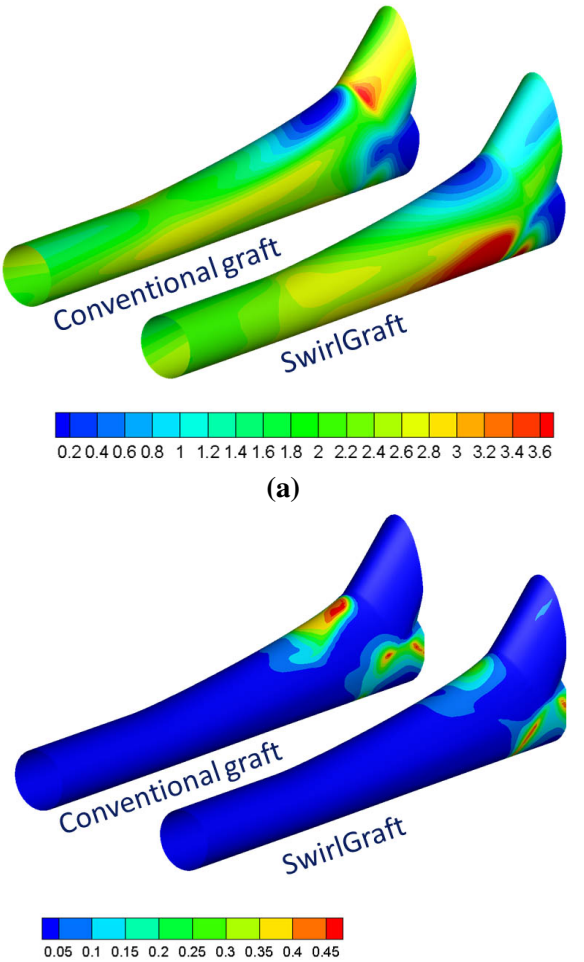

Figure 2: WSS [Pa]*(a)* and OSI *(b)*

4 CONCLUSIONS

The SwirlGraft effectively reduces low WSS and high OSI zones, but does not eliminate them. The reduction of WSS temporal gradients can be linked to the increase in HFI as suggested by Morbiducci et al. [4]. The statement that the SwirlGraft avoids stenoses should however be considered with care in clinical practice.

REFERENCES

[1] M. Allon, Current Management of Vascular Access, *Clinical Journal of the American Society of Nephrology*, 2, 786-800, 2007.

[2] M. Fillinger, Graft Geometry and Venous Intimal-Medial Hyperplasia in Arteriovenous loop grafts, *Journal of Vascular Surgery*, 11(4), 556-566, 1990.

[3] P. Roy-Chaudhury, L.M. Spergel, A. Besarab, A. Asif and P. Ravani, Biology of Arteriovenous Fistula Failure, *Journal of Nephrology*, 20, 150-163, 2007.

[4] U. Morbiducci, R. Ponzini, M. Grigioni and A. Redaelli, Helical Flow as Fluid Dynamic Signature for Atherogenesis Risk in Aortocoronary Bypass. A Numeric Study, *Journal of Biomechanics*, 40, 519-534, 2007.

2nd International Conference on Mathematical and Computational Biomedical Engineering – CMBE2011
March 30 – April 1, 2011, Washington D.C., USA
P. Nithiarasu and R. Löhner (eds)

NUMERICAL MODEL FOR CFD-SIMULATION OF THE FLOW FIELD IN THE ANASTOMOSIS REGION OF CORONARY BYPASSES

Marloes De Witte*, Abigail Swillens*, Lasse Løvstakken, Håvard Nordgaard**, Denis Van Loo***, Bram Trachet*, Jan Vierendeels**** and Patrick Segers***

* IBiTech-bioMMeda, Ghent University, Ghent, Belgium

** Department of Circulation and Medical Imaging, Norwegian University of Science and Technology, Trondheim, Norway

***Department of Physics and Astronomy (UGCT), Department of Soil Management, Ghent University, Ghent, Belgium

**** Department of Flow, Heat and Combustion Mechanics, Ghent University, Ghent, Belgium

Corresponding author: Marloes De Witte, Ph. D. fellow of the Research Foundation - Flanders (FWO), IBiTech-bioMMeda, Ghent University, De Pintelaan 185 Blok B, B-9000 Gent, Belgium, Marloes.DeWitte@UGent.be

SUMMARY

Coronary artery bypass surgery is a treatment for ischemic heart disease and can increase life quality and expectancy. The results after the treatment depend largely on the patency of the bypass grafts, which are used to bypass the narrowed arteries on the heart. Long-term patency is mainly determined by the progression of atherosclerosis and intimal hyperplasia (IH) within the bypass grafts, which are believed to be related to unfavourable wall shear stress (e.g. low and oscillatory WSS) exerted on the endothelial cells. To investigate the potential role of hemodynamic forces on the endothelial cells and the impact of the severity of the bypassed arterial stenosis on the flow fields, we developed a computational model of a LIMA-to-LAD anastomosis region obtained from a porcine in-vivo cast. In addition, the same porcine experiment provided the necessary up- and downstream boundary conditions for the simulations. The model has been applied to simulate the flow field in 5 cases, corresponding with 100, 97, 90, 75 and 0% LAD stenosis, in order to quantify the effect of the stenosis on resulting flow fields and on WSS distributions. Low stenosis degrees are associated with competitive LAD and LIMA flow and low WSS in the LIMA, which might contribute to WSS-related remodeling and suboptimal performance of the LIMA bypass.

Key Words: *LIM-to-LAD anastomosis, numerical modeling, CFD, wall shear stress.*

1. INTRODUCTION

Atherosclerosis may lead to flow-obstructing stenosis, a problem that frequently occurs in the coronary arteries and causes angina pectoris and heart infarction. In order to restore the blood supply to the heart, the atherosclerotic coronary arteries can be bypassed by means of a vascular graft. This treatment is called coronary artery bypass surgery. Different kinds of vessels may be used as bypass graft (vein or artery). In this work, the LIMA graft and LIMA-to-LAD anastomosis are studied (host: left anterior descending coronary artery, LAD; graft: left internal mammary artery, LIMA).

Despite the usually excellent long-term patency of the LIMA-graft, the LIMA-graft may shrivel and fail in the late course after the grafting procedure. This so-called 'string effect', is more likely to occur in conditions of competitive flow, where the native flow is substantial and disturbs the flow through the bypass grafts due to a non-significant stenosis [1].
It is known that hemodynamic forces, principally too low (WSS<±0.4-0.5Pa) and oscillatory WSS, may induce endothelial dysfunction and vascular remodeling and promote atherosclerosis and IH [2, 3]. In order to assess the susceptibility of the LIMA-graft to narrowing and shriveling, more insight has to be acquired in the complex flow field and the induced WSS in the LIMA-lumen. As WSS is still a challenging parameter to measure non-invasively, numerical simulations are necessary.

2. MAIN BODY

2.1 Materials and Methods

2.1.1 3D-geometry

A LIMA-to-LAD bypass was constructed in a pig [4]. During the procedure, flow and pressure measurements were performed in the proximal and distal LAD, and flow was measured in the LIMA. Three data sets were acquired, measured when the proximal LAD was completely occluded, partially occluded and fully open. Afterwards, the heart was removed from the euthanized pig's chest and the LIMA was fixated on the heart in order to preserve the angle between LAD and LIMA. Subsequently, a cast was made of the anastomosis region (with non-occluded LAD). This 3D-cast of the anastomosis region and surrounding vasculature was scanned using the micro-CT scanner of the Ghent University Centre for X-ray Tomography. Out of the resulting CT-images, a digital model (STL) was created using Mimics (Materialise, Belgium). The resulting basic model counted 2 circular inlets (LIMA and proximal LAD), and 13 circular outlets (12 septals and the distal LAD).
As the exact degree of stenosis was not known, (digital) models with proximal LAD stenoses of 97, 90 and 75% area reduction were created by extending the proximal LAD inlets of three basic models by means of three cylindrical tubes of which the mid luminal flow sections were reduced by respectively 97, 90 and 75% (figures 3B, C and D). The models for 0% and 100% stenosis were obtained by defining the proximal LAD inlet respectively as an inlet and as a wall (figures 3A and E). Finally, the resulting geometries were meshed in Gambit (Ansys, Inc., U.S.A.).

2.1.2 Boundary conditions

In order to identify the isolated effects of the stenoses as purely as possible, *one* set of boundary conditions (BC's) was used to simulate flow in the 5 different configurations. The BC's were extracted from the data measured during 100% LAD occlusion as this condition provided the most consistent and useful dataset.
The pressure measured at the proximal LAD was applied at both inlets (LIMA and proximal LAD) because no LIMA-pressure measurements were available. This induces an error since a time shift between both pressure waves is expected in real physiologic circumstances.
Since flow in the coronary circulation is dominated by active components during systole (e.g. the squeezing of the septals embedded in the myocardium) and more by passive components during diastole, two types of boundary conditions were created for systole and diastole. During the whole cardiac cycle, velocity profiles were assumed parabolic at the outlets.
As the exact distribution of blood flow towards the distal LAD and the septals is unknown, we arbitrarily assumed that 5% of the blood flow was going to the septals, while the remaining 95% was going to the distal LAD. During systole, the maximal velocity of the parabolic velocity profile at septal l $(l=1\text{-}12)$ was then calculated according to:

$$v_{systole}^{l,\max}(t) = -2 \times \left[\frac{0.05 \times Q_{LIMA}(t)}{A_l} \left(\frac{R_l^3}{\sum_{k=1}^{12} R_k^3} \right) \right]$$

with A_l and R_l respectively the area and radius of the circular outflow section of septal *l* and $Q_{LIMA}(t)$ the flow measured at the LIMA at time instant *t* during 100% proximal LAD occlusion. The maximal velocity of the parabolic velocity profile at the distal LAD was calculated according to:

$$v_{systole}^{LAD,\max}(t) = -2 \times \left[\frac{0.95 \times Q_{LIMA}(t)}{A_{LAD}} \right]$$

During diastole, the maximal velocities of the parabolic outlet velocity profiles at septal *l* and at the distal LAD at a time *t* were calculated by means of the conductances $C_l(t)$ and $C_{LAD}(t)$, given by respectively:

$$C_l(t) = \frac{0.05 \times Q_{LIMA}(t)}{P_{LIMA}(t) - P_{ra}} \left(\frac{R_l^3}{\sum_{k=1}^{12} R_k^3} \right) \qquad \text{and} \qquad C_{LAD}(t) = \frac{0.95 \times Q_{LIMA}(t)}{P_{LIMA}(t) - P_{ra}}$$

with $P_{LIMA}(t)$ the pressure applied at the LIMA (i.e., the pressure measured at the proximal LAD during 100% proximal LAD occlusion) and $P_{ra} \approx 0$ the pressure in the right atrium.
The obtained conductances (calculated from the measurements corresponding with 100% proximal LAD occlusion) were used to derive the maximal velocities of the parabolic velocity profiles at septal *l* and at the distal LAD according to:

$$v_{diastole}^{l/LAD,\max}(t) = -2 \times \left[C_{l/LAD}(t) \frac{P_{l/LAD}(t)}{A_{l/LAD}} \right]$$

with $P_{l/LAD}(t)$ the pressure at septal *l* or at the distal LAD. Velocities are thus dependent on the local pressures in the studied models.
During diastole, a semi-implicit calculation of the flow field is necessary since $P_{l/LAD}(t)$, a result of the flow simulations, must be known in order to calculate the corresponding outflow profile. An adapted algorithm was developed to accomplish this.
All simulations were performed using Fluent 12 (Ansys, Inc., U.S.A.). Two cardiac cycles were calculated to remove transient effects.

2.2 Results and Discussion

2.2.1 Effect of the stenosis on the flow and flow patterns

The total blood flow into the anastomosis region is not affected by the degree of proximal LAD stenosis. Lower flow from the LAD causes higher flow from the LIMA, and vice versa. However, the lower the degree of proximal LAD stenosis, the higher the inflow into the proximal LAD and the lower the inflow of blood into the LIMA, as illustrated in figure 1.
In all studied cases, the velocity contours at maximal inflow in slices distal from the anastomosis-region, show typical crescent velocity distributions with maximal velocities near the bottom wall of the LAD (figure 2A, slices 6-9). The angle between LIMA and LAD affects the velocity distribution in the anastomosis region: e.g. in slice 8 of figure 2A, velocities are higher near the back wall of the LAD due to the twisted position of the LIMA relatively to the LAD (figure 2B, top view of the LIMA-to-LAD anastomosis).

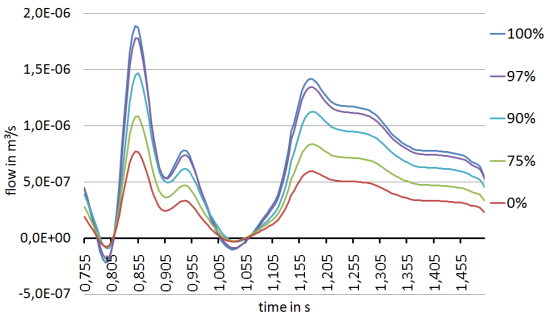

Figure 1: Plot of the flow at the LIMA (inlet) for 100, 97, 90, 75 and 0% LAD stenosis

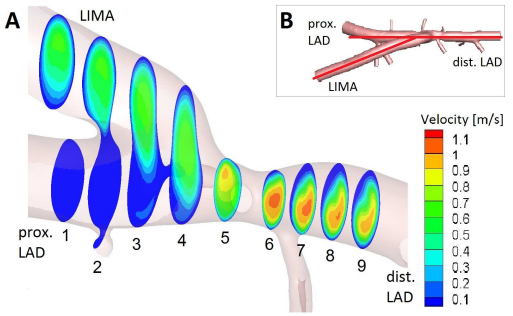

Figure 2: (A) Velocity contours in 9 cross-sectional planes at t=0.855s for 100% prox. LAD occlusion; (B) Top view of the LIMA-to-LAD anastomosis

2.2.2 Effect of the stenosis on the WSS-distribution

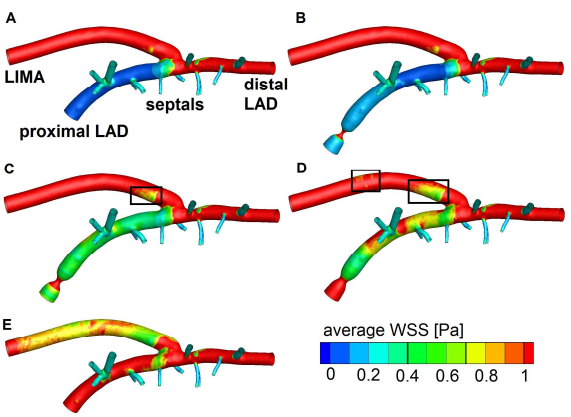

Figure 3: Average WSS (0-1Pa; WSS>1Pa = red) during one cardiac cycle for the cases of (A) 100%, (B) 97%, (C) 90%, (D)75% and (E) 0% proximal LAD occlusion

The average WSS in the LIMA (whole cardiac cycle) is clearly correlated to the blood flow through it: for a proximal LAD occlusion of 100 or 97%, the average WSS in the LIMA is higher than 1Pa (figures 3A and B); when the flow in the LIMA diminishes (90% stenosis), a zone of relatively low average WSS (0.3-0.8Pa) appears at the inner bend of the distal LIMA, as indicated in figure 3C. This zone of low average WSS expands when the degree of proximal LAD stenosis is further lowered (i.e. in the case of 75% stenosis, figure 3D) until it covers the whole LIMA when the proximal LAD is not occluded (figure 3E).

3. CONCLUSIONS

In conclusion, based on hemodynamic grounds, the LIMA may become more susceptible for vascular diseases and subsequent occlusion when the stenosis in the proximal LAD is less than severe.

REFERENCES

[1] M.B. Yilmaz, Y. Guray et al., Fate of internal mammary artery grafted to left anterior descending artery is influenced by native vessel stenosis and viable myocardium, *Angiology*, Vol. 60, Issue 2, 201-206, 2009.

[2] A.M. Malek, S.L. Alper and S. Izumo, Hemodynamic shear stress and its role in atherosclerosis, *JAMA*, Vol. 282, No. 21, 2035-2042, 1999.

[3] G.S. Kassab and J. Navia, Biomechanical considerations in the design of graft: the homeostasis hypothesis, *Annual Review of Biomedical Engineering*, Vol. 8, 499-535, 2006.

[4] H. Nordgaard, D. Nordhaug et al., Different graft flow patterns due to competitive flow or stenosis in the coronary anastomosis assessed by transit-time flowmetry in a porcine model, *European Journal of Cardio-Thoracic Surgery*, Vol. 6, Issue 1, 137-142, 2009

2nd International Conference on Mathematical and Computational Biomedical Engineering – CMBE2011
March 30 – April 1, 2011, Washington D.C., USA
P. Nithiarasu and R. Löhner (eds)

RESULTS OF THE FDA INTERLABORATORY COMPUTATIONAL STUDY IN A NOZZLE WITH A SUDDEN CONTRACTION AND CONICAL DIFFUSER

Sandy F.C. Stewart*, Prasanna Hariharan*, Eric G. Paterson†, Greg W. Burgreen‡, Varun Reddy† , Steven W. Day§, Matthew Giarra§, Keefe B. Manning†, Steven Deutsch†, Matthew R. Myers*, Michael R. Berman*, Richard A. Malinauskas*
*Food & Drug Administration
†Pennsylvania State University
‡Mississippi State University
§Rochester Institute of Technology

SUMMARY

A computational interlaboratory study was recently performed in a generic medical device consisting of a nozzle with a sudden contraction and a conical diffuser. Results from 28 computational fluid dynamics (CFD) simulations from around the world were compared to 2D planar particle image velocimetry (PIV) measurements performed at 3 laboratories. Flow rates covered the laminar, transitional, and turbulent regimes. The CFD results showed large velocity variations in comparison to experiment, much of which could be attributed to the turbulence models used. Simulations routinely underestimated the velocity in the sudden contraction. At the highest Reynolds number, four of the sixteen 3D simulations predicted some degree of the Coanda effect, where the jet issuing from the diffuser was deflected to one side by the adverse pressure gradient. However, no significant Coanda effect was observed in the 2D PIV experiments. This demonstrates the necessity of careful experimental validation in similar flow regimes.

Key Words: *CFD validation, standards, medical device regulation, best practices, blood flow.*

1. INTRODUCTION

CFD is a powerful tool used to develop complex medical devices, but its usefulness in assessing safety in a way that can help the regulatory process is still unknown. In the cardiovascular area, the main fluid component of interest is blood, which is extraordinarily difficult to model. The 50% cellular content can still only be fully modeled at extremely small scales, while the full chemistry of coagulation is too complex to be modeled without simplifications. One technique used is to consider hemolysis in a continuum fluid by assessing the effects of shear stress and exposure time. Most such models depend on empirical shear stress/exposure time data gathered over decades. However, if the physics isn't modeled correctly, then the computed biological effects cannot be trusted. Therefore, this interlaboratory study had two main goals: 1) to take a snapshot of the current state of the art in medical device fluid dynamics computations, and 2) to compare hemolysis levels predicted by the computations. This paper concentrates on goal #1, while goal #2 will be detailed in a future report.

2. METHODS

Participants in the computational interlaboratory study were asked to model flow in the generic tubular medical device containing a sudden contraction and conical diffuser (Figure 1), similar to models used previously (for example, Hinds et al. [1]).

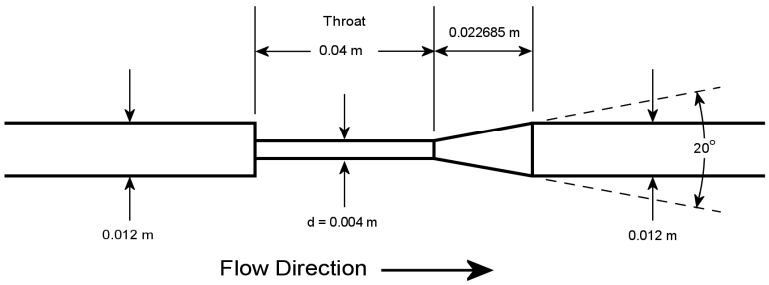

Figure 1. Conical diffuser nozzle used in computational round robin.

This model shares flow characteristics with some common medical devices (e.g., catheters, needles) and medical device problems (e.g., kinks in dialysis tubing). Throat Reynolds numbers (Re_t) were specified at 500, 2000, 3500, 5000, and 6500 under steady flow. A Newtonian viscosity of 0.0035 N-s/m^2 and density = 1056 kg/m^3 were specified. All other parameters (inlet/outlet lengths, mesh density, cell type, axisymmetric vs. 3D mesh, inlet boundary conditions, etc.) were left to the discretion of the individual participants. CFD was validated using 2D planar PIV performed at 3 labs (2 experiments at one lab, 1 each at the other two labs).

3. RESULTS

The CFD results showed a great deal of variation. At Re_t = 500, many of the participants used turbulence models, while the experiments demonstrated that the flow was laminar as would be expected from Re_t. However, even some of the laminar simulations did not accurately model the axial velocity along the nozzle centerline (Figure 2a). Problems in laminar models included failure to conserve the mass flow rate, and the use of outlet lengths that were not long enough for the flow to develop properly for the outlet boundary conditions used.

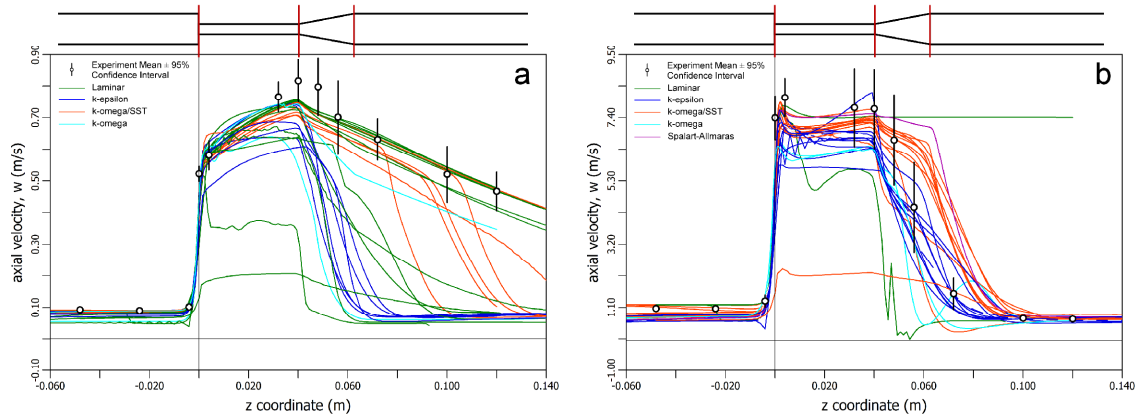

Figure 2. Axial velocity along nozzle centerline: a) Re_t = 500; b) Re_t = 6500.

Turbulence models more consistently matched the centerline velocity at Re_t = 6500 (Figure 2b). The various k-omega/shear stress transport (SST) models matched the throat centerline velocity

better than did the k-epsilon (KE) models, while the reverse was true within the diffuser. Selected velocity profiles at Re_t = 500 are shown in Figure 3. Experimental velocity profiles compared favorably with most of the laminar models, and some of the turbulent models, except at the sudden contraction where the CFD underestimated the measured velocities (Figure 3b). As in Figure 2a, the turbulent models and some of the laminar simulations did not agree with the experimental data downstream of the diffuser.

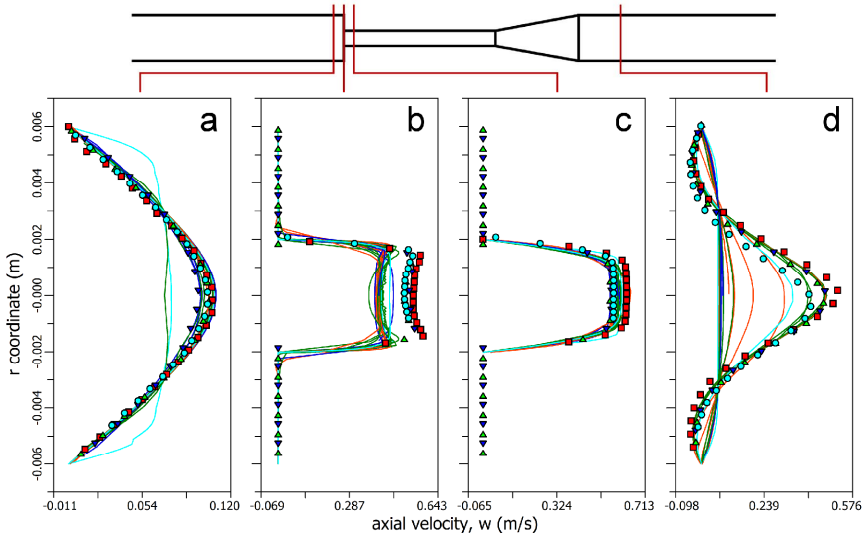

Figure 3. Axial velocity profiles at selected radial cuts for Re_t = 500. Symbols are experiments; lines are simulations color-coded by turbulence model as in Figure 2.

At Re_t = 6500 (Figure 4), the turbulent models again underestimated velocities at the sudden contraction. However, experimental data from one of the labs suffered from wall distortion in the acrylic model. In addition, several of the 3D simulations showed degrees of skewness downstream of the diffuser not seen in the experiments.

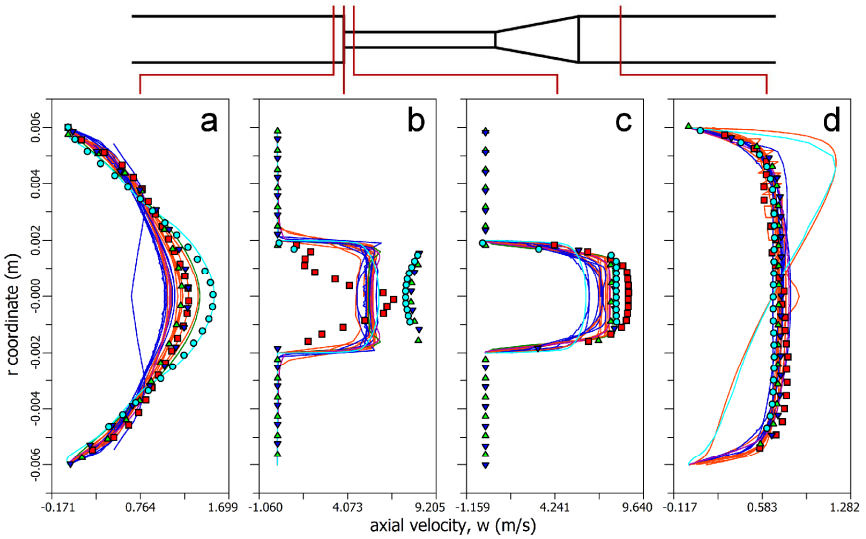

Figure 4. Axial velocity profiles at selected radial cuts for Re_t = 6500. Symbols are experiments; lines are simulations color-coded by turbulence model as in Figure 2.

Figure 5 shows the axial velocity contours from three 3D simulations at Re_t = 6500, provided by the participants. These contours are taken along a plane at the radial cut indicated in Figure 4d. Figure 5a is from a transient SST simulation with a hex mesh (red skewed line in Figure 4d). Figure 5b is from a steady SST simulation with a tetrahedral mesh. Figure 5c is from a steady k-epsilon simulation using a hex mesh. Not only are the velocity contours visibly skewed in the first two of the three simulations, but the two skewed contours have different maximum velocities. In contrast, the experimental data showed mostly symmetric profiles, with the caveat that they are averages of many image pairs. The existence of subtly skewed experimental data in Figures 3d (blue circles) and 4d (red squares) may have been caused by measurement errors; no Coanda effect to the extent seen in the simulations shown in Figures 4d and 5a was observed experimentally (but note that these were 2D PIV measurements in one plane).

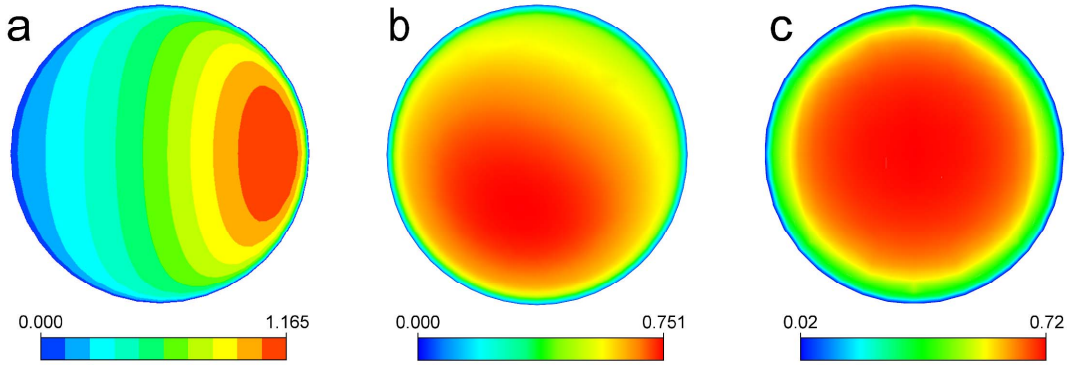

Figure 5. Axial velocity profiles at z = 0.012 m downstream of sudden contraction (as in Figure 4d) for three 3D simulations at Re_t = 6500. Blue = minimum velocity, red = maximum velocity.

4. CONCLUSIONS

The results of the computational interlaboratory study showed unexpected variations when compared to experiment, in part due to turbulence models being used at low Reynolds numbers. Turbulent simulations performed better at the higher flow rates; however, variations among the families of turbulence models at the higher Reynolds number were also observed, as shown in a previous study [3]. Other computational issues included modelers using outlet tubes that were too short, and not conserving the mass flow rate. Some of the simulations also showed extremely skewed jets issuing from the diffuser due to the adverse pressure gradient; however, this degree of skewness was not observed in the experiments. Thus validation of CFD by experiment of even simple models is necessary but must be performed with care.

REFERENCES

[1] M.T. Hinds, Y.J. Park, S.A. Jones, D.P. Giddens, and B.R. Alevriadou, Local hemodynamics affect monocytic cell adhesion to a three-dimensional flow model coated with E-selectin, *J Biomech,* 34, 95-103, 2001.

[2] K. Chao, V.A. Moises, R. Shandas, T. Elkadi, D.J. Sahn, and R. Weintraub, Influence of the Coanda effect on color Doppler jet area and color encoding. In vitro studies using color Doppler flow mapping. *Circulation,* 85, 333-41, 1992.

[3] E.J. Braga and M.J.S. de Lemos, Numerical simulation of turbulent flow in small-angle diffusers and contractions using a new wall treatment and a linear high Reynolds k-ε model, *Numerical Heat Transfer, Part A*, 2004, 45, 911–933.

2nd International Conference on Mathematical and Computational Biomedical Engineering - CMBE2011
March 30 - April 1, 2011, Washington D.C, USA
P. Nithiarasu and R. Löhner (Eds.)

VESSEL WALL MODELING FOR 1D HAEMODYNAMICS

Sergey S. Simakov[⋆], Yuri V. Vassilevski[⋆⋆], Victoria Yu. Salamatova[⋆⋆⋆]
Yuri A. Ivanov[†], Tatyana K. Dobroserdova[†]
[⋆]Moscow Institute of Physics and Technology, 141700, Institutski Lane 9, Dolgoprudny, Russia,
simakov@crec.mipt.ru
[⋆⋆]RAS Institute of Numerical Mathematics, 119333, Gubkina St. 8, Moscow, Russia,
vasilevs@dodo.inm.ras.ru
[⋆⋆⋆]RAS Institute for Nuclear Safety, 115191, B.Tulskaya St. 52, Moscow, Russia
[†]Moscow State University, 119991, Leninskie Gory, Moscow, Russia

SUMMARY

We present an approach of combining 1D model of global haemodynamics with vessel wall elasticity model representing the wall by a set of elastic fibers. Two applications are discussed: cava-filter implantation and atherosclerotic vascular network analysis.

Key Words: *mathematical modeling, blood flow, atherosclerosis, endovascular implants, vessel wall state equation.*

1 INTRODUCTION

We present an approach of combining 1D model of global haemodynamics [6] with vessel wall elasticity model representing the wall by a set of elastic fibers [2,3]. The approach is the two-stage procedure. At the first stage we develop a numerical vessel model which provides pressure to cross section area relationship (a wall state equation); at the second stage we employ the global haemodynamic model which uses the recovered relationship in each vessel. The approach allows us to simulate dynamics of cardiovascular system under surgical interventions or vascular diseases affecting the elastic properties of vessels. Using this approach we get around the problem of accounting for fluid-structure interaction [1,4].

We discuss two applications, cava-filter implantation [5] and atherosclerotic vascular network analysis [7]. Most biological soft tissues demonstrate nonlinear strain-stress relationships, in particular, at high stresses. The elastic fiber model can recover elastic responses to a deformation for Hookean and neo-Hookean materials as well as for collagen which reacts when the vessel is considerably deformed. Using the fiber model we developed numerical elastic models of cava vein with or without implanted cava-filter and atherosclerotic carotid arteries.

2 METHODS

The wall of cava vein is modeled as a set of elastic fibers composed of Hookean materials. All fibers can be divided into three types: elastin, smooth muscle and collagen. Collagen fibers are distributed in the wall in unstrained state and begin to respond to the deformation when the wall is

considerably deformed. The composition of elastic responses of fibers forms the spatial distribution of wall response to the deformation. This response can be interpreted as the counterbalance to the transmural pressure and the impact of the implant.

The wall of an atherosclerotic vessel is modeled as a three-layer cylindrical shell inflated by internal pressure. The axial strain is assumed to be negligible. The internal and external layers are thin-walled shells which represent the fibrous cap of the plaque and the vessel wall, respectively. The middle layer represents the lipid pool of the atherosclerotic plaque. The arterial wall and the atherosclerotic plaque are assumed to be isotropic and incompressible. We imitate their response to a deformation as the response of independent ring fibers to the same deformation (see fig. 1). The lipid pool elasticity model is based on its representation by a set of radial springs with the non-constant elasticity modulus. Spring stiffness is estimated through the solution of the deformation problem for the isotropic thick-walled cylinder under internal and external pressures. For both material models (Hookean and Neo-Hookean) we verified the model comparing with analytic solution for the simplest plaque shape (see fig. 1-A). The relative error in linear and non-linear cases does not exceed 2% for displacements in the whole range of feasible pressure values.

We studied three types of plaque shapes that are shown in Fig. 1. All three types are formed by the same outer and different inner surfaces. The inner surface corresponds to the fibrous plaque cover. The surfaces are represented by sets of fibers which are connected with springs. The first type (Fig. 1A) represents the connected coaxial cylindrical shells that corresponds to the lengthy plaques which are uniformly distributed over the vessel wall. The second type (Fig. 1B) is formed by the interior axial symmetric surface narrowing at the center of the vessel. The third type (Fig. 1C) is similar to the second one but is not axially symmetric.

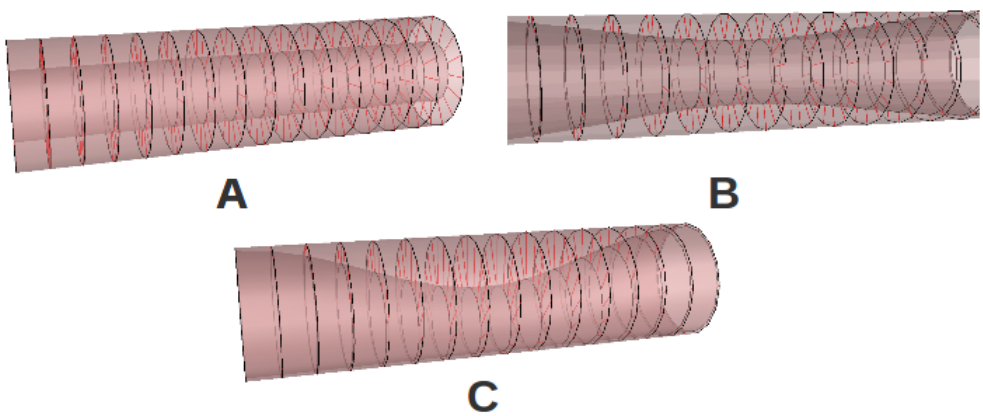

Figure 1: Plaque shapes, type 1 (A), type 2 (B) and type 3 (C).

3 RESULTS

We apply the Hookean (linear) and Neo-Hookean (nonlinear) material models for both healthy and atherosclerotic arteries. We compare both material models in terms of the computed wall state equation, in order to examine the difference between the two material models. Fig. 2 demonstrates the dependencies $p(S/S_0)$ for the cases of healthy vessel (left panel) and atherosclerotic vessel with a lengthy plaque (right panel) of lumen 10 % (see fig. 1-A). Parameters for the static equilibrium problem are set according to the properties of the common carotid artery.

For the healthy artery, we observe substantial deviation of the Hookean and Neo-Hookean curves $p(S/S_0)$ for pressures higher than 8 kPa. Since such high pressure is achieved no longer than 0.1 seconds within the cardiac cycle, the impact of the discrepancy in the wall state equations is almost negligible. For the atherosclerotic artery, the discrepancy in the wall state equations is more distinct. The substantial difference in pressures is observed at transmural pressures over 4 kPa as well as for negative transmural pressures. This results in higher sensitivity to inflating transmural pressure and higher resistance to deflating transmural pressure. We employed the computed wall state equations for atherosclerotic arteries in the 1D global blood flow model and studied the impact of atherosclerotic disease in different atherosclerotic networks.

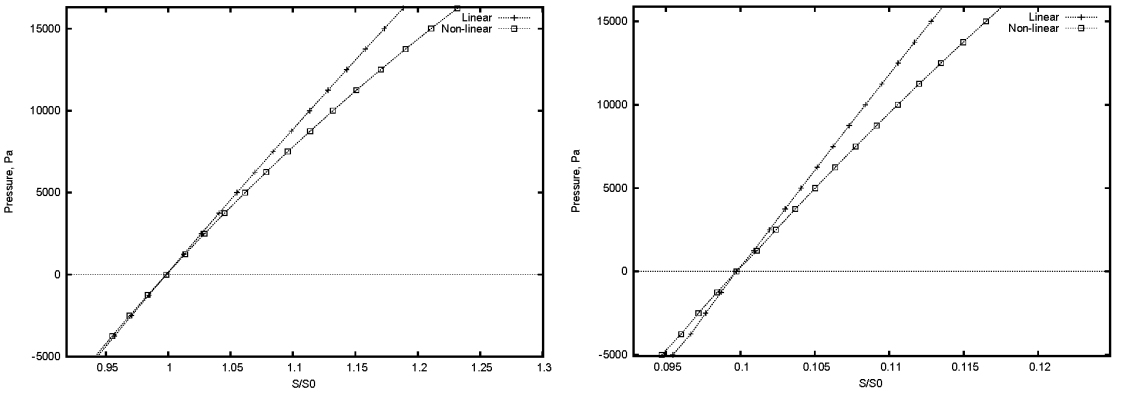

Figure 2: Comparison of common carotid wall state equations for Hookean and Neo-Hookean materials: healthy artery (left) and atherosclerotic artery (right).

We also developed the wall state equation for the cava vein on the basis of the elastic fiber model. The model is capable to reproduce circular, elliptic, and dumb-bell vascular cross sections under positive, zero, and negative transmural pressures, respectively (see fig. 3). The fiber model can be combined with the elastic model of a cava-filter. The latter is implanted into the vein in order to catch migrating thrombii. The combined elastic model produces pressure to cross section relationship for the system "vein-filter". The relationship allows us to study the impact of filter implantation to global haemodynamics.

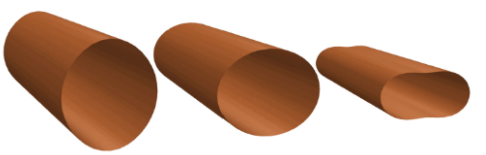

Figure 3: Venous cross section under positive, zero, and negative pressure loads.

4 CONCLUSIONS

The elastic properties of cava vein with or without implanted filter may be recovered via the elastic fiber model. The model is capable to reproduce the vein wall state equation in the whole range of transmural pressures. The elastic properties of atherosclerotic arteries may be approximated by the

fiber-spring three-layer models with Hookean or Neo-Hookean materials. Both models have been validated through the analytic solution of the elastic problem for the particularly shaped plaques. The numerical models of the elastic vessel wall are used for the recovery of the pressure to cross section relationship which is the input function for the global 1D haemodynamics model. The latter allows us to study the impact of regional atherosclerotic diseases and the implantation of endovascular filters to global haemodynamics.

5 ACKNOWLEDGEMENTS

This work was partially supported by the Federal Program "Academic and pedagogical staff of innovative Russia", RAS program "Basic Research for Medicine", RFBR grants 08-01-00159, 09-01-00115, 10-01-91055.

REFERENCES

[1] H.Y. Chen, L. Zhu, Y. Huo, Y. Liu and G.S. Kassab. Fluid–structure interaction (FSI) modeling in the cardiovascular system, *Computational Cardiovascular Mechanics: Modeling and Applications in Heart Failure*, chapter 9, 141-157, Springer, 2010.

[2] M.C. Lai and C.S. Peskin. An immersed boundary method with formal second order accuracy and reduced numerical viscosity, *Journal of Computational Physics* , 160, 705-719, 2000.

[3] M. Rosar, C. Peskin. Fluid flow in collapsible elastic tubes: a three-dimensional numerical model, *New York Journal of Mathematics.* 7, 281-302, 2001.

[4] L. Formaggia, A. Quarteroni and A. Veneziani. *Cardiovascular mathematics,* Heidelberg, DE: Springer, 2009.

[5] Y.V. Vassilevski, S.S. Simakov and S.A. Kapranov. A multi-model approach to intravenous filter optimization. *International Journal of Numerical Methods for Biomedical Engineering*, 26(7) 915-925, 2010.

[6] S.S. Simakov and A.S. Kholodov. Computational study of oxygen concentration in human blood under low frequency disturbances. *Mathematical Models and Computer Simulations*, 1(2), 283-295, 2009.

[7] Y.V. Vassilevski, S.S. Simakov, V.Yu. Salamatova, Yu.A. Ivanov and T.K. Dobroserdova. Blood flow simulation in atherosclerotic vascular network using fiber-spring representation of diseased wall. *Math.Models Natur.Phenom.*, to appear.

2nd International Conference on Mathematical and Computational Biomedical Engineering - CMBE2011
March 30 - April 1, 2011, Washington D.C, USA
P. Nithiarasu and R. Löhner (Eds.)

A Computational framework for uncertainty quantification and robust optimization of cardiovascular bypass graft surgeries

Sethuraman Sankaran[⋆] **and Alison L. Marsden**[⋆⋆]
[⋆]Postdoctoral Fellow, Department of MAE, UCSD, 9500 Gilman Drive La Jolla CA 92093-0411.
email: sesankar@ucsd.edu
[⋆⋆]Assistant Professor, Department of MAE, UCSD, email: amarsden@ucsd.edu

SUMMARY

We present a computational framework for virtual shape optimization of cardiovascular bypass graft surgeries through computational fluid dynamics (CFD) simulations. We show that performing uncertainty quantification with multiple sources of randomness and performing patient-specific optimization are feasible within our framework. We discuss hemodynamic implications of the optimized surgical geometry.
Key Words: *blood flow, uncertainty quantification, wall shear stress, bypass grafts.*

1 INTRODUCTION

It is well known that the fluid mechanics of bypass grafts impacts biomechanical responses and is linked to intimal thickening and plaque deposition on the vessel wall. In spite of this, quantitative information about the fluid mechanics is not currently incorporated into surgical planning and bypass graft design. In this work, we use a derivative free optimization technique for performing systematic design of bypass grafts. The optimization method is coupled to a three-dimensional pulsatile Navier Stokes solver. We systematically account for inevitable uncertainties that arise in cardiovascular simulations, owing to noise in medical image data, variable physiologic conditions, and surgical implementation. Uncertainties in the simulation input parameters as well as shape design variables are accounted for using the adaptive stochastic collocation technique. A derivative-free optimization framework is coupled with a stochastic response surface technique to make the problem computationally tractable. Two numerical examples are discussed - an idealized bypass graft around a stenosis and shape optimization of a patient-specific coronary artery bypass graft. We demonstrate that accounting for uncertainty could significantly change the optimal graft design compared to the deterministic case. Results show that small changes in the design variables from their optimal values should be accounted for in surgical planning.

2 MAIN BODY

2.1 Uncertainty Quantification

Simulations of blood flow in both healthy and diseased vascular models can be used to compute a range of hemodynamic parameters including velocities, time varying wall shear stress, pressure drops, and energy losses. Our confidence in the data output from cardiovascular simulations depends directly on our level of certainty in simulation input parameters. We present a stochastic

collocation framework [1] to compute the sensitivity of output parameters to input uncertainties in cardiovascular simulations. Uncertainties can arise from boundary conditions, geometrical parameters, or clinical data. These uncertainties result in a range of possible outputs which are quantified using probability density functions (PDFs). The objective is to systemically model the input uncertainties and quantify the confidence in the output of hemodynamic simulations.

2.2 Stochastic Optimization

There is tremendous scope to improve the outcome of cardiovascular surgeries (especially bypass grafts) by manipulating geometrical parameters. Some examples are the angle of attachment of graft to the parent arteries, location and size of anastomosis, size of graft, etc. In [2], a derivative free optimization method (SMF) is presented for performing optimization in cardiovascular systems. We have recently extended the SMF method to handle uncertainties for the purpose of performing robust design [3]. In surgical design, it is infeasible for surgeons to implement a design solution, say anastomosis angle, exactly. By enforcing robustness, we account for the fact that the implemented design solution can vary from the prescribed design.

θ_1	θ_2	$\mathcal{J}$	$\mathcal{J}_{\texttt{stoch}}$	OSI (mean/max)	WSSG (mean/max)
75^o	75^o	10.08	19.02	0.212/0.487	1.327/147.04
45^o	75^o	11.96	19.81	0.214/0.497	2.042/247.74
75^o	45^o	12.17	18.13	0.215/0.490	0.90/169.85

Table 1: The table summarizes results for the deterministic and stochastic optimization cases for problem 2. Det. stands for deterministic, opt. stands for optimal point and stoch. stands for stochastic. The stenosis radius, r_s, for the deterministic case was $0.425\texttt{cm}$ and $v = \bar{v}$. For the stochastic case, the velocity was chosen to be normally distributed, $v \sim \mathcal{N}(\bar{v}, (0.2\bar{v})^2)$ and radius was chosen to be uniformly distributed $r_s \sim \mathcal{U}(0.35, 0.5)$. All dimensions are in c.g.s. units.

The cost function for stochastic optimization is generally defined as:

$$\mathcal{J} = \sum_{i=1}^{N_c} \left(\alpha_i \mathbf{E}(C_i) + \sum_{j=1}^{N_m} \beta_{ij} \mathbf{M}^j(C_i) \right) \tag{1}$$

where $\mathcal{J}$ represents the robust objective function, C_i are quantities derived from hemodynamics that are to be minimized, α_i and β_{ij} represent weights that are attached to the different cost functions depending on their units and relative order of magnitudes, $\mathbf{E}(.)$ denotes the expectation operator and $\mathbf{M}^j(.)$ represents the j^{th} statistical moment. N_c and N_m represent the number of cost functions and number of statistical moments that are employed, respectively. The second moment can be used to capture standard deviation, and so on. The standard deviation is key to enforcing that the objective function is robust to fluctuations in the design variables.

The choice of cost function is problem specific and is a very important component of the problem definition. In bypass grafts, intimal thickening is usually observed near the heel and toe of the anastomosis attachment, the artery floor, and the suture line locations. Flow separation occurring just above the arterial floor contributes to increasing blood flow stagnation and residence times, leading to increased plaque deposition. In general, the cost function C could include WSS, WSSG, OSI, energy losses and other clinically relevant hemodynamic quantities.

A customized version of the Simvascular software package is used for cardiovascular geometry modeling as well as solving the Navier-Stokes equations. Machine language (tcl) scripts are interfaced with the software to generate models from their analytic description. These scripts generate

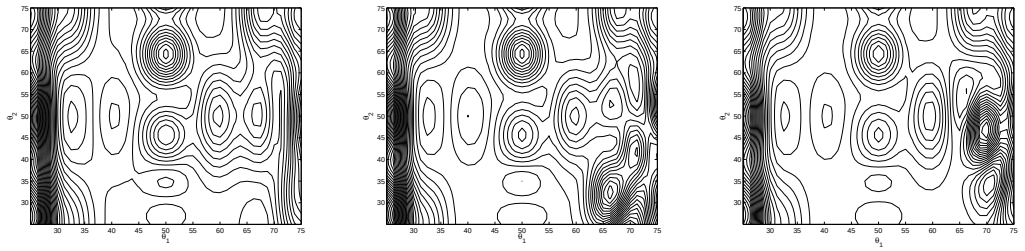

Figure 1: Contours of the mean cost function plotted over parameter space constructed using (left) the response surface with a coarse adaptive Smolyak sparse grid (middle) at an intermediate iteration in the optimization algorithm using Kriging interpolation and (right) termination of the optimization algorithm using Kriging interpolation.

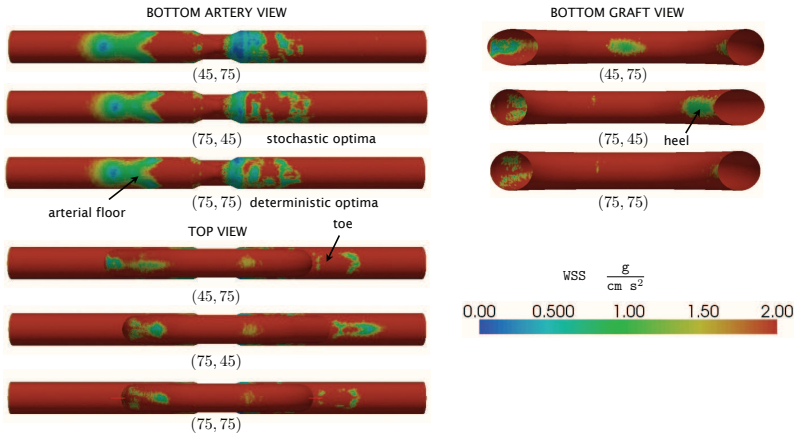

Figure 2: Three configurations for the deterministic case - the suboptimal configuration 45-75, suboptimal configuration 75-45 and deterministic configuration 75-75. The subscripts refer to three different projections so that important intimal thickening regions - bottom view of artery, top view and bottom view of the graft are shown.

two dimensional (2D) surfaces which are lofted and blended together to produce the problem geometry. A commercial software `MESHSIM` (Symmetrix Inc., Troy, N.Y.) is used to create a 3D tetrahedral mesh for these geometries. The optimization algorithm is implemented as a wrapper script over the Finite element framework to compute the cost function at specific parameters.

While there are potentially many cost functions, the objective we have chosen for this work is to minimize regions of low wall shear stress. In the first example, we present the design of anastomosis angles on a bypass graft constructed over a stenosis[4]. Table 1 shows a summary of the cost functions and the difference between deterministic simulations and stochastic simulations where standard deviations in the implementation anastomosis angles are accounted for. OSI and WSSG stand for oscillatory shear index and wall shear stress gradient. The table also shows that the optimal geometry is dependent on the choice of cost functions. The evolution of cost function through the optimization iterations is shown in Fig. 1. As the algorithm proceeds, the polling is restricted to a smaller subspace of the original space. Comparison of WSS for the three representative configurations are shown in Fig. 2. The deterministic optimum, $(75^o, 75^o)$, has almost zero low WSS area near the heel region and has the least cost function contribution at the arterial and heel regions amongst all configurations. Apart from the typically observed areas of low WSS in

the toe, heel and arterial floor regions, the section just downstream of the stenosis also contributes to the cost function in this problem. The top of the artery (the side where graft is anastomosed) has, in general, higher WSS than the toe, heel and arterial floor regions. In the second example, we parameterize and perform optimization on a patient specific geometry. Fig. 3 shows the construction of a patient specific CABG geometry and simulation results for a specific geometry. CABG models are first constructed based on a post-operative image from a patient. Saphenous vein grafts are parameterized using splines and pre-determined control points are manipulated to achieve desired anastomosis angles. A mathematical relation between the control parameter space and the motion of the control points is derived. This input is fed into our finite element framework to evaluate the cost function for each parametric input.

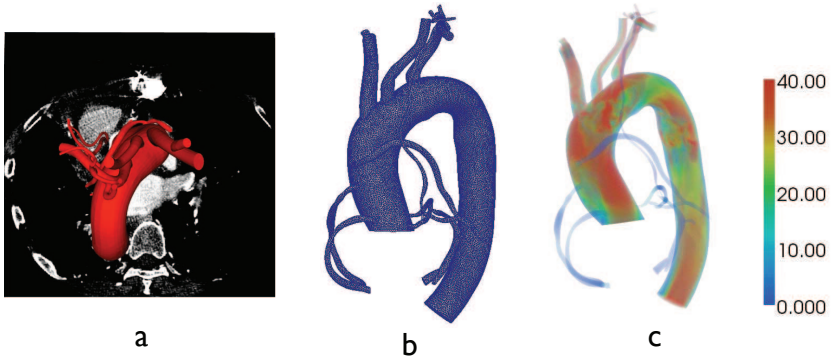

Figure 3: The figure shows (left) construction of a computational model of coronary artery bypass grafting from image data (center) a sample mesh and (right) the blood velocities at systole for a specific geometry.

3 CONCLUSIONS

We presented a framework for performing virtual optimization on patient-specific cardiovascular geometries. Uncertainties in the inputs as well as implementation are accounted for and a feasible non-intrusive algorithm is discussed. We show that uncertainties have to be accounted for and could change the optimal geometry. We also show the importance of cost function in virtual optimization of cardiovascular bypass graft surgeries.

REFERENCES

[1] S. Sankaran and A.L. Marsden, A stochastic collocation method for uncertainty quantification in cardiovascular simulations, *Journal of Biomechanical Engineering, in press.*

[2] A. L. Marsden, J. A. Feinstein, and C. A. Taylor., A computational framework for derivative-free optimization of cardiovascular geometries, *Computer Methods in Applied Mechanics and Engineering*, 197(21-24):1890–1905, 2008.

[3] S. Sankaran, C. Audet and A.L. Marsden, A method for stochastic constrained optimization using derivative-free surrogate pattern search and collocation, *Journal of Computational Physics*, 20(12), 4664-4682, 2010.

[4] S. Sankaran and A.L. Marsden, The impact of uncertainty on shape optimization of idealized bypass graft models in unsteady flow, *Physics of Fluids, under review.*

2nd International Conference on Mathematical and Computational Biomedical Engineering – CMBE2011
March 30 – April 1, 2011, Washington D.C., USA
P. Nithiarasu and R. Löhner (eds)

APPLICATION OF GENETIC ALGORITHM AND FINITE ELEMENT METHOD IN DESIGN OF THE SCAFFOLDS FOR TISSUE ENGINEERING

Marcin K. Heljak*, Wojciech Swieszkowski* Krzysztof J. Kurzydlowski*
*Faculty of Materials Science and Engineering, Warsaw University of Technology,
Poland, Woloska 141 02-507 Warsaw, m.heljak@inmat.pw.edu.pl

SUMMARY

The favourable scaffold for bone tissue engineering should have desired characteristic features, such as adequate mechanical strength and 3D open porosity, which guarantee suitable environment for tissue regeneration. In fact, optimization of such complex structures like bone scaffolds is a challenge for investigators. In the paper we attempt to use numerical modeling to evaluate material properties for the optimization of such a bone tissue engineering scaffold fabricated via the Fused Deposition Modeling technique. The optimization aims to achieve the best possible mechanical strength – degradation rate ratio [1]. We use a standard genetic algorithm for our optimization studies. This is an efficient method of discrete optimization, especially when a great number of degrees of freedom are taken into account. For the FDM scaffold [2], the number of degrees of freedom is equal to number of individual struts which structurally form the scaffold. Each individual strut is scrutinized for its role in the architecture and structural support it provides for the scaffold. Its contribution to the overall scaffold was studies based on five possible materials that the struts could be fabricated from. The optimized object was bi-modal scaffold for osteochondral defect repair [3]. The numerical models of the scaffolds were generated using ANSYS. The objective of the optimization is to find the scaffold with required properties for tissue engineering. The first step to solve this problem is to find what is the most desirable characteristic of such a scaffold. In fact, each scaffold could be described by many different characteristics, but in this study we are focused on desirable curve of scaffold degradation, which is the modulus change during the scaffold degradation process.

Key Words: *FEM, Genetic Algorithm, Scaffold, FDM.*

1. INTRODUCTION

The objective of the study was to propose a numerical tool which could help in developing scaffolds for tissue engineering. The first step to solve this problem is to find what is the most desirable characteristic of such a scaffold. In fact, each scaffold could be described by many different characteristics, but in this article we are focused on desirable curve of scaffold degradation, which is the modulus change during the scaffold degradation process.
The desirable curves of degradation were chosen arbitrarily to represent great number of ways in which scaffold mechanical function loss could proceed. The degradation time was split into three phases: early phase, middle phase and late phase of degradation. The curves from Figure 1 refer to bi-modal scaffold. The upper part should preserve mechanical function of softer type of tissue, whereas the lower part should preserve mechanical function of harder one.

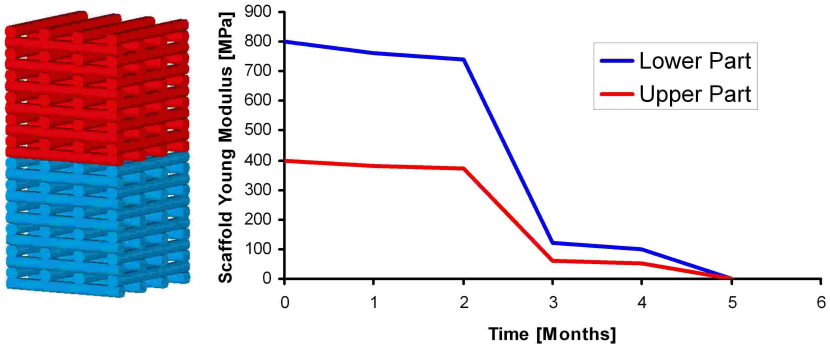

Figure 1. Desirable curves of degradation of the bi-modal scaffold

For this optimization study, we have selected five different polymeric materials (Table 1) [4] which could be used for scaffold fabrication. As a method of optimization of material selection was used genetic algorithm (GA). Finite element method (ANSYS) was used for evaluation (calculations of scaffold Young's modulus).

Table 1. Mechanical and degradation properties of used materials [4]

	Young Modulus [GPa]	Degradation Time [Months]
PGA – poly-glycolide acid	7.0	6 to 12
LPLA L – poly-lactide acid	2.7	>24
DLPLA DL – poly-lactide acid	1.9	12 to 16
PCL poly-caprolactone	0.4	>24
DLPLG poly(D,L-lactide-co-glycolide)	2.0	5 to 6

2. MAIN BODY

In case of the designed scaffolds the number of possible combinations of assigning k materials for n struts is expressed by below formula:

$$c = k^n ,$$

what means that systematically enumerating all possible candidates for the solution and checking which candidate satisfies the problem's statement (brute-force algorithm) is a problem solvable by exponential-time algorithms, which require computation time that grows as an exponential function of problem size. It is also hard to apply for this problem any analytical method of curve fitting because of the fact that evaluation of the fitness function of the problem requires finite element structural analysis. The possible alternatives are heuristic methods, often called methods of artificial intelligence, which are efficient tool for solving complex searching and optimization problems, especially when local extrema are expected. The heuristic search technique used in this work is the Genetic Algorithm (GA).

Genetic algorithms are algorithms searching the space of solutions base on the analogy to the biological evolution of species. Like in biology, the term of an individual is used, and it represents a single alternative solution. Genetic algorithms operate on populations of individuals.

An individual consists of chromosomes. Usually it is assumed that an individual has one chromosome, as in case of curve fitting problem presented in this paper. Chromosomes consist of genes which are equivalents of degrees-of-freedom of the model. In this study the number of degrees-of-freedom corresponds to number of scaffold struts, whereas the value of each gene corresponds to material type. The number of scaffold struts is 96. Each strut could be assigned as one of five polymeric materials, then values of genes are contained by the following set:

$$V = \{0, 1, 2, 3, 4\};$$

The values of genes have not any physical meaning. The only aim of these values is to define the given type of material. The adaptation (fulfilment of requirements) of given individual, which corresponds to particular strut blend is computed using fitness function. All the genes of an individual determine the fitness function value. Figure 2 shows flowchart representing the current schematic of the standard genetic algorithm coupled with structural analysis (finite element method) adopted in this study. The expected result of structural analysis is displacement of scaffold top, based on which we could calculate the scaffold stiffness.

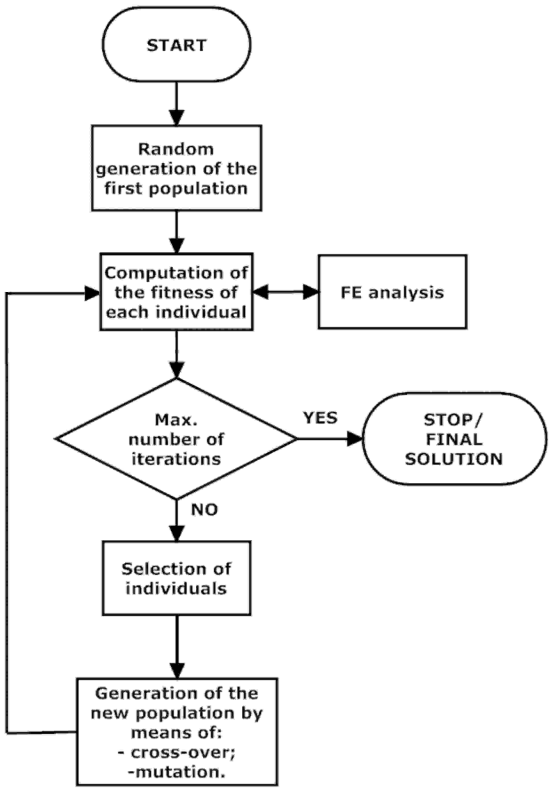

Figure 2. Flow-chart of a standard genetic algorithm coupled with FEM module

The best fitted curves of degradation of the designed scaffold and the resulted material assignement are shown in Figure 3. The figure shows, that PCL (the softest material among all used materials) fraction is especially high in the upper part of designed scaffold what is in the great accordance with expectations. Such choice of the materials assigning ensured the best

possible fitting to the desirable curves of degradation. This proved that finding optimal solution for this case is very difficult. The obtained results showed that the proposed method of scaffold optimization based on genetic algorithm is promising because of its efficiency (reduction of computational time) and required accuracy in comparison with systematic search algorithms (brute-force algorithms). FEM analysis of scaffold model takes particular time, then verification of all combination of material assigning could be hardly time-consuming if even possible in practice.

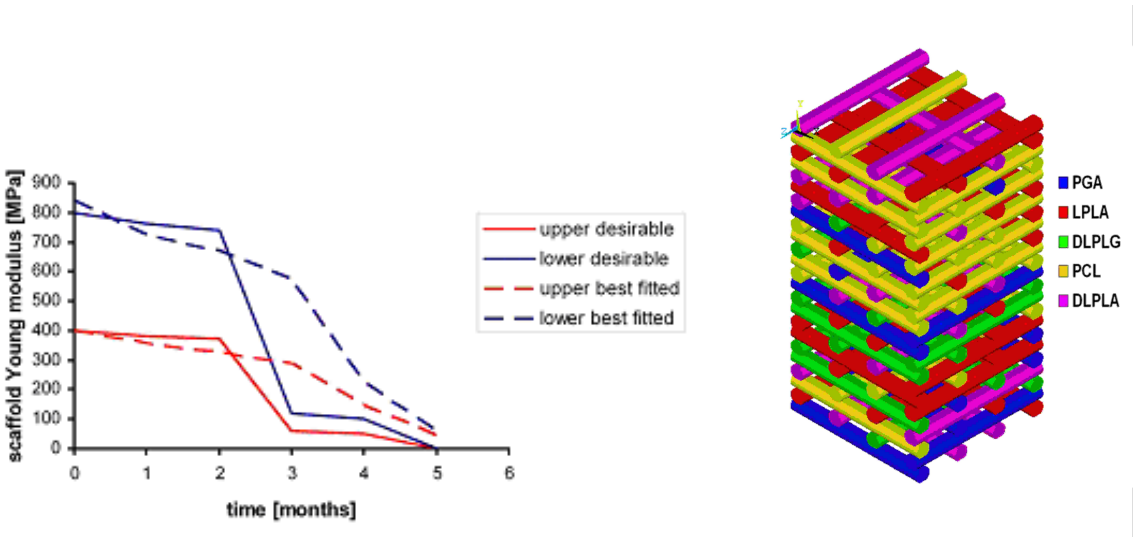

Figure 3. Obtained (the best fitted) curves of degradations of the bi-modal scaffold, which are the result of optimization and strut blend, which is the result of optimization corresponding to bi-modal design of scaffold

3. CONCLUSIONS

Developed method could be easily applied for any type of scaffold geometry (under condition that given scaffold is made of struts, what enables easily designing scaffolds well-matched for bone and cartilage defects). Although, we analyzed scaffold made of polymer materials the presented numerical tool could be used also for selecting biodegradable ceramics or composite materials for the scaffold struts fabrication.

REFERENCES

[1] T. Adachi, Y. Osako, M. Tanaka, M. Hojo, S.J. Hollister, Framework for optimal design of porous scaffold microstructure by computational simulation of bone regeneration, *Biomaterials* 2006;27:3964-3972.

[2] Dietmar W. Hutmacher, Maria Ann Woodruff. Design, In: Paul K. Chu, Xuanyong Liu, editors, Fabrication and Characterization of Scaffolds via Solid Free-Form Fabrication Techniques, *Biomaterials Fabrication and Processing Handbook*. CRC Press; 2008. p 45-67.

[3] Swieszkowski W, Tuan BH, Kurzydlowski KJ, Hutmacher DW., Repair and regeneration of osteochondral defects in the articular joints, *Biomol Eng*. 2007 Nov;24(5):489-95

[4] J. C. Middleton, A.J. Tipton. Synthetic biodegradable polymers as orthopedic devices. *Biomaterials* 2000;21:2335-2346.

2nd International Conference on Mathematical and Computational Biomedical Engineering - CMBE2011
March 30 - April 1, 2011, Washington D.C, USA
P. Nithiarasu and R. Löhner (Eds.)

Modelling Ventricular Function Under LVAD Support

M. McCormick*, David Nordsletten, Dave Kay* and Nic Smith****
*Computing Laboratory, Unversity of Oxford, OX1 3QD, UK
**Department of Biomedical Engineering and Imaging, King's College London, SE1 7EH, UK

SUMMARY

Numerical simulations provide a unique approach for investigating the impact of LVADs on pump function in the heart. Incorporating fictitious domain into a coupled fluid-solid mechanics framework, we have developed a method capable of simulating the full range of LV behaviour under support, including contact between the myocardium and the LVAD cannula. To extend the model to the full cardiac cycle, a simple valve model has been developed to facilitate the coupling of the model to circulatory Windkessel models. Simulations of LV function under support were performed of diastole and bringing the myocardium into suction. These results demonstrate the capabilities of the simulation methods and provide a framework for patient-specific optimisation studies to maximise the potential benefit from LVAD implantation.

Key Words: *Mechanical Heart Modelling, Fluid Mechanics, LVAD, Fictitious Domain.*

1 INTRODUCTION

Left ventricular assist devices (LVADs) are pumps most typically used as a *bridge to transplant* in heart failure patients [1].They reduce the mechanical load on the heart by pumping blood from the left ventricular (LV) apex directly to the aorta, bypassing the aortic valve. Despite the complexities of the device and its significant impact on the mechanical and hemodynamic function of the heart, patient selection for LVAD implantation is based on relatively simple, qualitatively based, clinical metrics [2]. Additionally, once implanted, there is little customisation to the patient nor tuning to the cardiac cycle. Optimising LVAD use, via patient specific tuning, to benefit cardiac function has the potential to provide substantial clinical gains [3]. Coupled fluid-solid simulations provide a novel tool for studying the behaviour of the ventricle under LVAD support and analysing its efficacy as a pump.

To fully capture ventricular function under support, coupled fluid-solid simulations of a supported LV must be able to describe the complete range of ventricular behaviour. This includes the capability to simulate the entire cardiac cycle, from diastole through to systole, and the interaction between the LVAD cannula and the myocardial wall. Such interactions occur either intermittantly, during systole, or, if cannula outflow is high, continuously as the myocardium is sucked onto the cannula [4]. Models must therefore incorporate, not only the interaction between the blood and the myocardial wall, but also the ability to simulate contact between fluid immersed rigid objects and encasing elastic bodies. Furthermore, to provide physiologically meaningful results, simulations of the complete cardiac cycle need to be coupled to models of the systemic and pulmonary circulatory systems [5] to provide feedback for the ventricular inflow and outflow boundary conditions.

Recently, Nordsletten et. al. [6] have developed a finite element fluid-solid mechanics algorithm, coupled using a non-conforming Lagrange multiplier approach, and have applied it in simulations of the diastolic and systolic behaviour of the normal LV [7]. McCormick et. al. [8] have

extended the algorithm, incorporating the fictitious domain (FD) method [9], to enable the simulation of fluid immersed rigid bodies and their interactions with coupled elastic bodies. The extended algorithm was used to simulate the interaction between the LVAD cannula, applied as a FD, and the ventricular endocardial wall. Applying these methods, to simulate an anatomical LVAD supported LV over the full cardiac cycle, will facilitate *in-silico* investigations enabling the identification and optimisation of metrics associated with LVAD function, such as flow rate, position and pulse sequencing. Furthermore, quantification of the work performed by the myocardium under LVAD support could lead to enhanced understanding of the factors underlying reverse remodelling, whereby myocardial function recovers to the point where the device can be explanted [3].

2 METHODS

2.1 Governing Equations

Blood flow is modelled as an incompressible, Newtonian fluid. On moving domains, such as the ventricular chambers, it is convenient to describe such flow using the Arbitrary Lagrange-Eulerian (ALE) form of the Navier-Stokes equations. The ALE framework enables the myocardial deformation to be transferred to the fluid domain by ensuring that the fluid domain is congruous with the myocardial wall, which is modelled as a hyperelastic incompressible solid.

At the fluid-solid interface boundary, conditions are applied to ensure that the fluid and solid domains do not detach or overlap during motion and that stresses are equal but opposite across the boundary. These conditions are met by equating velocities on the interface. The constraint is incorporated through a Lagrange multiplier, λ_c, that equates tractions on the fluid and solid interfaces. Since the fluid and solid problems tend to require different degrees of spatial refinement to adequately resolve their respective governing equations, a third interface domain is used to map the constraint across the boundary. This additional domain enables non-conforming fluid and solid meshes to be coupled.

The LVAD cannula is considered to be a rigid body immersed inside the fluid domain and can be approximated as a FD. The cannula boundary is enforced by prescribing the fluid velocity to be zero on the FD surface. This constraint is applied as an additional Lagrange multiplier, λ_{Fd}, equating fluid and FD tractions on the FD surface.

The action of the two Lagrange multipliers, λ_{Fd} enforcing the fluid velocity to be zero on the immersed rigid body and λ_c enforcing the fluid velocity to be equivalent to the solid velocity on the coupling interface, implicitly resolves the contact problem, with sufficient refinement, of a fluid immersed rigid body with an encasing elastic object. This enables the numerical scheme to simulate the full range of cardiac motion, including contact between the LVAD cannula and the myocardial wall.

2.2 Model Development

A model left ventricle was constructed based on 36 cine MRI sequences taken from a 70kg, healthy, male subject, apex to base [8]. Cubic hexahedral volume meshes were constructed from surfaces fitted to the images at end diastole. An idealised fibre geometry, $\pm 60^\circ$ relative to the sheet normal plane, was defined within the myocardial volume. The fluid domain was constructed using linear tetrahedral elements, formed by creating a surface mesh from the digitised endocardial surface. Cannula geometry was provided by Berlin Heart.[1]

[1] http://www.berlinheart.com

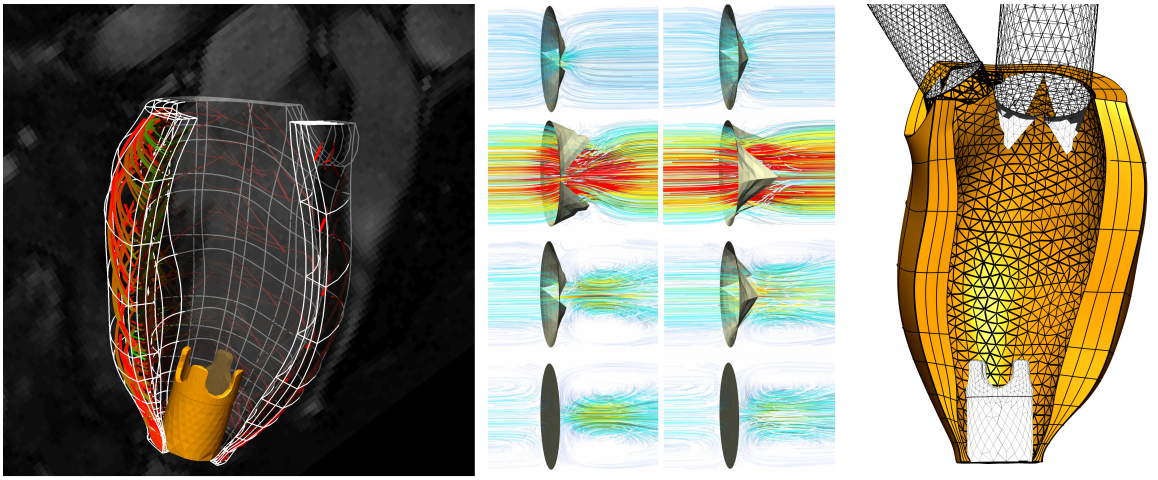

Figure 1: Left, cut away of the fitted solid mesh superimposed on an MRI slice, note the idealised fibres withing the myocardial wall. Centre, bicuspid (left) and tricuspid (right) valve models used on the mitral and aoric valve planes. Top to bottom shows the valves opening and closing as a function of flow velocity across the valve planes as a sinusoidal pressure profile is applied to the left edge. Streamlines are coloured by velocity magnitude, blue to red. Right, Final meshes for the fluid, solid, LVAD cannula and valves. Note the inflow and outflow cannula attached to the mitral and aortic valve planes required to enable pressure boundary conditions to be used.

To couple the model to Windkessel models of the systemic and pulmonary circulatory systems, it is preferable that pressure boundary conditions be applied at the mitral and aortic valves. This requires valve models to be incorporated into the simulation framework. Simple models of the bicuspid mitral and tricuspid aortic valves were developed where the valves were prescribed as FDs within the fluid domain. Valve opening was governed by the direction of λ_{fd} on the valves and the radius of the open valve was defined as a function of the flow volume across the valve plane, see figure 1.

3 RESULTS & DISCUSSION

In this study, simulations were performed of diastolic filling under support and suction of the ventricle onto the LVAD cannula, see figure 2. Outflow velocity via the LVAD cannula was prescribed to be constant at $0.45\text{m} \cdot \text{s}^{-1}$. Inflow across the mitral valve was defined based on ultrasound velocity measurements while the aortic valve was assumed to be closed. The mechanics problem was constrained by fixing both the mitral valve plane and the apex, where the LVAD cannula was attached. The Costa constitutive law [10] was used to define the passive material response of the myocardium.

During diastole, blood flow within the supported LV was observed to be dominated by the formation of large vortices, moving base to apex, which break down on reaching the cannula mouth. Due to continuous outflow via the LVAD cannula, myocardial deformation is minimal, causing the unloading of the ventricle. In contrast, when the ventricle is brought into suction, blood flow was observed to be largely uniaxial in the direction of the cannula mouth. Myocardial deformation was pronounced and contact between the endocardial wall and the cannula occured.

Incorporating the valve model outlined above into the model enables the assumptions of valve behaviour applied in these simulations to be removed. This facilitates more physiologically based simulations to be performed, where the pressure volume response from one cardiac cycle provides feedback for future heart beats. From this, any changes in simulated behaviour, such as flow rate, contractile strength, material stiffness, can be observed across multiple beats enabling their comparative effects to be determined.

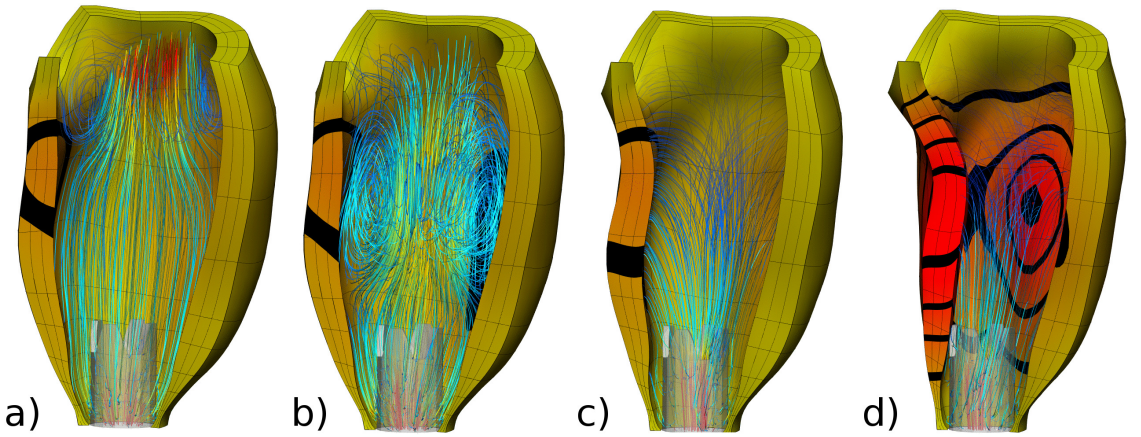

Figure 2: Simulations of LV function under support at various points within the cardiac cycle. a) and b) show diastole simulation results at early and late diastole. c) and d) show results from a simulation drawing the myocardium into suction. Streamline colour gives velocity magnitude, blue to red, while solid colour shows the displacement magnitude, yellow to red. Note the development of vortices within the ventricular chamber during diastole, these break down on reaching the LVAD cannula mouth.

This presents an optimisation problem, whereby pump function, currently set at a constant velocity in axial flow LVADs, could be tuned to the cardiac cycle. Of particular importance is the reduction in thromboembolic events, typically caused by blood pooling in the ventricular cavity caused by recirculations at the apex, and the optimisation of myocardial unloading. The techniques outlined in this paper provide a framework for patient specific simulations, based on clinical images, to address these issues, maximising the potential benefit from LVAD implantation.

ACKNOWLEDGEMENT

This work was supported by the European Commission (FP7-ICT-224485:euHeart), the United Kingdom Engineering and Physical Sciences Research Council (EP/G007527/1, the Woolf Fisher Trust the the IIE/Whitaker Foundation.

References

[1] F. Arabia, R. Smith, and et. al., "Success rates of long-term circulatory assist devices used currently for bridge to heart transplantation.," *ASAIO Journal*, vol. 42, pp. M542–M546, 1996.

[2] M. Williams and M. Oz, "Indications and patient selection for mechanical ventricular assistance.," *Ann. Thorac. Surg.*, vol. 71, pp. S86–S91, 2001.

[3] D. Burkhoff, S. Klotz, and D. Mancini, "LVAD induced reverse remodeling: basic and clinical implications for myocardial recovery.," *J. Caridac Failure*, vol. 12, pp. 227–239, 2006.

[4] K. Reesink, A. Dekker, and et. al., "Suction due to left ventricular assist: implications for device control and management.," *Artificial Organs*, vol. 31, pp. 542–549, 2007.

[5] Y. Shi, T. Korakianitis, and C. Bowles, "Numerical simulation of cardiovascular dynamics with different types of vad assistance.," *J. Biomech*, vol. 40, pp. 2919–29333, 2007.

[6] D. Nordsletten, D. Kay, and N. Smith, "A non–conforming monolithic finite element method for problems of coupled mechanics.," *J. Comp. Phys.*, vol. 20, pp. 7571–7593, 2010.

[7] D. Nordsletten, M. McCormick, P. Kilner, D. Kay, and N. Smith, "Fluid-solid coupling for the investigation of diastolic and systolic human left ventricular function.," *IJNMBE*, In Press.

[8] M. McCormick, D. Nordsletten, D. Kay, and N. Smith, "Modelling left ventricular function under assist device support.," *IJNMBE*, In Review.

[9] R. van Loon, P. Anderson, and F. van de Vosse, "A fluid–structure interaction method with solid–rigid contact for heart valve dynamics," *J. Comp. Phys.*, vol. 217, pp. 806–823, 2006.

[10] K. Costa, J. Holmes, and A. McCulloch, "Modeling cardiac mechanical properties in three dimensions.," *Phil. Trans. R. Soc.*, vol. 359, pp. 1233–1250, 2001.

2nd International Conference on Mathematical and Computational Biomedical Engineering – CMBE2011
March 30 – April 1, 2011, Washington D.C., USA
P. Nithiarasu and R. Löhner (eds)

A SALIENCY MAP-BASED VISUAL ATTENTION NEURAL NETWORK MODEL FOR DYNAMICAL SCENE ANALYSIS

Juan F. Ramirez-Villegas* and David F. Ramirez-Moreno*
*Computational Neuroscience, Department of Physiscs, Universidad Autonoma de Occidente, e-mails: juanfelipe.rv@gmail.com (Juan F.); dramirez@uao.edu.co (David F.)

SUMMARY

This work proposes a model for visual attention for dynamical scene analysis. In our model two main novelties were included: First, the calculation of motion saliency in a neural network with realistic dynamics and time response, and second, for the feature extraction stage, we complemented the color map calculation from Itti and Koch's model [1] by including red-cyan and green-magenta cells into the standard color double-opponent system. The network elicited strong transient responses to moving objects and, as expected, reached stability within a biologically plausible time interval. Modified color maps also elicited better responses than classical (Itti and Koch) ones at high statistical significance levels. There were no considerations to top-down processes or higher brain's neural motion analysis cortexes concerning complex motion patterns, learning or motion understanding.

Key Words: *Visual attention, saliency map, motion saliency, neural network, color double-opponent.*

1. INTRODUCTION

Biological evidence establishes that the primates' brain uses several serial visual processing provided that the visual system is not capable to process all visual inputs using purely parallel processing [1]. Nature deals with this problem by selecting fragments of visual information to be processed preferentially, and by changing the processing focus from a location to another in a serial strategy. There is a large quantity of experimental evidence in favor of two different processes during visual search: The so-called bottom-up and top-down visual processes [2]; while the first one is a fast, saliency-dependent and task-independent process, the second one is a slower, volition-dependent and therefore, task-dependent visual process. Conversely, objects in the visual field must compete for processing within approximately 30 different visual cortical areas [3]. As the ability to screen out objects during visual search tasks is contextual and primates often detect a single target in an array of non-targets, detections –for all the effects– depend largely on the correlation between targets and non-targets.

Up to this moment, many saliency-based models suitable to the analysis of natural scenes have been developed; although the main idea surround the principles underlined by Itti and Koch and therefore have resemblance with neurobiology, they do not consider the visual neural networks dynamics or time neural responses [6]-[9].

The present work develops a saliency-based visual attention model for dynamical scene analysis. Our approach expands the results obtained in [1] and [4] by proposing a motion saliency

computation and keeping the sudden-onset/offset signaling mechanism in a network of neural populations. Our bottom-up model integrates the saliency computation of real and synthetic dynamical scenes, avoiding the problem faced by the dynamical model in [4] when it is applied to moving targets or certain sudden-onset ones; i.e., the transient response of moving (or sudden-onset) non-salient stimuli cannot be forced to rise above the other objects by the network dynamics itself (in absence of motion detectors). The normalization problem is also solved by using synaptic depression [4] and additionally, we have made important complements on color saliency calculation based on certain experimental evidence [5].

2. METHODS

This model computes saliency using the three features studied by Itti and Koch: Intensity, orientation and color. These features are organized into 54 maps (6 for intensity, 24 for orientation and 24 for color).

This procedure covers three main well-studied feature maps: Intensity, orientation and color maps. Intensity contrast is extracted by standard band-pass filtering to calculate center-surround differences between the established resolution levels. Orientation contrast is extracted using standard Gabor pyramids for four orientations (namely 0º, 45º, 90º and 135º). On the other hand, color contrast is calculated on the basis of the evidence presented in [5], who suggests the existence of red-cyan and green-magenta cells.

Motion detection is accomplished by subtracting consecutive neural inputs into the dynamical equations. We encountered the results of this procedure highly similar to standard motion detectors (over the main peak of the transient response of the system). Given the systems' dynamics, population's Gaussian-shaped connections induce smoothing and therefore noise reduction. Moving stimuli become more salient than the others, showing that even if motion occurs far away from the most salient location in the scene, it would attract the attention of the viewer until its priority over non-moving or non-onset stimuli decays about 100 ms after motion [4]. In addition, Rather than implementing each neuron and their synapses, we used Naka-Rushton functions in mean field equations with dynamic synapses in order to describe the neurons' spike rates (they are derived from winner-take-all network approaches detailed in [10]). The most important equations describing the dynamics of the network are given below.

$$\tau_1 \frac{dT}{dt} = -T + \frac{C\left(E_{T_k} - rND + U_{SE}^{L}\left(\sum_j w_{ij}^{L} E_{T_j} \right) x_3 + x_1 T + M_T \right)_+^2}{\sigma^2 + \left(E_{T_k} - rND + U_{SE}^{L}\left(\sum_j w_{ij}^{L} E_{T_j} \right) x_3 + x_1 T + M_T \right)_+^2}, \quad (1)$$

$$\tau_1 \frac{dD}{dt} = -D + \frac{C\left(E_{D_k} - r(N-1)D - rT + U_{SE}^{L}\left(\sum_j w_{ij}^{L} E_{D_j} \right) x_4 + x_2 D + M_D \right)_+^2}{\sigma^2 + \left(E_{D_k} - r(N-1)D - rT + U_{SE}^{L}\left(\sum_j w_{ij}^{L} E_{D_j} \right) x_4 + x_2 D + M_D \right)_+^2}, \quad (2)$$

with: $C = 40.0$; $k = 3.0$; $\sigma = 120.0$; $\tau_1 = 20.0$; $\tau_2 = 10.0$; $U_{SE}^{L} = 1.2$,

where T is the spike rate of any neuron receiving an input about the target (most salient location), D is the spike rate of each of the N distraction neurons, the constant r describes the feedback inhibition strength (neurons' competition); similarly, M_T and M_D, describe the spike rate of any neuron receiving an input about a moving target and/or an input about a moving distractor, respectively; x_1, x_2, x_3 and x_4 are the variables representing the synaptic depression between laterally connected populations and input populations [4]. These synaptic depression variables respectively account for: Targets (Eq. 1) and distractors (Eq. 2). Constants C, τ, σ and U_{SE}^{L} are adjustable parameters of the system, where C is the maximum spike rate of the system, the time constant τ_n controls the frequency at which T and D reach their maximum value (in milliseconds), σ is the system's semi-saturation constant and U_{SE}^{L} defines the synaptic efficiency between intra-layer neural connections. The lateral connection weights w_{ij}^{L} among the neural populations in the saliency map are determined by an elliptical difference-of-Gaussians function. For all the effects, the saliency stimulus $E_T > E_D$.

The results of our approach are depicted in Figure 1 and Figure 2.

Figure 1. (a) Representative movie frames, the objects that move are marked using black circles. (b) (1) Time response representing the saliency map activity over 440 ms; (2) Initial saliency map activity before the motion occurs; (3)-(4) Saliency map's transient responses (overshoots).

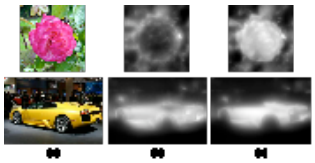

Figure 2. Color map comparison: (a) Input images; (b) classical color maps; (c) modified color maps.

Modified color map results (whose visual difference with respect to classical color maps are depicted in Fig. 2) showed that there are significant statistical differences ($p < 0.02$) with respect to the classical ones (those from the approach detailed in [1]). Moreover, as expected, the

coefficient of variation for classical maps has greater values than the coefficient of variation for modified ones, this basically illustrates that objects' activity is more disperse in classical maps. Moreover, the classic and modified color maps' target saliency levels showed remarkable significant differences ($p < 0.0001$) and for nearly all the cases the proposed modified color maps led to higher target saliency levels than classical ones.

3. CONCLUSIONS

Our model presents two main novelties: First, this work is an attempt to describe how visual system attends motion into a bottom-up strategy with realistic time responses and neural latencies as reported by neurophysiological evidence [4, 10]; this stage implies that there is not understanding, recognition, nor analysis regarding complex motions; and second, color representation was modified by including green-magenta and red-cyan cells regarding color-opponency mechanisms and experimental data obtained in [5]; according to our findings, at this stage, the color model in [1] needed revision, as color feature's codifying often failed to distinguish salient color objects when complex scenes were analyzed. In addition, we also showed the relevance of including motion detectors into the dynamics of the neural network; as the network itself, as proposed in [4], is insufficient to elicit an adequate response for certain moving stimuli. Besides, we showed the importance of keeping the synaptic depression effect on those moving stimuli for overall instantaneous saliency computation. This model can be applied to modeling other visual processing centers such as area MT, MST and 7a [8, 9]. It is expected that transient responses of the network present the same pattern as they were shown by our results. Top-down volitional control is necessary too in order to complete the overall attention scheme with realistic dynamics.

REFERENCES

[1] L. Itti and C. Koch, A saliency-based search mechanism for overt and covert shifts of visual attention, *Vision Research*, 40, 1489–1506, 2000.

[2] A. Treisman, M. Sykes and G. Gelade, Selective attention stimulus integration, In S. Dornie (Ed.), *Attention and performance VI* (pp. 333-361). Lawrence Erlbaum Associates: Hillside, New Jersey, 1977.

[3] R. Desimone and J Duncan, Neural mechanisms of selective visual attention, *Annu. Rev. Neurosci.*, 18, 193-222, 1995.

[4] M. de Brecht and J. Saiki, A neural network implementation of a saliency map model, *Neural Networks*, 19, 1467–1474, 2006.

[5] B. R. Conway, Spatial structure of cone inputs to color cells in alert macaque primary visual cortex (V-1), *The Journal of Neuroscience*, 21, 2768-2783, 2001

[6] D. Gao, V. Mahadevan and N. Vasconcelos, The discriminant center-surround hypothesis for bottom-up saliency, *Proceedings of Neural Information Processing Systems*, Vancouver, Canada, 2007

[7] J. H. Reynolds and D. J. Heeger, The normalization model of attention, *Neuron*, 61, 168-185, 2009.

[8] J. Mira, E. Delgado, M. T. Lopez, A. Fernandez-Caballero, M. A. Fernandez, A conceptual frame with two neural mechanisms to model selective attention processes, *Neurocomputing*, 71, 704–720, 2008.

[9] J. K. Tsotsos, Y. Liu, Y., J. C. Matinez-Trujillo, M. Pomplun, E. Simine and K. Zhou, Attending to visual motion, *Computer Vision and Image Understanding,* 100, 3-40, 2005

[10] H. R. Wilson, *Spikes, Decisions and Actions: The dynamical foundations of neuroscience,* Oxford University Press, 2004.

2nd International Conference on Mathematical and Computational Biomedical Engineering - CMBE2011
March 30 - April 1, 2011, Washington D.C, USA
P. Nithiarasu and R. Löhner (Eds.)

POINT-CLOUD METHOD FOR IMAGE-BASED BIOMECHANICAL ANALYSIS

Jing Qian⋆, Martin Chiang⋆ and Jia Lu⋆⋆
⋆Polymer Division, National Institute of Standards and Technology, Gaithersburg, MD. Email: jing.qian@nist.gov
⋆⋆Department of Mechanical and Industrial Engineering, University of Iowa, Iowa City, IA. Email: jia-lu@uiowa.edu

SUMMARY

This article introduces applications of the Discrete Gradient Method (DGM) in the field of computational biomedical engineering. Unlike the finite element method (FEM), this novel method can directly conduct mechanical analysis on point-cloud representations of organs, which are extracted from medical image. As a more efficient approach in patient-specific modeling, the procedure of carrying out DGM on point-cloud model is demonstrated. Examples shows that this method can reach a satisfied accuracy without introduce continuous approximation of the primary unknown field variables.

Key Words: *point-cloud, medical images, biomechanics analysis.*

1 INTRODUCTION

Pixel or voxel data from the medical images provide a point-cloud depiction for complicated anatomies that are difficult to describe in CAD geometry. Conventionally, a point-cloud model needs to be converted into finite element mesh in order to perform biomechanical or biomedical analysis. Although meshing generation tools have been significantly improved over the last decades, generating high quality meshes in complicated geometries remains a challenge. Recently, a family of solid mechanics solvers named discrete gradient method [1,2] were developed. Using this method, it is possible to conduct mechanical analysis on point-cloud representations of patient-specific organs without resorting to finite element method.

2 METHODOLOGY

The most noteworthy attribute of the discrete gradient method (DGM) is the absence of continuous interpolation (or approximation) of the primary unknown. The gradients of the unknown field are computed directly from nodal values using discrete differentials. Mathematically, the discrete gradient of nodal value at a node I can be given in the form

$$(\nabla^h u)_I = \sum_{J \in \Omega_I} \mathbf{R}^*_{IJ} u_J \ ,$$

where $\mathbf{R}^*_{IJ}$ is the defined vector interpolant, Ω_I represents the supporting nodes of node I. Therefore, this method bypasses the numerical complications associated with the construction of implicit shape functions employed in meshfree methods. To identify neighboring nodes and influence domain of each node, Delaunay triangulation is employed to tessellate the domain because the process is fully automatic and does not require user-specified algorithmic parameters such as the size of influence region.

Reference [1,2] described systematic approaches for constructing linearly consistent gradient formula and the derivation of weak form equations in the discrete setting. Furthermore, numerical tests show that the method not only has comparable accuracy and convergence rate as the displacement finite element method, but also displays robustness for large deformation simulations. As expected, this method resists numerical locking in the incompressibility limit and the thin element limit as well. One the other hand, stabilized scheme is also developed to avoid spurious modes that are common to nodal integration methods [3].

Radiographic images register different physical constituents (soft tissue, bone, fluid etc) by different grayscale values. Therefore, it is straightforward to identify a material constituent, or a specific organ comprised of certain material by extracting material points within certain range of grayscale value. The extracted point-cloud models from medical images provide a discrete representation of the organs upon which the mechanical analysis can be directly carried out using the discrete solvers [4]. The analysis consists of the following steps:

1. Segment images and extract point-cloud modes.
2. Tessellate the point domain into a set of non-overlapping, nodal-centered nodal cells.
3. At each node, approximate the gradient of the primary unknown by a linear combination of nodal values in a set of neighboring nodes.
4. Substitute the gradients into a Galerkin weak from to derive the algebraic equations governing the nodal variables.

3 EXAMPLE

After images segmentation, it is straightforward to represent each pixel by a node and yield point-cloud model of organs at the pixel resolution. However, pixel-resolution model usually contains too many nodes and the model size may be prohibitively large for mechanical analysis. To save the computational cost, the model can be made coarse by lumping several pixels into a node. Figure 1(a) shows a coarse skull extracted model from a stack of 400 CT scans with 9-fold reduction in spatial resolution. An impact pressure is applied over one small region in the forehead to initiate a stress wave. Figure 1(b) shows a snapshot of the stress wave at an instant.

4 CONCLUSIONS

In this article, We describe a point cloud method for the stress analysis in biological systems. The method takes a point-cloud derived from medical images as the geometric input, and utilizes DGM as the mechanical solver. Examples demonstrate the promising application of this solver in the field of patient-specific modeling.

REFERENCES

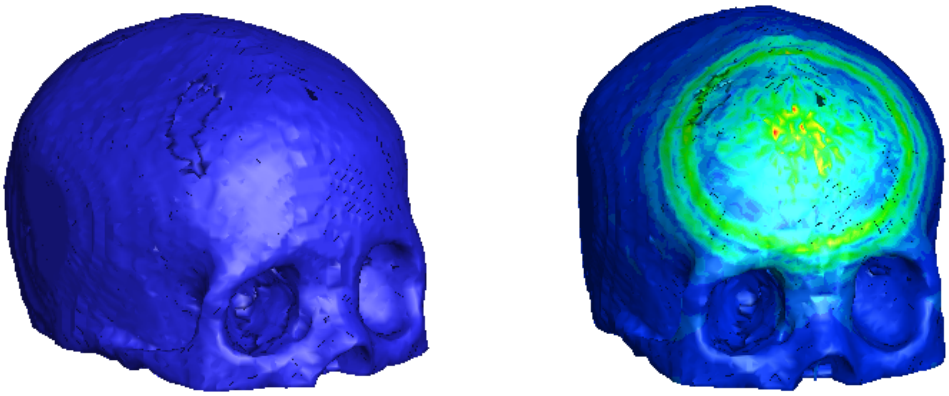

(a) (b)

Figure 1: Three dimensional skull model. (a) Point-cloud skull model extracted from CTs; (b) The propagation of stress wave in skull.

[1] J. Lu and J. Qian and W.M. Han, Discrete gradient method in solids mechanics, *Numerical Methods in Engineering*, 74, 619-641, 2008.

[2] J. Lu and J. Qian, Discrete gradient method over polygon mesh, *International Journal for Numerical Methods in Engineering*, 78, 505-527, 2009.

[3] J. Qian and J. Lu, A stabilized formulation for discrete gradient method, *International Journal for Numerical Methods in Biomedical Engineering*, DOI:10.1002/cnm.1337, 2009

[4] J. Qian and J. Lu, Point-cloud method for image-based biomechanical stress analysis, *International Journal for Numerical Methods in Biomedical Engineering*, Accepted for publishing, 2010

2nd International Conference on Mathematical and Computational Biomedical Engineering - CMBE2011
March 30 - April 1, 2011, Washington D.C, USA
P. Nithiarasu and R. Löhner (Eds.)

Hemodynamics in the lower-limb bypasses using wave separation and wave intensity analysis

Marie Willemet[⋆], Valérie Lacroix[⋆⋆], Emilie Marchandise[⋆] and Ashraf Khir[⋆⋆⋆]
[⋆]Université catholique de Louvain, Institute for Mechanics, Materials and Civil Engineering, Louvain-la-Neuve, Belgium. Email: marie.willemet@uclouvain.be
[⋆⋆]Université catholique de Louvain, Cliniques universitaires St-Luc, Bruxelles, Belgium
[⋆⋆⋆]Brunel Institute for Bioengineering, Brunel University, Uxbridge, United Kingdom

SUMMARY

While femoro-popliteal bypasses are a very common type of bypass surgery, failure of the graft within five years is still often observed. As causes of occlusion are not clearly understood yet, we intend to enhance the understanding of the hemodynamics in bypassed legs by analyzing the propagation of arterial waves in nearby vessels using the wave intensity analysis (WIA) method. While WIA has been largely applied to some systemic arteries, its application to lower-limb arteries has never been studied.

We acquire the physiological data invasively during surgery after the suture of the bypass graft. By using WIA, we describe the energies of individual waves observed in the leg. We compare these results with the analyses performed in the upper-limb arteries.

Through this work, we show that the WIA method provides a good analysis tool for bypassed lower-limbs arteries.

Key Words: *wave intensity analysis, wave separation, lower-limb bypass, PU-loop, blood flow.*

1 INTRODUCTION

When atherosclerosis, a widespread cardiovascular disease, affects a patient, its arterial network suffers from physiological changes such as an increase of the rigidity of the arterial wall or of its thickness. When the lower-limb arterial network is affected, it can lead in the worst cases to a total occlusion of a long segment of the femoral artery and as a consequence, to the lack of vascularization of the leg. In such cases, femoro-popliteal bypass remains the only surgical procedure to overcome the lesion.

When designing a bypass, a surgeon has many parameters to decide, e.g. the material and size of the bypass, the types and locations of anastomoses. These decisions are based on the patient's morphology, the surgeon's experience and literature advice; there exists no objective tool providing him with the best parameters. As a consequence, a high failure rate (up to 60%) is observed within the five years following the surgery [1].
The main effect responsible for the bypass failure is the development of intimal hyperplasia. The triggers for its formation are injury, circulating blood components, abnormal hemodynamics or impedance mismatch between the native vessel and the graft material [2]. Nowadays, the importance of these causes and the implication of the hemodynamics is not clearly understood yet.

Formulated by Parker et al. [3], the wave intensity analysis (WIA) is an efficient tool for studying wave propagation and reflection and for quantifying wave power and energy [4]. It has been widely used to aid the understanding of physiological events in the arterial system: i.a. in the aorta [3, 5], the coronaries [4] or the pulmonary circulation [6]. While it has also been applied to major systemic arteries (carotid and upper-limb arteries [7]), hemodynamics in lower-limb arteries has never been analyzed with the wave intensity analysis.

The aim of this work is twofold. First, to use the WIA method in the lower-limbs, as this has never been done in the literature. Second, to analyze hemodynamics in bypasses after surgeries and summarize the potential clinical benefits drawn from these analyses.

2 MATERIALS AND METHODS

Subjects. Four patients in advanced stage of atherosclerosis took part in this study. They all suffered from occlusion of the superficial femoral artery and were treated with femoro-popliteal bypass. Materials used for the bypass were either a synthetic material (Dacron, Gore-Tex), either the native saphenous vein. All patients gave their full agreement for taking part into this study.

Data acquisition. Data acquisition was performed during the bypass surgery, while patients were under anaesthesia. Measurements were performed after the suture of the graft, at four different locations in the leg: in the proximal common femoral artery, the proximal deep femoral artery, the popliteal artery and in the bypass graft (Figure 1). Pressure profiles were acquired invasively using a pressure catheter, while velocity profiles and mean diameters were measured using B-mode ultrasonography echodoppler. These measurements were not realized simultaneously, though they presented a constant heart rate. Signals were smoothed using a Savitzky-Golay filter and ensemble averaging was performed in order to provide simultaneous representative pressure and velocity waveforms.

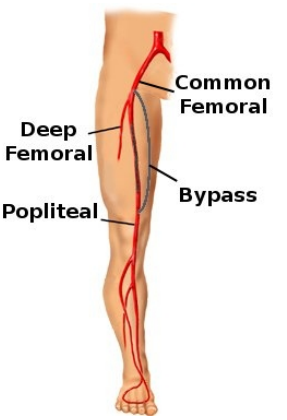

Figure 1: Lower-limb vessels with occluded superficial femoral artery

Theoretical background. The theoretical basis of WIA is the solution of the classical 1D conservation of mass and momentum equations [8]. Wave intensity, dI, is defined as the amount of energy carried by the wave per cross-sectional area of the vessel and can be calculated as $\mathrm{d}I = \mathrm{d}P\ \mathrm{d}U$, where $\mathrm{d}P$ and $\mathrm{d}U$ are the pressure and velocity differentials. Local pulse wave velocity (PWV) is calculated using the pressure-velocity loop during early systole [9].
With the use of the PWV, a traveling wave can be separated into its forward and backward components. While forward waves result from the contraction of the ventricle and ejection in the aorta, backward waves are created by the reflection at the bifurcations, discontinuities and peripheral resistive networks.

Waves are quantified by a measure of their energy: the cumulative intensity of each individual wave normalised by the sampling interval $\mathrm{d}t$:

$$\int_{T_{start}}^{T_{end}} \frac{\mathrm{d}P}{\mathrm{d}t}\frac{\mathrm{d}U}{\mathrm{d}t}\bigg|_{wave} \mathrm{d}t\ .$$

3 RESULTS AND CONCLUSION

Energies of waves are described in Table 1. Figure 2 shows the evolution of the wave intensities in the four vessels for a typical patient. Similarly to the upper-limb arteries [7], compression waves are observed in early systole: a forward-traveling of significant intensity (FCW) and a backward-traveling wave (BCW) of weak intensity. Though, only one forward-traveling expansion wave (FEW) is observed in the leg. A strong decrease of the wave intensities is observed as waves travel from the proximal to the distal arteries. This dissipation of wave energy might be explained by the tapering of the arteries and the impedance mismatch with the synthetic graft.

As showned by the analysis performed on the preliminary data set, WIA can also be efficiently applied to lower-limb arteries. Thanks to our current collaboration with vascular surgeons, additional data will be gathered in future months. On the one hand, post-operative measurements will corroborate the presented analysis. On the other hand, by extending our data set with pre-operative measurements, we will analyze the hemodynamics before the suture of the bypass graft, thereby describing the pathological condition of the occluded lower-limb.

Wave	Common Femoral	Deep Femoral	Bypass	Popliteal
FCW	21.06 ± 7.56	18.54 ± 19.26	12.62 ± 3.79	13.13 ± 9.60
BCW	2.99 ± 1.85	7.65 ± 14.08	1.03 ± 0.68	0.54 ± 0.35
FEW	6.81 ± 4.12	5.07 ± 5.83	2.72 ± 1.58	3.86 ± 4.52

Table 1: Mean data $\pm$ standard deviation $[kJ/(m^2 s^2)]$ of the cumulative intensity of individual waves, normalised by the sampling interval.

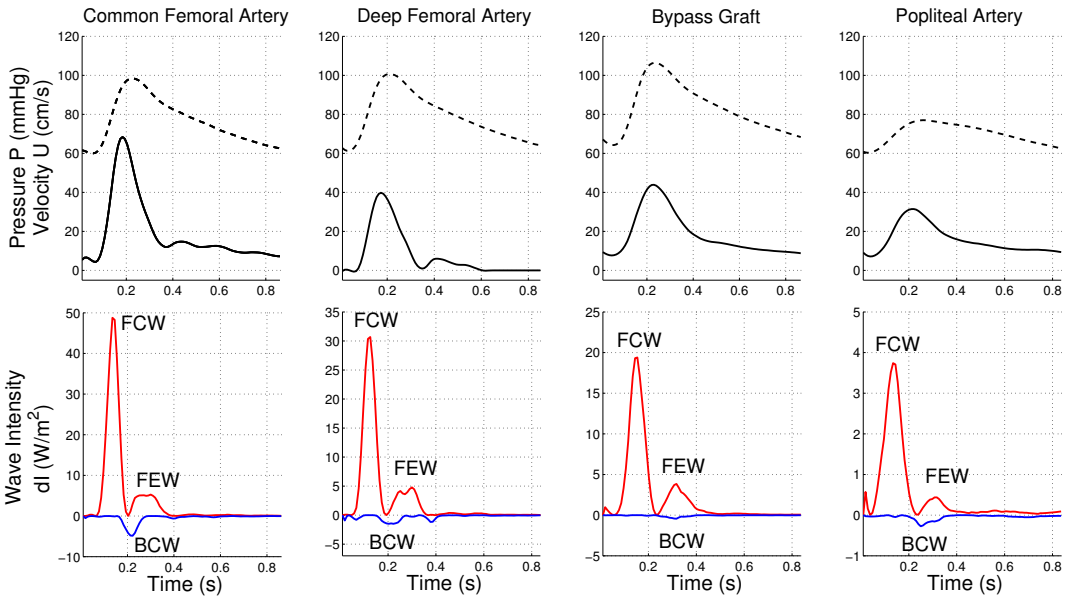

Figure 2: Pressure, velocity and wave intensities in the four vessels of the bypassed leg from a typical patient (From left to right: common femoral artery, deep femoral artery, femoro-popliteal bypass graft, popliteal artery). In the top, pressure is in dashed line, velocity in solid line. In the bottom, forward dI is in red, backward dI is in blue. Remark the different WI scales used for the four vessels.

Limitations of the method. Due to the invasive acquisition of the pressure signal, the methodology we used in this work can not easily be extended to large population of patients. Furthermore, it does not allow subject-specific pre-operative advice.
In cases of unsimultaneous measurements of pressure and velocity, care should be taken when aligning signals and when applying filtering. As mentioned in previous works, WIA method is sensitive to noise since the method implies the multiplication of two derivatives.
Furthermore, application of the method to pathological vessels needs a careful study of the morphology of the network (small tapered arteries, local stenoses).

REFERENCES

[1] L Norgren, W.R. Hiatt, J.A. Dormandy, M.R. Nehler, K.A. Harris, and F.G.R. Fowkes. Inter-society consensus for the management of peripheral arterial disease (TASC II). *European Journal of Vascular and Endovascular Surgery*, 33, 2007.

[2] Gerrit Jan Toes. *Intimal hyperplasia, the obstacle in bypass grafts*. PhD thesis, University of Groningen, 2002.

[3] K.H. Parker and C.J.H. Jones. Forward and backward running waves in the arteries: analysis using the method of characteristics. *Journal of Biomechanics*, pages 322–326, 1990.

[4] Alun D. Hughes, Kim H. Parker, and Justin E. Davies. Waves in arteries: A review of wave intensity analysis in the systemic and coronary circulations. *Artery Research*, 2 (2):51–59, 2008.

[5] Christopher J. H. Jones, Motoaki Sugawara, Yukiyoshi Kondoh, Keisuke Uchida, and Kim H. Parker. Compression and expansion wavefront travel in canine ascending aortic flow: wave intensity analysis. *Heart and Vessels*, 16:91–98, 2002.

[6] E.H. Hollander, J.J. Wang, G.M. Dobson, K.H. Parker, and J.V. Tyberg. Negative wave reflections in pulmonary arteries. *Am J Physiol Heart Circ Physiol*, 281:H895–902, 2001.

[7] A. Zambanini, S.L. Cunningham, K.H. Parker, A.W. Khir, S.A. McG Thom, and A.D. Hughes. Wave-energy patterns in carotid, brachial, and radial arteries: a noninvasive approach using wave-intensity analysis. *Am J Physiol Heart Circ Physiol*, 289:H270–276, 2005.

[8] Kim H. Parker, Christopher J. H. Jones, J. Rex Dawson, and Derek G. Gibson. What stops the flow of blood from the heart? *Heart and Vessels*, 4:241–245, 1988.

[9] A. W. Khir, A. O'Brien, J. S. Gibbs, and K. H. Parker. Determination of wave speed and wave separation in the arteries. *Journal of Biomechanics*, 34(9):1145–55, 2001.

2nd International Conference on Mathematical and Computational Biomedical Engineering – CMBE2011
March 30 – April 1, 2011, Washington D.C., USA
P. Nithiarasu and R. Löhner (eds)

COMPUTATIONAL RHEOLOGY OF SICKLE CELL

Oscar L. Castillo, Andrés L. Gonzalez
Department of Mechanical Engineering, Universidad de Los Andes, Cra. 1 Este No. 19A-40, ol.castillo28@uniandes.edu.co

SUMMARY

In this paper we implement a numerical algorithm to simulate flow of sickle cells in the microvasculature. Sickle cell disease (SCD) is caused by a defect in the hemoglobin structure [1]. As a consequence of this the shape and mechanical properties of red blood cells (RBC) are altered decreasing their ability to deform [2]. The objective of this work is to study micro-rheology of sickle cell disease in 3D using a hybrid numerical method [3]. The method used is composed of three major parts: Lattice Boltzmann Method (LBM) to solve the Navier-Stokes equations, linear Finite Element Method (LFEM) to solve the membrane elastic behavior and the Immersed Boundary Method (IBM) [13] as the framework for fluid-membrane interactions. Cells interaction phenomenon is also included using Morse potential [7]. It was found that apparent viscosity is dramatically increased due to the increase in membrane rigidity. The relationship between the apparent viscosity and membrane rigidity is approximately logarithmic; in agreement with the results found by Liu et al. [7]. Lateral migration of RBCs was also studied. It was observed that the rate of migration depends on cell rigidity. Normal red blood cells migrate faster than sickle cells towards the center of the flow. Apparent viscosity is strongly affected by cell-cell interaction potential. It was observed that apparent viscosity decreases with decreasing cell-cell interaction potential. The new contribution of this work is that it presents numerical correlation between anomalies in sickle cell and rheological properties of bulk blood including realistic sickle cell geometry, deformation model and cell-cell interaction in 3D domain.

Key Words: *Sickle Cell Disease, LBM, IBM, LFEM*

1. INTRODUCTION

Sickle cell disease (SCD) is a group of genetic disorders caused by the polymerization of hemoglobin inside Red Blood Cells (RBCs) [1]. Changes in RBCs geometry have been reported in many forms of the disease [8], some of the most common geometries are presented in figure 1. RBCs increase their membrane rigidity and usually increase their size; these two factors cause the cells to become stuck in blood vessels. The blockages deprive irrigation of oxygen to tissues and causes ischemia and infarction, which may cause organ damage [2]. This disease is chronic, lifelong and occurs most commonly in people from sub-Saharan Africa [3]. This disease is prevalent in zones where Malaria is or was common. Although disease is present in other ethnicities is much less common [2].

Development of computational tools to study therapeutic treatments is the ultimate objective of this work. Different authors have worked using several computational approaches, for example, Bagchi [13] used the Neo-Hookean constitutive model in order to represent the mechanical behavior of the RBC membrane. They model SCD by increasing the values of shear and bending modulus of the membrane. In his simulations it is evident that isolated sickle cells undergo only

tumbling motion in contrast with normal easily deformable RBC that undergo simultaneous tank-treading and tumbling motions. He also found that cells with normal deformability migrate faster than less deformable cells in lateral migration experiments. The main limitation of this approach is that simulations were performed using 2D models and without the characteristic geometry of sickle cells. Liu et al. [7] implemented an Immersed Finite Element Method and mesh-free methods using Mooney-Rivlin constitutive model to study aggregation phenomenon, in their work they showed that apparent viscosity increases with the increasing stiffness of the cells. Although their simulations were performed in the 3D domain clear relation between membrane deformability and apparent viscosity is not reported and variations in membrane geometry was neglected as well. Most of these authors have used IBM [11][12][15] to capture interaction between cells and surrounding fluid, they differ either in fluid solver or membrane representation.

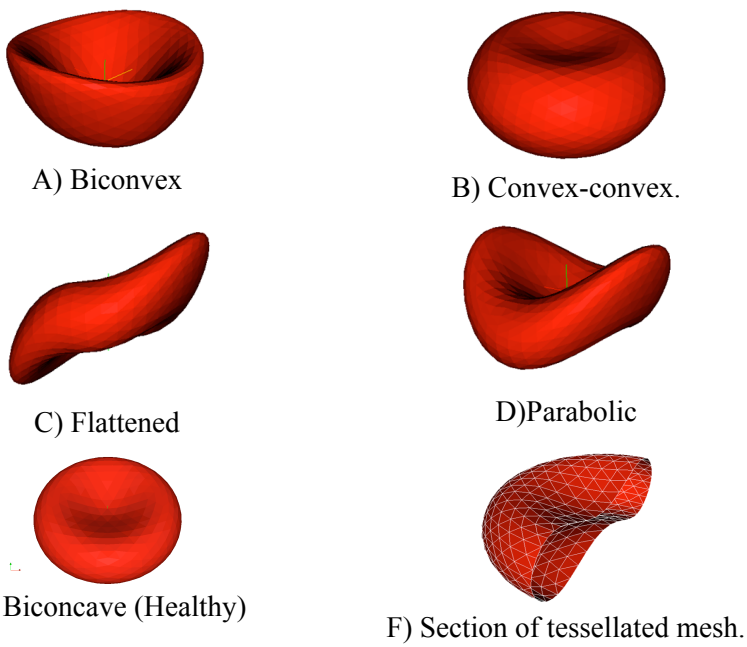

Fig. 1. - Common geometries of RBCs in sickle cell disease. Dimensions have been reported by many authors [4], [8], [14].

2. METHOD OVERVIEW

The method used in this work consists of a Eulerian Navier-Stokes solver for the incompressible fluid, a Lagrangian description of membranes, a framework to capture interaction of both systems and an interaction potential between nodes of different cells. Extensive validation of this method has been recently carried by Krüger et al. [3][6], moreover, the accuracy of the method when numerical parameters like mesh refinement, aspect ratio between elements of the Eulerian and Lagrangian descriptions and the effect of different stencils used in the definition of the delta function within the IBM framework, have been studied. In this work a D3Q19 unit cell for the LBM is used. Boundary conditions were implemented using the on site scheme proposed by Hecht et al. [4]. Linear Finite Element Method proposed by Charrier et al. [5] is used to model the RBC membrane, this approach have been used by several authors [9][10][11][12][15]. The Evans and Skalak constitutive equation is used to model the membrane. The general idea is to find the strain state of each element in the membrane through nodal displacements. Once strain state is calculated, nodal forces can be found using the selected constitutive model and the principle of

virtual work. Since every node is part of more than one element, summation over all elements that share that node is performed in order to find the total force. This force is then applied back to the surrounding fluid with the same magnitude but opposite direction using IBM.

3. PRELIMINARY RESULTS

In order to validate the behavior of the proposed algorithm, a common test has been performed. This test consists of a capsule suspended in a shear flow, as shown in Fig. 2. The presence of tank treading and the inclination angle agrees well with the models proposed by Barthès-Biesel [16]. For a mesh composed by 642 nodes and 1280 elements the variation in the inclination angle and angular velocity is less than 5% with respect to the analytical solution.

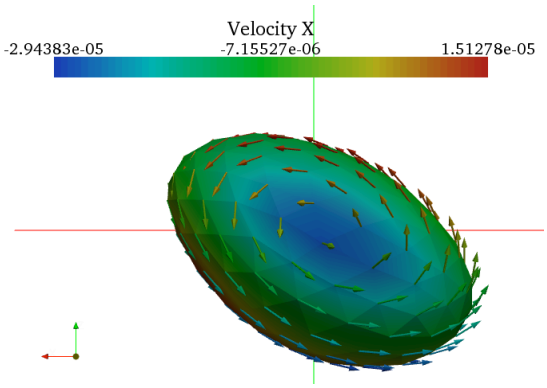

Tank treading behavior under shear flow, Ca = 0.001, Re = 0.002

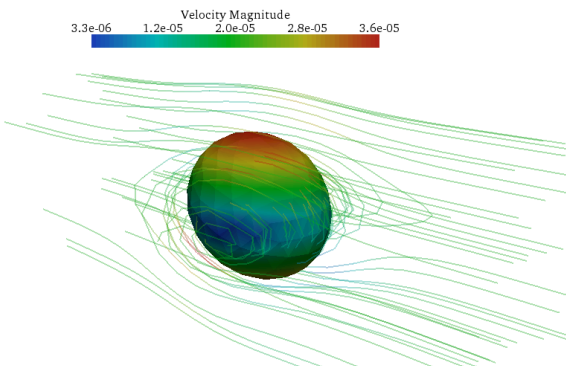

Stream lines around suspended capsule H/r=10, L/Δx=1.5.

Fig. 2. – Tank treading behavior of elastic capsule suspended in shear flow.

Fig. 3 shows the configuration used to perform measurements of apparent viscosities in relation with membrane rigidity and geometry. Eight sickle cells are suspended in a pressure driven flow. The increase in blood viscosity is observed for flows with presence of sickle cells. The relation between membrane rigidity and apparent effective viscosity is logarithmic. Lateral migration experiment confirms previous results where it has been observed that normal RBC with less rigid membranes migrate faster to the center of flow than more rigid cells.

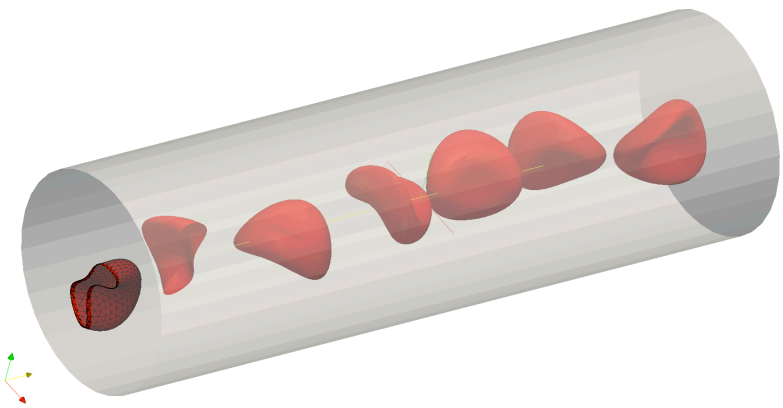

Fig. 3. Sickle Cells suspended in Hagen-Poiseuille flow, Re = 0.002. Every cell is composed by 642 nodes and 1280 elements. Fixed mesh is composed by 50x50x200 nodes.

4. CONCLUSIONS

We have used a hybrid numerical algorithm to investigate effect of sickle cells disease in blood rheology. Evans-Skalak constitutive model has been used to model membrane behavior. Morse potential has been included to simulate cell-cell interaction and aggregation phenomenon. This numerical method has been applied to study the effect of deformability of cell in bulk blood rheology. Effect of interaction potential in bulk rheology has been investigated as well. Extending this algorithm to hundreds of cells is straightforward, although optimization of the algorithms to run in parallel is needed in order to improve time efficiency of the simulations. Consistently, results have been found to be in agreement with previous works.

REFERENCES

[1] Platt, O.S., 1995. The sickle syndrome. In: Haldin, R.I., Lux, S.E., Stossel, T.P. (Eds.), Blood: Principles and Practice of Hematology. J. B. Lippincott, Philadelphia, pp. 1592–1700

[2] M.M. Dupin, I. Halliday, C.M. Care, L. Alboul, L.L. Munn, Modeling the flow of dense suspensions of deformable particles in three dimensions, Phys. Rev. E 75 (6) (2007) 066707_066717

[3] Krüger, T. Efficient and accurate simulations of deformable particles immersed in a fluid using a combined Immersed boundary lattice boltzmann finite element method. Computers and Mathematics with Applications (2010), doi:10.1016/j.camwa.2010.03.057

[4] Hecht, Martin. Implementation of on-site velocity boundary conditions for D3Q19 lattice Boltzmann. J. Stat. Mech. (2010) P01018.

[5] Charrier, J. M. Free and constrained inflation of elastic membranes in relation to thermoforming non-axisymmetric problems'' J. Strain Anal. 24, 55 1989.

[6] Feng, Z.-G. and Michaelides, E.E., 2004. The Immersed boundary-lattice Boltzmann method for solving fluid– particles interaction problems. Journal of Computational Physics, 195, 602–628.

[7] Liu, Y. and Liu, W.K., 2006. Rheology of red blood cell aggregation by computer simulation. Journal of Computational Physics, 220, 139–154

[8] Westcott, H. Vayo, Model Geometries for Sickled Erythrocytes. Bulletin of Mathematical Biolooy Vol. 49, No. 4, pp. 403-411, 1987.

[9] Sui, Y. A front-tracking lattice Boltzmann method to study flow-induced deformation of three-dimensional capsules. Computers & Fluids 39 (2010) 499–511

[10] Sui, Y. Numerical simulation of capsule deformation in simple Shear flow. Computers & Fluids 39 (2010) 242–250

[11] Dupin,M.M., et al., 2008. Efficiency oriented, hybrid approach for modeling deformable particles in three dimensions. Progress in Computational Fluid Dynamics, 8, 109–120

[12] Bagchi, Prosenjit. Mesoscale simulation of blood flow in small vessels. Biophysical Journal Volume 92 March 2007 1858–1877

[13] Peskin, C. S. 1977. Numerical analysis of blood flow in the heart. J. Comput. Phys. 25:220–233

[14] Evans, E.A. and Fung, Y.C., 1972. Improved measurements of the erythrocyte geometry. Microvascular Research, 4, 335–347.

[15] Eggleton, C.D. and Popel, A.S., 1998. Large deformation of red blood cell ghosts in a simple shear flow. Physics of Fluids,10, 1834–1845.

[16] D. Barthès-Biesel, Motion of a spherical microcapsule freely suspended in a linear shear flow, J. Fluid Mech. 100 (04) (1980) 831–853.

2nd International Conference on Mathematical and Computational Biomedical Engineering – CMBE2011
March 30 – April 1, 2011, Washington D.C., USA
P. Nithiarasu and R. Löhner (eds)

A Fluido-Chemical Model of Thrombus Formation

Jacopo Biasetti* and T. Christian Gasser*
*Department of Solid Mechanics, Royal Institute of Technology - KTH, Osquars Backe 1 - Stockholm, biasetti@kth.se – tg@hallf.kth.se

SUMMARY

Our understanding of the genesis and evolution of Abdominal Aortic Aneurysms (AAAs), with particular emphasis on Intra-Luminal Thrombus' evolution, may be improved by studying the complex interplay between fluid-dynamics and biochemistry. To investigate the evolution of pro-thrombotic chemicals inside the blood flow, in particular thrombin (factor IIa), a fluido-chemical model has been developed. To this end a series of convection-diffusion-reaction (CDR) equations describing the tissue factor pathway to thrombin have been solved on top of the biofluid dynamics problem. The proposed model integrates biochemistry and fluids dynamics, and hence, supports a comprehensive understanding of how ILT in AAAs may develop.

Key Words: *Intra-luminal thrombus, coagulation cascade, CFD, convection-diffusion-reaction equations.*

1. INTRODUCTION

Abdominal Aortic Aneurysms (AAAs) are frequently characterized by the presence of an Intra-Luminal Thrombus (ILT) known to affect biochemically [1] and biomechanically [2] their development. ILT's evolution is still under scientific debate, and little knowledge has surfaced regarding the chemical environment of the aortic blood flow; this being too often neglected in literature. Hence, the evolution throughout the fluid domain of chemical species related to the coagulation cascade, in particular thrombin (factor IIa), their distribution related to coherent vortical structures [3] and their effect on ILT evolution is the subject of the present work.

2. MAIN BODY

Idealized and patient specific AAAs have been considered, with the latter reconstructed from Computer Tomography-Angiography (CT-A) scans. The tissue factor pathway to thrombin [4] has been implemented first as a 1D time-dependent model [5] and later extended to a full 4D model (space-time) through a series of convection-diffusion-reaction (CDR) equations while the blood has been modeled as a non-Newtonian incompressible fluid using the Carreau-Yasuda model. The fluid-dynamics problem and the convection-diffusion-reaction equations have been solved in COMSOL (COMSOL AB). Triangular and tetrahedral meshes have been created for 2D-axialsymmetric and 3D simulations. The fluid-dynamics problem was discretized with Lagrange P_3P_2 elements and streamline diffusion and crosswind diffusion have been used for stabilization purposes [6]. Due to the convection-dominated nature of the CDR set of equations (Pe>>1) fine meshes, especially in regions of expected strong concentration gradients like the near wall

regions, Lagrange cubic elements and stabilization techniques like SUPG and crosswind diffusion have been used to avoid uncontrolled oscillations in the solution variables. Coherent vortical structures educed with the λ_2-method [3] and thrombin distribution have been evaluated in different AAAs. In particular the evolution of thrombin throughout the domain as a function of the damaged wall area has been studied.

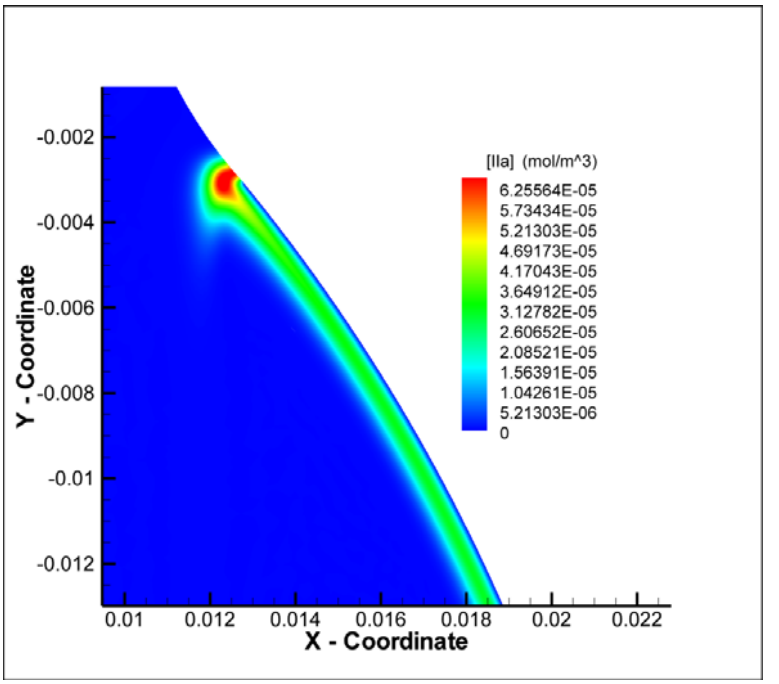

Figure 1: Example of thrombin (factor IIa) segregation in the near wall region due to a coherent vortical structure in the aneurysmatic bulge.

3. CONCLUSIONS

A concentration boundary layer develops naturally along the damaged aortic walls where the coagulation cascade is triggered. Vortical structures, which are strongly dependent from the geometry, determine the accumulation of chemicals in the near wall region and their distribution throughout the fluid domain. In particular, vortices can force the segregation of thrombin near the wall (Figure 1) increasing platelets activation and adhesion in the affected region, or force thrombin to follow a certain path along the aortic lumen. Naturally, vortex boundaries, due to the high shear stresses here present, increase the mixing of chemicals, creating a favorable environment for chemical reactions. In complex fluid domains, as is the case of patient-specific AAAs, the distribution of thrombin is dependent from the damaged wall areas. The present approach has the potential of elucidate fluid-driven ILT evolution in particular with regard to the regions with high platelets activation and platelet adhesion. However, more knowledge regarding the initial endothelial damage, for example its location and extension, is needed to validate the present approach.

REFERENCES

[1] M. Kazi et al., Influence of intraluminal thrombus on the structural and cellular composition of the abdominal aortic aneurysm wall, *J. Vasc. Surg.*, 38:1283-1292, 2003.

[2] W. R. Mower et al., Effect of intraluminal thrombus on abdominal aortic aneurysm wall stress, *J. Vasc. Surg.*, 33:602-608, 1997.

[3] J. Jeong and F. Hussain, On the identification of a vortex, *J. Fluid. Mech.*, 285:69-94, 1995.

[4] J.H. Lawson et al., A model for the tissue factor pathway to thrombin. I. An empirical study, *The Journal of Biological Chemistry.*, 269,37:23357-23366, 1994.

[5] K.C. Jones and K.G. Mann, A model for the tissue factor pathway to thrombin. II. A mathematical simulation, *The Journal of Biological Chemistry.*, 269,37:23367-23373, 1994.

[6] O.C. Zienkiewicz, R.L. Taylor and P. Nithiarasu, The finite element method for fluid dynamics, 6th edition, Elsevier.

[7] J. Biasetti et al., Hemodynamics of the normal aorta compared to fusiform and saccular abdominal aortic aneurysms with emphasis on a potential thrombus formation mechanism, *Ann. Biomed. Eng.*, 38: 380–390 2010.

2nd International Conference on Mathematical and Computational Biomedical Engineering – CMBE2011
March 30 – April 1, 2011, Washington D.C., USA
P. Nithiarasu and R. Löhner (eds)

EFFECT OF ROLL ANGLE ON THE BUBBLE TRANSPORT IN A SYMMETRIC BIFURCATING MICROCHANNEL

Poornima J[*] and Vengadesan S[**]
[*]Research Scholar (poornima.josyula@gmail.com); [**]Associate Professor (vengades@iitm.ac.in)
Department of Applied Mechanics, Indian Institute of Technology Madras, Chennai - 600036, India.

SUMMARY

In this paper, we present the numerical simulations carried out in a symmetric two-dimensional (2D) rectangular first generation bifurcating microchannel which mimics the human arteriole filled with blood as the liquid phase. In order to model the bubble transport, we introduce perfluorocarbon gas at the entrance of the microchannel, in the form of a non-dimensional bubble size, L_d (ratio of the dimensional bubble length to the parent tube diameter). For the two bubble sizes of L_d=1 and L_d=2 considered in the present study, the splitting behavior of the bubble under the effect of gravity is assessed and reported. The gravity effects are incorporated via the Bond number, Bo (ratio of the gravity forces to the surface tension forces); Roll Angle, Φ (angle which the plane makes with the horizontal); and Modified Bond Number, Bo^* (which takes into account the roll angle). The splitting ratio was found to be 1, when the roll angle was 0^0 (i.e. no gravity effect) for both the bubble sizes indicating a uniform distribution of bubble volume in both the daughter channels. When the gravity effects are incorporated, the splitting ratio was found to be decreasing with the increase in the roll angle.

Key Words: *arteriole, splitting ratio, roll angle, bubble transport.*

1. INTRODUCTION

The present work derives its motivation from a novel concept of gas embolotherapy which is used to treat tumors. The potential treatment modality is explained in [1]. Since rectangular microchannels have become popular in studying the blood flow phenomena *in vitro* under physiological conditions [2], for the current study; the human arteriole is modeled as a 2D symmetric rectangular bifurcating microchannel. The aim of our work is to arrive at the lodging and dislodging pressures for two non-dimensional bubble sizes, that is for, L_d=1 and L_d=2. Upon identifying the lodging & dislodging pressures, subsequent calculations are carried out to study the effect of gravity on the splitting behavior of these two bubble sizes. The effect of gravity is taken into account by introducing a non-dimensional modified Bond number, Bo^*.

2. COMPUTATIONAL MODEL AND SIMULATION PARAMETERS

The computational model for the present study is shown in Figure 1. The value of the bifurcating angle, θ is taken as 78^0, which matches the physiological value of the arterial branching in the human body [3]. Blood (as a Newtonian fluid) and Perfluorocarbon (PFC) gas are used as the working fluids. The Reynolds number ($Re = D_p U\rho/\mu$), based on the hydraulic diameter of the parent tube and properties of blood, is taken as 0.2. The Capillary number ($Ca = U\mu/\sigma$), based on the surface tension between blood and PFC, is calculated as 1.22×10^{-3}. Since the transport of the PFC bubble through the blood filled microchannel is a two-phase interfacial problem, the VOF scheme in the commercial CFD package, FLUENT® v. 6.3.26 [4] is used to carry out the simulations. Initially,

steady state calculations are carried out and the results obtained are used as an initial condition for the transient calculations. For transient calculations; at the inlet, pressure inlet boundary condition (a symmetric pressure gradient equal to the lodging and dislodging pressure, as according to the case considered) is imposed and at the outlets, pressure outlet boundary condition is imposed with a gauge pressure equal to 0.

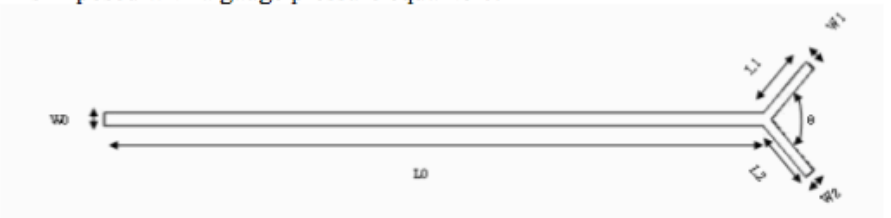

Figure 1: First generation bifurcation geometry where: L0 = 462.6 µm; W0 = 77.1 µm; L1, L2 = 360.828 µm; W1, W2 = 60.138 µm; θ = 78^0

3. RESULTS AND DISCUSSIONS

3.1. Identification of the Lodging and Dislodging Pressures

The lodging pressure for the two bubble sizes i.e. L_d=1 and L_d=2, is identified based on the following criteria:

$$\hat{t}_i \geq (20.\hat{t}_b) \quad (1)$$

Where:

(2)non-dimensional lodging time scale, $\hat{t}_i = \frac{\Delta t}{D_p U^{-1}}$; (3)non-dimensional bulk time scale, $\hat{t}_b = \frac{t_b}{D_p U^{-1}}$;

(4)dimensional bulk time scale, $t_b = L_d . \frac{D_p}{U}$; (5)non-dimensional instant time scale, $\hat{t}_i = \frac{t_i}{D_p U^{-1}}$

In the above equations, Δt is the time lag between instant when the bubble lodges at the bifurcation and instant upto when the bubble remains at the same position for a sufficiently long time. The non-dimensionalization of this time is given in Equation (2); t_i is the instant when the bubble is present in the channel; D_p – Hydraulic diameter of the parent tube (µm); U – Characteristic velocity of the blood ($m.s^{-1}$); L_d – Dimensionless bubble length.

Equation (1) suggests that for a bubble to lodge at the bifurcation at a particular pressure, the lodging time scale should be at least 20 times greater than the bulk time scale. To account for the sensitivity of the effect of the pressure on the bubble transport, the dislodging pressure is taken as 2-5% higher than that of the lodging pressure. An illustration for one of the bubble sizes i.e. L_d=1 lodging at the bifurcation at a pressure of 831.195 Pa is shown in Figure 2. A similar phenomena is observed for L_d=2.

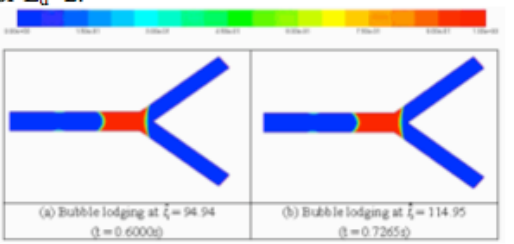

Figure 2 (a)–(b): Volume fraction contours of PFC for L_d=1 at a pressure of 831.195 Pa for the non-dimensional time of $\hat{t}_i$ = 94.94 and $\hat{t}_i$ = 114.95 respectively.

The identified lodging and dislodging pressure for both the bubble sizes is tabulated in Table 1.

Table 1: Lodging and dislodging pressures for bubble sizes, L_d=1 and L_d=2

Bubble size, L_d	Dislodging Pressure (Pa)	Lodging Pressure (Pa)
1	874.942	831.195
2	892.798	874.942

3.2. Effect of gravity on the splitting ratio

Eshpuniyani [5] defined splitting ratio (SR) as the ratio of the bubble volume in the bottom daughter channel (V_b) to the bubble volume in the top daughter channel (V_t) after it has passed through the first bifurcation. Additionally, we define a term *percentage of total volume fraction split,* $\%V_s$ given by Equation (6), which will help in identifying how much of the bubble volume splits into the top and bottom channels right after crossing the bifurcation point.

$$\%V_s = \frac{V_{daughter}}{V_t} \text{x100} \qquad (6)$$

where, $V_{daughter}$ refers to the volume of the bubble in either top or bottom daughter channel; V_t refers to the total volume of bubble at the bifurcation junction before splitting into the daughter channels. The value of Bond number ($Bo = \Delta\rho g D_p^2/\sigma$) calculated for the present study is $6.647\text{x}10^{-4}$. To understand the effect of roll angle (Φ), we have considered three values i.e. 0^0, 30^0 and 45^0 which correspond to the modified Bond numbers ($Bo^* = Bo.\sin(\Phi)$) 0, $3.323\text{x}10^{-4}$ and $4.700\text{x}10^{-4}$ respectively.

At the lodging pressure, the gravity does not have any significant effect on the splitting ratio of bubble (L_d=1), that is the bubble lodges at the bifurcation instead of splitting into the daughter channels even under the gravitational effect, as seen in Figure 3. A similar phenomena is observed for L_d=2. Further, the time for the lodging of the bubble conforms to Equation (1) for both the bubble sizes.

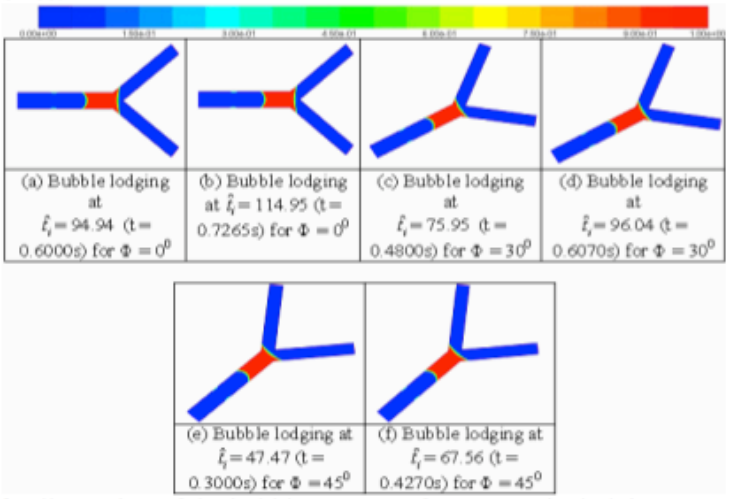

Figures 3 (a)-(f): Illustration of the bubble transport for L_d=1 at its lodging pressure of 831.195 Pa for different roll angles, $\Phi = 0^0$, 30^0, and 45^0

At the dislodging pressure, the effect of gravity on the splitting ratio is profound. From Table 2, it can be seen that with the increase in the roll angle, the splitting ratio decreased for both the bubble sizes. And also, it can be observed that for both the bubble sizes at $\Phi=0^0$, the splitting ratio was found to be 1 indicating that there is an equal distribution of the bubble volume to both

the channels. Physiologically, this suggests that the microbubble contrast agents would be uniformly distributed in the vicinity of the diseased organ/tissue.

Table 2: Effect of gravity on the splitting ratio for bubble sizes of L_d =1 and L_d = 2

Bubble Size, L_d	Non-Dimensional time (given by Equation (5))	Roll Angle, Φ (Degree)	Length of the bubble (μm)		Available Volume of the bubble (nL)		Splitting Ratio, SR = V_b/V_t	% of Total Volume Fraction Split, $\%V_s$ (given by Equation (6))	
			In the top channel (L_t)	In the bottom channel (L_b)	In the top channel (V_t)	In the bottom channel (V_b)		In the top channel	In the bottom channel
1	59.496	0^0	66.708	67.051	1.447	1.454	1.005	50.00	50.00
	134.81	30^0	67.072	66.376	1.455	1.440	0.9896	49.88	49.36
	90.352	45^0	67.394	66.563	1.462	1.444	0.9876	47.56	46.97
2	59.101	0^0	81.428	81.573	1.766	1.770	1.001	50.00	50.00
	64.085	30^0	82.522	79.144	1.790	1.717	0.9592	48.30	46.33
	32.992	45^0	81.277	76.577	1.763	1.661	0.9421	47.77	45.01

4. CONCLUSIONS

From the present study, the following conclusions are drawn:-

1) A non-dimensional lodging time scale (dependent on the bubble length) was proposed as an indicator to identify the lodging pressure.
2) At the lodging pressure of the bubble, there was no significant effect of the gravity on the bubble transport. The bubble lodged at the bifurcation conforming to the non-dimensional lodging time scale criteria for both L_d=1 and L_d= 2.
3) At the dislodging pressure of the bubble, it was found that with the increase in roll angle, the splitting ratio decreased, signifying the profound effect of the gravity on the bubble transport for both L_d=1 and L_d= 2.
4) At roll angle, $\Phi=0^0$, the splitting ratio was found to be 1 indicating that there is an equal distribution of the bubble volume to both the channels.

REFERENCES

[1] A. J. Calderón. A multiphase flow study of bubbles traveling through bifurcations for a novel gas embolotherapy technique. *Ph.D. Thesis* 2006; University of Michigan, USA.

[2] R. Lima, S. Wada, K. Tsubota, T. Yamaguchi. Confocal micro-PIV measurements of three-dimensional profiles of cell suspension flow in a square microchannel. Meas. Sci. Technol. 2006, **17**: 797–808.

[3] YC Fung. *Biomechanics: circulation*. Springer: New York, 1997.

[4] FLUENT user manual, Version 6.3.26, 2007.

[5] B. Eshpuniyani, J. B. Fowlkes, J. L. Bull. A bench top experimental model of bubble transport in multiple arteriole bifurcations. *Int. J. Heat and Fluid Flow* 2005; **26**: 865–872.

2nd International Conference on Mathematical and Computational Biomedical Engineering – CMBE2011
March 30 – April 1, 2011, Washington D.C., USA
P. Nithiarasu and R. Löhner (eds)

Fontan surgical design for improved hepatic flow distribution using CFD and derivative-free optimization

Weiguang Yang [1], Irene E. Vignon-Clementel [2], Guillaume Troianowski [3], Shawn Shadden [4], V. Mohhan Reddy [5], Jefferey A. Feinstein [6] and Alison L. Marsden [1]

1. Mechanical and Aerospace Engineering Department, University of California San Diego, La Jolla, CA 92093 w1yang@ucsd.edu and amarsden@ucsd.edu
2. INRIA Paris-Rocquencourt, 78153 Le Chesnay Cedex, France Irene.Vignon-Clementel@inria.fr
3. Institute for Computational and Mathematical Engineering, Stanford University, Stanford, CA 94305, USA guillaume.troianowski@gmail.com
4. Mechanical, Materials and Aerospace Engineering, Illinois Institute of Technology, Chicago, IL 60616, USA sshadden@gmail.com
4. Department of Cardiothoracic Surgery, Stanford University, Stanford, CA 94305, USA
5. Departments of Pediatrics and Bioengineering, Stanford University, Stanford, CA 94305, USA jaf@stanford.edu

SUMMARY

The Fontan procedure is a surgery to treat single ventricle heart defects, in which the patient's inferior vena cava (IVC) is connected to the pulmonary artery (PA) via a tube-shaped Gore-tex graft. Previous studies have demonstrated that the geometry plays an important role in Fontan hemodynamics. A novel Y-shaped design was recently proposed to improve upon traditional designs, and results showed promising improvements in energy dissipation, pressure levels, and flow distribution. In this study, we compare hemodynamic performance of three competing designs in five patients by performing patient specific flow simulations. The hepatic flow distribution, which is clinically related to the development of pulmonary arteriovenous malformations (PAVMs), is particularly studied. Results show that the geometry and boundary conditions significantly influence the hepatic flow distribution, and that overall the Y-graft design distributes hepatic flow more evenly than traditional designs. In the second part of this study, we couple particle tracking to shape optimization in an idealized model to optimize the hepatic flow distribution under a series of conditions. We observe that optimal hepatic flow distribution is consistent with the theoretical optimum derived from conservation of mass. A semi-idealized model which incorporates a patient specific SVC is also optimized to evaluate the effect of SVC geometry on flow distribution. Optimization results will then be used to improve performance in some underperforming patient specific models.

Key Words: *Blood flow, surgical design, optimization, CFD* .

1. INTRODUCTION

Singe ventricle heart defects are among the most challenging for pediatric cardiologists and surgeons to treat. Patients born with a single functional ventricle are cyanotic and the condition is uniformly fatal without surgical intervention. Typically a three-staged palliative surgery is performed. In the second stage, the bidirectional Glenn procedure, the superior vena cava (SVC) is connected to the pulmonary arteries (PAs). In the third and final stage, the Fontan procedure, the inferior vena cava (IVC) is connected to the PAs via a Gore-Tex tube forming a T-shaped junction. Although early survival rates following the Fontan procedure are greater than 90%, significant long term morbidity remains, including diminished exercise capacity, thromboembolic complications, protein-losing enteropathy, arteriovenous malformations and arrhythmias [1].

Advances in CFD, MRI and CAD have enabled detailed simulations of Fontan hemodynamics. The impact of geometry on Fontan hemodynamics has been demonstrated in multiple recent studies and is widely accepted in the engineering and clinical communities [2] [3] [4]. An offset design was the first design derived from simulations and adopted by surgeons to reduce energy loss [5]. Recently a new Y-shaped graft bifurcating the IVC flow has been proposed to replace traditional T-junction and offset designs [6][7]. Preliminary results show that the Y-graft design improves the energy efficiency, SVC pressure and hepatic flow distribution.

Recent studies have shifted the focus of computational studies from solely studying the energy dissipation to a multiple parameter approach. It was found that the hepatic flow distribution varies greatly with geometry of the Fontan connection and flow conditions. Although the pathogenesis of PAVMs remains unknown, there is adequate clinical data to indicate that lack of hepatic flow in the left or right pulmonary artery may cause PAVMs [8]. Thus, a surgical design based on energy dissipation alone without considering hepatic flow distribution may unnecessarily increase the risk of PAVMs. To assess the potential of the Y-graft to improve hepatic flow distribution, we virtually implanted Y and tube-shaped grafts into five patient specific Glenn models and simulated post- operative flow conditions. Each design was evaluated with multi-parameters [5] with particular attention paid to the hepatic flow distribution. To gain further physical understanding, we then employ an optimization framework to unveil the optimal shapes that distribute hepatic flow evenly under a series of flow conditions.

2. Method

Y-grafts with 20 mm diameter trunk and 15 mm diameter branches, and T-junction and offset designs with a 20 mm diameter were virtually implanted into five patient specific Glenn models (A-E) using a customized version of the Simvascular package. Multiple Y-graft and offset designs were implemented for patients B and E due to PA stenosis and heterotaxy.

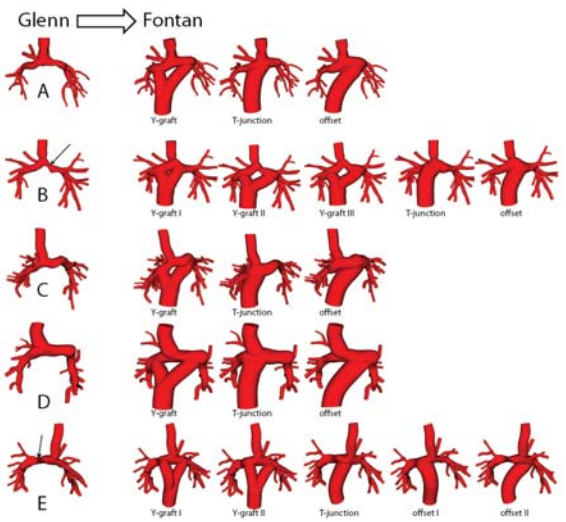

Fig 1: Original Glenn models and variations of Fontan geometries for five patients.

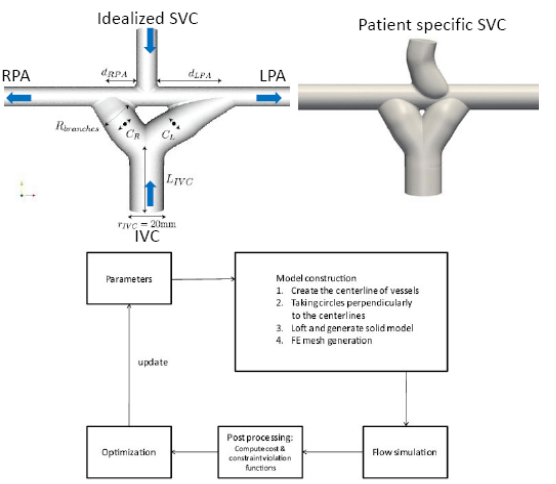

Fig 2: Model parameterization and optimization procedure. Patient specific SVC is also incorporated into the idealized model.

Flow simulations were performed with a stabilized finite element Navier-Stokes solver [9] assuming rigid walls and Newtonian flow. Final meshes consisted of approximately 1 to 1.5 million elements and adaptive meshing was used to ensure convergence. Pulsatile inflow and three element RCR circuit model were employed at the inlets and outlets respectively [10] [11]. A respiratory model [12] was superimposed on the IVC waveform.

Standard methods [7] were used to calculate the power loss, SVC pressure and wall shear stress for each model. To quantify the hepatic flow distribution, particles were released continuously at the inlet of the IVC and Lagrangian particle tracking was performed [12]. Particle tracking results are compared with the theoretical optima for the hepatic flow distribution which is derived from conservation of mass.

A shape optimization framework that employs Kriging surrogates and mesh adaptive direct search (MADS) has been developed for Fontan surgical design based on an idealized model [14]. In this study, we incorporate particle tracking into the optimization framework to systematically explore optimal shapes for the hepatic flow distribution. To evaluate the impact of SVC on the optimal design, we also optimize a semi-idealized model (Fig.2) which incorporates patient specific SVC and approximates PAs by a cylindrical tube. Improvements to the patient specific designs based on optimization results will be explored.

3. Results

Fig. 3 shows two patients' hepatic flow distribution in each design and the robustness of the Y-graft and offset designs to the changes of the pulmonary flow split. In patient A, the Y-graft design achieves the closest distribution to the theoretical optimum, even though patient A's right lung receives more than 80% of the total venous return. For the T-junction design, over 90% hepatic flow is skewed to the RPA because the SVC jet blocks the hepatic flow going to the LPA (Fig. 4). The offset design performs well under the original pulmonary flow split but skews the hepatic flow to the LPA when LPA resistance is reduced. In patient D, the offset design results in a highly uneven hepatic flow distribution when the pulmonary flow split is close to 50/50.

Fig. 5 shows the optimal shapes under two pulmonary flow splits using pulsatile flow. Both equal and unequal-branch designs achieve the same performance under an 80/20 pulmonary flow split (Fig. 6). The unequal-branch design could be ruled out due to higher energy loss, compared to the equal-branch design.

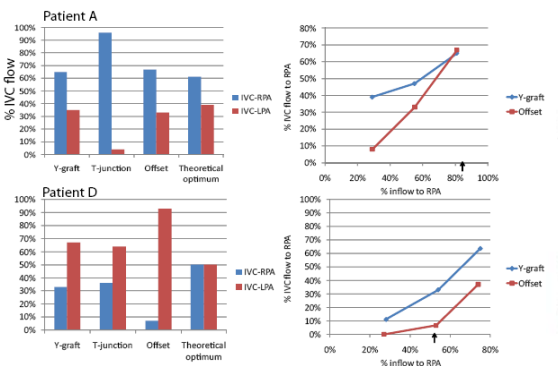

Fig 3: Left: Hepatic flow distribution in each design (amount of IVC flow in right and left lungs). Right: Robustness test for the Y-graft and offset designs. Patient's original pulmonary flow splits are marked by arrows.

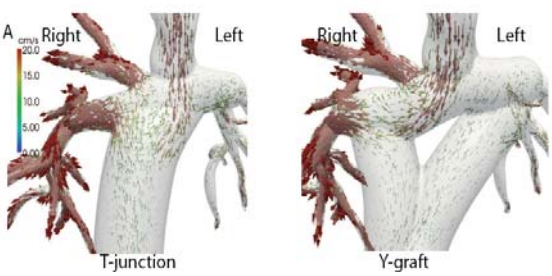

Fig 4: Time-averaged velocity vectors in the Y-graft and T-junction models for patient A.

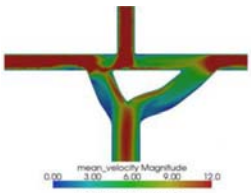

Fig 5: Optimal shapes for the hepatic flow distribution under two pulmonary flow splits. Theoretical optima are achieved.

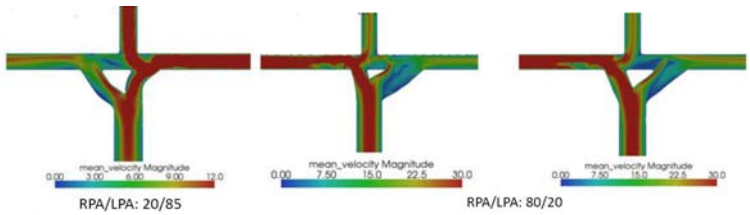

Fig 6: Both equal and unequal-branch designs achieve theoretical optimum.

4. CONCLUSIONS

We have demonstrated that Fontan geometry significantly influences the hepatic flow distribution. Overall, the Y-graft design results in more even hepatic flow distribution and moderate improvements in energy loss and SVC pressure. The offset design is able to achieve an even hepatic flow distribution for patients with highly unequal pulmonary flow splits, but is sensitive to variations in pulmonary flow split. The flow distribution optimization demonstrates that the optimal hepatic flow distribution can be theoretically achieved in an idealized model (Fig 6) under a large range of flow conditions. In conclusion, the results of this study indicate that the Y-graft design has potential for clinical application but that graft designs should be carefully tailored for individual patients prior to surgery.

REFERENCES

[1] B. S. Marino. Outcomes after the Fontan procedure. *Curr. Opin. Pediatr*., 14:620–626, 2002.

[2] K. K.Whitehead, K. Pekkan, H. D. Kitahima, S. M. Paridon, A. P. Yoganathan, and M. A. Fogel. Nonlinear power loss during exercise in single-ventricle patients after the Fontan: insights from computational fluid dynamics. *Circulation*, 116:I–165 – I–171, 2007.

[3] A. L. Marsden, V. Mohan Reddy, S. C. Shadden, F. P. Chan, C. A. Taylor, and J. A. Feinstein. A new multi-parameter approach to computational simulation for fontan assessment and redesign. *Congenital Heart disease*, 5(2):104–117, 2010.

[4] F. Migliavacca, G. Dubini, E. L. Bove, and M. R. de Leval. Computational fluid dynamics simulations in realistic 3-D geometries of the total cavopulmonary anastomosis: the influence of the inferior caval anastomosis. *J. Biomech. Eng.*, 125:805–813, 2003.

[5] G. Dubini, M. R. de Leval, R. Pietrabissa, F. M. Montevecchi, and R. Fumero. A numerical fluid mechanical study of repaired congenital heart defects: Application to the total cavopulmonary connection. *J. Biomech.*, 29(1):111–121, 1996.

[6] D. D. Soerensen, K. Pekkan, D. de Zelicourt, S. Sharma, K. Kanter, M. Fogel, and A. Yoganathan. Introduction of a new optimized total cavopulmonary connection. *Ann. Thorac. Surg.*, 83(6):2182–90, 2007.

[7] A. L. Marsden, A. J. Bernstein, V. M. Reddy, S. Shadden, R. L. Spilker, F. P. Chan, C. A. Taylor, and J. A. Feinstein. Evaluation of a novel Y-shaped extracardiac Fontan baffle using computational fluid dynamics. *J. Thocac. Cardio. Surg.*, 137(2):394–403, 2009.

[8] Y. Imoto, A. Sese, and K. Joh. Redirection of the hepatic venous flow for the treatment of pulmonary arteriovenous malformations after fontan operation. *Pediatr. Cardiol*, 27:490–492, 2006.

[9] C. A. Taylor, T. J. R. Hughes, and C. K. Zarins. Finite element modeling of blood flow in arteries. *Comput. Method. Appl. Mech. Engrg.*, 158(1-2):155–196, 1998.

[10] I. E. Vignon-Clementel, C. A. Figueroa, K. E. Jansen, and C. A. Taylor. Outflow boundary conditions for three-dimensional finite element modeling of blood flow and pressure in arteries. *Comput. Meth. Appl. Mech. Engrg.*, 195(29-32):3776–3796, 2006.

[11] Clementel IE, Figueroa CA, Jansen KE, Taylor CA. Outflow boundary conditions for 3d simulations of non-periodic blood flow and pressure fields in deformable arteries. *Computer Methods in Biomechanics and Biomedical Engineering. 13(5)*, 625-640, 2010

[12] A. L. Marsden, I. E. Vignon-Clementel, F. Chan, J. A. Feinstein, and C. A. Taylor. Effects of exercise and respiration on hemodynamic efficiency in CFD simulations of the total cavopulmonary connection. *Ann. Biomed. Eng.*, 35(2):250–263, 2007.

[13] S. C. Shadden and C. A. Taylor. Characterization of coherent structures in the cardiovascular system. *Annals of Biomedical Engineering*, 36(7):1152–1162, 2008.

[14] W. Yang, J. A. Feinstein, and A. L. Marsden. Constrained optimization of an idealized Y-shaped baffle for the fontan surgery at rest and exercise. *Comput. Meth. Appl. Mech. Engrg.*, 199(33-36):2135–2149, 2010.

MATHEMATICAL MODELING OF SWIRLING INTRACARDIAC FLOW USING EXACT SOLUTION OF UNSTEADY-STATE HYDRODYNAMIC EQUATIONS FOR THE CLASS OF SELF-ORGANIZING TORNADO-LIKE FLOWS OF VISCOUS MEDIUM

Bokeriya L.A.*, Kiknadze G.I. *, Bogevolnov A.V. **, Gorodkov A.Yu.*
* Bakulev Research Center for Cardiovascular Surgery, Moscow, Russia
(agorodkov@bk.ru)
**S.-Petersburg State University, Physical Dpt.

SUMMARY

A new approach to quantification and modeling of the intraventricular blood flow is proposed using the exact solution of unsteady-state hydrodynamic equations for the class of tornado-like viscous flows.

Key Words: *Swirling blood flow, exact solution of unsteady-state hydrodynamic equations.*

1. INTRODUCTION

The hydrodynamic structure of the blood flow in the heart and main vessels stays one of unsolved problems in cardiovascular physiology. Despite the existence of number of hypotheses, it is not any consented opinion on this matter at present. Many experimental studies performed during last 40 years demonstrate the swirling structural organization of blood flow in the ventricular cavity and aorta [Kuzmina, Zakharov, McDonalds, Rushmer, Ohlsson, et al.]. However, so far no mathematical methods have been applied for analysis and quantification of the blood flow structure. Importance of such analysis of blood flow structural properties is evident for the mathematical, numerical and laboratory modeling of blood circulation. This is also important for design and safety improvement of implantable devices, used in the cardiovascular surgery.

2. MAIN BODY

The quantification of swirling flow became feasible after the appearance in 1986 of the exact solution of Navier-Stocks and Continuity equations for the class of self-organizing swirling flows [Kiknadze G.I., Krasnov Yu.K., 1986].

$$\begin{cases} V_r = -C_0(t)r + \dfrac{2C_1(t)\nu}{r} \\ V_z = 2C_0(t)z + C_2(t) \\ V_\varphi = \left(\dfrac{\gamma_0}{2\pi r} + \dfrac{1}{2\pi}\sum_i \dfrac{\gamma_i}{r_i}\right)\cdot\Gamma\left[C_1(t)+1, \beta_i(t)r^2\right] \end{cases}$$

($V_r(t)$, $V_z(t)$, $V_\varphi(t)$ – radial, longitudinal and tangential velocity components; $C_0(t)$, $C_1(t)$, $C_2(t)$, $\beta_i(t)$ - independent time-functions; $\gamma_0(t)$, $\gamma_i(t)$ - time-dependent flow

circulations; $\Gamma[C_1(t)+1, \beta_i(t)r^2]$ – incomplete tabulated Γ-function [Gelfand I.M.]; ν - medium viscosity).

The velocity field of elementary single swirling jet of considered flow type is described by the following expressions:

$$\begin{cases} V_r = -C_0(t)\cdot r \\ V_z = 2C_0(t)\cdot z \\ V_\varphi = \dfrac{\Gamma_0(t)}{2\pi r}\left[1-\exp\left(-\dfrac{C_0 r^2}{2\nu}\right)\right] \end{cases}$$

where $\Gamma_0(t)$ – time-dependent jet circulation, $C_0(t)$-radial velocity gradient, reflecting the extent of jet convergence.

This solution describes the field of velocity and pressure in the axis-symmetrical flows where the medium element moves along the swirled converging trajectory. The longitudinal and radial velocity components do not depend on medium viscosity. So the energy losses in the flows of this type exist only in the tangential direction where the velocity depends on viscosity. As it is seen from the exact solution less the jet radius is, more the energy losses. The boundary interactions in these flows are determined by special structure of boundary layer consisted of the same micro vortexes that roll along the jet's outer layer providing the zero velocity on the jet margin. Here the share is replaced by rolling which explains the low values of hydrodynamic resistance inherent to these flows.

The principle of such flows generating and evolution was used in a number of various technical devices. As a result a significant heat-mass exchange intensification, decrease of resistance of flowed surfaces, an energy transformation processes were achieved in different industrial processes [Kiknadze G.I., et al., 2009].

Comparison of properties of tornado-like swirling flows and the flow of blood in the heart and main vessels reveals some evident similarities that allow the blood flow analysis using the above exact solution. These similarities may be summarized as low hydrodynamic resistance, anatomical convergence of the flow lumen, and spirally oriented trabecular profile on the inner surface of heart ventricles that should determine swirled structure of the flow [Gorodkov A.Yu., 2003].

The study of the flow structure in the heart and main vessels on the base of exact solution for the class of tornado-like flow is performed in the Bakulev Research Center for Cardiovascular Surgery (Moscow) since 1992. It was proved that the blood flow corresponds to the class of tornado-like flows by means of morphometry of corrosion casts of left ventricle and aorta, using 4D mapping of velocity field in the aorta by MRI. The values of main model parameters, responsible for the flow generation and evolution were estimated. These parameters are the time-dependent functions determined by the geometry of the flowing lumen of left ventricle and aorta [Bokerya L.A., et al., 2003, Kiknadze G., et al., 2009]. They change dynamically during cardiac cycle reflecting the extent of pulsatile flow unsteadiness. The only way to measure directly these parameters is the *in vivo* measurement of velocity field with sufficient spatial resolution. However this procedure seems to be very complex in the ventricular cavity due to necessity of taking into account a lot of events occurring in the contracting heart. Moreover, some features of the flows of this type could not be measured, like the structure and thickness of boundary layer. Therefore the physical and mathematical modeling remains the only way to study these flows.

A special channel was used to model a tornado-like swirling flow. The channel had a converged lumen and a set of twisting paddles inside the lumen. The channel

surface and the shape of paddles were designed in correspondence with the streamlines of tornado-like flows according to the exact solution. The water was used as a working fluid. The measurement of the main characteristics of the resulting flow revealed all the advantages of tornados – the absence of turbulence in a wide debits range, significant decrease of the resistance, additional flow acceleration provided by pressure gradients occurring due to the flow twisting. The measured flow characteristics have unambiguously proved the equivalence of the experimentally generated flow and the flow described by the exact solution.

A finite volume algorithm is often used currently in the investigational practice in order to obtain the detailed 4D reconstruction of the velocity and pressure fields in different parts of the circulation. This method marked the beginning of a set of program packages intended to study the medium flowing around the bodies of complex spatial configuration, such as ANSYS CFX and ANSYS FLUENT. These programs were successfully used to reconstruct the velocity field, to estimate the energy balance in the flows, to minimize the turbulence behind various bodies flowing by media, etc.

Using ANSYS CFX and ANSYS FLUENT a hydrodynamic computation of the flow inside the channel, which was used as a physical model for the tornado flow generation, was performed. The flow was carried out in twisted and rectilinear modes under several debit ranges. The flow reconstruction showed significant perturbations in the flow if debit exceeded the laminar rate (Fig. 1). The velocity and acceleration rates corresponded to the channel section areas, that is contrary to experimental results. The computational analysis of flow concluded that there is not any advantage of swirling flow mode in comparison with rectilinear one.

Fig. 1

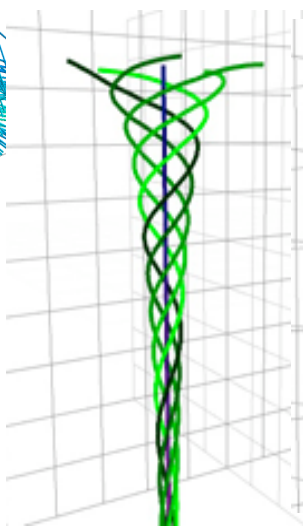

Fig. 2

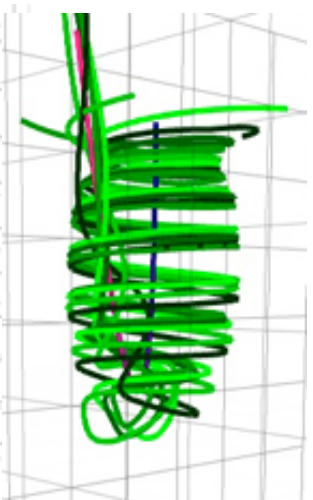

Fig. 3a

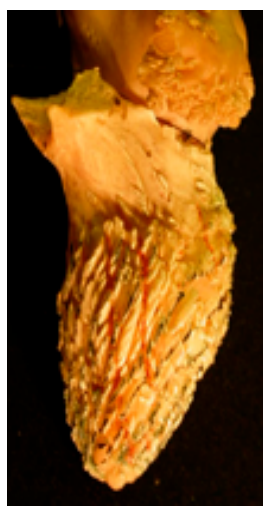

Fig. 3b

On the base of exact solution a qualitative mathematical model was worked out which traces the paths of liquid particles injected in the axis-symmetrical flow according to the directions of tornado streamlines. The model provides the setting of axis length and curvature, the setting of medium viscosity, and the setting of plots of time-dependent functions determining the swirling structure of the flow changing due to cardiac contraction: the radial velocity gradient ($C_0(t)$; jet circulation $\Gamma_0(t)$, and a distance between the particle's position in the flow and the origin point of the cylindrical coordinate system of swirling jet $Z_0(t)$).

Under the condition of rectilinear axis and constant values of functions $C_0(t)$, $\Gamma_0(t)$, and $Z_0(t)$ the streamlines reconstruction shows exactly the structure of flow generated in a channel used in experiment (Fig. 2). In the case of curved axis and dynamically changed functions $C_0(t)$, $\Gamma_0(t)$, $Z_0(t)$ it becomes possible to obtain an asymmetrical flow pattern

reproducing the shape of left ventricular cavity as it is seen on the left ventricular cast (Fig. 3a, b)

3. CONCLUSIONS

The exact solution of unsteady-state hydrodynamic equations for the class of swirling tornado-like viscous flows adequately reproduces the spatial streamlines orientation in the model channel in conformity with experimental results; matching the time-dependent parameters determining the flow configuration and the position of curvilinear flow axis allows reproducing of asymmetrical flow following the shape of the left ventricular cavity.

REFERENCES

[1] Burakovskiy V.I., et al. The Pattern of Flow in the Heart Left Ventricle (Experimental Study).Бураковский В.И., Доброва Н.Б., Кузьмина Н.Б., Агафонов А.В., Роева Л.А., Дрогайцев А.Д., Навроцкая В.В. Характер потока крови в левом желудочке сердца (экспериментальное исследование). Экспериментальная хирургия и анестезиология. 1976; №3: 13-16. [Rus.]

[2] Zakharov V.N., et al. Bio-hydromechanics of Blood Movement in the Heart and Main Vessels. Захаров В.Н., Полуэктов Л.В., Кремлев Н.И., Гунин А.Г., Самойлов В.А. Биогидромеханика движения крови в полостях сердца и магистральных сосудах (Клинико-экспериментальное исследование). Новосибирск, 1989. (31 с.).[Rus.]

[3] McDonald D. Blood Flow in Arteries. Edward Arnold Ltd. 2nd Ed. London, Arnold, 1974.

[4] Ohlsson N.-M. Left Heart and Aortic Blood Flow Patterns in the Dog. Precision Motion Analysis of Hhigh Speed (270 frames/sec.) Cine-fluorographic Recordings. Acta Raiol. 1962; suppl. 213:1-80.

[5] Rushmer R.F. Cardiovascular dynamics. 3rd edition. Philadelphia, Saunders, 1970.

[6] Kiknadze G.I., Krasnov Yu.K. Evolution of a spout-like flow of a viscous fluid. Sov. Phys. Dokl. 1986; 31(10): 799-801.

[7] Guelfand I.M., et al. The General Γ-functions, Exponents and Hypergeometrical functions. Гельфанд И.М., Граев М.И., Ретах В.С. Общие гамма-функции, экспоненты и гипергеометрические функции. Успехи математических наук, 1998; 53(1): 3-60. [Rus.]

[8] Kiknadze G.I., Gachechiladze I.A., Gorodkov A.Yu.. Self-organization of Tornado-like Jets in Flows of Gases and Liquids and the Technologies Utilizing this Phenomenon. Proc. ASME 2009 Heat Transfer Summer Conference. Jul. 19-23. 2009, San Francisco, CAL. USA HT2009-88644: p.1-14.

[9] Gorodkov A.Yu. Intraventricular Flow Analysis on the Base of the Morphometry of the Trabecular Shape and Orientation on the Inner Surface of Left Ventricle. А.Ю. Городков. Анализ структуры внутрисердечного закрученного потока крови на основании морфометрии трабекулярного рельефа левого желудочка сердца Бюлл. НЦССХ им. А.Н. Бакулева РАМН, 2003, №9, с. 61-65. [Rus.]

[10] Kiknadze G., Gorodkov A., Bogevolnov A. Intraventricular and Aortic Blood Flow Analysis and Reconstruction Using the Exact Solution of Non-stationary Hydrodynamic Equations foe the Class of Twisted Converging Viscous Flows. Proc.1st International Conference on Mathematical and Computational Biomedical Engineering – CMBE2009. June 29 – July 1, 2009, Swansea, UK. P. Nithiarasu and R. Löhner (eds).

[11] Bokerya L.A., et al. Velocity Field Analysis in the Swirling Aortic Flow Using 3D Mapping with MRI. Л.А. Бокерия, А.Ю. Городков, Д.А. Николаев, Г.И. Кикнадзе, И.А. Гачечиладзе. Анализ поля скоростей закрученного потока крови в аорте на основании 3D картирования с помощью МР-велосиметрии Бюлл. НЦССХ им. А.Н. Бакулева РАМН, 2003, №9, с. 71-74. [Rus.]

Poster Sessions

2nd International Conference on Mathematical and Computational Biomedical Engineering – CMBE2011
March 30 – April 1, 2011, Washington D.C., USA
P. Nithiarasu and R. Löhner (eds)

MODELING HEAT AND MASS TRANSFER IN RADIANT WARMER

Marek J. Rojczyk*, Ireneusz A. Szczygieł**
Institute of Thermal Technology, Silesian University of Technology
ul. Konarskiego 22, 44-100 Gliwice, Poland,
* Marek.Rojczyk@polsl.pl, ** Ireneusz.Szczygiel@polsl.pl

SUMMARY

The main object of this study is to develop 3D model of infant radiant warmer and to understand the heat transfer phenomena between an infant placed in a radiant warmer and the environment. A complete numerical simulation was done by using ANSYS software. The model was used in the Computational Fluid Dynamics (CFD) analysis with the usage of commercial code FLUENT. The analysis involves both the flow, convection and radiation heat transfer as well as the turbulence modeling. The experiments was done to validate a numerical solution. This results will be used to optimise the incubator parameters.

Key Words: *radiant warmer, premature infant, CFD, heat transfer, fluid mechanics*

1. INTRODUCTION

According to WHO (World Health Organization) the term of premature infant is a baby who was born between 22nd and 37th week of pregnancy. This term is not exact because it is hard to determine the right term of conception. The lowest chance to stay alive and grow healthy has got the babies who were born before 28th week. This group has the biggest underdevelopment indicator and mortality rate. A big Number of premature infants decreases because of decreased total number of delivery. The reason of premature childbirth strongly depends on a social and medical indicator e.g.: the mother's age, it should be lower than 16 and bigger than 35, work time more than 40 hours per week, environment pollution, genetic defects, population's oldness or sterile aspect of life. Premature infants are weaker and their organs are not well developed it strongly depends on weight which is an organ indicator because it verifies if the newborn has a chance to quick recovery Children who were premature born, usually have a low weight Chiswick in 1986 divided birth weight it 4 categories, table 1- shows that schedule [4-6].

Table 2. Birth weight categories (Chiswick M. 1986).

Category	Birth-weight (grams)
Low Birth Weight (LBW)	<2500
Very Low Birth Weight (VLBW)	<1500
Extremely Low Birth Weight (ELBW)	<1000
Incredibly Low Birth Weight (ILBW)	<800

The largest problem in neonatology is to keep them alive but it is not the only thing. Very important is 2 or 6 years control and stimulation of the premature birth children, with neurologist, respiration, oculist, etc. rehabilitation, as well. As it was mentioned above the problem with

healthy growth of a premature indents is a long process which does not finish after leaving hospital however better treatment at once delivery give more chances to quicker get the same condition as healthy children. Thanks to many researches and inventing a modern medical devices therapy can be carried out better than in the past was. One kind of a special rescue device is an incubator: closed – which is well known and open – called a radiant warmer.
The best solution is to place them in a closed incubator and to guarantee the optimal thermal conditions for development. However, in the case of free access to infants is the most important aspect, an open incubator should be used.
A purpose of this project is to build a numerical model and to understand the phenomena of heat transfer between an infant and surrounding environment in a radiant warmer in order to ensure the optimal temperature of body. The attention was paid on natural convection, radiation and conduction only and not on other aspects of the heat transfer. Other possible occurrences- like evaporation, for example are more advanced and will be developed in further work.

2. FUNDAMENTALS OF THERMAL CONTROL; RADIANT WARMER

2.1 Heat balance equation

The human normal temperature is different in case of skin measured in the stomach: 36.2-37.2°C and on the core body, measured in rectum: 36.5-37.5°C as an effect of energy balance: heat generation and losses into the environment. The heat balance equation is presented by ASHRAE [1]:

$$M - W = Q_{sk} + Q_{res} = (C + R + E_{rsw} + E_{dif}) + (C_{res} + E_{res}) \quad (1)$$

Where: M – metabolic energy production; W – mechanical work, Q_{sk} – skin heat loss; Q_{res} – heat loss through respiration; C – convective skin heat loss; R – radiative skin heat loss; E_{rsw} – evaporative skin heat loss (through sweating); E_{dif} – evaporative skin heat loss (through moisture diffusion); C_{res} – convective heat loss from respiration; E_{res} – rate of evaporate heat loss from respiration.

2.2 Infant thermoregulation

Premature infants (born before 32 week) with Very Low Birth Weight (<1500 gram) have handicapped thermoregulation system, so it cannot keep the constant temperature longer than little while, as e.g. grown-up person. Foetal exchanges 85% of heat trough placenta and only 15% through the skin which is thin and not well developed and loses the heat more rapidly that normal baby. Therefore, after delivery there should be ensured a neutral environment with neutral temperature which is not the same for every infant and depends on body weight and birth age. Generally even low fluctuation (even about 1°C) of core body temperature can be dangerous for infants' life. Consequently, closed incubators and radiant warmer are really essential [6].

2.3 Radiant warmer

Model of the open incubator used in the presented study was built on the bases of "Babytherm 8010 Radiant Warmer", constructed by Dräger Medical – Germany, which is installed in "Upper Silesian Child and Mother's Centre of Health" in Katowice [2]. Figure 1 shows the real model of the incubator. The incubator consists of two main elements: of heat production: a lamp (1) with infrared bulbs, and a bed (2) with a heating up mattress. In this project there were analysed two cases which do not use a radiator lamp but a mattress only. The full model analyses will be possible in the future because standard models of radiation which are implemented in Fluent Solver solve an diffusion radiation only, while the main part of radiator lamp in this device is an

reflector. For this case an own radiation solver is being created basing on the MONTE CARLO method [3].
The Model Design pre-processor was used to create 3D geometry (middle), and to discritise the whole domain in the considered region (right) [5]. Due to the restrictions of the hardware and computational time it is important to find a compromise between number of cells and solution accuracy. An unstructured (triangular) mesh which is comprised of 340000 elements was used.

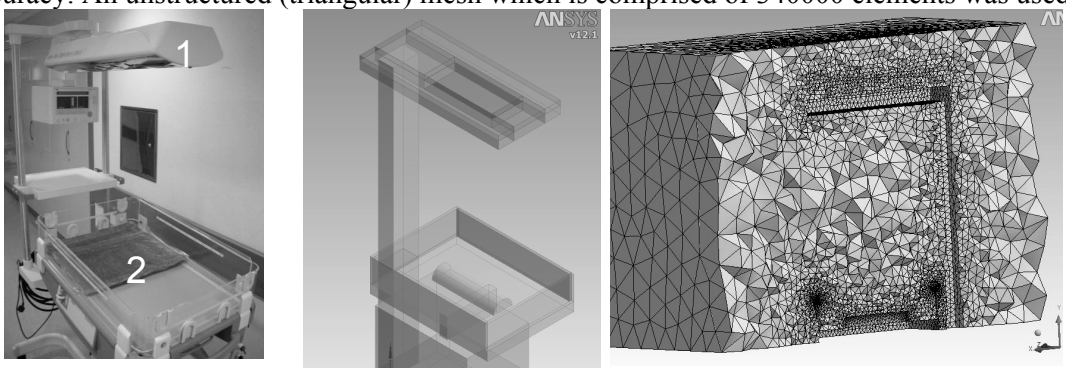

Figure 1: Real model (left), 3D Design Modeller model (middle), meshed model (right).

3. COMPUTATIONAL FLUID DYNAMICS ASPECTS

FLUENT solver was used to solve heat and flow phenomena. A 3D model was analysed. The following settings were assumed. Firstly, all of processes are considered as a steady–state. The fluid as an in-compressible ideal gas was admitted. Air is viscous and analyzed by $k-\varepsilon$, RNG (renormalization group) turbulence model. Radiation is considered by Discrete Ordinate radiation model [4] which permission describes diffusive radiation between baby skin and surrounded devices.

4. CALCULATIONS AND THEIR SOLUTIONS

The calculations were done in the case of baby who was not protected. The aim was to observe how much time it takes to obtain the hypothermia. This problem will be solved by comparing two solvers: Fluent – which modeling what is being done in the space surrounding baby and own solver (which is connected to Fluent) which can calculate a core temperature. Numerical solution is shown in Figure 2 where the temperature distribution was presented (left) and temperature distribution with vectors speed of

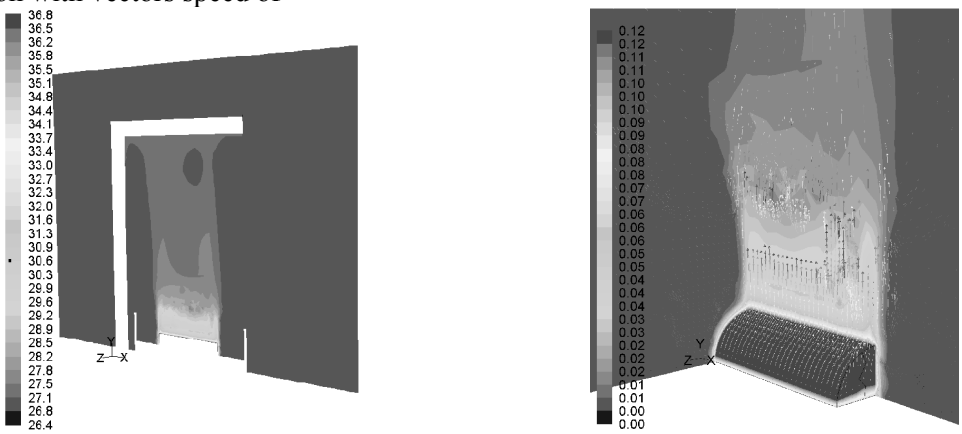

Figure 2: Temperature distribution, whole model °C (left), temperature distribution with vectors m/s (right).

air (right). In both cases the highest value of temperature and air velocity are the highest above an baby model because of natural convection. The total heat loss through convection and radiation is about 10W.
To validate above numerical simulations a laboratory stand was constructed. The part of the laboratory devices was shown on figure 3. It is a model of a baby (1), with a thermocouples (2) to monitor a temperature in a model and above where is the biggest temperature gradient is.

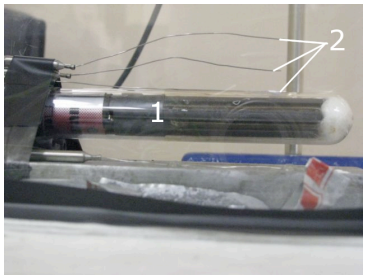

Figure 3: The model of a infant baby (1) with thermocouples (2).

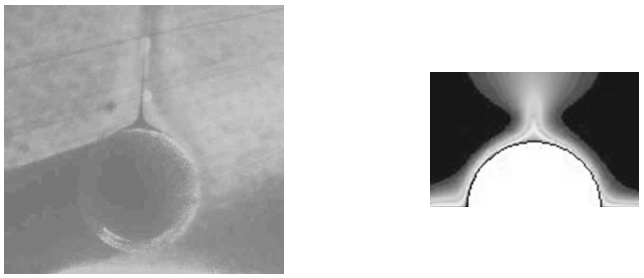

Figure 4: Flow field above infant model. An experimental solution (left), an numerical solution (right). The shine on the left hand site it figure 4 left is a reason of that the laser was on the right hand side model.

In the figure 4 (left)it is shown the experimental flow field surrounding the heater. In the figure 4 (right) a numerical solution next to the baby model. These experiments show that the temperatures are the same on the body surface as well as above it. In both cases, a duck is shown very well. It is characteristic for a natural convection. Velocity distribution was measured by using a PIV method and it is 0.06 m/s. It means it is almost the same as in the case of numerical model. The additional protection for a baby is the transparent shields in incubator which are also being modelled and tested by laboratory devices.

5. CONCLUSIONS

Radiant warmer is a very important device in every delivery room. Nowadays, devices are very modern, but there are still places which should be improved. The optimalisation of this equipment is really important but making experiments within baby is unacceptable. The CFD (Computational Fluid Dynamics) can give a proper solutions with a numerical model without exposing the premature infants. The experiments presented above prove that this numerical model can be used successfully to future researches with MONTE CARLO radiation model to modelling full incubator usage. A full model with a tool to solve core temperature will be presented in a conference.

REFERENCES

[1] ASHARE *Fundamentals Handbook.* Physiological principles, comfort and health, Atlanta 1989.
[2] Babytherm 8040/8010 radiant warmer. Instruction for use. Dräger Medical AG & Co. KGaA
[3] Fluent 6.3. User guide, Lebanon, NH, USA: Fluent Inc.; 2006
[4] Parsons K.C. *Human Thermal Environments*… Taylor & Francis, London, NY 2003
[5] Radshaw M., Rivers R., Rosenblatt D. *Born too early. Special care for your preterm baby.* Oxford University Press Inc. 1985
[6] Szczapa J. *Podstawy neonatoligii* Wydawnictwo Lekarskie PZWL, Warszawa 2008

2nd International Conference on Mathematical and Computational Biomedical Engineering – CMBE2011
March 30 – April 1, 2011, Washington D.C., USA
P. Nithiarasu and R. Löhner (eds)

ESTIMATION OF PULSE WAVE VELOCITY DERIVED FROM 2D AND 4D FLOW-SENSITIVE MAGNETIC RESONANCE IMAGING

Andrew L. Wentland*, Alex Frydrychowicz, Kevin M. Johnson*, Chris J. Francois**, Thomas M. Grist**, and Oliver Wieben***

* Department of Medical Physics, University of Wisconsin School of Medicine & Public Health, Madison, WI, USA

** Department of Radiology, University of Wisconsin School of Medicine & Public Health, Madison, WI, USA

SUMMARY

Pulse wave velocity (PWV) is a useful biomarker of vascular stiffness. We investigated the use of a 4D radially undersampled, volumetric, and dynamic flow-sensitive MRI acquisition for computing PWV. An analysis package was created that allowed for the computation of PWV from this 4D velocity encoded data set, from a series of targeted 2D velocity acquisitions, and by mapping the 2D slice locations to the 4D data set. PWV was computed in five volunteers with four methods: time-to-upstroke (TTU), time-to-peak (TTP), time-to-foot (TTF), and cross-correlation (XCorr). TTU, TTP, and XCorr calculations from the 4D data set provided results consistent with previously published studies. 2D results tended to be erroneous secondary to flow waveforms with a poorly defined systolic upstroke. 4D measurements repeated for the five volunteers demonstrated a moderate degree of reproducibility after excluding TTF calculations.

Key Words: *pulse wave velocity, phase contrast, magnetic resonance imaging, atherosclerosis*

1. INTRODUCTION

In recent years there has been an increasing body of research into magnetic resonance imaging (MRI)-based techniques for evaluating atherosclerosis. MRI provides user-independent, non-invasive measurements without the need for ionizing radiation. In addition to anatomical imaging, velocity-sensitive phase contrast (PC) MR measurements can provide velocity maps with one-, two-, and three-directional velocity encoding. From such data sets, patient-specific functional parameters to assess atherosclerotic burden can be derived, including the calculation of pulse wave velocity (PWV) [1, 2]. As arteries are stiffened by the growth of atherosclerotic plaques, the pulse wave of blood down the aorta is accelerated because of the loss of elastic recoil in the vessel [3]. The calculation of PWV is dependent on the amount of time the aortic blood flow waveform shifts for flow waveforms progressively downstream the aorta. The majority of studies on PWV have focused on calculating PWV from a series of 2D PC images along the length of the aorta [4, 5]. These flow measurements are acquired as an image series that provides maps of the through-plane velocity component during the entire cardiac cycle, prescribed perpendicular to the vessel path of interest. For PWV analysis, these methods are highly dependent on accurate cardiac triggering and the distance calculation between the imaging planes, as derived from additional volumetric scans. Other investigators have explored the use of 4D PC MRI [2] for computing PWV, but the lengthy volumetric acquisitions with Cartesian sampling usually require compromises in temporal resolution, which is vital to PWV calculations.

Over the last few years we have developed a 4D PC MRI technique, termed PC VIPR (Phase Contrast with Vastly-undersampled Isotropic Projections), that makes use of radial undersampling to significantly reduce scan time [6] while maintaining high spatial resolution. In addition to providing three-directional velocity information over the entire cardiac cycle, this PC MRI technique has been successfully used to compute pressure gradients as validated in animal studies [7] and to estimate wall shear stress [8]. Since the PC VIPR technique provides flow information over a large anatomic region, we explored the use of this approach for computing PWV measurements in the thoracic aorta. The purpose of this study was to i) introduce a user-friendly tool for the computation of PWV from both 2D and 4D PC MR data sets, to ii) assess the

feasibility of computing PWV from a radially undersampled 4D PC MR (PC VIPR) technique, and to iii) assess the reproducibility of the 4D analysis approach.

2. METHODS OF COMPUTING PWV

2.1 Data Acquisition

Five healthy volunteers (1 male; 4 females; average age = 35.8 ± 16.7 years, range = 22 - 59 years) were included in this HIPAA-compliant study, which was approved by our local IRB. Written informed consent was obtained prior to participation. Inclusion criteria were BMI<30 and no history of smoking or cardiovascular disease. 4D PC VIPR data were acquired on a 3T MR scanner (MR750, GE Healthcare, Waukesha, WI) with a 32-channel body coil (NeoCoil, Pewaukee, WI), retrospective ECG cardiac gating, adaptive respiratory gating (50% efficiency), a 1.25 mm^3 isotropic spatial resolution, 26-34 times frames/cardiac cycle (32-33.5ms), and a scan time of ~11.5 minutes. 2D PC images were acquired in the ascending aorta, aortic arch, and in the proximal and supra-diaphragmatic descending aorta in repeated breath holds. Scan parameters included: a temporal resolution of 63 ± 13 time frames (ave. ~10.7ms), prospective ECG cardiac gating, a spatial resolution of 1.6x1.6mm^2, and a slice thickness of 7mm.

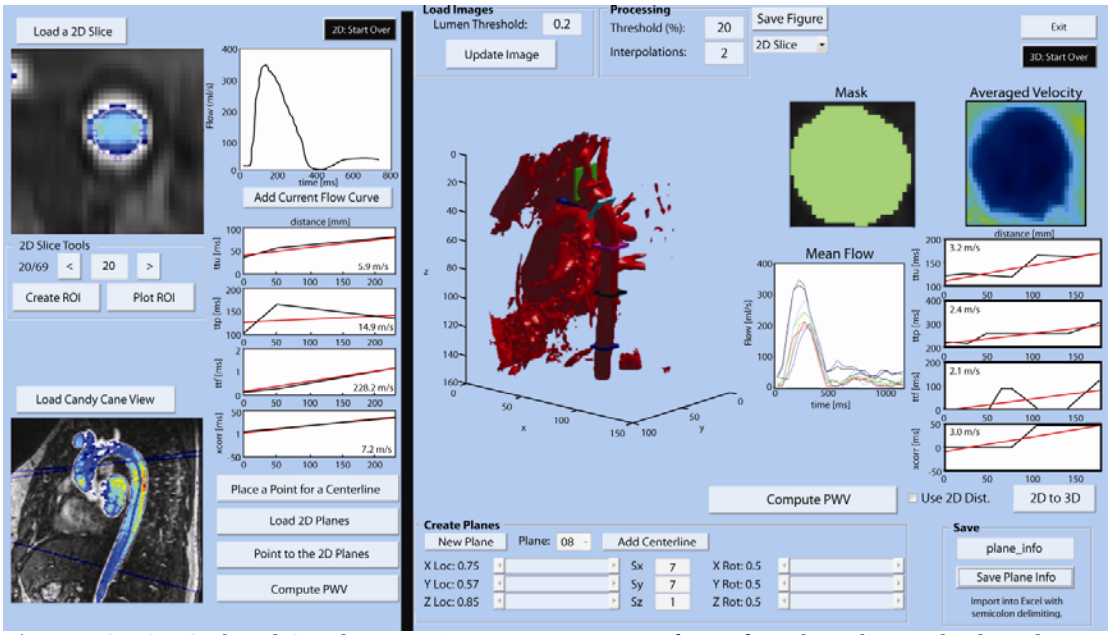

Figure 1. *A MATLAB-based GUI demonstrating 2D measurements of PWV from three slices and independent 4D measurements of PWV from 8 planes along the aorta.*

2.2 Graphical User Interface Development

An interactive graphical user interface (GUI) was implemented in MATLAB (version 7.9, The MathWorks, Cambridge, MA), as shown in Figure 1. The tool allowed for the computation of PWV from 2D and 4D data independently, and also for the correlation of 2D and 4D data.

The workflow for the analysis of 2D PC MR data is as follows: a time series is first loaded and displayed in the GUI. A region of interest (ROI) is placed on any time frame in the 2D series and copied to the other time frames. A flow curve is generated from the ROI by velocity integration over the selected area. After this flow curve is loaded to memory, the next 2D series is loaded from a different anatomical position. Once the flow curves from all 2D series are evaluated, a 'candy-cane' view of the aorta derived from a 3D angiogram is loaded and used to estimate points along the vessel center. From these points a cubic spline interpolant is generated to derive a centerline along the aorta. The orientation of each 2D slice is mapped to the 'candy-cane' view; the intersection between each 2D plane with the centerline is identified and used to calculate the distance between planes along the centerline.

The workflow for the analysis of 4D data is as follows: a surface-shaded 3D display of the aorta is generated from the complex difference information. 2D planes are placed interactively and

obliquely to be perpendicular to the vessel orientation at several points along the aorta. For each plane, the centroid is computed. The coordinates of each centroid are used to compute a cubic spline interpolant along the vessel lumen that is then used to calculate the distance between each of the planes.

The planes from the 2D measurements can also be loaded into the GUI to synthesize planes from the 4D data at equivalent orientations. Since MRI images can be prescribed in any plane, the 2D slices were acquired obliquely to the vessel; as such, the same orientation of each 2D plane was recreated in the 4D data set. The distance between planes was computed from the 'candy-cane' view, since the 3-4 planes used in the 2D analysis would be insufficient for defining an appropriate spline three-dimensionally.

2.3 PWV Algorithms

Four methods of computing PWV were used: time-to-upstroke (TTU), time-to-peak (TTP), time-to-foot (TTF), and cross-correlation (XCorr), with the latter three previously described by [2, 9] (Figure 2).

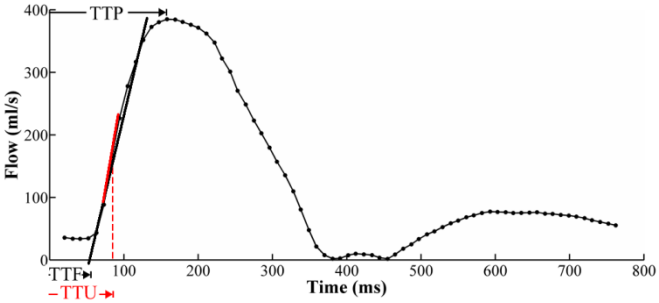

Figure 2. *Blood flow in the aorta demonstrating the time-to-peak (TTP), time-to-foot (TTF), and time-to-upstroke (TTU).*

The TTP was identified as the time point of the global maximum flow rate for each of the flow waveforms. TTF was identified as the intersection of the abscissa with a line fitted to the data points along the upstroke between 20 and 80% of the maximum flow rate. XCorr was computed as the amount of time each flow waveform had to shift relative to the initial flow waveform for maximum correlation, computed as

$$(f \star g)[n] = \sum_{m=-\infty}^{\infty} f^*[m]g[n+m]$$

Finally, TTU was computed from the second-order finite difference of the flow waveform as:

$$f'' \approx \frac{f[n+h] - 2f[n] + f[n-h]}{h^2}$$

```
flow_padded = [0 flow_points 0];
second_der = (-flow_padded(1:end-2) + 2*flow_padded(2:end-1) -flow_padded(3:end))/Δt;
```

where h = Δt = temporal resolution or frame # and f[n] = `flow_points` = the flow waveform.

The maximum rate of change along the upstroke of the flow waveform was identified as the zero crossing of the second derivative of the flow waveform. The time point corresponding to this zero-crossing was recorded for computing TTU.

As shown in Figure 1, the distance between each plane was plotted versus the TTU, TTP, TTF, and XCorr time points. The PWV for each method was computed as the inverse slope of a line fitted to these data [2].

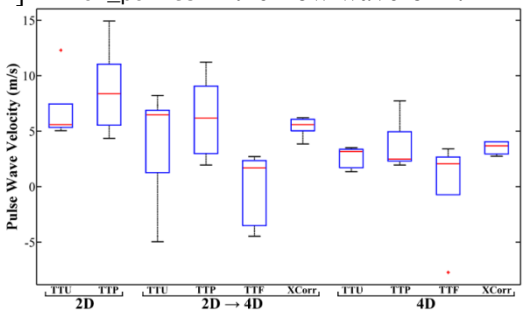

Figure 3. *Box plots of PWV measurements for five volunteers as calculated from 2D PC slices, with the 2D slices mapped to the 4D PC VIPR data set, and with the 4D data independently.*

3. RESULTS & DISCUSSION

3.1 PWV Calculations in Five Volunteers

PWV was computed for five volunteers using the 2D approach, the 4D approach, and the 2D → 4D comparison (Figure 3). Best agreement with data typically described in the literature [2] was found for 4D TTU, TTP, and XCorr and 2D → 4D XCorr measurements. For the 4D data, the XCorr method was the least variable, whereas the TTU method was the least variable for the 2D data set. 4D independent measurements were less variable than measurements acquired from the 2D → 4D approach. 2D TTF, 2D XCorr, and 4D TTF revealed non-physiological results. This was of special note since 2D scans are widely used for PWV calculation and can be considered a

reference standard. The erroneous TTF and XCorr results are likely due to the lack of measurements at the beginning of the cardiac cycle for planes close to the heart. Time frames from our prospectively gated 2D PC acquisition often began during the upstroke of the flow waveform, especially in the ascending aorta. As a result, a foot could not be accurately defined; since parts of the characteristic waveform were missing for planes in the ascending aorta, and more completely defined for planes downstream, cross-correlation was often erroneous.

3.2 4D Reproducibility Calculations

4D independent measurements of PWV were repeated for the five volunteers (Table 1) to assess the dependence of the measurements on plane placement and hence slight variations in flow waveforms. There was no statistical difference between the two sets of measurements as evaluated with a Student's t-test ($p = 0.61$). A Pearson's correlation coefficient was computed for evaluating the reproducibility of the data. The correlation of the raw data was not significant ($rho = 0.01$; $p = 0.97$). A lack of time points at the beginning of the flow waveform led to erroneous foot calculations and therefore sporadic TTF measurements. Calculating the Pearson correlation coefficient from the TTU, TTP, and XCorr data only led to better correlation, although this was not quite statistically significant ($rho = 0.50$, $p = 0.059$). The TTU, TTP, and XCorr measurements were more robust and may prove to be more reproducible as we continue to recruit subjects to our study.

Table 1. *Average ± standard deviation of 4D PWV measurements for five volunteers. Measurements were repeated for comparison.*

	PWV (m/s)	
	4D #1	4D #2
TTU	2.66 ± 0.98	3.06 ± 0.70
TTP	3.74 ± 2.35	4.74 ± 2.45
TTF	0.38 ± 4.56	5.20 ± 6.28
XCorr	3.54 ± 0.61	4.16 ± 0.84

4. CONCLUSIONS

We successfully demonstrated the feasability of estimating PWV measurements in vivo from a 4D PC VIPR acquisition using a MATLAB-based tool specifically designed for analyzing 2D and 4D data sets. For most methods of computation, our PWV measurements in healthy volunteers were similar to previously reported PWV measurements [2, 5]. The radial sampling scheme employed in our 4D acquisition allowed for higher temporal resolution than previously publised 4D techniques [2] with a clinically feasible scan time (~11.5 min). Although the PC VIPR technique provided inferior temporal resolution to the 2D acquisition, the PC VIPR acquisition provided PWV measurements that were less variable than measurements obtained from the 2D PC slices. Not all methods of computing PWV were compatible with our data sets—producing particularly erroneous results with the TTF method. In future work we will investigate a retrospectively gated 2D acquisition that is not limited by such trigger delays. In order to complete such an acquistion in a breathhold, we will explore 2D radially undersampled acquisitions. Additionally, we are actively recruiting more subjects to increase the statistical power of our results.

REFERENCES

[1] S. Laurent, S. Katsahian, C. Fassot, A. I. Tropeano, I. Gautier, B. Laloux, and P. Boutouyrie, "Aortic stiffness is an independent predictor of fatal stroke in essential hypertension," *Stroke*, vol. 34, pp. 1203-6, 2003.

[2] M. Markl, W. Wallis, S. Brendecke, J. Simon, A. Frydrychowicz, and A. Harloff, "Estimation of global aortic pulse wave velocity by flow-sensitive 4D MRI," *Magn Reson Med*, vol. 63, pp. 1575-82.

[3] M. Bock, L. R. Schad, E. Muller, and W. J. Lorenz, "Pulsewave velocity measurement using a new real-time MR-method," *Magn Reson Imaging*, vol. 13, pp. 21-9, 1995.

[4] B. D. Bolster, Jr., E. Atalar, C. J. Hardy, and E. R. McVeigh, "Accuracy of arterial pulse-wave velocity measurement using MR," *J Magn Reson Imaging*, vol. 8, pp. 878-88, 1998.

[5] H. B. Grotenhuis, J. J. Westenberg, P. Steendijk, R. J. van der Geest, J. Ottenkamp, J. J. Bax, J. W. Jukema, and A. de Roos, "Validation and reproducibility of aortic pulse wave velocity as assessed with velocity-encoded MRI," *J Magn Reson Imaging*, vol. 30, pp. 521-6, 2009.

[6] T. Gu, F. R. Korosec, W. F. Block, S. B. Fain, Q. Turk, D. Lum, Y. Zhou, T. M. Grist, V. Haughton, and C. A. Mistretta, "PC VIPR: a high-speed 3D phase-contrast method for flow quantification and high-resolution angiography," *AJNR Am J Neuroradiol*, vol. 26, pp. 743-9, 2005.

[7] D. P. Lum, K. M. Johnson, R. K. Paul, A. S. Turk, D. W. Consigny, J. R. Grinde, C. A. Mistretta, and T. M. Grist, "Transstenotic pressure gradients: measurement in swine--retrospectively ECG-gated 3D phase-contrast MR angiography versus endovascular pressure-sensing guidewires," *Radiology*, vol. 245, pp. 751-60, 2007.

[8] E. T. Bieging, B. R. Landgraf, K. M. Johnson, A. Frydrychowicz, A. L. Wentland, O. Wieben, and C. J. Francois, "In vivo 3D Magnetic Resonance Wall Shear Stress Estimation in Ascending Aortic Aneurysms," *Journal of Magnetic Resonance Imaging*, 2010.

[9] E. H. Ibrahim, K. R. Johnson, J. M. Shaffer, and R. D. White, "Evaluation of Different Techniques for Measuring Pulse Wave Velocity using 3 Tesla MRI," presented at ISMRM, Stockholm, Sweden, 2010.

2nd International Conference on Mathematical and Computational Biomedical Engineering – CMBE2011
March 30 – April 1, 2011, Washington D.C., USA
P. Nithiarasu and R. Löhner (eds)

DIGITAL SIGNAL CONTROLLER DM 330011 BASED REAL TIME SYSTEM FOR DETECTION OF ECG SIGNAL

D. Bansal*, M. Khan and A.K. Salhan*****

* Manav Rachna International University, Faridabad, Haryana, India,
dipali.bansal@yahoo.co.in
** Jamia Millia Islamia (A Central University), New Delhi, India.
khanmunna@yahoo.com
***Defence Institute of Physiology and Allied Sciences, DRDO, Delhi, India
ashoksalhan@yahoo.com

SUMMARY

Commercialization of digital signal controllers (DSC) allows development of compact and noise immune system for ECG detection. Proprietary amplifier and filter system is however, required to acquire them and the output is generally analyzed offline using LCD displays. Inexpensive dspic DSC DM330011 from microchip is used in this paper for detection of ECG. Analog output of developed amplifier and notch filter system is fed to the DSC kit, processed, interfaced to computer and viewed on simulated oscilloscope. Developed MATLAB algorithm give digitally filtered and peak detected ECG resulting in a relatively inexpensive stand alone solution to real time medical monitoring.

Key Words: *Digital signal controller, ECG, MATLAB, Peak detection, Real time.*

1. INTRODUCTION

Major modernization in bio-signal detection and processing are viable in the key areas such as compaction of sizes, low power consumption, enhanced efficiency and reliability, additional memory, quick response and lengthened battery performance. This was primarily handled through micro controllers which has gradually being substituted by Digital Signal Processors (DSP) based controls. Digital Signal Processors in combination with Microcontrollers make Digital Signal controllers (DSC) which allow computerized automatic investigation of human bio-signals and facilitate improved computational speeds, simple acquisition and interfacing arrangement, capacity to work on vast data and development of stand alone compact and cost effective system. Extensive work has been done in the area of ECG signal detection and analysis using DSP processors and micro controllers developed by Texas Instruments (T.I) that result in a real time system on chip solution [1], [2], [3], [4], [11]. Further signal analysis and filtering is done using Wavelets [5], [8], Template matching methods [6] or Correlation technique [12] on these embedded designs that enable portable monitoring [9] and spectral analysis [10].

Many other manufacturers like Hyperstone [13], [15], Motorola [14], STMicroelectronics [16] etc also allow the fast execution of algorithm for bio-signal processing based on DSP systems. However, for acquiring and viewing the bio-signal there is an additional requirement of ADC, filters, commercial amplifiers and LCD displays which make the entire arrangement expensive and complex [7]. This paper implements the development of a Microchip dsPIC digital signal controller DM330011 and computer based relatively cost effective real time system for acquisition and analysis of ECG waveform. The project work includes self developed amplifier, 50 hertz notch filter, digital filter and peak detection algorithm in MATLAB.

2. MAIN BODY

Experimental set up for dsPIC DSC based real time system for acquisition of ECG signal on a computer is shown in Figure 1 and its block diagram is sketched in Figure 2. Front end of the measurement system consists of Ag-AgCl sensors, amplifier system, hardware band-pass filter, fifty hertz notch filter, Digital signal controller and a personal computer. The amplifier and filter system is already tested using TL-084C differential amplifiers [18] and notch filter using 741 op-amps. MPLAB starter kit dsPIC digital signal controller DM 330011 board is used for continuous monitoring and automatic analysis of ECG. The starter kit has features of dsPIC 33FJ 256 GP 506 and is a general purpose fixed point Digital Signal Controller (DSC) used for speech processing. Filtered analog output signal obtained from the front end of ECG amplifier system is routed through the line-in socket to the 12 bit analog to digital converter (ADC) module in the on board kit for software processing, ruling out the need of an extra ADC. The incoming bio-signal is amplified and sent to the ADC module on the dsPIC33F device through an anti-aliasing filter [19].

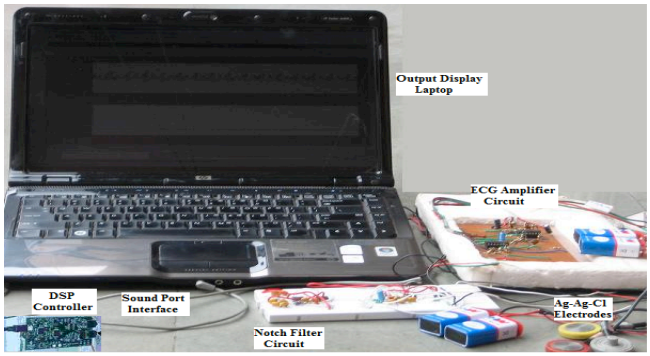

Fig. 1. Experimental set up for dsPIC DSC based System for acquisition of ECG Signals on a Computer

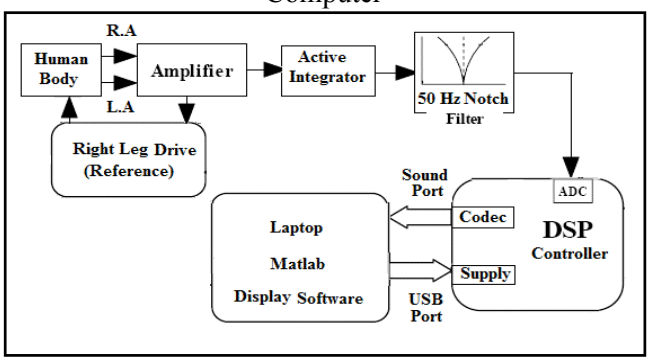

Fig. 2. Block diagram of DSC based Real Time System for acquisition of ECG Signal on a Computer

The dsPIC33F device on the starter kit is pre-programmed with a Record and Playback application that uses the audio codec to play back the recorded signal [19]. The processed signal finally appears in an analog form at the output port after passing through the Codec in the kit and feeds the output amplifier after converting this digital signal to analog. This output is interfaced directly to the sound port of the PC and the result is viewed on the virtual oscilloscope programmed in MATLAB. The Zero phase band-pass filter and peak detection algorithm tested and implemented in MATLAB are verified in the development software tool provided by dsPIC.

Microcontroller based systems used earlier lack the complicated processing power requirements but the DSP kits used these days for medical monitoring have sufficient power for long-lasting use [20]. The design implemented in this work ensures sophisticated real time processing of bio-signals using MicroChip's DSC kits that requires less power, is compact in size and is cost effective. Figure 3 shows snap shot of filtered ECG Signal as recorded in DSC DM330011 displayed in MATLAB virtual oscilloscope and Figure 4 is the snap shot of peak detected ECG Signal recorded on DSC DM330011. Advantage of using DSC over usual microcontrollers is that DSC uses Harvard architecture having separate memories for data and instructions whereas others use the Von Neumann architecture that uses a single memory to hold both data and instructions, thus providing higher speed [21]. For acquiring the bio-signal especially ECG, commercially available amplifiers and ADC are utilized which make the entire system cumbersome and expensive. MPLAB's dsPIC digital signal controller DM 330011 kit used in this project has on-board ADC which enables reduction in the complexity of the medical monitors. The amplifier system required are custom made, have already been tested on a MATLAB based GUI and are relatively cost effective.

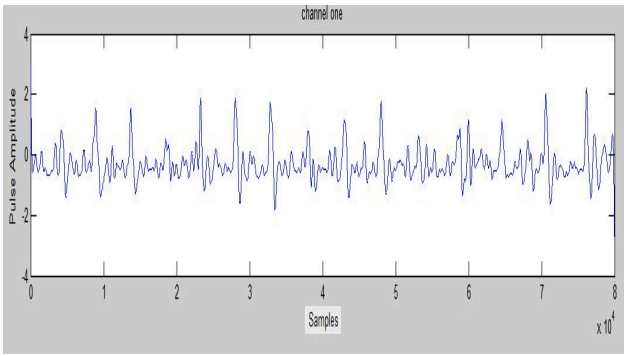

Fig. 3. Filtered ECG Signal recorded in DM330011 displayed in MATLAB virtual oscilloscope

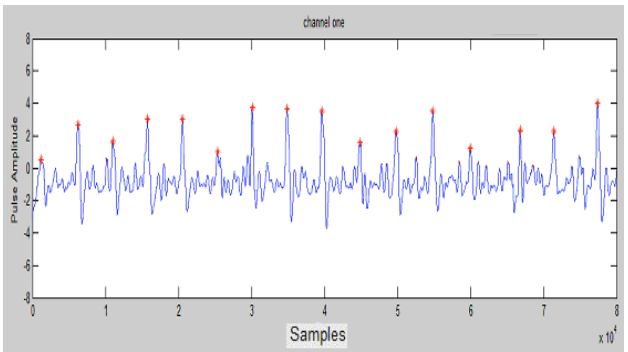

Fig. 4. Peak detected ECG Signal recorded in DM330011 displayed in MATLAB virtual oscilloscope

3. CONCLUSIONS

High cost of portable medical monitors limits their wider use by local masses. A low-cost, embedded solution can help overcome this problem. The cost of a personal medical monitor can be reduced through use of new technologies which use displaying powers of a computer and microcontroller and digital signal processing as an integrated system. The arrangement discussed in this paper results in an inexpensive stand alone computer based solution to real time implementation of medical monitor for acquiring and analyzing ECG waveform. The embedded system can be further programmed to calculate the heart rate, heart rate variability and cardiac output. The algorithm tested in MATLAB can further be targeted to the DSC to obtain an embedded solution to medical monitoring.

REFERENCES

[1] M. Raju. Heart-Rate and EKG Monitor Using the MSP430FG439, Texas Instruments Application Report, SLAA280A–Revised September 2007.

[2] Y. Yang, D. Yin & R. Freyer. Development of a digital signal processor-based new 12-lead synchronization electrocardiogram automatic analysis system, Comput Methods Programs Biomed, 69, 1, 2002, pp. 57-63.

[3] D. Pani, S. Argiolas and L. Raffo. A DSP Algorithm and System for Real-Time Fetal ECG Extraction, Computers in Cardiology, 2008, 35, pp. 1065−1068.

[4] J. S. Sahambi, S. N. Tandon and R. K. P. Bhatt. DSP based enhanced data acquisition system, Biomed Sci Instrum., 1995, 31, pp. 247-250.

[5] J. S. Sahambi, S. N. Tandon, R. K. P. Bhatt, An Automated Approach to Beat by Beat QT- Interval Analysis, IEEE Engineering in Medicine and Biology, May/June 2000, pp. 97-101.

[6] S. Mohammad, Z. Lim, Y. Lin, A. Sani, K. Zanjani, M. Paracha & J. Jenkins. Real-Time ECG Analysis Using a TI TMSC54x Digital Signal Processing Chip, Computers in Cardiology, 2003, 30, pp. 541−544.

[7] C. S. Ho, H. T. Wu, D. M. Lu, C. H. Lin, S. H. Ho and K. H. Chou. Development of a Measurement System for Electrocardiograms and Its Application to Remote Home Care, Proceedings of 2005 CACS Automatic Control Conference, Tainan, Nov 18-19, 2005.

[8] Lin Qi, Y. Zhang and J. Bai. Development of Portable ECG Monitor On Low-cost DSP, IFMBE Proceedings, Vol. 14/6, JC 27, pp. 4058-62.

[9] E. Jovanov, P. Gelabert, R. Adhami, B. Wheelock and R. Adams. Real Time Holter Monitoring of Biomedical Signals, DSP Technology and Education Conference DSPS'99, August 4-6, 1999, Houston, Texas.

[10] D. Raskovic, E. Jovanov, T. Martin, S. Hanief and P. Gelabert. Energy Profiling of DSP Applications, A Case Study of an Intelligent ECG Monitor, Proc. of DSPS fest 2000, Houston, Texas, Aug. 2-4, 2000.

[11] S. Hoferichter, B. U. Köhler, C. Hennig and R. Orglmeister, On-Line QRS-Detection Using the TMS320C6701, Proc. of 3rd European DSP Education & Research Conference, Paris, 2000.

[12] A. C. Buttfield and M. P. Bolton. Real time measurement of RR intervals using a digital signal processor, J. Med. Eng. Technol., 29, 1, 2005, pp. 8-13.

[13] S. Kondra, C. Yew, F. Ahmad and U. G. Hofmann. Prototype of a Patient Monitoring Device based on an embedded RISC/DSP system, ICMP 2005/BMT Conference, Nuremberg, Germany, September 2005.

[14] F. Iacob and C. Popescu. A DSP based processing system for Electrocardiographic signals, http://www.ee.bilkent.edu.tr/~signal/BCSP

[15] M. C. Chang, Z. X. Lin, C. W. Chang, H. L. Chan & W. S. Feng. Design of a System-on-Chip for ECG signal processing, 2004 IEEE Asia-Pacific Conference on Circuits & Systems, December 6-9, 2004, pp. 441-444.

[16] I. A. Khatib, F. Poletti, D. Bertozzi, L. Benini et al, A Multiprocessor System-on-Chip for Real-Time Biomedical Monitoring and Analysis: Architectural Design Space Exploration, 43rd Design Automation Conference (DAC 06).

[17] BDTI's Pocket Guide to Processing Engines for Embedded Applications. http://www.BDTI.com/benchmarks.html

[18] D. Bansal, M. Khan & A. K. Salhan. A computer based wireless system for online acquisition, monitoring and digital processing of ECG waveforms, Journal of Computers in Biology & Medicine,39:4, Jan 2009, 361-367.

[19] Microchip. MPLAB Starter kit for dsPIC Digital Signal Controllers. User's guide. www.microchip.com.

[20]D. Raskovic, E. Jovanov and K. Kavi. Hierarchical Digital Signal Processing, ISPACS 2001, Nashville, TN, Nov. 20-23, 2001.

[21] Processor Comparison: Texas Instruments C6000 DSP and Motorola G4 PowerPC, www.pentek.com

2nd International Conference on Mathematical and Computational Biomedical Engineering – CMBE2011
March 30 – April 1, 2011, Washington D.C., USA
P. Nithiarasu and R. Löhner (eds)

CONTROLLABLE SEPARATION OF SSDNA MOLECULES BY A POLARIZED CNT MEMBRANE SUBJECTED TO A PULSED ELECTRIC FIELD

Y.H. Xie and A.K. Soh
Department of Mechanical Engineering, The University of Hong Kong, Pokfulam Road, Hong Kong

SUMMARY

In this manuscript, molecular dynamics simulations have been carried out to study controllable separation of ssDNA molecules through polarized CNT membrane subjected to pulsed electric field. Through adjusting the periodicity of the applied pulsed field, some DNA oligonucleotides can be transported across nanopore, while other strands were restricted inside nanopore owing to the continuous switching of direction of the pulsed electric field. Besides, a sufficiently self-diffusion process was important to prevent the translocated DNA polymer from being driven back inside nanotube.

Keywords: *DNA molecules, pulsed electric field, CNT membrane.*

1. INTRODUCTION

In recent years, carbon nanotubes (CNTs) exhibit great promise for serving as nanometer-scale channels or pores in view of their structural simplicity and robustness. These nanostructures have been regarded as good candidates for controllable transport of water molecules, ionic flow, protons and polymers [1, 2]. For example, Gao et al. [2] reported the dynamic processes of spontaneously inserting DNA fragments inside the hollow cavity of nanotubes, and the critical size of CNT allowing the occurrence of these encapsulation phenomena was determined.

2. MODELING AND SIMULATION

Figure 1 presents the schematic of a simulated CNTs-DNA system. The proposed bio-nano-system is composed of four hexagonally packed zigzag carbon nanotube bundles; a homogeneous single-stranded DNA (ssDNA) molecule varied in terms of length and composition, e.g. purine nucleotides: adenine (A) and guanine (G), and pyrimidines nucleotides: thymine (T) and cytosine (C); water as an explicit solvent; and additional sodium ions for electrically neutralizing the whole system. Four individual nanotubes, with a hexagonal lattice in the x-y plane and the tube axis aligned with the z axis, are assembled by prescribing the tube-to-tube interval of the hexagonally packed arrays as 0.34nm. The DNA strand is initially aligned with the axis of one of the four assembled nanotubes, and situated at the entrance of the pore such that the nearest axial distance between the DNA and CNT atoms is 0.2nm. In most simulations, the ssDNA molecules with diameter of approximately 1.3nm are electrophoretically driven inside zigzag (20, 0) nanopores of 1.56nm in diameter. This setup is based on the expectation that ssDNA would be straightened from its randomly coiled native conformation during its permeation, indicating that the ssDNA chain must enter and exit the nanopore in a single-file or one-dimensional fashion.

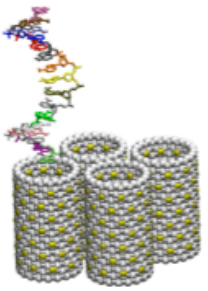

Fig. 1. A proposed nanotube membrane-DNA model. The DNA strand is initially placed at the entrance of one of the four packed nanotubes with a separation of 0.2nm.

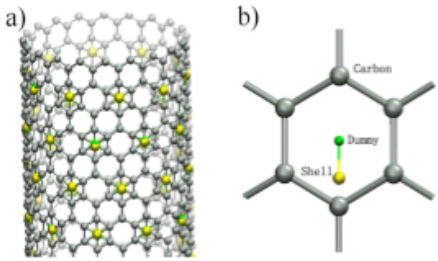

Fig. 2. The schematics of a shell CNT model. (a) Symmetrical arrangement of a polarized CNT with the conjugation of shell-dummy pairs; (b) A polarizable hexagonal cell with a shell particle coupled to a dummy atom via a spring-like connection.

The polarization of zigzag (20, 0) nanotube can be achieved via the motion of a network of negatively charged shell particles, which assists the charge redistribution in this tube, and physically reflects the electronic degrees of freedom in response to an external electric field. From a viewpoint of modeling, a polarizable carbon nanotube is constructed by periodically distributing a number of shell particles within this tube (Figure 2a); each shell particle is located near the center of a hexagonal cell and surrounded by six carbon atoms positioned at the vertices of the cell (Figure 2b). The CNT atom involved in polarization is assigned a charge of $q_C = 0.05e$, and the shell particle is given a charge of $q_s = -0.3e$. For zigzag (20, 0) SWNTs, the value of the axial polarizability per hexagonal cell is calculated to be 0.129nm^3. In addition, a new term called polarization potential energy, i.e. $U_{pol} = \frac{1}{2}\sum_{i=1}^{N}\frac{p_i^{ind}\cdot p_i^{ind}}{4\pi\varepsilon_0\alpha_{zz}}$, is incorporated into the classical force field for carbon nanotubes, in order to account for the response of nanotubes to the external field, where ε_0 is the vacuum dielectric constant; α_{zz} is the axial polarizability of one individual unit; p_i^{ind} denotes the electric field-induced dipole moment per hexagonal cell.

Molecular dynamics simulations are carried out by using a versatile package called GROMACS [3] to implement a united-atomic force field GROMACS87 in combination with nanotube polarization. A rhombic-shaped box, with edges approximately tangent to the outer wall of the nanotubes, is used to build up the simulation cell, and an infinite nanotube membrane can be obtained by defining periodic boundary conditions (PBC). The length of the box edge in the *x*-*y* plane is set as ~3.9nm with interior angles equal to 60° or 120°, while the box dimension in *z* direction is chosen according to the lengths of CNT and ssDNA molecules. The SPC216 [4] model is used to deal with water solvent. The long-range electrostatic interactions can be precisely evaluated by the Particle-Mesh Ewald (PME) treatment [5]. The LINCS algorithm [6] is employed to integrate Newton's equations of motion by adopting a time-step of 1fs. After a 100ps equilibration in the *NPT* ensemble, which is of necessity to ensure a constant volume of system, a typical *NVT* ensemble is implemented in the simulations upon the imposition of external electric field. A low temperature of 1K with time constant 1fs for coupling is assigned to the shell-dummy pairs, and the values of T = 300K and 0.1ps is applied to other atoms. The electric field applied in our simulations is at least 0.3V/nm, which is an order higher than the field strengths adopted in experiments. However, a strong enough electric field is compulsory to promote such a nanometer-scale translocation process within the nanosecond timescale.

Prior to separating biological molecules of different lengths and compositions by an alternating current (AC) or pulsed electric field, it is desirable to characterize the dependence of the translocation time τ_{trans} on the DNA length. In principle, for the case where a DNA molecule of length $L_{DNA} = Na$ is electric field-driven through a

nanopore of length $L_{CNT} = Ma$ with M and N being the number of monomers and $a = 0.4$nm being the base-to-base distance along the DNA polymer, the resulting translocation time exhibits a nonlinear dependence on the DNA length when $N < M$. In particular, the ssDNA polymers of different lengths in the case of $N < M$ usually spend the proximate translocation time in transporting through nanopore, which however becomes proportionally increased for larger N. This discipline was also demonstrated by both the experimental observations [7] and the theoretical analysis [8].

Due to our limited computational resource, which only allow simulations of nanoseconds in timescale and nanometers in dimension, a 2.4nm-thick zigzag (26, 0) nanotube membrane is designed to transport a homogeneous nucleotides of 8, 16, 24 cytosine (C8, C16, C24) or 16 adenine bases (A16). Further separation of these ssDNA fragments of different sizes or compositions can be accomplished by imposing a pulsed AC electric field across the system along z direction, as shown in Figure 3a and b. For a clear visualization, these biological molecules are aggregated at the entrance of an infinite nanotube membrane. In the actual MD simulation, each bio-nano-system is only composed of one four-packed carbon nanotubes and a single DNA strand.

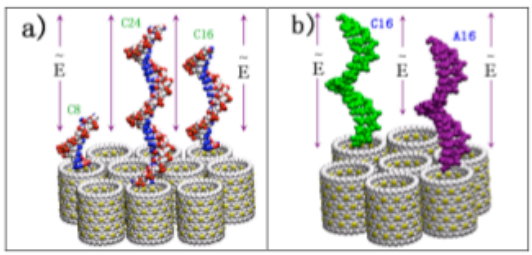

Fig. 1. A designed polarizable carbon nanotube membrane used to transport or separate ssDNA molecules of (a) different lengths; (b) different compositions, under an adjustable alternating current or pulsed electric field.

To estimate the first passage time of an individual ssDNA molecule, a direct current (DC) electric field of strength $E_0 = 0.5$V/nm is applied to each of the simulated systems containing C8, C16, C24 or A16. Figure 4 displays an obvious increase of the first translocation time as a function of the DNA length in the case that the ssDNA oligonucleotides are larger than the selected nanopore length. Note that the difference of N value between two neighboring ssDNA molecules, such as C8 and C16, C16 and C24, is set to be appropriately large, in order to achieve an obvious difference in translocation time. In fact, the ssDNA molecules adopted in experiments [9] mostly consisted of hundreds or thousands of nucleotides, and the length difference between two neighboring DNA polymers was at least tens of bases. Both of these two assumptions were made to ensure a significant difference in the translocation time of the simulated ssDNA molecules, which was necessary for the sake of the later DNA separation process. The unique feature of this separation technique is the use of an adjustable pulsed electric field to control driving of one specific DNA fragment through nanopore for each set of translocation events, with other molecules being kept inside nanopore or back to the *cis* side of nanopore.

To illustrate the relative position of ssDNA molecule with respect to nanopore, a distance from the last atom of ssDNA to the exit side of CNT is denoted by dz, as shown in Figure 5. This variable also gives an efficient judgment on whether ssDNA molecules have been driven outside nanopore, for example, $dz \leq 0$ indicates that the last atom of ssDNA fragment is leaving the hollow cavity of nanotube. For each separation round, one specific DNA oligonucleotide should be translocated, and it would be better that the permeation of this specific ssDNA molecule be achieved within the first half of the periodicity. Otherwise, the initially helical conformations of DNA oligonucleotides would be significantly altered via several periodicities of pulsed electric field. Due to the unpredicted adhesions of different DNA polymers to the sidewall of nanotubes, the uncertain conformations seriously hinder their motion inside nanopore, and ultimately encumber the prescribed separation process.

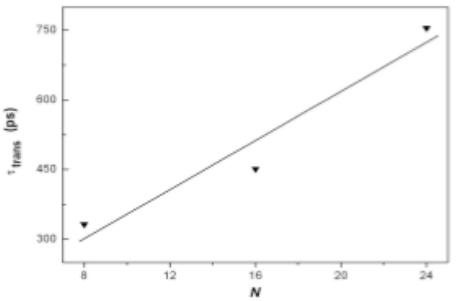

Fig. 2. The first translocation time of ssDNA molecules as a function of their length in the case where all the DNA strands are longer than the simulated nanotube membrane.

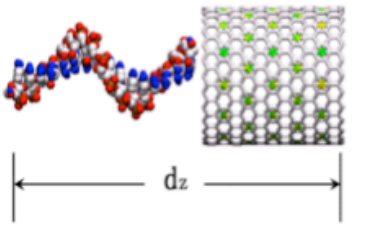

Fig. 5. Axial distance from the last atom of DNA strand to the exit side of nanotube.

3. CONCLUSION

A pulsed electric field-induced translocation and separation technique has been developed based on MD simulations. The difference in the passage time for ssDNA molecules of different sizes or compositions becomes a key issue to accomplish a successful separation. Through adjusting the periodicity of the applied pulsed field, some DNA oligonucleotides can be transported across nanopore, while other strands are restricted inside nanopore owing to the continuous switching of direction of the pulsed electric field. Besides, a sufficiently self-diffusion process is important to prevent the translocated DNA polymer from being driven back inside nanotube.

REFERENCES

[1] Joseph S et al. (2003) Electrolytic transport in modified carbon nanotubes. Nano Lett. 3:1399-1403

[2] Gao H, Kong Y, Cui D (2003) Spontaneous insertion of DNA oligonucleotides into carbon nanotubes. Nano Lett. 3: 471-473

[3] Van der Spoel et al. (2001). Gromacs User Manual, version 3.2. Groningen, Netherlands

[4] Teleman O, Jonsson B, Engstrom S (1987) A molecular-dynamics simulation of a water model with intramolecular degrees of freedom. Mol. Phys. 60:193-203

[5] Darden T, York D, Pedersen L (1993) Particle mesh ewald – an n.log(n) method for ewald sums in large systems. J. Chem. Phys. 98: 10089-10092

[6] Hess B et al. (1997) LINCS: A linear constraint solver for molecular simulations. J. Comput. Chem. 18:1463-1472

[7] Meller A, Nivon L, Branton D (2001) Voltage-driven DNA translocations through a nanopore. Phys. Rev. Lett. 86:3435-3438

[8] Loebl HC et al. (2003) Simulation studies of polymer translocation through a channel. Phys. Rev. E 67: 04191

[9] Kasianowicz JJ et al. (1996) Characterization of individual polynucleotide molecules using a membrane channel. Proc. Natl. Acad. Sci. U.S.A. 93:13770-13773

2nd International Conference on Mathematical and Computational Biomedical Engineering - CMBE2011
March 30 - April 1, 2011, Washington D.C, USA
P. Nithiarasu and R. Löhner (Eds.)

MODELING AND CONTROL OF AN INDUCIBLE GENE EXPRESSION SYSTEM

Nathalie Barbosa, Andres Olarte, Carlos A. Clavijo and Hernando Diaz*
*National University of Colombia, Bogota, hdiazmo@unal.edu.co

SUMMARY

The tetracycline-responsive repressor/operator system has proved to be useful for studying the functions of different genes. This document presents a mathematical model of a cellular system that uses this system to regulate GFP expression on a graded way in a modified macrophage cell line. It is also shown that the model can be linearized by feedback. This may allow to accurately control the expression of the gene.

Key Words: *Gene activation and repression, mathematical model, nonlinear model feedback linearization.*

1 INTRODUCTION

Tetracycline (Tet) has been used to control gene activation and repression in many cell lines. This antibiotic is utilized as an exogenous signal for a cellular system that uses a combination of a repressor and a specific promoter that blocks the expression of a particular gene located downstream such promoter. However, Tet could be also used in the opposite fashion: gene transcription only occurs when Tet is added to the cell culture [2]. In addition to the on-off behavior, this system allows production of intermediate levels of gene expression.

Currently in our laboratory, a monocyte cell line (U937) is being developed to include a tetracycline-mediated gene expression system. This cell line will be used as an experimental model to identify host-cell genes, that are necessary for the infection by *Leishmania spp.* Several studies suggest that the macrophage expression gene patterns are affected by the infection [4]. Therefore, we are implementing an experimental system that can generate diverse transcription levels depending on Tet dosage scheme.

A methodology using *in silico* experimentation was proposed as a first step for designing the experimental system. Several authors have built mathematical models to describe genetic circuits and gene transcription processes. Elowitz and Leibler, for instance, present a synthetic network, comprised of three repressor proteins designed to work as an oscillator [1]. Gardner *et al.* developed a synthetic, bistable gene-regulatory network in *E. coli* using two different repressors; in their work, an exogenous pulse of anhydrotetracycline (aTc) switches the network state [3]. Rossi *et al.* proposed a different class of transcriptional control: Rheostat Converted to On/Off Switch. A graded rheostat mechanism is converted to an on/off switch when either transactivators or transrepressors compete for the same DNA regulatory element [7]. Kramer *et al.* introduced a mammalian epigenetic circuitry capable of switching between two stable trasgene expression states after transient administration of two alternate drugs [6].

This paper presents a model for graded regulation of gene expression on a cell line. Then it is shown that the nonlinear model can be linearized using feedback.

2 MATHEMATICAL MODEL OF GRADED GENE EXPRESSION

Building a dynamical model of the gene expression activity requires consideration of the species involved: Tetracycline repressor (TR), tetracycline (Tet), green fluorescent protein (GFP) and the corresponding messenger RNA concentration $(mRNA_{GFP})$. In this case, in the absence of the inducer (Tet), the tetracycline repressor (TR) binds to an operator and suppresses transcription from the adjacent promoter. Addition of tetracycline allows its binding to TR, interrupting its interaction with the operator and allowing transcription. The final product of transcription is GFP (green fluorescent protein) that can be measured by fluorescence microscopy or fluorometry.

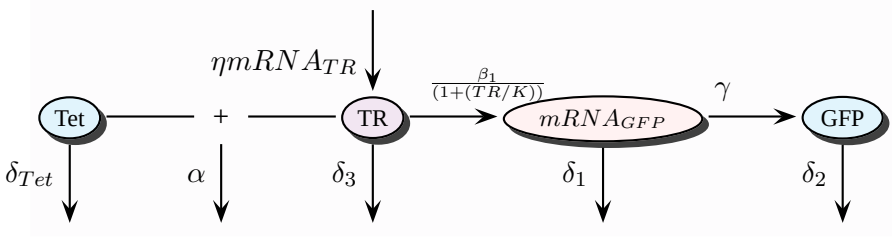

Figure 1: Tetracycline repressor-activator gene expression diagram

Figure 1 illustrates the interactions. Considering instantaneous balances for the different species and simple mass action reaction rates with a Hill function, one obtains:

$$\frac{dTR}{dt} = -\delta_3 TR - \alpha TRTet + \eta\, mRNA_{TR} + \nu\,(Tot_{TR} - TR) \tag{1a}$$

$$\frac{dmRNA_{GFP}}{dt} = -\delta_1 mRNA_{GFP} + \frac{\beta_1}{1 + \left(\frac{TR}{K}\right)^n} \tag{1b}$$

$$\frac{dGFP}{dt} = -\delta_2 GFP + \gamma mRNA_{GFP} \tag{1c}$$

$$\frac{dTet}{dt} = -\delta_{tet} Tet - \alpha TRTet + \zeta u + (\delta_3 + \nu)\,(Tot_{TR} - TR) \tag{1d}$$

where δ_1, δ_2, δ_3 and δ_{tet} are decay rates for the corresponding species, α represents the $Tet - TR$ association constant and ν is the dissociation rate. η and γ represent translation rates of $mRNA$.

Equation (1b) shows how the $mRNA$ production is related to the amount of TR in the modified cell. In the absence of TR $mRNA_{GFP}$ reaches a maximum value. The first term on (1b) considers the protein degradation. The second term, $\frac{\beta_1}{1+\left(\frac{TR}{K}\right)^n}$, is a Hill function describing the repression of protein synthesis. The free parameter K is the concentration of repressor required for half-maximum repression of the target promoter. β describes the maximum protein production rate. This rate goes from β_1 in absence of TR to $\beta_1/1 + \frac{TR}{K}^n$ in a full repression state.

The model response after a single Tet dosage, applied at $t = 20h$, is shown on figure 2. Model parameters have been obtained from published results. It can be seen that the GFP response, in absence of Tet, is fully repressed. When tetracycline is added to the system, the active repressor level diminishes enabling the production of $mRNA_{GFP}$ and then GFP. This behavior is consistent with the expected response.

3 FEEDBACK LINEARIZATION AND CONTROL DESIGN

Our interest is to control the transcription level at varying amounts, depending on the Tet dosage scheme. Geometric control provides conditions under which the nonlinear system may be transformed into a linear system using a state transformation and a nonlinear feedback control law.

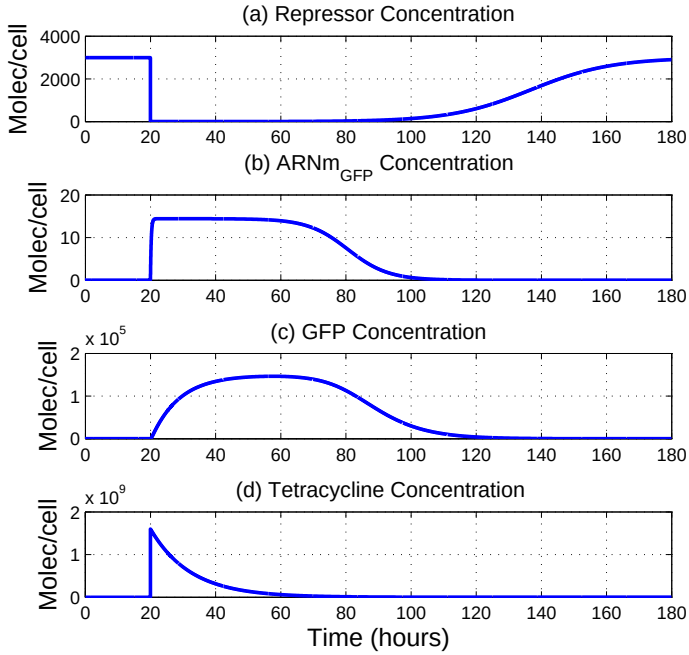

Figure 2: Model response for a single tetracycline dosage applied at $t = 20h$

The transformation can be found using tools from differential geometry [5]. For equations (1), the control law

$$u = \omega(x) + \sigma(x)\, v \tag{2}$$

will produce a system whose dynamics are linear. In the last equation, $\omega(x)$ and $\sigma(x)$ are non-linear functions of the original variables (TR, $mRNA_{GFP}$, GFP, Tet), too complicated to be included in this summary. v is an additional control signal designed to produce a response as desired. The existence of this transformation also proves that the system is controllable. The equivalent linearized system is described by the equations

$$\dot{z}_1 = z_2; \quad \dot{z}_2 = z_3; \quad \dot{z}_3 = z_4$$
$$\dot{z}_4 = \frac{-\omega(x)}{\sigma(x)} + \frac{1}{\sigma(x)} u = v$$

Implementation of the control law in the experimental phase of the study requires that the control signals satisfy some practical actuator constraints: The maximum actuator dose is set to a fixed number of molecules per cell. To simplify the implementation, the control signal has two different values: zero or maximum level. A time varying input $u(t)$ is obtained through a PCM (pulse code modulation) process.

Some examples of a closed loop system response, satisfying the actuator constraints are shown on figure 3. The expression level was set at four different set points. As shown, the GFP expression level tracks adequately the reference set point. The input signals for a few time intervals are also presented.

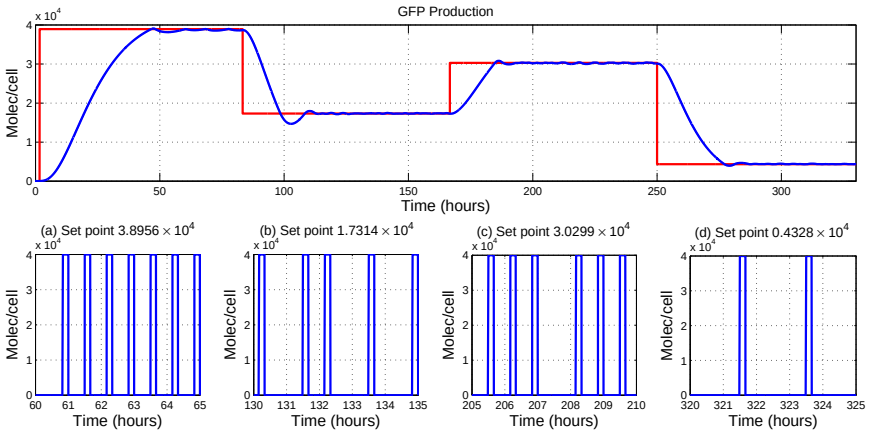

Figure 3: Closed loop system response. (1) GFP concentration (blue), Set point (red). (2) Dosage Scheme on several set points.

4 CONCLUSIONS

The mathematical model presented here describes adequately the dynamics of the tetracycline-responsive repressor/operator system for gene expression. In addition, the resulting model can be linearized by nonlinear state feedback. This opens the way for designing linear system-based controllers. It has also been shown that the process described by this model can be controlled to track a varying reference signal.

References

[1] Michael B. Elowitz and Stanislas Leibler. A synthetic oscillatory network of transcriptional regulators. *Letters to Nature*, 443:335–338, 2000.

[2] S. Freundlieb, C. Schirra-Mller, and H. Bujard. A tetracycline controlled activation/repression system with increased potential for gene transfer into mammalian cells. *J Gene Med.* ., 1:4–12, 1999.

[3] Timothy S. Gardner, Charles R. Cantor, and James J. Collins. Construction of a genetic toggle switch in *Escherichia coli*. *Letters to Nature*, 403:339–342, 2000.

[4] David J. Gregory, Robert Sladekand, Martin Olivier, and Greg Matlashewski. Comparison of the effects of leishmania major or leishmania donovani infection on macrophage gene expression. *Infection and Immunity*, 76(3):1186–1192, 2008.

[5] Alberto Isidori. *Nonlinear Control Systems*. Springer Verlag, 1995.

[6] Beat P Kramer, Alessandro Usseglio Viretta, Marie Daoud-El Baba, Dominique Aubeland Wilfried Weber, and Martin Fussenegger. An engineered epigenetic transgene switch in mammalian cells. *Nature Biotechnology*, 22:867–870, 2004.

[7] Fabio M.V. Rossi, Andrew M. Kringstein, Albert Spicher, Oivin M. Guicherit, and Helen M. Blau. Transcriptional control: Rheostat converted to on/off switch. *Mol Cell*, 6(3):723–728, September 2000.

A new fractal model of chromosome and DNA processes

Kais Bouallegue
Department of Electrical Engineering, High Institute of Applied Sciences and Technology of Sousse, Tunisia.

Cit Taffala (ISSAT), 4003 Sousse Tunisie,

kais_Bouallegue@yahoo.fr

SUMMARY

Key Words: *Fractal, chromosome, mitosis, meiosis, DNA processes.*

1 INTRODUCTION

Fractals and chaos offer a rich environment for exploring and modeling the complexity of nature. In a sense, fractal geometry is used to describe, model and analyze the complex forms found in nature. Fractal has found a wide application in biology and medicine. A fractal is an object that displays self-similarity under magnification and can be constructed using a simple motif (an image repeated on ever-reduced scales). Fractals have generated a great deal of interest since the advent of the computer. The problem of identifying a chromosome becomes a challenge to find out to which one of the model it belongs [3][2].Many different models have been proposed for mitotic chromosome including a hierarchical coiling model[4],a tube model[1] and radial loop model[5].

In section 2 we present a algorithm inspired from Julia set, in section 3 we model duplication process with making a cascade fractal processes on chromosome. Section 4 some results are presented to show a model of mitosis and meiosis processes on chromosomes. Consider the following recurrent system :

$$\begin{cases} x_{n+1} = \mu x_n - \nu y_n + \beta \dfrac{z_n}{\sqrt{x_n^2 + y_n^2}}(\gamma x_n - \lambda y_n) + X_c \\ y_{n+1} = \mu x_n + \nu y_n + \beta \dfrac{z_n}{\sqrt{x_n^2 + y_n^2}}(\lambda x_n + \gamma y_n) + Y_c \\ z_{n+1} = 2\alpha z_n - z_{n-1} + Z_c \end{cases} \quad (1)$$

with $\alpha^2 + \beta^2 = 1$; $\gamma^2 + \lambda^2 = 1$; $\mu = \alpha\gamma$ and $\nu = \alpha\lambda$

The implementation of the recurrent system 1 shows a compressed cube-shaped recurrent state behavior.

Figure 1 illustrates the result:

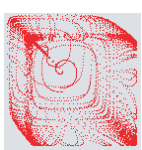

Figure 1: Compression statements

We apply a transformation to states x_n, y_n and z_n by an arctangent function

$$\begin{cases} u_n = \arctan(x_n) \\ v_n = \arctan(y_n) \\ w_n = \arctan(z_n) \end{cases} \tag{2}$$

Figure 2 shows the behavior of state vectors after processing:

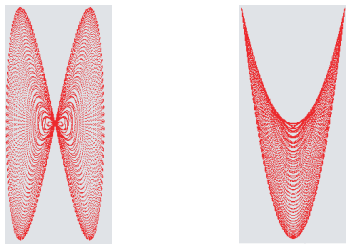

(a) Attractor behavior of chromosome (b) Attractor behavior of chromosome Y

Figure 2: Behavioral states after processing

2 Fractal Algorithm

We demonstrate that fractal processes is a useful concept for understanding exterior and interior processes of DNA and characteristics of chromosome structure of chromosomes. A combination between system 1 and Julia fractal process gives the result in figure 3.

Algorithm 1 computation $(v_{k+1}, u_{k+1}) = P(u_k, v_k)$

if $u_k < 0$ **then**
  $u_{k+1} = \sqrt{[\sqrt{[(u_k)^2 + (v_k)^2]} + \frac{u_k}{2}]}$
  $v_{k+1} = \frac{v_k}{2u_{k+1}}$
end if
if $u_k = 0$ **then**
  $u_{k+1} = \sqrt{\frac{\mid v_k \mid}{2}}$
  if $u_k > 0$ **then**
    $u_{k+1} = \frac{v_k}{2v_{k+1}}$
  end if
  if $u_k < 0$ **then**
    $v_{k+1} = 0$
  end if
end if
if $u_k > 0$ **then**
  $v_{k+1} = \sqrt{[\sqrt{[(u_k)^2 + (v_k)^2]} - \frac{u_k}{2}]}$
  $u_{k+1} = \frac{v_k}{2u_{k+1}}$
  if $v_k < 0$ **then**
    $v_{k+1} = -v_{k+1}$
  end if
end if

Figure 3 shows a results of implementation of model.

Figure 3: Butterfly Chromosome and Y chromosome

3 Model of duplication process

3.1 Duplication inter chromosomal

Gene duplication is known to have played a major role in the evolution of almost all life on Earth of genomic data from numerous plants such as grasses

The duplication leading to an increase of chromosomal material resulting in a repetition, a copy of an insertion of a chromosome or chromosomes. Figure 4 show the presence of multiple chromatid running side by side along the longitudinal axis of parental chromosome.

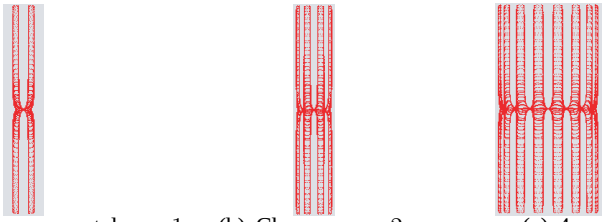

(a) Chromosome parental $n = 1$ (b) Chromosome $2n$ (c) 4n

Figure 4: Multi duplication

All the chromosome replication occurs at the centromere. Figure 4 shows the insertion of new chromosome between the two arms of parental chromosome and this operation is done for every phase of replication. Replication is a multiple of $2n$. The centromere is the base home during replication.

4 Model of cellular division

There are many processes in cellular division , we show two processes the first one is mitosis and the second a meiosis.

4.1 Mitosis process model

Mitosis is a form of eukaryotic cell division that produces two daughter cells with the same genetic component as the parent cell. Mitosis, although a continuous process, is conventionally divided

into five stages: prophase, prometaphase, metaphase, anaphase and telophase.

Figure 5 illustrated a level of model mitosis process :

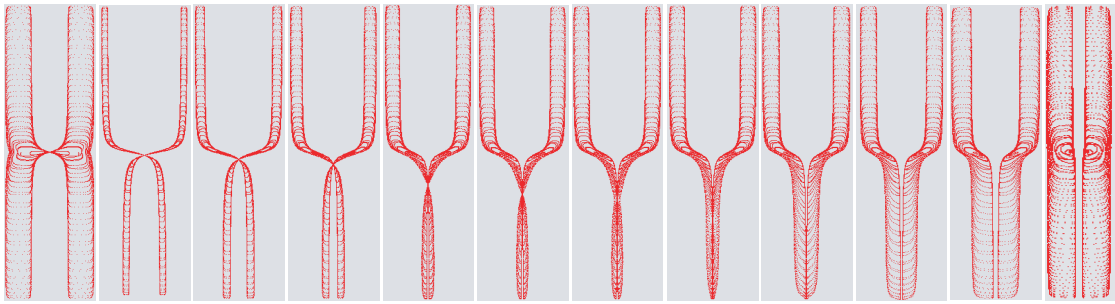

(a) (b) (c) (d) (e) (f) (g) (h) (i) (j) (k) (l)

Figure 5: Mitosis process

4.2 Meiosis

Meiosis comprises the four phases of a mitosis starting from two duplicated chromosomes made up each of four chromatids.

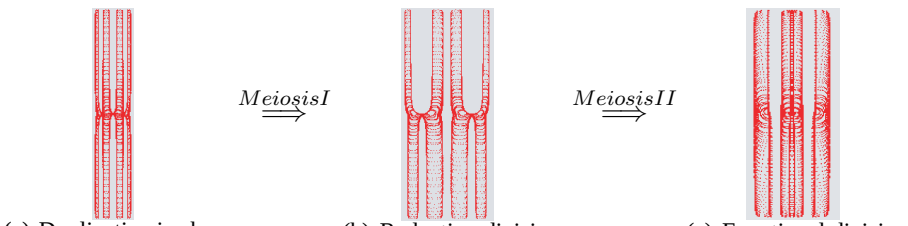

(a) Duplication in chromosome (b) Reduction division (c) Equational division

Figure 6: Meiosis

5 CONCLUSIONS

In this paper, we have provided the first exact and efficient model of chromosome and DNA processes for a long stating open problem. DNA is the molecule that not only encodes the information that organism needs to live but also processes that reproduce themselves. We count, to, continue research to apply the models developed in this paper for the identification, localization and diagnosis of certain inherits of genetic origin.

REFERENCES

[1] SeDat,J.& Manuelidis,L. Cold Spring Harb. Symp. quant., *biol* , **42**, 331,1978.

[2] Manabu Takahashi. A Fractal Model of Chromosomes and DNA Replication. J. theor.biol. (1989) 141, 117-146.

[3] Tony Y. T. Chan. Unsupervised classification of noisy chromosomes, *Bioinformatics*, **17**, 438-444,2001.

[4] Bak,A.,L,Zeuthen,J. CRIK, F.H (1977) F.H.C., *Chromosoma* , **199**, 46-247,1977.

[5] Mardesen,M.P.F. & Laemmli, U,K. , *cell* , **17**, 849, 1979.

2nd International Conference on Mathematical and Computational Biomedical Engineering – CMBE2011
March 30 – April 1, 2011, Washington D.C., USA
P. Nithiarasu and R. Löhner (eds)

Finite Element Analysis on the Fluid Filtration in a Capillary-Tissue System

Ying HE*,** and Ryutaro HIMENO**
*Department of Modern Mechanics, University of Science and Technology of China,
Mail Box 4, Hefei, 230027 Anhui, China
Email: yhe@ustc.edu.cn
**Advanced Computing Center, RIKEN,
2-1 Hirosawa, Wako-shi, 351-0198 Japan

SUMMARY

The Fluid filtration across the wall is particularly important in certain pathological conditions and cancer treatment. Thus, it is of importance to study the flow through the capillaries and tissues. In this study, the blood flow and filtration through a straight tube surrounded by tissues were studied. The domains consist of blood flow region described by the Stokes equation and the porous region described by the Darcy equation. The flows inside the capillary and tissue region were computed simultaneously by a nodal replacement scheme at the tube wall region. The pressure and flow velocity distribution for different filtration coefficient in capillary and tissue were obtained and the effect of the permeability was well reflected

Key Words: *Blood flow, Permeable tube, Fluid filtration, FEM, porous media*

1. INTRODUCTION

It is believed that pathological conditions are affected more by events within microcirculation than by events within the interior of large vessels. There are a lot of small pores in the capillary wall so as to let water across it but to prevent ions and macromolecules to pass, which functions as a semi-permeable wall. The circulation of tissue fluid is essential to the regulation of blood pressure and volume. Too much or too less fluid in tissue will lead to Edema or Dehydration. At the arterial end of the capillary, fluid is squeezed out of the capillary by blood pressure and at the venous end, fluid will re-enter into the capillary by osmotic attraction.

The momentum and mass transfer studies in permeable tubes are important in the understanding of nephron function and fluid convection in the treatment of cancer by the therapeutic macromolecules. Chaturani[1] developed a mathematical model for solute transfer in an ultrafiltering glomerular capillary. The axial distribution of hydrostatic and osmotic pressure and the total solute clearance have been obtained and it is found that the osmotic pressure has relatively greater influence on capillary mass transfer than the hydrostatic pressure. Lei et al [2] proposed a three-porous-medium model to describe the extravascular transport and transvascular exchange. The analytical solutions show that the elevated interstitial pressure is a major barrier in the penetration of macromolecular drug into tumors. Shahed [3] employed two-phase equations for particle and fluid to express the blood flow in a permeable tube and provided a perturbation solution for the two phase flow. It is shown that the volume fraction of the particles has a significant effect on the plasma flow. In Bhardwaj & Tandon's work[4], the blood flow through a permeable capillary was divided into three layers, which includes the core region with constant

velocity, Casson's fluid flow region and cell free plasmatic layer. The analytical solutions of filtration velocity in different positions well described the filtration and re-absorption process.

Pozrikidis [5,6] carried out a series work to study the blood and interstitial flow through a solid tumor with a single tube and a vascular network by boundary element method. The axial blood through a capillary was described by Poiseuille's law, and the plasma fluid across the vasculature into the surrounding interstitium was expressed by Starling's law. At the bifurcation of the vessel network, the mass balance for blood flow and extravasation flux was constructed between the neighboured nodes. The interstitial pressure at the vessel surface can be computed by a boundary integral formation which expresses the relationship between blood, interstitial, and tumor surface pressure and Green's function of Laplace equation corresponding to the tumor surface. The blood and interstitial pressure can be computed numerically by coupling the integral and differential equations. The results illustrated the effect of the interstitial flow and vascular permeability on the factional plasma leakage and demonstrated the effect of length of capillary tree. His work presented a framework for describing the blood and fluid flow through the interstitium and has been developed for different applications. For example, Sun et al [7] employed the same model of Pozrikidis [2] to investigate fluid flow through a curved permeable vessels in a solid tumor.

The purpose of this study is to use a finite element analysis to investigate the blood and fluid flow in a capillary network and the surrounded tissue simultaneously. As the first step, the blood and fluid flow through a straight tube and the surrounded tissue was investigated. A nodal replacement scheme was employed to couple the computation in different flow regimes and some primary results were obtained.

2. SIMULATION MODEL

The Krogh cylinder tissue model with a permeable tube embedded was employed. The blood flow in the capillary is considered as Stokes flow and its pressure can be expressed as Laplace equation

$$\nabla^2 P_b = 0 \tag{1}$$

By assuming the tissue as an isotropic porous medium, the interstitial pressure also satisfies Laplace equation

$$\nabla^2 P_i = 0 \tag{2}$$

The interstitial velocity can be described by Darcy equation

$$\mathbf{U} = -\kappa \nabla P_b \tag{3}$$

The fluid exchange between blood and fluid in tissue is assumed to obey Starling's law

$$q_e = L_p (P_b - P_i) \tag{4}$$

It is considered that Darcy velocity at the tube surface is equal to that provided by Starling's law, therefore, the boundary condition can be written as

$$\frac{\partial P}{\partial n} \equiv \mathbf{n}(\mathbf{x}) \cdot \nabla P_b(\mathbf{x}) \cong -\frac{q_e}{\kappa} = -\frac{L_p}{\kappa}(P_b - P_i) \tag{5}$$

Eq.(1) was discretized by employing the Galerkin Weighting, which is written as

$$\int_\Omega [\mathbf{N}]^T \left(\frac{\partial^2 P_b}{\partial x^2} + \frac{\partial^2 P_b}{\partial y^2} \right) d\Omega = \int_\Gamma [\mathbf{N}]^T \frac{\partial p_b}{\partial n} d\Gamma - \int_\Omega \left(\frac{\partial [\mathbf{N}]}{\partial x}\frac{\partial P_b}{\partial x} + \frac{\partial [\mathbf{N}]}{\partial y}\frac{\partial P_b}{\partial y} \right) d\Omega = 0 \tag{6}$$

Substituting Eq. (5) into the line integral, Eq. (6) becomes

$$\int_\Omega [\mathbf{N}]^T \left(\frac{\partial^2 P_b}{\partial x^2} + \frac{\partial^2 P_b}{\partial y^2} \right) d\Omega = \int_\Gamma [\mathbf{N}]^T \left[-\frac{L_p}{\kappa}(P_b - P_i) \right] d\Gamma - \int_\Omega \left(\frac{\partial [\mathbf{N}]}{\partial x}\frac{\partial P_b}{\partial x} + \frac{\partial [\mathbf{N}]}{\partial y}\frac{\partial P_b}{\partial y} \right) d\Omega = 0 \tag{7}$$

The effect of vessel wall permeability can thus be imposed in the first term of right hand in Eq. (7). Using the same approximation, Eq. (2) can be discretized into the same form as Eq. (7). In

the implementation of numerical analysis, the two different flow regimes were included in a single computational domain and the computation in every flow regime was implemented iteratively until it reaches steady. The schematic diagram of the nodal replacement scheme is shown in Fig. 1. AB and A_1B_1 represent the boundaries in the blood and tissue side, which have the same coordinates. Since the computation for blood and tissue regime is carried out iteratively, the blood and interstitial pressure at the interfacial nodes can be represented by the parameters at the previous and present time, that is, the pressure P_b and $P_{\underline{i}}$ in Eq. (7) can be expressed by P_{new} and P_{old}. Thus, the effect of interfacial surface can be evaluated in a single computational domain.

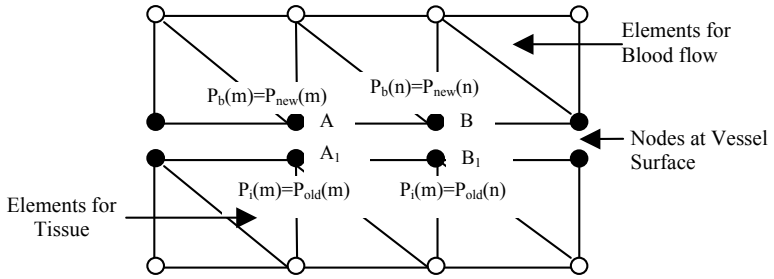

Fig. 1 Schematic diagram for linking the blood and tissue regime

3. Results and Summary

In the simulation, the inlet, outlet, and tissue surface pressure were prescribed. Fig. 2 gives the pressure distribution in tissue and tube and Fig. 3 shows the pressure variation of blood and interstitium at the tube surface along the flow direction when filtration coefficient is different. It can be seen that with the filtration coefficient increasing, the pressure gradient becomes greater, and the interstitial pressure is greater than that of blood near the outlet. The blood flow vector field when filtration coefficient is 10^{-7} m/Pas is shown in Fig. 4. Due to the low pressure gradient in the middle of the tube, the blood velocity becomes lower and when the flow is near the outlet, the blood velocity gradually increases.

In summary, a finite element analysis was conducted to investigate the fluid filtration in a simple capillary-tissue system and some primary results have been obtained. It will be extended to apply in analyzing the blood and fluid flow in tissues with complex vasculature.

Acknowledgements

The authors wish to acknowledge the financial support by JSPS invitation fellowship program. The first author is grateful for the financial support by Anhui Provincial Natural Science Foundation No. 11040606M09.

REFERENCES

1. Charturani, P. and Ranganatha, T.R., Solute transfer in fluid flow in permeable tubes with application to flow in glomerular capillaries, Acta, Mechanica, Vol 96 (1993), pp.139-154.
2. Lei, X.X., We, W. Y. et al , Mass transfer in solid tumors(1)—fluid dynamics, Applied mathematics and mechanics, 19(1998), 1025-1032.
3. Shahed M. E., Blood flow in a capillary with permeable wall, Physica, A 338 (2004) 544-558.
4. Bhardwaj R, and Tandon, PN, A model of fluid filtration and reabsorption in a capillary-tissue exchange system, Ultra Science, Vol. 20(2008), pp.633-642
5. Pozrikidis, C. and Farrow D.A., A model of fluid flow in solid tumors, Annals of Biomedical Engineering, Vol. 31(2003), pp.181-194.

6. Pozrikidis, C., Numerical simulation of blood and interstitial flow through a solid tumor, J. Math. Biol. Vol. 60(2010), pp.75-94.

7. Sun, Q., Wu, GX, Ovenden, N, Numerical simulations of blood flow through a permeable curved vessel in a solid tumor, proceedings of the 5th International Conference on Fluid Mechanics, Aug. 15-17, 2007, Shanghai, New Trends in Fluid Mechanics Research.

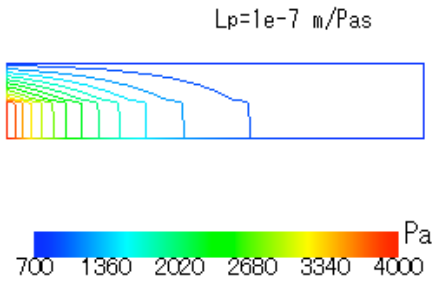

Figure 2 Fluid pressure distribution in the capillary-tissue system

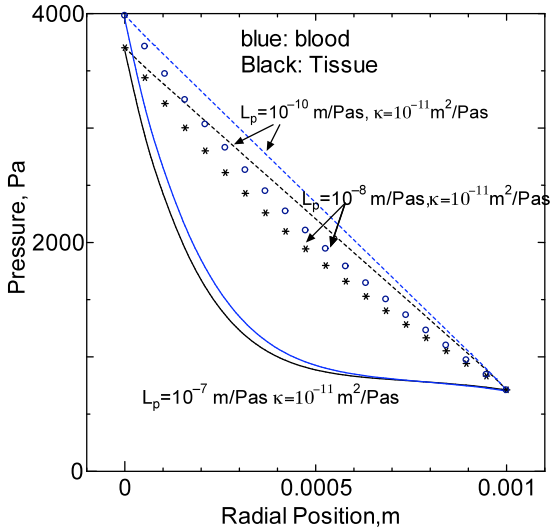

Figure 3 Blood and Interstitial Pressure Variations Profiles at the Vessel Wall for Different Filtration coefficients

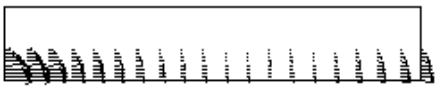

Figure 4 Blood Velocity Field in the capillary when the filtration coefficient is 10^{-7} m/Pas

2nd International Conference on Mathematical and Computational Biomedical Engineering – CMBE2011
March 30 – April 1, 2011, Washington D.C., USA
P. Nithiarasu and R. Löhner (eds)

A CONSTITUTIVE MODEL FOR VASCULAR TISSUE THAT INTEGRATES FIBRIL, FIBER AND CONTINUUM LEVELS

T.C. Gasser[*] , G. Martufi[*] and M. Auer[**]
* Department of Solid Mechanics, The Royal Institute of Technology (KTH), Stockholm, Sweden, tg@hallf.kth.se, martufi@kth.se
** VASCOPS GmbH, Graz, Austria, martin.auer@vascops.com

SUMMARY

Our current understanding of vascular pathologies like Abdominal Aortic Aneurysms (AAAs) might be enriched by investigating the interplay between the tissue's internal architecture (histology) and its macroscopic mechanical properties. A microfiber model approach that accounts for the complex 3D arrangement of collagen is suggested, where constitutive relations for collagen fibers are integrated over the unit sphere, which in turn defines the tissue's macroscopic mechanical properties. A collagen fiber is represented by a bundle of Proteoglycan (PG) cross-linked collagen fibrils, where a triangular distribution function accounts for the dispersion of straightening stretches, i.e. the stretch required straightening a separated collagen fibril. The proposed constitutive model is able capture the non-linear mechanics of the aortic wall and demonstrates good predictive capability.

Key Words: *Arterial mechanics, multiscale modeling, structural constitutive model, aorta, collagenous tissue.*

1. INTRODUCTION

Collagen is the most abundant protein in mammals and gives mechanical strength, stiffness and toughness to many soft biological tissues. Malfunction of collagen turnover is believed to define later stages of Abdominal Aortic Aneurysms (AAAs) [1], i.e. local and permanent dilatations of the aorta in the abdomen, which are frequently observed in the elderly male population. AAA rupture is lethal in 3 out of 4 cases and predicting aneurysm growth and rupture risk could significantly improve the clinical management of aneurysms.

A fundamental understanding of how the tissue's internal architecture impacts its macroscopic mechanical properties and vice versa is vital to any biomechanical constitutive model. In that respect a structural model [2] is suggested, which integrates fibril, fiber and continuum levels of the vascular tissue. Specifically, cross-linked collagen fibrils are thought to form collagen fibers, which in turn are integrated over the unit sphere to define the tissue's macroscopic properties.

2. MAIN BODY

As suggested previously, the vascular wall is modelled as an isotropic matrix material with embedded bundles of collagen, where their alignment is defined by an orientation density

function [3]. Specifically, an assemblage of Proteoglycan (PG) linked [4] collagen fibrils defines a bundle of collagen, i.e. a collagen fiber.

Consequently, collagen is modelled at the fibril level and each collagen fibril has its own intermediate configuration $\Omega_{st\,i}$, where multiplicative kinematics relates fibril deformation to the (macroscopic) tissue deformation. Specifically, $\mathbf{F}_{st\,i}$ maps the collagen from Ω_0 to $\Omega_{st\,i}$, i.e. it straightens the *i*-th wavy collagen fibril, and $\mathbf{F}_{c\,i}$ elastically stretches the fibril and maps it into its spatial configuration Ω. The orientation of the collagen fiber is denoted by the unite direction vectors **N** and **n** in the referential and spatial configurations, respectively.

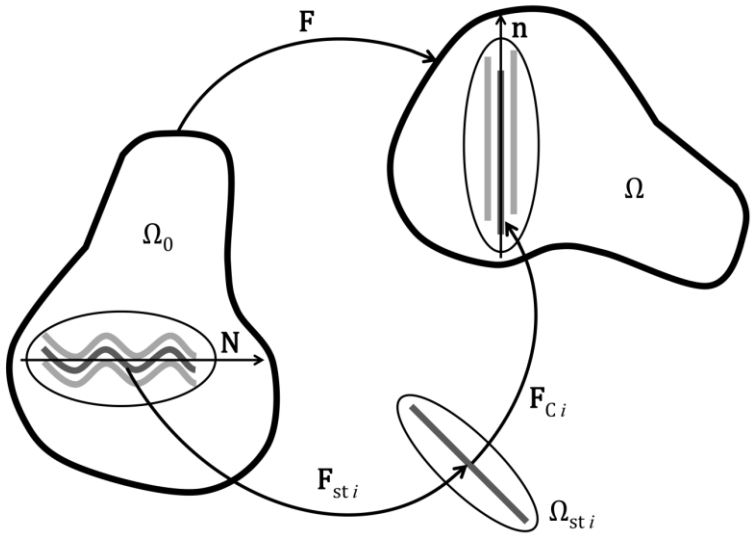

Figure 1: Arterial tissue as a collagen fibers reinforced material. A collagen fiber is assembled by collagen fibrils of different waviness that are interconnected by Proteoglycan (PG) bridges. The *i*-th collagen fibril has its own intermediate configuration $\Omega_{st\,i}$, where it is straightened and starts carrying load during the deformation $\mathbf{F}_{c\,i}$.

A triangular density distribution function captures the distribution of fibrils' reference waviness within a particular collagen fiber, and hence relates the stretch of the fibril to the stretch of the fiber. Likewise, affine transformation of the collagen fibers within the macroscopic continuum is assumed. Finally, similar to micro-plane constitutive models, the macroscopic stress at the material point is derived by integration over all collagen fibers, i.e. integration over the unit sphere [2]. Specifically, spherical t-designs are used to perform this integration [5, 6, 7] and the constitutive has been integrated in a Finite Element (FE) environment.

Data from in-vitro testing [8] of the aortic wall were used to validate the proposed constitutive model. Specifically, material parameters were estimated from stretch-stress characteristics of uniaxial tensile tests, where a constant collagen orientation density distribution reflects the isotropic properties of the aortic wall; see Figure 2(left). In a second step these material parameters were used to predict the stretch-stress response of the aortic wall under equibiaxial stretch, and hence test the predictive capability of the model; see Figure 2(right).

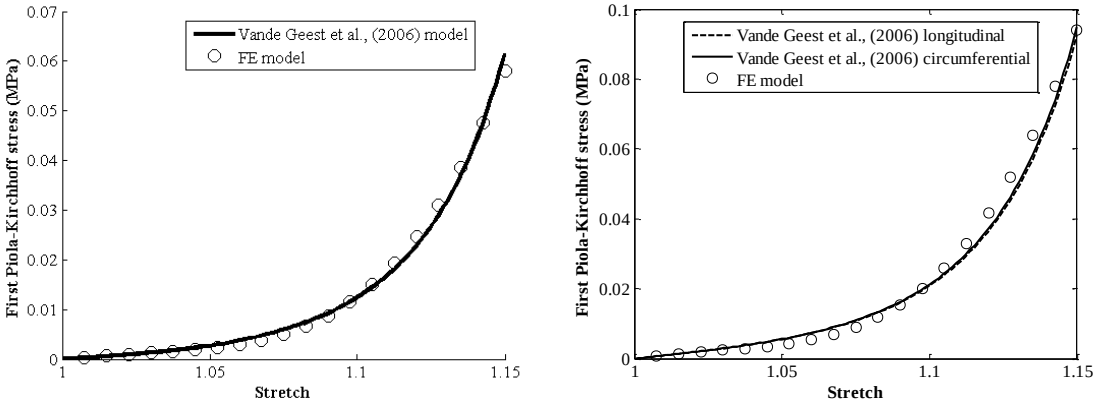

Figure 2: Properties of the proposed constitutive model. (Left) Material parameter estimation based on stretch-stress characteristics of uniaxial tensile testing of aortic tissue. (Right) Prediction of the equibiaxial stretch-stress properties of aortic tissue in comparison to in-vitro test data.

Finally, the stress distribution within patient specific normal and aneurysmatic aortas were invested and related to stress predictions based on alternative constitutive models reported in the literature.

3. CONCLUSIONS

The proposed constitutive model has a strong biological motivation and links the collagen fibril's level with the tissue's macroscopic length scale. Such a structural view is important to understand the interplay of the tissue's histology (internal architecture) and its macroscopic mechanical properties. Apart from understanding the tissue's passive properties a structural constitutive models may be helpful to understand the impact of collagen turn-over on the macroscopic properties of tissue and vice versa [9].

The suggested constitutive model is able to capture the non-linear mechanics of the aortic wall and demonstrates good predictive capability. Specifically, material parameters identified from uniaxial tensile test can be used to predict the response under planar biaxial loading. However, it is noted that an isotropic tissue was considered in the present study, which might explain that information from uniaxial testing is sufficient to predict biaxial properties.

The numerical analysis of patient specific aortas demonstrated the efficiency and robustness of the FE implementation of the proposed multiscale model. Macroscopic stress predictions did not differ much between the suggested and earlier proposed constitutive models, however, the multi-scale approach followed in the present work provides information at different length scales. The model is thought to be enriched by a collagen turn-over model to simulate growth of AAA growth.

REFERENCES

[1] E. Choke and G. Cockerill and W. R. Wilson and S. Sayed and J. Dawson and I. Loftus and M. M. Thompson. A review of biological factors implicated in Abdominal Aortic Aneurysm rupture. *Eur. J. Vasc. Endovasc. Surg.*, 30:227-244, 2005.

[2] Y. Lanir. Constitutive equations for fibrous connective tissues. *Journal of Biomechanics* 16(1), 1-12, 1983.

[3] T.C. Gasser, R.W. Ogden, G.A. Holzapfel. Hyperelastic modelling of arterial layers with distributed collagen fibre orientations, *J. R. Soc. Interface*, 3 :15-35, 2006.
[4] J. E. Scott. Elasticity in extracellular matrix 'shape modules' of tendon, cartilage, etc. A sliding proteoglycan-filament model. *J. Physiol*., 553,2:335–343, 2003.
[5] R. H. Hardin and N. J. A. Sloane. McLaren's improved snub cube and other new spherical designs in three dimensions. *Discrete Comput. Geom*., 15:429–441, 1996.
[6] S. Federico, T.C. Gasser. Non-linear elasticity of biological tissues with statistical fibre orientation, *J R Soc Interface*, 7:955-966, 2010.
[7] T.C. Gasser. An irreversible constitutive model for fibrous soft biological tissue: A 3D microfiber approach applied to Abdominal Aortic Aneurysms. *Acta Biomaterialia* (submitted)
[8] J.P. Vande Geest, M.S. Sacks, D.A. Vorp. The Effects of Aneurysm on the Biaxial Mechanical Behavior of Human Abdominal Aorta. *Journal of Biomechanics* 39, 1324-1334, 2006.
[9] J.D. Humphrey. Remodelling of a collagenous tissue at fixed lengths, *J Biomech Eng*, 121:591–597, 1999.

2nd International Conference on Mathematical and Computational Biomedical Engineering - CMBE2011
March 30 - April 1, 2011, Washington D.C, USA
P. Nithiarasu and R. Löhner (Eds.)

Myocardial tissue deformation due to pacemaker lead contact - The impact of material anisotropy.

Caroline Forsell and T.Christian Gasser
Department of Solid Mechanics, School of Engineering Science, Osquars Backe 1, SE-100 44 Stockholm, Sweden, carfor@kth.se, tg@hallf.kth.se

A Pacemaker electrodes can cause lead penetration of the heart wall. A good understanding of ventricular failure is required to better understand this complication and be able to optimize the lead tip design. Implementation of a good model for ventricular tissue is important for this understanding. Here an anisotropic model have been implanted to compare with an isotropic model. Examples are done where we look at the response in the tissue from the deep penetration of a pacemaker.

Key Words: *myocardium, fracture, penetration failure, soft biological tissue, pacemaker lead perforation, constitutive properties, FEM, non-linear.*

1 INTRODUCTION

Lead perforation acute or delayed are rare but serious complications of an implanted pacemaker device [1]. Naturally, a sound knowledge of ventricular failure mechanisms may help to understand and to prevent this complication. To this end numerical simulations, based on the Finite Element (FE) Method for example, of in-vivo lead-tissue interactions may serve as an essential step in the lead tip design process.

Numerical simulations largely depend on the constitutive description, and for ventricular tissue numerous non-linear formulations have been reported in the literature. Examples are the "pole-zero" law Hunter et al.[2], the poroelastic model for the passive myocardium by Yang et al.[3],[4] and the model suggested by Humphrey et al.[5], to mention a few of them.

While the internal architecture (histology) of the ventricular wall clearly motivates an anisotropic mechanical description, one could argue that the gross characteristics can be captured by an isotropic model. The present work investigates to what extent the constitutive description influences the deformation of the ventricular wall, where specifically the impact of material anisotropy is studied.

2 MAIN BODY

2.1 Anisotropic Hyperelasticity

Following earlier work, e.g., [6] and references therein, we assume an additive decomposition of the strain energy function

$$\Psi = \Psi^{\infty}_{\mathrm{vol}}(J) + \Psi_{\mathrm{iso}}(\bar{\mathbf{F}}) \tag{1}$$

into volumetric Ψ_{vol} and isochoric Ψ_{iso} material responses, where $\bar{\mathbf{F}} = J^{-1/3}\mathbf{F}$ and $J = \det\mathbf{F}$ denote the isochoric deformation gradient and the volume ratio, respectively.

We consider a particular class of models $\Psi_{\text{iso}} = \Psi_{\text{iso}}(I_1, I_4, I_1 I_4)$, i.e. where the strain energy function depends on $I_1 = tr(\bar{\mathbf{C}})$, $I_4 = \alpha^2 = \mathbf{N}\bar{\mathbf{C}}\mathbf{N}$ and a mixed term $I_1 I_4$. Here, $\bar{\mathbf{C}} = \bar{\mathbf{F}}^{\mathrm{T}}\bar{\mathbf{F}} = J^{-2/3}\mathbf{C}$ and $\mathbf{N}$ (with $|\mathbf{N}| = 1$) denote the modified Right Cauchy Green strain and referential myocardial fiber direction of the tissue, respectively.

Thus, the Second Piola Kirchoff stress reads [7]

$$\mathbf{S} = \mathbf{S}_{\text{vol}} + \bar{\mathbf{S}}, \tag{2}$$

where $\mathbf{S}_{\text{vol}} = 2\partial\Psi_{\text{vol}}/\partial\mathbf{C}$ and $\bar{\mathbf{S}} = 2\partial\Psi_{\text{iso}}/\partial\mathbf{C}$ are volumetric and isochoric stress contributions.

2.2 Strain energy

As a particular example the anisotropic constitutive model proposed in Humphrey et al.[5] has been selected. This model has been proven useful in many studies [8],[9]and its strain energy function falls in the class represented by the framework detailed above.

Specially, the strain energy function is described as

$$\bar{\Psi}^{\infty} = c_1(\sqrt{I_4} - 1)^2 + c_2(\sqrt{I_4} - 1)^3 + c_3(I_1 - 3) + c_4(I_1 - 3)(\sqrt{I_4} - 1) + c_5(I_1 - 3)^2 \tag{3}$$

were $c1, ..., c5$ are material constants.

2.3 Numerical example

Pacemaker lead-tissue interaction is simulated, where a rigid penetrator (rounded tip and diameter 1.32 mm) is pushed down on a disk (thickness 10 mm and diameter 50 mm) of myocardial tissue. The penetrator's displacement is prescribed and the elastic force-displacement response is computed, see Figure 1(left). The anisotropic constitutive description predicts a much lower reaction force than the isotropic formulation, although the isotropic model is thought to reflect the gross behavior of myocardial tissue. Specifically, in simple tensile test in fiber and cross fiber directions, the isotropic response was defined to be in between of both anisotropic predictions, see Figure 1(right).

3 CONCLUSIONS

Material anisotropy largely effects the deformation characteristics of myocardial tissue induced by a rigid penetrator. The anisotropic model is more flexible and predicted an about a 50% lower reaction force than the isotropic constitutive description. Specifically, the anisotropic model deforms more in the (softer) cross fiber direction, which in turn unloads the (stiffer) fiber direction and causes the overall softer response. The investigated example nicely illustrates the importance of anisotropic models to describe soft tissue materials.

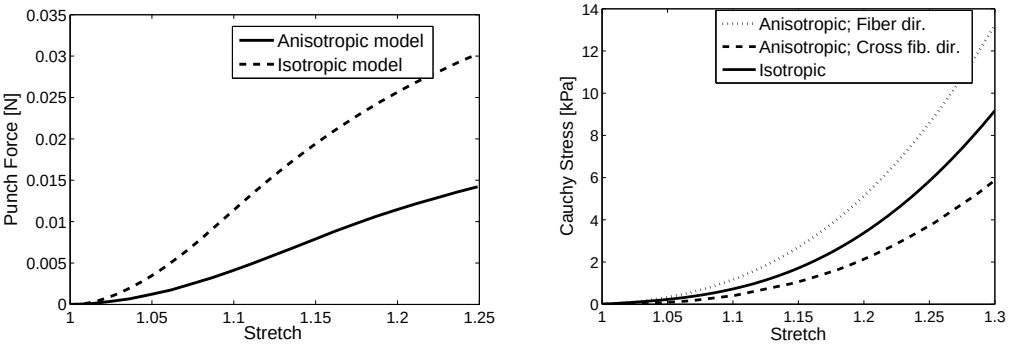

Figure 1: (Left) Force-displacement response when pushing a rigid penetrator into myocardial tissue. Predictions are based on an anisotropic and isotropic model for the myocardium. (Right) Simple tension in fibre and cross fibre direction of myocardial tissue using an anisotropic and an isotropic model.

REFERENCES

[1] M. N. Khan, G. Joseph, Y. Khaykin, K. M. Ziada, B. L. Wilkoff, Delayed lead perforation: a disturbing trend., Pacing and Clinical Electrophysiology 28 (2005) 251–253.

[2] P. J. Hunter, Myocardial constitutive laws for continuum models of the heart, in: S. Sideman, R. Beyer (Eds.), Molecular and Subcellular Cardiology, Plenum Press, New York, 1995, pp. 303–318.

[3] M. Yang, L. A. Taber, The possible role of poroelasticity in the apparent viscoelastic behaviour of passive cardiac muscle, J. Biomech. 24 (1991) 587–597.

[4] M. Yang, L. A. Taber and E. Clark, A nonlinear poroelastic model for the trabecular embryonic heart, J. Biomech. Engng 116 (1994) 213–223.

[5] J. D. Humphrey, R. K. Strumpf, F. C. P. Yin, Determination of constitutive relation for passive myocardium – Part I and II, J. Biomech. Eng. 112 (1990) 333–346.

[6] J. A. Weiss, B. N. Maker, S. Govindjee, Finite element implementation of incompressible, transversely isotropic hyperelasticity, Comput. Meth. Appl. Mech. Eng. 135 (1996) 107–128.

[7] R. W. Ogden, Non-linear Elastic Deformations, Dover, New York, 1997.

[8] H. R. B. B. Chaudhry, T. Findley, Stresses and strains in the passive left venricle, Journal of biological systems 29 (1996) 745–752.

[9] M. Y. L. A. Taber, W. W. Podszus, Mechanics of venricular torsion, J. Biomech. 4 (1996) 535–554.

2nd International Conference on Mathematical and Computational Biomedical Engineering - CMBE2011
March 30 - April 1, 2011, Washington D.C, USA
P. Nithiarasu and R. Löhner (Eds.)

Numerical Implementation of a Continuum Level Thrombosis Model: Simulation of Thrombus Growth and Fluid-Thrombus Interaction

Stefan B. Samra*, Eric G. Paterson**
Applied Research Lab and Dept. of Mechanical and Nuclear Engineering: The Pennsylvania State University, P.O. Box 30 State College, PA 16804
*sbs5018@psu.edu, **egp11@psu.edu

SUMMARY

In the present study a continuum level thrombosis model from the literature, [1] and [2], is solved numerically using the finite volume based code, OpenFOAM. The model governs the transport of several important haemostatic components including blood platelets, chemical activator, and a representative platelet cohesion stress. Simulations are performed to demonstrate the ability of the model to capture a growing clot and the alterations in the flow field due to its presence under general conditions. Simulations for a stenosed vessel are also presented, which predict clot growth patterns qualitatively similar to experimental results from the literature [3].

Key Words: *thrombosis, platelets, OpenFOAM, numerical modeling, blood flow.*

1 INTRODUCTION

1.1 General Background and Clinical Implications of Thrombosis

The blood clotting process, or haemostasis, is essential to life. When injury to a blood vessel occurs, platelets bind to the damaged site and a clot forms in order to seal off the opening thus preventing blood loss. Through similar biological mechanisms, an unwanted blood clot, or thrombus, can also form under certain circumstances within the bloodstream. Thrombosis occurs in situations where clotting is detrimental to the patient and is therefore distinguished from regular haemostasis. One condition that can lead to thrombus formation is atherosclerosis. Plaque that builds up over time causes a local narrowing of the blood vessel. These regions can develop blood clots which may grow to fully block flow or break away (embolize) and travel downstream. The surfaces of artificial blood contacting devices are often prone to the formation of a thrombus as well. Such devices include heart pumps, replacement heart valves, stents, and in general any foreign artificial device implanted in the blood stream.

As a thrombus grows it decreases the quantity of oxygen supplied to cells and organs downstream of the clotting site. Furthermore, if embolization occurs the now separated clot can travel and become lodged in narrower vessels, causing a sudden decrease in oxygen supply to cells and organs downstream of the lodging point. Depending on the blood vessel in question embolization can lead to heart attack, stroke, and pulmonary embolism, by blocking oxygen transport to the heart, brain, and lungs respectively. According to the American Heart Association, as of 2006, an estimated 17.6 million American adults suffered from coronary heart disease leading to one in every six deaths [4]. In 2006, stroke occurred in 6.4 million American adults causing one in every

18 deaths that year [4]. Pulmonary embolism caused 8,702 deaths in the U.S. in 2007 [5]. Based on its implications there exists a need to study thrombosis and the blood clotting process. Specifically, there is interest in the numerical prediction of thrombosis and thromboembolism. One potential application of numerical thrombosis modeling is optimizing the design of blood contacting devices by minimizing their propensity to develop clots. In the current study, a theoretical model from the literature developed by Aaron Fogelson et al. is numerically implemented within the open source software OpenFOAM.

2 MODEL FORMULATION AND CASE STUDIES

2.1 Theoretical Model: Principles and Assumptions

The continuum model presented here aims to predict platelet aggregation, a major component of thrombosis. Platelet aggregation is the process by which blood platelets, which are normally present in the human circulation, become activated and bind to each other as well as to the vessel wall. These platelet clusters, or aggregates, create the framework for a blood clot. The model used here is borrowed from work done by Dr. Aaron L. Fogelson from the University of Utah and others over the past several years; Fogelson 1992 [1], Fogelson 2008 [2]. The model consists of seven scalar, vector, and tensor transport partial differential equations that govern several quantities fundamental to platelet aggregation. Blood is assumed to be a continuous homogeneous Newtonian fluid of constant density and viscosity. The Incompressible Navier Stokes Equations are employed to model the blood flow itself, which is presently assumed to be laminar. Platelets, both activated and non-activated are incorporated in the model using scalar transport equations for the concentrations of each. A scalar transport equation for a single chemical activator, which promotes platelet activation, is also included. A scalar field variable representing the concentration of inter-platelet links is also solved for in the model. One important distinction is that initial triggers of thrombus formation are not currently incorporated in the model, which focuses on the actual growth of the clot and its interactions with the surrounding fluid. Therefore, a clot must be manually initiated in some way. In the current study this is achieved by prescribing a nonzero chemical activator concentration at some predetermined spatial location within the flow field, as Fogelson does in his case studies. When non-activated platelets are in the presence of this chemical activator they become activated themselves and subsequently secrete activator of their own. A stress tensor transport equation also exists in the model. The cohesive stress tensor represents platelet to platelet bonding strength, which increases in regions with high activated platelet concentrations to represent the fact that activated platelets bind to each other causing an aggregate. Platelet wall bonding is not explicitly accounted for as the present study is primarily focused on clot growth and its interaction with the flow field. The cohesive stress tensor field interacts with the fluid by bringing the velocity to zero in regions where stresses are sufficiently high. These regions can be interpreted as effective no slip boundaries, and in the model, they represent platelet aggregates. The cohesive stress is incorporated as a body force source term in the momentum equation in order to achieve the coupling between the growing thrombus and the velocity field. Hence, no slip boundaries that grow with time (blood clots) are present without the need for any alterations in the computational domain or boundary conditions, which is a major advantage of this approach.

2.2 Case Study 1: 2D Poiseuille Channel Flow

A two dimensional rectangular structured grid is generated to simulate thrombus growth in a vessel with an injured wall. Wall boundary cells in a small region on the grid's lower wall and horizontal center are initialized with a nonzero value for chemical activator concentration. All internal fields

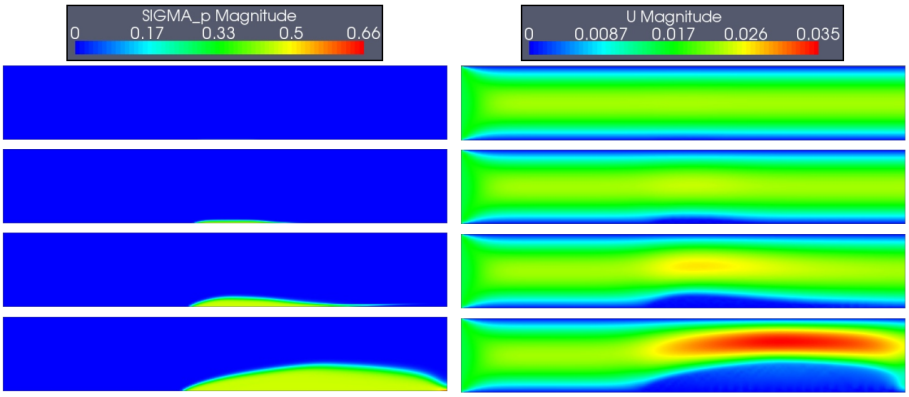

Figure 1: simulation contour plots of platelet cohesive stress magnitude and resulting velocity field magnitude at successive times. velocity in m/s and cohesive stress in m^2/s^2. cohesive stress is normalized by fluid density.

are prescribed to be zero initially and a uniform inlet velocity is imposed. Flow is driven by a pressure gradient and moves from left to right. The Reynolds Number based on total channel height is 300. Solutions of the model equations are given in Figure 1. It can be seen that as time proceeds, platelets become activated and generate a high cohesive stress starting in the immediate vicinity of the injury. The velocity profiles indicate that regions with sufficiently high cohesive stress present with zero velocity (no slip boundary or blood clot). Furthermore, a region of accelerated flow is observed where the effective channel area is reduced due to the growth of the clot. Diffusion of chemical activator enables clot growth to occur perpendicular to streamlines initially. However, as the flow is accelerated due to the growing thrombus, advection tends to dominate and the clot grows mostly in the downstream direction.

2.3 Case Study 2: Pressure Driven Flow Through a 2D Stenosed Vessel

A vessel stenosis, essentially a local reduction of flow area, is commonly encountered in the form of an atherosclerotic plaque. Stenosed vessels are prone to thrombosis due to high shear rates as well as stagnation regions that develop as a result of the blockage. An experimental analysis of clot formation with a stenosed geometry is performed in Narracott 2005 [3]. In [3], an in vitro study is performed using hypercoaguable milk flowing through a cylindrical tube with a sudden contraction and expansion. Clot formation is observed along the walls downstream of the stenosis with increased magnitude at locations closer to the throat (Figure 2 RHS).

In the present study, a two dimensional grid is generated with the same area reduction used in [3]. Simulation results are given in Figure 2 LHS for a Reynolds Number of 300. A nonzero chemical activator concentration is prescribed initially at the two (top and bottom) internal corners on the downstream side of the stenosis in order to initiate platelet activation which is presumed to occur at theses stagnation regions. As time evolves, platelets activate in the two adjacent stagnation regions and the platelet cohesion stress increases there. As chemical activator diffuses in the transverse direction towards the central flow a clot begins to grow outward in this direction, but ultimately advection forces clot growth to continue predominantly in the streamwise direction. The present study is not quantitatively based off of [3], but the results present similar clot growth patterns seen in the stenosed vessel experiments.

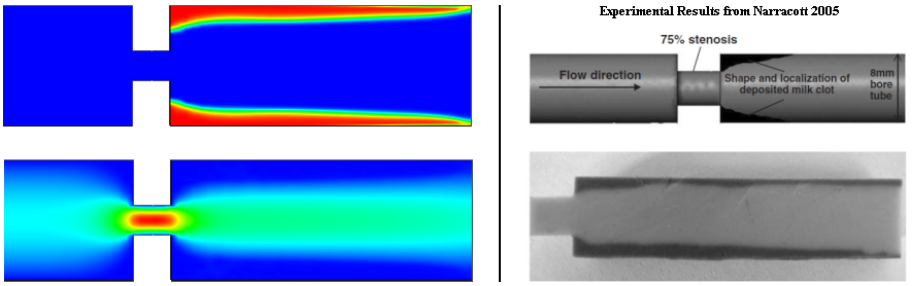

Figure 2: Left: contour plots of cohesive stress magnitude (top) and resulting velocity field magnitude (bottom) during clot formation. blue=0, red=maximum field value. Right: schematic of experimental results (top) and cast of test section with dark casting representing clot location (bottom), both taken from [3].

3 CONCLUSIONS

In summary, an existing theoretical platelet aggregation model has been implemented within the framework of OpenFOAM, an open source CFD software. The model tracks several quantities fundamental to the platelet aggregation process, their influence on thrombus formation, and coupling between a growing clot and the surrounding flow field. It has been demonstrated with the model solutions that as platelets become activated the development of a clot persists and grows as a changing no slip boundary with the fundamental fluid thrombus interactions captured. Furthermore, model simulations have demonstrated results qualitatively similar to experiments in the literature for the case of a stenosed vessel. By solving the model equations using open source software, the current code can be improved upon by other researchers without the need to explicitly recode solutions to the general model equations. In this respect, future increase in model sophistication and specificity is facilitated more easily. Specifically, Implementation of clot initiation mechanisms and quantitative correlation to experimental results might be subjects for future investigation.

References

[1] A.L. Fogelson. Continuum models of platelet aggregation: Formulation and mechanical properties. *SIAM Journal on Applied Mathematics*, 52:1089–1110, 1992.

[2] A.L. Fogelson and R.D. Guy. Immersed-boundary-type models of intravascular platelet aggregation. *Computer Methods in Applied Mechanics and Engineering*, 197(25-28):2087–2104, 2008.

[3] A. Narracott, S. Smith, P. Lawford, H. Liu, R. Himeno, I. Wilkinson, P. Griffiths, and R. Hose. Development and validation of models for the investigation of blood clotting in idealized stenoses and cerebral aneurysms. *J Artif Organs*, 8:56–62, 2005.

[4] American Heart Association. Heart disease and stroke statistics – 2010 update. Technical report, Dallas, Texas: American Heart Association, 2010.

[5] American Heart Association. Venous thromboembolism and pulmonary embolism – statistics. Technical report, American Heart Association, 2007.

2nd International Conference on Mathematical and Computational Biomedical Engineering – CMBE2011
March 30 – April 1, 2011, Washington D.C., USA
P. Nithiarasu and R. Löhner (eds)

Importance of thoracic aortic curvature in the pathogenesis of thoracic aortic dissection

D.P. Nathan, T.J. Eperjesi, A. Pouch, A.S. Jassar, C. Xu, J.H. Gorman, R.C. Gorman, B.M. Jackson
University of Pennsylvania, Philadelphia, PA, USA

1. INTRODUCTION

Aortic dissections involve either the ascending (Stanford type "A") or descending (Stanford type "B") thoracic aorta. Type B aortic dissections account for approximately one-third of dissections, and usually occur distal to the left subclavian artery.[1-2] Aortic dissections result from a tear in the aortic wall intima, leading to the creation of a false lumen within the media, and the separation of the false lumen from the true lumen by an intimal flap. While the pathogenesis of type B dissections remains uncertain, increased shear stress and momentum effects may play important roles.

In younger patients, the left subclavian artery arises from the top, or outer, curvature of the aortic arch (type I arch). In contrast, in older patients the left subclavian artery arises below the plane perpendicular to the top, or outer, curvature of the aortic arch (type II arch). These age-related changes in the configuration of the aortic arch are illustrated in Figure 1. Age-related geometric changes in the thoracic aorta may therefore result in decreased curvature distal to the left subclavian artery in older patients, which in turn might explain the decreased incidence of aortic dissection in older patients.

Using curvature as a proxy for momentum and shear stress effects, the curvature distal to the supraaortic vessels and in the descending thoracic aorta was calculated. In addition, aortic curvature distal to the left subclavian artery was compared between patients with type I and type II aortic arches.

2. MAIN BODY

Patients with normal thoracic aortas on electrocardiogram-gated computed tomography angiography (ECG-gated CTA) were retrospectively identified from radiologic records. Each subject underwent ECG-gated CTA scanning as part of their care dictated by their treating physician, and not for the purposes of this study. Exclusion criteria included renal dysfunction precluding administration of intravenous contrast, penetrating atherosclerotic ulcer, intramural hematoma, thoracic aortic aneurysm or ectasia, and history of thoracic aortic surgery. Indications for ECG-gated CTA included evaluating for embolic source (n=4) and valve disease (n=4). Study approval was obtained from the Institutional Review Board.

In order to assess for the possible effects of aortic arch configuration, patients were classified by the location of the left subclavian artery with respect to the outer (greater) curvature of the aortic arch (Figure 1). In the type I arch group (n=3), the left subclavian artery arose from the top, or

outer curvature of the aortic arch. In the type II arch group (n=5), the left subclavian artery arose below the plane perpendicular to the outer (greater) curvature of the aortic arch.

ECG-gated CTA was performed using 64-slice scanners (Siemens Medical Solutions, Malvern, PA) with IV injection of 80–120 mL of nonionic iodinated contrast (Omnipaque 350, GE Amersham, Milwaukee, WI). The ECG-gated CTA scan data were analyzed using Amira (Visage Imaging™, San Diego, CA) to detect the centerline of the aortic flow lumen (Figure 1). The linesets of the aortic centerline had between 60 and 80 points. MATLAB® (Mathworks, Natick, MA) was then used to analyze the linesets of the aortic centerlines. Three 10^{th} degree polynomials were fit to the curves, providing x, y and z position as a function of arc length.

Curvature was computed as

$$k = |r' \times r''| / |r'|3$$

where r' is the first derivative of the position polynomial, and r'' is the second derivative. All the curves were then translated with respect to arc length so that the left subclavian arteries were aligned, and scaled such that all descending thoracic aortas would have uniform arc lengths. Student t-test and ANOVA were used as appropriate in statistical analysis with SPSS software (SPSS Inc, Chicago, Illinois).

Curvature results are presented in Table 1 and Figure 2. The curvature distal to the left subclavian artery was greater than in the descending thoracic aorta (22.8 ± 7.0 m^{-1} versus 9.1 ± 6.4 m^{-1}, p=.020). In addition, the curvature distal to the left subclavian artery was greater in patients with type I arches compared to type II arches (29.7 ± 1.6 m^{-1} versus 18.7 ± 5.2 m^{-1}, p=0.013).

3. CONCLUSIONS

These results indicate that there is increased curvature distal to the left subclavian artery, which may account, in part, for the genesis of type B dissections at this location. Moreover, patients with a type I arch have greater curvature, which may explain why aortic dissections tend to occur in younger patients.

Table 1. Aortic curvature in the aortic arch and descending thoracic aorta

	Thoracic Aortic Curvature (m^{-1})			
	Descending thoracic aorta	Distal to left subclavian artery	Distal to left common carotid artery	Distal to innonimate artery
All patients (n=8)	9.1 ± 6.4	22.8 ± 7.0*	19.5 ± 5.5	21.1 ± 7.7
Type I aortic arch (n=3)	4.1 ± 2.6	29.7 ± 1.6**	25.4 ± 1.6	24.8 ± 5.3
Type II aortic Arch (n=5)	12.1 ± 6.1	18.7 ± 5.2	16.0 ± 3.2	19.0 ± 8.6

*P=0.020 for comparison between curvature in descending thoracic aorta and distal to left subclavian artery for all patients.

**P=0.013 for comparison between curvature distal to left subclavian artery in patients with type I and II arches.

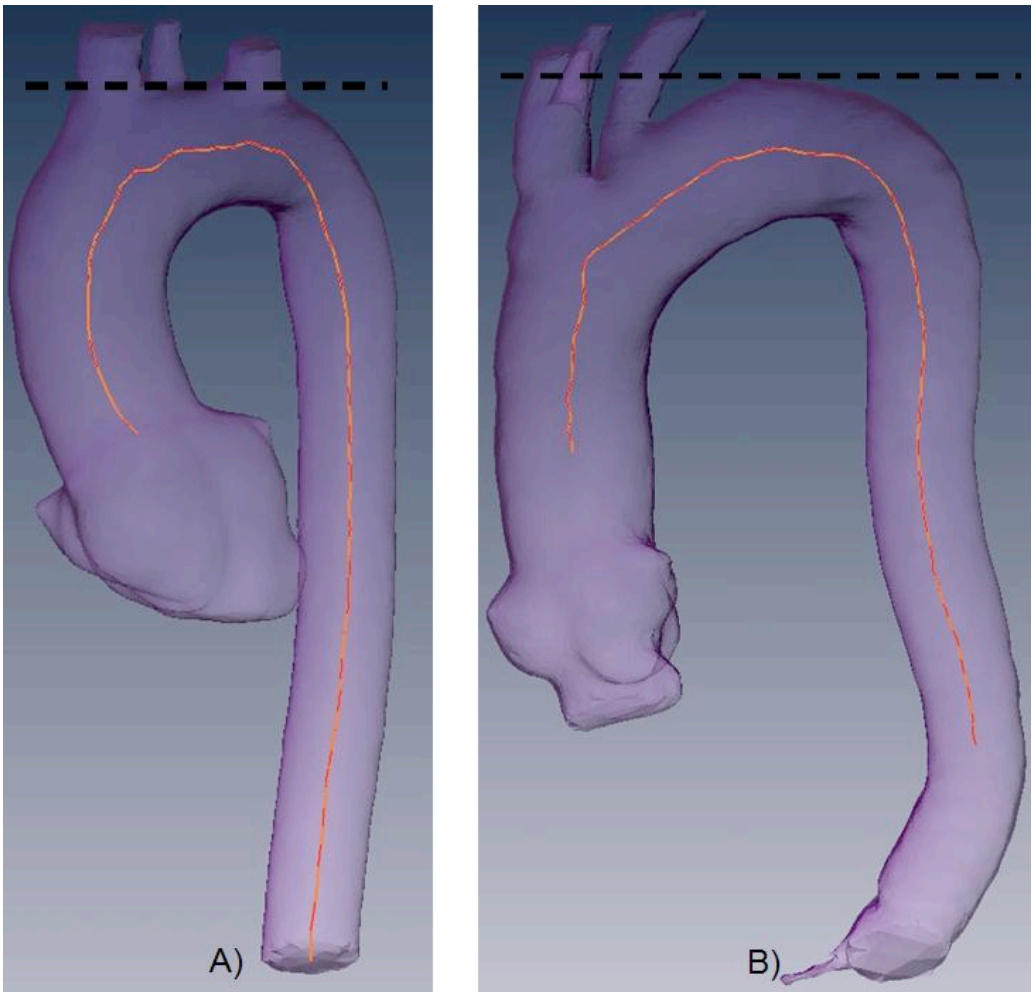

Figure 1. Aortic arch classification and centreline. A) Left subclavian artery originates from top of greater (outer) curvature (type I arch). B) Left subclavian artery originates from below greater (outer) curvature (type II arch).

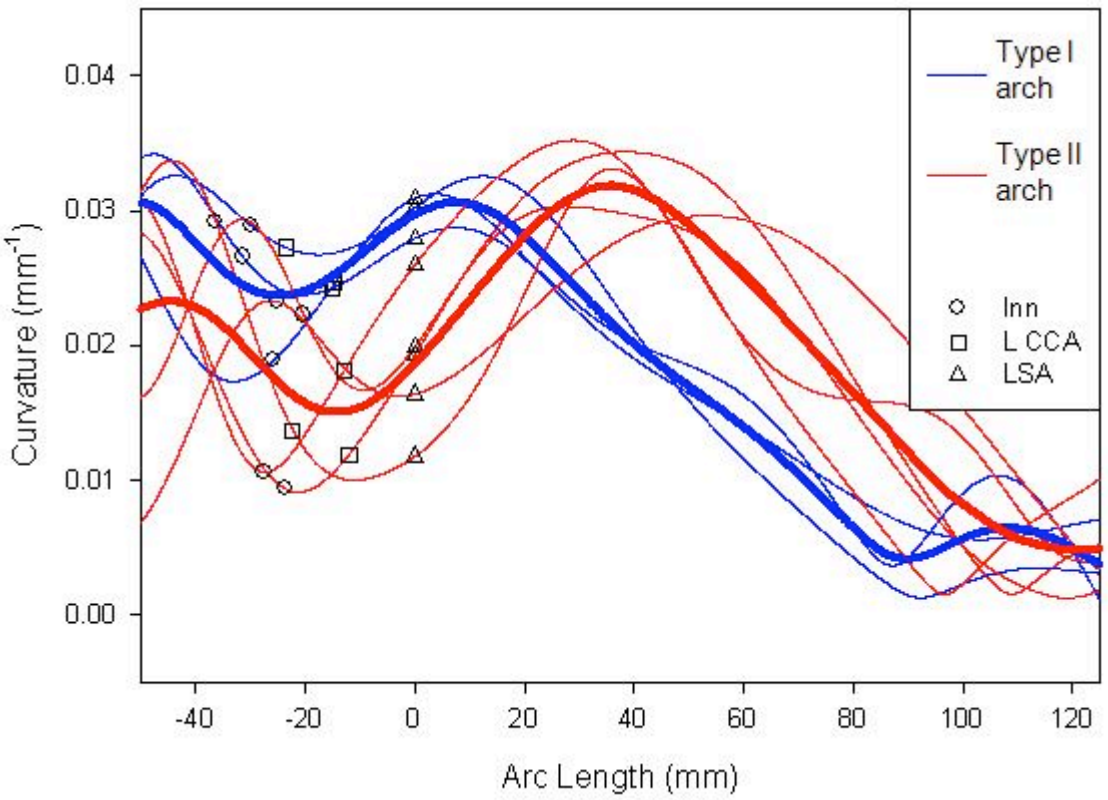

Figure 2. Curvature of thoracic aortic arch and descending thoracic aorta by arch configuration.

REFERENCES

1. Meszaros I, Morocz J, Szlavi J, et al. Epidemiology and clinicopathology of aortic dissection. Chest. 2000;117:1271-1278.
2. Clouse WD, Hallett JW Jr, Schaff HV, et al. Acute aortic dissection: population-based incidence compared with degenerative aortic aneurysm rupture. Mayo Clin Proc. 2004;79:176-180.
3. Morrison TM, Choi G, Zarins CK, et al. Circumferential and longitudinal cyclic strain of the human thoracic aorta: age-related changes. J Vasc Surg. 2009;49:1029-1036.
4. Lam RC, Lin SC, DeRubertis B, et al. The impact of increasing age on anatomic factors affecting carotid angioplasty and stenting. J Vasc Surg 2007;45:875–880.

2nd International Conference on Mathematical and Computational Biomedical Engineering - CMBE2011
March 30 - April 1, 2011, Washington D.C, USA
P. Nithiarasu and R. Löhner (Eds.)

Blood flow dynamics in patient specific arterial network in head and neck

S. Rhode[⋆], M. C. Paul[†], E. Martens[⋆⋆] and D. F. Campbell[⋆⋆⋆]
[⋆†]School of Engineering, University of Glasgow, Glasgow G12 8QQ, UK, [⋆]st.rhode@gmail.com,
[†]Manosh.Paul@glasgow.ac.uk
[⋆⋆]Department of Mechanical Engineering, University of Applied Sciences, 76133 Karlsruhe, Germany
[⋆⋆⋆]Department of Oral & Maxillofacial Surgery, Queen Margaret's Hospital, Fife, UK

SUMMARY

This paper shows a steady simulation of blood flow in the major head and neck arteries as if they had rigid walls, using patient specific geometry and CFD software FLUENT®. The Artery geometry is obtained by CT–scan segmentation with the commercial software ScanIP™. A cause and effect study with various Reynolds numbers, viscous models and blood fluid models is provided. Mesh independence is achieved through wall y^+ and pressure gradient adaption. It was found, that a Newtonian fluid model is not appropriate for all geometry parts, therefore the non–Newtonian properties of blood are required for small vessel diameters and low Reynolds numbers. The k–ω turbulence model is suitable for the whole Reynolds number range.
Key Words: *patient specific model, blood flow dynamics, non–Newtonian model*

1 INTRODUCTION

A better understanding of patient specific blood flow should inform pharmacodynamic simulations of regional drug concentrations, for instance intra arterial catheter placement positioning in chemotherapy for cancer of the head and neck. The ongoing development in computation resources allow engineers to simulate blood flow in vessels in a more realistic way then one decade ago. In contrast to ideal geometry, where many assumptions are required, the patient specific geometry, which is obtained from CT or MRI–scans [1, 2], offers detailed knowledge of flow dynamics including three dimensional vortices. This paper contains a cause and effect study of boundary conditions and material models for a steady simulation with rigid walls and provides conclusions, how to ensure the quality of CFD simulations in a patient specific model.

2 STEADY SIMULATION

The blood flow simulation in head and neck vessels with patient specific geometry was started with a model of the right common carotid artery, shown in Fig. 1. The geometry does not contain the major neck veins, hence the pressure value is not directly comparable with blood pressure measures. It is desirable to include as many geometrical details as possible for further studies, meaning major neck veins and a model including smaller peripheral arterial and venous blood vessels. The Reynolds number was calculated on a cross section near the pressure inlet bc with the velocity magnitude. The geometry was created with the software ScanIP™[3]. A patient's head

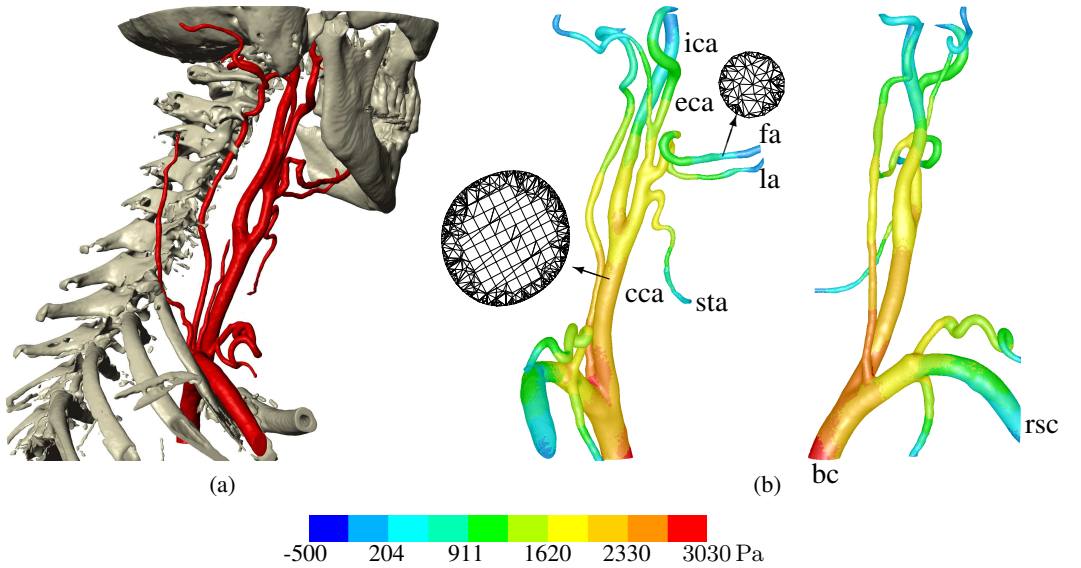

Figure 1: Artery and skull after segmentation (a). Total pressure on the wall for the highest Reynolds number $Re = 3972$. $k - \omega$ turbulence and blood as Newtonian medium was used (b). The pressure inlet is bc–brachiocephalic artery. All the other limits are pressure outlets, rsc–right subclavian artery, cca–common carotid artery, sta–superior thyroid artery, la–lingual artery, fa–facial artery, eca–external carotid artery and ica–internal carotid artery.

and neck CT–Scans were segmented to generate a volume mesh. Using gray scale values, vessels were marked throughout the slices and segmented into a volume. The volume was imported into GAMBIT [4] for remeshing. The CFD simulation was solved by FLUENT®. Blood flow in the human body is pulsatile. In general, a transient CFD simulation takes a very long computational time and requires extensive memory and disk capacity in comparison with a steady simulation. A cause and effect study is compulsory to set up a realistic transient simulation with appropriate parameters. Therefore, it is good to begin with a steady simulation to study the effects of various meshes, turbulence models and material models.

The mesh consists of hexahedron elements in the artery core and tetrahedron elements for the vessel wall. Due to this separation, the core elements have a perfect quality, the skewness being close to zero. The focus was on the tetrahedron elements next to the wall. To resolve the boundary layer, it is required to create a fine mesh next to the wall. The mesh refinement and independence test was done by wall y^+ adaption and pressure gradient adaption in FLUENT®. For the most critical case with the maximum Reynolds number, a value of $y^+ = 5.9$ was achieved, which is slightly above the recommendation of $y^+ < 5$, found in [5] and [6, chapter 12.11.1]. The impact on the simulation results, during the mesh adaption process, was monitored by the velocity magnitude of the bc–inlet and ica–, fa–outlets, shown in Fig. 2. After finding an appropriate mesh, a series of simulations was made. It was decided to vary the Reynolds number in eight steps at the pressure inlet bc in a typical range $676 \leq Re \leq 3972$, given by [7, chapter 3] for the brachiocephalic artery. In order to simplify the simulation, fluid structure interaction was not considered, hence rigid walls were set up for this model.

First, the fluid model of blood was Newtonian and the $k - \omega$ turbulence model was used. In [6, chapter 7.2.2] best practice guidelines are described for an approximate setup for the turbulent kinetic energy k and specific dissipation rate ω for fully developed turbulent pipe flows. The range of Re extends from laminar over transitional to turbulent, measured by the critical Reynolds number for pipe flows $Re = 2300$. However, in pulsating blood flow it is rather improbable that full developed turbulent flow will occur. Neither the entrance length nor the time are long enough

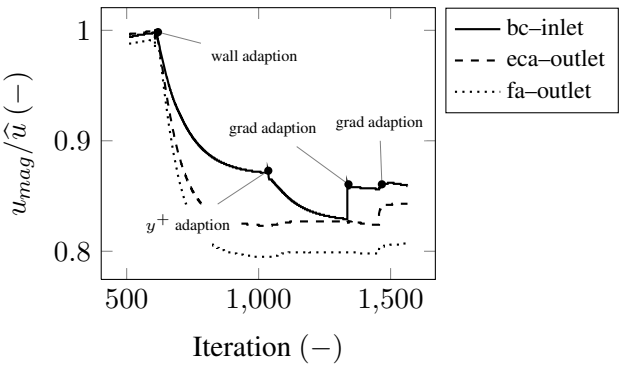

Figure 2: The mesh quality is examined by monitoring mass averaged velocity at pressure inlet and two pressure outlets, using the $k-\omega$ turbulence model, taking blood as a Newtonian medium with the highest Reynolds number, $Re = 3972$. The velocity is normalised for each variable with their maximum value. The first mesh adaption for all cells adjacent to the wall results in decreasing velocity values. The change after the wall y^+ adaption in the smaller arteries (eca and fa–outlet) is marginal, the maximum value of wall y^+ is 5.9. The following velocity gradient adaption was stopped when the value change was below 3 %.

for a fully established turbulent flow. Nevertheless low turbulent effects will be present and have to be taken into account. In a transient simulation, choosing between laminar and turbulent is required in the pre processing. Later on, simulations were done with laminar viscous model and the non–Newtonian power law fluid model. The difference between the $k-\omega$ model in a standard or SST version to laminar viscous model is negligible for low Reynolds numbers, Fig. 3a. The k – ω model is appropriate for low Reynolds number flow with standard or SST option. The difference between both $k-\omega$ models on high Reynolds number is marginal, Fig. 3b.

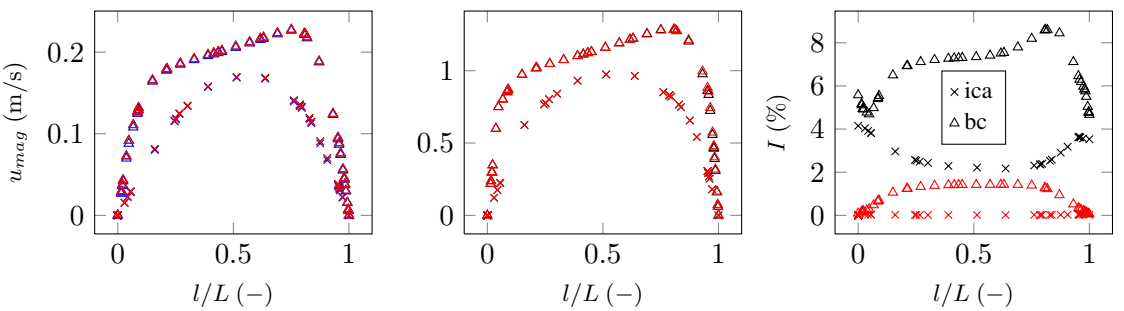

(a) $Re = 676$, black: $k-\omega$, blue: laminar, red: SST $k-\omega$

(b) $Re = 3972$, black: $k-\omega$, red: SST $k-\omega$

(c) black: $Re = 3972$, red: $Re = 676$

Figure 3: Velocity profiles of line probe ica and bc for low and high Reynolds numbers with various viscous model approaches, Fig. (a) and (b). In (a), the difference between booth k–ω models and laminar viscous model is negligible, contrary to (b). In Fig. (c) the turbulence intensity is shown. The blood fluid model is Newtonian.

Blood is a non–Newtonian fluid. Its viscosity depends on the shear rate. For small shear rates, the viscosity increases. Approximately from $\dot{\gamma} > 100\,\mathrm{s}^{-1}$, the viscosity is constant as for a Newtonian fluid, dealt with in [8, chapter 1.2.2]. In [9, chapter 6.4.2], different fluid models are introduced with typical parameters for blood. Every model has advantages and disadvantages, and a comparison is studied in [10]. It was decided to use the power law model for a comparison between Newtonian and non–Newtonian fluid. Fig. 4 shows the influence of the viscous assumption on the simulation results. For small vessels on small Reynolds numbers it is not valid to use a Newtonian model, shown by Fig. 4b. The influence decreases with higher Reynolds numbers and increasing vessel diameter, Fig. 4a and (c). Further studies with various non–Newtonian models are required.

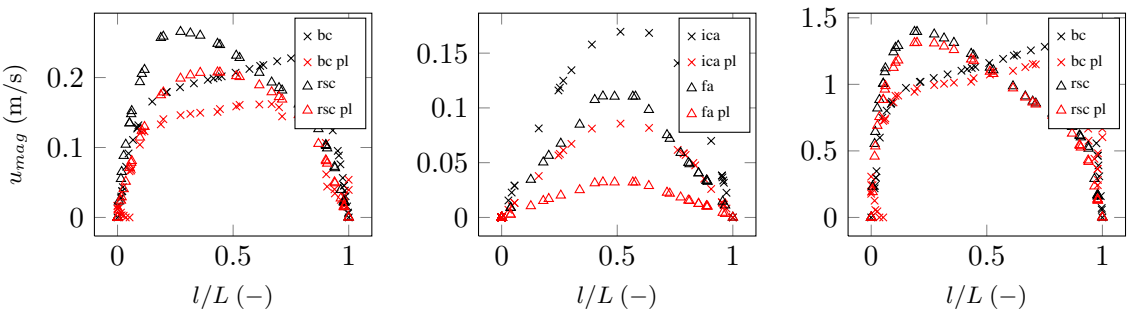

(a) Inlet pressure 150 Pa (b) Inlet pressure 150 Pa (c) Inlet pressure 3000 Pa

Figure 4: Velocity profiles with various blood models. Black markers show blood as a Newtonian medium, red markers as non–Newtonian power law. The non–Newtonian approach results in lower velocity values, due to more viscosity on low shear rate. This effect is more relevant in low Reynolds number flow and in small vessels. The difference between both material models is approximately $50\,\%$, shown in Fig. (b). In contrast, Fig. (c) shows approximately similar functions. The length of line–bc is $L = 0.0121\,\mathrm{m}$, of line–rsc $L = 0.0093\,\mathrm{m}$, of line–ica $L = 0.0057\,\mathrm{m}$ and of line–fa $L = 0.0029\,\mathrm{m}$.

3 CONCLUSIONS

A mesh independent solution is produced with wall y^+ and pressure gradient adaption in FLUENT®. A maximum value of $y^+ = 5$ is desirable. The $k - \omega$ turbulence model is able to provide approximately similar results as the laminar viscous model for low Reynolds numbers. For further simulations the Newtonian fluid model approach is not desirable. The small arteries with low Reynolds number values require a non–Newtonian fluid model with increasing viscosity on low shear rates. A study of the fluid structure interaction is necessary to estimate the influence of the vessel deformation on the simulation results.

REFERENCES

[1] C. A. Taylor and C. A. Figueroa. Patient-specific modeling of cardiovascular mechanics. *Annu Rev Biomed Eng*, 11:109–134, 2009.

[2] T. Schenkel, S. Krittian, K. Spiegel, S. Höttges, M. Perschall, and H. Oertel. The Karlsruhe Heart Model KaHMo: A modular framework for numerical simulation of cardiac hemodynamics. In *IFMBE Proceedings Volume 25/4, World Congress on Medical Physics and Biomedical Engineering, September 7-12, 2009, Munich, Germany*, pages 615–618. Springer, September 2009.

[3] Simpleware LTD, Innovation Centre Rennes Drive Exeter EX4 4RN, UK. *ScanIP™, +ScanFE™ and +ScanCAD™ Reference Guide*, 2010.

[4] Fluent Incorporated, Centerra Resource Park 10 Cavendish Court Lebanon, NH 03766. *Gambit 2.4 User's Guide*, 2007.

[5] S. M. Salim and S. C. Cheah. Wall y + Strategy for Dealing with Wall–bounded Turbulent Flows. In *Proceedings of the International MultiConference of Engineers and Computer Scientists 2009 Vol II*, IMECS, Hong Kong, March 2009. ISBN 978-988-17012-7-5.

[6] Fluent Incorporated, Centerra Resource Park 10 Cavendish Court Lebanon, NH 03766. *Fluent 6.3 User Guide*, 2007.

[7] Y. C. Fung. *Biodynamics : Circulation*. Springer, Berlin, 1984. ISBN 3-540-90867-6 ; 0-387-90867-6.

[8] K. B. Chandran, A. P. Yoganathan, and S. E. Rittgers. *Biofluid Mechanics : The Human Circulation*. Taylor & Francis Group, Boca Raton, Fl, 2006. ISBN 978-0-8493-7328-2.

[9] L. Formaggia. *Cardiovascular Mathematics : Modeling and simulation of the circulatory system*. MS&A ; 1SpringerLink : Bücher. Springer-Verlag Milan, Milano, 2009. ISBN 978-88-470-1152-6. In: Springer-Online.

[10] M. M. Molla and M. C. Paul. LES of non–Newtonian physiological blood flow in a model of arterial stenosis, 2010. Submitted for publication in Medical Engineering & Physics.

2nd International Conference on Mathematical and Computational Biomedical Engineering - CMBE2011
March 30 - April 1, 2011, Washington D.C, USA
P. Nithiarasu and R. Löhner (Eds.)

SIMULATION AND ANALYSIS OF FLOW IN DIFFERENT GEOMETRICAL ARRAYS OF A VASCULAR GRAFT

García J. F.⋆, Gonzalez A.⋆, Carolina Vallecilla⋆, Briceño J.C.⋆
⋆ Department of Mechanical Engineering. University of Los Andes. Bogotá- Colombia.

SUMMARY

Blood flow dynamics has a fundamental role in the success of vascular grafts. In particular, shear stress and secondary flows are involved in platelet activation and aggregation. In order to investigate these three dimensional flow characteristic, a program was developed and applied to the results of computational simulations, that allows to evaluate shear stress and residence time values to get a level of platelet activation. The geometries used, are a simplification of real geometries obtained by injection - corrosion method and angiography images. The results show that shear stress reached values out of normal in the anastomosis region, and secondary flow in the post - anastomosis region.

Key Words: *blood flow dynamics, wall shear stress, graft, platelet activation, computational fluid dynamics.*

1 Introduction

Cardiovascular diseases are the principal cause of death in the world. The bioengineering group of the University of Los Andes has development a regenerative vascular graft of porcine small intestine submucosa. The animal experiments in veins had an important rate of occlusion, so the study of flow is relevant to improve the graft design and implant protocol. Several groups have proposed computational evaluation of flow characteristics in cardiovascular devices and pathologies. In these studies, shear stress along the particle trace was involved in blood damage[1]. Other studies analyzed the flow in axisymmetric stenosis, and created a platelet activation index, based on shear stress and exposure time [2], however there is a shear stress threshold for platelet activation independent of the exposure time to each shear stress. Furthermore, most studies are interested in designing vascular grafts improving the anastomosis in bypass surgery, not in a vessel replace [4, 3]. In this work, we analyze the flow through a simplified geometry of real collagen graft in jugular vein of rabbits. Animal experiments have shown persistent occlusion of grafts. We explain the occlusion evaluating flow variables only and the possible relationship with physiological variables in the occlusion. The real geometry is obtained in the first minute after surgery by injection - corrosion method, and with help of angiography images we build a group of simplified geometries with different relation between graft and vessel diameter. FLUENT (Version 12.1.2, ANSYS) was used based on the finite volume method. We created a particle distribution at intel of the model to be trajectorized. The results was exporting to MATLAB for further analysis of platelet activation.

2 Methods

Three principal objectives were achieved in this study. First, simplified computational geometries based on real geometries and diagnostic images. Second, the computational whole volume flow and particle trajectories. Third, the results of simulation were processed to derive the full 3D shear stress tensor and platelet activation levels. The geometries were created in Solid Edge (Synchronous Technology 2 - SIEMENS CAD software) with different relation of diameters vessel - graft and different diameter of anastomosis, the vessel diameter is constant ($3mm$) and the relation have a range from 1 to 1.5, the last one equivalent to the actual diameter of graft in rabbits. The geometries were meshed with tetragonal elements changing the grow rate. The simulation results showed that the adopted model with 800.000 elements and a refined model with 1'600.000 element have less than 1% of difference between head loss pressure. The boundary conditions are pressure at outlet ($P = 666Pa$) and a velocity paraboloid profile at inlet with average velocity ($V = 0.1\frac{m}{s}$) for the worst case. Steak lines were used to determinate the shear stress and exposure time, a Lagrangian tracking approach was employed with the displacement of each streak line being computed using forward Euler integration of the velocity over a time interval. The streak lines began at the geometry inlet and not all ended at the outlet, some streak lines enter in vortexes.

The results of streak lines are exported to MATLAB, and the stress tensor (ST) at a given point in space was constructed as follows:

$$ST = \begin{bmatrix} \sigma_{xx} & \tau_{xy} & \tau_{xz} \\ \tau_{yx} & \sigma_{yy} & \tau_{yz} \\ \tau_{zx} & \tau_{zy} & \sigma_{zz} \end{bmatrix} \tag{1}$$

where σ is the normal stress and τ is the shear stress. Once the shear stresses were determined, the eigen values were found for every point of trajectories, providing the 3D principal stresses, and the maximum shear stress.

$$\tau_{max} = \sigma_{3D} = \frac{(\sigma_{max} - \sigma_{min})}{2} \tag{2}$$

The obtained data is processed to calculate a level of platelet activation (LPA) [2]:

$$LPA = \sum \tau t_i \tag{3}$$

where τ is the maximum shear stress calculated by equation 2, and t_i is the exposure time exported from the simulation.

The program create a group of symbolic platelets simulating the whole blood volume, a number corresponding to trajectories is randomly selected, and randomly putted in each trajectory, for these group the program calculate the LPA and find the maximum shear stress. A platelet is activated if the LPA is higher than $1.7Pa * s$ or if τ_{max} is higher than $10.5Pa$ [2]. This values are considered for young platelets, the capability to get activated decrease with the age of the platelet [5]. The information is saved and the platelets return to the blood volume, which is randomly mixed. A degeneration factor is included for platelets, replacing randomly some of them in each cycle for new platelets. This cycle is repeated ten times to calculate the percentage of platelets activated. The complete process is repeated ten times to get an average for eliminate the random effect. Results are analyzed and related to possible physiological factors that could accelerate the activation and occlusion process.

3 Results

The principal characteristic of the geometries is the influence of the sutures that creates a parachute shape, the geometries created have six differents relation of diameters for 1.0 to 1.5, and three different diameters of anastomosis $D = 2.5mm, 2mm, 1.5mm$ (Figure 1). The computational simulation shows zones of secondary flow after the first anatomosis, size of this zones increase with diameter ratio (Figure 2). Number of activated per cycle platelets increases when the anastomosis diameter decreases and there is not a general relation with the diameter ratio (Figure 3).

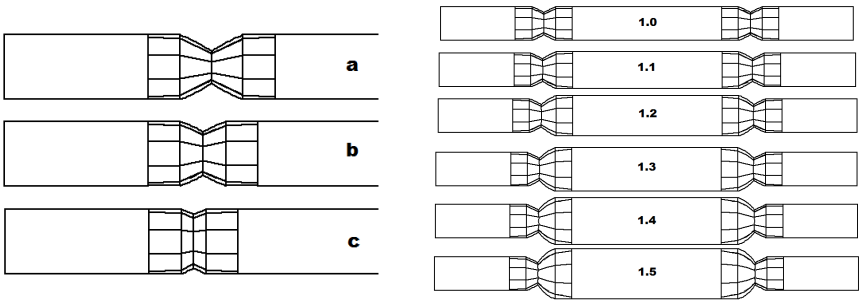

Figure 1: Simplified geometries, different anastomosis diameter (Left), different diameter ratio (Right)

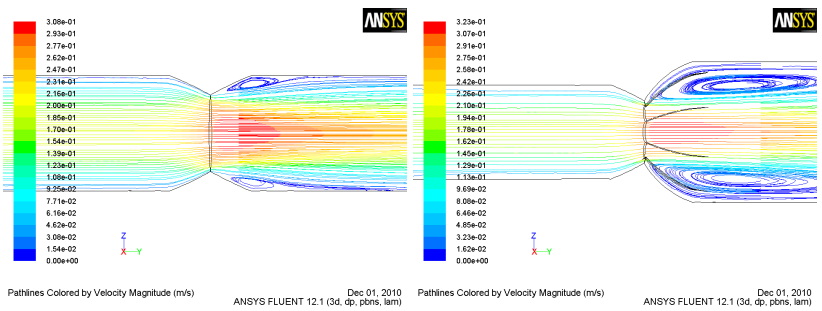

Figure 2: Zones of secondary flows, $D = 2mm$, $\frac{D_{graft}}{D_{vessel}} = 1$ (Left), $\frac{D_{graft}}{D_{vessel}} = 1.5$ (Rigth)

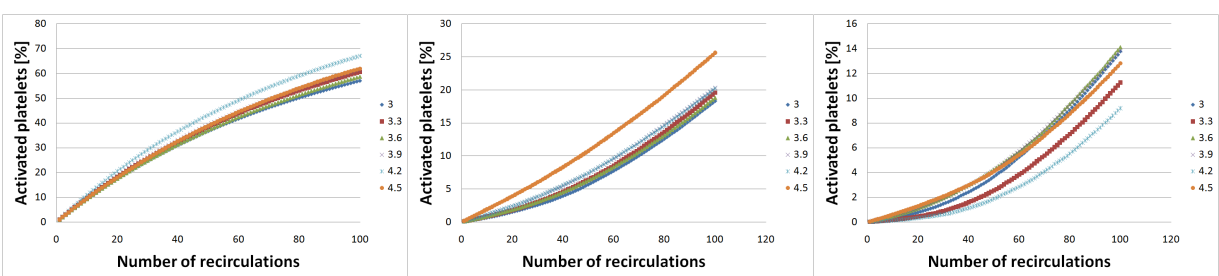

Figure 3: Number of platelet activated after each cycle, $D = 1.5mm$ (Left), $D = 2mm$ (Center), $D = 2,5mm$ (Rigth)

4 Discussion

The results suggest that relation of the LPA with the anastomosis diameter has a maximum between $D = 1.5mm$ and $D = 2.5mm$. Behavior of shear stress have a relation with the relation of diameters and the anastomosis diameter. If the relation of diameter increases, behavior of shear stress register higher values and more population in high values. LPA and shear stress were the two activation factors taken into account, LPA has low values at anastomosis diameters $D = 2.5mm$ and $D = 1.5mm$, and shear stress has low values at $D = 2.5mm$. In general the two factors have minimum values at small relation of diameters. The analysis suggest a relation of diameter $\frac{D_{graft}}{D_{vessel}} = 1$ for the size of the secondary flow zones, also suggest an anastomosis diameter closer to vessel diameter. When a platelet is activated its morphology changes to get more chances of aggregation with other platelets and adhesion to vascular wall. Besides, collagen, the main graft material, is recognized by platelets like presence of injury and gets them activated starting a coagulation process. If enough platelets get aggregated coating starts and the possibility of adhesion to graft wall increases. Physiological factors help flow variables to occlude the graft, but the largest number of platelets and coagulation factors are present 7 to 10 days after injury. This period of time is important because the occlusion could occur during those conditions.

5 Conclusion

In this simplified model, the analysis of flow variables and the activation of platelets suggest an important role of geometry, especially the anastomosis diameter, in the phenomenon of occlusion in collagen vascular grafts. This analysis could be related to physiological coagulation factors and increase the probability of occlusion. An improvement in implantation method is recommended, trying to reduce the influence of suture, avoiding the reduction of diameter at the anastomosis. Another important moment of flow evaluation is the period between 7 to 10 days after surgery, when a inflammatory response happens and the number of platelets increase to a maximum. Future works can include a platelet aggregation model to make a more accurate prediction of occlusion.

References

[1] Chua, L. P.. Su, B.. Lim, T. M.. Zhou, T.. Numerical Simulation of an Axial Blood Pump. Artificial Organs. Volume 31. Issue 7. Blackwell Publishing Inc. 1525-1594.

[2] D. Bluestein; L. Niu; T. Schophoerster; M. K. Dewanjee. Fluid mechanics of arterial stenosis: Relationship to the development of mural thrombus. Annals of Biomed. Eng, 25:344-356.

[3] Aike Qiao, Youjun Liu, Zhihong Guo, Wall shear stresses in small and large two-way bypass grafts, Medical Engineering & Physics, Volume 28, Issue 3, April 2006, Pages 251-258.

[4] Ming Lei, Joseph P. Archie, Clement Kleinstreuer, Computational design of a bypass graft that minimizes wall shear stress gradients in the region of the distal anastomosis, Journal of Vascular Surgery, Volume 25, Issue 4, April 1997, Pages 637-646.

[5] Fulton, John F. A Textbook of Physiology. W. B. Saunders Company. Seventeenth edition. Philadelphia, 1955. Pages 524 - 526.

2nd International Conference on Mathematical and Computational Biomedical Engineering – CMBE2011
March 30 – April 1, 2011, Washington D.C., USA
P. Nithiarasu and R. Löhner (eds)

ASYMMETRIC ARTERY STENOSIS - NUMERIC MODEL

M. Brand[1], M. Teodorescu[2], I. Avrahami[3], J. Rosen[4]

[1] Department of Mechanical Engineering and Mechatronics, Faculty of Engineering, Ariel University Center of Samaria, Ariel, Israel, mosheb@ariel.ac.il
[2] Department of Automotive Engineering, School of Engineering, Cranfield University, Bedford, UK, m.s.teodorescu@cranfield.ac.uk
[3] Afeka College of Engineering, Tel Aviv, Israel, IditA@afeka.ac.il
[4] Department of Computer Engineering, Baskin School of Engineering, University of California, Santa Cruz , CA, USA, rosen@ucsc.edu

SUMMARY

Main cause of restenosis after balloon angioplasty is a result of the stresses generated in the artery as well as from the stent artery interaction. Understanding the factors that are involved in this interaction, and the ability to evaluate the stresses that are formed in the artery, could help to lessen the number of failures. The goal of the present study is to develop computationally efficient numerical models for estimating the contact stresses between the stent and the artery, and to investigate their influence upon stent design, artery and plaque parameters. The artery was taken as a two dissimilar layers model, with non-linear hyper-elastic properties and asymmetric blocking. Solution of this problem is undertaken using a two dimensional model.
For cases of arteries with identical blocking percentages and identical mechanical properties but with different geometry of the blocked strata, the contact stresses for an artery with asymmetric blocking is lower than that received for the symmetric case.

Key Words: *Stent, Mechanical stress, Finite element method.*

1. INTRODUCTION

At the final stage of the balloon angioplasty a stent is inserted into the artery. The stent keeps the internal space of the artery, the lumen, from decreasing, and for this end it requires a specific geometry and mechanical properties [1]. Main cause of restenosis after stent implantation is due to stresses generated in the artery by the stent [2]. The mismatch between the stent and the artery cause high stresses in the arterial wall as well as local injury of the artery. These factors cause formation of new layer producing a narrowing of the arterial lumen and increase the risk for a restenosis [3-5]. In most cases, the shape of the blocked arteries is asymmetric [6, 7]. In this study we formulate numerical models in order to calculate the stresses formed at the artery's wall. We considered typical net structure stents which inserted into arteries with an asymmetric blocking. The arteries contain two different layers with non linear and hyper elastic material properties. The case to be studied treats an artery with an asymmetric blocking around the longitudinal axis. In order to calculate the stresses formed at the artery's wall in these cases, a dimensionless parameter - Damage Factor (DF), was defined. This factor is the average value of the interface pressure between stent and artery- Psa, normalized relative to a value of average blood pressure Pb; DF= Psa/ Pb. Knowledge of this factor is important for choosing the correct size and type of stent for each patient.

2. NUMERIC MODEL

A Model of an Artery with Asymmetric Blocking

In many of the cases, the structure of the plaque is asymmetric. In previous study [8, 9] we showed that it is possible to compute the stresses developed in the artery wall by using a plane numerical 2D model, wherein the results received from this model constitute a good approximation to the results arrived at using the more accurate three dimensional model.
In order to calculate the stress developed at the wall of the artery, we will select a typical case representing the problem described in Fig. 1. Since prior to inserting the stent the blocked artery undergoes inflating by a balloon in order to open the lumen, we will calculate first the shape of the artery as received following the inflating stage. Later on we will derive a model of this artery following the insertion of the stent into it, and compute the stresses generated in the artery wall.

Geometry of an Artery with Asymmetric Blocking after the Inflation

A two dimensional model was formulated to compute the shape of the artery after its inflation. The mechanical properties of these layers were characterized by the properties of a hyper-elastic non-linear material, as was presented in detail in previous study [8, 9].

Simulation of artery inflation by a balloon was made by inserting a rigid cylinder into the volume of the blocked artery. The solution of this problem provides the geometry of the blocked artery following the inflating process (Fig. 2). It can be seen that during the inflating process the healthy part of the artery is stretched. This fact stems from the high stiffness of the blocking plaque strata relative to the stiffness of the healthy layer.

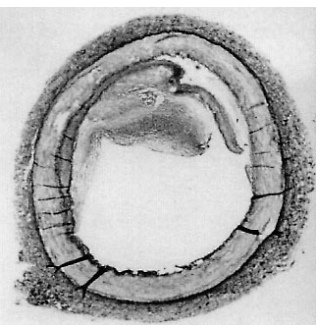

Fig. 1 - Histology of a blocked artery [10].

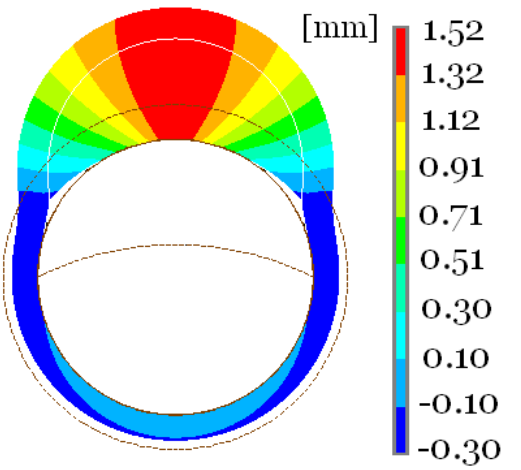

Fig. 2 - Geometry and radial displacements of an artery with asymmetric blocking after its inflation (colored sectors) relative to its state before inflation (dashed line).

Calculation of the geometrical shape after inflation enables to formulate a model of a stent inserted into an artery with asymmetric blocking.

Stent-Artery Interaction for Asymmetric Blocking

Symmetry of the blocked strata around the vertical axis enables to formulate the problem using a symmetric sector containing nine stent's beams in an 180° sector (Fig. 3). The boundary conditions are similar to those defined in cases of the symmetric blocking [8].

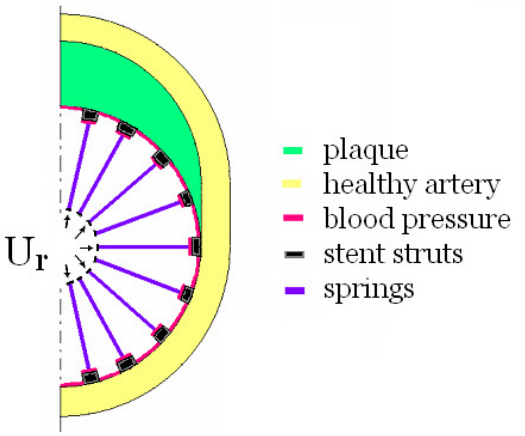

Fig. 3 - Geometry of a two dimensional numerical model of an artery with asymmetric blocking

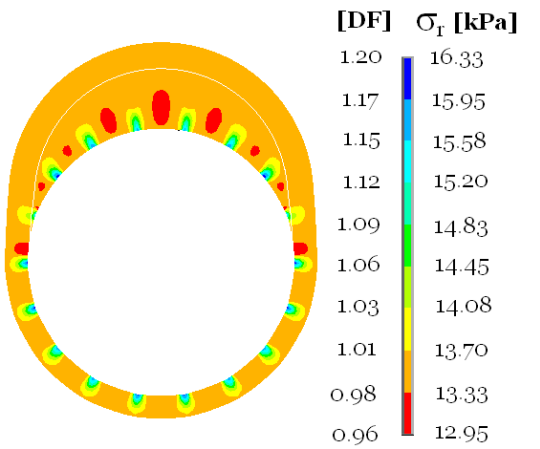

Fig. 4 – Radial stresses and Damage Factor generated at a 3.75 mm diameter artery into which a 4.25 mm diameter stent was inserted

Results

The case selected for presenting the results in this section is a 3.75 mm diameter artery with 40% asymmetric blocking, into which a stent of 4.25 mm diameter was inserted. The radial stresses σ_r for this case are depicted in Fig. 4. A comparison of these results to the results obtained for a case of an artery with symmetric blocking and identical blocking percentage shows that the Damage Factor for an artery with asymmetric blocking is lower than that received for the symmetric case. For the case of an artery with symmetric blocking, the Damage Factor at the stent-artery interface is equal to 1.35. For the artery with asymmetric blocking case, the Damage Factor at the various zones at which the stent's beam is in contact with the artery – is found to be less than 1.2.

A viable explanation for this phenomenon is that it stems from the fact that the stiffness of the plaque strata is higher than the stiffness of the healthy artery. Hence, when the blocking is symmetric, the plaque stratum is located along the circumference of the entire inner volume of the artery, and thus causes larger radial stiffness of the blocked artery's structure. In contra distinction, in the case of a blocking which is asymmetric, part of the artery's wall contains only a healthy layer, which causes lower radial stiffness of the structure.

3. CONCLUSIONS

Solution of this problem is undertaken using a two dimensional model. Two arteries with identical blocking percentages and identical mechanical properties but with different geometry of the blocked strata will have different radial stiffness which eventually influences the stresses generated at the artery's wall. The Damage Factor for an artery with asymmetric blocking is lower than that received for the symmetric case.

REFERENCES

[1.] Schrader, C. S., and Beyar, R., 1998, Evaluation of the Compressive Mechanical Properties of Endoluminal Metal Stents, Cathet Cardiovasc. Diagn., 44, pp. 179–187.

[2.] De Belder, A., and Thomas, M. R., 1998, The Pathophysiology and Treatment of In-stent Restenosis, Stent, 1(3), pp. 74–82.

[3.] Akiyama, T., Di Mario, C., Reimers, B., Ferraro, M., Moussa, I., Blengino, S., and Colombo, A., 1997, Does the High-Pressure Stent Expansion Induce More Restenosis? J. Am. Coll. Cardiol., 29, p. 368A.

[4.] Oesterle, S. N., Whitbourn, R., Fitzgerald, P. J., Yeung, A. C., Stertzer, S. H., Dake, M. D., Yock, P. G., and Virmani, R., 1997, The Stent Decade: 1987 to 1997, Am. Heart J., 136, pp. 578–599.

[5.] Rachev, A., Manoach, E., Berry, J., and Moore, J. E., Jr., 2000, A Model of Stress-Induced Geometrical Remodeling of Vessel Segments Adjacent to Stents and Artery/Graft Anastomoses, J. Theor. Biol., 206, pp. 429–443.

[6.] Kiousis, DE; Gasser, TC; Holzapfel, GA, 2007, A numerical model to study the interaction of vascular stents with human atherosclerotic lesions, Annals of Biomedical Engineering, Vol. 35, No. 11, pp. 1857–1869

[7.] Holzapfel, G; Stadler, M; Gasser, TC, 2005, Changes in the mechanical environment of stenotic arteries during interaction with stents: Computational assessment of parametric stent designs, Journal of Biomechanical Engineering-Transactions of the ASME, Volume: 127 Issue: 1, Pages: 166-180

[8.] M. Brand, M. Ryvkin, S. Einav, J. Rosen, 2009, Numerical Models of an Artery with a Net Structured Stent, WC 2009, IFMBE Proceedings Vol. 25/IV, pp. 1341–1344

[9.] M. Brand, M. Ryvkin, S. Einav ,I. Avrahami, J. Rosen, M. Teodorescu, Numerical Models of an Artery with Different Stent Types, 2010, IFMBE Proceedings 29, pp. 545–548

[10.] Bom N., de Korte C.L., Wentzel J.J., Krams R., Carlier S.G., van der Steen A.W.F., Slager C.J., Roelandt J.R.T.C., 2000, Quantification of plaque volume, shear stress on the endothelium, and mechanical properties of the arterial wall with intravascular ultrasound imaging, *Z Kardiol 89: Suppl 2, II/105-II/111*

2nd International Conference on Mathematical and Computational Biomedical Engineering – CMBE2011
March 30 – April 1, 2011, Washington D.C., USA
P. Nithiarasu and R. Löhner (eds)

FINITE ELEMENT ANALYSIS OF STENTLESS VALVE IMPLANT IN PATIENT-SPECIFIC AORTIC ROOT GEOMETRY

F. Auricchio*, M. Conti*, S. Morganti*§, P. Totaro and M. Viganò****
*Structural Mechanics Department, Università degli Studi di Pavia, Via Ferrata 1, 27100 Pavia, Italy
§ simone.morganti@unipv.it
**IRCCS Policlinico San Matteo, Cardiac Surgery Department, Viale Golgi 19, 27100 Pavia, Italy

Key Words: *Stentless valve, Finite Element Analysis (FEA) , patient-specific modeling.*

1. Introduction

In case of aortic valve leaflet disease, the implant of a stentless biological prosthesis represents an excellent option for aortic valve replacement (AVR) in older and often sicker patients due to its several advantages (Oses et al., 2010). In particular, it provides a more physiological hemodynamic performance and a minor trombogeneticity avoiding the use of anticoagulants. Moreover, a continuos suture technique for implantation is adopted, which may reduce cardiopulmonary by-pass and crossclamp times (Beholz et al., 2006). The clinical outcomes of AVR are related to an appropriate choice of both prosthesis size and replacement technique, which are, at present, strictly related to surgeon's experience and skill. Therefore, also this treatment, like most reconstructive procedures in cardiac surgery, remains more art than science (David, 2002). Nowadays computational methodologies represent a useful tool both to investigate the aortic valve behavior, in physiologic and pathologic conditions (Auricchio et al., 2010), and to reproduce virtual post-operative scenarios (Soncini et al., 2009). The present study aims at supporting the AVR procedure planning through a patient-specific Finite Element Analysis (FEA) of stentless valve implantation.

2. Materials and methods

We evaluate the implant of three different sizes of stentless tissue valves in one aortic root model. Each prosthesis is placed along three different supra-annular suture lines, defining thus nine different scenarios. The host aortic root model is based on patient-specific geometrical data obtained from Computed Tomography - Angiography (CT-A). Firstly, we perform FEA to simulate the prosthesis placement inside the patient-specific aortic root; then, we reproduce, again by means of FEA, the diastolic closure of the valve to evaluate both the coaptation and the stress/strain state. An isotropic hyperelatic Mooney-Rivlin material is adopted to represent the material behavior of aortic leaflets and root tissue. All the analyses are performed using the Abaqus Explicit solver.

3. Results and discussion

For the assumed material properties and aortic bulb geometry under investigation, the results of the prosthesis placement allow to compare the internal stress state for each simulated combination

of prosthesis size and suture line, proving that, both the valve size and the anatomic asymmetry of the Valsalva sinuses, affect the prosthesis placement procedure (see Figure 1a). In dealing with the simulation of valve closure (see Figure 1b), we are able to establish a relation between valve size, suture line and coaptation parameters, as shown in Figure 2.

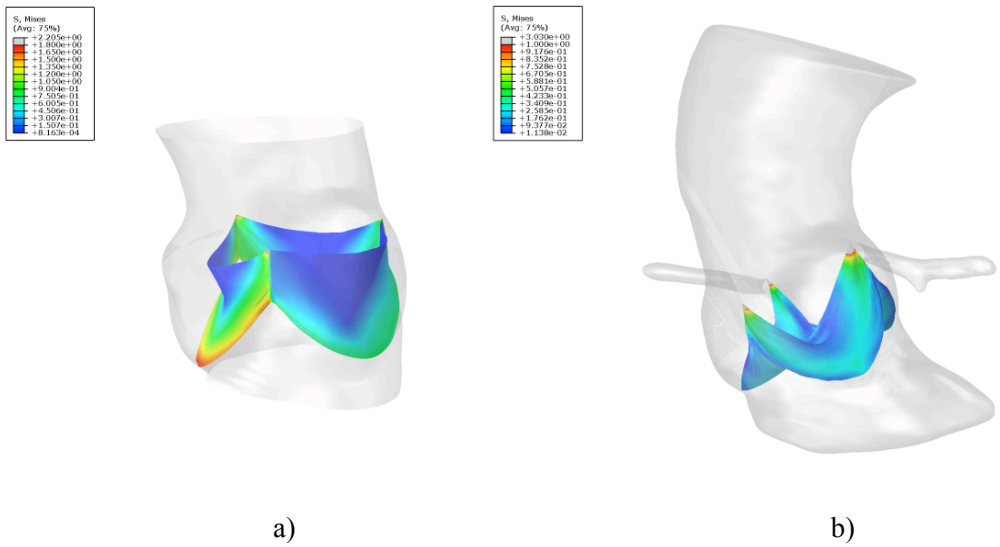

a) b)

Fig.1: Results of implant simulation: (a) valve placement; (b) valve closure.

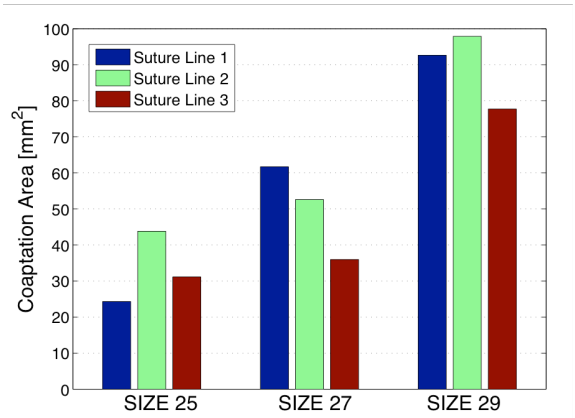

Fig.2: Post-closure comparison.

4. Conclusions

Besides the intrinsic limitation related to the complex system under investigation, we conclude that the proposed methodology offers a useful tool to evaluate the stentless valve implant aiming at anticipating surgical operation guidelines during the procedure planning.

REFERENCES

[1] P. Oses, J.-P. Guibaud, N. Elia, G. Dubois, G. Lebreton, M. Pernot and X. Roques, Freedom SOLO valve: early- and intermediate-term results of a single centre's first 100 cases, *European Journal of Cardiothoracic Surgery*. doi:10.1016/j.ejcts.2010.04.038, 2010.

[2] S. Beholz, S. Dushe and W. Konertz, Continuous Suture Technique for Freedom Stentless Valve: Reduced Crossclamp Time, *Asian Cardiovascular and Thoracic Annals,*14,128-133, 2006.

[3] T. David, Aortic Valve Sparing operations, *Annals of Thoracic Surgery,* 73,1029-1030, 2002.

[4] F. Auricchio, M. Conti, S. Demertzis and S. Morganti, Finite element analysis of aortic root dilation: a new procedure to reproduce pathology based on experimental data, *Computer Methods in Biomechanics and Biomedical Engineering,* in press.

[5] M. Soncini, E. Votta, S. Zinicchino, V. Burrone, A. Mangini, M. Lemma, C. Antona and A. Redaelli, Aortic root performance after valve sparing procedure: a comparative finite element analysis, *Medical Engineering and Physics,* 31, 234-243, 2009.

2nd International Conference on Mathematical and Computational Biomedical Engineering – CMBE2011
March 30 – April 1, 2011, Washington D.C., USA
P. Nithiarasu and R. Löhner (eds)

Intracranial Aneurysms: towards discrimination of hemodynamically stable and unstable 3D virtual patient specific geometries

R. Ouared*, O. Brina*, A. Narata*, A. Marcos*, P. Bijlenga*, K. Schaller*, K.Lovblad* and V. Pereira*
*Hospital of Geneva, Rue Gabrielle-Perret-Gentil 4
1211 Genève 14
rafik.ouared@unige.ch, olivier.brina@hcuge.ch, vitor.mendespereira@hcuge.ch

SUMMARY

In a recent study led in our group at hospital of Geneva we made a non-exhaustive analysis of the impact of segmentation on several geometrical and hemodynamic factors based on seven patient-specific aneurysm models obtained in one month of clinical activity at hospital of Geneva. Comparison of different segmentation protocols and hemodynamic boundary conditions has been made using both ANOVA and visual analysis. Incidence of threshold variations on several geometry and hemodynamic factors is shown as well as uncertainties ranging between 10 and 300%. Moreover and interesting enough, a brand new result has emerged from this study: hemodynamic figures appeared unchanged in three out of seven cases. A methodology is then proposed to check for stability of geometry which could definitely change our approach in using blood flow simulation: "stable" geometries -not sensitive to segmentation and boundary conditions – would give credit to hemodynamic-based assessments, while 'unstable' geometries -very sensitive to segmentation and boundary conditions- , would require more caution in hemodynamic-based predictions.

Key Words: *Blood flow, wall shear stress, aneurysm, stable geometry.*

1. INTRODUCTION

Intracranial aneurysms are still a challenge for current neuroscience research. Computational Flow Simulations is generating very nice qualitative figures and enthusiasming physicians about its clinical application potential. Clinical validation is needed for most of the assumptions acquired with CFD analysis. Indeed, blood flow solvers are reliable if the running conditions are accurately known or they may largely introduce uncertainties in hemodynamic prediction leaving rupture risk analysis and stent treatment planning meaningless [2].

One of the main sources of uncertainty can be the geometrical factor. The segmentation process can bias both the geometrical dimensions and forms of the virtual vessel structures with unpredictable consequences on blood flow virtual behaviour. In practice, operators or automated algorithms try to find a compromise in order to reconstruct both aneurysms and vessels with the same parameterization. The level of noise and artefact in image datasets is such that operators usually seek of having a good quality of the 3D-rendered image of the vascular tree for subsequent meshing processes, with relatively less care seeking accuracy and precision.

Moreover, conditions of contrast injection and image acquisition modalities can very much impact the quality and accuracy of the final outcome.

The aim of this study is neither to find the most accurate segmentation and reconstruction process leading to the most accurate hemodynamic-based predictions, nor to find the best boundary conditions prescriptions for simulation. Instead, it is rather to show limitations of the whole simulation pipeline, which can influence CFD results and in which manner.

2. MAIN BODY

Seven patients harbouring non-ruptured intracranial saccular aneurysms that underwent endovascular treatment at University Hospital of Geneva on March 2009 were selected. We excluded all ruptured, dissected, partially thrombosed or fusiform aneurysms. All patients were submitted to a diagnostic angiogram with 3D acquisitions on a mono-plan angiographic system Allura FD20 (Philips Medical Systems, Best the Netherlands). The images were acquired with 3D rotational angiography (3DRA) modality: 120 projection views over 240 ° C-arm rotation were acquired during 4 seconds around the region of interest initially placed at the isocenter of the C-arm. Contrast agent was injected with a constant flow rate of 3cc/s during 6 seconds (4 seconds to cover acquisition run plus 2 seconds' X-rays' delay). The 256x256x256 reconstruction matrix captures a region of interest (ROI) of 74.54 mm. Courtesy of Philips Medical Systems, has allowed to emulate Xtravision segmentation and 3D-surface rendering offline for persistency of intensity level thresholds which were not available on the Xtravision.

We compare the effect of segmentation by setting seven different procedures with regard to parent vessel truncation and intensity level threshold, namely: "icamax", "icamin", "noicamax5d", "noicamax10d", "noicamin5d", "noicamin10d" and "philips". The latter is a reference isosurface extraction procedure related to the Xtravision. "icamax" and "icamin" models were reconstructed with the whole internal carotid artery from the distal cervical segment to intracranial ICA bifurcation. The minimal threshold was tuned until visualisation of noise around the siphon region vanishes. The maximal threshold was fixed at the level before holes appear in the petrous part of the internal carotid artery. "noicamax10d" and "noicamin10d" models were reconstructed with the proximal and distal extremities clipped from the vascular tree. The proximal ICA segment was corresponding to about 10 times the diameter size of the artery at the level of aneurysm neck. "noicamax5d" and "noicamin5d" correspond to proximal ICA clipping of about 5d. To analyze the incidence of threshold variation on geometry and hemodynamic factors we have used dataset 1 made of {"philips", "icamax", "icamin", "noicamax10d", "noicamin10d"}. To analyse stability of geometries with regard to geometry and boundary conditions variations we have used dataset 2: { philips", "icamax", "icamin", "noicamax5d", "noicamin5d"}.
High quality surface and volumetric finite element grids made of tetrahedral and triangular elements have been produced with ICEM tool to mesh the geometrical models. While meshing, manned intervention was required to define the aneurysm neck. Blood flow is modelled as an incompressible Newtonian fluid described by Navier-Stockes (NS) equation. Rigid no-slip boundary conditions were applied on wall. Inlet and outlet boundary conditions used prescriptions from the 1D model [3]. Constant 1D plug flow [4] was applied on inlets. Outlet pressures were taken to 0 corresponding to absolute pressures between 9000 and 10000 Pa. Implicit numerical scheme formulation was used with fixed time-step of 0.08s. Two 80-time-steps cardiac cycles were computed. Persistency of intermediate results was applied to last cycle only. The calculations took between 45 mns and 3 hours for every run on a 4-Quad 2.80 Ghz CPU HP server running PVM parallel system on 4 partitions and 12 Gbytes memory. The number of elements was varying between 800000 and 3 millions corresponding to more than 1700

elements per mm3. Post-processing has been fully automated thanks to ANSY CEL integrated programming language and Matlab programming toolkits (The MathWorks, version 7.9.0.R2009b). Manned definition of aneurysm neck and aneurysm body has allowed full automatization of post-processing.

Three models out of seven were found hemodynamically stable with regard to segmentation and boundary conditions. Figure 1 shows the instability of one of the models and both the impact of segmentation and boundary conditions on some of the views. Segmentation procedures in dataset 2 are considered here.

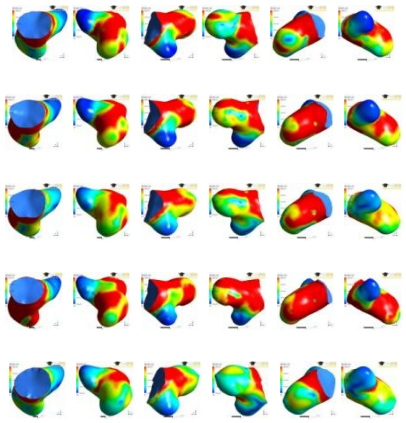

Figure 1: time-cycle-average of wall shear stress. First row corresponds to segmentation Philips, 2nd row to icamax, 3rd row to icamin, 4th raw to noicamax5d and 5th row to noicamin5d. From left to right, the six projection views; X, -X, Y, -Y, Z, -Z. The red color correspond to wss higher than 3 Pa.

Figure 2 shows correlations between intensity threshold variation and some of the geometrical factors through linear regressions. Segmentation procedures in dataset 1 are considered here. Slopes corresponding to outlet and neck surface are quite high in comparison with the other factors. Impact on neck surface may partly reflect manned intervention.

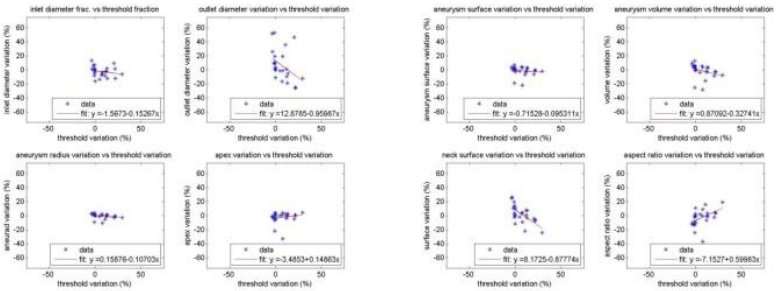

Figure 2: Correlations between intensity thresholds and various geometrical factors; row1 from left to right: inlet diameter, outlet diameter, aneurysm surface, aneurysm volume. Row 2 from left to right: aneurysm radius, apex, neck surface, aspect ratio.

Figure 3 shows correlations between intensity threshold variation and some of the hemodynamic factors through linear regressions. Segmentation procedures in dataset 1 are considered here. Slopes corresponding to maximum time-cycle-averaged wall shear stress and mean wall shear stress variations are quite high in comparison with the other factors. The other factors but those related to pressure and velocity, have statistically the same variation as intensity threshold.

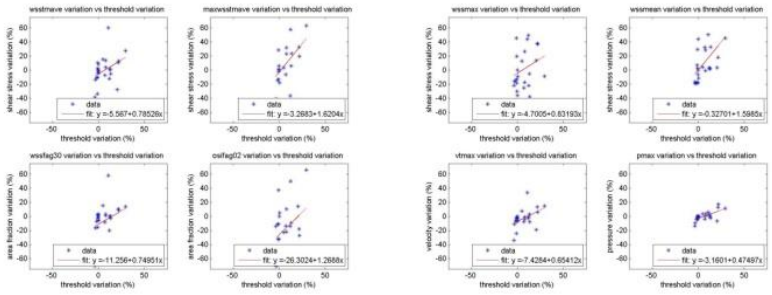

Figure 3: Correlations between intensity thresholds and various hemodynamic factors in aneurysm; row1 from left to right: time-cycle-averaged wall shear stress, maximum time-cycle-averaged wall shear stress, maximum wall shear stress, means wall shear stress. Row 2 from left to right: area fraction of time-cycle-averaged wall shear stress larger than 3.0 Pa, area fraction of oscillating shear stress index larger than 0.2, maximum time-cycle-averaged of blood flow velocity in aneurysm, max pressure in aneurysm. The red lines correspond to the robust linear fit.

ANOVA analysis made on those datasets has allowed to obtain three classes of errors: (95% CI) on geometry and hemodynamic factors: less than 30%, between 30% and 60% and larger than 60%. Errors on geometry factors are restricted to the first two classes while those on hemodynamic factors span over all the three classes.

3. CONCLUSIONS

Segmentation procedures can present a major influence on CFD results. It is found that it is possible to discriminate between hemodynamically stable and instable 3D virtual geometry models. This finding suggests a new approach in using blood flow simulation with confidence to support clinical decisions. Opportunities to standardize segmentation and simulation processes are opened. Correlations of several geometry and hemodynamic factors with intensity threshold have been measured. ANOVA analysis has established classes of errors, which can be used in estimating simulation uncertainties.

REFERENCES

[1] J.R.Cebral, M.A.Castro, J.E.Burgess, R.S.Pergolizzi, M.J.Sheridan and C.M.Putman, Characterization of Cerebral Aneurysms for Assessing Risk of Rupture By Using Patient-Specific Computational Hemodynamics Models, *Am. J. Neuroradiol.*, 26, 2550-2559, 2005.

[2] A.G.Radaelli, L.Augsburger, J.R.Cebral, M.Ohta, D.A.Rufenacht, R.Balossino, G.Benndorf, D.R.Hose, A.Marzo, R.Metcalfe,P.Mortier, F.Mut, P.Reymond, L.Socci, B.Verhegghe, A.F.Frangi, Reproducibility of haemodynamical simulations in a subset-specific stented aneurysm model- A report on the Virtual Intracranial Stenting Challenge 2007, *Journal of Biomechanics*, 41, 2069-2081, 2008.

[3] P.Reymond, F.Merenda, F.Perren, D.Rufenacht and N.Stergiopulos, Validation of a one-dimensional model of the systemic arterial tree, *Am. J. Physiol. Heart Circ. Physiol.*, 297: H208-H222, 2009.

[4] A.Marzo, P.Singh, P.Reymond, N.Stergiopulos, U. Patel, R.Hose, Influence of inlet boundary conditions on the local haemodynamics of intracranial aneurysms, *Computer Methods in Biomechanics and Biomedical Engineering*, 1-14, 2009.

2nd International Conference on Mathematical and Computational Biomedical Engineering - CMBE2011
March 30 - April 1, 2011, Washington D.C, USA
P. Nithiarasu and R. Löhner (Eds.)

Influence of siphon bends on the flow patterns of the internal carotid artery

M. Piccinelli⋆ and T. Passerini⋆
⋆Department of Mathematics and Computer Science, Emory University, 400 Dowman Dr., W401 Atlanta, GA 30322, marina@mathcs.emory.edu, tiziano@mathcs.emory.edu

SUMMARY

The aim of this study is to evaluate how, at physiological flow rates, subsequent and sudden changes in direction, curvature and torsion induced by siphon bends influence the final distribution of hemodynamic variables.

Key Words: *blood flow, wall shear stress, aneurysm, geometry.*

1 INTRODUCTION

Numerous studies in the last decades have underlined the central role of hemodynamics in the localization and progression of vascular pathologies, among which cerebral aneurysms. While conclusive results have not been reached yet, it is well established that vascular geometry has a major effect on fluid dynamics. This in turn has affirmed the need for understanding the complex relationship between anatomy and haemodynamics. A district of particular interest in the cerebral vasculature is the internal carotid artery (ICA). The two ICAs (together with the basilar artery) are responsible for the perfusion of the brain, being the feeding arteries of the circle of Willis. Therefore, the hemodynamics enviroment in the intracranial circulation depends on the flow conditions in the the ICAs. This was noted for instance by Hans et al. [1] who reported on a case of spontaneous regression of two supraophthalmic aneurysms after endovascular closure of the right ICA. Furthermore, ICAs are typical sites of aneurysm development.

One of the most striking anatomical characteristic of the ICA is its being S-shaped in the terminal region, which has the form of a siphon. This siphon can be represented as the non-planar sequence of planar bends, and as such is known to induce secondary motion in the blood flow, yielding complex spatial patterns of the wall shear stress. Recent studies by Takeuchi et al. pointed out that the shape of the siphon determines a flattened velocity profile at the terminal bifurcation of the ICA, while the velocity profile at the bifurcation of the middle cerebral artery (MCA) results sharpened [3]. In other word, the siphon could have a potential protective effect on the vascular wall at the terminal bifurcation of the ICA (the estimated hemodynamic stresses resulted much lower than at the bifurcation of the MCA).

On the other hand, the morphology of the siphon may vary significantly in the population. The curvature of the bends, the radius and the torsion of the ICA could have different effects on the flow features. Parametric studies on idealized geometries have been conducted to classify the flow patterns when varying the geometry or the flow regimes. Lee et al. considered steady flow in three-dimensional non-planar double bend geometries, at different Reynolds numbers. They observed that non-planarity of the bends has the biggest effects on mixing and swirling of flow [3]. With

a similar perspective, Niazmand et al. considered steady flows in S-shaped bends with different sweep angles and at different Reynolds number, and reported on the strong dependence of flow patterns on both Reynolds number and bend sweep angle [4]. In particular, for high Reynolds numbers, depending on the bend sweep angles the secondary vortex pattern of the first bend may persist partially or totally throughout the second bend.

The knowledge gained from idealized geometries cannot typically be applied straightforward to anatomically correct geometries. The hemodynamics strongly depend on the local details of the vessel morphology (e. g. non circular sections, non uniform radius, different angles and curvature of the bends). On the other hand, given the presumed role of the ICA siphon in flattening the velocity profile at the terminal bifurcation, it is expected that the geometry of the bends correlates with the flow features in the ICA consistently across the population. In other words, a similar parametric analysis to that proposed on idealized geometries can be conducted on patient specific geometries, with a proper choice of the geometrical parameters. In this work we describe the methods that we use to characterize the vessel morphology in an objective and semi-automatic way. The parameters chosen to describe the vessel geometry are described in the methods section, where we also report on the observed hemodynamics quantities. Preliminary analysis on a limited number of cases are then presented.

2 METHODOLOGY AND RESULTS

Geometric analysis and synthesis of a vascular tree is in general a challenging task, both for the extreme anatomical variability of in vivo morphologies and for the availability of many potential quantities of interest. In order to enable quantitative comparisons of geometric features across a wide population, standardized and robust methods for geometric quantities definition and measurement are in order. The methodologies described in the following are implemented in the Vascular Modeling ToolKit (*www.vmtk.org*), an open source software packages for segmentation, geometric characterization of vascular structures and data post processing routines. The hemodynamics computations have been performed with a software based on LifeV (*www.lifev.org*), a C++ software library of algorithms and data structures for the numerical solution of partial differential equations.

Six 3D patient-specific surface models of cerebral vasculature were selected from the Aneurisk database (the Aneurisk project, 2005-2008); in all cases, the subject did not present aneurysms along the internal carotid artery. The models had been previously segmented from 3D rotational angiography images by means of the segmentation tools available within VMTK. For each complete surface model, the vessels downstream the terminal bifurcation of the ICA were removed. Similarly, the small side branches originating from the ICA, namely posterior communicating artery and ophthalmic artery, were removed in order to isolate the carotid siphon. Each siphon model was then objectively subdivided into individual bends following these steps [6]: (i) the centerline of each vessel was extracted and its curvature and torsion computed; (ii) starting from the ICA bifurcation and moving in the upstream direction, each bend was identified as centered in a curvature peak and delimited by two enclosing (proximal and distal) torsion peaks. Three variants were then constructed for each siphon model. The first variant comprised the three successive siphon bends preceding the terminal bifurcation. The second model included the last two bends, and the third model included only the latter bend. 18 models were finally available for the CFD simulations. Figure 1A depicts the three configurations analysed for one of the siphon models.

A geometric characterization of the siphon models was performed and parameters that are likely to play a role in determining the flow patterns were computed by means of the tools available within VMTK [7]. Mean radius, length, mean and peak curvature and mean torsion were calculated for

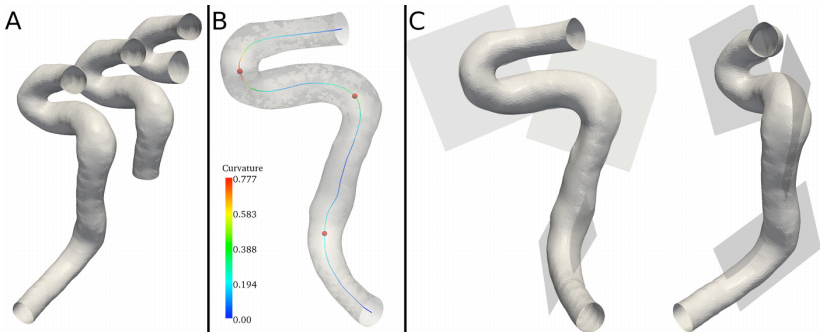

Figure 1: A. 1-, 2- and 3-bend model for one of the ICA siphon analyzed; B. curvature profile of the 3-bend model centerline and identification of the curvature peaks; C. two different views of the 3-bend model with the osculating planes approximating the bends.

each bend. Moreover, to characterize the way two consecutive bends are linked together, each bend was approximated with its osculating plane constructed at the curvature peak, and the angle between two consecutive "approximating" planes was evaluated. In a similar way, the torsion values evaluated at the bend borders were computed, as a measure of how fast the osculating plane is twisting in space along the centerline. Figure 1C shows the approximating planes for one of the three-bend models.

Computational fluid dynamics simulations were carried out in all of the geometric models (1-, 2- and 3-bends siphon models) imposing an unsteady flow condition at the model inlets. The boundary condition featured the same time pattern in all the simulated cases, while the amplitude of the prescribed flow rate was tuned in each case. For each three-bend ICA model, the inflow condition was defined such that the time averaged Reynolds number on the inlet section was equal to 350, found to describe with a good approximation the flow regime of an ICA flow rate in the range of physiological values [8]. The same flow rate was then prescribed in the simulations on the corresponding two-bend and one-bend models. The wall shear stress (WSS) was computed for each simulated case, and the time-averaged WSS was considered as a synthetic descriptor of the shear load exerted by the blood flow on the arterial wall, under unsteady flow conditions.

For each set of variants of each siphon models (1-, 2- and 3- bends models), we plan to compare the computed flow features in order to evaluate (i) to what extent the WSS distribution along the vessel wall is influenced by upstream portions of the model; (ii) how the concatenation of bends affects the distribution of flow features along the vessel and particularly at the outflow, in particular with respect to the geometry of the bends (e. g. slow vs. abrupt changes in osculating planes orientation). Post processing methodologies available within VMTK are going to be employed to perform these comparisons. The siphon model is topologically equivalent to a cylinder, therefore it can be mapped onto a rectangular parametric space. After this mapping step, it is possible to perform point-to-point comparisons of variable fields defined over the surface of different geometrical models [9]. Figure 2 (LEFT) displays the result of this mapping procedure on one of the cases analysed. To evaluate the distribution of hemodynamics variables on the 3D volume, the velocity fields of all the three configurations can be sliced at the same positions along the models centerlines. This allows to compare the velocity profiles in the different models (Figure 2 RIGHT).

3 CONCLUSIONS

While it is well-known that vascular geometry has a major impact on haemodynamics, it is still difficult to qualitatively predict and quantitatively evaluate its effects on hemodynamics variables

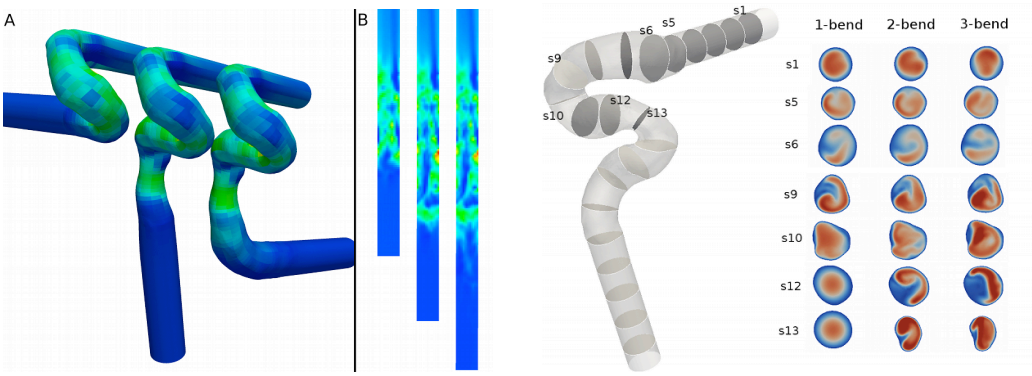

Figure 2: LEFT: Wall shear stress distribution on the 1-, 2- and 3-bend configurations of one of the siphons simulated over the 3D surface models (A) and after mapped onto rectangular spaces (B). RIGHT: Slices over the velocity field for positions along the artery centerline common to all the three configurations (velocity magnitude plotted).

such as WSS, velocity distribution and more in general flow patterns. In particular, the carotid siphon represents an interesting case due to the sequence of bends that characterizes its anatomy. We present robust computational techniques that allow the investigation of these aspects in patient-specific geometrical models with the goal of identifying potential relationship between geometric vascular features (curvature, torsion, rate of change of osculating planes) and haemodynamic variables.

REFERENCES

[1] F. J. Hans, T. Krings, M. H. T. Reinges and M. Mull, Spontaneous regression of two supraophthalmic internal cerebral artery aneurysms following flow pattern alteration. *Neuroradiology*, 46 (6), 469-73, 2004.

[3] S. Takeuchi, T. Karino, Flow patterns and distributions of fluid velocity and wall shear stress in the human internal carotid and middle cerebral arteries, *World Neurosurgery*, 73 (3), 174-85, 2010.

[4] K. Lee, K. H. Parker, C. Caro and S. J. Sherwin, The spectral/hp element modelling of steady flow in non-planar double bends, *International Journal for Numerical Methods in Fluids*, 57, 519-529, 2008.

[5] H. Niazmand and E. R. Jaghargh, Bend sweep angle and reynolds number effects on hemodynamics of s-shaped arteries, *Annals of Biomedical Engineering*, 38 (9), 2817-28, 2010.

[6] M. Piccinelli, S. Bacigaluppi, E. Boccardi, B. Ene-Iordache, A. Remuzzi, A. Veneziani and L. Antiga, Geometry of the ICA and recurrent patterns in location, orientation and rupture status of lateral aneurysms: an image-based computational study, *Neurosurgery*, in press, 2010.

[7] M. Piccinelli, A. Veneziani, D. A. Steinman, A. Remuzzi and L. Antiga, A framework for geometric analysis of vascular structures: application to cerebral aneurysms, *IEEE Transactions on Medical Imaging*, 28(8), 1141-55, 2009.

[8] T. Passerini, Computational hemodynamics of the cerebral circulation: multiscale modeling from the circle of Willis to cerebral aneurysms, *PhD Thesis*, Politecnico di Milano, 2009.

[9] L. Antiga and D. A. Steinman, Robust and objective decomposition and mapping of bifurcating vessels, *IEEE Transactions on Medical Imaging*, 23(6), 704-713, 2004.

Aneurysm enlargement utilizing a fiber-based growth model

Fred Nugen, Luca Dedé, Thomas JR Hughes

Institute for Computational Engineering and Sciences
The University of Texas at Austin

Motivation

Aneurysms are common, life-threatening, and poorly understood. It is nearly impossible to observe the disease process which leads to aneurysms, especially in early stages. As a result, little is known about causes of the disease, and there is no strongly-correlated marker of patient prognosis. Several things are known. An aneurysm's mechanical environment has a strong influence over its behavior; weakening of the arterial wall is the main proponent of aneurysm rupture; and remodeling and turnover are chief mechanisms of weakening. We utilize these principles to build computational and analytic tools that can reconstruct the disease process and serve as a predictor of patient prognosis.

Overview

We have developed a theoretical formulation, a modeling pipeline, and a set of simulation tools for the prediction of enlargement of aneurysms. The constitutive relations describe a neo-Hookean elastin background matrix and two families of supporting collagen fibers with exponential stiffening. The collagen fibers change their structure through growth and remodeling, as described in [1]; briefly, stress induces growth (addition of mass), and natural turnover of cells in the body induces remodeling. The two together can induce aneurysm enlargement.

The modeling paradigm is multiscale in time, with one timescale on the order of seconds (the cardiac cycle) where hemodynamic stimuli are produced, and the other on the order of weeks to months (the aneurysm's enlargement) where growth and remodeling occur. Computation will proceed using a staggered approach, switching between the two timescales.

The simulation will build on existing technologies for modeling tissue as a solid anisotropic elastic material [2]. Isogeometric analysis with NURBS is used, based on its suitability for describing organic geometries, previous successes analyzing both fluid and structures, and robustness with respect to large deformations.

Enlargement Mechanisms

Enlargement is an increase in dilatation. The enlargement mechanisms we employ involve turnover of collagen. Collagen fibers are assumed to have a

finite lifespan. Old collagen fibers are removed by the body and replaced with new ones. New fibers are placed at a fixed rate of pre-stretch (regardless of any other fibers), and the mass rate of fiber placement may not equal the decay rate. Through these mechanisms, fibers may lengthen or contract, and may increase or decrease in number. An aneurysm may increase or decrease in size, and increase or decrease in mass.

Lesion initiation

We investigate two major categories of aneurysms: aneurysms initiated by elastin degradation, and aneurysms initiated by high wall shear stress.

Elastin Degradation

While aneurysm formation is clearly multi-factorial, localized degradation of the elastin layer within the wall of an artery is believed to be the predominant biomechanical feature.

One method of modeling lesion initiation is to postulate that the elastin layer has completely degraded in a specified region and to allow blood pressure and remodeling and turnover to dictate lesion progression. This technique has been extensively tested by many researchers and is generally found to formulate fusiform aneurysms in a manner consistent with what is observed in patients with the disease.

High Wall Shear Stress

A second method of postulating lesion initiation is by using geometric features of the shape of the artery as the main proponent of vessel weakening. In this way, aneurysm development is not as predetermined by the user as with specified elastin degradation, but rather arises more naturally from features specific to the patient in question.

Areas of abnormally high (and low) WSS are known to be predictive of aneurysm enlargement and rupture. Moreover, abnormal WSS indicates disease progression during all phases of aneurysm formation: initiation, enlargement, and rupture. Initiation often occurs at sharp bends and T-junction branches, sites of high WSS in healthy arteries. Enlargement is predicted by the size and intensity of jets of blood flow onto the distal wall of an aneurysm. The neck and distal wall of many saccular aneurysms is a site of continued high WSS, which may be a factor leading to continued weakness and rupture.

In order to obtain WSS, a fluid calculation is performed and averaged over a cardiac cycle. This function is used as a seed for degradation of elastin and for determining the growth rates of fibers within the wall at each point. Growth and remodeling are computed until enough deformation has occurred that a new fluid calculation is warranted. The process repeats, switching back and forth between the timescales.

We believe these investigations may provide an understanding for enlargement of saccular aneurysms.

Verification and Validation

The proposed implementation is verified on geometries representing healthy arteries under normal conditions. One of the requirements is a stability check: ensuring the simulation tools predict that healthy arteries remain healthy.

We have begun a pilot clinical study to validate the results. By using patient-specific geometries from longitudinal image data, we can quantify attributable risk of aneurysm growth and remodeling due to mechanical factors. Validation comes as follows: two image datasets are obtained from the same subject, spaced about one year apart. A simulation is run beginning from a geometry representing the early dataset, and is used to predict the geometry of the later dataset. The results of this study will be used to drive avenues of further biomechanical research as well as to suggest the utility of performing large-scale studies.

Future Work: Fluid-Solid-Growth Models

All of the above modeling paradigms lead toward the combination of fluid mechanics, solid mechanics, growth mechanics, and patient-specific geometries into one consistent supermodel. Ideally, the supermodel will be valid at all timescales from the cardiac cycle to growth and remodeling. As each piece is tested, we will expand it little by little into progressively richer scenarios until we can make strong statements about disease risk in particular individuals.

The modeling systems involved in this work are necessary steps to providing better conclusions as to the behavior and mechanical nature of diseased arteries, as well as to improve the overall predictive capability of simulation tools. Physicians who use these tools will better understand aneurysm dynamics, improve their morbidity and mortality rates, and save lives.

[1] S. Baek, K.R. Rajagopal, J.D. Humphrey,
"A theoretical model of enlarging intracranial fusiform aneurysms,"
Transactions of the ASME, 128:142--149, February 2006, DOI:10.1115/1.2132374.

[2] Y. Bazilevs, V.M. Calo, Y. Zhang, and T.J.R. Hughes,
"Isogeometric fluid-structure interaction analysis
with applications to arterial blood flow,"
Computational Mechanics, 38:310--322, 2006, DOI:10.1007/s00466-006-0084-3.

2nd International Conference on Mathematical and Computational Biomedical Engineering - CMBE2011
March 30 - April 1, 2011, Washington D.C, USA
P. Nithiarasu and R. Löhner (Eds.)

Towards the Validation of a Virtual Coiling Technique Using a Real Versus a Simulated Bolus Injection

Hernán G. Morales[⋆†], Ignacio Larrabide[†⋆], Maria-Cruz Villa-Uriol[⋆†], Adrianus J. Geers[⋆†] and Alejandro F. Frangi[⋆†‡]

[⋆] Center for Computational Imaging & Simulation Technologies in Biomedicine (CISTIB), Universitat Pompeu Fabra, Barcelona, Spain

[†] Networking Center on Biomedical Research (CIBER-BBN), Barcelona, Spain

[‡] Institució Catalana de Recerca i Estudis Avançats (ICREA), Barcelona, Spain

alejandro.frangi@upf.edu

SUMMARY

Endovascular coiling is a well-established therapy to treat intracranial aneurysms. However, its outcome is not always predictable. The purpose of this work is to present the first step towards the validation of a virtual coiling technique based on the comparison of *in vivo* medical images and computational fluid dynamics (CFD) modeling with a bolus injection. A patient harboring a coiled aneurysm was selected. A three-dimensional vascular geometry derived from medical image was used. The aneurysm geometry was virtually coiled using a technique that dynamically plans the path that each coil would follow during their insertion. Afterwards, a CFD model was constructed simulating the bolus injection using the time-intensity curves (TIC) obtained from a digital subtracted angiography image sequence. A qualitative comparison between real and virtual angiographic images, and the quantitative differences between TIC were assessed. As a result, the CFD model properly reproduced the global aspects of the injected contrast agent along the vascular model, including the branches downstream the coiled aneurysm.

Key Words: *blood flow, aneurysm, coiling, time-intensity curve*

1 INTRODUCTION

Intracranial aneurysms are arterial dilatations often occurring at branching points in the circle of Willis. One of their treatment options is endovascular coiling [1]. This minimally invasive treatment tries to prevent rupture by the insertion of biocompatible metal alloy coils to block the blood flow into the aneurysm. However, coiling outcome is not always predictable and thereby, being able to assess the hemodynamic alterations induced by coiling could have the potential to impact clinical practice at pre-operative planning and post-treatment diagnosis.

Computational fluid dynamics (CFD) modeling has grown as a valuable tool for better understanding of hemodynamics. Nonetheless, to evaluate the reliability and accuracy of numerical approaches, a proper validation is mandatory. Virtual angiography has been proposed as a tool to validate CFD studies on hemodynamics [2]. This work presents the first step towards the validation of a virtual coiling technique for intracranial aneurysms by CFD modeling with virtual angiography.

2 MATERIALS AND METHOD

2.1 Patient Information

A 37-years old female harboring a right middle cerebral artery bifurcation aneurysm was selected for this study. Two three-dimensional rotational angiography (3DRA) images of this aneurysm, before and after endovascular coiling, were acquired using a Philips Integris System (Philips Healthcare, Best, The Netherlands). A digital subtracted angiography (DSA) image sequence was also acquired synchronized with the bolus injection of a contrast agent (during 2.5 s at 4 ml/s). DSA images were acquired at 60 frames per second for a period of 7.8 s. The information about the number of coils, and their respective diameters and lengths were also recorded.

2.2 Numerical Approach

To model the blood flow with the bolus injection for this patient, geometrical and hemodynamic information was extracted from the medical images as follows:

Vascular models: A three-dimensional (3D) representation of the vascular luminal surface was extracted from the region of interest of a 3DRA image obtained before coiling, using a geodesic active region method combined with an image intensity standardization technique [3]. Then, the resulting 3D geometry was cropped, cleaned and smoothed.

The same method was applied on the 3DRA image after coiling without contrast and the resulting 3D geometry was combined with the aneurysm surface previously created to extract a similar volume where the coils were actually inserted. This new volume was called coiled region. Afterwards, a virtual coiling technique [4] was applied to coil the model, using as input the diameters and lengths of the coils inserted in the real aneurysm.

The virtual coiling technique sequentially inserts the coils by advancing its tip through a planned path, starting from an initial position and direction inside the coiled region. To build the path, the coiling technique avoids coil migration outside the coiled region and the collisions between coils by smoothly changing the advancing tip direction. If the coil tip is trapped by other coils, the technique retreats the coil tip and redirects its advance. As a result, the virtual coiling produced a similar representation of the real inserted coils, including the small coil segment protruding in the parent artery of this specific aneurysm (Fig. 1). The generated packing density, defined as the ratio between the coils and coiled region volumes, was 43%.

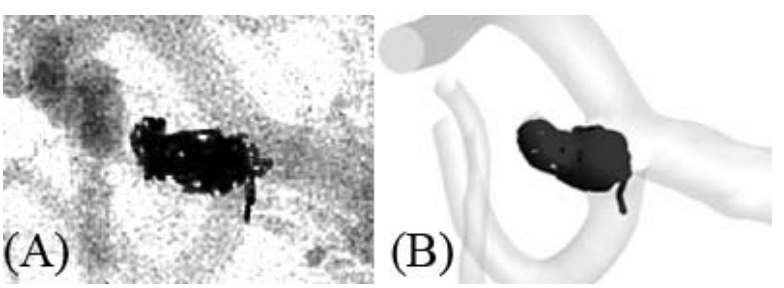

Figure 1: (A) Medical image. (B) Geometrical models of the vasculature and virtual coils.

Computational Fluid Dynamics: Once the geometric models were obtained, a volumetric mesh was created. The mesh was generated using the commercial software ANSYS ICEM-CFD v11 (Ansys Inc., Canonsburg, PA). This volumetric mesh was exported in ANSYS CFX v11 (Ansys Inc., Canonsburg, PA) to compute the fluid flow. Blood was modeled as a Newtonian incompressible fluid with viscosity and density of 0.00375 Pa·s and 1060 kg/m^3 respectively. Flow was

assumed to be laminar. Vessel wall and coil surfaces were imposed as rigid with no-slip boundary condition. At the outlets, a traction-free boundary condition was applied. For the inlet flow boundary condition, a physiological blood flow waveform from a normal individual was imposed. This flow waveform was scaled based on the estimation of the mean flow velocity, calculated with a time-intensity curve (TIC) approach [5] at different locations in the vasculature. Besides, the increase of flow rate due to the bolus injection was considered using the information of the real contrast injection (Fig. 2B). The cardiac period was 0.6 s, and it was derived from the averaged time differences between consecutive peaks or valleys, presented in the TIC (Fig. 2B).

To compute the contrast propagation through the vasculature, a scalar field of its concentration was solved from a transport equation following the strategy of previous CFD studies [6][7]. The TIC at the inlet region of the DSA images was imposed as boundary condition for the contrast concentration at the inlet of the CFD model (see Fig. 2B) with a homogeneous distribution. The TICs computed from the CFD simulation were calculated using the contrast concentration at the four control regions defined in the medical images (A-D in Fig. 2A). Each TIC was normalized based on the highest value of each curve. The visualization of the virtual angiography images were done by volume rendering as was previously performed on a similar CFD study of blood flow with bolus injection [8].

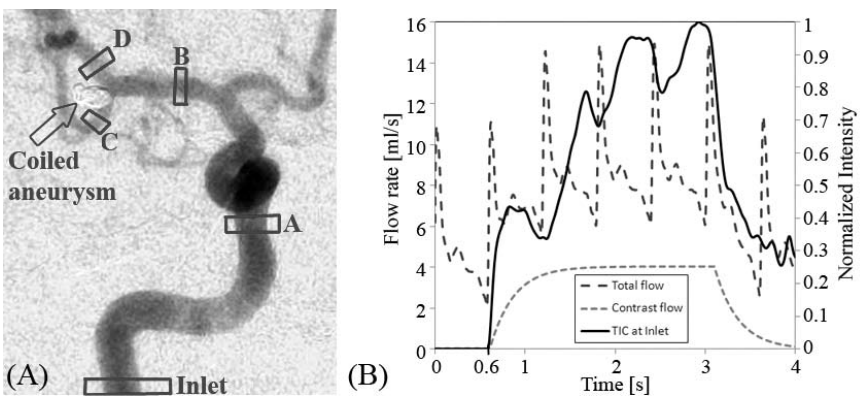

Figure 2: (A) DSA image with the control regions for TIC measurements. (B) TIC at inlet of the image and flow rates of contrast and total flow.

3 RESULTS

Figure 3 compares DSA images with the corresponding virtual angiography obtained from the CFD model at two different time instants during the contrast filling phase. Once the vasculature was full of contrast, the intensity oscillations of the TIC (see Fig. 4) were not visible. Qualitatively, the intensity of the contrast shows a good correspondence between the DSA images and the virtual angiography.

In Fig. 4, the TICs of both *in vivo* and CFD are presented at the control regions in the vasculature. The plots show in total 4 s, including the initial part of the wash-out phase. This was done since the superposition of the arteries of interest with other arteries and veins downstream, introduces important changes in the background of the medical images, generating an overestimation of the TIC after the fourth second. The CFD model was able to capture the global flow characteristics obtained from the intensity of the contrast injection, including the regions downstream the aneurysm (Fig. 4C and D). A good agreement between the TICs was observed, especially when the contrast arrived at the control regions, peaks and valleys of the TIC and the intensity gradient during the filling and wash-out phases.

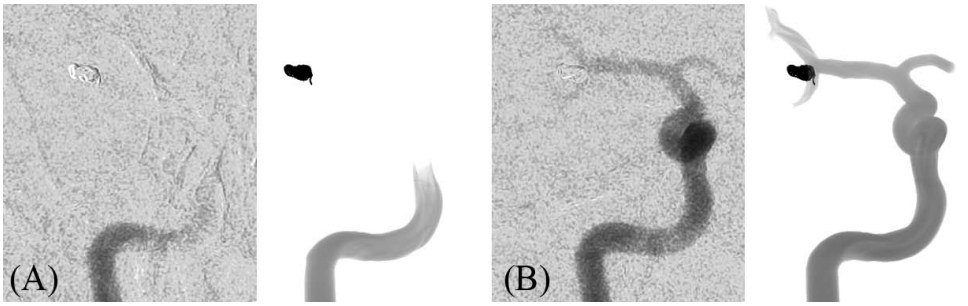

Figure 3: Visualization of *in vivo* and virtual angiography images at (A) 0.7 s and (B) 0.9 s.

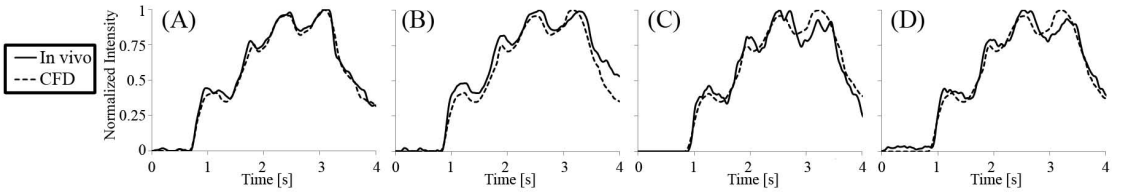

Figure 4: Comparison of the TIC of the *in vivo* images and CFD model. (A)-(D) correspond to the four control regions defined in Fig. 2A.

4 CONCLUSIONS

We have presented a comparison between *in vivo* images and a CFD model of blood flow with a bolus injection in one patient-specific aneurysm, as a first approach for the validation of a virtual coiling technique. Good agreement was found between the *in vivo* medical images and virtual angiography results, as well as between the TICs along the vasculature including downstream the coiled aneurysm.

REFERENCES

[1] van Gijn, J. and G.J. Rinkel, Subarachnoid haemorrhage: diagnosis, causes and management. *Brain*, 2001. 124(Pt 2): p. 249-78.

[2] Ford, M.D., *et al.*, Virtual angiography for visualization and validation of computational models of aneurysm hemodynamics. *IEEE Trans Med Imaging*, 2005. 24(12): p. 1586-92.

[3] Bogunovic, H. *et al.*, Automated Segmentation of Cerebral Vasculature with Aneurysms in 3DRA and TOF-MRA using Geodesic Active Regions: an Evaluation Study, *Medical Physics*, *In Press.*

[4] Morales, H. *et al.*, Influence of Coil Packing Rate and Configuration on Intracranial Aneurysm Hemodynamics, *World Congress on Medical Physics and Biomedical Engineering*. 2009. p. 2291-2294.

[5] Bogunovic, H. and Loncaric, S. Blood flow and velocity estimation based on vessel transit time by combining 2D and 3D X-ray angiography. *Med Image Comput Comput Assist Interv*, 2006. 9(Pt 2): p. 117-24.

[6] Larrabide, I. *et al.*, Fast virtual deployment of self-expandable stents: Method and in vitro evaluation for intracranial aneurysmal stenting. *Med Image Anal*, 2010. *In press.*

[7] Sun, Q. *et al.*, Phantom-based experimental validation of computational fluid dynamics simulations on cerebral aneurysms. *Medical Physics*, 2010. 37(9): p. 5054-5065.

[8] Cebral, J.R., *et al.*, Computational fluid dynamics modeling of intracranial aneurysms: qualitative comparison with cerebral angiography. *Acad Radiol*, 2007. 14(7): p. 804-13.